Validating models of channel flow, ductile extrusion and exhumation – The Greater Himalayan Sequence, Annapurna Massif

Andrew John Parsons

Submitted in accordance with the requirements for the degree of Doctor of Philosophy

The University of Leeds

School of Earth and Environment

April, 2015

The candidate confirms that the work submitted is his/her own, except where work which has formed part of jointly-authored publications has been included. The contribution of the candidate and the other authors to this work has been explicitly indicated below. The candidate confirms that appropriate credit has been given within the thesis where reference has been made to the work of others.

Chapter 2 and 4 contain research from the following jointly-authored publications.

Parsons, A. J. *et al.* 2014. Geology of the Dhaulagiri-Annapurna-Manaslu Himalaya, Western Region, Nepal. 1:200,000. *Journal of Maps*, 1-11. DOI: 10.1080/17445647.2014.984784

All work included within the thesis is directly attributable to the candidate.

This copy has been supplied on the understanding that it is copyright material and that no quotation from the thesis may be published without proper acknowledgement.

The right of Andrew John Parsons to be identified as Author of this work has been asserted by him in accordance with the Copyright, Designs and Patents Act 1988.

© 2015 The University of Leeds and Andrew John Parsons

Acknowledgements

This work would not have been possible without the guidance and supervision given by Richard Phillips and Geoff Lloyd. Thank you both for seeing the potential in me and giving me the opportunity to pursue my interests. I am very grateful for your encouragement and support and I could not have completed this research without it.

Thank you to my external supervisors, Rick Law and Mike Searle. Your knowledge and expertise have been invaluable and this project would not have been possible without your input. Thank you also for the excellent company on fieldwork and at conferences. I also thank Dave Wallis for always being ready to answer my questions and for supplying a constant source of inspiration and enthusiasm towards my work.

Thank you to Eric Ferré for inviting me to the U.S. and taking the time to teach me the dark art of rock magnetism. Thank you to Gerry Heij and Amanda DeRienzo for your kind and generous hospitality during my time in Illinois. To my good friend, Jarek Trela and your family – thank you for my first proper thanksgiving (!) and for all the good times spent (and still to be had) across the U.S.

I am grateful to Richard Walshaw for his guidance and patience, whilst training and assisting me on the electron microscope and microprobe and to Harri Wyn-Williams for all the time spent preparing my samples. Dave Mainprice is thanked for the training and assistance provided for the use of MTEX. Thanks must also be given for the outstanding support provided by Suka Ghale, Basan Sherpa and all of the Nepalese porters who assisted on field work. Thank you all for guiding me around your beautiful country and inviting me into your homes.

Thank you to all my friends, old and new, for all the good times had and support given and for making my time in Leeds and 8.152 (the best office in Leeds) the most memorable and enjoyable experience possible. Finally, thank you to my family for helping me pursue and achieve my goals and for the unfailing encouragement and support you have given throughout my studies.

- ABSTRACT -

Himalayan orogenesis is commonly explained with models of channel flow, in which the metamorphic core, referred to as the Greater Himalayan Sequence (GHS), forms a partially molten, rheologically weak mid-crustal flow. Geochronological and thermobarometric studies from the Himalaya provide support for the channel flow model, however, strain-related model predictions are unresolved and the model remains controversial. Additionally, wedge-extrusion, underplating / thrust-stacking and tectonic wedging models are favoured by many as alternative explanations for the formation of the Himalaya.

In this thesis, strain-related predictions of the channel flow model for Himalayan orogenesis are tested with field-based structural studies together with laboratory-based microstructural and magnetic fabric analyses. Orogen-perpendicular transects along the Modi Khola and Kali Gandaki valleys in the Annapurna-Dhaulagiri Himalaya of central Nepal were chosen for study. Samples were collected from the GHS and bounding units for crystallographic preferred orientation (CPO) and anisotropy of magnetic susceptibility analyses (AMS). Both techniques were used to quantify deformation fabric strength, which provides a proxy for relative strain magnitude. These data, combined with geochronological and thermobarometric constraints, reveals the kinematic evolution of the GHS in the Annapurna-Dhaulagiri Himalaya. These data can be directly compared to predictions implied by the channel flow model in order to assess its validity.

The results support the channel flow model as a viable explanation of the mid-crustal evolution of the GHS. However, lower temperature deformation indicates that exhumation of the GHS was facilitated through wedge-extrusion and thrust-stacking. The development of the Himalayan orogen in the Annapurna-Dhaulagiri region is best explained by models that allow channel flow, wedge-extrusion and thrust-staking to occur in a single orogen. Similar ‘composite models’ for Himalayan orogenesis have been proposed recently by other authors and reflect a growing understanding of how rheological controls on orogenesis can vary both spatially and temporarily.

Table of Contents

List of Tables

List of Figures

Chapter 3

Appendix

Chapter 4

Appendix

Chapter 5

Chapter 6

Chapter 7

Supplementary Data CD Contents

CHAPTER 2

- CHAPTER 2 - Parsons et al. 2014 Article.pdf
- CHAPTER 2 - Parsons et al. 2014 MAP.pdf
- CHAPTER 2 - Field & Sample Data.xlsx

CHAPTER 3

- Garnet-Biotite Thermometry
  - Sample Images
    - P12055
      - P12055.pdf
      - P140314_P12055_2.tif
    - P12058
      - P12058.pdf
      - P170314_P12058_BSE_2.tif
    - P12060
      - P12060.pdf
      - P180314_P12060_BSE.tif
  - Biotite Probe Data (unprocessed).xlsx
  - Garnet Probe Data (unprocessed).xlsx
- Zr in Ti Thermometry
  - P12053
    - P12053.pdf
    - P12053_BSE.png
    - P12053_GRAINS.pdf
    - Plus individual titanite grain images
  - P12054
    - P12054.pdf
    - P12054_BSE.png

        - P12054_GRAINS.pdf
        - Plus individual titanite grain images
    - P13031
        - P13031.pdf
        - P13031_BSE_2.png
        - P13031_GRAINS.pdf
        - Plus individual titanite grain images
    - P13032
        - P13032.pdf
        - P13032_BSE.png
        - P13032_GRAINS.pdf
        - Plus individual titanite grain images
    - ZR in Ti (unprocessed).xlsx

CHAPTER 4

- CHAPTER 4 - Complete AMS dataset.xlsx
- CHAPTER 4 - Hysteresis Data 2012.xlsx
- CHAPTER 4 - Hysteresis Data 2013.xlsx

CHAPTER 5

- CHAPTER 5 - AMS & CPO Strain Proxy values.xlsx

List of Abbreviations

AD	Annapurna Detachment
Amp	Amphibole
AMS	Anisotropy of Magnetic Susceptibility
An	Anorthite
And	Andesine
BLG	Grain Boundary Bulging dynamic recrystallisation
BSE	Back Scattered Electron
Bt	Biotite
C	Strength Parameter
Cal	Calcite
CBS	Chess Board Subgrains
Chl	Chlorite
Clz	Clinozoisite
CPO	Crystallographic Preferred Orientation
Cpx	Clinopyroxene
CT	Chomrong Thrust
DD	Deurali Detachment
Dol	Dolomite
EBSD	Electron Back Scattered Diffraction
EDS	Energy Dispersive Spectroscopy
F	Fold generation
FeOx	Iron Oxide
GBAR	Grain Boundary Area Reduction
FORC	First Order Reversal Curve
Fsp	Feldspar
GBM	Grain Boundary Migration dynamic recrystallisation
GCT	Great Counter Thrust
GHS	Greater Himalayan Sequence
Grt	Garnet
I	Intensity
Ilm	Ilmenite
ITS	Indus-Tsangpo Suture
IYSZ	Indus-Yarlung Suture Zone
J	J-index
KG	Kali Gandaki
Ksp	K-Feldspar
KSZ	Kalopani Shear Zone
Ky	Kyanite
L	Lineation generation
LGHS	Lower Greater Himalayan Sequence
LHD	Lesser Himalayan Duplex
LHS	Lesser Himalayan Sequence
LVZ	Low Velocity Zone
M	Misorientation index
m.u.d.	Multiples of Uniform Distribution
MBT	Main Boundary Thrust

MCT	Main Central Thrust
MCTZ	Main Central Thrust Zone
MD	Machapuchare Detachment
MD	Multidomain
MFT	Main Frontal Thrust
MHT	Main Himalayan Thrust
MK	Modi Khola
MKSZ	Modi Khola Shear Zone
Msc	Muscovite
MSD	Magnetostatic Single Domain
MT	Munsiari Thrust
Myr	Million years
NHA	North Himalayan Antiform
ODF	Orientation Distribution Function
Olg	Oligoclase
PF	Pole Figure
PGR	Point-Girdle-Random index
Phl	Phlogopite
Plg	Plagioclase
Py	Pyrite
Pyh	Pyrrhotite
PSD	Pseudo Single Domain
PT	Pressure-Temperature
PTt	Pressure-Temperature-time
Qtz	Quartz
R	Random (of PGR index)
RSCM	Raman Spectroscopy of Carbonaceous Material
RSM	Relative Strain Magnitude
Rt	Rutile
S	Schistosity generation
Scp	Scapolite
SD	Single Domain
SEM	Scanning Electron Microscope
SF	Smoothing Factor
SGR	Subgrain Rotation dynamic recrystallisation
SI	Système International
SIA	Superstructure-Infrastructure Association
Sil	Sillimanite
SP	Superparamagnetic
SPO	Shape Preferred Orientation
STD	South Tibetan Detachment
STDS	South Tibetan Detachment System
SZ	Subhimalayan Zone
THS	Tethyan Himalayan Sequence
Tt	Titanite
UGHS	Upper Greater Himalayan Sequence
UMM	Upper Mustang Massif
USD	Uniaxial Single Domain
U-stage	Universal-stage
VPSC	Visco-Plastic Self Consistent (modelling)
WNFS	Western Nepal Fault System
YS	Yarlung Suture

- CHAPTER 1 -

VALIDATING MODELS OF CHANNEL FLOW, EXTRUSION AND EXHUMATION FOR THE HIMALAYAN OROGEN: OVERVIEW AND RATIONAL

1.1. Introduction

The Himalayan orogen is frequently cited as a unique natural laboratory for studying geological processes at a wide range of spatial and temporal scales. However, the tectonic evolution of the Himalayan-Tibetan orogenic system remains disputed and continues to provide new insights into the crustal processes that have shaped past and present continental collision zones. The kinematic evolution of the metamorphic core of the Himalayan orogen, referred to as the Greater Himalayan Sequence (GHS – Figure 1.1), is the central focus of all models of Himalayan orogenesis (e.g. Grujic *et al.*, 1996; Beaumont *et al.*, 2001; Bollinger *et al.*, 2006; Robinson *et al.*, 2006; Searle *et al.*, 2006; Kohn, 2008; Mukherjee, 2013a; He *et al.*, 2014; Montomoli *et al.*, 2014). Understanding the temporal and spatial distribution of strain across the GHS is paramount to validation of these models (e.g. Grujic *et al.*, 1996; Grasemann *et al.*, 1999; Jessup *et al.*, 2006; Larson & Godin, 2009; Mukherjee & Koyi, 2010; Law *et al.*, 2011; Kellett & Grujic, 2012; Law *et al.*, 2013).

The aim of this thesis is to test the validity of models for Himalayan orogenesis through quantified structural and microstructural analysis of the GHS, with a specific focus on the channel flow model for the Himalayan orogen (e.g. Beaumont *et al.*, 2001; Godin *et al.*, 2006; Searle *et al.*, 2006). This model assumes that the GHS represents a rheologically weak, partially molten, mid-crustal channel that flowed laterally southwards, due to lateral pressure gradients produced by the overburden of the thickened Tibetan Plateau (Beaumont *et al.*, 2001; Searle *et al.*, 2011). The channel flow model is based upon and supported by both geological and geophysical observations (Searle & Rex, 1989; Nelson *et al.*, 1996; Grujic *et al.*, 2002; Rapine *et al.*, 2003; Searle *et al.*, 2003; Unsworth *et al.*, 2005; Godin *et al.*, 2006; Hollister & Grujic, 2006; Klemperer, 2006; Searle *et al.*, 2006; Larson & Godin, 2009; Rippe & Unsworth, 2010; Cottle *et al.*, 2011; Law *et al.*, 2011; Kellett & Grujic, 2012; Law *et al.*, 2013; Mukherjee, 2013a; Rolfo *et al.*, 2014) and has been tested numerically by a series of thermo-mechanical models (Beaumont *et al.*, 2001; 2004; Jamieson *et al.*, 2004; 2006; Jamieson & Beaumont, 2013). However, the strain and deformation-related predictions made by the channel flow model are yet to be fully tested (e.g. Grujic *et al.*, 1996; Grasemann *et al.*, 1999; Williams *et al.*, 2006; Larson & Godin, 2009; Law *et al.*, 2013) and alternative models of Himalayan orogenesis are still favoured by many (e.g. Bollinger *et al.*, 2006; Robinson *et al.*, 2006; Kohn, 2008; Webb

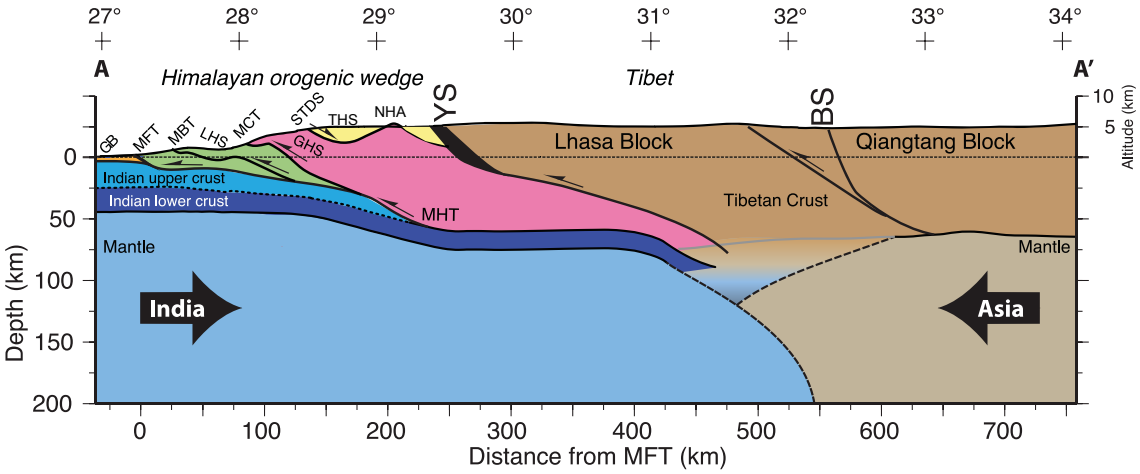

Figure 1.1. Cross sectional architecture of the Himalayan-Tibetan orogenic system. After Godin & Harris (2014). BS, Bagong Suture; GB, Ganga basin; GHS, Greater Himalayan sequence; LHS, Lesser Himalayan sequence; MBT, Main Boundary thrust; MCT, Main Central thrust; MFT, Main Frontal thrust; MHT, Main Himalayan thrust; NHA, North Himalayan Antiform; STDS, South Tibetan detachment system; THS, Tethyan Himalayan sequence; YS, Yarlung(-Tsangpo) Suture.

et al., 2011b; He *et al.*, 2014; Montomoli *et al.*, 2014).

In this chapter, the channel flow model is presented, alongside current alternative models. The fundamental geological requirements for model validation are then outlined with a list of criteria used to test the channel flow model. Finally, a means to test the validity of these models is proposed and the structure and content of this thesis is described.

1.2. Tectonic models of Himalayan orogenesis

Understanding the kinematic evolution of the GHS represents the central focus of all models of Himalayan orogenesis and remains a highly debated topic (e.g. He *et al.*, 2014; Larson & Cottle, 2014; Montomoli *et al.*, 2014; Robinson & Martin, 2014). Before any model can be considered plausible, it must first demonstrate that it is consistent with existing data sets and is compatible with well-documented geological features recorded across the orogen. Of most importance for the Himalaya, are working models consistent with: (*a*) the inverted metamorphic sequence at the base of the GHS; (*b*) coeval motion on the bounding shear zones of the GHS; and (*c*) well-constrained thermobarometric and geochronological data for partial melting, prograde and retrograde metamorphism, exhumation and erosion (e.g. Le Fort, 1975; Vannay & Hodges, 1996; Guillot *et al.*, 1999; Godin *et al.*, 2001; White *et al.*, 2002; Garzione *et al.*, 2003; Searle *et al.*, 2003; Harris *et al.*, 2004; Godin *et al.*, 2006; Blythe *et al.*, 2007; Jessup *et al.*, 2008; Kohn, 2008; Imayama *et al.*, 2010; Streule *et al.*, 2010a; Corrie & Kohn, 2011; Nadin & Martin, 2012; Carosi *et al.*, 2014; Kohn, 2014; Larson & Cottle, 2014; Martin *et al.*, 2014; Larson & Cottle, 2015). The persistence of these criteria has

led current models for development of the Himalayan orogen to fall into one of four general classes of tectonic models (Figure 1.2) : (*1*) Channel flow (e.g. Beaumont *et al.*, 2001; Grujic *et al.*, 2002; Searle *et al.*, 2003; Beaumont *et al.*, 2004; Jamieson *et al.*, 2004; Jain *et al.*, 2005; Grujic, 2006; Jamieson *et al.*, 2006; Searle *et al.*, 2006; Jamieson & Beaumont, 2013; Mukherjee, 2013a); (*2*) Wedge extrusion (Burchfiel & Royden, 1985; Burchfiel *et al.*, 1992; Hodges *et al.*, 1993; Hodges *et al.*, 1998; Grasemann *et al.*, 1999); (*3*) Duplexing/underplating (e.g. Robinson *et al.*, 2006; Kohn, 2008; Carosi *et al.*, 2010; Corrie & Kohn, 2011; Montomoli *et al.*, 2014; Robinson & Martin, 2014); and (*4*) Tectonic wedging (Yin, 2006; Webb *et al.*, 2007; Webb *et al.*, 2011a; Webb *et al.*, 2013; He *et al.*, 2014). In some cases, proposed models contain elements of two or more of these four classes (e.g. Larson *et al.*, 2010; Spencer *et al.*, 2012; Jamieson & Beaumont, 2013; Mukherjee, 2013a; Wang *et al.*, 2013; He *et al.*, 2014; Larson & Cottle, 2014).

Whilst the main focus of this thesis is to test the validity of channel flow models, in doing so, alternative models also need to be considered. The four model end-members are outlined below and a detailed introduction is given to the channel flow model. A critical evaluation of these models is presented in Chapter 7, following the presentation and discussion of new research amassed in this thesis (Chapters 2-6).

1.3. Channel flow model for Himalayan orogenesis

The fundamental physics behind the channel flow model (Figure 1.2a) is derived from basic concepts of fluid mechanics that describe the movement of a viscous fluid between two rigid plates (Turcotte & Schubert, 2002). Channel flow is driven by a horizontal pressure gradient and/or shearing related to motion of the channel walls and can be defined by a specific velocity structure (Figure 1.3). In geodynamics, channel flow concepts have been used to explain a number of geological processes including asthenospheric counter flow, lower-crustal channels, intra-crustal channels, subduction channels and salt tectonics (Godin *et al.*, 2006).

Channel flow models for the Himalayan orogen assumes that the GHS forms an exhumed portion of a mid-crustal channel flow that developed beneath the Himalaya and Tibetan Plateau (Beaumont *et al.*, 2001; Godin *et al.*, 2006; Grujic, 2006; Harris, 2007). Following initial collision between India and Eurasia, crustal thickening and heating was followed by widespread partial melting at mid-crustal levels, resulting in the development of a weak, low viscosity channel located between rigid upper and lower crust (Beaumont *et al.*, 2001; Godin *et al.*, 2006). Below a threshold viscosity, southwards return-flow of the channel initiated. This flow was driven by a horizontal

(*a*) CHANNEL FLOW

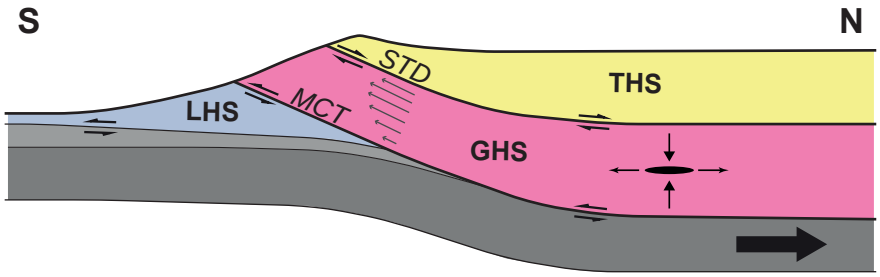

(*b*) WEDGE EXTRUSION

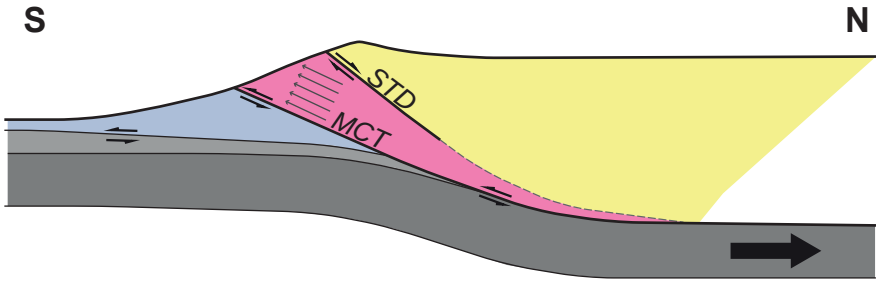

(*c*) DUPLEX (*Single Thrust Sheet*)

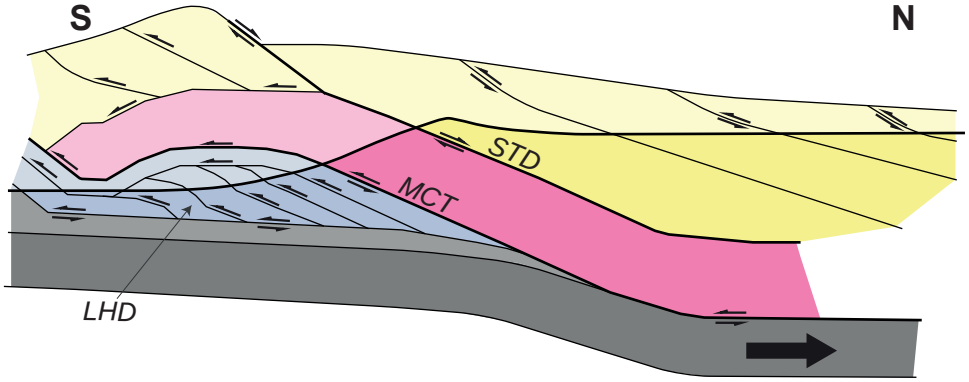

(*d*) DUPLEX/UNDERPLATING (*Internal Thrusting*)

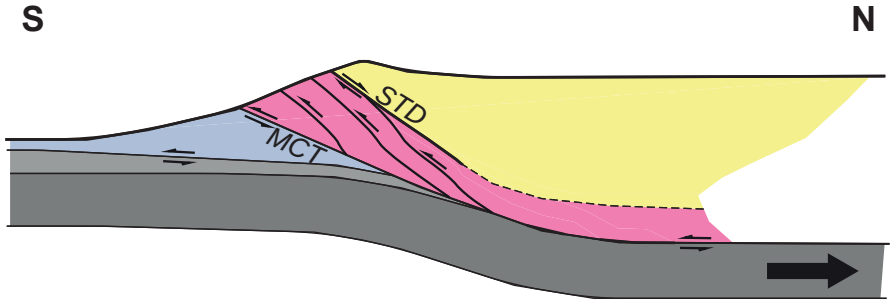

(*e*) TECTONIC WEDGING

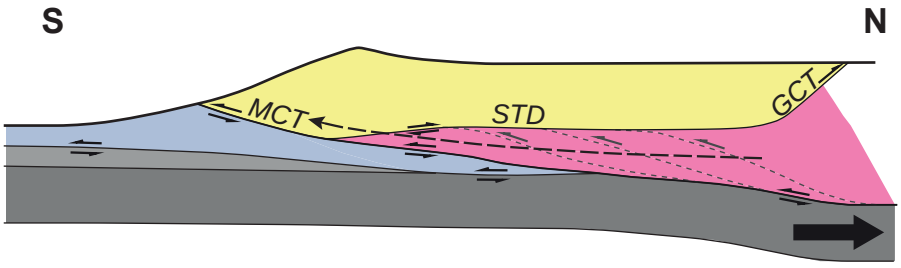

Figure 1.2 Models of Himalayan orogenesis

pressure gradient produced by the relative topographic elevations and crustal thicknesses of the Tibetan plateau and Indian continent and from shear stresses due to the northwards underthrusting of the lower Indian continental crust (Beaumont *et al.*, 2001; Beaumont *et al.*, 2004; Grujic, 2006). Uplift and exhumation of the channel was facilitated by coeval shearing on upper and lower bounding brittle-ductile shear zones and driven by focused erosion along the Himalayan front and the underthrusting Indian lower crust (Beaumont *et al.*, 2001; Godin *et al.*, 2006; Grujic, 2006). Relatively low viscosities were maintained during exhumation due to continued partial melting (Harris & Massey, 1994; Streule *et al.*, 2010a; Jamieson *et al.*, 2011; Searle, 2013).

Two scenarios are predicted for exhumation of the channel: (*1*) When erosion, exhumation and extrusion rates are coupled, an '*active channel*' may be exhumed (Beaumont *et al.*, 2001; Godin *et al.*, 2006; Grujic, 2006). In such a situation, exhumation is driven in part by the same lateral pressure gradient driving mid-crustal flow and the channel continues to deform internally as it exhumes and denudes at the topographic surface (Beaumont *et al.*, 2001; Godin *et al.*, 2006; Grujic, 2006). (*2*) Alternatively, when extrusion rates exceed exhumation and erosion rates, the channel cools and strengthens at depth and is exhumed as a rigid '*channel plug*' (also refered to as a palaeo-channel; Beaumont *et al.*, 2004; Godin *et al.*, 2006; Grujic, 2006). Some authors predict that this second scenario may be more likely, due to the effects of strain localisation and an increase in viscosity at lower temperatures (Godin *et al.*, 2006; Grujic, 2006). It has been noted that the kinematics of this late stage channel plug exhumation may be more akin to models of wedge extrusion (*see below*) (Grujic, 2006). During extrusion and exhumation, the inverted metamorphic sequence at the base of the GHS is produced, either by recumbent folding of isograds during extrusion of the channel through a fixed thermal field (Searle & Rex, 1989; Searle *et al.*, 1999; Searle *et al.*, 2008), or though differential syn-metamorphic shearing within the GHS,

---

Figure 1.2. Models of Himalayan orogenesis. Schematic cross sections of the Himalaya (not to scale) showing different end-member tectonic models. All cross sections follow same key; *Yellow – THS; Purple – GHS; Blue – LHS; Light Grey – Indian Upper crust; Dark Grey – Indian Lower Crust.* Thick black arrow shows northwards motion of Indian Lower Crust. (*a*) Channel flow – grey arrows in GHS represent velocity relative to the down going slab. Black arrows and ellipse show vertical shortening + horizontal stretching of GHS. (*b*) Wedge extrusion - grey arrows in GHS represent velocity of a rigid wedge relative to the down going slab. Dashed line of STD reflects uncertainty of structure at depth associated with model (e.g. Burchfield *et al.* 1992). (*c*) Duplex – GHS deforms as a single thrust sheet within a duplex. *LHD – Lesser Himalayan Duplex.* Modified from Robinson *et al.,* 2006. (*d*) Duplex/Underplating – GHS deforms internally as a thrust stack. Dashed line of STD reflects structural uncertainty at depth associated with model. (*e*) Tectonic wedging – Wedge may form a thrust stack (e.g. grey dashed lines – Webb *et al.* 2013). Tectonic wedging occurs at depth and does not involve exhumation. Dashed black arrow shows exhumation path of wedge during subsequent duplexing of LHS. *GCT – Great Counter Thrust.* Modified from He *et al.,* 2014.

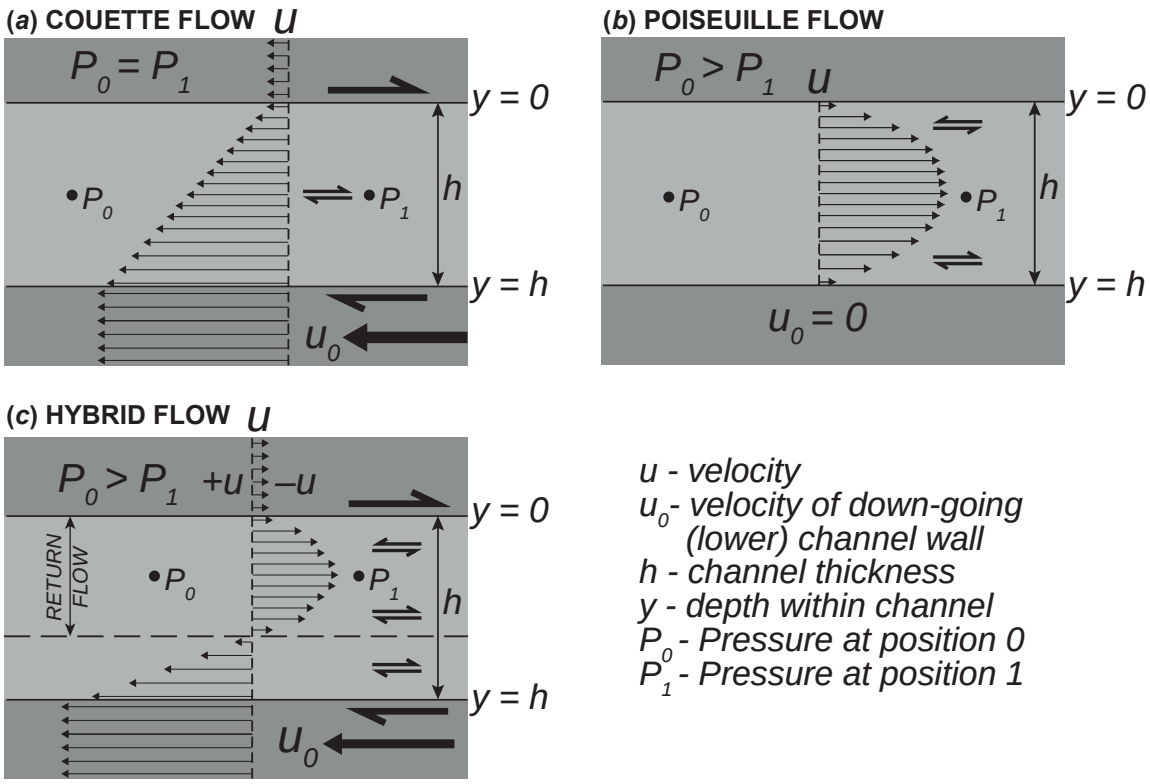

Figure 1.3. 1-Dimensional channel flow velocity profiles. After Grujic 2006. All models follow same key, displayed in figure. Channel defined by light grey rectangle. Rigid channel walls defined by dark grey rectangles. No slip boundary conditions apply (see text for discussion) (*a*) Couette flow – due to dextral shear between channel walls. Pressure gradient between P_0 and P_1 = 0. (*b*) Poiseuille flow – due to positive pressure gradient between P_0 and P_1. Channel walls are stationary. (*c*) Hybrid flow. Due to combined effects of dextral shear between channel walls plus a positive pressure gradient between P_0 and P_1. Return flow occurs in the opposite direction to the down-going (bottom) channel wall.

translating material from hotter hinterland crustal regions southwards over cooler foreland material (Grujic *et al.*, 1996; Jamieson *et al.*, 2004; Jamieson & Beaumont, 2013).

The channel flow model places a crucial dependence on widespread partial melting of the mid crust for the reduction in viscosity required for crustal flow (Beaumont *et al.*, 2001; Beaumont *et al.*, 2004; Grujic, 2006; Jamieson *et al.*, 2011). Leucogranites in the GHS, which are found along the entire central-eastern sections of the Himalaya, are most commonly the product of fluid-absent muscovite dehydration and at higher temperatures, biotite dehydration reactions (Harris & Massey, 1994; Harris *et al.*, 1995; Streule *et al.*, 2010a; Searle, 2013). The initial heat source for melting is likely to be a combination of radiogenic heating and thermal relaxation during crustal thickening (Zhang *et al.*, 2004; Streule *et al.*, 2010a). Continued melting of the GHS during extrusion and exhumation is suggested to have been driven by decompression melting (Harris & Massey, 1994; Streule *et al.*, 2010a). It has been noted that Himalayan

granites are significantly enriched in uranium and contain highly radiogenic Pb isotopes that point to a source rock with high concentration of Th and U (Searle *et al.*, 2010).

Experimental deformation of rocks shows that an increase in melt fraction from 0 to 0.07 (i.e. 7%) is accompanied by a ~90% reduction in strength (Rosenberg & Handy, 2005). An intermediate strength drop is also recorded between a melt fraction of 0.2 and 0.6 (Rosenberg & Handy, 2005). Similar observations are recorded by deformation experiments of partially molten synthetic granite that produce flow laws with a power law exponent of 1.8 (Rutter *et al.*, 2006). Consequently, as long as melt migration and melt production are balanced, only small amounts of partial melting are required to reduce the viscosity of large portions of the crust (Rosenberg *et al.*, 2007; Jamieson *et al.*, 2011).

1.3.1. Geophysical observations

The sub-surface structure of the Himalayan-Tibetan orogenic system has been interpreted from a variety of geophysical data, including seismic reflection surveys (e.g. Nelson *et al.*, 1996; Schulte-Pelkum *et al.*, 2005; Nábelek *et al.*, 2009; Zhang & Klemperer, 2010), seismic tomography (e.g. Shapiro *et al.*, 2004; Guo *et al.*, 2009; Huang *et al.*, 2009), magnetotelluric surveys (e.g. Wei *et al.*, 2001; Unsworth *et al.*, 2005) and gravity anomaly surveys (e.g. Jin *et al.*, 1996; Cattin *et al.*, 2001).

One of the motivations behind the development of the channel flow model was the results of the INDEPTH geophysical survey (Figure 1.4) (Nelson *et al.*, 1996). The INDEPTH seismic profile identified a distinct ‘bright spot’, characteristic of a fluid horizon, north of the Indus suture zone between 15 and 20 km depth (Brown *et al.*, 1996; Nelson *et al.*, 1996). This ‘bright spot’ is coincident with a low seismic velocity zone of similar dimensions and lateral extent, as well as a high conductivity layer identified by magnetotelluric data that persists up to 70 km south and 50-100 km north of the Indus suture zone (Figure 1.4) (Nelson *et al.*, 1996; Wei *et al.*, 2001; Unsworth *et al.*, 2005). The coincidence of these observations, combined with more recent geophysical surveys, has led many authors to postulate the existence of a mid-crustal partially molten low viscosity layer beneath the Tibetan Plateau, in which the ‘bright spot’ and low velocity zone represent pooling of magma and/or aqueous fluid (Nelson *et al.*, 1996; Unsworth *et al.*, 2005; Hodges, 2006; Searle *et al.*, 2006; Guo *et al.*, 2009; Huang *et al.*, 2009; Zhang & Klemperer, 2010; 2011). It is postulated that this partially molten layer connects to the GHS at depth and that the Main Central Thrust (MCT) and South Tibetan Detachment (STD), which bound the GHS above and below (Figure 1.1), connect to the upper and lower boundaries of the low velocity zone beneath the Himalaya (Figure 1.4) (Makovsky *et al.*, 1996; Nelson *et al.*, 1996; Hauck *et al.*, 1998;

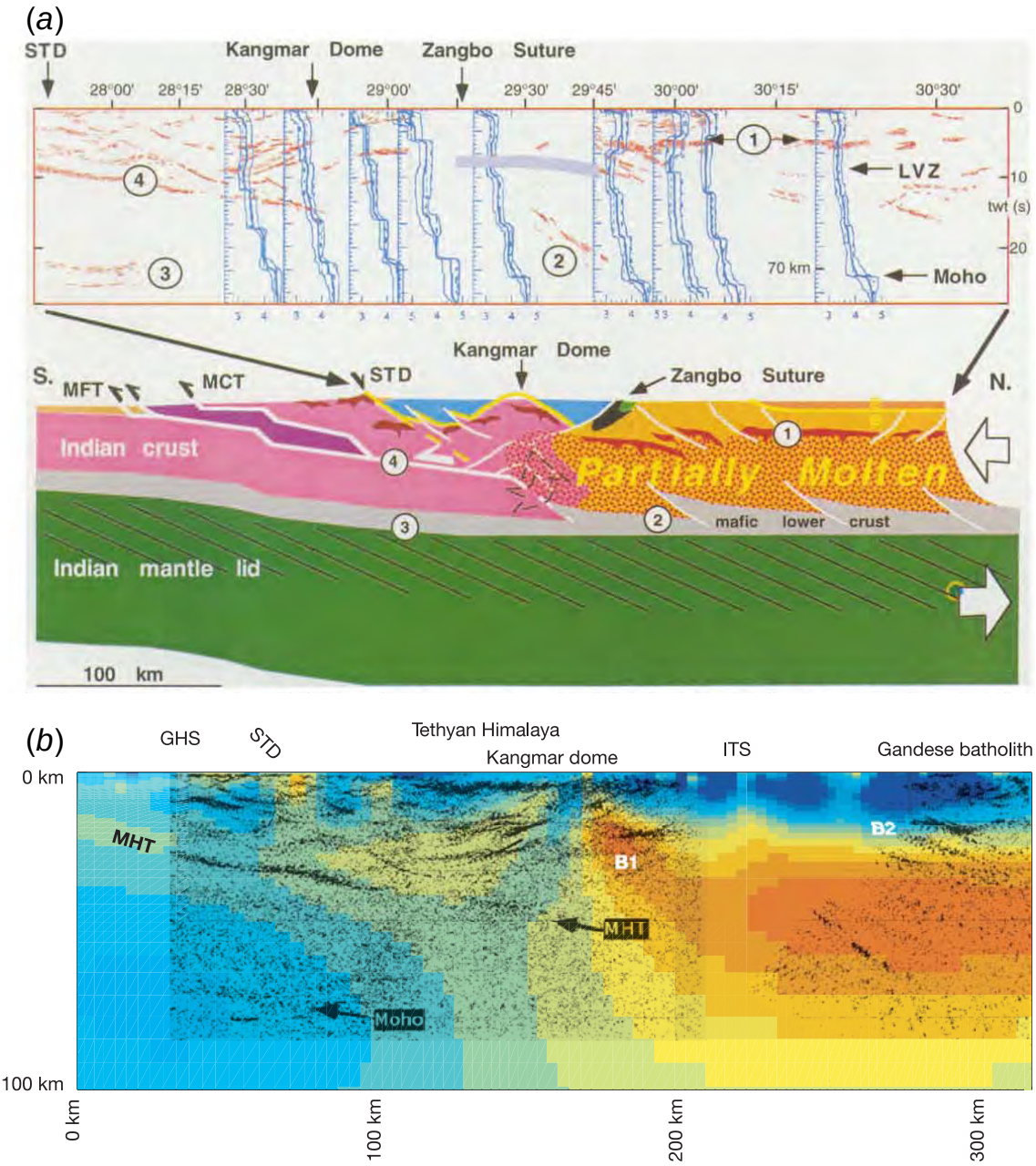

Figure 1.4 INDEPTH profile results and interpretations.

Unsworth *et al.*, 2005; Guo *et al.*, 2009; Zhang & Klemperer, 2010).

Current research continues to consider the lithospheric structure and rheology of the Himalayan-Tibetan orogenic system and whether a partially molten mid crust presently exists beneath the Tibetan Plateau (e.g. Guo *et al.*, 2009; Huang *et al.*, 2009; Nábelek *et al.*, 2009; Rippe & Unsworth, 2010; Yang *et al.*, 2012; Hacker *et al.*, 2014; Li *et al.*, 2014). Whilst these studies provide useful insight into how such processes may occur, they do not necessarily relate to the mid-crustal processes responsible for the kinematic evolution of the GHS, which took place during Eocene to Miocene times (e.g. Godin *et al.*, 2006; Jessup *et al.*, 2008; Kohn, 2008; Corrie & Kohn, 2011; Kohn & Corrie, 2011). Consequently, the present day structure and deformation of the Tibetan mid crust is not discussed further.

1.3.2. Thermo-mechanical models of channel flow

Many early geological and geophysical observations suggested that the GHS may have flowed internally as a large partially molten mid-crustal shear zone (e.g. Searle & Rex, 1989; Burchfiel *et al.*, 1992; Grujic *et al.*, 1996; Nelson *et al.*, 1996; Grasemann *et al.*, 1999; Searle *et al.*, 1999). More recently, thermo-mechanical finite element simulations of channel flow have greatly advanced our understanding of the mechanisms by which channel flow may occur within the Himalayan-Tibetan orogenic system (Beaumont *et al.*, 2001; Jamieson *et al.*, 2002; Beaumont *et al.*, 2004; Jamieson *et al.*, 2004; Beaumont *et al.*, 2006; Culshaw *et al.*, 2006; Jamieson *et al.*, 2006; Jamieson & Beaumont, 2011; Jamieson & Beaumont, 2013).

The finite element models have a 2-dimensional vertical plane-strain design that simulates lithospheric plate motion within a subduction zone (Beaumont *et al.*, 2001; Jamieson *et al.*, 2002; Beaumont *et al.*, 2004). Plate motion is controlled by a prescribed mantle velocity, whilst the model crust is allowed to thicken and deform during collision, with a temperature dependant viscous power-law creep rheology, based on experimentally derived flow laws of various geological materials (Beaumont *et al.*, 2004). A thermal model simulates diffusion, advection and radiogenic heat production and thermal and mechanical models are coupled such that both velocity and thermal fields evolve and change together during each simulation (Beaumont *et al.*, 2004). Additionally, these models include a surface denudation component that is sensitive to topographic slope and a prescribed climate function that simulates spatial

---

Figure 1.4. INDEPTH profile results and interpretations. (*a*) Results of the INDEPTH seismic survey (From Nelson *et al., 1996*). Top profile shows a composite section of the seismic reflection data (red) and the 1-D shear wave velocity profile (blue). The solid light blue rectangle represents the shear wave low velocity zone. The bottom profile shows the geological interpretation of the INDEPTH survey, with numbers 1-4 corresponding to important geological features. (1) 'Bright spot' beneath Tibetan Plateau at the top of the shear wave low velocity zone interpreted as pooling of magma at the top of a partially molten mid-crustal layer. (2) North dipping structures in the Indian lower crust. (3) The Moho at *ca.* 75 km depth beneath the Tethyan Himalaya. (4) The Main Himalayan Thrust displaces Indian mid-crust over Indian lower crust. The Main Himalayan Thrust appears to intersect the shear wave low velocity zone and is interpreted as the lower boundary to the mid-crustal partially molten layer (Nelson *et al.,* 1996). *LVZ, low velocity zone; MCT, Main Central Thrust; MFT, Main Frontal Thrust; STD, South Tibetan Detachment.* (*b*) Resistivity profile along the INDEPTH section (From Unsworth *et al.,* 2005). Warm colours (yellow-orange) = low resistivity, cool colours (blue) = high resistivity. The INDEPTH seismic reflection profile (black stipple) is overlain onto a magnetotelluric profile from the same line of section. The profile shows that the low resistivity regions are coincident with the seismic bright spots, B1 and B2, and that a low resistivity region also exists in the hangingwall of the Main Himalayan Thrust (Unsworth *et al.*, 2005). *GHS, Greater Himalayan Sequence; ITS, Indus-Tsangpo Suture; MHT, Main Himalayan Thrust; STD, South Tibetan Detachment.*

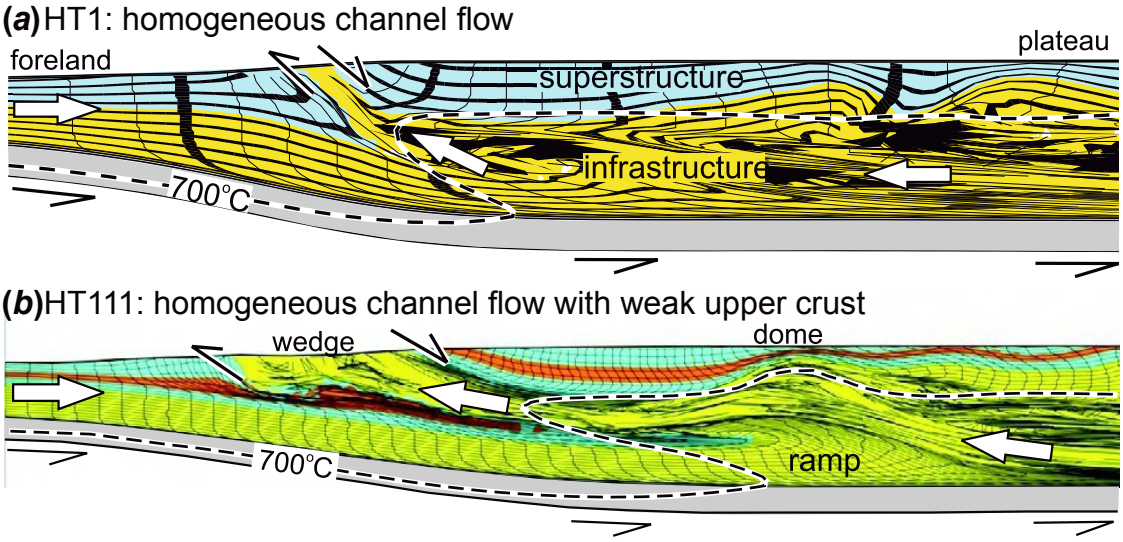

Figure 1.5. Thermo-mechanical channel flow models HT1 and HT 111. From Jamieson & Beaumont (2013). Both models show final model configuration of a deformed grid pattern. Colours represent crust with different rheological properties. 700 ^{o}C isotherm corresponds to the initiation of modelled melt weakening (*a*) Homogenous channel flow model HT1 (Beaumont *et al.*, 2001; Jamieson *et al.*, 2004) with coupled erosion and extrusion resulting in exhumation of an 'active channel'. (*b*) Homogeneous channel flow with a weak upper plate model HT111 (Jamieson *et al.*, 2006). Upper-crustal instability results in hinterland upper-crustal extension, channel upwelling and dome formation (Jamieson & Beaumont 2013).

and temporal variations in erosion rates (Beaumont *et al.*, 2004). Importantly, the model simulates the rheological effect of partial melting. Model elements at a temperature of ≤700 ^{o}C have a viscosity defined by a given flow law (~10^{20} – 10^{22} Pa s), whereas model elements at a temperature of ≥750 ^{o}C are given a 'Melt Weakening' viscosity of 10^{19} Pa s (Beaumont *et al.*, 2004). It is noted by the authors that this is a conservative estimate of the viscosity of partially molten rock (Beaumont *et al.*, 2004).

The finite element models demonstrate that following an 'incubation period' of 10-20 Myr, thermal relaxation due to crustal thickening, and radiogenic heat production should raise mid-crustal temperatures significantly (Beaumont *et al.*, 2001; Beaumont *et al.*, 2004). This prompts a reduction in viscosity from flow law values to 'Melt Weakening' values, which subsequently leads to lateral flow of a rheologically weak mid-crustal channel towards the margin of the thickened crust (Beaumont *et al.*, 2001; Beaumont *et al.*, 2004). Additionally, these models demonstrate that when rates of extrusion and erosion are balanced, the individual processes may become dynamically coupled, leading to the focused extrusion and exhumation of the mid-crustal channel at the margin of the thickened crust (Beaumont *et al.*, 2001; Beaumont *et al.*, 2004; Jamieson *et al.*, 2004; Jamieson & Beaumont, 2013).

Importantly, with an initial model set-up designed to reflect the Himalayan-Tibetan orogenic system (Model HT1 & HT111; Beaumont *et al.*, 2001; Beaumont *et al.*, 2004;

Jamieson *et al.*, 2004; Jamieson *et al.*, 2006), the final geometry produces many similarities to the salient geological features of the Himalaya and Tibet (Figure 1.5). By varying boundary conditions (e.g. channel thickness, erosion rates, upper-crustal rheology, convergence rates), the finite element models were able to recreate features such as: an inverted metamorphic sequence at the base of the GHS; coeval shearing on the MCT and STD; a hinterland plateau; gneissic domes; 'syntaxes' (e.g. Nanga Parbat); a foreland thrust belt; and out-of-sequence thrusting. Additionally, the particle pathways of model elements exposed at the topographic surface at the end of each simulation closely match thermobarometric and geochronological data sets produced along the length of the central-eastern Himalaya (Jamieson *et al.*, 2004; Jamieson *et al.*, 2006). This ability to numerically simulate geological features of the Himalaya based on variable rheological boundary conditions provides significant support to the validity of the channel flow model for the Himalayan orogen.

1.3.3. Strain & velocity profiles

The predicted strain and velocity profiles are perhaps the most indicative characteristics of channel flow that could be used to test the validity of such models. Two end-member velocity profiles are commonly recognised when describing flow of a viscous material between parallel channel walls (drawn relative to a stationary channel wall) (Turcotte & Schubert, 2002): (*1*) Couette flow; and (*2*) Poiseuille flow. Couette flow (Figure 1.3a) occurs in response to viscous drag forces produced by relative horizontal parallel motion of the channel walls (Turcotte & Schubert, 2002; Grujic, 2006). Under such circumstances, velocity is greatest adjacent to the moving channel wall and decreases to zero towards the stationary wall, (assuming no-slip boundary conditions – fluid in contact with a channel wall has the same velocity as the channel wall) (Turcotte & Schubert, 2002; Grujic, 2006). Couette flow of a linear-viscous material has a uniform strain rate (i.e. straight line velocity profile) and vorticity (i.e. ratio of simple shear to pure shear), dominated by non-coaxial deformation (Turcotte & Schubert, 2002; Grujic, 2006).

Poiseuille flow (Figure 1.3b) describes the flow of a viscous material between stationary channel walls and is controlled by an applied pressure gradient within the channel (Turcotte & Schubert, 2002; Grujic, 2006). Poiseuille flow produces a curved velocity profile with the largest velocity in the middle of the flow and the smallest velocity at the channel margins (Turcotte & Schubert, 2002; Grujic, 2006). Poiseuille flow of a linear-viscous material has a non-uniform strain rate and vorticity, with highest strain rates and vorticity at the channel margins and lowest strain rates and vorticity towards the channel centre (Turcotte & Schubert, 2002; Grujic, 2006). Additionally,

vorticity has opposite shear sense at the top and bottom of the channel (Turcotte & Schubert, 2002; Grujic, 2006).

The mode of flow is a function of the relative plate velocities, channel thickness, channel viscosity and horizontal pressure gradient (assuming uniform crustal densities) (Turcotte & Schubert, 2002; Beaumont *et al.*, 2004; Grujic, 2006; Mukherjee, 2014). Typically, high viscosity channels are dominated by Couette flow and channel material is under-plated on to the upper channel wall (Turcotte & Schubert, 2002; Grujic, 2006). Low viscosity channels are dominated by Poiseuille flow in the direction of the positive pressure gradient (Turcotte & Schubert, 2002; Grujic, 2006). Following a change in boundary conditions, a change in flow modes between Couette-dominated flow to Poiseuille-dominated flow (or vice-versa) may occur (Grujic, 2006).

Channel flow during formation of the Himalayan orogen is proposed to occur after a reduction in viscosity and a possible relaxation of the no-slip boundary conditions along the upper shear zone of the GHS, which led to a change from northwards Couette-dominated flow to southwards Poiseuille-dominated return-flow (Grujic *et al.*, 1996; Beaumont *et al.*, 2004; Grujic, 2006). Widespread partial melting is the mechanism proposed for the viscosity decrease (Beaumont *et al.*, 2001). As such, crustal flow associated with the channel flow model for Himalayan orogenesis is driven by opposed channel wall motion and pressure gradients and has a Hybrid velocity structure, (Figure 1.3c), representing a composite of both Couette and Poiseuille flow (Mancktelow, 1995; Grujic, 2006). For a linear-viscous fluid, the shape of the Hybrid velocity profile is indicative of the proportionality between shear driven and pressure gradient driven flow (Turcotte & Schubert, 2002; Grujic, 2006). For a non-Newtonian fluid with power law rheology, the shape of the velocity profile may also be temperature and/or stress dependent (Turcotte & Schubert, 2002). Thus, when considering channel flow of geological materials, any deviations from the model Hybrid velocity profile (Figure 1.3c) may provide information on the rheological properties of the channel (Grujic, 2006).

1.3.4. Caveats & outstanding issues

Despite the extensive geological and geophysical data that support channel flow during the Himalayan orogen, the models have a number of caveats. The thermo-mechanical models on which much of the theory is based do not model melt production directly and instead only simulate the rheological effects of partial melting with melt fractions of <10% (Jamieson *et al.*, 2011). Consequently, melt migration and concentration leading to development of large accumulations of magma are not considered (Jamieson *et al.*, 2011). Where large magma bodies form, buoyancy forces become significant and

vertical ascent of magma should follow to produce plutons and granite cored gneiss domes (Jamieson *et al.*, 2011). The effects of shear heating are also neglected by these models (Beaumont *et al.*, 2004), although some authors suggest that shear heating may be an important factor in the ductile evolution of the GHS (Mulchrone & Mukherjee, 2015).

The extent to which channel flow models are representative of the whole of the Himalaya has also been questioned (Godin *et al.*, 2006; Harris, 2007). The original thermo-mechanical channel flow model (Beaumont *et al.*, 2001) was based on data from the INDEPTH transect (Nelson *et al.*, 1996), which was conducted across the southern part of the Tibetan Plateau to north Sikkim. Whilst lithologies within the GHS are remarkably constant across the length of the Himalaya, the relative proportions of these lithologies do vary (e.g. Le Fort, 1975; Upreti, 1999; Yin, 2006). This is important as the thermo-mechanical models simplify the rheological properties of the model crust by applying either a flow law-derived viscosity or a '*Melt Weakening*' viscosity depending on the model crust temperature. In reality, the variable proportions of different lithologies in the GHS, some of which are less susceptible to partial melting than others (e.g. calc-silicate gneiss and orthogneiss; Godin *et al.*, 2006; Harris, 2007) are likely to produce orogen-parallel variation in viscosity. This may be reflected by variations in the PTt paths recorded from the GHS along the orogen (Kohn, 2014). Additionally, the thermo-mechanical channel flow models require a channel thickness of 10-20 km for crustal flow to be an effective form of extrusion (Beaumont *et al.*, 2004; Jamieson *et al.*, 2004; Godin *et al.*, 2006; Jamieson *et al.*, 2006). The thickness of the GHS varies along the length of the orogen and it remains unclear as to whether sections with a structural thickness of <10 km (e.g. the Annapurna region; Hodges *et al.*, 1996; Larson & Godin, 2009) are too thin to have flowed.

Another potential caveat in the channel flow model is the assumption of plane strain deformation (Beaumont *et al.*, 2004; Culshaw *et al.*, 2006; Jamieson & Beaumont, 2013). These 2-dimensional thermo-mechanical models cannot account for past and present orogen-parallel deformation recorded across the Himalaya (e.g., Brun *et al.*, 1985; Pêcher, 1991; Pêcher *et al.*, 1991; Gapais *et al.*, 1992; Guillot *et al.*, 1993; Scaillet *et al.*, 1995; Vannay & Steck, 1995; Coleman, 1996; Argles & Edwards, 2002; Hurtado, 2002; Webb *et al.*, 2007; Jessup & Cottle, 2010; Styron *et al.*, 2011; Xu *et al.*, 2013). The authors of the thermo-mechanical channel flow models acknowledge this and suggest that in nature, orogen-parallel flow of a mid-crustal channel may occur and could have significant effects on the kinematic evolution of the orogen (Culshaw *et al.*, 2006; Jamieson & Beaumont, 2013). These caveats highlight the limitations of current numerical simulations that typically require a degree of simplification of the natural

phenomena they are designed to simulate. Nevertheless, the models provide valuable insight into the rheological controls of orogenesis and suggest that under the right circumstances, mid-crustal channel flow is a likely response to widespread partial melting (Jamieson *et al.*, 2011; Jamieson & Beaumont, 2013). In order to properly evaluate the validity of the channel flow model, a set of criteria that can be tested against geological observations is required.

1.3.5. Criteria for channel flow

Based on the principles of mid-crustal channel flow outlined above, the following criteria are proposed as supporting evidence for channel flow processes during the formation of the Himalayan orogen (Mancktelow, 1995; Beaumont *et al.*, 2001; Beaumont *et al.*, 2004; Jamieson *et al.*, 2004; Godin *et al.*, 2006; Grujic, 2006; Jamieson *et al.*, 2006; Williams *et al.*, 2006; Harris, 2007).

1) High grade metamorphic rocks bound above and below by sub-parallel syn-metamorphic ductile shear zones with opposite shear senses that were active at the same time.
2) An inverted metamorphic profile at the base of the channel and a right-way-up metamorphic profile at the top of the channel.
3) Significant syn-tectonic partial melting capable of sustaining channel flow through a reduction in rock strength relative to stronger over- and underlying crustal layers.
4) Pervasive general shear throughout the channel with a concentration of deformation on the channel margins; deformation at the margins has a larger component of non-coaxial strain relative to deformation in the channel centre.
5) Hybrid velocity profiles indicative of combined northwards Couette flow (plate motion driven) and southwards Poiseuille flow (pressure gradient driven).
6) Kinematic inversion of the STDS relating to a switch from northwards Couette-flow to southwards Poiseuille–dominated return-flow.
7) Identification of the STDS as a stretching fault with a fixed hangingwall, separating an overlying low metamorphic grade *superstructure* with upright folds, thrust faults and steep foliation from an underlying high metamorphic grade *infrastructure* of horizontal shearing and recumbent folding produced during non-coaxial flow.
8) Progressive variations in metamorphic histories across the channel interior and metamorphic discontinuities across channel boundaries.

1.4. Alternative models of Himalayan orogenesis

In order to evaluate the validity of the channel flow model, alternative models for Himalayan orogenesis must also be considered. This is particularly important when such models are presented as evidence against the occurrence of channel flow (e.g. Robinson *et al.*, 2006; Webb *et al.*, 2007; Kohn, 2008; Montomoli *et al.*, 2014).

1.4.1. Wedge extrusion

Wedge extrusion models (Figure 1.2b) consider the GHS to be a northward-tapering wedge of extruding material, exhumed via normal and reverse sense motion on upper and lower bounding shear zones (e.g. Burchfiel & Royden, 1985; Burchfiel *et al.*, 1992; Hodges *et al.*, 1993; Hodges *et al.*, 1998; Dézes *et al.*, 1999). Most wedge extrusion models follow similar principles to the critical wedge concept (Platt, 1986), which proposes that exhumation and extrusion of a metamorphic core can become dynamically coupled with denudation in order to maintain a critically stable wedge. The earliest of these models (e.g. Burchfiel & Royden, 1985) suggest that extrusion of the GHS was driven by gravitational collapse and N-S extension of the upper shear zone (STDS) as a result of topographic instability (Royden & Burchfiel, 1987; Burchfiel *et al.*, 1992; Hodges *et al.*, 1998).

Some wedge models propose an alternation of activity between the upper and lower bounding shear zones in order to maintain a critically stable wedge (e.g. Hodges *et al.*, 1993; Hodges *et al.*, 1996). However, displacement on the STDS due to gravitational collapse is predicted to be on the order of 10's of km (Royden & Burchfiel, 1987; Hodges *et al.*, 1998; Dézes *et al.*, 1999), whereas, microstructural and thermobarometric studies suggest displacement on the STDS was on the order of 100-200 km (Searle *et al.*, 2003; Searle *et al.*, 2006). As such, wedge extrusion driven by gravitational collapse and crustal extension alone is considered improbable (Searle *et al.*, 2003; Searle, 2010; Law *et al.*, 2011). Alternatively, wedge extrusion may be driven by tectonic overpressure due to foreland converging bounding shear zones (Mancktelow, 1995), pressure gradients due to variations in crustal thickness, density or any combination of the three (Grujic, 2006). Exhumation and erosion of the wedge may be dynamically coupled (Hodges *et al.*, 1993; Chemenda *et al.*, 1995; Hodges *et al.*, 1996; Grujic, 2006).

Wedge extrusion models for the Himalayan orogen may be divided into two types: (*1*) ductile wedge extrusion; and (*2*) rigid wedge extrusion. Based on observations in the Bhutan Himalaya, the ductile wedge extrusion model assumes the GHS represents a zone of distributed general shear that deformed as a mid-crustal flow with the same or

similar strain and velocity profile to the hybrid flow model in Figure 1.3c (Grujic *et al.*, 1996; Grasemann *et al.*, 1999; Grasemann & Vannay, 1999). This model is a predecessor to the channel flow model and differs only in the geometric structure of the GHS (i.e. wedge vs channel). The main drawback of the model is that the proposed amounts of coaxial thinning of the wedge (Grujic *et al.*, 1996; Grasemann *et al.*, 1999) require a volume increase within the centre of the wedge (Grasemann *et al.*, 2006) to satisfy strain compatibility (Grasemann *et al.*, 1999). Whilst melt migration within the wedge may provide the necessary volume flux to satisfy these conditions, without the addition of material from a mid-crustal channel towards the hinterland, continued erosion and exhumation of the wedge can only lead to a net volume loss (Harris, 2007). As such the wedge geometry places limits on the extent of extrusion (Harris, 2007). More recent studies from Bhutan attribute the apparent wedge-morphology of the GHS to late stage out-of-sequence thrusting (Grujic *et al.*, 2002). Cross section restoration of these thrusts revealed a channel-like geometry with parallel sided boundaries and a minimum N-S transport-parallel length of 200 km (Grujic *et al.*, 2002). Based on these principles, the ductile wedge model as described by Grujic *et al.* (1996) should be considered as a variant of the channel flow model.

Rigid wedge models (Figure 1.2b) consider the GHS to have behaved as a relatively solid block during extrusion and exhumation with little or no internal deformation (Burchfiel & Royden, 1985; Hodges *et al.*, 1993; Chemenda *et al.*, 1995). Extrusion of the wedge is facilitated though motion on discrete bounding faults, which accommodate most or all of the strain (Chemenda *et al.*, 1995). Microstructural and metamorphic observations indicate that the GHS *is* internally deformed and that at least part of this deformation occurred synchronously with decompression melting (e.g. Grujic *et al.*, 1996; Jessup *et al.*, 2006; Searle *et al.*, 2006; Kellett *et al.*, 2010; Searle *et al.*, 2010; Cottle *et al.*, 2011). Consequently, rigid wedge extrusion cannot explain the entire kinematic evolution of the GHS. Whilst channel flow and rigid wedge models define opposing end members of strain distribution, the two models may co-exist in the same orogenic system (Godin *et al.*, 2006; Grujic, 2006). In such cases, the rigid wedge model may be used to explain the extrusion and exhumation of a channel plug that develops during cooling and crystallisation of an active channel (Beaumont *et al.*, 2001; Godin *et al.*, 2006; Grujic, 2006; Harris, 2007). Extrusion of the rigid plug is aided by dynamical coupling of mid-crustal flow, extrusion and erosion (Beaumont *et al.*, 2001; Godin *et al.*, 2006; Grujic, 2006; Harris, 2007). This poses a potential problem as the margins of a denuded channel plug are likely to preserve deformation relating to both channel flow and rigid wedge extrusion, or relating to rigid wedge extrusion only (Grujic, 2006).

1.4.2. Duplex / under-plating model

Models of duplexing or out-of-sequence thrusting are widely used to explain the development of the Himalaya since the late Miocene and largely involve deformation within the Himalayan foreland fold thrust belt (e.g. Paudel & Arita, 2000; Decelles *et al.*, 2001; Robinson *et al.*, 2003; Bollinger *et al.*, 2004; Pearson & Decelles, 2005). More recently, models of duplexing, under-plating and out-of-sequence thrusting have been used to explain earlier hinterland extrusion and exhumation of the GHS (Figure 1.2c,d) (Robinson *et al.*, 2006; Martin *et al.*, 2010; Corrie & Kohn, 2011; Montomoli *et al.*, 2014). These models propose that the GHS was exhumed and extruded during duplex development driven by development of a critical-tapered thrust wedge and deformed either as a single thrust sheet (Figure 1.2c) (Robinson *et al.*, 2006; Robinson, 2008) or as thrust stack internally dissected into several thrust slices (Figure 1.2d) (Carosi *et al.*, 2010; Martin *et al.*, 2010; Corrie & Kohn, 2011; Montomoli *et al.*, 2013; Khanal *et al.*, 2014). In the former situation (Figure 1.2c), it has also been suggested that faulting on the STDS occurred at least in part due to the southwards migration of active faulting within the duplex (England & Molnar, 1993; Robinson & Pearson, 2013). In the latter situation (Figure 1.2d), thrust stack development within the GHS took place as it extruded southwards in a similar manner to the wedge extrusion model, with each new thrust slice under-plating the last (Martin *et al.*, 2010; Corrie & Kohn, 2011; Larson & Cottle, 2014). Within these thrust stacks, the age and temperature of peak metamorphism decrease down section with distinct discontinuities in temperature and age occurring between slices (Corrie & Kohn, 2011; Larson & Cottle, 2014). Where identified, the timing of internal thrusting in the GHS relative to metamorphism varies from pre- and syn-peak metamorphic (e.g. Carosi *et al.*, 2010; Imayama *et al.*, 2012; Montomoli *et al.*, 2013; He *et al.*, 2014) to post-peak metamorphic (e.g. Vannay & Hodges, 1996; Grujic *et al.*, 2002; Wang *et al.*, 2013; Larson & Cottle, 2014). In the former, internal thrusting is usually in-sequence and facilitates exhumation-related metamorphism (e.g. Carosi *et al.*, 2010). In the latter, internal thrusting is usually out-of-sequence and deforms and advects earlier formed metamorphic isograds (e.g. Vannay & Hodges, 1996).

Internal thrust stacking of the GHS (Figure 1.2d) requires a localisation of strain between thrust slices in order to produce the observed discontinuities in age and metamorphic temperature within the GHS (e.g. Carosi *et al.*, 2010; Larson & Cottle, 2014). In general, thrust stacking models do not consider the effects of thinning and stretching to play an important role during extrusion, and imply a horizontal, rather than vertical, shortening direction. Additionally, some models assume/require that melt migration does not cut across the discontinuities between thrust slices (He *et al.*, 2014).

1.4.3. Tectonic wedging

Tectonic wedging (Figure 1.2e) is a variant on standard duplex models and assumes that the Himalayan orogen formed as a passive roof duplex system (Yin, 2006; Webb *et al.*, 2007; Webb *et al.*, 2011a; Webb *et al.*, 2013; He *et al.*, 2014). These models are derived from models applied to the core of the Canadian Cordillera (Price, 1986) and are commonly applied to fold-thrust belt settings (e.g. Banks & Warburton, 1986; Mora *et al.*, 2014). The initial configuration of these models (Figure 1.2e) assumes the GHS represents a crustal scale thrust slice located between the THS and LHS, which tapers southwards (Yin, 2006; Webb *et al.*, 2007). Beyond this tapered point towards the foreland, the southward continuation of the MCT places the THS over the LHS (Yin, 2006; Webb *et al.*, 2007). The MCT and STD converge at the tapered point of the GHS, thereby forming a floor thrust – roof thrust association with the GHS.

The tectonic wedging model assumes that the STDS forms as a passive roof backthrust to a duplex system (Banks & Warburton, 1986) and re-emerges northwards as the Great Counter Thrust (GCT) (Yin, 2006), which forms an orogen scale backthrust within the India-Asia suture zone (Yin *et al.*, 1999). At the front (south) of the system, the LHS under-thrusts the THS with top-to-the-south motion. Towards the hinterland, top-to-the-north motion on the STDS is achieved by greater southwards motion of the footwall (GHS) relative to the hangingwall (THS). This implies that the GHS effectively pierces southwards through the contact between the LHS and THS. The model proposes that earlier top-to-the-south shear in the STDS relates to earlier deformation that occurred on the MCT between the THS and LHS and/or variations in the relative motion between the GHS and THS (Yin, 2006).

More recent versions of the tectonic wedging model allow internal thrust stack development of the GHS to occur (Webb *et al.*, 2013; He *et al.*, 2014). These models assume that complete emplacement of the GHS occurred at depth and that exhumation of the GHS took place after emplacement due to surface erosion and footwall uplift through later duplexing of the LHS (Webb *et al.*, 2013). Webb *et al.* (2011, 2013) state that tectonic wedging is distinct from channel flow models because during the former, emplacement occurs in the Miocene with no surface directed extrusion and exhumation, whilst during the latter, emplacement occurs between the Eocene-Oligocene and surface directed extrusion and exhumation occurs during the Miocene (Webb *et al.*, 2011a; Webb *et al.*, 2013). Additionally, it has been proposed that no other processes can explain the interpreted merger of the MCT and STD and, on this basis, the tectonic wedge model has been extrapolated to the rest of the GHS (Yin, 2006; Webb *et al.*, 2007; Webb *et al.*, 2011a; Webb *et al.*, 2013; He *et al.*, 2014).

1.5. Composite models

The models outlined above, including the channel flow model are often considered as end-members of orogenic processes (e.g. Searle & Szulc, 2005; Robinson *et al.*, 2006; Kohn, 2008; Carosi *et al.*, 2010; Webb *et al.*, 2011a). More recently, some models of Himalayan orogenesis have incorporated multiple elements from two or more of these 'end-member' models in recognition of the dynamic behaviour of an entire orogenic system during its rheological evolution (Beaumont *et al.*, 2004; Jamieson *et al.*, 2006; Larson *et al.*, 2010; Spencer *et al.*, 2012; Jamieson & Beaumont, 2013; Mukherjee, 2013a; Wang *et al.*, 2013; He *et al.*, 2014; Larson & Cottle, 2014). This concept of composite orogenic systems built from distinct orogenic domains dominated by different tectonic processes will be discussed in more detail in Chapter 7 in the context of the new research presented in this thesis, combined with a synthesis of previously published work.

1.6. Validating models of channel flow, extrusion and exhumation for the GHS: Research outline and objectives

Our understanding of the kinematic responses of orogenic systems to changes in rheological boundary conditions continues to grow. However, much of this understanding is rooted in the results of numerical simulations (e.g. Willett *et al.*, 1993; Mancktelow, 1995; Beaumont *et al.*, 2001; Beaumont *et al.*, 2004; Whipple & Meade, 2004; Butler *et al.*, 2013; Jamieson & Beaumont, 2013; Whipp *et al.*, 2014). Whilst the power and sophistication of these models is truly remarkable, concepts based on numerical simulation require validation from natural observations. Channel flow (Figures 1.2a, 1.4 & 1.5) has been used to explain the evolution of the GHS in a variety of locations along the length of the Himalaya (e.g. Grujic *et al.*, 2002; Jain *et al.*, 2005; Searle & Szulc, 2005; Lee *et al.*, 2006; Searle *et al.*, 2006; Cottle *et al.*, 2009; Larson *et al.*, 2010; Streule *et al.*, 2010a; Yan *et al.*, 2011; Spencer *et al.*, 2012; Mukherjee, 2013a; Rolfo *et al.*, 2014). In most cases channel flow has been proposed as a viable model based on macrostructural field relations and thermobarometry and geochronology data sets (e.g. Jessup *et al.*, 2008; Cottle *et al.*, 2009; Searle *et al.*, 2010; Streule *et al.*, 2010a; Spencer *et al.*, 2012). Fewer studies have been able to test the strain and velocity related criteria (Jain *et al.*, 2005; Mukherjee & Koyi, 2010; Mukherjee, 2013b) and to date, investigations of the strain-related criteria have mostly been limited to vorticity and strain rate estimations from quartz microstructures (e.g. Grasemann *et al.*, 1999; Grujic *et al.*, 2002; Law *et al.*, 2004; Jessup *et al.*, 2006; Larson & Godin, 2009; Law *et al.*, 2011; Law *et al.*, 2013). These studies are restricted to quartz dominated lithologies due to the complex controls of annealing, static recrystallisation and flow partitioning in high grade metamorphic rocks with

polymineralic assemblages. Consequently, the distribution and characterisation of strain across the whole of the GHS and the resulting velocity profiles are yet to be determined.

This thesis addresses these issues by employing a variety of techniques to determine the strain distribution across the GHS and bounding units. These include crystallographic preferred orientation (CPO) analysis via electron back scattered diffraction (EBSD) methods (Prior *et al.*, 1999) and anisotropy of magnetic susceptibility (AMS) analysis (Tarling & Hrouda, 1993; Borradaile & Jackson, 2004). Together, these techniques are capable of determining proxies of relative strain for all lithologies within the GHS, regardless of their mineral composition and structural heterogeneity (Bunge, 1982; Borradaile, 1991; Housen *et al.*, 1995; Skemer *et al.*, 2005; Barth *et al.*, 2010; Morales *et al.*, 2011; Ferré *et al.*, 2014; Morales *et al.*, 2014), thereby overcoming the problems associated with classic strain analysis techniques (Ramsay & Huber, 1983; Passchier & Trouw, 2005). Combining these techniques with field structural and microstructural analyses, provides a means to construct vertical strain profiles through the GHS and bounding units that can be compared to modelled strain and velocity profiles of channel flow (Mancktelow, 1995; Turcotte & Schubert, 2002; Beaumont *et al.*, 2004; Grujic, 2006).

In order to construct strain profiles for the GHS and bounding units, the chosen study area must have easy access and good exposure from which detailed sample suits can be obtained. Additionally, the chosen study area must have a comprehensive set of thermobarometric and geochronological constraints in order to test all of the criteria for channel flow listed in *Section 1.3.5.* It may also be advantageous to study an area with an atypical structural or lithological framework so as to test the limitations of the channel flow model.

The Annapurna-Dhaulagiri region of central Nepal is located in the middle of the Himalayan mountain belt (Figure 1.6). The area contains numerous trekking routes and road sections that traverse through entire structural sections of the GHS and bounding units. Thanks to the relative ease of access to the region, the area has been geologically mapped in detail (Colchen *et al.*, 1986; Hodges *et al.*, 1996; Godin, 2003; Larson & Godin, 2009; Martin *et al.*, 2010; Searle, 2010; Parsons *et al.*, 2014) and has been the subject of numerous structural, thermobarometric and geochronological studies (Bouchez & Pêcher, 1981; Le Fort *et al.*, 1987; Nazarchuk, 1993; Kaneko, 1995; Hodges *et al.*, 1996; Vannay & Hodges, 1996; Godin *et al.*, 2001; Hurtado *et al.*, 2001; Hurtado, 2002; Godin, 2003; Beyssac *et al.*, 2004; Kellett & Godin, 2009; Larson& Godin, 2009; Martin *et al.*, 2010; Searle, 2010; Corrie & Kohn, 2011; Kohn & Corrie, 2011; Nadin & Martin, 2012; Carosi *et al.*, 2014; Martin *et al.*, 2014; Larson &

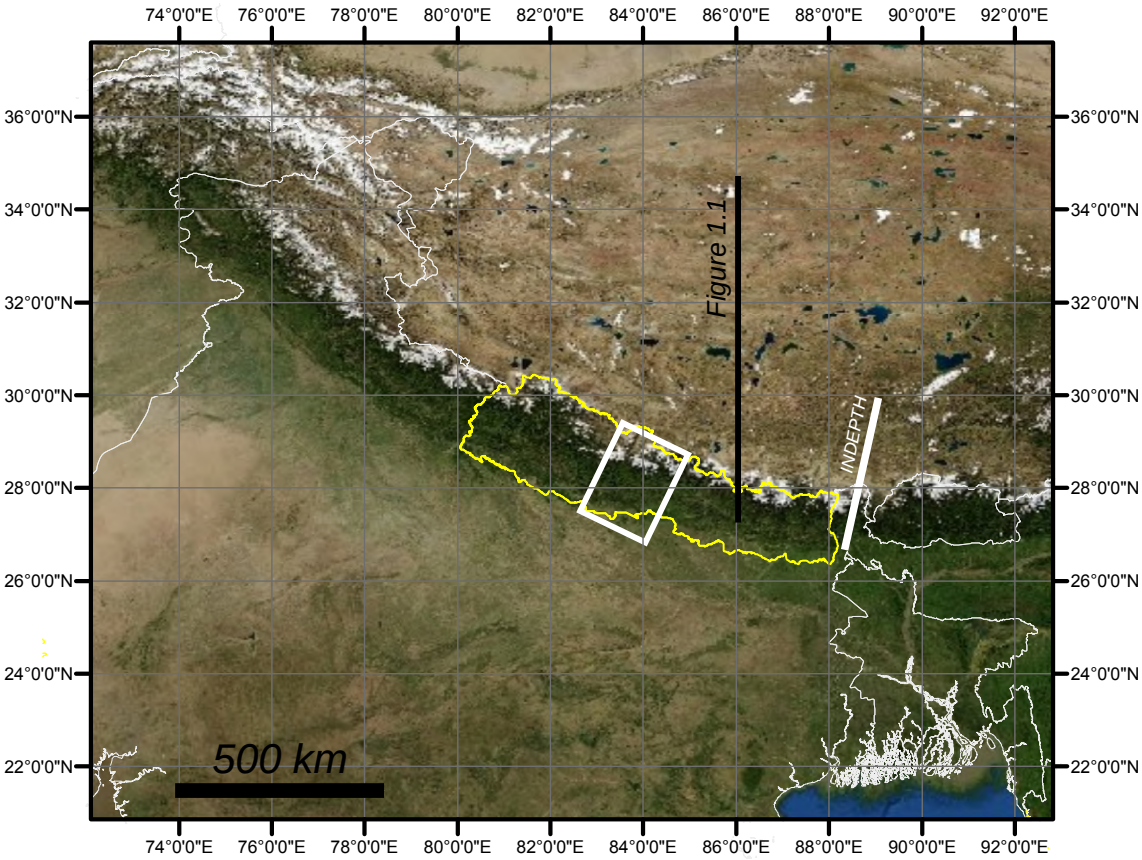

Figure 1.6. Geographic location of the Annapurna-Dhaulagiri region, central Nepal. White box shows location of study area. Yellow outline shows the Nepalese boarder. White line shows the location of the INDEPTH profile (Nelson *et al.*, 1996). Black line shows location of cross section in Figure 1.1.

Cottle, 2015). Additionally, the GHS in the Annapurna-Dhaulagiri region differs from typical sections of the GHS upon which the channel flow model was based, with lower than typical volumes of leucogranite and sillimanite grade rocks, a smaller than typical structural thickness (<10 km), a late stage kinematic reversal on the STD and E-W extension in the northern parts of the region (Brown & Nazarchuk, 1993; Nazarchuk, 1993; Hodges *et al.*, 1996; Godin *et al.*, 1999; Hurtado *et al.*, 2001; Godin, 2003; Godin *et al.*, 2006). Based on these criteria, the Annapurna-Dhaulagiri Himalaya of central Nepal is selected as favourable location to test the validity of the channel flow model and determine its limitations for explaining along-strike variations in the structural and lithological framework of the GHS. The structure of this research and its aims and objectives are as follows.

- Evaluate the structural and lithological framework of the Annapurna-Dhaulagiri Himalaya (*Chapter 2*).
- Determine the thermo-kinematic evolution of the GHS and bounding units in the Annapurna-Dhaulagiri region through microstructural observations and CPO analysis via EBSD (*Chapter 3*).

- Determine the influence of deformation on magnetic fabric development in samples from the GHS and bounding units and where possible make kinematic interpretations from these fabrics (*Chapter 4*).
- Assess the relationship between strain and CPO and AMS fabric development to determine vertical strain profiles of the GHS and bounding units from these analyses (*Chapter 5*).
- Construct relative velocity profiles of the GHS and bounding units from the strain profiles (*Chapter 6*).
- Compare strain and velocity profiles of the GHS and bounding units with simplified analytical models of 1D channel flows to determine kinematic implications (*Chapter 6*).
- Based on the findings of this research, combined with previously published constraints, evaluate the criteria for channel flow outlined in *Section 1.3.5.* and assess the validity of the channel flow model for the Annapurna-Dhaulagiri region (*Chapter 7*).
- Consider the atypical features of the Annapurna-Dhaulagiri region and assess whether they are compatible with the channel flow model or whether alternative explanations are required (*Chapter 7*).
- Consider the validity of all models proposed for the Himalayan orogen in light of the new research presented in this thesis and previous observations, and assess the apparent dichotomy between models of contrasting styles (e.g. channel flow versus thrust stacking) (*Chapter 7*).
- Based on the finding of this research and of others, determine the kinematic evolution of the Annapurna-Dhaulagiri region during the Himalayan orogen (*Chapter 7*).

- CHAPTER 2 -

GEOLOGICAL FRAMEWORK OF THE ANNAPURNA-DHAULAGIRI HIMALAYA

2.1. Introduction

Robust kinematic interpretation of microstructural observations requires a solid understanding of the geological framework from which they derive. In this chapter the regional geological framework of the Annapurna-Dhaulagiri Himalaya is presented, based upon petrological and structural observations made during this study. These observations are supplemented (where cited) with additional data from previously published work, including thermobarometric and geochronological constraints. Geological maps are presented with sample locations and accompanying sample transects, cross sections and stratigraphic columns. The maps, cross sections and stratigraphic columns are based on a newly published geological map of *'Western Region, Nepal'* produced as part of this study (Parsons *et al.*, 2014). The accompanying memoir published with this map, which describes the construction method and the geology found outside of the Annapurna-Dhaulagiri Himalaya is available in the supplementary materials CD. This chapter concludes with a description of the atypical features of the region that differ from other parts of the Himalaya. An initial consideration for their significance to the kinematic evolution of the region is discussed, prior to further evaluation in Chapter 7 based on the findings of this thesis.

2.2. The Himalayan orogen

During the final closure of Neotethys at *ca.* 50 Ma (Searle *et al.*, 1987; Green *et al.*, 2008; Najman *et al.*, 2010), the India-Asia collision resulted in the initiation of mountain building processes along the Himalaya (Figure 2.1). The Himalayan belt has been under a continuous state of convergence since that time, resulting in uplift and erosion of the world's largest mountain peaks (Searle *et al.*, 2011). In Western Region, Nepal, the Himalaya can be divided into four tectonic units separated by orogen parallel faults and shear zones (Figure 2.2). From SW to NE these units are the Subhimalayan Zone (SZ), the Lesser Himalayan Sequence (LHS), the Greater Himalayan Sequence (GHS) and the Tethyan Himalayan Sequence (THS) (Le Fort, 1975). This chapter focuses on the lithology and structure of the GHS and bounding units from the Annapurna-Dhaulagiri Himalaya. For a brief a description of the geology of Western Region beyond the Annapurna-Dhaulagiri Himalaya see Parsons *et al.* (2014; supplementary CD) and others (Le Fort, 1975; Stöcklin, 1980; Colchen *et al.*, 1986; Upreti, 1999; Paudel & Arita, 2000).

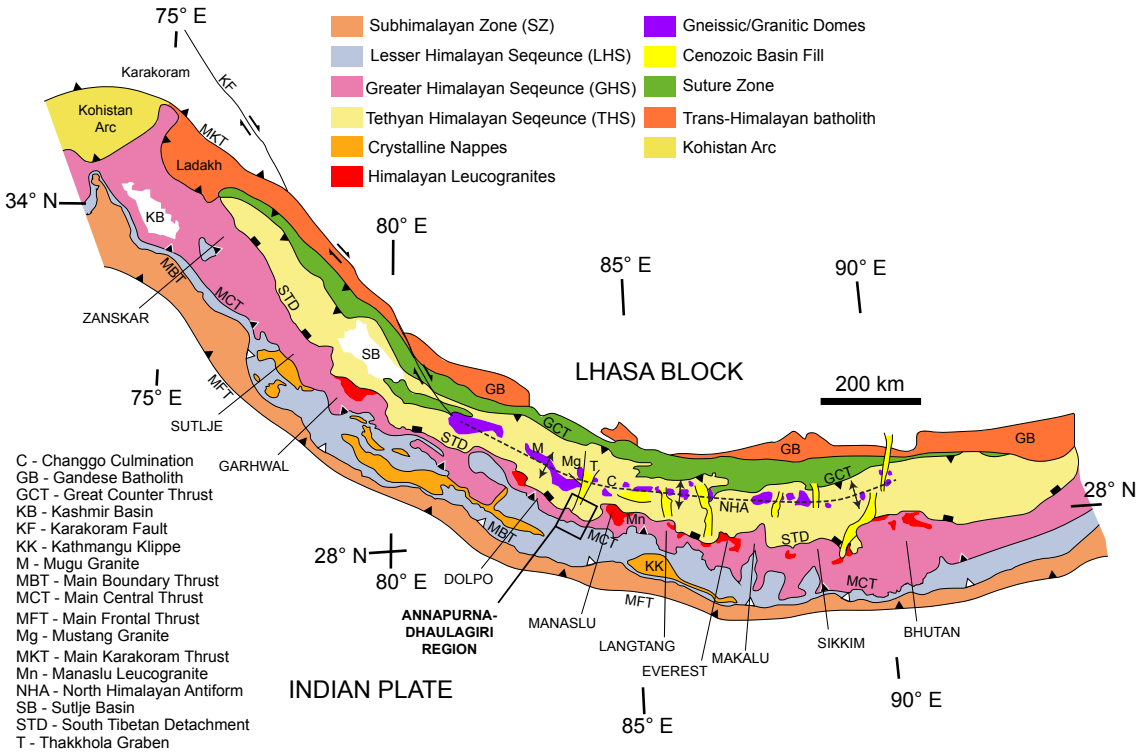

Figure 2.1. Simplified geological sketch map of the Himalayan orogen. After Goscombe *et al.* (2006), Searle *et al.* (2008) and Law *et al.* (2013).

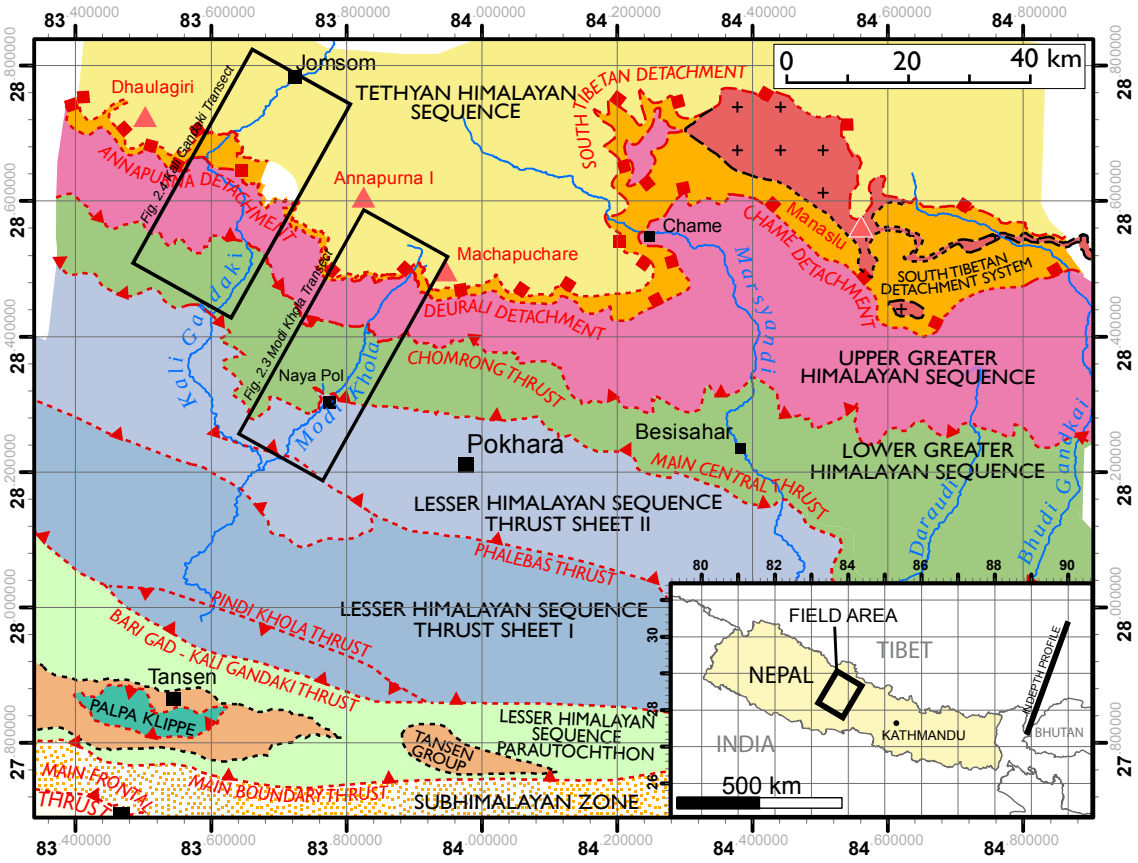

Figure 2.2. Simplified tectono-stratigraphic map of Western Region, Nepal. Major tectonic units and bounding faults and shear zones are labelled. Black boxes show extent of Modi Khola and Kali Gandaki transects. Inset map shows field area location in relation to the rest of Nepal. After Parsons *et al.* (2014).

2.3. Study area: The Annapurna-Dhaulagiri Himalaya

The central Himalaya in north Western Region, Nepal, is dominated (from east to west) by the peaks of Dhaulagiri (8167 m), Annapurna I (8091 m) and Manaslu (8156 m), which form part of a high mountain massif. Rivers flow between these peaks along steep sided valleys that trend approximately NE-SW. This study focuses on two orogen-perpendicular transects located along the Kali Gandaki and Modi Khola valleys (Figure 2.2). Rocks from the uppermost LHS, GHS and THS are exposed across this area making it a logistically suitable location to sample through the major units of the Himalayan orogen. The region was first described in detail by Le Fort (1975) and later by Colchen *et al.* (1986). Importantly, extensive structural, geochronological and metamorphic studies from the region provide the necessary PTt constraints to interpret strain data in terms of the local deformation history (e.g., Le Fort et al., 1987; Stöcklin, 1980; Bouchez & Pêcher, 1981; Arita, 1983; Pêcher, 1989; Brown & Nazarchuk, 1993; Nazarchuk, 1993; Kaneko, 1995; Hodges *et al.*, 1996; Vannay & Hodges, 1996; Godin *et al.*, 1999a; Godin *et al.*, 1999b; Godin *et al.*, 2001; Godin, 2003; Bollinger *et al.*, 2004; Martin *et al.*, 2005; Paudel & Arita, 2006b; Kellett & Godin, 2009; Larson & Godin, 2009; Martin *et al.*, 2010; Corrie & Kohn, 2011; Kohn & Corrie, 2011; Carosi *et al.*, 2014; Martin *et al.*, 2014; Larson & Cottle, 2015).

The Modi Khola transect is approximately 38 km long and can be accessed along trekking paths between Naya Pol and Annapurna Base Camp and along a road section between Kushma and Naya Pol (Figure 2.3). 59 orientated samples from the LHS, GHS and THS were collected along this transect, with 49 for optical and electron microscopy and 10 for magnetic fabric analysis. The Kali Gandaki transect is approximately 48 km long and runs along a road section and trekking paths between Beg Khola and Jomsom (Figure 2.4). 104 orientated samples from the GHS and THS were collected from this transect; 73 for optical and electron microscopy and 31 for magnetic fabric analysis. The relative structural positions of these samples are displayed in Figure 2.5. A full sample and structural data list is provided in the supplementary materials CD.

2.4. Tectono-stratigraphy

The geology of the Annapurna-Dhaulagiri Himalaya comprises the uppermost LHS, GHS, and THS. The GHS is bound below by the Main Central Thrust (MCT) and above by the South Tibetan Detachment (STD) and, in this study, is divided into the Lower GHS (LGHS), Upper GHS (UGHS) and South Tibetan Detachment System (STDS). The LGHS and UGHS are separated by the Chomrong Thrust (CT), whilst the UGHS and STDS are separated by the Annapurna Detachment (AD) in the Kali Gandaki

valley and the Deurali Detachment (DD) in the Modi Khola valley (Brown & Nazarchuk, 1993; Hodges *et al.*, 1996; Vannay & Hodges, 1996; Larson & Godin, 2009). Internally, the UGHS is deformed by the Kalopani Shear Zone (KSZ) in the Kali Gandaki valley and the Modi Khola Shear Zone (MKSZ) in the Modi Khola valley (Hodges *et al.*, 1996; Vannay & Hodges, 1996). These tectonic units are well exposed in the Modi Khola and Kali Gandaki valleys and the foothills between. Stratigraphic columns and cross sections for both transects are presented in Figures 2.5, 2.6 & 2.7.

This study follows the definitions of the GHS and MCT proposed by Searle *et al.* (2008) and used by Larson and Godin (2009) for the same region. These studies propose that the MCT is the basal thrust to the GHS, which incorporates the entire section of stratigraphy metamorphosed above chlorite grade and pervasively sheared due to extrusion during the Himalayan orogeny (Searle *et al.*, 2008). Such a proposal differs from other studies in the same region that define the GHS as amphibolite facies, leucogranite bearing rocks (Martin *et al.*, 2005; Martin *et al.*, 2010; Corrie & Kohn, 2011; Carosi *et al.*, 2014). In these other studies, the CT as defined here, is named as the MCT; the MCT as defined here is named as the Ramgarh Thrust; and the LGHS as defined here is named as Lesser Himalayan rocks (Martin *et al.*, 2005; Martin *et al.*, 2010; Corrie & Kohn, 2011; Carosi *et al.*, 2014).

2.4.1. Lesser Himalayan Sequence (LHS)

The LHS is exposed in the Modi Khola transect along a road section between Kushma and Naya Pol (Figure 2.3). Here, quartzites and chlorite-bearing semipelitic metasedimentary rocks with a stratigraphic thickness of at least 4000 m are observed. These rocks belong to the Fag Fog Quartzites described by Stöcklin (1980). Peak metamorphic conditions in LHS rocks exposed in the Modi Khola transect did not exceeded chlorite grade (Paudel & Arita, 2006a, b).

2.4.2. Lower Greater Himalayan Sequence (LGHS)

The LGHS is well exposed in the Kali Gandaki transect (Figure 2.4), exhibiting a structural thickness of ~6100 m, but poorly exposed in the Modi Khola transect (Figure 2.3), with a structural thickness of ~5700-6650 m. The LGHS consists of metasedimentary rocks (quartzites, pelites and semipelites, metacarbonates and dolomitic marbles) and a discontinuous layer of augen orthogneiss. Detrital zircon U-Pb ages suggest that the LGHS protoliths were deposited between approximately 1886-1831 Ma (Decelles *et al.*, 2000).

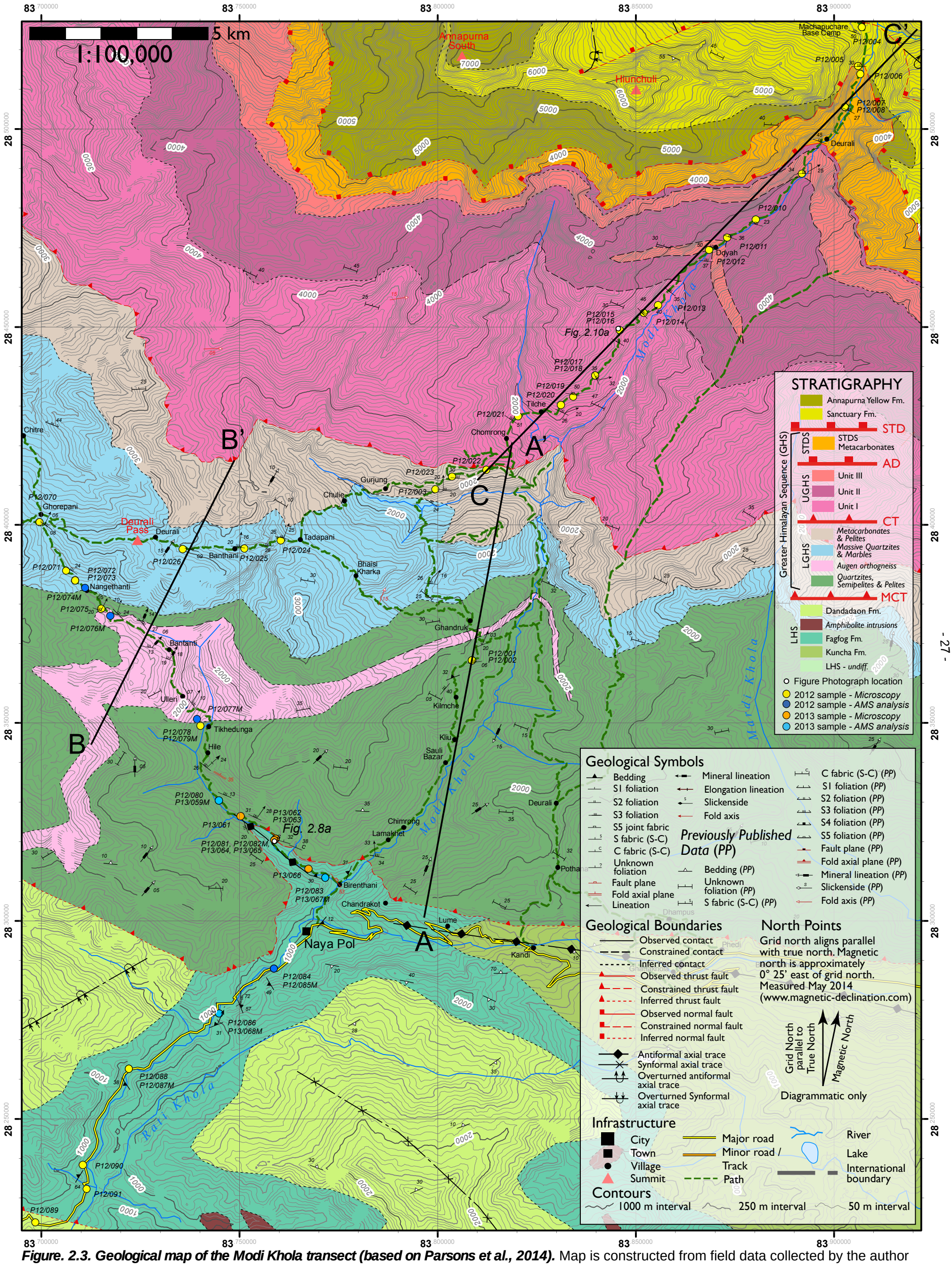

Figure. 2.3. Geological map of the Modi Khola transect (based on Parsons et al., 2014). Map is constructed from field data collected by the author and from previously published data (Colchen ***et al.,*** 1986; Paudel & Arita, 2006ab; Martin ***et al.,*** 2010). Cross sections constructed from the map are presented in Figure 2.6. For a description of the LHS strata (not described in this chapter) see Parsons ***et al.*** (2014).

Figure. 2.4. Geological map of the Kali Gandaki transect (based on Parsons et al.(2014). Map constructed from field data collected by the author and from previously published data (Colchen et al., 1986; Godin, 2003; Larson & Godin, 2009). Cross sections constructed from the map are presented in Figure 2.7. For a description of the THS strata (not described in this chapter) see Parsons et al. (2014).

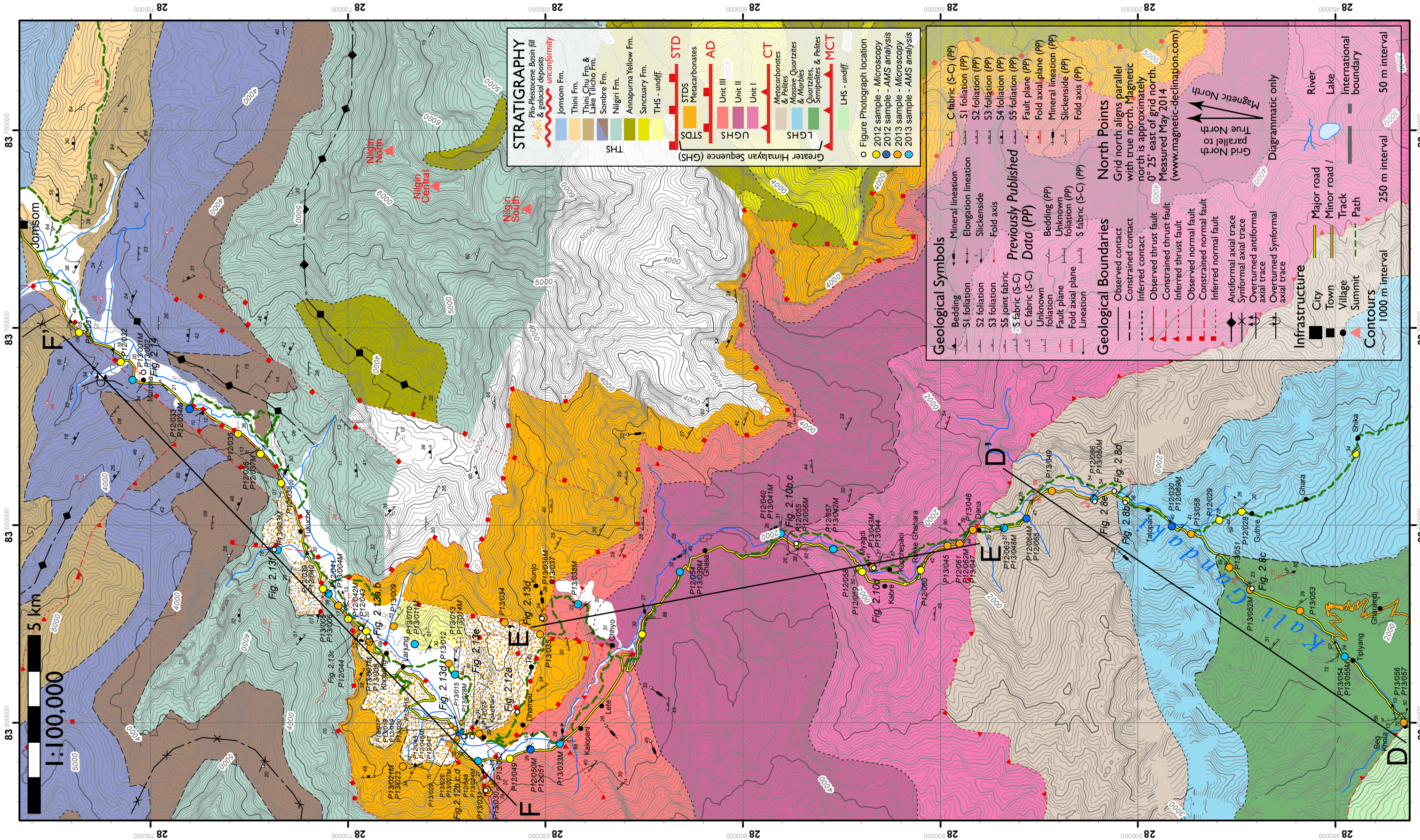

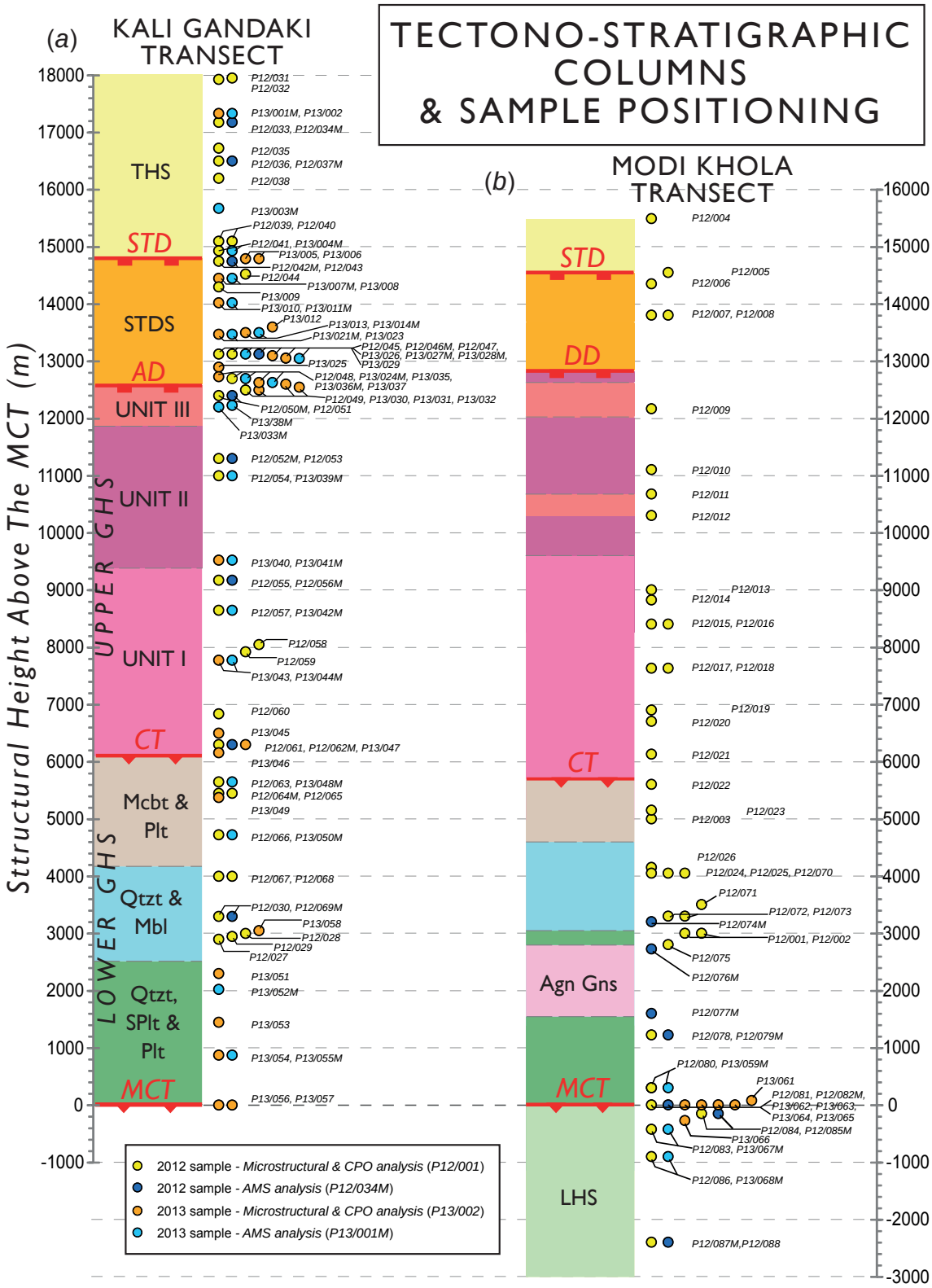

Figure 2.5. Tectono-stratigraphic columns and sample structural position above the MCT for the Annapurna-Dhaulagiri transects. (*a*) Kali Gandaki transect. (*b*) Modi Khola transect. Unit thicknesses and structural position of samples are determined from cross sections (Figures 2.6 & 2.7). Key for unit classification is given in Figures 2.3 & 2.4.

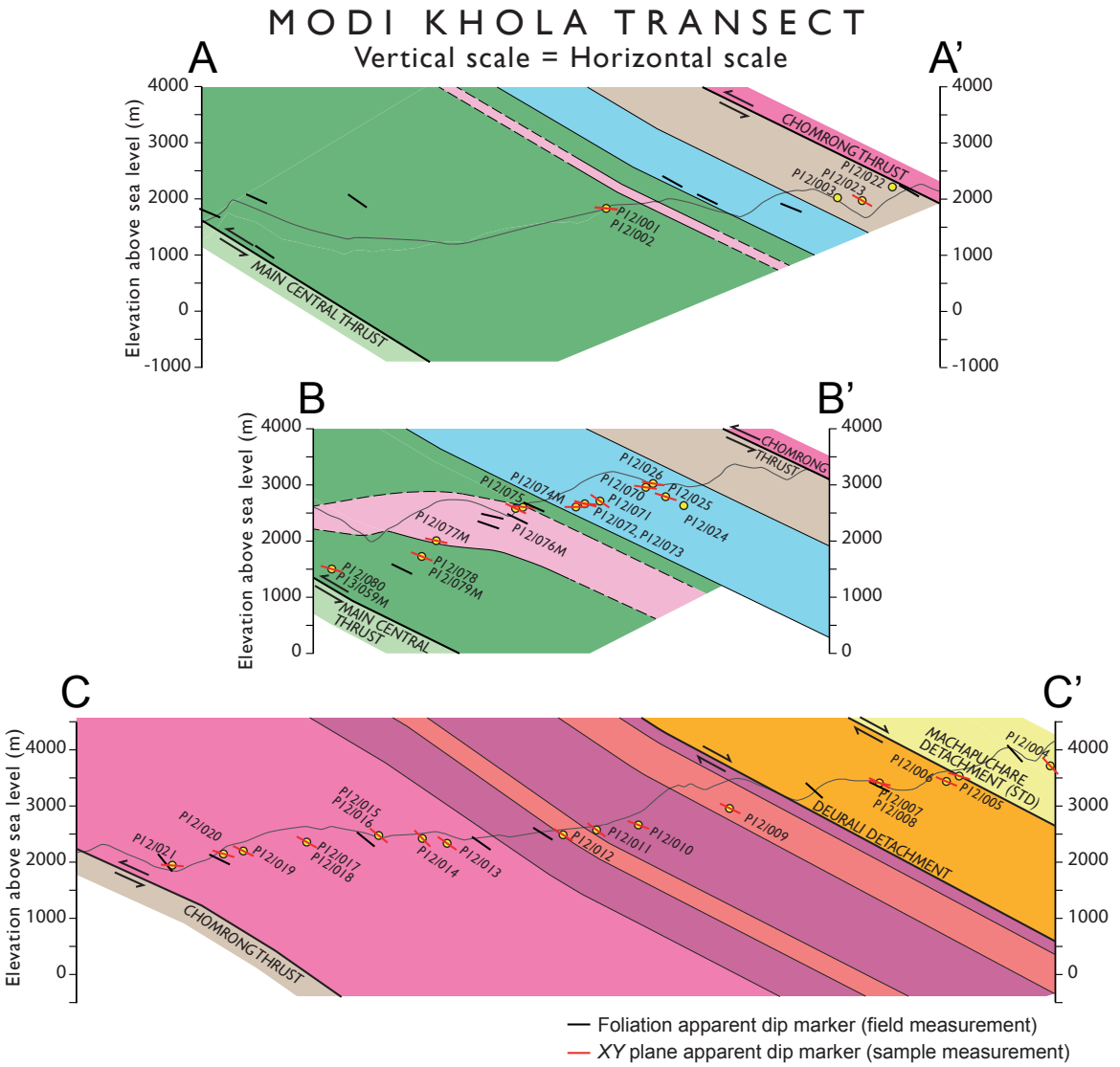

Figure 2.6. Cross sections for the Modi Khola transect. Constructed from Figure 2.3. Yellow dots indicate sample positions. Vertical scale = horizontal scale.

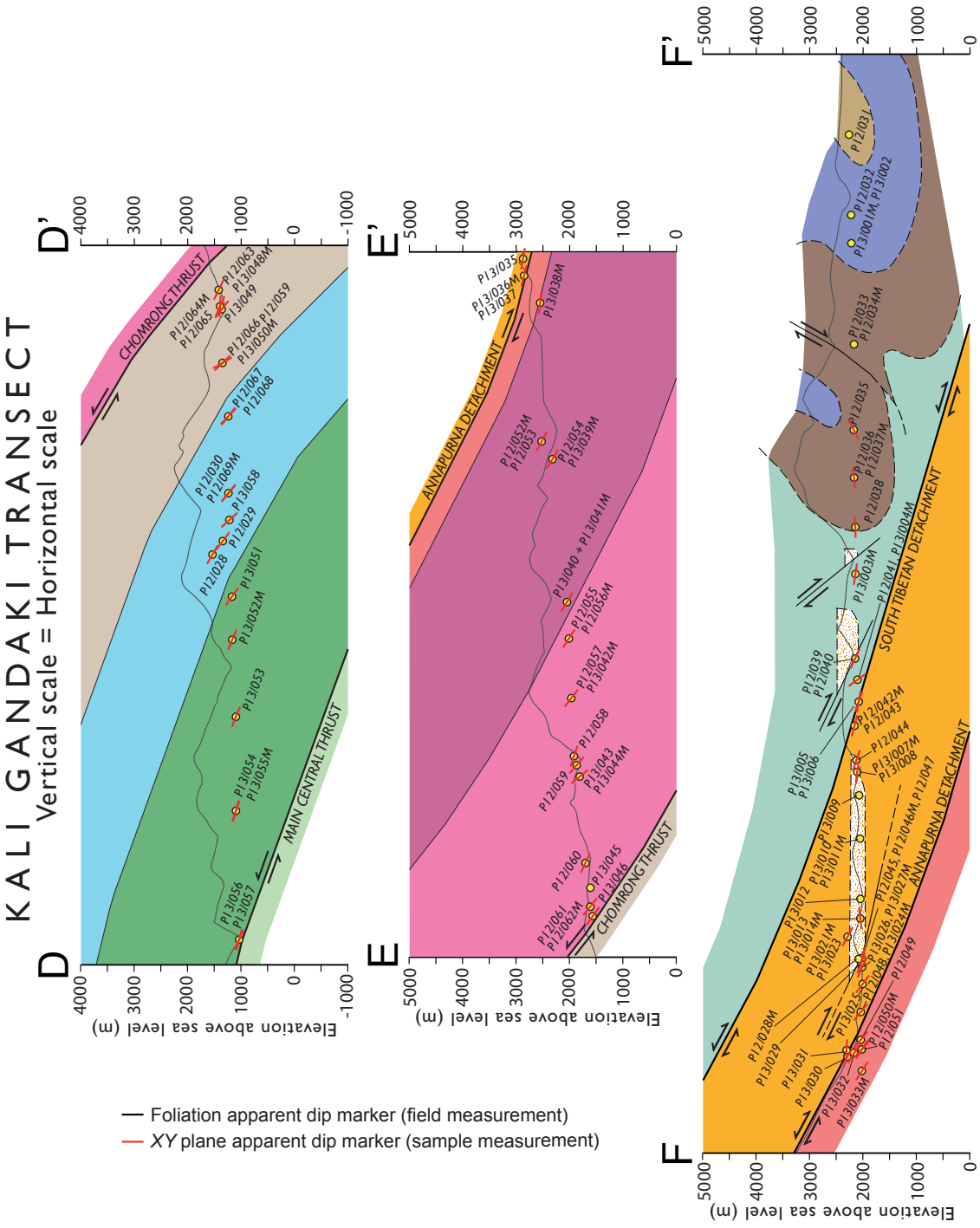

Figure 2.7. Cross sections for the Kali Gandaki transect. Constructed from Figure 2.4. Yellow dots indicate sample positions. Vertical scale = horizontal scale.

At the base of the LGHS, the MCT forms a 10-20 m thick shear zone. Across the shear zone, 2-4 m thick alternating layers of quartzite/semipelite horizons and friable shale horizons are observed (Figure 2.8). Shale horizons contain a high concentration of quartz veins. Within the quartzite horizons, thin (<1 cm) chloritic layers are observed. In the thickest quartzite horizons, cross-bedding structures are sometimes preserved.

The lowermost portion of the LGHS comprises a unit of undifferentiated and often interbedded quartzites pelites and semipelites with a structural thickness of ~2500-3000 m (Figure 2.5). Quartzites typically contain 5-20% mica. Semipelitic and pelitic units contain variable proportions of muscovite, biotite and chlorite, with chlorite content greatest towards the base of the unit and biotite content greatest towards the top of the unit. Towards the top of the unit, staurolite and chloritoid pseudomorphs after staurolite are occasionally observed. Pelitic layers commonly contain graphitic lamellae between mica sheets. Sericitised plagioclase, K-feldspar, tourmaline, apatite and ilmenite form the most common accessory phases within this unit (<5% volume of rock). The distribution of quartz and mica within these rocks varies from an even and homogeneous distribution to segregated bands.

Within the unit of undifferentiated metasedimentary rocks is a laterally discontinuous layer of orthogneiss. This orthogneiss, referred to as the Ulleri augen gneiss by previous authors (e.g. Le Fort, 1975) is exposed in the Modi Khola transect, with a variable thickness of approximately 200-1600 m. It is not observed in the Kali Gandaki transect. The augen orthogneiss is dominated by cm-scale albite augen distributed between segregated layers of quartz and mica that define a weak S-C fabric (Berthé *et al.*, 1979). Mica layers contain muscovite and chlorite. K-feldspar is also present. The orthogneiss is interpreted as a pre-Himalayan syndepositional intrusion (Pêcher & Le Fort, 1977), and has zircon U-Pb ages of ~1831 Ma (Decelles *et al.*, 2000).

Above the unit of undifferentiated metasedimentary rocks is a unit of massive quartzite and dolomitic marble (marble defined as >80% carbonate) with an approximate thickness of 1700 m in the Kali Gandaki transect and 1550-800 m in the Modi Khola transect (Figure 2.5). Quartzites comprise >95% quartz and <5% muscovite. Dolomitic marbles contain >80% dolomite, <20 % quartz and <5 % mica, which is present as phlogopite and muscovite.

The uppermost unit of the LGHS consists of interbedded layers of dolomitic metacarbonates (metacarbonate defined as >50-80 % carbonate) and calc-pelitic metasedimentary rocks with an approximate thickness of 1100 m in the Modi Khola transect and 1950 m in the Kali Gandaki transect (Figure 2.5). Calc-pelite rocks contain roughly equal proportions of mica, quartz, dolomite ± calcite and commonly have thin

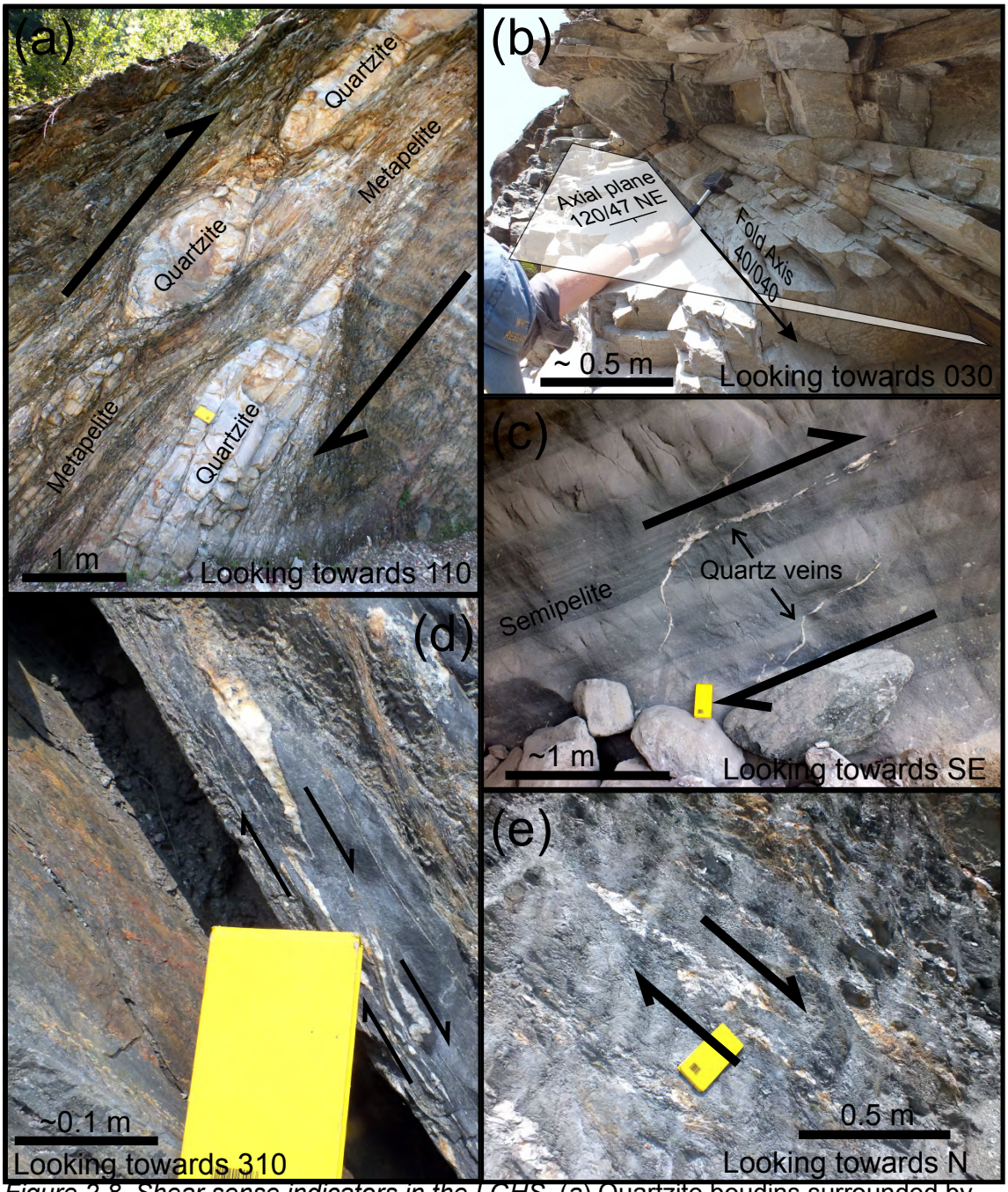

Figure 2.8. Shear sense indicators in the LGHS. (*a*) Quartzite boudins surrounded by metapelitic rocks in the MCT in the Modi Khola transect. (*b*) F3 'Flattening folds' within the Massive Quartzite & Marble Unit in the Kali Gandaki transect. F3 Fold hinges and hinge planes are parallel to the regional L3 stretching lineation and S3 foliation, respectively. (*c*) Sheared quartz veins in the Quartzite, Semipelite and Pelite unit in the Kali Gandaki transect. Shear sense is top-to-the-SW. (*d-e*) Top-to-the-NE sheared calcite veins in the Metacarbonate and Pelite unit on the Kali Gandaki transect. See Figures 2.3 & 2.4 for photo locations.

graphitic lamellae between mica sheets. Mica grains are present as phlogopite and muscovite. Garnet has also been reported in these rocks (Kaneko, 1995; Corrie & Kohn, 2011), although none were observed in this study.

In the LGHS in the Modi Khola transect, an up-section increase in temperature from ~400 °C to ~500-600 °C has been determined from Raman spectroscopy of

carbonaceous material (RSCM) (Bollinger *et al.*, 2004) and garnet-biotite thermometry (Kaneko, 1995; Martin *et al.*, 2010; Corrie & Kohn, 2011). Pressure estimates derived from garnet-plagioclase barometry range between ~7-10 kbar (Martin *et al.*, 2010; Corrie & Kohn, 2011).

2.4.3. Upper Greater Himalayan Sequence (UGHS)

The UGHS is ~6500-7050 m thick in the Kali Gandaki transect and ~7150 m thick in the Modi Khola transect (Figure 2.5**)**. Within the UGHS, the Kalopani shear zone (KSZ) and the Modi Khola shear zone (MKSZ) deform the upper portions of the sequence during syn- to post-peak metamorphic top-to-the-southwest shearing (Hodges *et al.*, 1996; Vannay & Hodges, 1996). Detrital zircon U-Pb ages suggest that the UGHS protoliths were deposited between approximately 800-480 Ma (Decelles *et al.*, 2000). The UGHS is divided into Unit I, Unit II and Unit III (e.g. Searle, 2010)

2.4.3.1. Unit I

Unit I is 3300 m thick in the Kali Gandaki transect and 3900 m thick in the Modi Khola transect (Figure 2.5) and consist of high grade schists, gneisses, migmatites and leucogranites. The bulk mineral assemblage of the schists and gneisses is dominated by biotite, quartz, plagioclase ± garnet ± kyanite ± K-feldspar. Apatite, tourmaline and rutile form common accessory minerals. Kyanite is first observed at ~400-450 m above the unit base in both the Kali Gandaki and Modi Khola transects. In the Modi Khola transect, small amounts of sillimanite are also observed in a few samples, the lowest of which is positioned ~3300 m above the base of Unit I. Sillimanite is not observed in Unit I in the Kali Gandaki transect. Garnet is commonly present as almandine, but occasionally recognised as pyrope. Garnets commonly contain inclusions of quartz, plagioclase, biotite and rutile. In some cases, garnet cores contain ilmenite inclusions, whilst rims contain rutile inclusions. Rutile inclusions are also observed within the largest kyanite crystals. In a minority of samples from the Kali Gandaki transect but commonly in the Modi Khola transect, garnet grains show signs of retrogression and resorption and are sometimes observed breaking down to biotite, plagioclase and quartz. Plagioclase compositions are most commonly characteristic of oligoclase, but albite and andesine compositions are also recognised. Muscovite is sporadically observed most commonly as a secondary mineral phase but is identified as a primary phase at the very base of Unit I in the Kali Gandaki transect. Secondary paragonite is also observed in the lowermost Unit I samples from the Modi Khola transect. Migmatites typically concentrate into foliation parallel bands ~10-50 m thick, whilst leucosomes and small (<1 m thick) leucogranite bodies are present throughout Unit I (Figure 2.9). Where present, the degree of partial melting estimated from outcrop

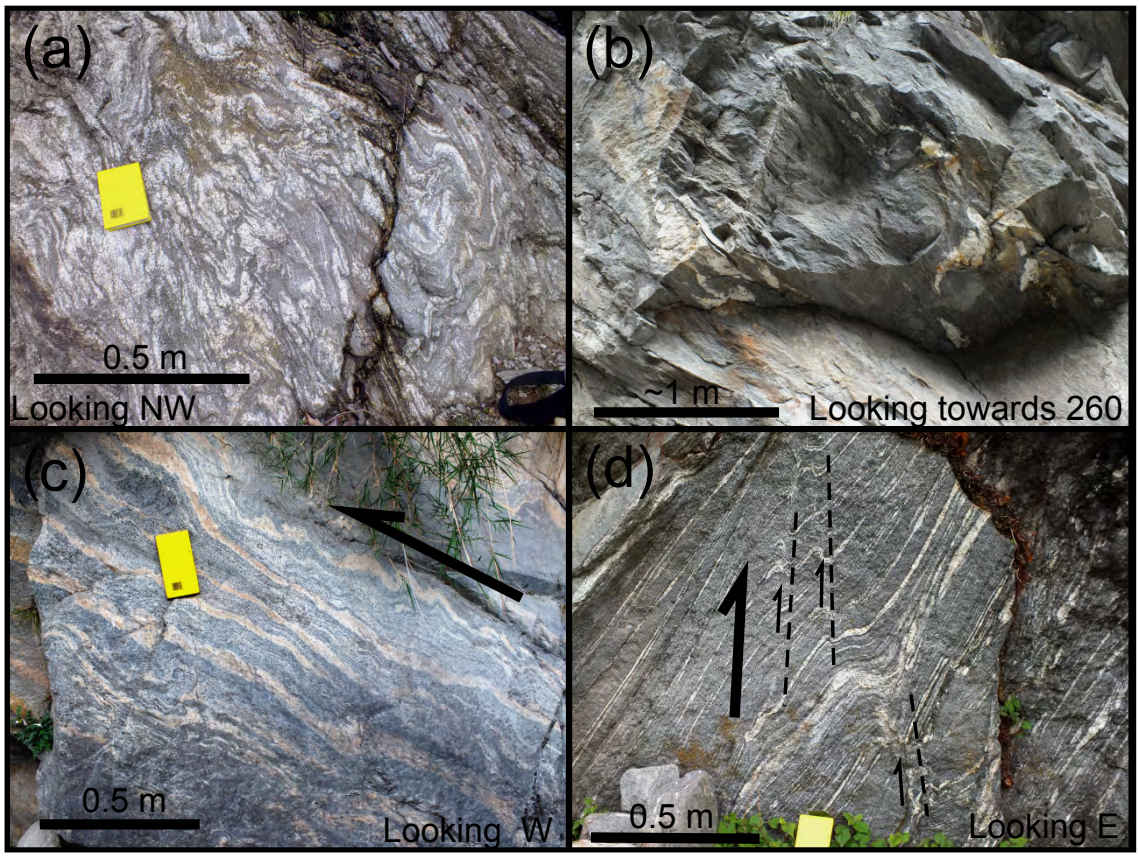

Figure 2.9. Leucosome structures in the UGHS. (*a*) Folded leucosomes in Unit I migmatite from the Modi Khola transect. (*b*) Amorphous leucosomes bodies in Unit I, Kali Gandaki transect. (*c*) Banded leucosomes in Unit I migmatites in the Kali Gandaki transect. Leucosomes record top-to-the-S shearing along a S3 foliation-parallel shear plane. Deformation features suggest that deformation occurred during partial melting, prior to crystallisation of leucosomes. (*d*) Banded leucosomes in Unit I migmatites in the Kali Gandaki transect. S3 leucosome fabric is deformed by S4 thrust-tip-folds. See Figures 2.3 & 2.4 for photo locations.

appearance is 10-40% in the Modi Khola transect and 5-20% in the Kali Gandaki transect.

2.4.3.2. Unit II

Unit II is ~2500 m thick in the Kali Gandaki transect (Figure 2.5). In the Modi Khola transect, Unit II is interlayered with Unit III and has a combined thickness of ~2250 m (Figure 2.5). Unit II dominantly consists of high grade calc-silicate gneiss. In the Modi Khola transect, pelitic gneisses are also present. Where retrogression has not occurred, the bulk mineral assemblage of the calc-silicate gneisses comprises variable proportions of quartz, calcite, clinopyroxene, plagioclase, K-feldspar, phlogopite, scapolite, clinozoisite and titanite. Plagioclase compositions range between labradorite, andesine and oligoclase and internal zoning between these compositions is commonly observed. Clinopyroxene compositions vary between diopside and augite. Where retrogression is evident, scapolite and clinopyroxene are less common and intergrowth textures of clinozoisite, quartz, biotite, plagioclase and calcite are observed. Amphibole

is also observed in retrogressed samples from Unit II, particularly in samples from the Modi Khola transect, where retrogression appears to be more significant.

Subordinate pelitic gneiss within Unit II of the Modi Khola transect comprises quartz, plagioclase, garnet, kyanite, biotite and muscovite. Resorption textures of garnet, biotite and kyanite and intergrowth textures of secondary muscovite are observed in these rocks. In the Kali Gandaki transect, leucosomes are rare within Unit II and where present are typically <10 cm thick and <50 cm long. In the Modi Khola transect leucogranite sills are commonly seen in the uppermost section of Unit II at the top of the UGHS.

2.4.3.3. Unit III

Unit III is >700 m thick in the Kali Gandaki transect (Figure 2.5). In the Modi Khola transect two layers of Unit III are present between rocks from Unit II. These layers are ~400 and ~600 m thick (Figure 2.5). Unit III is dominated by orthogneiss and leucogranite with subordinate layers and pods of calc-pelitic and calc-psammitic gneiss. Albite, K-feldspar, quartz, biotite and muscovite form the bulk mineral assemblage of the orthogneiss and leucogranite, while apatite and tourmaline form common accessory phases. It is unclear whether or not muscovite is present as a primary or secondary mineral or both. Garnet is observed only in orthogneiss from the Modi Khola transect although it has previously been reported in leucogranites from Unit III in the Kali Gandaki transect (Larson & Godin, 2009). U-Pb geochronology (Hodges *et al.*, 1996; Godin *et al.*, 2001) suggests that the orthogneiss protolith was emplaced as a granitic pluton during the Early Ordovician.

The pelitic gneiss layers in Unit III were not sampled during this study but are reported to contain sillimanite together with biotite and kyanite bearing leucosomes (Arita, 1983; Godin *et al.*, 2001; Larson & Godin, 2009; Searle, 2010). Within the Kali Gandaki transect, subordinate calc-psammitic gneiss is present at the very top of Unit III and contains labradorite, biotite, clinozoisite, amphibole and quartz. The top of Unit III is bound by the Annapurna Detachment in the Kali Gandaki transect (Figure 2.6) and the Deurali Detachment in the Modi Khola transect (Figure 2.5) (Searle, 2010).

2.4.3.4. UGHS metamorphism

The UGHS in the Annapurna-Dhaulagiri region equilibrated within the kyanite stability field (Carosi *et al.*, 2014). In the Modi Khola transect, peak metamorphic temperatures and pressures of 750-825 ^{o}C and 12-14 Kbar are recorded (Kaneko, 1995; Martin *et al.*, 2010; Corrie & Kohn, 2011). In the Kali Gandaki transect, peak metamorphic temperatures and pressures of ~650-700 ^{o}C and 5-10 Kbar are recorded by Le Fort *et*

al. (1987) and of ~500-750 ^{o}C and 6-12 kbar by Vannay and Hodges (1996). However, the exact method by which peak temperatures for the Kali Gandaki transect were obtained is unclear and it has been suggested that these values are probably an under-estimate (*D. Waters & M. Kohn pers. comms. 2014*).

U-Pb zircon and monazite geochronology indicates that the UGHS has been subjected to prograde metamorphism at temperatures exceeding 700 ^{o}C between 48-18 Ma and partial melting between 41-18 Ma (Nazarchuk, 1993; Hodges *et al.*, 1996; Godin *et al.*, 2001; Corrie & Kohn, 2011; Carosi *et al.*, 2014; Larson & Cottle, 2015). Peak metamorphic temperatures were attained between 35-30 Ma in Unit III and 25-20 Ma in Unit I and Unit II (Corrie & Kohn, 2011; Kohn & Corrie, 2011).

2.4.4. South Tibetan Detachment System (STDS)

The STDS forms the uppermost part of the GHS and is bound below by the Annapurna Detachment (AD) in the Kali Gandaki transect (Brown & Nazarchuk, 1993) and the Deurali Detachment (DD) in the Modi Khola transect (Hodges *et al.*, 1996) (Figures 2.6 & 2.7). The top of the STDS is bound by the STD (Searle, 2010), which is also referred to as the Machapuchare Detachment (MD) in the Modi Khola transect (Hodges *et al.*, 1996). The STDS is 2200 m thick in the Kali Gandaki transect and 1700 m thick in the Modi Khola transect (Figure 2.5).

The STDS consists of metacarbonate and marble and contains leucogranite sills and dykes in the middle to lower portions. In the Kali Gandaki transect, subordinate calc-silicate gneiss is present at the base of the STDS. Marbles and metacarbonates are dominated by calcite and contain variable proportions of quartz, plagioclase, mica ± K-feldspar ± dolomite. Mica is most commonly present as phlogopite with minor amounts of muscovite. In the Kali Gandaki transect, biotite and chlorite porphyroblasts are present in the middle to upper portion of the STDS. Plagioclase compositions fall within the bytownite-oligoclase range. Calc-silicate gneiss at the base of the STDS in the Kali Gandaki transect is composed of clinopyroxene, amphibole, clinozoisite, plagioclase, K-feldspar, quartz, biotite ± titanite ± calcite.

2.4.5. Tethyan Himalayan Sequence (THS)

The THS is well exposed throughout the upper reaches of the Kali Gandaki valley (Figure 2.4). In this transect, cross section restoration of the THS indicates that the undeformed sequence has a stratigraphic thickness of 11 km (Godin, 2003). The THS is only weakly metamorphosed near its base and does not contain any leucogranites. In the Kali Gandaki transect, the Nilgir Fm., Sombre Fm. and Thini Chu & Lake Tilicho Fm. (Figure 2.4), which comprise limestones, dolostones, and calc-semipelitic and

calc-pelitic rocks were sampled. In the Modi Khola transect, only the Annapurna Fm. and Sanctuary Fm. were sampled from the lower 1 km of the THS which consist of limestone, semipelitic, calc-semipelitic and calc-pelitic rocks (Figure 2.3). The full stratigraphic framework of the THS is described in detail by Gradstein *et al.* (1992), Garzanti (1999) and Godin (2003).

2.4.6. Mid Miocene to recent sedimentation

In the upper Kali Gandaki valley north of Kalopani and into Upper Mustang and Tibet, the Thakkhola graben has deformed the THS since the Mid-Miocene during E-W extension (Figure 2.4) (Hurtado *et al.*, 2001; Garzione *et al.*, 2003). Basin fill within the Thakkhola graben is Mid-Miocene to Plio-Pleistocene in age and is characterised by poorly consolidated fluvial, lake and glacial deposits (Garzione *et al.*, 2003; Baltz & Murphy, 2009; Adhikari & Wagreich, 2011).

2.5. Structural framework

The Annapurna-Dhaulagiri region records a complex history of polyphase deformation. In order to understand the kinematic evolution of the region it is helpful to define distinct fabric generations. Table 2.1 and 2.2 lists the details of five fabric generations observed across the Annapurna-Dhaulagiri region. These are based upon the foliation classification defined by Godin (2003) for deformation fabrics in the UGHS, STDS and THS in the Kali Gandaki valley. This classification scheme has been expanded to fabrics in the LGHS and LHS. Field structural data collected during this study are described below using this classification and are displayed in Figures 2.10 & 2.11.

2.5.1. LHS

Bedding (S0) in the LHS strikes approximately NW-SE with an average dip of 43^{o} and is gently folded into low amplitude open folds with a 1-2 km wavelength (Figure 2.10). Cross bedding and ripple surface sedimentary structures are commonly preserved. In some cases, quartzites in the LHS have a bedding-parallel foliation and a weak NE-SW trending mineral lineation. It is unclear what fold (F?) and foliation (S?) and lineation (L?) generation these fabrics belong to but their similarity in orientation with fabrics in the GHS suggests that they formed during the Himalayan orogen.

2.5.2. LGHS

The MCT is deformed with a well-defined S-C fabric, observed in the shale and semipelitic layers with S-planes ($S3_S$) orientated at 058/57 NW and 156/63 NE and C-planes ($S3_C$) orientated at 075/39 NW and 147/24 NE in the Modi Khola and Kali Gandaki transects respectively (Figure 2.10 & 2.11). Mineral lineations from the MCT

	LHS	LGHS	UGHS	STDS	THS (From Godin 2003)
S0	Bedding. ~NW-SE strike, 43^{o} average dip	-	-	-	-
S1	-	Microscopic fabric preserved in pelites - Deformed by S2 + S3.	-	-	-
S2	-	Microscopic fabric preserved in pelites - Crenulation cleavage deforms S1 foliation.	-	-	-
S3	-	119/25 NE - Regional transpositional fabric	116/42 NE - Transpositional fabric, parallel to structural and lithological boundaries	112/36 NE - Transpositional fabric, parallel to structural and lithological boundaries, related to top-to-the-north shearing	STDS parallel foliation. Present at base of THS, deforms S1 and S2
L3	-	19/028 - Regional mineral stretching lineation	29/067 - Regional mineral stretching lineation	29/067 - Regional mineral stretching lineation	-
F3	-	Localised folding related to top-to-the-south shearing. Fold hinge planes have ~E-W strike, sub-vertical dip.	Localised folding related to top-to-the-south shearing. Sub-parallel to S3	Localised folding related to top-to-the-north shearing	Regional shear-related fold transposes S1 and S2 into parallelism with S3
S4	-	Crenulation cleavage in pelitic rocks deforms S3	Syn- to post-metamorphic top-to-the-south shear fabric	Syn- to post-metamorphic top-to-the-south shear fabric, with associated S4 parallel thrust planes	-
S?	Weak bedding parallel foliation (Rare)	-	-	-	-
L?	Weak NE-SW trending lineation (Rare)	-	-	-	-
F?	Low amplitude open folds with NW-SE striking fold hinge planes deforms bedding, foliation and lineation	-	-	-	-

Table 2.1. Fabric generations from the Modi Khola transect. Based on Godin (2003)

(L3) in the Modi Khola transect are orientated at 31/030. In the Modi Khola transect, meter-sized quartzite boudins are observed within a pelitic layer (Figure 2.8a). Above the MCT, regional foliation in the LGHS (S3) has a mean orientation of 119/25 NE in the Modi Khola transect (Figure 2.10) and 128/36 NE in the Kali Gandaki transect (Figure 2.11). Mineral lineation (L3) has an average trend of 19/028 and 41/028 in each transect respectively.

S-C fabrics, shear bands and folded quartz veins are observed within semipelitic and pelitic lithologies throughout the LGHS. Microstructural analysis of pelitic rocks from the LGHS indicates that the regional foliation (S3) transposes an earlier crenulation cleavage (S2).

Table 2.2. Fabric generations from the Kali Gandaki transect. Based on Godin (2003)

	LGHS	UGHS	Unit I	Unit II	Unit III	STDS	THS (From Godin 2003)
S0	-	-	-	-	-	-	Bedding deformed by km-scale F2 folds
S1	Microscopic fabric preserved in pelites - Deformed by S2 + S3.	-	-	-	-	-	Sub-parallel to bedding. Deformed by km-scale F2 folds
S2	Microscopic fabric preserved in pelites - Crenulation cleavage deforms S1 foliation.	-	-	-	-	-	Crenulation cleavage, axial-planar to km-scale F2 folds deforms S1 and S0
F2	-	-	-	-	-	-	Overturned to upright km-scale folds with NW-SE striking hinge planes
S3	128/36 NE - Regional transpositional fabric	118/38 NE - Transpositional fabric, parallel to structural and lithological boundaries	112/48 NE	109/35 NE	145/36 NE	157/29 E - Transpositional fabric, parallel to structural and lithological boundaries, related to top-to-the-north shearing	STDS parallel foliation. Present at base of THS, deforms S1 and S2
L3	41/028 - Regional mineral stretching lineation	41/022 - Regional mineral stretching lineation	41/002	29/000	29/078	16/087 - Regional mineral stretching lineation	-
F3	Localised folding related to top-to-the-south shearing 'Flattening folds' within quartzites and marbles with L3 & S3 parallel hinges and hinge planes	-	-	-	-	Localised folding related to top-to-the-north shearing	Regional shear-related fold transposes S1 and S2 into parallelism with S3
S4	~E-W Strike, Sub-vertical dip. Crenulation cleavage in pelitic rocks deforms S3.	Sub-parallel to S3. Syn- to post-metamorphic top-to-the-south shear fabric.	-	-	-	151/41 E - Syn- to post-metamorphic top-to-the-south shear fabric, with associated S4 parallel thrust planes	Sub-parallel to S3, always steeper, with associated thrust faults
F4	-	-	-	-	-	129/28 NE - Localised folding related to top-to-the-south shearing deforms S3 foliation and leucogranite bodies.	Kink folds deform S1, S2, S3
S5	178/70 W - Normal faults and associated joint sets	192/83 W - Normal faults and associated joint sets	-	-	-	195/76 E	N-S striking, sub-vertical cleavage. Normal faults and associated penetrative cleavage.

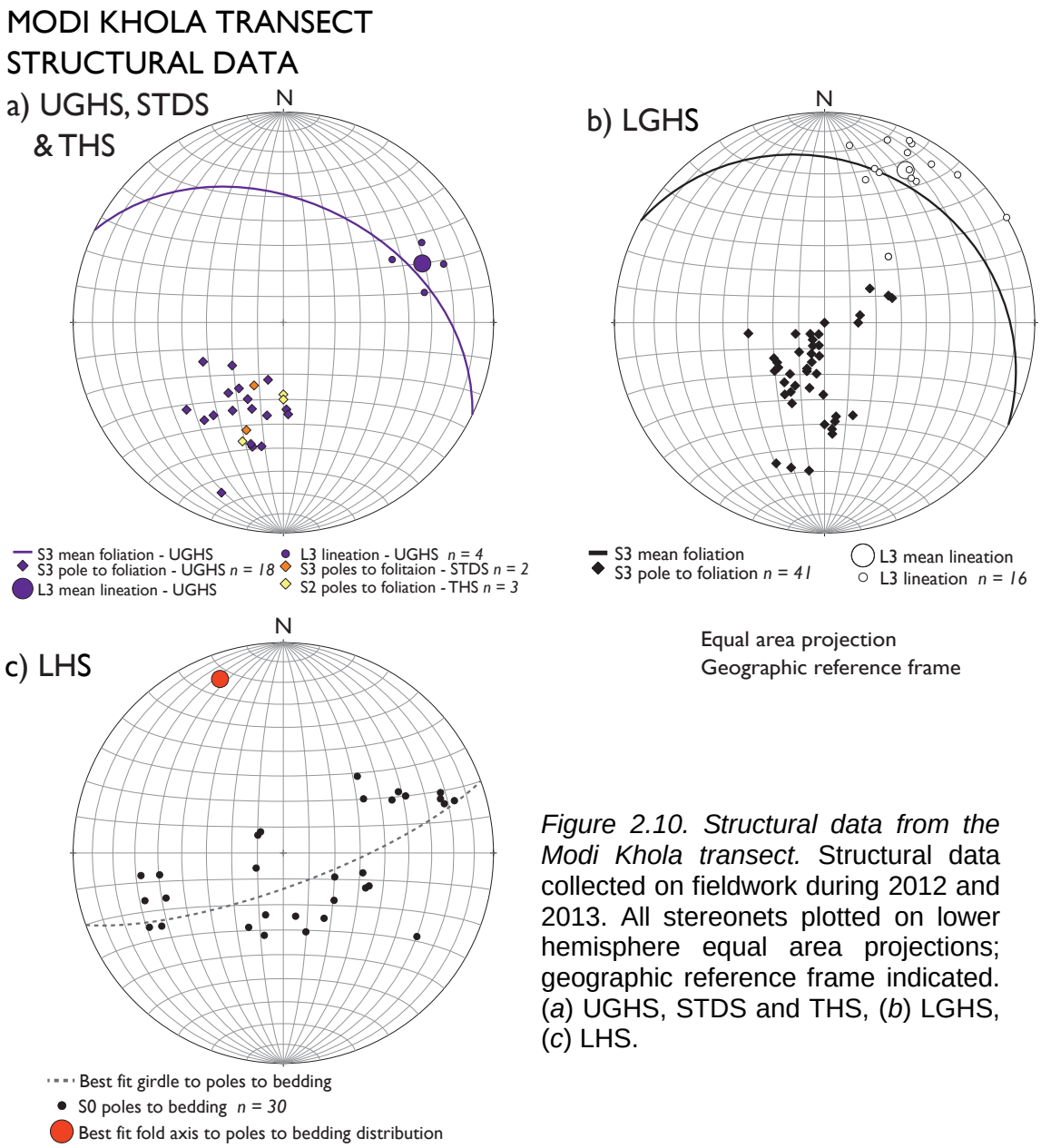

Figure 2.10. Structural data from the Modi Khola transect. Structural data collected on fieldwork during 2012 and 2013. All stereonets plotted on lower hemisphere equal area projections; geographic reference frame indicated. (*a*) UGHS, STDS and THS, (*b*) LGHS, (*c*) LHS.

Within semipelitic and pelitic layers, the mica layers and segregated mineral bands define the foliation as a spaced cleavage. A sub-vertical crenulation cleavage (S4) is sometimes observed striking approximately E-W in pelitic horizons.

In the massive quartzite and marble unit, a strong foliation (S3) and lineation (L3) is defined by mica and quartz or calcite/dolomite alignment and shape preferred orientation (SPO). Quartz veins in the pelitic layers are often folded and commonly show a top-to-the-southwest shear sense (F3). In the Kali Gandaki transect, F3 folds observed within the massive quartzites and marble unit have S3-parallel hinge planes and L3-parallel fold hinges (Figure 2.8b). A minority of quartz veins found above the massive quartzite and marble layer in the Kali Gandaki transect show a top-to-the-north shear sense (Figure 2.8c-e). Top-to-the-north shear above the massive quartzite and marble unit does not necessarily imply that this unit is in extension and there is no

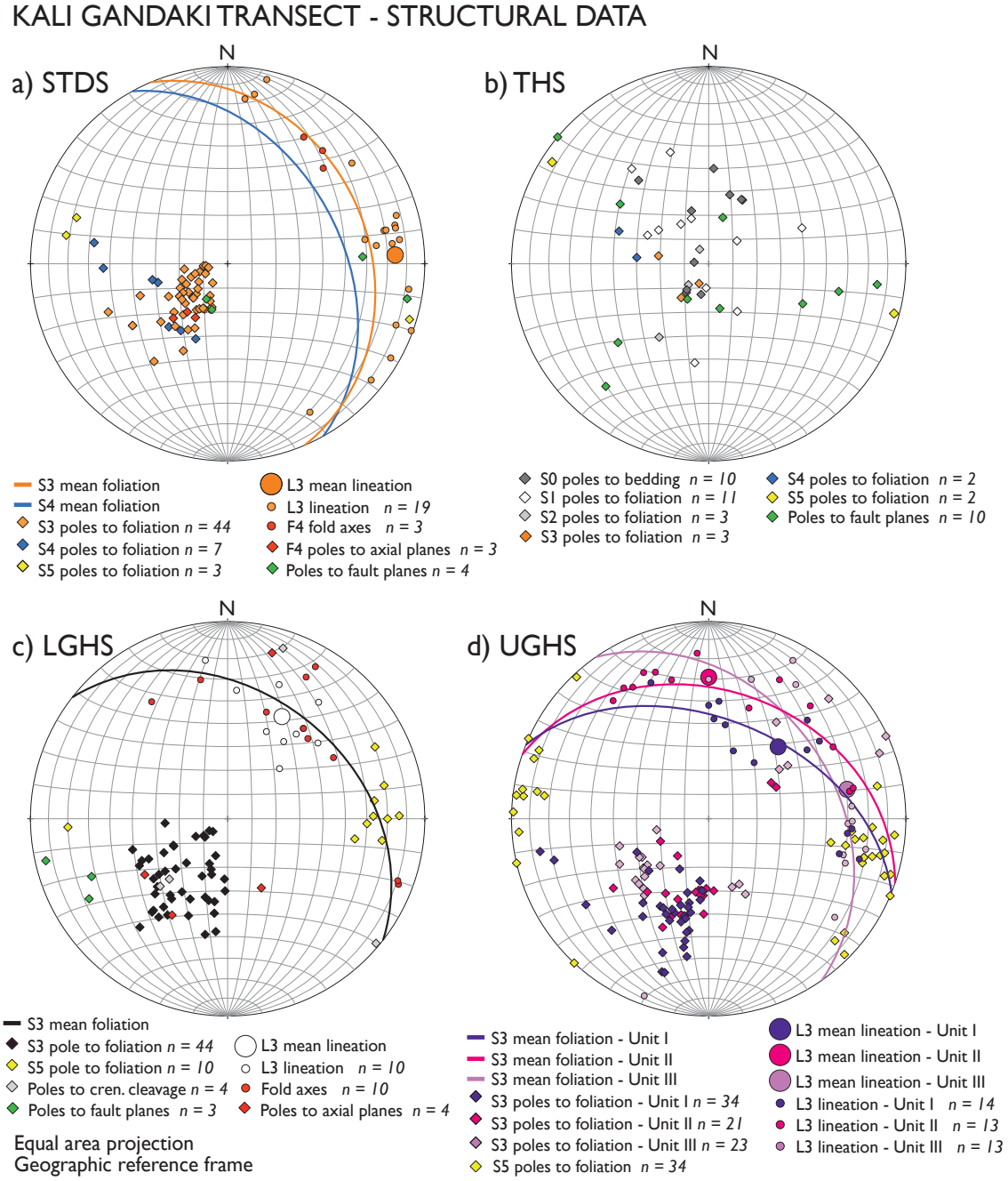

Figure. 2.11. Structural data from the Kali Gandaki transect. Structural data collected on fieldwork during 2012 and 2013. All stereonets plotted on lower hemisphere equal area projections; geographic reference frame indicated. (*a*) STDS, (*b*) THS, (*c*) LGHS, (*d*) USGH.

additional evidence to support such an interpretation. Localised top-to-the-north shearing above the massive quartzite and marble unit only implies that the quartzite and marble unit moved southwards relative to the overlying metapelitic rocks. It is suggested here that localised top-to-the-north shearing occurred during southwards rigid body translation of the massive quartzite and marble units, whilst the overlying metapelitic rocks shortened internally as evident from the S4 crenulation cleavage (Table 2.2). Consequently, the massive quartzite and marble layer has a greater southwards velocity than the overlying metapelitic rocks, resulting in localised top-to-

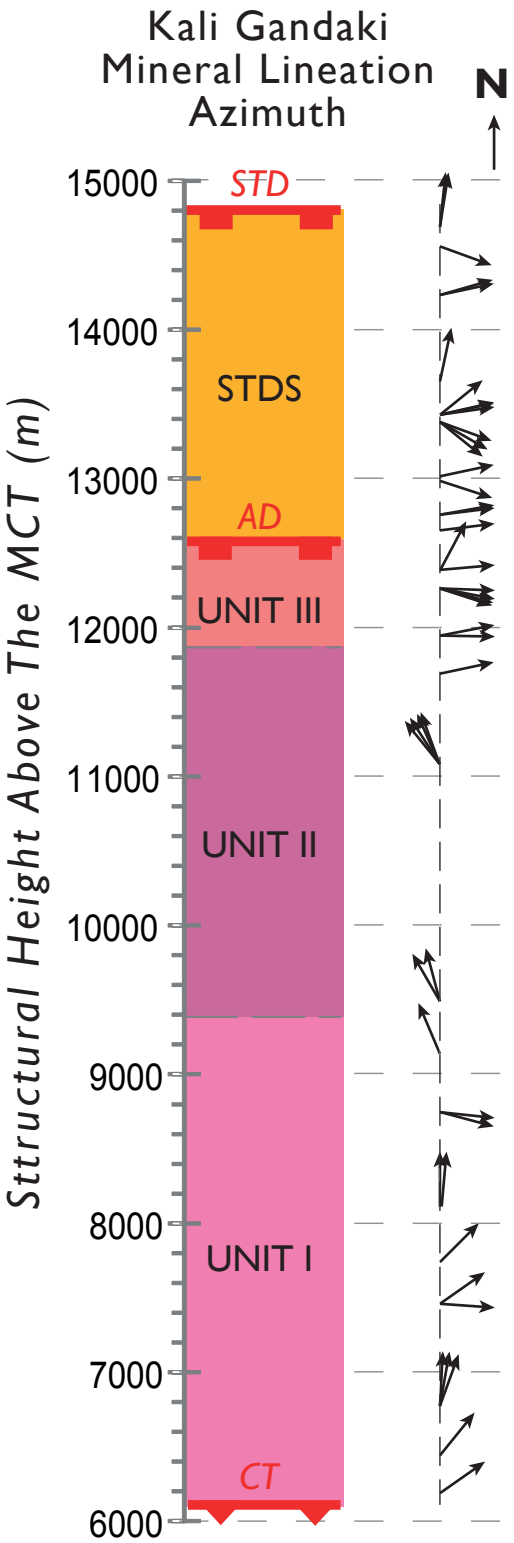

Figure 2.12. Mineral lineation azimuth in the UGHS & STDS, Kali Gandaki transect.

the-north shearing at the interface between the two units.

In the Kali Gandaki transect, late stage normal faults and fractures are recorded with a mean orientation of 178/70 W (Figure 2.11). These are correlated here with the S5 fracture and fault set observed in the UGHS, STDS and THS. This fabric (S5) relates to deformation in the Thakkhola graben (Hurtado *et al.*, 2001; Godin, 2003). A single $^{40}Ar/^{39}Ar$ muscovite cooling age from the LGHS suggests that the sequence exhumed through the closure temperature for Ar loss at 7 Ma (Martin *et al.*, 2014).

2.5.3. UGHS

At the base of the UGHS, the Chomrong Thrust (CT) (Figure 2.6 & 2.7) displays a well-defined S-C fabric (S3) with a top-to-the-southwest shear sense. Crystallisation ages of undeformed leucogranite dykes indicate that motion on the CT occurred before 22-18.5 Ma (Nazarchuk, 1993; Hodges *et al.*, 1996). Approximately 50-100 m up-section of this, on the roadside north of Dana (Figure 2.4), a 5 m thick mylonitic quartzite layer is observed, presumably associated with this motion.

Regional foliation in the UGHS (S3) has a mean orientation of 116/42 NE in the Modi Khola transect and 118/38 NE in the Kali Gandaki transect. Mineral lineations (L3) have a mean orientation of 29/067 and 41/022 in the Modi Khola and Kali Gandaki transects, respectively (Figures 2.10 & 2.11). In the Kali Gandaki transect structural data can be subdivided into the constituent units of the UGHS. Unit I has a mean S3 foliation and L3 mineral lineation of 112/48 NE and 41/022. Unit II has a mean S3 foliation and L3 mineral lineation of 109/35 NE and 29/000 (Figure 2.11). Unit III has a mean S3 foliation and L3 mineral

lineation of 145/36 NE and 29/078 (Figure 2.11), but these do not include data from outcrops of Unit III found on the NE bank of the Kali Gandaki, opposite Lete (Figure 2.4). Foliation in these outcrops dip 36-89^{o} towards the SW and it is likely that these rocks have been deformed by later normal faulting associated with the Thakkhola graben in the upper Kali Gandaki valley (See section 2.4.6). Figure 2.12 shows variations in mineral lineation azimuth with relative structural position in the UGHS and STDS of the Kali Gandaki transect. From bottom to top of the section, lineation azimuth varies with a range of northward to eastward plunging in Unit I, north-northwestern plunging in Unit II and northeastward to southeastward plunging in Unit III and the STDS. The cause for this shift in mineral lineation azimuth is unclear but implies that the kinematic transport direction (*X*) across the UGHS and STDS is not uniform. Instead, it appears that the transport direction varies with, and is partitioned between the different litho-tectonic units, perhaps due to differences in their rheological properties.

Folding (F3) is observed throughout the UGHS, particularly in the migmatitic sections (Figure 2.9a,c). Leucosome bodies have a variety of shapes, ranging from irregular bodies to foliation-parallel layers. In some cases these parallel leucosome layers are deformed by later internal shearing and boudinage (Figure 2.9c).

S3 foliation in Unit III in the Kali Gandaki transect is deformed by the Kalopani Shear Zone (KSZ), which forms a 5-10 m thick top-to-the-southwest reverse sense mylonitic zone (S4), north of Kalopani (Vannay & Hodges, 1996). Similar observations (S4) have been recorded from the top of the UGHS in the Modi Khola valley, relating to deformation on the Modi Khola Shear Zone (MKSZ) (Hodges *et al.*, 1996). The timing of deformation on the KSZ and MKSZ is interpreted as syn- to post-peak metamorphic (Hodges *et al.*, 1996; Vannay & Hodges, 1996). Across the UGHS, localised S4 deformation structures are observed, deforming the regional S3 foliation (Figure 2.9d). Late stage normal faulting and fracture development (S5) associated with deformation in the Thakkhola graben is also observed in the UGHS of the Kali Gandaki transect. S5 fractures have a mean orientation of 192/83 W (Figure 2.11).

Uniform $^{40}Ar/^{39}Ar$ muscovite cooling ages from the UGHS suggest that the sequence was extruded and exhumed to the surface as a coherent single block some time between ~16-12 Ma (Vannay & Hodges, 1996; Godin *et al.*, 2001; Martin *et al.*, 2014). Consequently, shearing on the KSZ and MKSZ must have occurred before this time at a temperature above the muscovite closure temperature for Ar loss (Vannay & Hodges, 1996).

2.5.4. STDS

New mapping in the Kali Gandaki transect (Parsons *et al.*, 2014) relocates the STD north of its previously mapped position (e.g. Larson & Godin, 2009; Searle, 2010) as rocks previously mapped as part of the THS, actually fit definition of GHS rocks as given by Searle (2010) and Searle *et al.* (2008). The new position of the STD is based on an up-section transition from metacarbonate rocks with biotite porphyroblasts and only S3 ± S4 related observable deformation (STDS) to chlorite grade metacarbonate rocks with S1-S4 related observable deformation (THS). This new position reflects the upper structural limit of complete transposition of S1 and S2 fabrics into parallelism with S3. The mapped position of the AD at the base of the STDS in the Kali Gandaki valley is unchanged from Brown and Nazarchuk (1993).

At the base of the STDS, the DD and AD form foliation-parallel normal-sense ductile shear zones with associated mylonitic fabrics and deformed foliation-parallel leucogranite sills (Figure 2.13). In the Modi Khola transect, S3 foliation in the STDS has a mean orientation of 112/36 NE (Figure 2.10). In the Kali Gandaki transect S3 foliation has a mean orientation of 157/29 E and L3 mineral lineations have a mean orientation of 16/087, which is similar to L3 lineations in Unit III of the UGHS (Figure 2.11 & 2.12). This foliation is commonly accompanied by S3-parallel calcite veins. In the Kali Gandaki transect, S3 foliation in the STDS is locally deformed by an S4 foliation with a mean orientation of 151/41 E (Figure 2.11). A similar S4 on S3 fabric relationship is described at the base of the STDS in the Modi Khola transect relating to deformation on the MKSZ (Hodges *et al.*, 1996). Both folding and boudinage of strata are observed in the STDS. The STD bounds the top of the STDS. In the Kali Gandaki transect the STD is identified by the disappearance of S1 and S2 foliations, which are common in the THS, and the dominance of the S3 foliation and lineated biotite porphyroblasts. There is no discrete principal slip surface associated with the STD in the Kali Gandaki transect. In the Modi Khola transect, the STD was not directly sampled due to access limitations. U-Pb chronology of deformed and undeformed leucogranites suggest that the DD was active at ~22.5 Ma (Hodges *et al.*, 1996) and that motion on the AD had ceased by ~22 Ma (Godin *et al.*, 2001). In the Modi Khola transect, the STD was active after 18.5 Ma but may have initiated before this time (Hodges *et al.*, 1996).

In the Kali Gandaki transect the STDS contains folds with normal (top-to-the-north) and reverse (top-to-the-south) senses of vergence. Normal sense F3 folds are associated with normal sense shearing in the STDS and development of the S3 foliation (Figure 2.14). Locally, F4 folds with a top-to-the-south reverse sense vergence deform S3

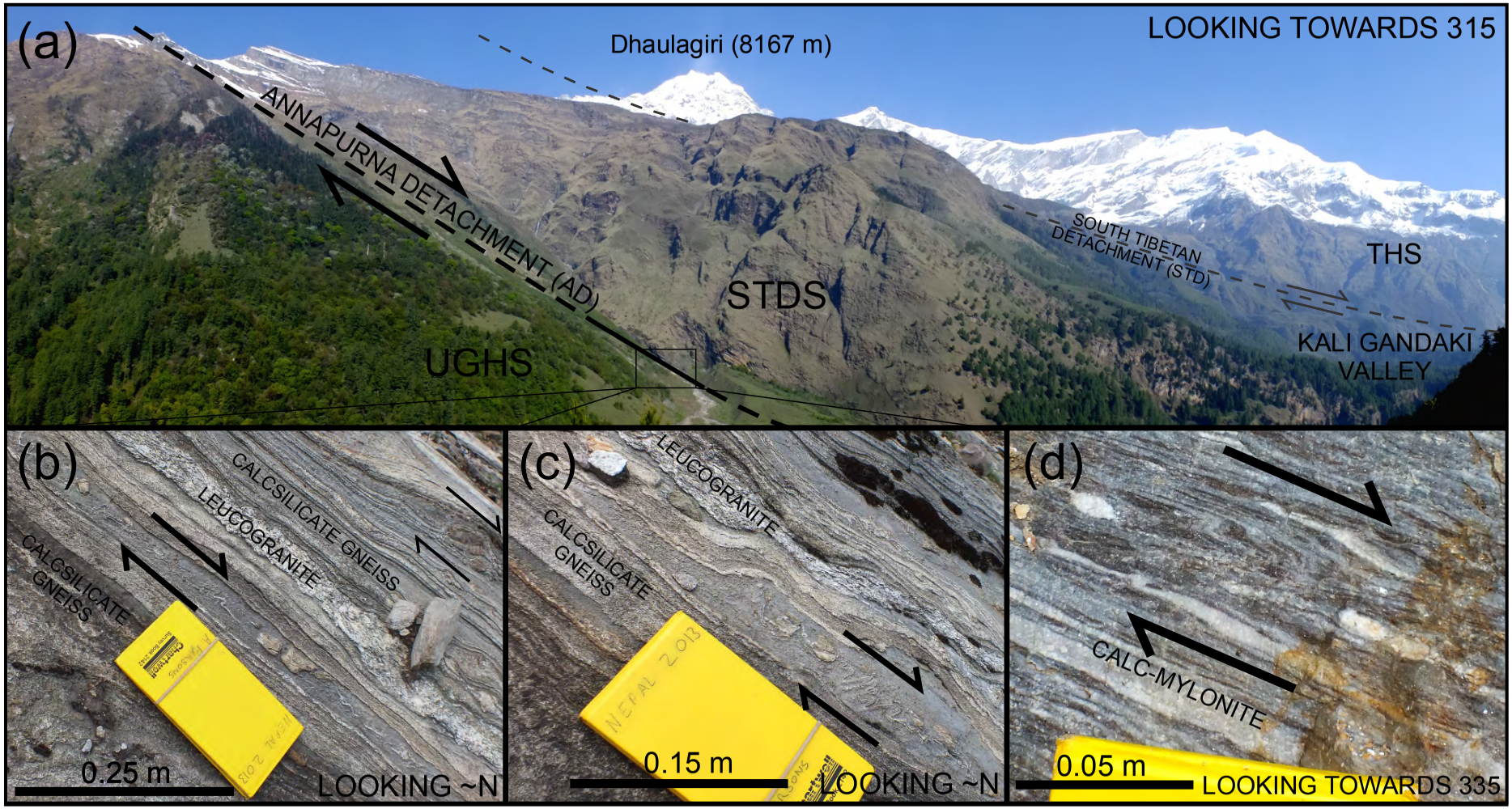

Figure 2.13. Annapurna Detachment (AD) exposed on the Kali Gandaki transect. (*a*) Panoramic photograph of the AD. The AD is accessible at the mouth of the gorge highlighted by small black box, where (*b*) and (*c*) are located. (*b-c*) Sheared and boudinaged calc-silicate gneiss and leucogranite from the AD, recording top-to-the-E normal sense motion. (*d*) Top-to-the-ENE normal sense shearing recorded by a calc-mylonite from the AD, observed at a different location to (*c*) and (*d*). See Figure 2.4 for photo locations.

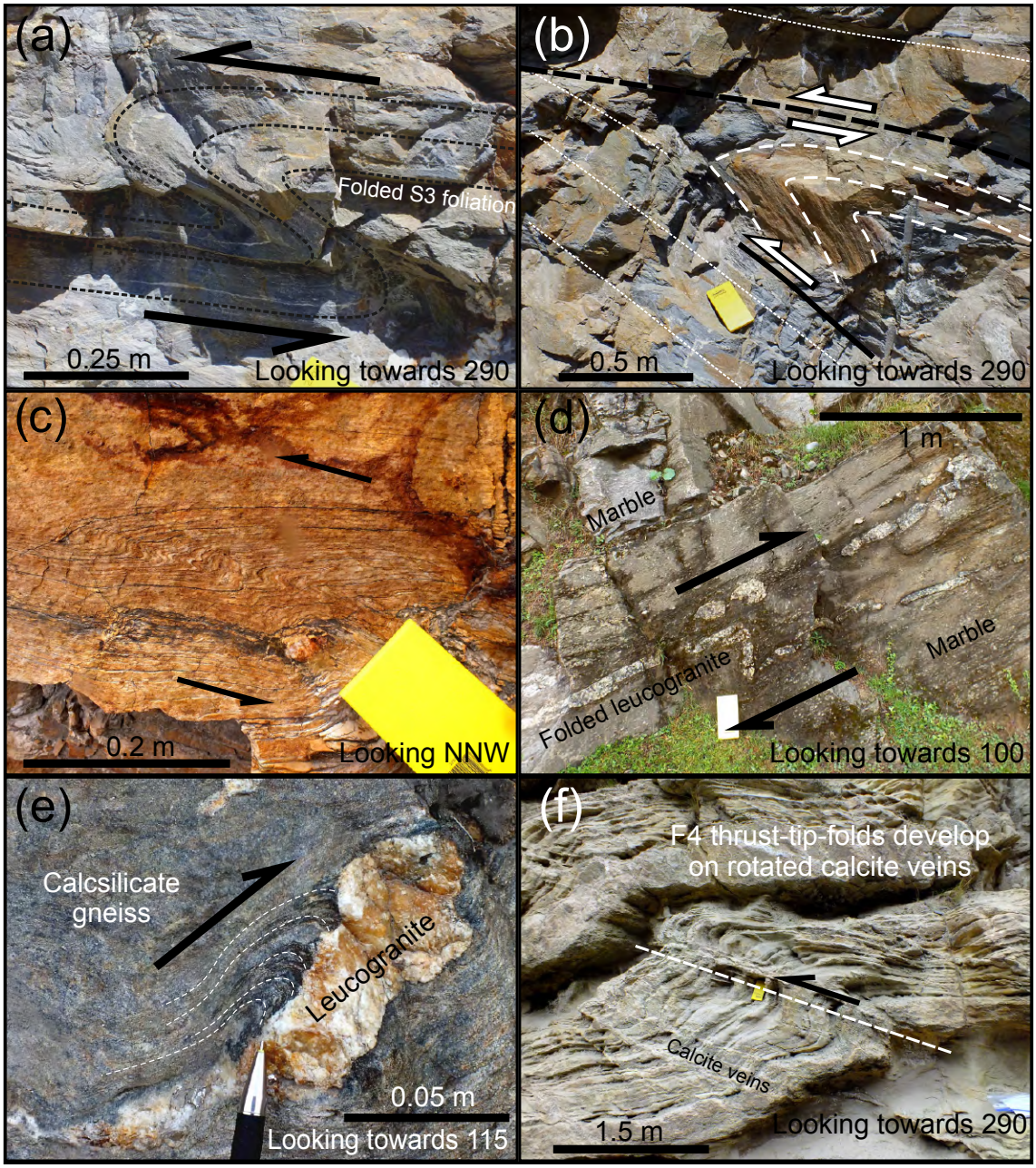

Figure 2.14. Top-to-the-S reverse sense shearing in the STDS and THS, Kali Gandaki transect. (*a-c*) F4 folding and associated top-to-the-SW thrusting deforms S3 foliation in the STDS. F4 folds hinge planes are sub-parallel to S4 foliation. (*d*) Folded and boudinaged leucogranite in the STDS recording top-to-the-S reverse sense motion. Boudins appear to be shortened parallel to the shear direction, suggesting that they formed prior to top-to-the-S shearing. (*e*) Top-to-the-S shearing of S3 foliation on the margin of a leucogranite intrusion in the STDS. Structure suggests that reverse sense shearing occurred after leucogranite emplacement. (*f*) F4 thrust-tip-folding in the THS. S4 related compression has rotated pre-existing calcite veins during top-to-the-S F4 thrust and fold development. See Figure 2.4 for photo locations.

foliation (Figure 2.14). Hinge planes of F4 folds have a mean orientation of 129/28 NE. The timing and orientation of these folds relative to the S3 foliation suggests that they are associated with the development of S4 foliation (F4) in the THS. Leucogranite intrusions in the STDS in the Kali Gandaki transect are also deformed by F4 folding (Figure 2.14d,e). Additionally, brittle thrusts faults are observed in the STDS in the Kali Gandaki transect, parallel to S4. An L4 lineation was not identified. In the Kali Gandaki

transect, the youngest deformation in the STDS is defined by a set of sub-vertical fractures (S5) and associated sub-vertical N-S trending normal faults. S5 fractures have a mean orientation of 195/76 E (Figure 2.11).

2.5.5. THS

The THS is bound by the STD below and the Indus-Yarlung Suture Zone (IYSZ) above (Searle, 2010). The IYSZ is exposed in southern Tibet, north of the mapped area. The structure of the THS in the Kali Gandaki transect has been extensively studied by Godin (2003). In the Kali Gandaki transect (Figure 2.4), bedding (S0) and S1 foliation are sub-parallel. Km-scale F2 folds and an associated S2 axial planar crenulation cleavage deform S1 and S0 (Figure 2.15) (Godin, 2003). F2 folds in the southernmost exposures of the THS are overturned and verge northwards with south dipping hinge planes that are folded into parallelism with the STD (Godin, 2003; Searle, 2010). Northwards of the STD, F2 fold hinge planes progressively rotate, becoming upright in exposures close to Jomsom (Kali Gandaki transect) and dip northwards, north of Jomsom (Godin, 2003; Searle, 2010). These large folds are related to crustal thickening prior to extrusion and exhumation of the GHS (Godin, 2003; Godin *et al.*, 2011). S3 transpositional foliation is present at the base of the THS where S2 cleavage is folded (F3) into parallelism with S3. North dipping S4 foliation and associated thrust faults and kink bands are found throughout the THS S5 foliation forms a N-S striking, sub-vertical cleavage, related to E-W extension of the Thakkhola graben (Hurtado *et al.*, 2001; Godin, 2003).

2.5.6. Thakkhola graben & the Dangardzong fault

The Thakkhola graben is bound to the west by the N-S striking, E-W extending Dangardzong normal fault (Hagen, 1959; Bodenhausen & Egeler, 1971; Bordet *et al.*, 1971), which has a vertical throw of ~4000 m (Figure 2.15 & 2.16). On the eastern side of the upper Kali Gandaki valley, the graben is bound by a series of en-echelon faults known collectively as the Muktinath Fault (Hagen, 1959; Bordet *et al.*, 1971). Sub-vertical NE trending normal faults related to the Thakkhola graben are found throughout the THS and occasionally within the STDS. An associated sub-vertical N-S trending fracture set and cleavage (S5) is observed in the THS, STDS, UGHS and LGHS. Additionally, low angle normal faults are observed within the STDS and lower THS, with east-dipping principal slip surfaces separating GHS/THS footwall rocks and Plio-Pleistocene basin fill hangingwall rocks. These structural associations support suggestions that the STDS is the southern basin-forming margin of the Thakkhola graben (e.g. Godin *et al.*, 2001; Hurtado *et al.*, 2001; Searle, 2010). This is supported

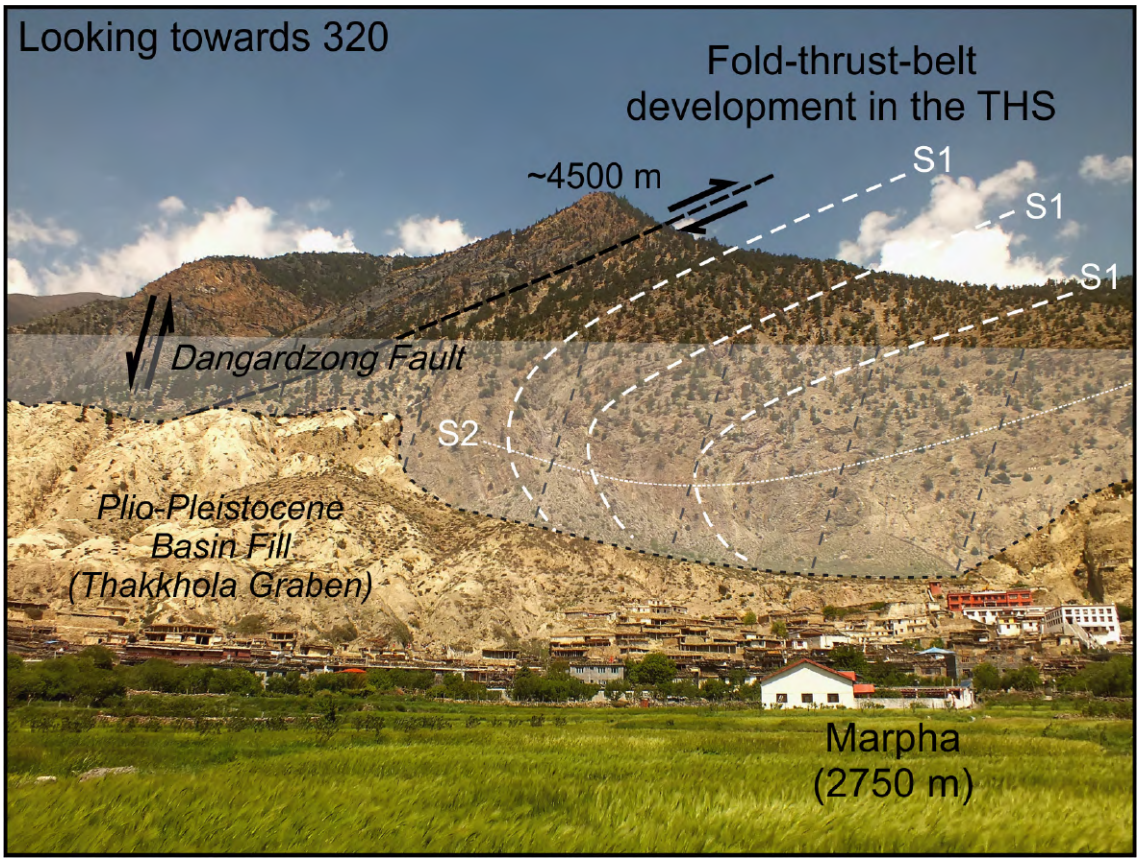

Figure. 2.15. Km-scale folding and late stage extensional faulting in the THS, Kali Gandaki transect. Compressional structures in the THS relate to fold-thrust belt development in the early stages of the Himalayan orogen. F2 folding deformed bedding-subparallel S1 foliation and developed an S2 axial planar foliation. The Dangardzong fault forms the western basin-bounding structure to the Thakkhola graben. Associated basin fil sediments are preserved in the hangingwall of this structure. See Figure 2.4 for photo locations.

by a $^{40}Ar/^{39}Ar$ muscovite cooling age of ~12 Ma from the STDS that is interpreted to be hydrothermally produced due to fluid flow during E-W extension (Godin *et al.*, 2001).

2.5.7. Metamorphic & granitic domes

North of the study area in the Mustang region of the Kali Gandaki valley, the Mugu and Mustang granite domes form the basin margins of the Thakkhola graben (Figure 2.16) (Krummenacher, 1971; Fuchs, 1973; Sorkhabi & Stump, 1993; Le Fort & France-Lanord, 1995; Harrison *et al.*, 1997; Guillot *et al.*, 1999; Hurtado, 2002; Garzione *et al.*, 2003). The Mustang granite is a semi-circular dome in the footwall of the Dangardzong fault that covers an area of *ca.* 325 Km^2 and is characterised by a porphyritic to megacrystic granitic pluton (Le Fort & France-Lanord, 1995; Hurtado, 2002). The Mugu granite is a fine to medium grained two-mica leucogranite with pegmatites containing sillimanite, garnet, tourmaline, biotite and muscovite (Fuchs, 1977; Le Fort & France-Lanord, 1995; Hurtado *et al.*, 2007). The Mugu granite forms an elongate leucogranite batholith that trends NNW over an area of *ca.* 1600 km^2; possibly the largest leucogranite body in the Himalaya (Hurtado, 2002). Deformed and undeformed dykes

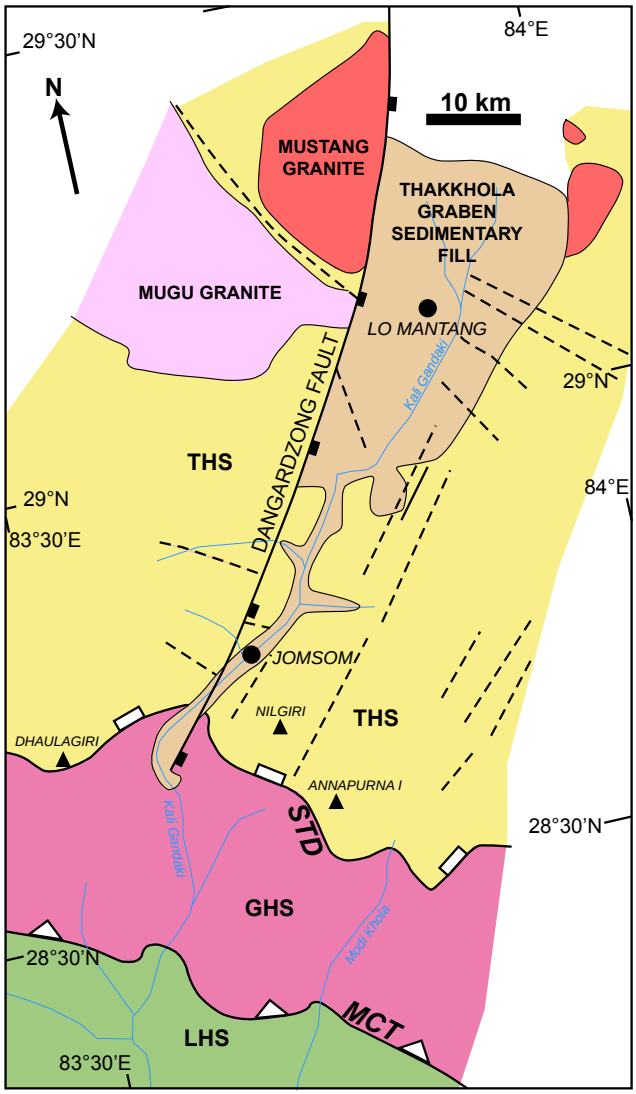

Figure 2.16. Simplified geological map of the Thakkhola graben and Mustang and Mugu granite domes. All units and major structures are labelled on the map. Unnamed normal faults are indicated by dashed lines. Modified after Hurtado *et al.*, 2001 and Hurtado, 2002.

belonging to the Mugu granite cut the Mustang granite and surrounding country rock (Hurtado, 2002). The two granite bodies are interpreted to represent multiple phases of anatexis (Le Fort & France-Lanord, 1995; Hurtado *et al.*, 2007). U-Pb and Th-Pb crystallisation ages indicate that the Mustang granite formed between ~23-24 Ma (Hurtado, 2002), whilst the Mugu granite had a protracted history of emplacement during ~21-17 Ma (Harrison *et al.*, 1997; Hurtado, 2002; Hurtado *et al.*, 2007).

The Mugu and Mustang granites form the core of the Upper Mustang Massif (UMM); a gneissic dome of amphibolite facies calc-silicate gneisses and schists, marbles and calc-phyllites (Fuchs, 1973; Hurtado, 2002). The Dangardzong fault bounds the edge of the UMM, placing biotite grade Tethyan sedimentary rocks in its hangingwall against the sillimanite grade UMM in its footwall (Hurtado, 2002). $^{40}Ar/^{39}Ar$ muscovite ages indicate that the UMM was exhumed above the muscovite closure temperature for Ar loss (380-450 ^{o}C; Harrison *et al.*, 2009) between 15-17 Ma (Guillot *et al.*, 1999; Hurtado, 2002). Additionally, indistinguishable $^{40}Ar/^{39}Ar$ muscovite ages of 17-18 Ma from the footwall and hangingwall of the Dangardzong fault in the Mustang region suggest that both walls exhumed together and hence that faulting occurred before this time (Hurtado, 2002). Mylonitic fabrics with a top-down-to-the-southeast shear sense in the UMM along the edge of the Dangardzong fault suggest that the uplift and exhumation of the UMM may have been kinematically linked to the initial opening of the Thakkhola graben, forming in the same manner as a core-complex (Hurtado, 2002).

2.6. Atypical geological features of the Annapurna-Dhaulagiri Himalaya

This section identifies the observations made from this and previous studies that distinguish the Annapurna-Dhaulagiri region from other parts of the Himalaya. These observations have implications for the local rheological properties of the GHS and form some of the central discussion points presented in the rest of this thesis.

2.6.1. Reduced volumes of leucogranite and sillimanite grade rocks

In the Annapurna-Dhaulagiri region, the volume of leucogranite and sillimanite grade rocks is noticeably lower than elsewhere in the Himalaya (Nazarchuk, 1993; Hodges *et al.*, 1996; Larson & Godin, 2009; Parsons *et al.*, 2014). A key feature in the architecture of the GHS is a high concentration of leucogranite dykes, sills and injection complexes throughout the UGHS and STDS, which typically have maximum combined thicknesses of 100's to 1000's of meters (Figure 2.1) (e.g. Garhwal - Scaillet *et al.*, 1990; Langtang - Inger & Harris, 1992; Manaslu - Harrison *et al.*, 1999; Zanskar - Walker *et al.*, 1999; Bhutan - Grujic *et al.*, 2002; Everest - Searle *et al.*, 2003; Sikkim - Searle & Szulc, 2005; Makalu - Streule *et al.*, 2010a). In the Annapurna-Dhaulagiri region, leucogranite bodies are no larger than 10's of meters in thickness and injection complexes are only observed in the Modi Khola transect and are less densely packed with dykes and sills than typically observed in other regions (Nazarchuk, 1993; Hodges *et al.*, 1996; Larson & Godin, 2009; Parsons *et al.*, 2014). Leucogranite volumes decrease westwards from the Modi Khola transect to the Kali Gandaki transect. The presence of the 3-4 km thick Manaslu leucogranite pluton (Figure 2.2) (Le Fort, 1975, 1981; Colchen *et al.*, 1986), ~70 km east of the Modi Khola transect, suggests that the westwards decrease in leucogranite may be a regional trend.

In general, Himalayan leucogranites are the product of isothermal decompression melting during Early Miocene metamorphism (Harris & Massey, 1994; Searle *et al.*, 2010; Streule *et al.*, 2010a), a process that may still occurring beneath the western syntaxis of Nanga Parbat (e.g. Zeitler *et al.*, 1993). The UGHS in the Annapurna-Dhaulagiri region is dominated by kyanite grade metamorphism, dated between the mid Oligocene to early Miocene (Godin *et al.*, 2001; Corrie & Kohn, 2011; Kohn & Corrie, 2011), synchronous with leucogranite production (Nazarchuk, 1993; Hodges *et al.*, 1996; Harrison *et al.*, 1999; Godin *et al.*, 2001; Larson & Cottle, 2015). Sillimanite is almost entirely absent and only reported from the very top of the UGHS (Arita, 1983; Nazarchuk, 1993; Hodges *et al.*, 1996; Godin *et al.*, 2001; Larson & Godin, 2009; Searle, 2010; Parsons *et al.*, 2014). These observations suggest that decompression

melting during sillimanite grade retrogression did not play an important role during exhumation of the GHS in the Annapurna-Dhaulagiri region. Importantly, reduced melt volumes in the UGHS may have resulted in an increased effective viscosity (*Section 1.3*), relative to other regions, which would hinder the ability of the UGHS to deform via mid-crustal channel flow (Harris, 2007).

2.6.2. Thickness of the UGHS

The UGHS has a structural thickness of ~7 km in the Annapurna-Dhaulagiri region. This is significantly lower than observed elsewhere in the Himalaya (Figure 2.1), where UGHS equivalent stratigraphy have structural thicknesses of 10-15 km (Bhutan - Grujic *et al.*, 2002; Manaslu - Searle & Godin, 2003; Garhwal - Webb *et al.*, 2011b), 20 km (Langtang - Inger & Harris, 1992; Sikkim - Searle & Szulc, 2005) and 30 km (Everest-Makalu - Searle *et al.*, 2003; Jessup *et al.*, 2006; Streule *et al.*, 2010a). The threshold viscosity for mid-crustal channel flow is, in part, controlled by the channel thickness, with thinner channels requiring a lower threshold viscosity (*Section 1.3*) (Grujic *et al.*, 1996; Turcotte & Schubert, 2002; Beaumont *et al.*, 2004). This was demonstrated by thermodynamic numerical simulations of the Himalayan orogen (Beaumont *et al.*, 2001; Beaumont *et al.*, 2006), which were able to sustain mid-crustal channel flow of a homogenous material when channel thicknesses exceeded 10 km. Based on these concepts, the combined effects of a reduced structural thickness and melt volume may imply that the rheological properties of the UGHS in the Annapurna-Dhaulagiri region differ when compared to equivalent strata in other regions.

2.6.3. Reversal of shear sense in the STDS

The STDS forms a top-to-the-north shear zone at the top of the GHS that is observed continuously across the entire orogen (Burg *et al.*, 1984; Burchfiel *et al.*, 1992). In the Kali Gandaki transect, the top-to-the-north (normal) shear fabric is overprinted by a later top-to-the-south (reverse) shear fabric (Figure 2.14 plus Godin *et al.*,1999a and Larson & Godin, 2009). If the STDS formed in response to mid-crustal flow of the underlying crustal material, then the development of this structure reflects the rheological contrast between the strong hangingwall (THS) and weak footwall (UGHS) (e.g. Means, 1989; Williams *et al.*, 2006; Searle, 2010; Kellett & Grujic, 2012). In such a situation, this implies that the STDS is inherently linked to the rheology of the Himalayan orogen. Consequently, the observed top-to-the-south shear overprint reported in the STDS of the Kali Gandaki transect may be a response to a change in the relative rheological properties of the GHS and THS. Thermo-mechanical simulations of channel flow suggest that instability of the upper channel wall (i.e. the THS) could lead to upper crustal extension and top-to-the-south motion on the STDS

as the THS extends southwards faster than the underlying GHS (Beaumont *et al.*, 2004; Jamieson *et al.*, 2006).

2.6.4. Orogen-parallel deformation of the THS and GHS

Stereographic projection of structural data from the UGHS and STDS in the Kali Gandaki transect (Figure 2.11) show an abrupt transition from Unit I and Unit II to Unit III and the STDS from N and NE dipping foliations and mineral lineations to orogen-parallel NE and E dipping foliations and ENE and E plunging mineral lineations. Elsewhere in the Himalaya, such orogen-parallel dip and plunge directions in the STDS and upper UGHS are uncommon (Burg *et al.*, 1984; Burchfiel *et al.*, 1992; Kellett & Godin, 2009; Kellett *et al.*, 2010; Cottle *et al.*, 2011; Law *et al.*, 2011). However, similar E-W orientated lineations have been documented locally in the Manaslu Himalaya from both field structural observations and AMS data (Pêcher, 1991; Guillot *et al.*, 1993) and from other regions further afield in the Himalayan orogen (Xu *et al.*, 2013).

Orogen-parallel deformation of the Himalayan orogen has been recognised in a variety of situations across the mountain belt. Orogen-parallel extension has affected the upper crust of the Himalayan orogen since the late Miocene to the present day (e.g., Hurtado *et al.*, 2001; Jessup & Cottle, 2010; Lee *et al.*, 2011; Styron *et al.*, 2011). Within the THS of the Kali Gandaki valley (Figure 2), E-W extension of the Thakkhola graben is well documented and has deformed the THS since at least 11 Ma (Hurtado *et al.*, 2001; Garzione *et al.*, 2003). Hurtado (2002) presents geochronological data, which suggests that E-W extension initiated before 17 Ma during formation and deformation of the Mustang and Mugu metamorphic domes, which form the footwall of the Dangardzong fault of the Thakkhola graben (Figure 2.16). The occurrence of post-Miocene orogen-parallel deformation in the THS is easily reconciled with present day deformation occurring across the Tibetan Plateau (Styron *et al.*, 2011). Models of strain partitioning into reverse-sense faulting and strike-slip faulting due to oblique convergence between the Indian plate and the arcuate Himalayan orogen provide a favourable explanation for this phenomenon. These processes are suggested to be responsible for development of the Western Nepal Fault System (WNFS), which links the frontal thrust system with the hinterland Karakoram Fault Zone (e.g. Mccaffrey & Nabelek, 1998; Styron *et al.*, 2011; Murphy *et al.*, 2014; Whipp *et al.*, 2014). Interestingly, the WNFS lies only 70 km west of the Thakkhola graben and whilst there is no surficial evidence of a kinematic link, it may be possible that the two structures formed in response to the same stress regime.

Observations of orogen-parallel deformation within the STDS and GHS (e.g. Pêcher *et al.*, 1991; Guillot *et al.*, 1993; Vannay & Steck, 1995; Coleman, 1996; Xu *et al.*, 2013)

are less understood and it is not known whether explanations for the present day orogen-parallel spreading in the THS can be applied to the mid-crustal deformation history of the GHS and STDS. However, orogen-parallel variations in the thickness, lithology and melt content of the GHS that both orogen-perpendicular *and* orogen-parallel pressure gradients may have existed during mid crustal deformation (e.g. Hurtado, 2002; Xu *et al.*, 2013). Some authors have speculated whether or not the STDS and the Thakkhola graben are kinematically linked in this region (Godin *et al.*, 2001; Hurtado *et al.*, 2001; Garzione *et al.*, 2003). E-W lineations recorded in the STDS may support such a link. Importantly, most models of Himalayan orogenesis (e.g. Beaumont *et al.*, 2001; Vannay & Grasemann, 2001; Grujic, 2006; Webb *et al.*, 2007; Robinson, 2008; Larson *et al.*, 2010) assume deformation occurred under a plain strain regime and hence cannot explain the observed orogen parallel deformation of the GHS.

2.7 Conclusions

Field observations from the Annapurna-Dhaulagiri region highlight several features that are *atypical* of the Himalaya orogen. Low volumes of leucogranite and sillimanite grade rocks suggest that isothermal decompression was not an important part of the structural evolution of the region. Additionally, low melt volumes and a reduced structural thickness suggest that the GHS in the Annapurna-Dhaulagiri Himalaya may have been rheologically stronger than equivalent structural/stratigraphic sections in other regions. Reversal of shear sense on the STDS could relate to a change in the rheological structure of the orogen, and may be explained by an increase in the rheological strength of the UGHS relative to the THS during mid-crustal deformation. Additionally, evidence of orogen-parallel deformation within the upper UGHS and STDS may indicate that mid-crustal deformation was driven by both orogen-perpendicular and orogen-parallel pressure gradients. Such processes may stem from or be accountable for lateral variations in lithology, thickness and melt content observed in the GHS across the orogen.

These observations and interpretations indicate that the rheological properties of the GHS are laterally variable on a regional scale. Such factors must be accounted for when attempting to apply tectonic models derived from specific and possibly distinct Himalayan regions to the rest of the orogen. Following a presentation of the results of this thesis in Chapters 3-6, these atypical features shall be discussed further in Chapter 7 and their implications for models of Himalayan orogenesis will be evaluated.

- CHAPTER 3 -

THE THERMO-KINEMATIC EVOLUTION OF THE ANNAPURNA-DHAULAGIRI HIMALAYA

3.1. Introduction

Detailed microstructural analysis is useful for understanding the deformation mechanisms by which tectonic processes occur. Petrofabric analysis provides information on the deformation conditions occurring for plastically deformed rocks, and allows for distinction between dislocation creep, dynamic recrystallisation and diffusive mass transfer mechanisms (e.g. Vernon, 2004; Passchier & Trouw, 2005). Additionally, crystallographic preferred orientation (CPO) analysis of the major mineral assemblages provides an indication of the crystal slip systems active during deformation (e.g. Nicolas & Poirier, 1976; Lister & Williams, 1979; Mainprice *et al.*, 1986; Schmid & Casey, 1986; Wenk *et al.*, 1987; Law, 1990; De Bresser & Spiers, 1997; Barber & Wenk, 2001; Morales *et al.*, 2011; Morales *et al.*, 2014). Importantly, this information provides an invaluable constraint on the temperature ranges at which deformation occurred (e.g. Barber *et al.*, 1981; Mainprice *et al.*, 1986; Wenk *et al.*, 1987; Burkhard, 1993; Okudaira *et al.*, 1995; Kruhl, 1996; De Bresser & Spiers, 1997; Kruhl, 1998; Stipp *et al.*, 2002; Rosenberg & Stünitz, 2003; Delle Piane *et al.*, 2008; Law, 2014).

In this chapter, microstructural observations from samples of the GHS and bounding units in the Annapurna-Dhaulagiri region are reported. This is followed by a detailed description of CPO fabrics of quartz, calcite, dolomite and feldspar measured via Electron Back Scattered Diffraction (EBSD) techniques. A literature summary of available deformation microstructure and CPO fabric thermometers is then provided and used to determine deformation temperatures from the reported microstructures and CPO. Additionally, garnet-biotite Fe-Mg exchange thermometry and Zr-in-titanite thermometry is conducted on 3 and 4 samples from the UGHS of Kali Gandaki transect, respectively. These data, combined with previously published thermometry from both the Modi Khola and Kali Gandaki transect are synthesised to construct deformation temperature profiles of the GHS and bounding units. Finally, these profiles and their implications for the thermo-kinematic evolution of the Annapurna-Dhaulagiri Himalaya are discussed and compared to existing models for Himalayan orogenesis.

Identifying how the distribution of deformation in the GHS and bounding units evolved through dynamic PTt space is fundamental to understanding the kinematic evolution the Himalayan orogen. The data presented in this chapter suggest that channel flow, wedge extrusion and duplexing/underplating (*Sections 1.3-1.4*) were *all* integral to the structural development of the Himalaya. Importantly, the results highlight the dominant

role that rheology has on controlling mid-crustal processes in an evolving orogenic system.

3.2. Deformation microstructures & textures

Microstructural analysis of samples was conducted via optical microscopy of thin sections cut in the *XZ* plane of the kinematic reference frame (*X* parallel to principal stretching direction and inferred transport direction, *Z* normal to foliation). Sample locations are presented in Figures 2.3 to 2.7. *X* is always towards the down dip direction of the measured lineation. The direction of *X* on the thin sections varies between left and right due to differences in the relative orientations of the sample slices cut for thin section preparation. As such shear senses determined from these thin-sections are given in terms of geographic (i.e. top-to-the-northeast) rather than kinematic (i.e. sinistral) shear sense. A full list of all samples analysed can be found in the Supplementary Data CD.

In the descriptions below, the term ‘microstructure’ is used to define a visible crystal structure (e.g. grain boundary morphology, deformation lamellae, subgrains, etc). The term ‘texture’ is used to describe a visible collection of microstructures that forms a distinct compositional structure (e.g. dynamic recrystallisation textures such as grain boundary migration, static recrystallisation textures, grain boundary area reduction textures, etc.). The term ‘fabric’ is used to describe alignments of crystal axes or crystal shapes, and may or may not be visible with optical microscopy (e.g. shape and crystallographic preferred orientations).

3.2.1. LHS

Quartz microstructures in the LHS are typically characterised by static recrystallization textures (also known as foam texture) with euhedral crystal shapes and polygonal grain boundaries. In addition, quartz deformation microstructures, including undulose extinction, deformation lamellae, fluid inclusion trails and brittle fracturing, are common and partially annealed grain boundary bulging (BLG) dynamic recrystallisation textures are also observed (Figure 3.1a). Consequently, the apparent degree of deformation is low compared to samples from the GHS (see below). Relict quartz grains (presumably detrital) appear to have resisted static recrystallization and often contain deformation bands.

3.2.2. LGHS

Partially annealed quartz deformation microstructures in quartzites and semipelites show a progressive transition from a dominance of BLG and subgrain rotation (SGR)

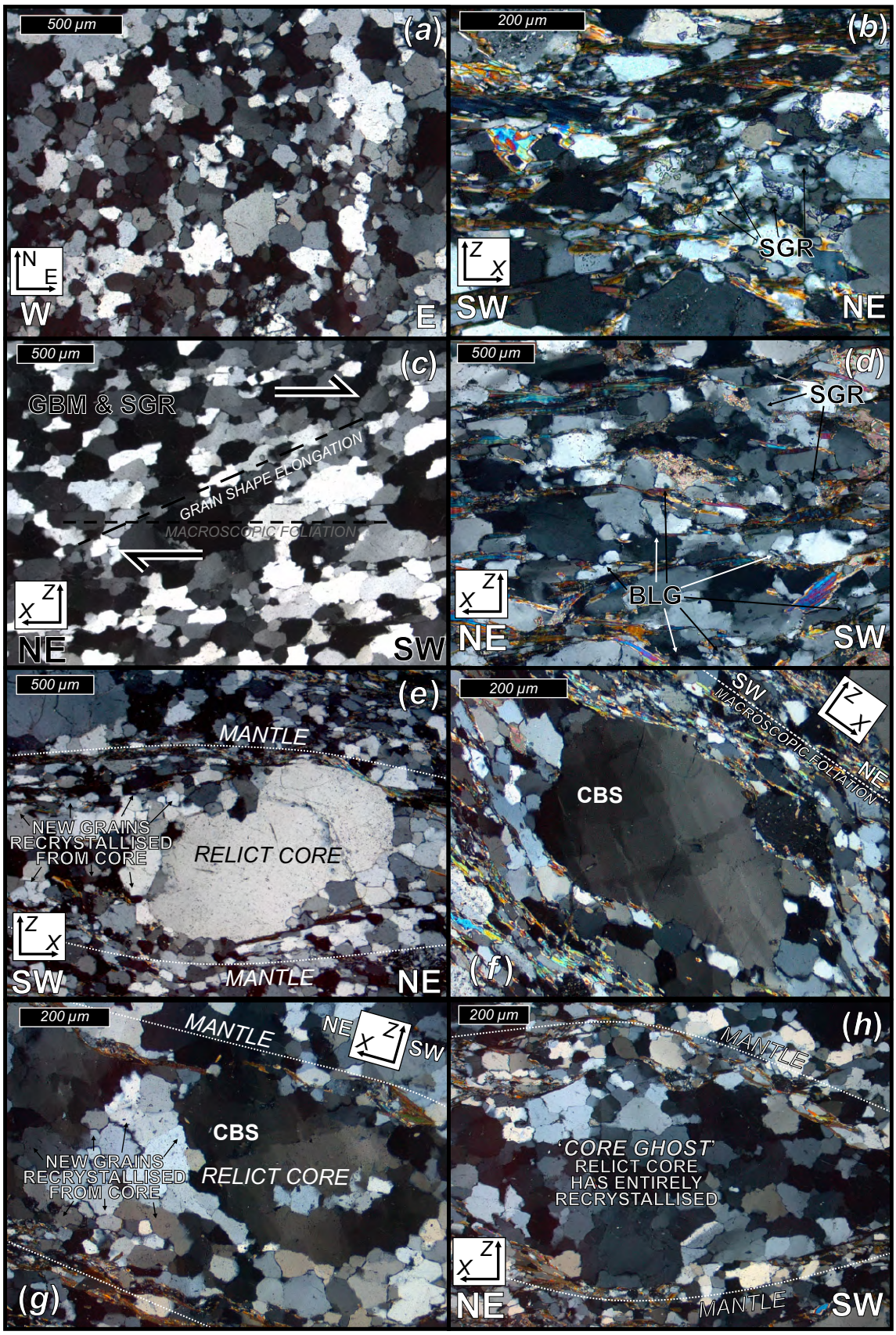

Figure 3.1. Quartz microstructures - LHS & LGHS.

dynamic recrystallisation textures at the base of the LGHS to a dominance of SGR and grain boundary migration (GBM) at the top of the LGHS (Figure 3.1b-d). In the lower portion of the LGHS, quartz porphyroclasts with a larger grain size than the

surrounding matrix are observed (Figure 3.1e-g**)**. Where present, quartz Shape Preferred Orientation (SPO) displays a top-to-the-southwest shear sense (Figure 3.1c). In the Modi Khola transect, quartz porphyroclasts contain deformation bands and subordinate subgrains. In the Kali Gandaki transect, some samples contain quartz porphyroclasts with chess board subgrain (CBS) textures (P13/051, P13/052, Figure 3.1f-g), which form at higher temperatures than SGR and BLG textures (Kruhl, 1996; Stipp *et al.*, 2002; see review by Law, 2014 and references therein). The edges of these porphyroclasts are often partially recrystallized to smaller matrix sized grains, thus forming core-mantle structures (Passchier & Trouw, 2005). These core-mantle structures are usually surrounded by an outer layer of mica, which defines the original grain size and shape of the partially recrystallised quartz core. In some cases, these relict cores are entirely recrystallized, leaving a micaceous layer surrounding an aggregate of matrix-sized quartz grains (Figure 3.1h). These aggregates are referred to as 'ghost cores' to reflect their development from an earlier core-mantle structure. The porphyroclasts are interpreted as relict grains left over from a higher temperature quartz deformation fabric.

In the metapelitic layers, several fabrics are observed (Figure 3.2). The earliest fabric (S1) is preserved in individual quartz-white mica microlithons oriented at high angle to the regional foliation (S3). These microlithons form the relict hinges of a microscopic crenulation cleavage (S2) oriented at an intermediate angle to the regional foliation (S3). This crenulation cleavage is deformed and transposed by the cross cutting S3 foliation (S3) (Figure 3.2a). S1 relict fold hinges contain a higher volume of quartz than the rest of the rock and form a spaced cleavage, parallel to S2. The high angle S1

Figure 3.1. Quartz microstructures – LHS & LGHS. All micrographs viewed in *XZ* plane of kinematic reference frame, except for (*a*), which is viewed in the horizontal plane of the geographic reference frame. (*a*) P12/084 – LHS, Modi Khola. Quartz microstructures indicative of low temperature, low stain deformation. (*b*) P13/053 – LGHS, Kali Gandaki. SGR ± BLG dynamic recrystallisation textures. (*c*) P12/030 – LGHS, Kali Gandaki. SGR + minor GBM dynamic recrystallisation textures. Grain shape elongation inclined against the macroscopic foliation indicates a top-to-the-SW sense of shear. (*d*) P13/049 – LGHS, Kali Gandaki. BLG + SGR dynamic recrystallisation textures. (*e*) P12/078 – LGHS, Modi Khola. Relict quartz porphyroclast has been partially recrystallized into smaller matrix quartz grains to form a core-mantle structure. Shape of relict grain suggests a dextral sense of shear however the core-mantle structure shows no shear sense. (*f-g*) P13/052, P13/051 – LGHS, Kali Gandaki. Relict quartz porphyroclast with CBS texture. Relict grains form partially recrystallised cores of larger core-mantle structures. Samples have been rotated with respect to the microscope to highlight sub grains. (*g*) P13/051 – LGHS, Kali Gandaki. Recrystallised matrix grains surrounded by a layer of mica that defines shape and size of a 'ghost core'. The original relict quartz core has been entirely recrystallized into smaller matrix grains, but the mica layer that surrounded the porphyroclast has remained intact. Sample locations presented on Figures 2.3 & 2.4. Full sample description presented in sample list in the Supplementary Data CD.

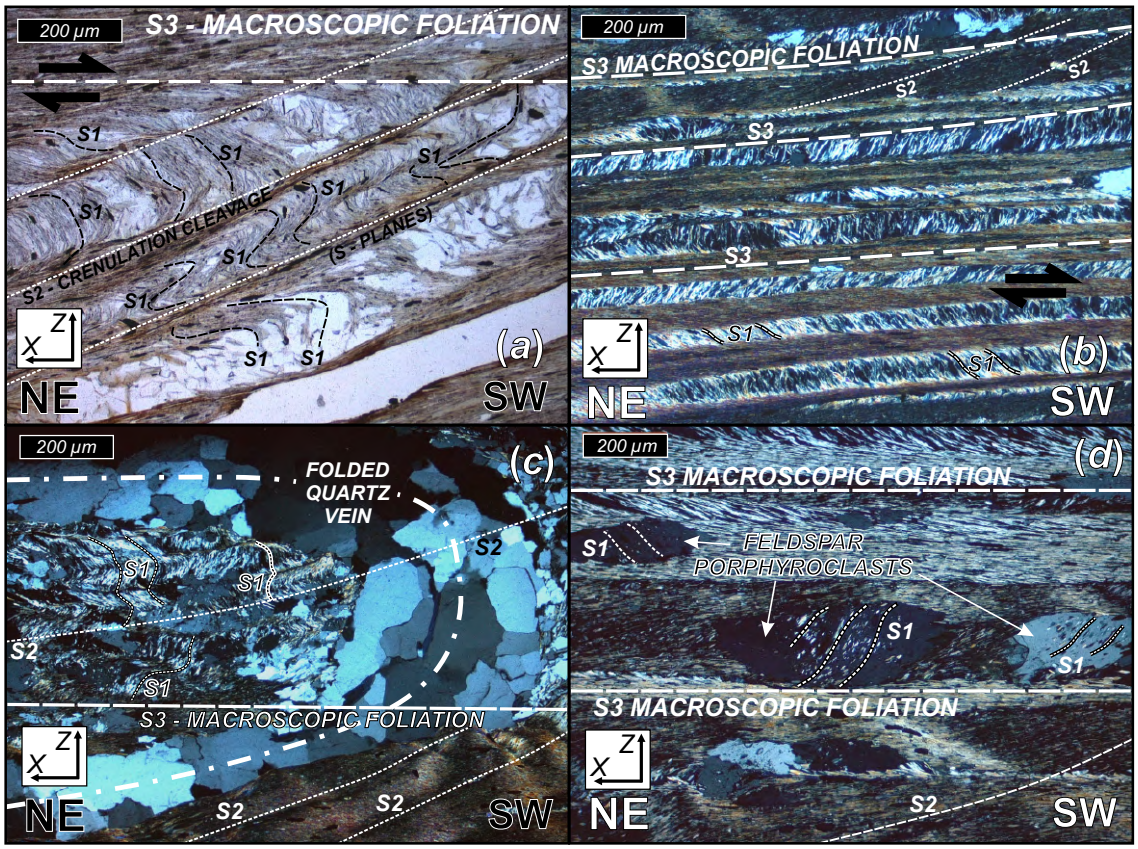

Figure 3.2. Polyphase deformation of metapelitic rocks – P12/071, LGHS, Modi Khola. All micrographs viewed in *XZ* plane of kinematic reference frame. (*a*) The earliest fabric (S1) is preserved at a high angle to the regional foliation, in the relict hinges of a subsequent crenulation cleavage (S2). Repetition of quartz-rich relict fold hinges and micaceous crenulation cleavage forms an S2-parallel spaced cleavage. S2 crenulation cleavage is inclined against the macroscopic foliation (S3). S3 forms the regional foliation and deforms and transposes S2. (*b*) S2 crenulation cleavage hinges form microlithons that preserve an S1 fabric. Microlithons are sub-parallel to the regional S3 top-to-the-SW shear fabric. (*c*) Isoclinally folded quartz vein with S2 parallel fold hinge trace. Fold hinge zones preserve a micaceous S1 foliation. (*d*) Feldspar porphyroclasts aligned parallel to S3 with micaceous inclusions. Orientation of inclusion trails suggests that feldspar porphyroclasts grew after or during development of the S2 crenulation cleavage; porphyroclast preserve deformed S1 fabric. Sample locations presented on Figures 2.3 & 2.4. Full sample description presented in sample list in the Supplementary Data CD

foliation is also preserved as mica inclusion trails in feldspar porphyroclasts (Figure 3.2d). Isoclinally folded quartz veins are also observed with S2 parallel axial traces (Figure 3.2c).

Within the metacarbonates (50-80% carbonate) and dolomitic marbles (≥80% carbonate) at the top of the LGHS, dolomite and calcite grains have a tabular shape with long axes orientated sub-parallel to the foliation (S3) and show signs of grain boundary area reduction (GBAR) (Figure 3.3). Calcite grains commonly display type I and II twinning and occasionally preserve type III twins (Figure 3.3a), following Burkhard (1993). Dolomite grains are also twinned. Where preserved, quartz grains commonly display BLG and SGR recrystallisation textures and less commonly display

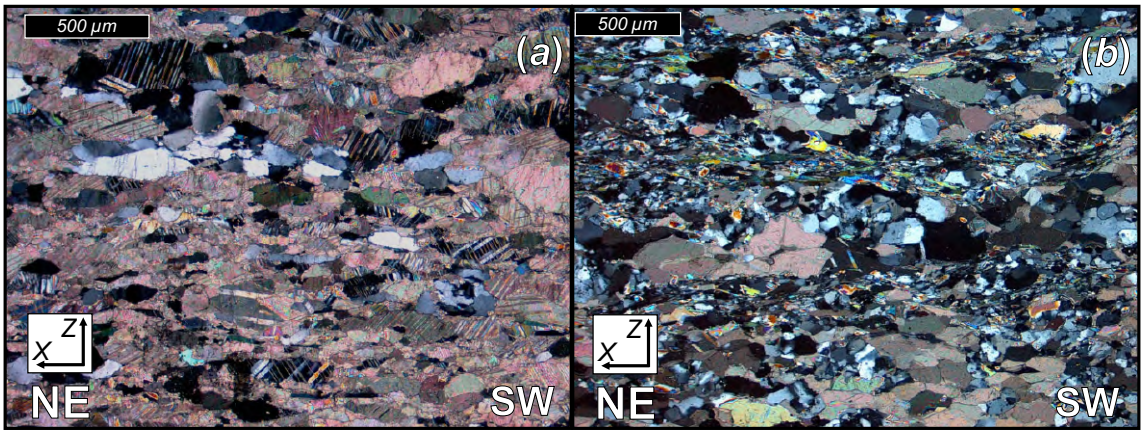

Figure 3.3. Metacarbonate / Marble microstructures – LGHS. Both micrographs viewed in *XZ* plane of kinematic reference frame. (*a*) P12/026 – marble, Modi Khola. Tabular grains of calcite and dolomite aligned parallel to the regional foliation. Type I and type II twinning is observed. (*b*) P12/068 – metacarbonate, Kali Gandaki. Calcite microlithons surrounded by quartz and mica layers. Sample locations presented on Figures 2.3 & 2.4. Full sample description presented in sample list in the Supplementary Data CD.

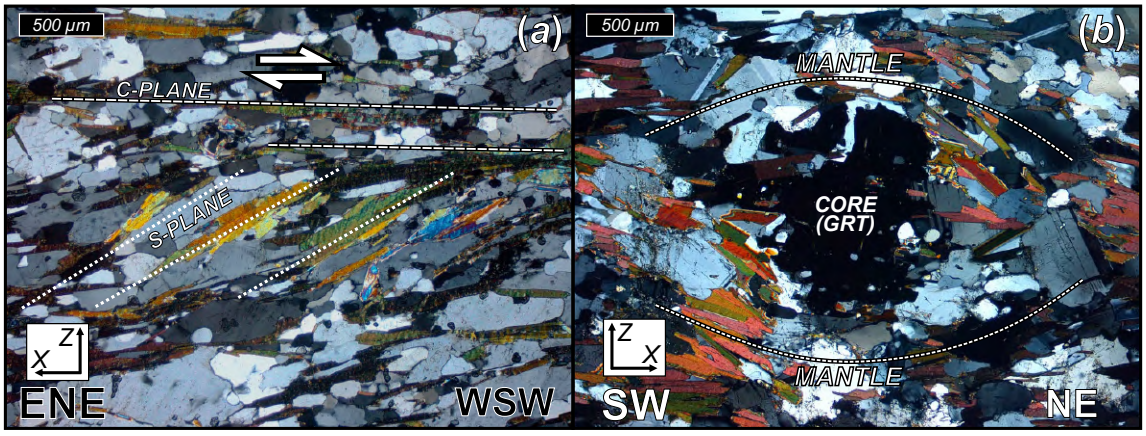

Figure 3.4. Shear sense indicators in the UGHS. Both micrographs viewed in *XZ* plane of kinematic reference frame. (*a*) P3/046 – Unit I, Kali Gandaki. Top-to-the-WSW S-C fabric from hangingwall of the CT. (*b*) P12/059 – Unit I, Kali Gandaki. Core-mantle structure around a garnet porphyroblast with no discernible shear sense. Sample locations presented on Figures 2.3 & 2.4. Full sample description presented in sample list in the Supplementary Data CD.

GBM recrystallisation textures.

3.2.3. UGHS

The UGHS displays a variety of high temperature deformation microstructures. GBAR of all minerals is common throughout the UGHS, with tabular and elliptical grains orientated with their long-axes parallel to foliation, except for secondary muscovite that does not always display a preferred orientation. Grain SPO does not give any indication of shear sense, except for samples P13/045, P3/046 and P12/061 from the base of the UGHS in the Kali Gandaki transect, which have a well-defined top-to-the-WSW S-C fabric (Berthé *et al.*, 1979) and quartz SPO (Figure 3.4a). These basal samples from the Kali Gandaki transect display SGR and GBM quartz recrystallisation

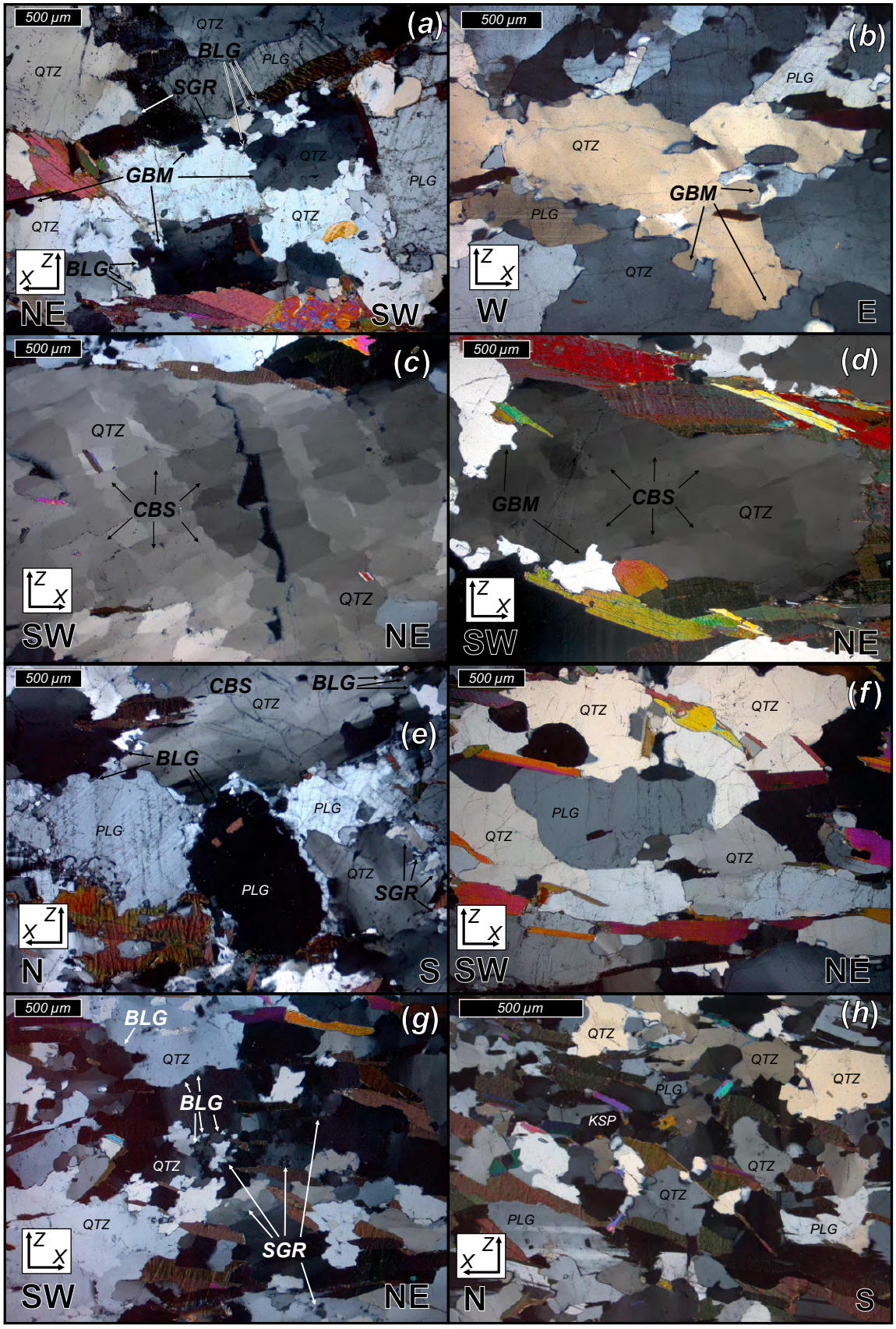

Figure 3.5 Quartz microstructures - UGHS

textures. Quartz microstructures observed in the rest of the UGHS in the Kali Gandaki transect and in the whole of the UGHS in Modi Khola transect are dominated by GBM ± CBS recrystallisation textures (Figure 3.5).

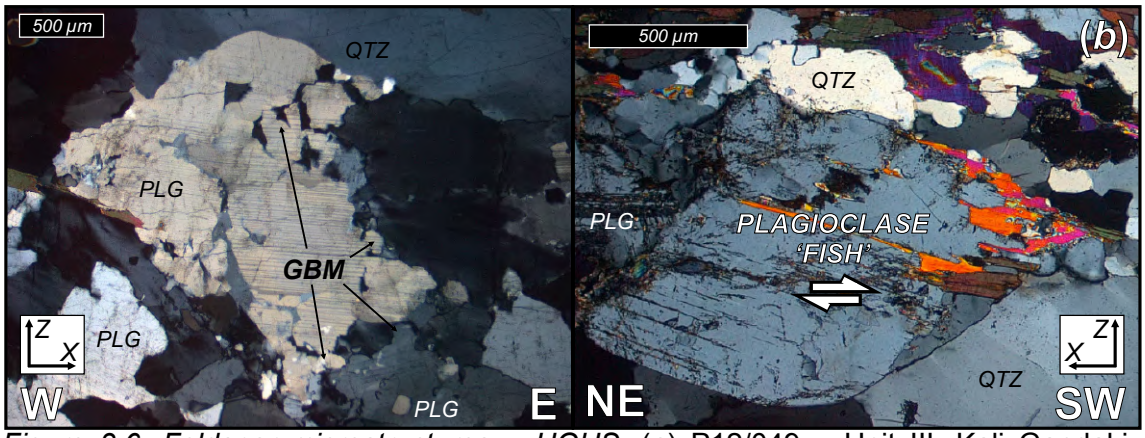

Figure 3.6. Feldspar microstructures – UGHS. (*a*) P12/049 – Unit III, Kali Gandaki. GBM dynamic recrystallisation of plagioclase. (*b*) P12/059 – Unit I, Kali Gandaki. Diffusive mass transfer of plagioclase, during top-to-the-SW shearing. Sample locations presented on Figures 2.3 & 2.4. Full sample description presented in sample list in the Supplementary Data CD.

In the Modi Khola transect, quartz microstructures also display a subordinate overprint of BLG + SGR recrystallisation textures (Figure 3.5a,e,g). This overprint is not observed in the UGHS in the Kali Gandaki transect (Figure 3.5b,f,h). Feldspar grains display GBM and BLG recrystallisation textures and diffusion creep textures (e.g. 'fish' grain shapes) (Passchier & Trouw, 2005) and both growth and deformation twins are common (Figure 3.6). Myrmkitic feldspars are observed throughout the UGHS and are most common in the Modi Khola valley. Garnet porphyroblasts commonly contain inclusions and are sometimes mantled by grains of mica, but these structures rarely show any indication of rotation (Figure 3.4b).

3.2.4. STDS

Calcite and dolomite grains in the STDS have an elongate tabular shape with grain long axes parallel or sub parallel to the foliation. Where SPO long axes are inclined to the foliation, either top-to-the-NW to top-to-the-SE (normal motion; P12/045, P13/005, P13/025, P13/026) or top-to-the-ESE to top-to-the-SW (reverse motion; P12044,

Figure 3.5. Quartz microstructures – UGHS. (*a*) P12/015 – Unit I, Modi Khola. GBM dynamic recrystallisation of quartz with a subordinate low temperature deformation overprint of SGR + BLG textures. (*b*) P12/049 – Unit III, Kali Gandaki. GBM dynamic recrystallisation of quartz with no lower temperature deformation overprint. (*c*) P12/017 – Unit I, Modi Khola. CBS textures in large quartz porphyroclasts. (*d*) P12/058 – Unit I, Kali Gandaki. CBS textures in large quartz porphyroclasts. (*e*) P12/012 – Unit III, Modi Khola. GBM dynamic recrystallisation and CBS textures in quartz with a subordinate low temperature deformation overprint of SGR + BLG textures. (*f*) P12/060 – Unit I, Kali Gandaki. GBM of quartz with no lower temperature deformation overprint. (*g*) P12/017 – Unit I, Modi Khola. GBM dynamic recrystallisation of quartz with a subordinate low temperature deformation overprint of SGR + BLG textures. (*h*) P12/055 – Unit I, Kali Gandaki. GBM of quartz with no lower temperature deformation overprint. Sample locations presented on Figures 2.3 & 2.4. Full sample description presented in sample list in the Supplementary Data CD.

P13/006, P13/008) sense shear is indicated locally, with most top-to-the-SW sense SPOs produced in the upper portion of the STDS (Figure 3.7). Field structural observations (Figure 2.13) indicate that the top-to-the-southwest fabrics are younger (S4) than the top-to-the-NE fabrics (S3). Type I and II twinning of calcite is commonly observed in the STDS. In the Kali Gandaki transect, type III calcite twinning is observed in samples from the base of the STDS and dolomite twinning is observed in samples from both the upper and lower margins. Partial annealing and calcite and dolomite GBAR textures are also observed in the STDS in the Kali Gandaki transect; GBM and BLG textures are less commonly observed. At the very top of the STDS, STD-related mylonitic calcite textures are observed. In the Modi Khola transect, dolomite from the top of the STDS displays deformation twins.

Quartz grains in the lower half of the STDS from the Modi Khola transect display GBM and CBS recrystallisation textures with a subordinate overprint of BLG recrystallisation textures, whilst plagioclase displays GBM + GBAR textures. In the Kali Gandaki transect, quartz grains in the STDS are less deformed. Where present, amalgamations of quartz grains show SGR and BLG textures in the lower portion of the STDS. More commonly, quartz grains are present as circular, isolated grains with no deformation microstructures, surrounded by calcite.

At the base of the STDS in the Kali Gandaki transect, hornblende porphyroblasts form core-mantle structures with a top-to-the-E shear sense. Phlogopite and biotite are commonly found in rocks from the STDS (Figure 3.7). These minerals often form a spaced cleavage, separated by bands of calcite and quartz that define the foliation in the rock. The upper half of the STDS in the Kali Gandaki valley contains biotite porphyroblasts, some of which are retrogressed to chlorite. In the middle of the STDS, these porphyroblasts are equant and euhedral in shape and locally form core-mantle structures with either top-to-the-S (Figure 3.7c) or top-to-the-ESE (Figure 3.7g) shear senses. Towards the top of the STDS, these biotite porphyroblasts become increasingly flattened, boudinaged and rotated, with an alignment parallel to foliation (Figure 3.7a,c,g,h). These mineral fabrics are related to S3 and L3 foliation and lineation development, which pre-date the N-S striking, sub-vertical S5 cleavage and fracture set. In addition, these fabrics are parallel to S3 and L3 structures in Unit III of the UGHS, and associated shear fabrics observed on the AD. As such, E-W orientated SPO and CPO fabrics described from the STDS are related to E-W directed pervasive shearing on the AD during ductile extrusion of the GHS. They do not record deformation associated with the E-W extension of the Thakkhola graben.

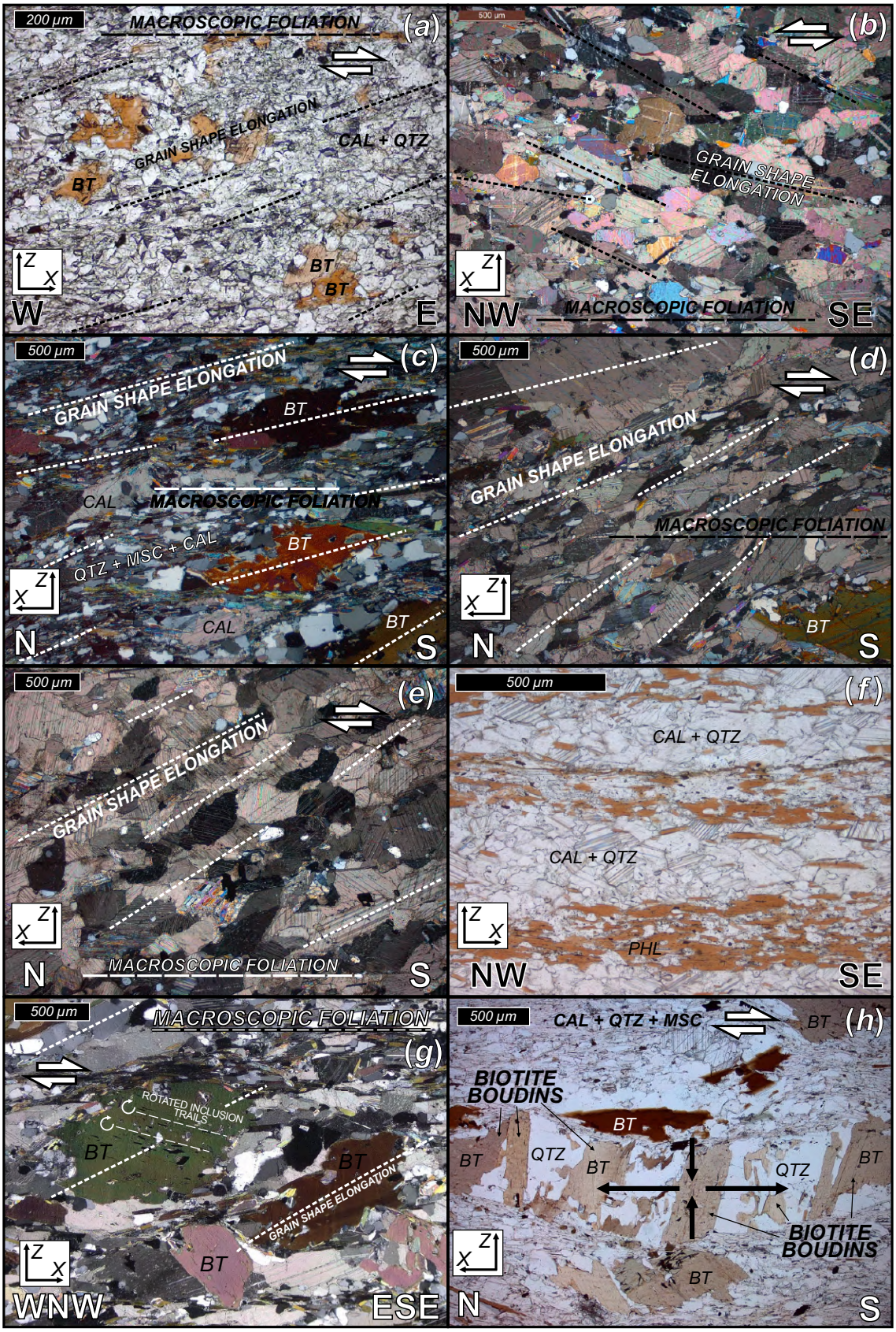

Figure 3.7. Shear sense indicators in the STDS - Kali Gandaki.

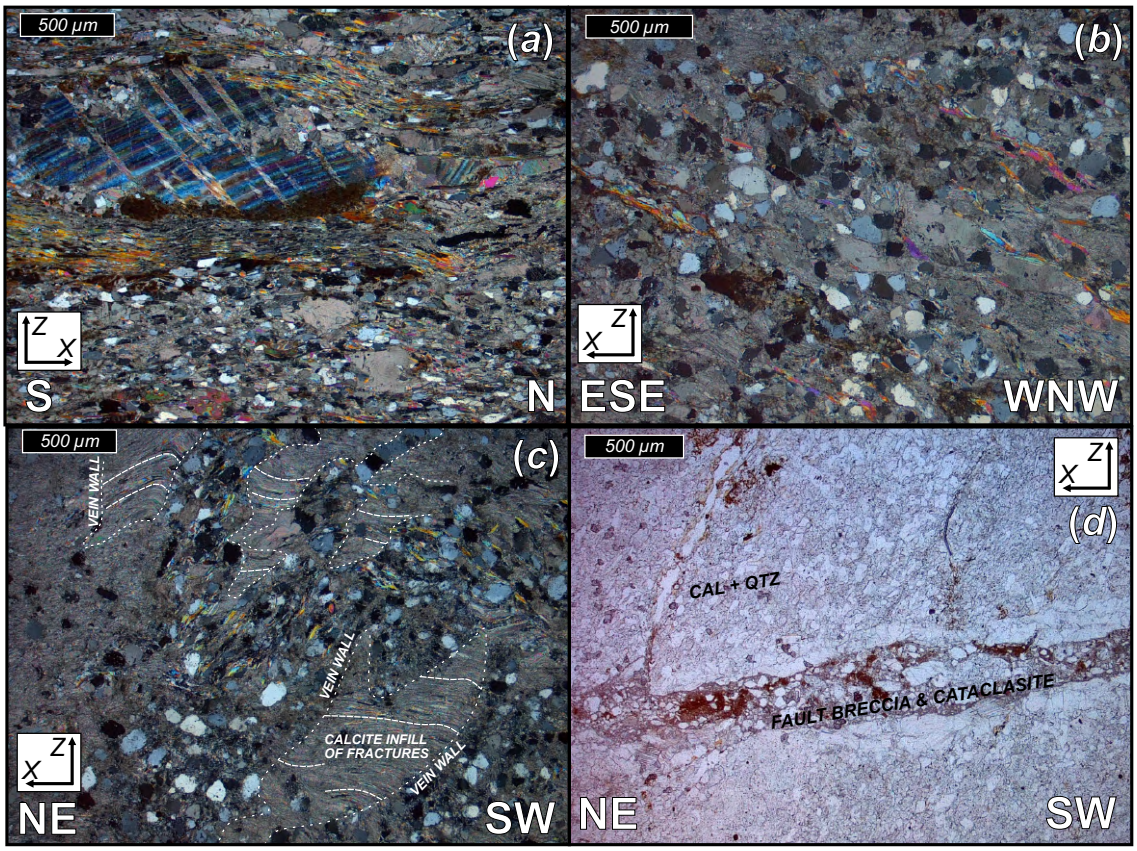

Figure 3.8. Microstructures in the THS – Kali Gandaki. (*a*) P12/037 – Type I and II calcite twins. Mica and calcite accommodate intracrystalline deformation whilst quartz behaves as isolated rigid grains. (*b*) P12/038 – Isolated undeformed quartz grains in a calcite matrix. Mica grains define a top-to-the-ESE shear fabric. (*c*) P12/039 – Calcite 'feathered wing-like' structures are interpreted to be the result of rapid calcite growth within fractures. Isolated quartz grains are undeformed. (*d*) P12/039 - Fault breccia and cataclasite within fractured metacarbonate rock. Sample locations presented on Figures 2.3 & 2.4. Full sample description presented in sample list in the Supplementary Data CD.

3.2.5. THS

Microstructures in the THS have been studied in detail using samples from the Kali Gandaki transect. At the base of the THS, microstructures record both brittle and

---

Figure 3.7. Shear sense indicators in the STDS – Kali Gandaki. (*a*) P13/005 – Grain shape elongation of calcite, quartz and mica records top-to-the-E (normal) sense shear from the footwall of the STD. (*b*) P13/026 - Grain shape elongation of calcite and dolomite records top-to-the-NW (normal) sense at the base of the STDS. (*c*) P13/008 - Grain shape elongation of calcite, quartz and mica matrix grains and biotite porphyroblasts records top-to-the-S (reverse) sense shear from top of the STDS. (*d*) P13/008 - Grain shape elongation of calcite records top-to-the-S (reverse) sense shear from top of the STDS. (*e*) P13/006 - Grain shape elongation of calcite records top-to-the-S (reverse) sense shear from the footwall of the STD. (*f*) P12/045 – Spaced cleavage of phlogopite-rich bands and calcite- and quartz-rich bands at the base of the STDS with no discernible shear sense. (*g*) P12/044 – Grain shape elongation of biotite porphyroblasts records top-to-the-ESE (normal) sense shear. Inclusion trails in biotite record a dextral rotation relative to the foliation. (*h*) P13/008 – Boudinage of biotite porphyroblast. Quartz infills gaps between boudins. Sample locations presented on Figures 2.3 & 2.4. Full sample description presented in sample list in the Supplementary Data CD.

ductile deformation. Calcite grains are small and anhedral and commonly display type I and occasionally type II twins, with signs of grain growth around equant grains of undeformed quartz (Figure 3.8). Bands of mica grains with a high aspect ratio, oriented parallel to the foliation, are common, as are foliation-cross-cutting fractures and cataclastic calcite (Figure 3.8). 'Feathered wing-like' calcite amalgamations are also observed that appear to have formed as vein-calcite precipitating rapidly into voids and fractures that formed during deformation (Figure 3.8d). These microstructures are observed in the lower ~1.5 km of the THS and are interpreted as deformation relating to motion on the STD. Above this structural level, microstructures are dominated by the local foliation, which is commonly picked out by a spaced cleavage between mica and quartz and/or calcite bands that is likely to correlate with the regional S1 foliation (*See section 2.5.5.*). A cross cutting crenulation cleavage (S2) is also commonly observed. In the Modi Khola transect, a semipelite contains quartz grains with low temperature transitional brittle-crystal plastic structures such as undulose extinction, deformation lamellae and fractures.

3.3. Crystallographic preferred orientations (CPOs) & active slip systems

Quartz, calcite and dolomite CPOs are studied to determine shear sense (Behrmann & Platt, 1982), strain geometry (e.g. Lister & Williams, 1979; Vollmer, 1990) and which crystal slip systems were active during deformation (e.g. Schmid & Casey, 1986; Bestmann & Prior, 2003). The latter may also provide an indication of the temperature at which each CPO formed (e.g. Barth *et al.*, 2010; Law, 2014).

CPO analysis was conducted on samples from the Kali Gandaki and Modi Khola transects via Scanning Electron Microscopy (SEM), using Electron Back Scattered Diffraction (EBSD) (Prior *et al.*, 1999). SEM/EBSD analyses were carried out using an FEI Quanta 650 FEGSEM with an Oxford Instruments INCA 350 EDX system, 80mm X-Max SDD detector and a KE Centaurus EBSD system. Square samples (~17-18 mm) were prepared in resin blocks and polished initially with alumina powders and diamond paste and finally using a colloidal silica solution (Lloyd, 1987). EBSD data were collected via automated stage movement from the *XZ* plane of the kinematic reference frame (*X* parallel to principle stretching direction and inferred transport direction, *Z* normal to foliation), measuring CPOs of the major constituent minerals of each sample. Oxford Instruments Channel5 software was used for data acquisition and MTEX open source software toolbox (Bachmann *et al.*, 2010) for MATLAB (MathWorks, Inc.) was used for data processing and pole figure plotting. CPOs are graphically represented on pole figures (stereographic projections) contoured in multiples of uniform distribution (m.u.d.). For all pole figures, *X* plots to the right and represents the down dip azimuth of the transport direction. This consistency in

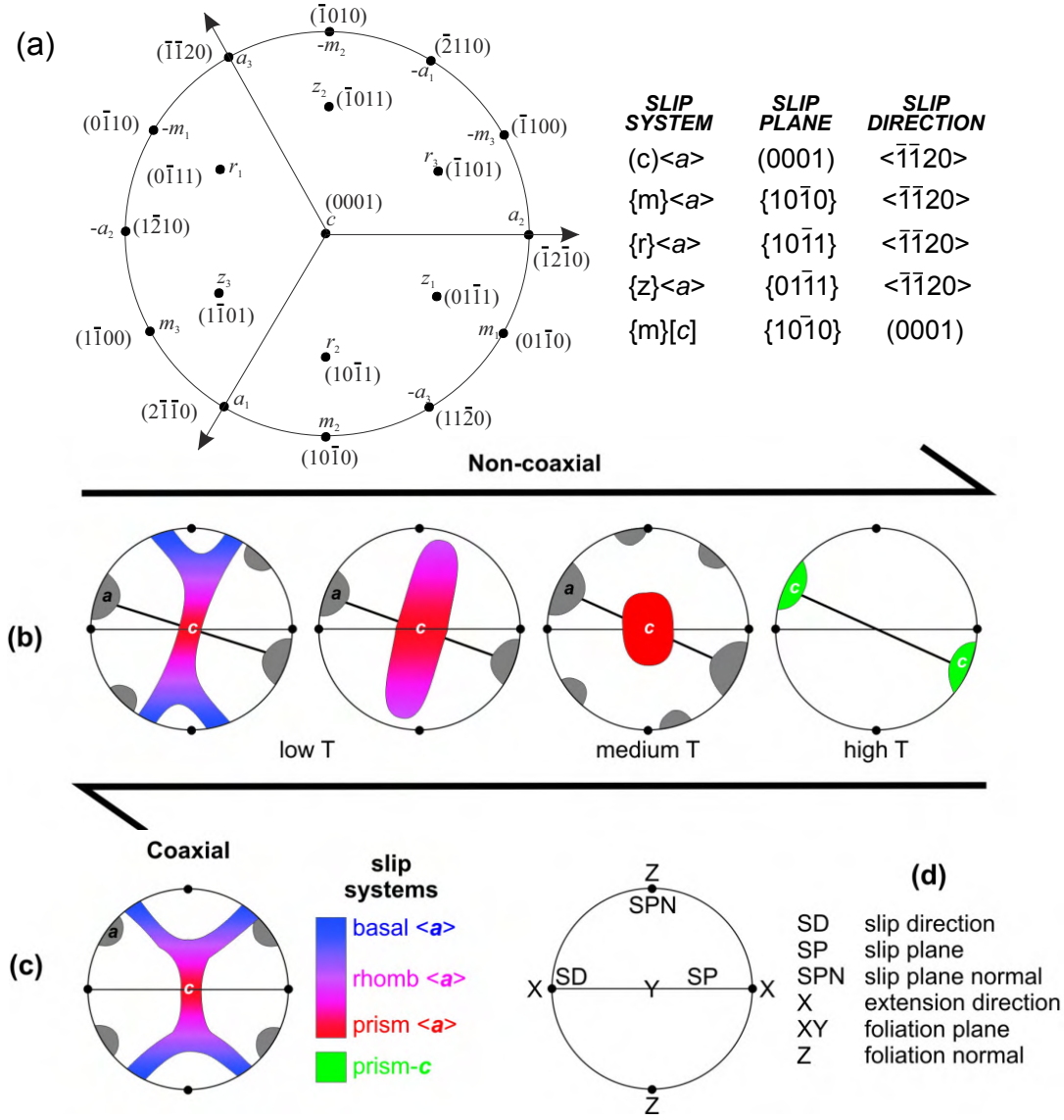

Figure 3.9. Quartz slip systems and a- and c-axis CPO development. (*a*) Quartz poles to planes and crystal axes orientation for the dominant crystal slip systems (After Linker *et al.*, 1984). Subsidiary poles to planes and axes (e.g. s', ξ, ξ', π and π' see Linker *et al.*, 1984). (*b*) Schematic pole figures showing temperature dependent CPO development of *a*-axes (grey maxima) and *c*-axis (coloured maxima) during non-coaxial dextral shear. As temperatures increase, CPOs record a transition in active slip systems from (c)<*a*> + {r}<*a*> + {z}<*a*> + {m}<*a*> slip (low temperature), to {r}<*a*> + {z}<*a*> + {m}<*a*> slip, to {m}<*a*> slip and finally to {m}[*c*] slip (high temperature). (*c*) *c*-axis crossed girdle CPOs develop through combined (c)<*a*> + {r}<*a*> + {z}<*a*> + {m}<*a*> slip – i.e. Mixed <*a*> slip. (*d*) Diagrammatic explanation of stereographic representation of pole figures in the *XZ* plane of the kinematic reference frame. (*b*) and (*c*) produced by G.E. Lloyd, modified from Passchier & Trouw (2005), after Nicolas & Poirier (1976), Lister & Hobbs (1980), Schmid & Casey (1986).

orientation means that all dextral shear sense indicators indicate a normal (up-dip) shear sense and all sinistral shear sense indicators indicate a reverse (down-dip) shear sense. To allow for comparison with other CPO analyses (e.g. Mainprice *et al.*, 1993; Ismaïl & Mainprice, 1998; Barth *et al.*, 2010; Mainprice *et al.*, 2014), the *J*-index is used to describe *c*-axis CPO strength and ranges from 1 for random a CPO fabric to infinity for uniformity (Bunge, 1982). In Chapter 5, CPO strength and its relationship to strain is

explored in detail and other CPO strength parameters are considered. The full CPO data set is provided in the appendix.

3.3.1. Quartz

Quartz CPOs were analysed from samples along the entire length of both transects. Pole figures were constructed for the <*a*>, {m}, (c), {r} and {z} crystallographic axes, plotted with an equal-area antipodal projection (Figures A.3.24a-f). During crystal plastic deformation, quartz can deform via <*a*> slip on the (c), {m}, {r} and {z} planes (*r* and *z* planes collectively referred to as {r/z} planes) and also by {m}[*c*] slip (Figure 3.9) (Baëta & Ashbee, 1969; Linker *et al.*, 1984; Mainprice *et al.*, 1986; Schmid & Casey, 1986). Typically, (c)<*a*> slip (i.e. slip on the basal plane in one of the three <*a*> directions) is common at lower greenschist facies conditions (~300-400 ^{o}C), whilst {m}<*a*> and {r/z}<*a*> slip becomes increasingly active with increasing temperature through middle greenschist to lower amphibolite facies conditions (~400-650 ^{o}C) (Baëta & Ashbee, 1969; Mainprice *et al.*, 1986; Schmid & Casey, 1986; Lloyd *et al.*, 1992; Lloyd & Freeman, 1994) At temperatures above ~650-700 ^{o}C, {m}[c] slip can occur (Mainprice *et al.*, 1986), although it is suggested that this requires the presence of water (Mainprice *et al.*, 1986; Morgan & Law, 2004).

Active quartz slip systems can be determined from *a*- and *c*-axis distributions (Figure 3.9a,b). (Tullis, 1977; Lister & Williams, 1979; Schmid & Casey, 1986). Commonly, <*a*> slip occurs on a combination of (c), {m} and {r/z} planes to produce crossed girdle distributions of *c*-axes when viewed in the *XZ* kinematic plane (Figure 3.9c). Crossed girdle shape and symmetry provide information on the strain geometry (Lister, 1977; Behrmann & Platt, 1982). Type I crossed girdles (Figure 3.10a) are indicative of a plane strain geometry (Lister, 1977). Type II crossed girdles (Figure 3.10b) have been related to several factors including constrictional strain geometry (Lister, 1977) or 'dry' high temperature (>650 ^{o}C) dynamic recrystallisation (Morgan & Law, 2004), when {m}[*c*] slip is less prevalent (Law, 2014). The degree of symmetry of *c*-axis distributions in the *XZ* plane is potentially a qualitative indicator of the degree of coaxial (symmetrical distribution) to non-coaxial (asymmetrical distribution) deformation (Lister *et al.*, 1978; Barth *et al.*, 2010) (Figure 3.10c). CPO asymmetries produced by non-coaxial deformation also give an indication of shear sense (Behrmann & Platt, 1982) (Figure 3.10c,d). With increasing strain, under non-coaxial plane strain deformation conditions, quartz *c*-axis distributions initially develop crossed girdle fabrics, which then develop into single girdle fabrics and finally a single point maxima distribution (Figure 3.10d) (Carreras *et al.*, 1977; Schmid & Casey, 1986; Heilbronner & Tullis, 2006).

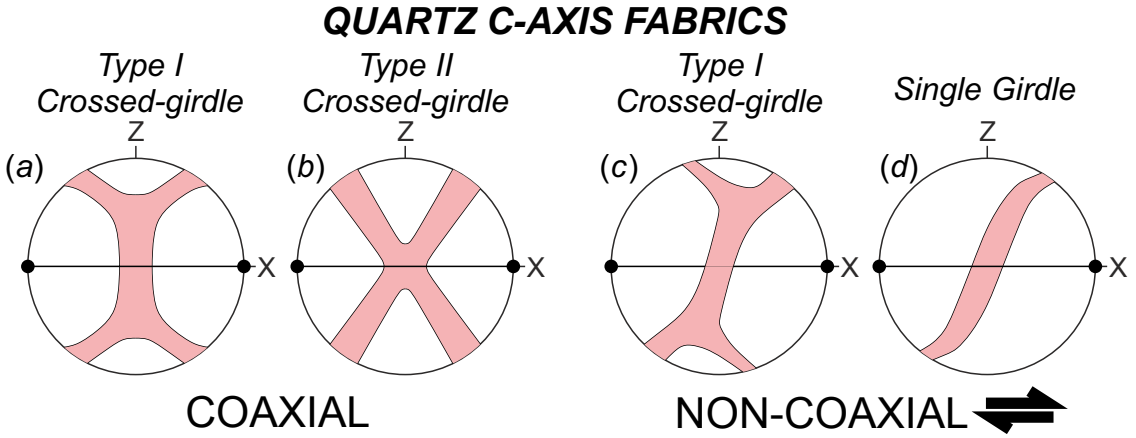

Figure 3.10. Quartz c-axis CPO development. (*a*) Type I crossed girdle develops under plane strain. (*b*) Type II crossed girdle develops under constrictional strain. (*c*) Asymmetric crossed girdle fabrics develop during non-coaxial deformation and provide an indication of shear sense. (*d*) With increasing strain crossed girdles become single girdles and finally point maxima parallel to the *Y* direction.

In the Annapurna-Dhaulagiri samples, the strongest CPO fabrics were consistently measured in quartzites. Well-developed quartz CPOs were also found in semipelites and some gneisses, where quartz represents a major constituent of the bulk mineralogy and forms load-bearing domains within the sample. At the base of the Modi Khola transect, in the LHS, quartz CPOs are weak with poorly defined fabrics that are suggestive of (c)<*a*> slip, but with no discernible shear sense (Figure 3.11a). In the LGHS, quartz CPOs incrementally strengthen up-section. In the lower portion of the LGHS, *c*-axis CPOs display weak to intermediate strength (*J* = 1.1-1.6) type I crossed-girdle fabrics, often with a weak asymmetry indicative of a sinistral shear (i.e. top-to-the-SW reverse sense) (Figure 3.11b). In the upper portion of the LGHS, quartz CPOs are stronger (*J* = 1.1-3.8) and develop asymmetric single girdle *c*-axis distributions with a sinistral shear sense (top-to-the-SW), with remnants of type I crossed girdle fabrics (Figure 3.11c). Both crossed girdle and single girdle fabrics display a greatest concentration of *c*-axis orientations parallel to the *Y* direction, indicative of {m}<*a*> slip with minor contributions from (c)<*a*>, {r/z}<*a*> slip. The strongest and most asymmetric quartz CPO fabric in the LGHS of the Modi Khola valley is found at the top of the sequence. However, the outcrop from which this sample (P12/022) was recovered was not *in-situ* and so it is not possible to distinguish between normal and reverse sense shearing.

Quartz CPO fabrics in the UGHS in the Modi Khola valley (Figure A.3.24b) are poorly developed, which may reflect the polymineralic composition of these rocks and the effects of static recrystallisation and GBAR. At the base of the UGHS, quartz CPO fabrics appear to reflect a poorly developed (c)<*a*> fabric (P12/021 & P12/020). Quartz CPO fabrics from samples up-section of this display either poorly defined {m}[*c*] slip fabrics (P12/019) or {m}<*a*> slip fabrics (P12/016) (Figure 3.11e-g). In some cases,

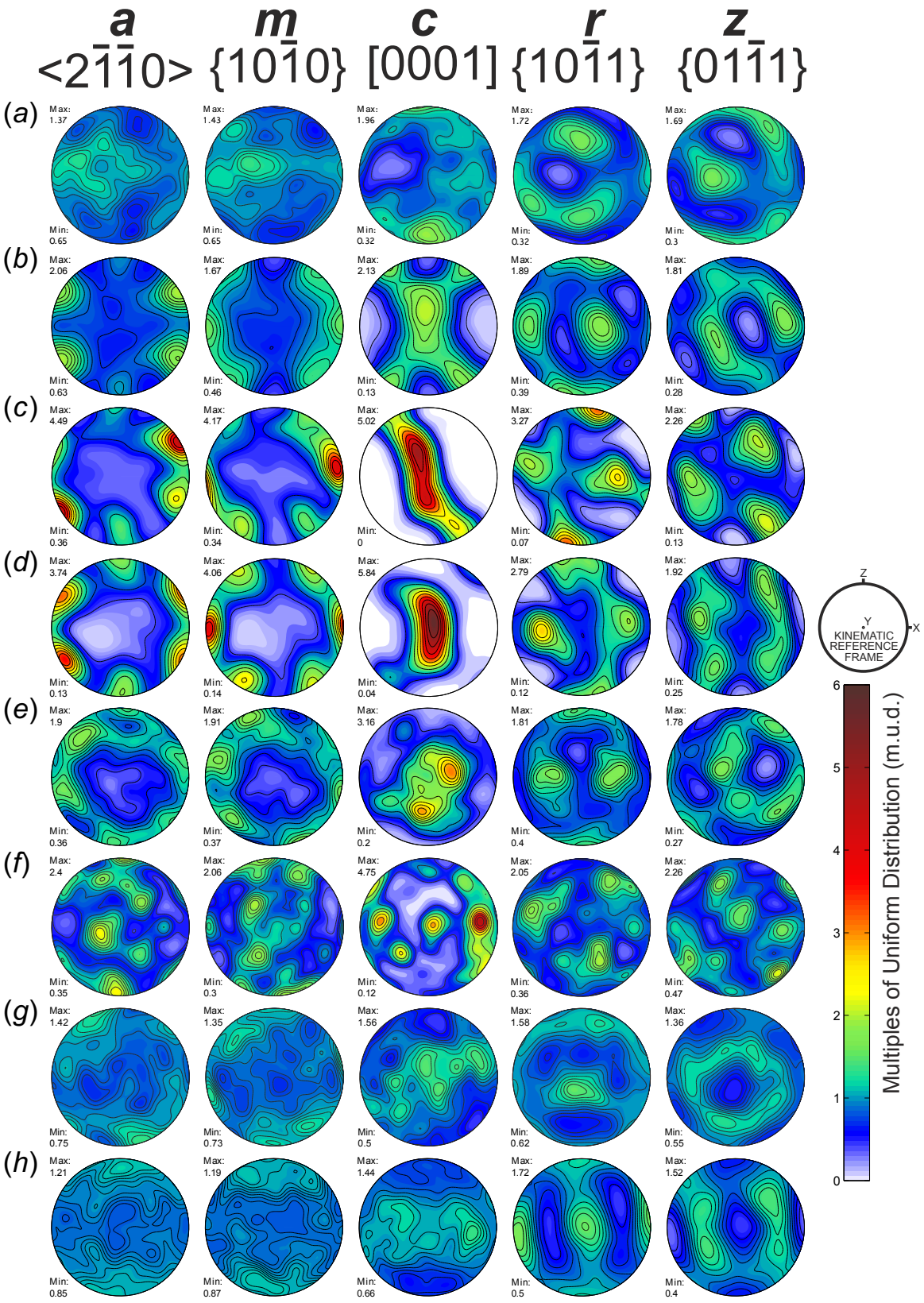

Figure 3.11 Selected quartz CPOs.

features of both of these fabrics are observed (P12/017). Occasionally, *c*- and *a*-axis maxima indicate a sinistral shear sense (top-to-the-SW). Where present, poorly formed type I *c*-axis crossed girdle fabrics are symmetrical and no shear sense can be inferred (P12/013, P12/104). In the STDS, a weak quartz {m}[*c*] slip fabric is observed in a metacarbonate sample (P12/008). A leucogranite sample collected from the same locality displays (*c*)<a> and {m}<*a*> slip CPO fabrics with a dextral shear (top-to-the-

NE) asymmetry (P12/007). At the top of the STDS in the Modi Khola transect a siliceous marble from the same area (P12/006) displays an intermediate strength quartz CPO fabric, with a *c*-axis girdle sub-parallel to the *XY* plane. In this sample, quartz is present as isolated single grains surrounded by calcite with no signs of internal deformation. In this situation, mechanical rotation of quartz grains that are elongate in the [*c*] direction (e.g. Stallard & Shelley, 1995) and/or preferential dissolution-precipitation growth along the *c*-axis is suggested to be responsible for the formation of the *c*-axis girdles / maxima parallel to the *XY* plane (e.g. Hippertt, 1994; Ihinger & Zink, 2000), rather than {m}[*c*] slip (Figure 3.11h). In the THS, a psammitic metasedimentary rock (P12/004) displays a weak type I crossed girdle *c*-axis fabric.

In the Kali Gandaki transect, quartz CPO fabrics in the LGHS (Figure A.3.24c) are mostly weak and poorly formed. At the base of the LGHS, quartz CPOs are very weak (*J* = 1.1-1.2) and display *c*-axis girdles parallel to the *XY* plane (P13/054, P13/057). The low-grade conditions indicated by the petrology of these samples and the high mica content within these rocks, suggest that these fabrics were formed by preferential dissolution-precipitation growth in the direction of the *c*-axis during phyllonitisation (e.g. Hippertt, 1994; Ihinger & Zink, 2000), rather than high temperature (>650 ^{o}C) {m}[*c*] slip. Quartz CPOs from the massive quartzite and marble unit in the middle of the LGHS (Figure 2.4) display strong (*J* = 1.3-4.1) type I crossed girdle (P12/027) or single girdle (P12/030) *c*-axis fabrics with a sinistral shear (top-to-the-SW) asymmetry (Figure 3.11b,c). These fabrics show a dominance of {m}<*a*> slip with minor contributions of (c)<*a*> and {r/z}<*a*> slip. At the top of the LGHS in the Kali Gandaki transect, quartz CPOs from the dolomitic marble and metacarbonate unit display weak (*J* = 1.2-1.3) (c)<*a*> slip fabrics (P12/065, P13/049) with a sinistral shear sense (top-to-the-SW). Weak *c*-axis maxima parallel to the stretching lineation (*X*) from this unit (P12/066) are interpreted as the product of preferential dissolution-precipitation growth in the direction

Figure 3.11. Selected quartz CPOs. All plotted in *XZ* plane of kinematic reference frame with down-dip direction of *X* to the right. Plotted with antipodal equal area projection. (*a*) P12/088 – LHS, Modi Khola. CPO is indicative of (c)<*a*> slip. (*b*) P13/062 – LGHS, Modi Khola. CPO is indicative of mixed<*a*> slip and displays a type I *c*-axis crossed girdle. (*c*) P12/030 – LGHS, Kali Gandaki. CPO is indicative of mixed<*a*> slip with a dominance of {r/z}<*a*> and {m}<*a*> slip. Single *c*-axis girdle fabric indicates a sinistral shear sense (top-to-the-SW). (*d*) P12/061 – UGHS, Kali Gandaki. CPO is indicative of {m}<*a*> slip under coaxial deformation. (*e*) P13/045 – UGHS, Kali Gandaki. Poorly defined CPO is indicative of {m}<*a*> slip. (*f*) P12/058 – UGHS, Kali Gandaki. CPO is indicative of {m}[*c*] slip. (*g*) P13/040 – UGHS, Kali Gandaki. CPO is indicative of {m}[*c*] slip with a sinistral shear sense (top-to-the-S). (*h*) P12/045 – STDS, Kali Gandaki. Pseudo {m}[*c*] slip CPO is interpreted as the product of rigid body rotation and/or preferential dissolution-precipitation growth along the *c*-axis, which aligns grain long axes into parallelism with the foliation (see text for further discussion). Contoured for multiples of uniform distribution (m.u.d.). Sample locations presented on Figures 2.3 & 2.4. Full sample description presented in sample list in the Supplementary Data CD.

of the *c*-axis (Hippertt, 1994; Ihinger & Zink, 2000) during phyllonitisation.

At the base of the UGHS in the Kali Gandaki section, a quartz *c*-axis CPO (Figure A.3.24d) forms a single girdle fabric, with remnants of a type I crossed girdle, indicative of {m}<*a*> slip plus minor (c)<*a*> and {r/z}<*a*> slip during non-coaxial sinistral shear (P13/046). Immediately above this, a thin quartzite layer produces a very strong (*J* = 3.7) and well defined type I *c*-axis crossed girdle distribution with no asymmetry and a point maxima parallel to the *Y* direction, indicative of {m}<*a*> slip during coaxial deformation (P12/061) (Figure 3.11d). Across the rest of the UGHS, quartz CPO measured from gneisses and schists is characterised by poorly defined {m}<*a*> slip fabrics (e.g. P12/051, P12/053, P13/032) and better defined {m}[*c*] slip fabrics (e.g. P12/054, P12/058, P12/059, P13/040) (Figure 3.11f,g). These fabrics show no asymmetry expect for P12/054 and P13/040 in Unit II, which are indicative of non-coaxial sinistral shear (top-to-the-S/SE) plus flattening (e.g. Barth *et al.*, 2010). The uppermost quartz CPO from the UGHS (P13/030) displays a (c)<*a*> slip fabric with a sinistral shear sense (top-to-the-WSW).

In the STDS in the Kali Gandaki section, quartz CPOs (Figure A.3.24e) are very weak (*J* = 1.1-1.3), and consistently produce *XY*-parallel *c*-axis maxima/girdles (Figure 3.11h). Quartz within these rocks is typically present as isolated grains surrounded by weaker phases (e.g. calcite and dolomite) and shows no evidence for intracrystalline deformation. Consequently, mechanical rotation of quartz grains resulting in a shape controlled CPO (e.g. Stallard & Shelley, 1995) is the most likely explanation for these fabrics.

In the THS, quartz CPO fabrics are very weak to random (*J* = 1.0-1.3) (Figure A.3.24f). *XY*-parallel *c*-axis maxima/girdle fabrics are common (e.g. P12/041, P12/038) and most likely result from shape-controlled mechanical rotation (e.g Stallard & Shelley, 1995) and/or preferential dissolution-precipitation growth in the direction of the *c*-axis (e.g. Hippertt, 1994; Ihinger & Zink, 2000). Towards the top of the Kali Gandaki transect, a calc-semipelite sample (P12/035) displays a low maximum intensity but well defined (c)<*a*> slip CPO fabric.

3.3.2. Calcite & Dolomite

Calcite and dolomite pole figures were constructed for the <*a*>, {m}, (c), {e}, {f} and {r} crystallographic axes and the $< 40\bar{4}1 >$ twinning direction (referred to as <*D1*> from here on) and $< \bar{2}021 >$ and $< 10\bar{1}1 >$ slip directions (referred to as <*D2*> and <*D3*> respectively from here on), plotted on an equal-area antipodal projection (Figure A.3.25a-d). At low temperatures (< 300 ^{o}C), calcite deforms by twinning on the {e} plane in the <*D1*> direction (Burkhard, 1993; De Bresser & Spiers, 1997). Dynamic

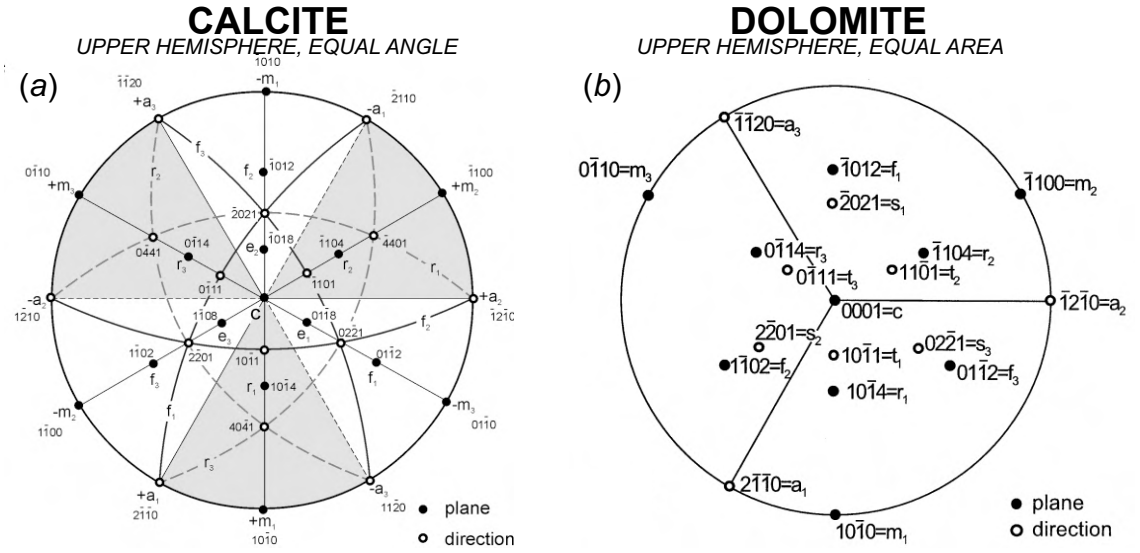

SLIP SYSTEM	SLIP PLANE	SLIP DIRECTION
(c)<*a*>	(0001)	$<\bar{1}\bar{1}20>$
{r}<*a*>	$\{10\bar{1}4\}$	$<\bar{1}\bar{1}20>$
{r}<*D2*>	$\{10\bar{1}4\}$	$<\bar{2}021>$
{f}<*D2*>	$\{01\bar{1}2\}$	$<\bar{2}021>$
{f}<*D3*>	$\{01\bar{1}2\}$	$<10\bar{1}1>$
TWIN SYSTEM	**TWIN PLANE**	**TWIN DIRECTION**
{e}<*D1*>	$\{01\bar{1}8\}$	$<40\bar{4}1>$

SLIP SYSTEM	SLIP PLANE	SLIP DIRECTION
(c)<*a*>	(0001)	$<\bar{1}\bar{1}20>$
{r}<*a*>	$\{10\bar{1}4\}$	$<\bar{1}\bar{1}20>$
{f}<*D2*>	$\{01\bar{1}2\}$	$<\bar{2}021>$
TWIN SYSTEM	**TWIN PLANE**	**TWIN DIRECTION**
{f}<*D3*>	$\{01\bar{1}2\}$	$<10\bar{1}1>$

Figure 3.12. Calcite and dolomite crystallography and slip & twin systems. (*a*) Calcite slip directions (white dots) poles to slip planes (black dots). Slip and twin systems listed below. After Bestman & Prior, 2003. (*b*) Dolomite slip directions (white dots) and poles to slip planes (black dots). Slip and twin systems listed. After Leiss & Barber, 1999.

recrystallisation of calcite begins at ~250 °C and dominates above 300-400 °C (Barber *et al.*, 1981; Evans & Dunne, 1991; Weber *et al.*, 2001). Above 300-400 °C, {r}<*D2*> slip ± {r}<*a*> slip dominates with subordinate {f}<*D2*> between 300-600 °C and subordinate {f}<*D3*> and (c)<*a*> slip between ~550-800 °C (Figure 3.12a) (De Bresser & Spiers, 1997; Pieri *et al.*, 2001; Bestmann & Prior, 2003).

Due to the many directions in which dislocation glide can occur in calcite, not all active slip systems produce CPOs which align parallel or perpendicular to the shear plane (Figure 3.13) (Trullenque *et al.*, 2006). Nevertheless, calcite CPOs can provide information relating to strain geometries and shear sense. Comparison of natural, experimental and numerically simulated calcite CPOs indicate that coaxial deformation results in orthorhombic symmetry, whilst non-coaxial deformation usually results in monoclinic asymmetry (Figure 3.14a,b) (Wenk *et al.*, 1987; Lafrance *et al.*, 1994; Trullenque *et al.*, 2006). It has also been suggested that on some occasions a distinction can be made between 'Low Temperature' and 'High Temperature' calcite CPOs (Figure 3.14c) (Wenk *et al.*, 1987; Leiss & Molli, 2003; Trullenque *et al.*, 2006). Care must be taken when interpreting calcite CPO asymmetries as shear sense indicators as non-coaxial intracrystalline deformation (i.e. twinning) can rotate *c*-axis maxima *against* the shear direction, whilst dynamic recrystallisation rotates *c*-axis

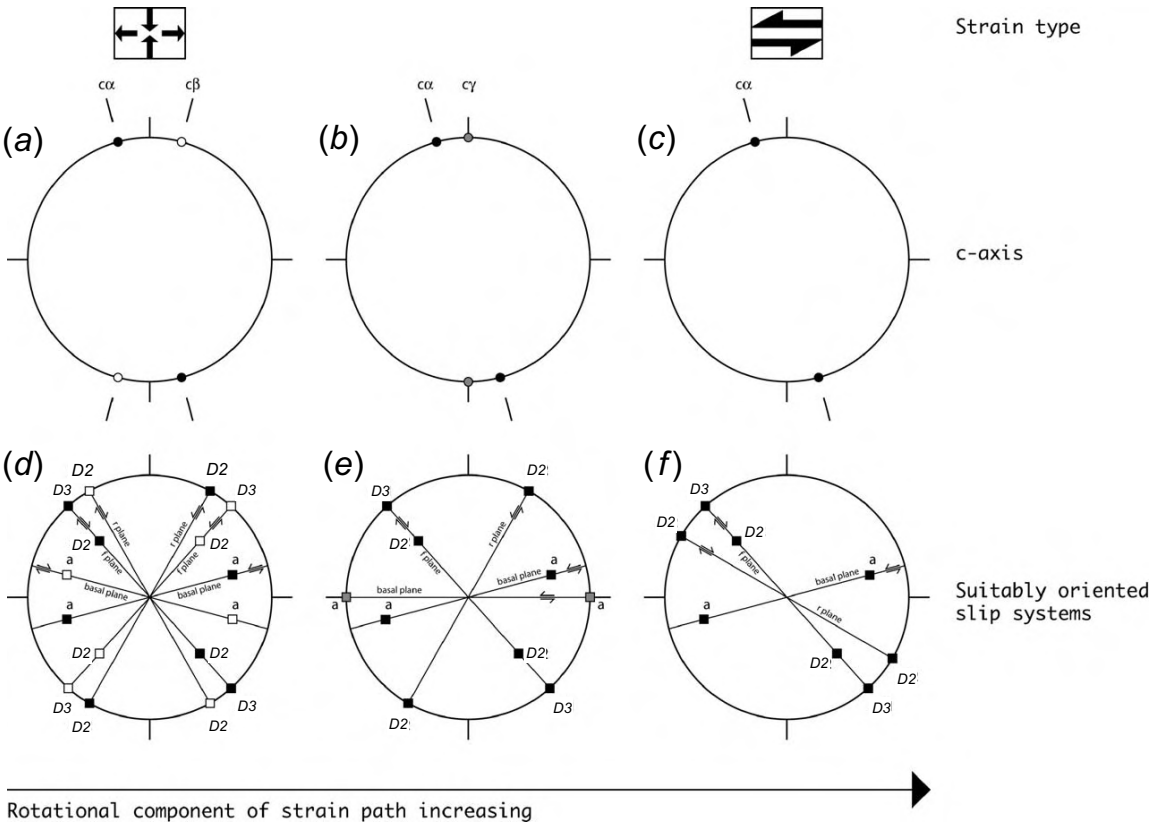

Figure 3.13. Calcite slip system CPO. (*a*) Orientation of *c-axis* maxima during coaxial deformation. Two maxima form: cα (black dots) and cβ (white dots). (*b*) Orientation of *c-axis* maxima during coaxial + non-coaxial deformation (i.e. general shear). Two maxima form: cα (black dots) and c*γ* (grey dots). (*c*) Orientation of *c-axis* maxima during non-coaxial deformation. One maxima forms: cα (black dots). (*d*) Orientation of slip planes and slip directions during coaxial deformation. Black squares correspond to cα maxima orientation, white squares correspond to cβ maxima orientation. (*e*) Orientation of slip planes and slip directions during coaxial + non-coaxial deformation (i.e. general shear). Black squares correspond to cα maxima orientation, grey squares correspond to c*γ* maxima orientation. (*f*) Orientation of slip planes and slip directions during non-coaxial deformation. Black squares correspond to cα maxima orientation. After Trullenque *et al.* 2006.

maxima *towards* the direction of shear (Lafrance *et al.*, 1994; Pieri *et al.*, 2001; Trullenque *et al.*, 2006; Oesterling *et al.*, 2007). Consequently, interpretations of calcite CPOs should be accompanied with microstructural observations.

In dolomite, (c)<*a*> slip dominates below 300 °C (Barber *et al.*, 1981). At intermediate temperatures (300-600 °C), twinning on the {f} plane in the <*D3*> direction is favoured (note that twinning of dolomite does not occur outside of this temperature range), with subordinate (c)<*a*> and {f}<*D2*> slip, whilst at high temperatures (>550 °C), {f}<*D2*> slip dominates (Barber *et al.*, 1981). Slip on the {r}<*a*> system may also occur in dolomite at intermediate to high temperatures, but is always subordinate to the other slip systems (Figure 3.12b) (Barber *et al.*, 1981; Barber *et al.*, 1994).

The relationship between dolomite CPO distribution and strain geometry is less well understood than that of calcite. Wenk and Shore (1975) found a sharp transition from

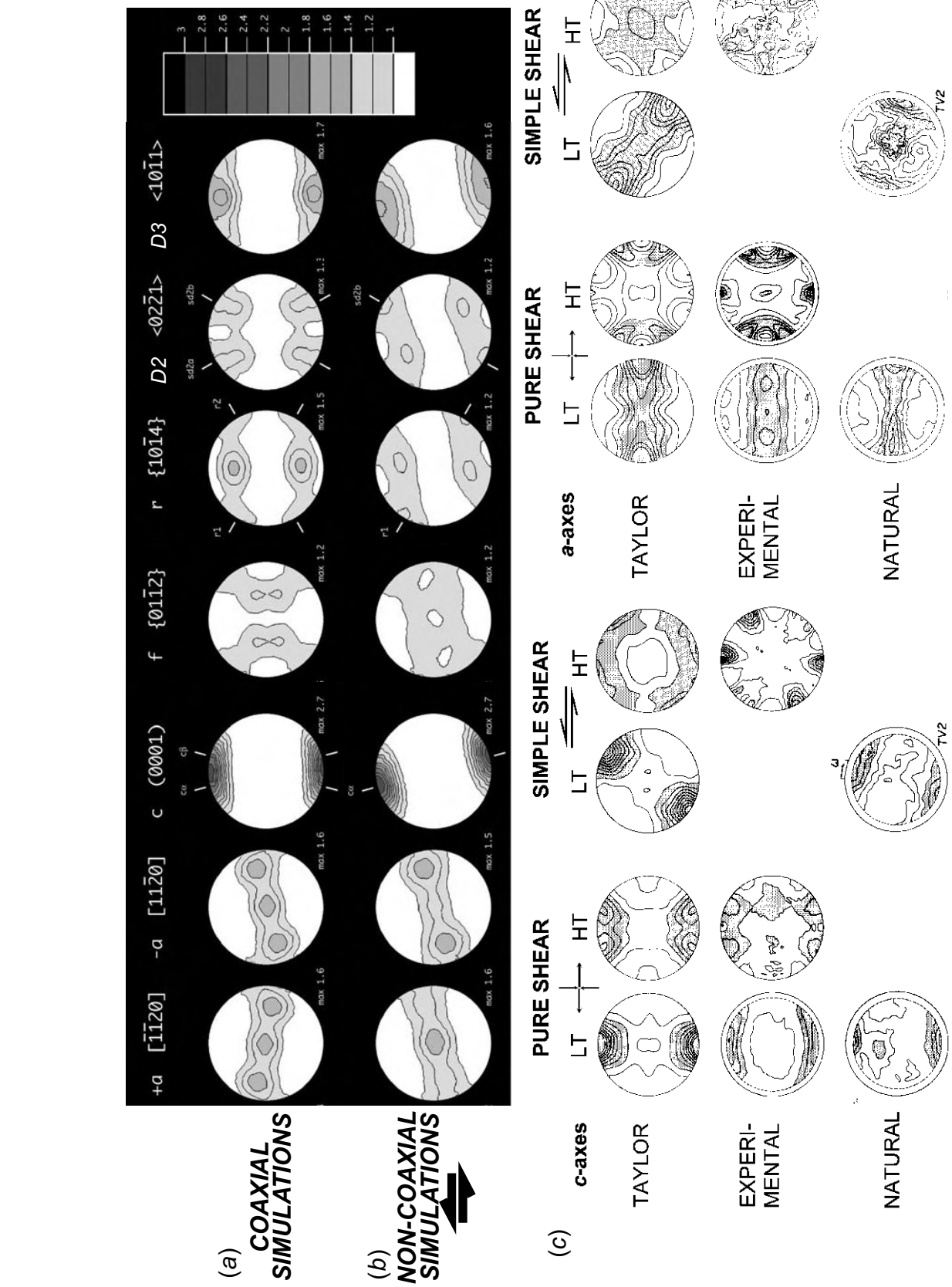

Figure 3.14. Calcite CPO fabrics. (*a*) Simulated calcite CPOs produced during coaxial deformation (After Trullenque *et al.* 2006). (*b*) Simulated calcite CPOs produced during non-coaxial deformation (After Trullenque *et al.* 2006). (*c*) 'Low Temperature' and 'High Temperature' calcite *a*-axis and *c-axis* CPO produced from Taylor-Bishop-Hill simulation, experimental deformation and naturally deformed samples (From Leiss & Molli 2003; after Wenk *et al.* 1987).

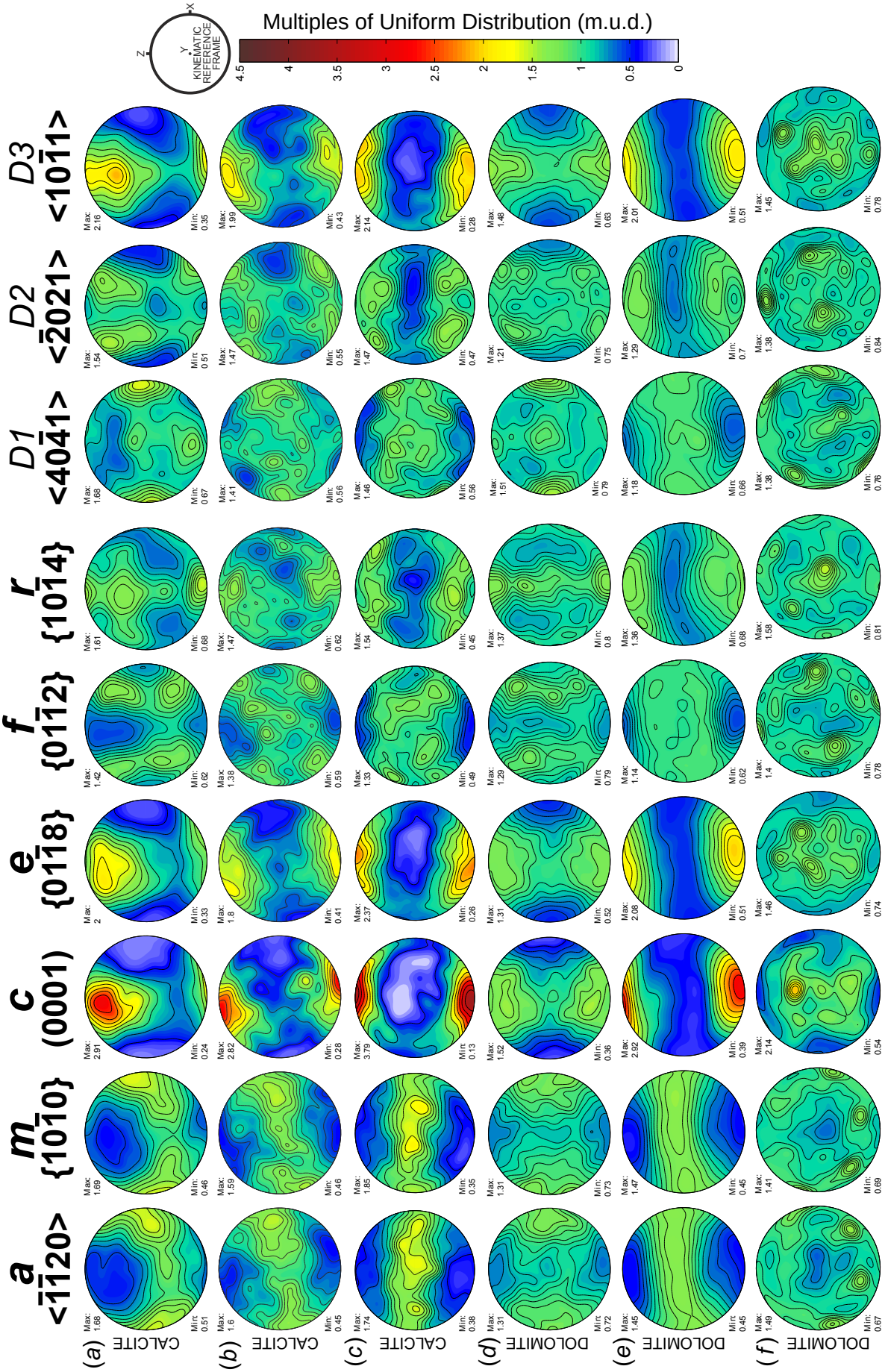

Figure 3.15 Selected calcite and dolomite CPOs.

weak to strong *c*-axis maxima in experimentally deformed dolomite at temperatures above 700 °C, due to a change in deformation mechanism from twinning at intermediate temperatures to recrystallisation at high temperatures. Non-coaxial deformation results in monoclinic CPOs with *c*-axis maxima at a high angle to the flow plane and an *a*-axis girdle with stronger concentrations sub-parallel to *X* (Delle Piane *et al.*, 2009). Under such conditions, dolomite *c*-axis asymmetries can be used as a shear sense indicator. However, as with calcite, the *c*-axis maxima of dolomite can rotate both *against* and *towards* the direction of shear (Leiss & Barber, 1999; Delle Piane *et al.*, 2009). Under such conditions, dolomite *c*-axis asymmetries can be used as a shear sense indicator. However, as with calcite, the *c*-axis maxima of dolomite can rotate both *against* and *towards* the direction of shear (Leiss & Barber, 1999; Delle Piane *et al.*, 2009). There are no experimental examples of coaxially deformed dolomite CPOs. Recrystallisation under high temperature (700-800 °C) static conditions produces orthorhombic CPOs with broad *c*-axis maxima parallel to *Z* and a wide *a*-axis girdle parallel to *X* (Delle Piane *et al.*, 2009).

Due to differences in slip systems, dolomite is stronger than calcite at low temperatures (<550 °C) and weaker than calcite at high temperatures (>550 °C) (Delle Piane *et al.*, 2008). Consequently, strain partitioning in calcite-dolomite aggregates is common and relative differences in CPO strength between these minerals can provide an indication of deformation temperature (Delle Piane *et al.*, 2008).

In the Modi Khola transect (Figure A.3.25a), a dolomitic marble from the top of the LGHS (P12/026) has a well-defined monoclinic CPO, with *c*- and *r*-axis maxima sub-parallel to the *Z* direction and an *a*-axis girdle sub-parallel to the *XY* plane (Figure 3.15). This CPO is favourably configured for (c)<*a*> and {r}<*a*> slip, although the orientation of {f} poles and <*D2*> and <*D3*> axes may also relate to *f*-twinning, as seen in thin section ± {f}<*D2*> slip. The *c*-axis fabric indicates a sinistral shear sense (top-to-the-SW). Strong calcite and dolomite CPOs (*J* = 1.3-2.3) from the top of the STDS in

---

Figure 3.15. Selected calcite and dolomite CPOs. All plotted in *XZ* plane of kinematic reference frame with down-dip direction of *X* to the right. Plotted with antipodal equal area projection. (*a*) P12/066 – LGHS, Kali Gandaki. Calcite CPO fabric is similar to simulated and experimental 'Low Temperature' coaxial fabric. (*b*) P13/049 – LGHS, Kali Gandaki. Calcite CPO fabric is similar to simulated and experimental 'Low Temperature' non-coaxial fabrics with a sinistral shear (top-to-the-SW). (*c*) P12/006 – THS, Modi Khola. Calcite CPO fabric is similar to simulated and experimental 'High Temperature' non-coaxial fabrics. (*d*) P12/068 – LGHS, Kali Gandaki. Dolomite CPO configuration is similar to simulated and experimental coaxial calcite CPOs. (*e*) P13/005 – STDS, Kali Gandaki. Dolomite CPO configuration is similar to simulated and experimental non-coaxial calcite CPOs. (*f*) P12/067 – LGHS, Kali Gandaki. 'Type II' dolomite CPO with *c*-axis maxima parallel to *Y*. The cause of this CPO is unknown. Sample locations presented on Figures 2.3 & 2.4. Full sample description presented in sample list in the Supplementary Data CD.

the Modi Khola transect, produced similarly orientated orthorhombic calcite and dolomite CPOs, with similar CPO strengths. These fabrics are comparable to natural and experimental 'Low Temperature' fabrics (Wenk *et al.*, 1987; Leiss & Molli, 2003), and are similar to simulated coaxial fabrics (Trullenque *et al.*, 2006). Calcite CPO display the necessary orientations required for {e} twinning, {*r*} slip, {f} slip and (c)<*a*> slip (Trullenque *et al.*, 2006).

In the Kali Gandaki transect (Figure A.3.25b) calcite and dolomite from the metacarbonates and marbles at the top of the LGHS have intermediate strength CPOs (*J* = 1.2-1.5). Where present in the same sample, calcite produces stronger CPOs than dolomite. Calcite CPO configurations are similar to 'Low Temperature' *c*-axis fabrics (e.g. Wenk *et al.*, 1987; Leiss & Molli, 2003). Observed {f}, <*D2*> and <*D3*> fabrics (Figure 3.15) vary between coaxial (P12/066, P12/068) and non-coaxial (P12/063, P13/049) configurations (e.g Trullenque *et al.*, 2006). The relative configuration of glide plane, slip direction girdles and point maxima indicate that all twinning and slip systems may have been active in these samples, but only {e} twinning, {r}<*a*> slip and (c)<*a*> slip could have occurred parallel to the stretching lineation / transport direction. Some calcite CPOs in the LGHS display a sinistral shear sense (top-to-the-SW). Two types of dolomite CPO configurations are recorded in the LGHS. Type I dolomite CPO (Figure 3.15) is comparable to coaxial calcite CPOs (e.g Trullenque *et al.*, 2006) and are favourably oriented for (c)<*a*> and {r}<*a*> slip parallel to *X* ± subordinate {f}<*D2*> slip ± {f} twinning (e.g. P12/068, P12/066, P12/063). Type II dolomite CPO (Figure 3.15f) have broad *c*-, *e*- and *r*-axis maxima centred on the *Y* direction and poorly defined *a*- and *f*-axis girdles parallel to the *XZ* plane (i.e. around the periphery of the pole figure). Distributions of <*D2*> and <*D3*> produce a broad, weak maximum around *Y*. There are no experimental examples of type II dolomite CPO and it is unclear what deformation mechanisms were responsible for its origin.

In the UGHS in the Kali Gandaki transect, calcite CPOs from calc-silicate gneisses in Unit II are poorly defined in terms of topology but have strong *c*-axis maxima parallel to *Z* and *a*-axis girdles parallel to the *XY* plane (Figure 3.15). These CPO configurations are most suggestive of deformation via {c}<*a*> slip ± {f} slip.

In the STDS (Figure A.3.25c), calcite CPO strength generally decreases up-section (*J* = 1.0-3.4). Typically, calcite CPOs have configurations comparable to 'Low Temperature' non-coaxial deformation fabrics (Wenk *et al.*, 1987; Leiss & Molli, 2003; Trullenque *et al.*, 2006). These calcite CPOs are most favourably orientated for {e} twinning, {*r*}<*a*> slip and {c}<*a*> slip in the *XY* plane parallel to *X*, but also well-formed {f} girdles and <*D2*> and <*D3*> small circle girdles and maxima indicative of {r}<*D2*> slip and {f} slip (Figure 3.15). Samples with calcite-dolomite aggregates from the middle

and top of the STDS all have dolomite fabrics that are stronger than calcite fabrics. The strongest dolomite CPOs are found at the very top of the STDS (P13/005, P13/006) and display a similar configuration to natural and experimental 'High Temperature' non-coaxial calcite CPOs (Wenk *et al.*, 1987; Leiss & Molli, 2003; Trullenque *et al.*, 2006). These dolomite CPOs are favourably orientated for (c)<*a*> slip and {r}<*a*> slip in the *XY* plane and {f} slip in the *XZ* plane. In the middle of the STDS, Type II dolomite CPO is recorded (P13/029). In this sample, calcite has a larger grain size and only a weak to random CPO. This may be explained by weakening of calcite CPO during static recrystallisation (Delle Piane *et al.*, 2009) or it may imply that dolomite was the weaker phase in these rocks during crystal plastic deformation (Delle Piane *et al.*, 2008). Across the STDS, a few calcite and dolomite CPOs display either clockwise or anticlockwise rotation about the *Y* axis. Recrystallisation appears to be significant in all samples in the STDS, which suggests that these rotations locally record both sinistral (top-to-the-WSW; P12/043) and dextral (top-to-the-ESE; P12/044) non-coaxial shear.

In the THS in the Kali Gandaki transect (Figure A.3.25d), calcite and dolomite CPOs are generally weak (J = ~1.0-1.2) with the exception of the lower- and uppermost samples (P12/041 and P12/033) which have strong calcite CPOs (J = 1.9 and 2.9). Discernible fabrics are comparable to experimental 'Low Temperature' CPOs (Wenk *et al.*, 1987). Calcite CPOs are favourably orientated for {f} twinning ± {c}<*a*> slip ± {r}<*a*> slip parallel to *X* in the *XZ* plane. Dolomite CPOs are favourable for {c}<*a*> ± {r}<*a*> slip parallel to *X* in the *XZ* plane. At the base of the THS, calcite CPOs display a sinistral shear sense (top-to-the-W; P12/041) that correlates with the observed SPO in thin section. Structurally above this, recrystallized calcite and dolomite CPOs (P12/039) from the footwall to a low angle normal fault (150/26 NE) have dextral (top-to-the-NE) shear sense. The strong calcite CPO from the top of the Kali Gandaki transect (P12/033) may relate to deformation on the Dangardzong fault during extension in the Thakkhola graben (*Section 2.5.6.*), as suggested by the sample location and normal-shear-sense SPO observed in thin section.

3.3.3. Plagioclase & K-feldspar

Plagioclase and K-feldspar pole figures were constructed for the <100>, <010>, <001> directions, and for the (100), (010) and (001) poles to planes (Figure A.3.26). Pole figures were plotted for both upper and lower hemisphere equal-area projections. Within the LHS, LGHS, STDS and THS, deformation temperatures and/or relative feldspar volumes are sufficiently low for feldspar to behave as rigid grains that accommodate little deformation. Consequently, only feldspar CPOs from the UGHS, where temperatures were sufficient for significant intracrystalline deformation and recrystallisation, are discussed.

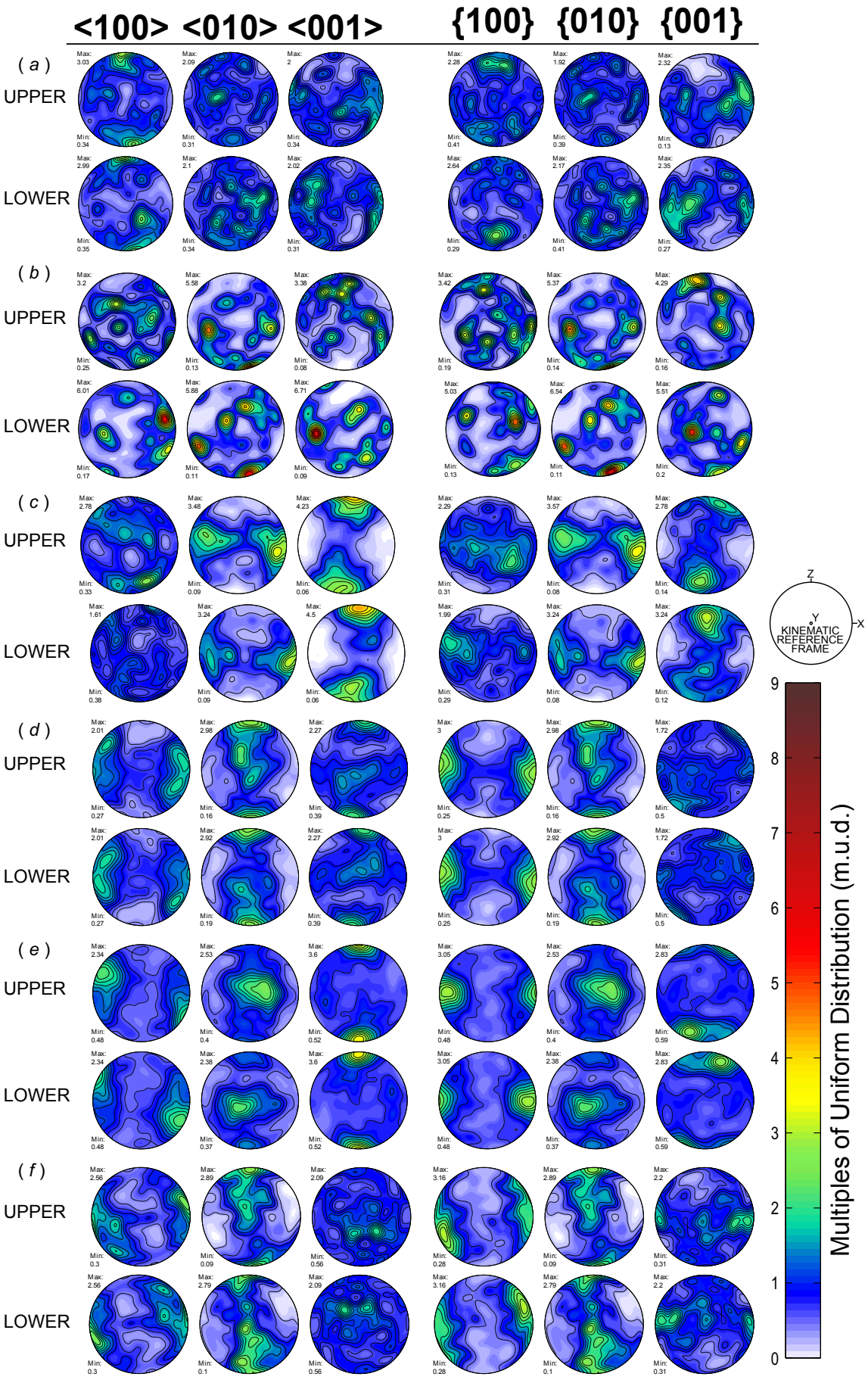

Figure 3.16 Selected feldspar CPOs.

During intracrystalline deformation of plagioclase at medium to high grade conditions, (010)<001> slip, and slip in the <110> direction on a plane anywhere between (001) and {111} are common, whilst (001)<100> and (010)<100> slip is also reported (Olsen & Kohlstedt, 1985; Heidelbach *et al.*, 2000; Stünitz *et al.*, 2003). At high strain, high temperature conditions (600-700^{o} C), diffusion creep becomes an important deformation mechanism, which can cause a weakening of CPO fabrics (Schulmann *et al.*, 1996; Bons & Den Brok, 2000; Rosenberg & Stünitz, 2003). In some cases, diffusion creep derived feldspar CPOs may differ from dislocation creep derived feldspar CPOs (Bons & Den Brok, 2000; Heidelbach *et al.*, 2000). Torsional deformation experiments indicate a rotation of the (010) pole around the *Y* direction occurs in the *opposite* direction to the applied shear, due to the activation of (010)<001> slip (Ji *et al.*, 2004; Barreiro *et al.*, 2007).

The mechanical behaviour of K-feldspar is similar to plagioclase, and involves similar slip systems, the commonest being slip on the (010) plane in the <100>, <010>, <001> and <101> directions (Gandais & Willaime, 1984; Fitz Gerald & Stünitz, 1993; Menegon *et al.*, 2008). K-feldspar exhibits brittle to semi-brittle behaviour at low to intermediate temperatures (<700 ^{o}C). Above 400-450 ^{o}C, crystal plastic deformation of K-feldspar begins (Fitz Gerald & Stünitz, 1993) and intracrystalline-deformation-derived CPO may develop (Ishii *et al.*, 2007). Diffusion creep is also an important deformation process, particularly at low differential stresses and has been shown to weaken CPO and/or produce new CPO configurations that relate to anisotropic crystal growth rates of K-feldspar (Menegon *et al.*, 2008; Fukuda *et al.*, 2012). In some cases, diffusion creep may be the only viscous deformation mechanism occurring, resulting in strain free grain interiors with no intracrystalline deformation (Fukuda *et al.*, 2012; Negrini *et al.*, 2014).

High temperature deformation microstructures (*Section 3.2.3*) suggest that feldspar CPO record both dislocation creep ± diffusion creep driven deformation (Figure 3.6). In the Modi Khola transect (Figure A.3.26a), feldspar CPOs from Unit I have no discernible fabric. Strong point maxima produced by large individual grains that dominate the population of orientation measurements are common (Figure 3.16b). The orientations of these maxima have no relation to the kinematic reference frame and are

Figure 3.16. Selected feldspar CPOs. All plotted in *XZ* plane of kinematic reference frame with down-dip direction of *X* to the right. Plotted with both upper and lower hemisphere equal area projection. (*a-c*) Plagioclase CPOs, (*e-f*) K-feldspar CPOs. (*a*) P12/013 – Unit I, UGHS, Modi Khola. (*b*) P13/045 – Unit I, UGHS, Kali Gandaki. (*c*) P12/054 – Unit II, UGHS Kali Gandaki. (*d*) P13/031 – STDS, Kali Gandaki. (*e*) P13/032 – Unit III, UGHS, Kali Gandaki. (*f*) P12/010 – Unit II, UGHS, Modi Khola. Contoured for multiples of uniform distribution (m.u.d.).

not an indication of high finite strains. These CPOs are essentially random fabrics, dominated by the orientations of the largest grains which represent a large percentage of the analysed sample area. In Unit II and Unit III, a minority of CPO configurations (P12/012, P12/010) are favourably orientated for (010)<110> ± (010)<001> slip (Figure 3.16f), although these fabrics are still weak and poorly defined. Some CPOs have a well-defined topology with maxima aligned perpendicular and/or orthogonal to the *X*, *Y* and *Z* directions but do not record slip on the *XY* plane in the *X* direction (P12/009, P12/011). These fabrics may relate to deformation driven by diffusion creep, which is occasionally observed from microstructures in these samples. The strongest feldspar CPO in the Modi Khola transect is from a leucogranite from the STDS (P12/007). This sample has a strong, well-defined oligoclase CPO due to the presence of large grains, favourably orientated for (001)<110> slip. K-feldspar CPO is weaker but still defined and favourably orientated for (010)<100> and/or (001)<100> slip. The presence of subgrains suggests that intracrystalline deformation of feldspar may have occurred. However, myrmkite and perthite textures indicate that dissolution-precipitation was also a significant deformation mechanism.

Feldspar CPOs in the Kali Gandaki transect (Figure A.3.26b) are similar to those described above. In Unit I, most feldspar CPOs are very weak to random in strength and configuration (Figure 3.16b). A minority of CPO configurations are favourably orientated for (001)<110> slip (e.g. P12/059). Some samples produce ordered fabrics that do not correspond to slip systems but may be derived from diffusion creep controlled deformation (e.g. P12/060). In Unit II, sample P12/054 records a strong, well defined albite CPO favourably aligned for (001)<110> slip (Figure 3.16c), whilst K-feldspar CPO are configured for slip on (010) (P12/053, P13/040). Unit III produces strong well-defined plagioclase and K-feldspar CPO (P12/049, P13/030, P13/031; Figure 3.16d). These are aligned for (001)<110> slip or (010)<001> and (010)<100> slip. The strongest feldspar CPOs are found at the base of the SDTS (P13/032). These are configured for (001)<110> slip in andesine and (010)<100> slip of K-feldspar (Figure 3.16e). Neither of the transects contain feldspar CPOs that show definitive evidence of rotation due to non-coaxial deformation.

3.4. Thermal profile of the Annapurna-Dhaulagiri Himalaya

3.4.1. Microstructural deformation temperature constraints

Table 3.1 contains a list of deformation microstructures, textures and crystal slip systems known to be active in quartz, calcite, dolomite and feldspar at specific temperature ranges, as determined from natural and experimental samples.

Mineral	*Microstructure / Slip System*	*T (°C)*	*Source*
Quartz	Grain boundary buldging dynamic recrystallisation (BLG)	270-390	Stipp et al 2002
	BLG-SGR transition	390-420	Stipp et al 2002
	Subgrain rotation dynamic recrystallisation (SGR)	420-490	Stipp et al 2002
	SGR-GBM transition	490-530	Stipp et al 2002
	Grain boundary migration dynamic recrystallisation (GBM)	>530	Stipp et al 2002
	Chessboard subgrains (CBS)	>650	Khrul 1996
	Quartz c-axis crossed girdle opening angle	Variable	Khrul 1998
	(c)<a> slip	300-400	Baëta & Ashbee, 1969, Mainprice et al., 1986, Schmid & Casey, 1986
	Mixed <a> slip	400-500	Baëta & Ashbee, 1969, Mainprice et al., 1986, Schmid & Casey, 1986
	{m}<a> slip	500-700	Baëta & Ashbee, 1969, Mainprice et al., 1986, Schmid & Casey, 1986
	{m}[c] slip	>650	Mainprice et al 1986
Calcite	Type I twinning	<200	Burkhard 1993, Ferrill et al 2004
	Type II twinning	200-300	Burkhard 1993, Ferrill et al 2004
	Type III twinning	250-300	Burkhard 1993, Ferrill et al 2004
	Low Temperature' (LT) CPO configuration	<300-400	Wenk et al 1987
	High Temperature' (HT) CPO configuration	>300-400	Wenk et al 1987
	Calcite CPO strength > dolomite CPO strength	<550	Delle Piane et al 2008
	{r} slip	>300	De Bresser & Spears 1997
	{f}<D2> slip	300-600	De Bresser & Spears 1997
	{f}<D3> slip	550-800	De Bresser & Spears 1997
	(c)<a> slip	500-800	De Bresser & Spears 1997
Dolomite	{f} twinning	300-600	Barber et al 1981
	Dolomite CPO strength > calcite CPO strength	>550	Delle Piane et al 2008
	Dolomite CPO strength = calcite CPO strength	500-600	Delle Piane et al 2008
	(c)<a> slip	<300	Barber et al 1981
	(c)<a> + {f} slip	300-600	Barber et al 1981
	{f} slip	>550	Barber et al 1981
Feldspar	BLG + SGR dynamic recrystallisation	450-650	Tullis & Yund 1991, Fitz Gerald & Stünitz 1993, Altenberger & Wilhelm 2000
	SGR + GBM dynamic recrystallisation	>550	Fitz Gerald & Stünitz 1993, Rosenberg & Stünitz 2003
	Diffusion creep associated strength drop	>600	Altenberger & Wilhelm 2000, Rosenberg & Süunitz 2003

Table 3.1. Deformation temperature constraints. Compilation of published deformation temperature constraints for quartz, calcite, dolomite and feldspar, determined from microstructural observations and slip system activities. See text for discussion.

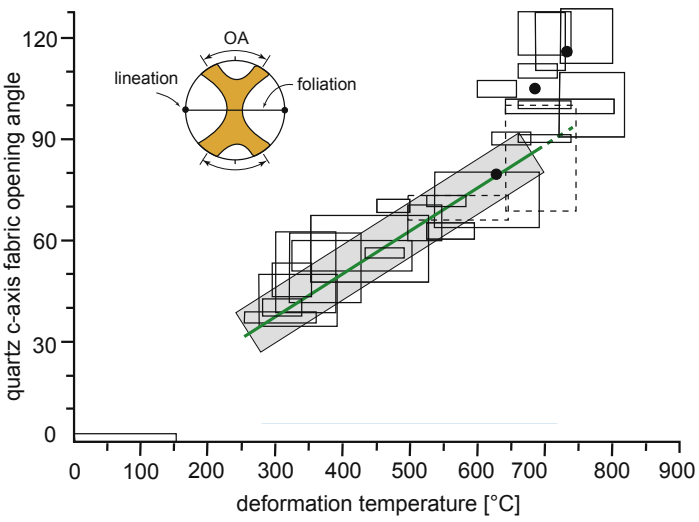

Figure 3.17. Quartz c-axis opening angle thermometer of Kruhl (1998). Green line shows linear best fit relationship between opening angle and deformation temperature under 'average geological strain rates'. Grey box corresponds to ±50 °C uncertainty. Black outlined boxes and black filled circles represent individual data sets from which thermometer was calibrated. In each case, opening angles were measured in rocks with an independently constrained temperature. The size and position of each box reflects the range of opening angles and temperatures measured in each data set. Data sets were compiled by Kruhl (1998), Morgan & Law (2004) and Law (2014). Modified from Law (2014), after Kruhl (1998) and Morgan & Law (2004).

Identification of these microstructures in samples collected from the Modi Khola and Kali Gandaki transects provides an indication of the likely temperature ranges through which they were deformed. Microstructures and textures are identified in thin section (*Section 3.2*), whilst active crystal slip systems are inferred from CPO configurations (*Section 3.3*). The microstructures used to constrain deformation temperatures are described below. *Section 3.3* described the crystal slip systems used to determine deformation thermometry.

Kruhl (1998) presented a quartz deformation thermometer based on the opening angle of *c*-axis crossed girdle fabrics. Quartz *c*-axis crossed girdle fabrics develop though dislocation glide on the (c), {m} and {r/z} planes in the <*a*> direction (Tullis, 1977). The relative critical resolved shear stress of each of these slip systems varies with temperature in such a way that the angle between the two crossed girdles increases with temperature (Figure 3.17) (Kruhl, 1998). Opening angles are determined from the radial angle between crossed girdle *skeletons* drawn on contoured *c*-axis pole figures. Temperature estimates have an uncertainty of ±50 °C to reflect the potential variable influence of strain rate and hydrolytic weakening on opening angles in the natural data sets used by Kruhl (1998) to develop this deformation thermometer (Law, 2014). EBSD derived quartz *c*-axis crossed girdle opening angles are displayed in Figure 3.18. A selection of these samples were also analysed using an optical microscope and Leitz universal stage (U-stage) for a comparison of methods. All U-stage derived opening angle analysis produced temperatures within error of the EBSD data set. U-stage data are presented in the appendix (Figure A.3.27).

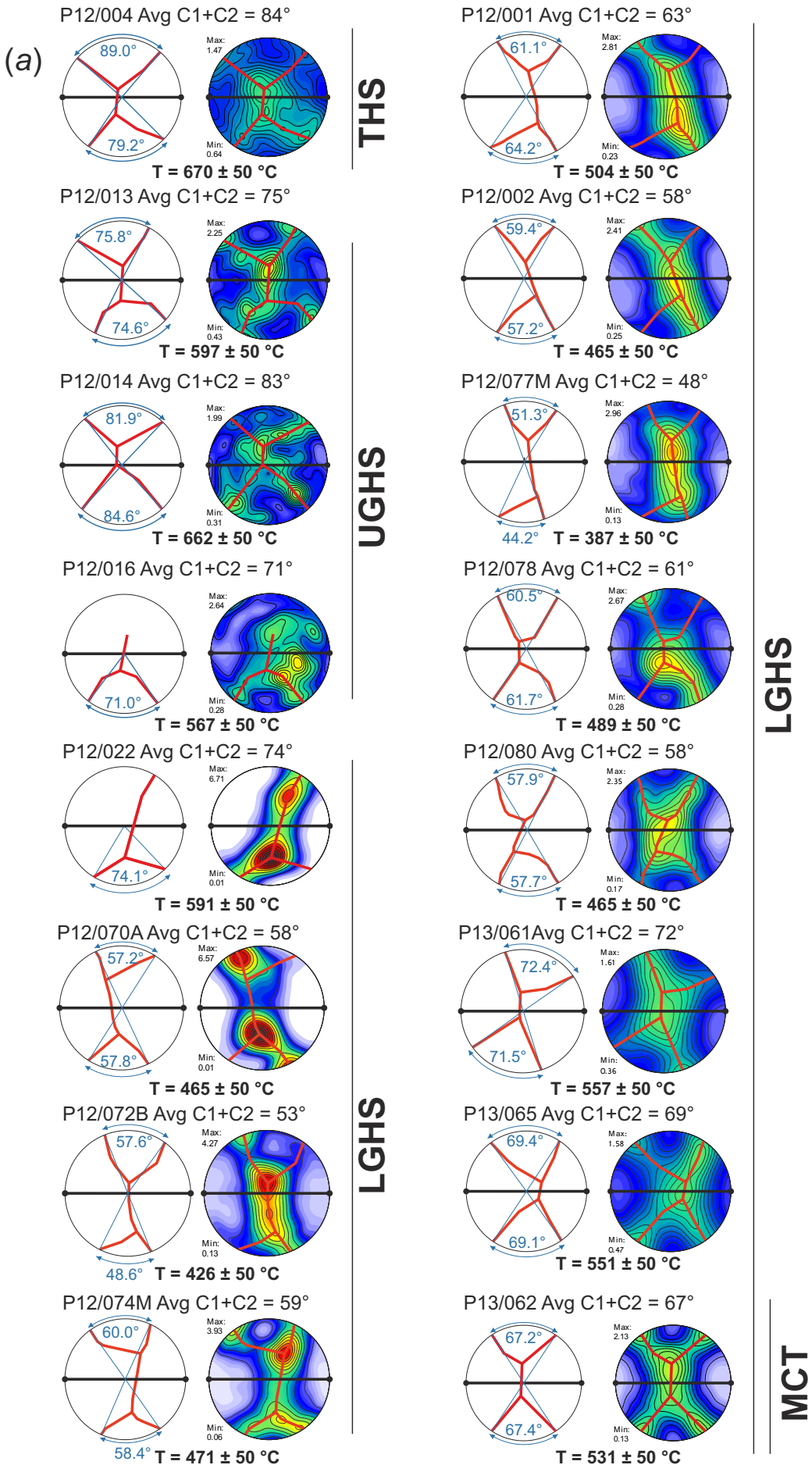

Figure 3.18. Quartz opening angle thermometry results

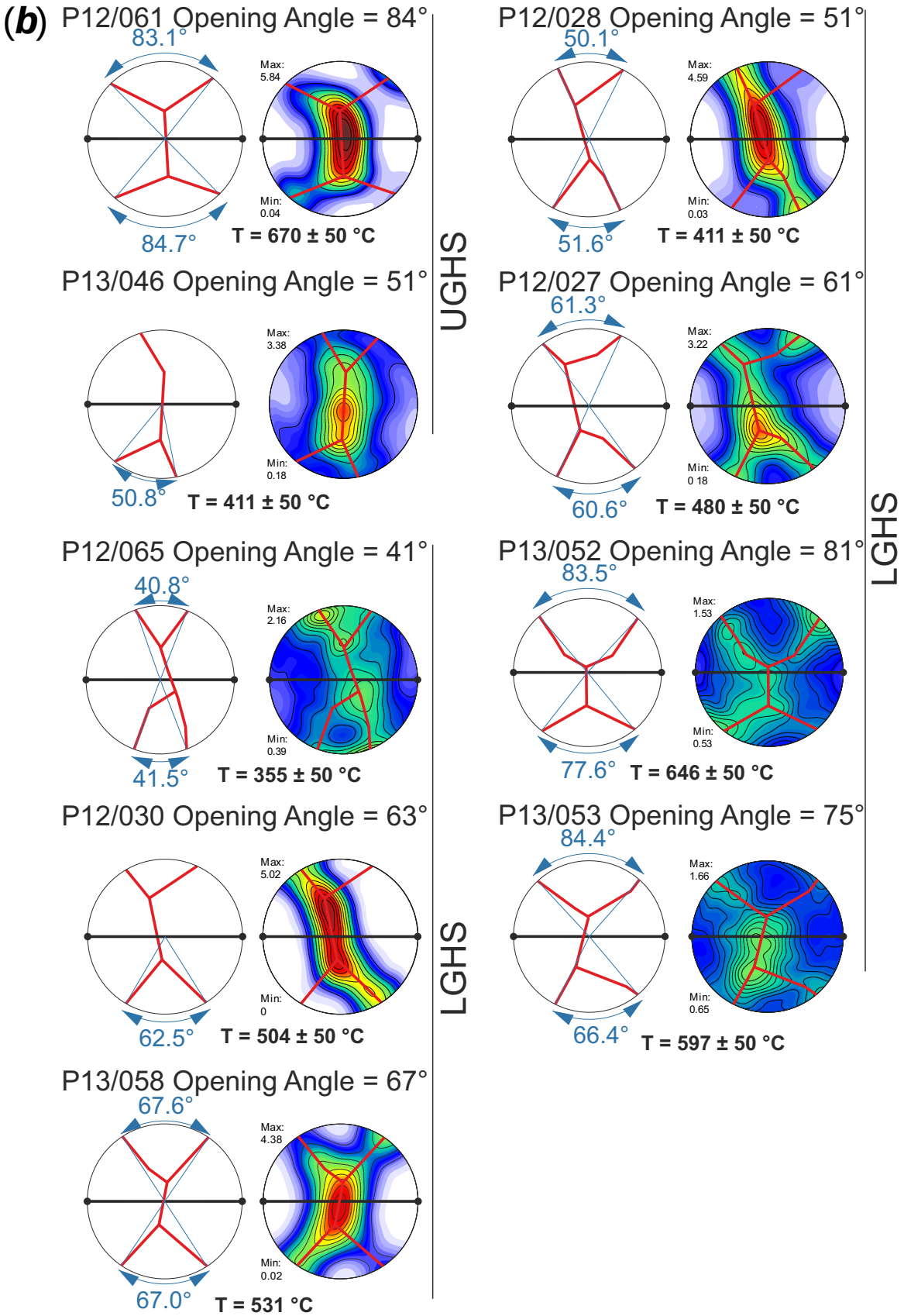

Figure 3.18. Quartz c-axis opening angle thermometry data. (*a*) Modi Khola results. (*b*) Kali Gandaki results. Opening angles are measured from the red fabric 'skeletons', which are drawn on top of the quartz *c*-axis pole figures. Temperatures are determined from the average best-fit opening angle of each fabric skeleton using the Kruhl (1998) thermometer. All temperatures have a ±50 °C uncertainty. Sample locations presented on Figures 2.3 & 2.4. Full sample description presented in sample list in the Supplementary Data CD.

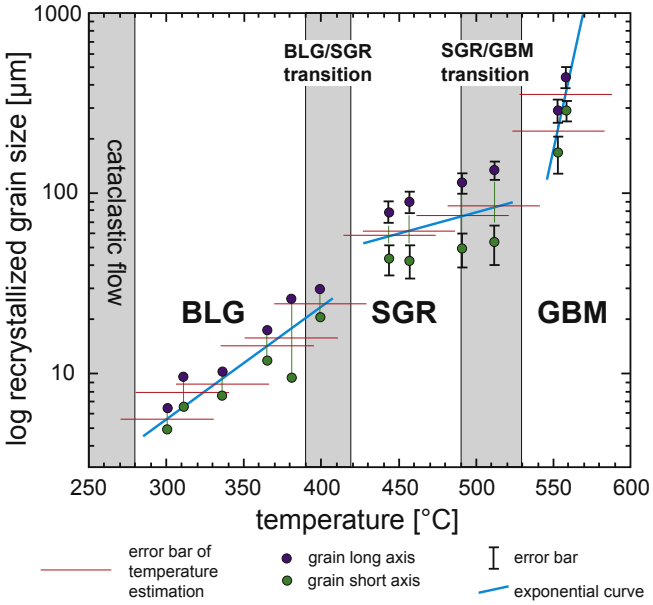

Figure 3.19. Temperature dependent dynamic recrystallisation mechanisms of quartz and associated grain sizes from the Tonale Line Fault Zone (Stipp et al., 2002). Dynamic recrystallisation mechanisms include: grain boundary bulging (BLG), subgrain rotation (SGR) and grain boundary migration (GBM). Grey bars represent transitional zones between recrystallisation mechanisms. From Law (2014) after Stipp *et al.* (2002).

Stipp *et al.* (2002) presented a deformation temperature thermometer for quartz based on recrystallisation microstructures recorded in quartz veins from the Tonale Line shear zone in the Italian Alps. These rocks were deformed along the margin of the Adamello pluton and subjected to contact metamorphism during shearing (Stipp *et al.*, 2002). Variations in quartz recrystallisation microstructures were correlated with a well-constrained gradient of decreasing temperature traced away from the pluton, determined from the syn-kinematic metamorphic mineral assemblages of surrounding polymineralic metasedimentary rocks. The thermometer predicts that at geological strain rates of ~10^{-12} to 10^{-14} s^{-1} the dominant quartz microstructures evolve from (*1*) grain boundary bulging recrystallisation (BLG; ~280-390 °C) to (*2*) subgrain rotation recrystallisation (SGR; ~420-490 °C) to (*3*) grain boundary migration recrystallisation (GBM; >530 °C) (Stipp *et al.* 2002) (Figure 3.19). Beyond the contact aureole, where temperatures did not exceed 280 °C, quartz displayed brittle behaviour (Stipp *et al.* 2002). Additionally, at high temperatures (>650 °C), chessboard subgrain patterns are often observed in quartz, which result from combined (c)<*a*> and {m}[*c*] slip (Kruhl, 1996).

Calcite twinning microstructures provide a low temperature (<400 °C) deformation thermometer (Burkhard, 1993; Ferrill *et al.*, 2004). Analysis of naturally deformed limestones deformed at known temperature ranges reveal the dominance of thin twins (Type I) below 170 °C and thick twins (Type II) above 200 °C (Burkhard, 1993; Ferrill *et al.*, 2004). Above 250 °C, the onset of dynamic recrystallisation can result in curved, tapered and lensoid thick twins (Type III) that may become patchy and serrated (Type IV) with increasing amounts of recrystallisation (Burkhard, 1993; Ferrill *et al.*, 2004). At higher temperatures and strains, dynamic recrystallisation and twin migration work to remove twins (Burkhard, 1993; Ferrill *et al.*, 2004). The use of this thermometer is limited, however, as calcite twins only form under low strain and recrystallisation may

occur at temperatures below 250 °C (Burkhard, 1993; Ferrill *et al.*, 2004). An additional constraint is provided by the presence or absence of dolomite twins, which form at 300-600 °C (Barber *et al.*, 1981).

Variations in feldspar recrystallisation mechanisms provide some indication of deformation temperatures (e.g. Tullis & Yund, 1991; Fitz Gerald & Stünitz, 1993; Altenberger & Wilhelm, 2000; Stünitz *et al.*, 2003) Recrystallisation of feldspar occurs at temperatures of >450 °C (Tullis & Yund, 1991; Fitz Gerald & Stünitz, 1993). Correlation between naturally deformed feldspar with known temperature constraints with experimental deformation studies suggests that plagioclase develops BLG + SGR recrystallisation textures between 450-650 °C (Tullis & Yund, 1991; Fitz Gerald & Stünitz, 1993). SGR + GBM recrystallisation textures are more common at temperatures of >550 °C (Fitz Gerald & Stünitz, 1993; Rosenberg & Stünitz, 2003). Additionally, at high temperatures (approx. >600 °C) and strains, diffusion-creep becomes the dominant deformation mechanism of feldspar and generally accommodates more strain than dislocation creep mechanisms (Dell`Angelo *et al.*, 1987; Altenberger & Wilhelm, 2000; Bons & Den Brok, 2000; Rosenberg & Stünitz, 2003; Menegon *et al.*, 2008). Studies of naturally deformed tonalite indicate that the transition from dominant dislocation to diffusion creep mechanisms is also associated with a decrease in strength of feldspar relative to biotite and quartz. (Altenberger & Wilhelm, 2000; Rosenberg & Stünitz, 2003)

3.4.2. Metamorphic temperature constraints

Temperatures indicated by analyses of metamorphic mineral assemblages provide additional constraints for the thermo-kinematic evolution of the GHS and bounding units. Peak metamorphic temperatures are particularly useful for determining an upper bound for deformation temperatures. Previously published metamorphic temperatures from the Modi Khola transect are derived from garnet-biotite thermometry (Kaneko, 1995; Corrie & Kohn, 2011), Zr-in-titanite thermometry (Corrie & Kohn, 2011) and Raman spectroscopy of carbonaceous material (RSCM) thermometry (Beyssac *et al.*, 2004). In the Kali Gandaki transect, previously published grt-bt thermometry (Le Fort *et al.*, 1987) is supplemented by grt-bt and Zr-in-titanite thermometry measured in this study. The new thermometry data are presented below. The full data set, including back-scattered electron (BSE) images of sample thin sections with analysis locations is included in the supplementary CD.

3.4.2.1 Garnet-biotite (grt-bt) Fe/Mg exchange thermometry

Three samples were selected for grt-bt thermometry from Unit I of the UGHS in the Kali Gandaki transect (P12/055, P12/058, P12/060). Sample mineral assemblages are summarised in Table 3.2. Garnet grains in samples P12/058 and P12/060 are 5-10 mm and 0.5-1 mm in diameter, respectively and are euhedral to subhedral. Garnet grains in P12/055 are 0.5-5 mm in diameter and are anhedral and the largest of these grains show significant signs of resorption.

Major element analyses were conducted using wavelength dispersive X-ray spectroscopy with a JEOL 8230 electron microprobe using *Probe for EPMA* (Probe Software Inc.); see Table 3.2a for analytical conditions. Garnet rims and cores and biotite cores were analysed and line-traverses with ~50-100 μm spacing between spot analyses were conducted on the largest grains. The largest biotite grains furthest away from garnet grains were selected for analysis to limit the effects of diffusion between garnet and biotite after metamorphism (Dasgupta *et al.*, 2004). If present, biotite grains in the middle of biotite amalgamations were preferentially chosen. For each grain analysis location, three individual spot analyses were conducted with 10-20 μm spacing.

Corrections were made to the data, based on the compositional errors recorded by standards that were analysed before, after and between each sample analysis. After correction, garnet and biotite compositions with oxide wt% totals <98% and >102% were discarded (assuming a 4% H_2O content in biotite; e.g. Fleet, 2003). An average composition for each grain analysis location (i.e. rim, core or intermediate position between rim and core) was then calculated from the individual spot analyses conducted at that location.

Peak metamorphic temperatures were calculated using the garnet-biotite thermometer of Ferry and Spear (1978) to allow for comparison with Corrie and Kohn (2011), who also used this calibration for grt-bt thermometry of samples from the Modi Khola transect. In order to account for retrograde exchange reactions that can occur at high temperatures, peak metamorphic garnet compositions were identified as those with the lowest Mn and Fe/(Fe+Mg) (Kohn *et al.*, 1992; Corrie & Kohn, 2011).

In samples P12/055 and P12/060 the smallest garnets were excluded as these had homogenous compositions with Mn and Fe/(Fe+Mg) volumes equal to the highest Mn and Fe/(Fe+Mg) volumes of the larger grains, and are therefore unlikely to represent peak metamorphic compositions. Garnet compositions were paired with an average

(*a*)

Mineral Analysis	Acclerating Voltage (kV)	Current (nA)	Beam size (µm)	On-peak count times (s) Si	Ti	Al	Cr	Fe	Mn	Mg	Ca	Ba	Na	K	F
Biotite	15	10	2	10	20	10	20	30	20	20	20	15	10	10	40
Garnet	15	30	<1	10	20	10	20	30	20	20	20	-	10	10	-

(*b*)

Sample	Mineralogy	Garnet Inclusions	Mineral	Cation Per Unit Formula Fe	Mn	Mg	Ca	T (°C)
P12/055	Qtz + Bt + Grt + Plg (An% 0-30) + Ky + Msc (secondary) + Rt	Qtz + Plg + Bt + Rt	Biotite	2.462	-	2.667	-	-
			Garnet 1	1.955	0.083	0.575	0.404	774
			Garnet 2	1.963	0.149	0.531	0.385	734
							Sample average temperature:	**754 ± 29**
			Mineral	**Fe**	**Mn**	**Mg**	**Ca**	**T (°C)**
P12/058	Qtz + Bt + Grt + Plg (An% 0-30) + Ky	Qtz + Rt + Py + Chl	Biotite	2.298	-	2.811	-	-
			Garnet 1	2.128	0.088	0.714	0.080	780
			Garnet 2	2.160	0.068	0.716	0.069	773
			Garnet 3	2.143	0.077	0.707	0.085	772
							Sample average temperature:	**775 ± 13**
			Mineral	**Fe**	**Mn**	**Mg**	**Ca**	**T (°C)**
P12/060	Qtz + Bt + Grt + Plg (An% 0-30) + Msc + Ilm	Qtz + Rt + Py	Biotite	2.348	-	2.840	-	-
			Garnet 1	2.063	0.100	0.610	0.236	724
			Garnet 2	2.101	0.103	0.582	0.227	695
			Garnet 3	2.105	0.103	0.582	0.226	695
			Garnet 4	2.077	0.095	0.610	0.229	721
							Sample average temperature:	**709 ± 22**

Table 3.2. Garnet-biotite major element analyses experimental set-up and results. (*a*) Electron microprobe conditions and on-peak count times for each element analysis. High and low off-peak count times are half on-peak count times. (*b*) Garnet-biotite Fe, Mn, Mg and Ca compositions and thermometry results. See text for discussion.

(*a*)

Samples	Acclerating Voltage	Current (nA)	Beam size (µm)	On-peak count times (s) Nb	Si	Zr (PETJ)	Zr (PETH)	Zr (PETH)	Ti	Al	Fe	Ca	K	F
P12/053, P12/054A	15	200	1	80	10	240	180	200	10	20	40	10	40	-
P13/031, P13/032				90	10	240	180	205	10	20	40	10	40	200

(*b*)

Sample	Unit	Mineralogy	Spot Analysis	Rim/Core	Zr (ppm)	T (°C)
P12/053	UGHS Unit II	Cal + Qtz + Plg (An 0-66%) + Ksp + Scp+ Clz + Tt+Cpx + Phl	P053_T2_2	Rim	91.92	751
			P053_T2_2	Rim	130.47	769
			P053_T2_2	Rim	108.92	760
			P053_T5_2	Rim	59.96	730
			P053_T7_2	Rim	85.84	747
			P053_T8_3	Rim	92.22	751
			P053_T8_3	Rim	84.56	747
			P053_T8_3	Rim	106.57	759
			P053_T9_2	Rim	108.31	759
			P053_T9_2	Rim	88.83	749
			P053_T9_2	Rim	73.04	739
					Sample average rim temperature (°C)	**750 ± 45**
			Spot Analysis	**Rim/Core**	**Zr (ppm)**	**T (°C)**
P12/054A	UGHS Unit II	Cal + Qtz + Plg (An 0-66%) + Ksp + Scp+ Clz + Tt + Cpx + Msc	P054_T1_1	Core	183.92	788
			P054_T1_1	Core	158.07	780
			P054_T2_1	Core	176.08	785
			P054_T2_1	Core	152.16	777
			P054_T3_1	Core	200.81	793
			P054_T3_1	Core	203.59	793
			P054_T6_1	Core	165.41	782
			P054_T8_1	Core	148.27	779
			P054_T8_1	Core	164.6	782
			P054_T9_1	Core	181.68	787
			P054_T9_3	Core	181.95	787
			P054_T10_1	Core	179.4	786
			P054_T10_1	Core	196.67	792
			P054_T16_1	Core	148.95	776
			P054_T16_1	Core	128.42	768
					Sample average core temperature (°C)	**785 ± 45**
			Spot Analysis	**Rim/Core**	**Zr (ppm)**	**T (°C)**
P13/032	UGHS Unit III	Cal + Qtz + Plg (An 0-66%) + Ksp + Scp+ Clz + Tt + Bt	P032_T7_1	Core	141.76	774
			P032_T7_3	Rim	91.03	750
			P032_T11_2	Rim	90.53	750
			P032_T12_4	Core	132.75	770
			P032_T13_1	Core	87.87	749
			P032_T13_2	Core	96.69	754
			P032_T13_3	Core	108.11	759
			P032_T13_4	Rim	62.41	731
					Sample average whole grain temperature (°C)	**755 ± 50**
			Spot Analysis	**Rim/Core**	**Zr (ppm)**	**T (°C)**
P13/031	STDS	Cal + Qtz + Plg (An 0-66%) + Ksp + Scp+ Clz + Tt + Cpx + Amp + Grt	P031_T3_1	Core	69.58	737
			P031_T3_3	Rim	87.71	749
			P031_T6_1	Core	42.34	713
			P031_T8_3	Rim	56.41	726
			P031_T10_2	Core	137.62	772
			P031_T12_1	Core	35.56	704
			P031_T12_4	Rim	31.14	698
			P031_T13_1	Core	108.28	759
			P031_T15_1	Core	44.92	715
					Sample average whole grain temperature (°C)	**730 ± 60**

Table 3.3. Titanite trace element analyses experimental set-up and results. (*a*) Electron microprobe conditions and on-peak count times for each element analysis. High and low off-peak count times are half on-peak count times. Zr concentrations were analysed with three spectrometers using PETJ and PETH crystals. (*b*) Titanite Zr concentrations and thermometry results. See text for discussion.

biotite core composition calculated for each sample. Temperatures were calculated for specific garnet grains and were then used to calculate an average sample temperature at an assumed pressure of 10 kbar, based on constraints from Corrie and Kohn (2011). Errors were calculated from one standard deviation of the average sample temperature, plus the error associated with ±2 kbar pressure, plus a 6^{o} C error associated with the calibration (Ferry & Spear, 1978). The results are displayed in Table 3.2b.

3.4.2.2. Zr-in-titanite thermometry

Four samples of calc-silicate gneiss (P12/053, P12/054 – Unit II; P13/032 - Unit III; P13/031 – STDS) from the Kali Gandaki transect were selected for trace element analysis of Zr in titanite (Table 3.3). P13/031 and P13/032 were sampled from immediately above and below the AD, respectively. Zircon was identified in all samples, rutile was not observed. Titanite grains are subhedral to anhedral and are often tabular in shape, with grain sizes ranging between ~50-400 μm. Some grains displayed patchy zonation in BSE images and a minority displayed oscillatory zonation, but most appeared homogeneous.

Major and trace element analyses were conducted using wavelength dispersive X-ray spectroscopy with a JEOL 8230 electron microprobe using *Probe for EPMA* (Probe Software Inc.); see Table 3.3a for analytical conditions. Spot analyses were conducted on the largest titanite grains on rims, cores and individual zones (where present), except for P12/054 where only cores were analysed. Corrections were made to the data based on the compositional errors recorded by standards analysed before, after and between each sample analysis. After correction, titanite with oxide wt% totals <97% and >102% were discarded.

Temperatures were calculated using the Zr-in-titanite thermometer of Hayden *et al.* (2008) from the sample average titanite Zr concentrations (ppm) at an assumed pressure of 12 kbar, $a(TiO_2)$ of 0.8 and $a(SiO_2)$ of 1, based on constraints from Corrie and Kohn (2011). Errors were calculated from one standard deviation of the average temperature, plus the error associated with ±2 kbar pressure and ±0.2 $a(TiO_2)$. The highest temperatures in P12/053 were calculated from rim concentration of Zr and are assumed to reflect peak metamorphic conditions (Kohn & Corrie, 2011). Titanite rim and core temperatures from P13/031 and P13/032 were within error of each other and only titanite core temperatures were calculated for P12/054. These may reflect crystallisation temperatures rather than peak metamorphic temperatures and thus provide a minimum bound for peak metamorphic conditions. The results are displayed in Table 3.3b.

3.4.3. Deformation temperature profiles

The deformation and metamorphic temperature constraints described above are compiled into tectono-stratigraphic columns for the Modi Khola and Kali Gandaki transects to reveal the preserved deformation temperature profiles for each transect (Figures 3.20 & 3.21).

3.4.3.1. Modi Khola transect

At the base of the Modi Khola transect (Figure 3.20) in the LHS, brittle and low temperature ductile quartz microstructures and active slip systems define a deformation temperature range of <280 ^{o}C to 300-400 ^{o}C.

In the LGHS, quartz microstructures show a progression in deformation temperatures from ~280-490 ^{o}C in the lower ~1 km, to 420-530 ^{o}C above this structural level. Quartz mixed <*a*> slip indicative of 400-500 ^{o}C deformation temperatures observed across the LGHS supports this interpretation. Additionally, quartz CPO from the LGHS augen gneiss unit display {m}<*a*> slip fabrics indicative of deformation at 500-700 ^{o}C. Quartz *c*-axis opening angles in the immediate hanging wall of the MCT record temperatures of 500-600 ^{o}C. Above this, opening angles record temperatures of ~350-500 ^{o}C in the lower portion of the LGHS and 400-550 ^{o}C in the upper portion. In the immediate footwall of the CT, opening angles record a temperature of ~550-650^{o}C. Dolomite twinning and slip system activity suggestive of deformation between 300-600 ^{o}C at the top of the LGHS are in agreement with quartz derived deformation temperatures. Grt-bt and RSCM thermometry indicate peak metamorphic temperatures of ~475-600 ^{o}C (Beyssac *et al.*, 2004; Corrie & Kohn, 2011), whilst grt-bt thermometry from garnet rims produces temperatures of ~400-450 ^{o}C (Kaneko, 1995). These temperatures coincide with the upper and lower bounds of deformation temperature estimates in the LGHS. This suggests that the LGHS has recorded and preserved progressive deformation

Figure 3.20. Deformation temperature profile for the Modi Khola transect. Each box corresponds to a particular deformation microstructure or active slip system observed in samples from the Modi Khola transect. The size and position of each box represents the temperature range over which each microstructure/slip system is active (horizontal-axis) and structural height above the MCT at which they are observed (vertical-axis). Numbers within each box correspond to a particular microstructure or slip system, listed to the right of the profile. Temperature constraints are determined from published sources presented in Table 3.1. Zone of dashed red lines indicates where syn-tectonic partial melting is observed. The lower bounding temperature of 750 ^{o}C of this melt zone corresponds to minimum temperature for fluid absent melting of muscovite at ~10 kbar, based on White *et al.* (2001). Overlain on the profile are quartz opening angle thermometry results (white circles – this study), plus RSCM thermometry (grey triangles – Beysaac *et al.* 2004), garnet-biotite thermometry (light grey squares; garnet rim temperatures – Kaneko 1995; medium grey squares; garnet core temperatures – Kaneko 1995; dark grey squares; peak metamorphic temperatures – Corrie & Kohn 2011) and Zr-in-titanite thermometry (grey diamonds – Corrie & Kohn 2011).

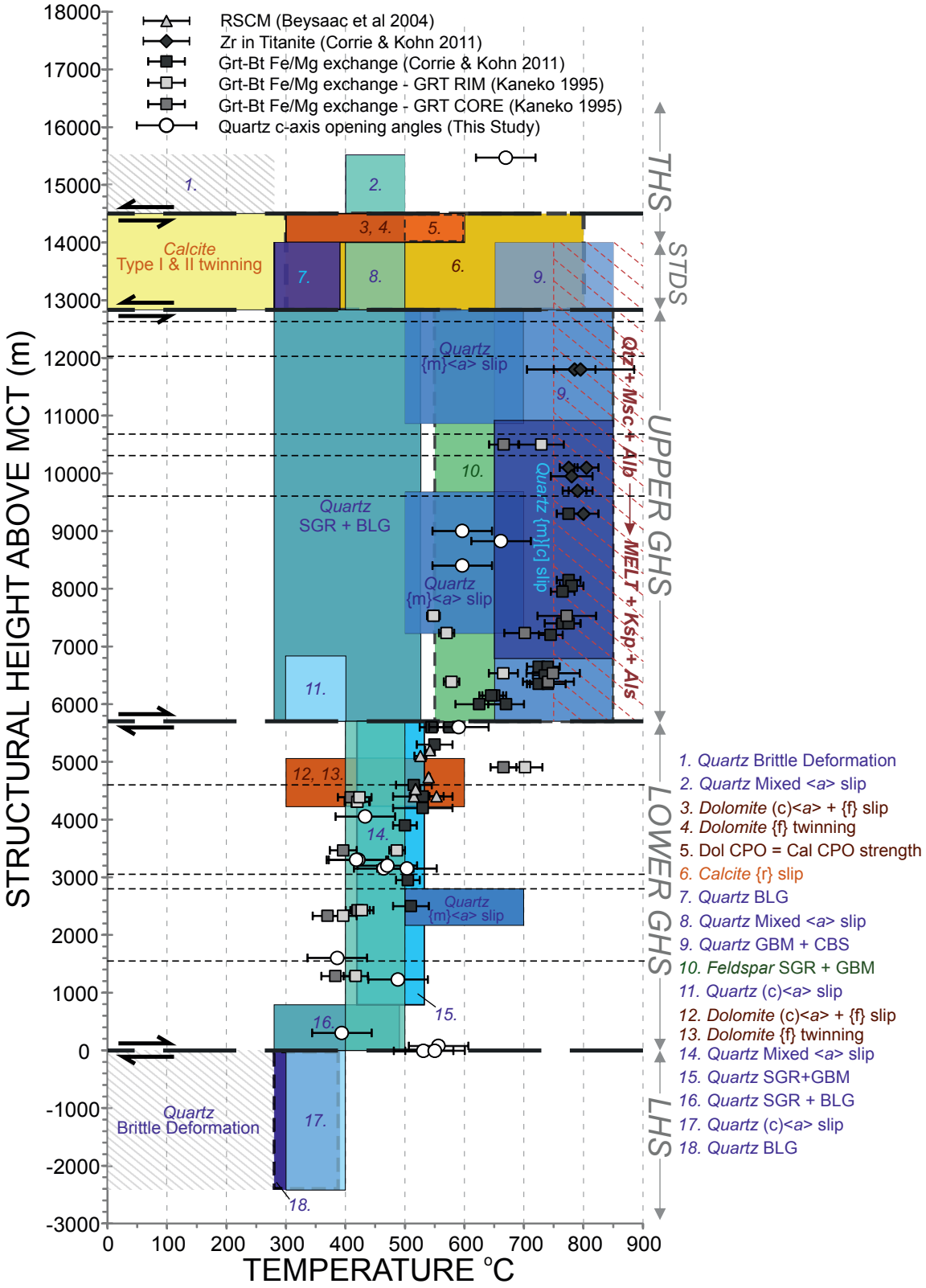

Figure 3.20. Deformation temperature profile for the Modi Khola transect

from peak conditions of ~500-600 °C through a cooling retrograde path. The correlation between garnet rim temperatures and the lower deformation temperature bounds may also imply that deformation was continuous from peak conditions through to ~400-450 °C during cooling. These observations are comparable to similar studies from elsewhere in the Himalaya that report up-section increasing deformation temperature gradients through LGHS-equivalent tectono-stratigraphy (Bouchez & Pêcher, 1981; Yakymchuk & Godin, 2012; Law *et al.*, 2013; Larson & Cottle, 2014).

In the UGHS of the Modi Khola transect, inferred deformation temperatures range from high (>650 °C) through to intermediate (280-530 °C) temperatures (Figure 3.20). Across the whole UGHS, quartz microstructures record high temperature deformation (>650 °C). A subordinate overprint of intermediate to low temperature deformation suggests that deformation may have continued between 280-530 °C. Active quartz slip systems determined from CPO configurations record a trend in deformation temperatures from 300-400 °C in the lower 1 km, through 500-700 °C and >650 °C in the middle ~4km to 500-700 °C in the upper ~2 km. Quartz *c*-axis opening angles from the middle of the UGHS record temperatures of ~550-700 °C. Feldspar microstructures from across the UGHS show high temperature recrystallisation textures of >550 °C.

Temperatures derived from metamorphic mineral assemblages indicate that peak deformation temperatures in the UGHS did not exceed 850 °C. Peak metamorphic temperatures increase from ~580-700 °C at the base of the UGHS, through to ~700-800 °C at 0.5-1 km above the CT, to ~750-850 °C at >1.5 km above the CT (Corrie & Kohn, 2011). Garnet rim temperatures of 550-600 °C in the lower half of the UGHS and ~700 °C in the middle of the UGHS (Kaneko, 1995) fall both within the temperature range of recorded active quartz slip systems and *c*-axis fabric opening angle temperatures. These are interpreted as the lower temperature bound of major ductile deformation in the UGHS. This implies that deformation in the UGHS occurred at a peak temperature of 750-850 °C and continued down to a temperature of ~550-600 °C.

In the STDS in the Modi Khola transect, the thermal profile is only poorly constrained due to a small sample size (Figure 3.20). In the lower half of the STDS, high temperature (>650 °C) quartz microstructures are observed with the same subordinate low temperature (280-500 °C) overprint as reported from the UGHS. Across the STDS calcite microstructures and CPO fabrics indicate deformation above and below ~300 °C. At the top of the STDS, dolomite microstructures and CPO fabric shape and strength relative to calcite CPO strength indicate deformation temperatures of 500-600 °C, and 300-600 °C. These observations suggest that the STDS was active at a temperature of >500 °C, but may have continued to deform down to 390-280 °C (Figure 3.20).

Only the lowest 1 km of vertical structural section of the THS is sampled from the Modi Khola transect (Figure 3.20). Brittle and intermediate temperature ductile deformation is recorded by quartz at <280 °C and 400-500 °C, respectively. Anomalous quartz *c*-axis fabric opening angles indicating temperatures of 620-720 °C do not fit with the chloritic composition of these rocks and are considered to be an over estimate, perhaps due to hydrolytic weakening (e.g. Law, 2014).

3.4.3.2. Kali Gandaki transect

At the base of the Kali Gandaki transect (Figure 3.21), deformation temperatures inferred from quartz microstructures in the LGHS increase from 280-420 °C in the immediate hanging wall of the MCT, through to 280-490 °C at structural levels between 0.2-1.7 km above the MCT and 420-530 °C at structural levels >1.7 km above the MCT. At the top of the LGHS in the dolomitic marble and metacarbonate unit, quartz recrystallisation microstructures indicate a wider range of deformation temperature (280-530 °C). Additionally, relict quartz porphyroclasts in the lower portion of the LGHS preserve the remnants of an earlier high temperature (>650 °C) deformation. Active quartz slip systems generally record deformation between 400-500 °C in the LGHS, and an additional lower temperature deformation (300-400 °C) in the upper ~2 km of the LGHS. Quartz *c*-axis fabric opening angles (this study, Larson & Godin 2009) record temperatures of 500-700 °C ~2 km above the MCT, ~400-550 °C in the middle portion of the LGHS, and 300-400 °C in the top 1 km. This up-section decrease in quartz opening angle temperatures in the LGHS in the Kali Gandaki transect does not fit with the classic inverted metamorphic profile of the GHS. However, microstructural observations suggest that the higher temperatures recorded at the base may relate to a an older (perhaps pre Himalayan) high temperature deformation, as suggested by relict porphyroclasts with chess board subgrain textures. Likewise, at the top of the LGHS, the recorded lower temperature quartz opening angles may relate to a younger, lower temperature deformation that post-dates the main phase of pervasive ductile shear recorded above and below this sample. As such, whilst the quartz opening angle temperatures do not fit the inverted metamorphic profile, they do not necessarily refute it if they record deformation at different stages. Calcite and dolomite microstructures and CPO configurations in the upper 2 km of the LGHS record both intermediate (300-600 °C and 500-600 °C) and low (<300 °C and >250 °C) deformation temperatures. A garnet core metamorphic temperature of ~620 °C recorded at the top of the LGHS (Le Fort *et al.* 1987) correlates reasonably well with the calcite and dolomite derived deformation temperatures. These observations are comparable to similar studies from elsewhere in the Himalaya that record increasing deformation temperatures, up-section

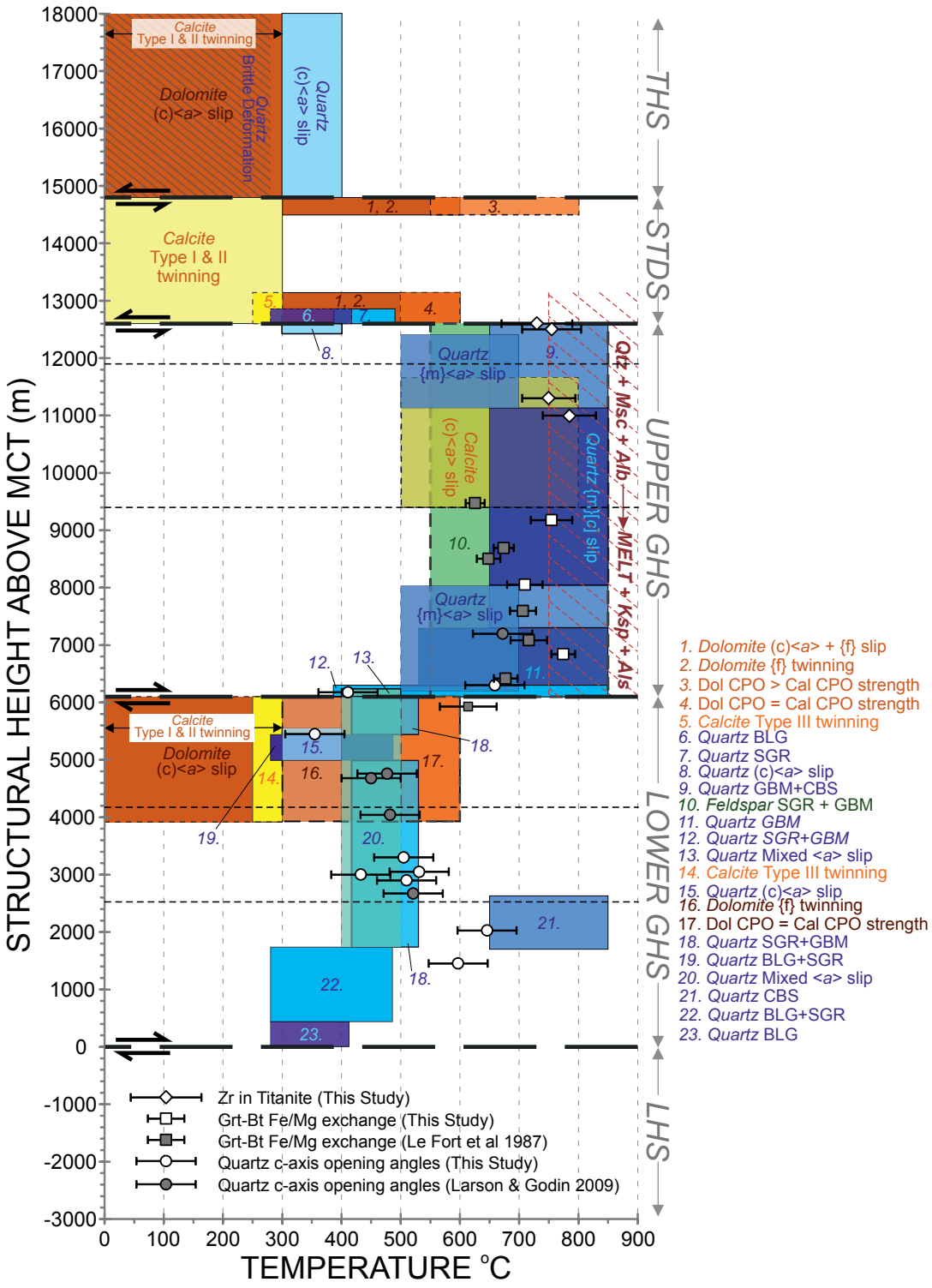

Figure 3.21. Deformation temperature profile for the Kali Gandaki transect. See Figure 3.20 for explanation of profile. Overlain on the profile are quartz opening angle thermometry results (white circles – this study; grey circles – Larson & Godin 2009), garnet-biotite thermometry (white squares – this study; grey squares – Le Fort *et al. 1986*) and Zr-in-titanite thermometry (white diamonds – this study) data.

through LGHS-equivalent tectono-stratigraphy (Bouchez & Pêcher, 1981; Yakymchuk & Godin, 2012; Law *et al.*, 2013; Larson & Cottle, 2014).

In the UGHS in the Kali Gandaki transect high temperature (>500 ^{o}C) deformation is recorded over a smaller temperature range than in the Modi Khola transect. Feldspar microstructures from across the UGHS indicate deformation temperatures of >550 ^{o}C. In the lower ~1 km of the UGHS, quartz recrystallisation microstructures indicate deformation temperatures from >530 ^{o}C to 420-530 ^{o}C. Quartz microstructures from the rest of the UGHS in the Kali Gandaki transect are entirely dominated by high temperature deformation (>650 ^{o}C). The intermediate to low temperature subordinate deformation overprint (280-530 ^{o}C) observed in the UGHS in the Modi Khola transect is absent from the UGHS in the Kali Gandaki transect. Active quartz slip systems record a change in deformation temperatures from 400-500 ^{o}C at the base of the UGHS, to 500-700 ^{o}C at structural levels between 0.2-2 km above the CT, followed by a ~3 km thick middle section of the UGHS at temperatures >650 ^{o}C. Above this, deformation temperatures decrease up-section from 500-700 ^{o}C in the upper portion of the UGHS to 300-400 ^{o}C in the immediate footwall of the AD. Deformation temperatures inferred from active calcite slip systems (>500 ^{o}C) fit with this trend. Quartz *c*-axis fabric opening angles from the immediate hangingwall of the CT indicate temperatures of 360-460 ^{o}C. At ~100 m above the CT, opening angles from the lower portion of the UGHS indicate temperatures of ~610-720 ^{o}C. The variation in quartz deformation temperatures with vertical structural position indicates an inverted temperature profile in the lower portion of the UGHS, followed up-section by a right-way-up thermal profile.

Metamorphic mineral assemblages in the UGHS suggest that peak deformation temperatures did not exceed ~700-825 ^{o}C (this study, Le Fort *et al.*, 1987). Quartz *c*-axis fabric opening angle thermometry results fall close to or within error of these metamorphic temperature estimates. This coincidence suggests that the main phase of high temperature retrogressive deformation in the UGHS began at ~700-825 ^{o}C and continued during cooling to temperatures of ~600-700 ^{o}C. Consequently, the main phase of penetrative deformation in the UGHS in the Kali Gandaki transect occurred over a smaller temperature range than in the Modi Khola transect.

Within the STDS of the Kali Gandaki transect (Figure 3.21), dolomite, calcite and quartz microstructures, coupled with CPO fabrics from the lowermost 0.5 km of vertical structural section, record deformation between 500-600 ^{o}C and down to as low 250-300 ^{o}C during cooling. Calcite twins across the whole of the STDS record low strain deformation at <300 ^{o}C. The central portion of the STDS is devoid of any useful deformation temperature indicators. Calcite CPOs define ‘Low Temperature’ fabrics whilst in the uppermost 0.4 km of vertical section, dolomite CPOs are similar to ‘High

Temperature' calcite configurations (*sensu* Wenk *et al.*, 1987). Dolomite microstructures and CPO configurations in the top 0.4 km of the STDS record deformation at 300-600 ^{o}C and >550 ^{o}C respectively. A single Zr-in-titanite temperature (this study) from the immediate hangingwall of the AD, indicates a peak temperature of 730 ± 60 ^{o}C at the base of the STDS.

In the THS in the Kali Gandaki transect (Figure 3.21), brittle and low temperature ductile deformation of quartz indicate deformation temperatures of <280 ^{o}C and 300-400 ^{o}C, respectively. Calcite and dolomite microstructures and CPO fabrics also indicate that deformation temperatures in the THS were low (<300 ^{o}C).

3.5 Kinematic interpretations

Deformation and metamorphic temperature profiles for both sampling transects described above, mimic the well documented inverted metamorphic sequence observed up-section through the lower portions of the GHS along the central and eastern Himalaya (e.g. Le Fort, 1975; Yin, 2006). The gradational changes in deformation temperatures indicated in both deformation temperature profiles (Figures 3.20 & 3.21) help identify specific tectonic units with distinct deformation histories that are potentially similar to other parts of the Himalaya. The correlation between peak temperatures of metamorphism and peak deformation temperatures, and the overprinting relationship of lower temperature on higher temperature microstructures, indicates that these profiles record progressive deformation on a retrograde path (Figure 3.22). The thermo-kinematic evolution of the GHS in the Annapurna-Dhaulagiri region can be divided into three distinct deformation stages (Figure 3.23), defined by the distribution and migration of deformation through evolving temperature regimes.

The earliest deformation stage (Figure 3.23a) is characterised by penetrative coaxial and non-coaxial shearing recorded throughout the UGHS, which occurred at, and close to, peak metamorphic temperatures (~700-850 ^{o}C) (Figure 3.22). Field observations confirm that this deformation took place contemporaneously with partial melting (Figure 2.9) under conditions suitable for mid-crustal channel flow (Figure 3.23a) (Beaumont *et al.*, 2004; Grujic, 2006; Jamieson *et al.*, 2011). Strain geometries determined from microstructures (core-mantle structures, S-C fabrics, SPO) and CPO fabrics suggest that the degree of coaxial deformation increases towards the middle of the UGHS and that non-coaxial deformation dominates the margins. Coaxial 'flattening folds' and high temperature quartz chessboard subgrain textures observed in the massive quartzite and marble unit of the LGHS may also correspond to this early deformation stage. Such observations are compatible with the geological criteria for channel flow presented in *Section 1.3.5*.

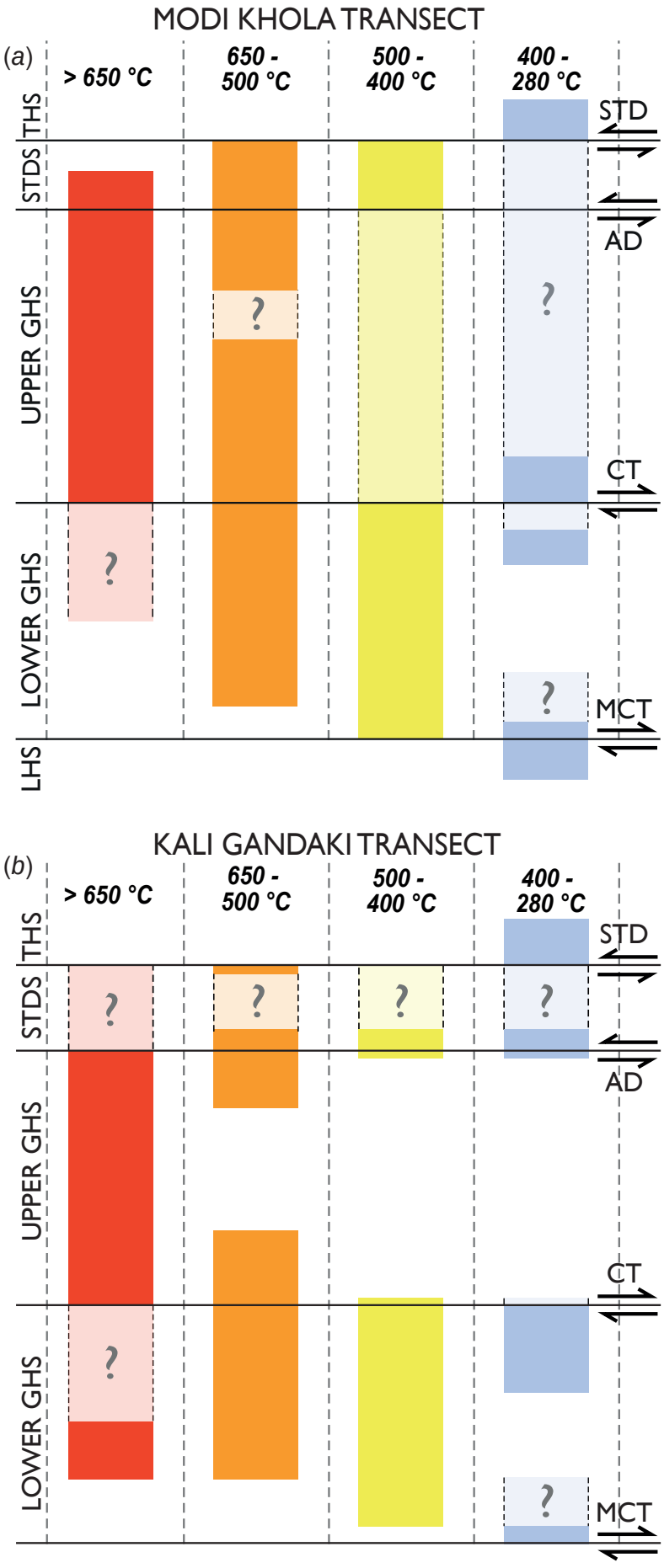

Figure 3.22. Deformation temperature summary profiles. (*a*) Modi Khola transect. (*b*) Kali Gandaki transect. Each column corresponds to a different temperature range. Horizontal solid lines mark positions of shear zones that bound the major tectonic units. Solid coloured bars indicate structural positions in which evidence was found for deformation under specific temperature ranges. Note: where a progressive history of deformation under different conditions can be recognised, individual structural positions can be keyed to multiple deformation temperature ranges. Pale coloured bars with dashed margins correspond to subordinate (i.e. weak) deformation. Question marks denote sections where deformation temperatures are poorly constrained.

Mid crustal channel flow is dependent upon a viscosity drop below some threshold level (Beaumont *et al.*, 2004; Grujic, 2006). As temperatures decrease, viscosity increases and the ability of the UGHS to deform through ductile flow and associated extrusion is significantly reduced. A transition from a pervasive extrusive flow to rigid block behaviour is likely to occur when this threshold viscosity is exceeded and this should coincide with a migration of deformation from the now rigid centre of the UGHS to its rheologically weaker margins. Such a transition is identified from the reduction (Modi Khola) and cessation (Kali Gandaki) of penetrative deformation in the UGHS at ~550-650 ^{o}C. This reduction/cessation of deformation coincides with the highest metamorphic and deformation temperatures recorded in the adjacent STDS and LGHS rocks. Such temperatures may correspond to a threshold viscosity for mid-crustal flow of the UGHS. Below these temperatures, deformation migrates to weaker lithologies (i.e. quartzites, marbles and metapelites) present in the underlying LGHS and overlying STDS.

The second deformation stage (Figure 3.23b) occurs at temperatures of ~400-600 ^{o}C and corresponds to the exhumation of the UGHS as a rigid block, facilitated by ductile shearing in the LGHS (Figure 3.22). This is supported by kinematic indicators such as S-C fabrics and crystal fabrics, which suggest deformation in the LGHS was dominantly non-coaxial. During this stage, deformation is pervasively distributed throughout the LGHS, which behaves as a large shear zone (Figure 3.23b). Such processes are comparable to those invoked by wedge extrusion models (e.g. Burchfiel & Royden, 1985; Grujic *et al.*, 1996; Grasemann *et al.*, 1999) and models for extrusion and exhumation of a solid 'channel flow plug' (e.g. Beaumont *et al.*, 2001). In the Kali Gandaki transect, deformation at these temperatures is also recorded in the STDS. Structural field observations and calcite SPOs have shown that the STDS in this transect has been subjected to a late stage top-to-the-SW/SE, overprinting the older top-to-the-NW/ESE shear (Figures 2.9 & 3.7). This late deformation overprint may be responsible for the intermediate deformation temperatures that also affect the uppermost portion of the UGHS.

The final stage of ductile deformation relates to the localisation of deformation on the MCT and CT (Figure 3.23c) at temperatures of 400-280 ^{o}C (Figure 3.22). The localisation of low temperature quartz, calcite and dolomite deformation 1-2 km below the CT in the LGHS (Figures 3.20 & 3.21) is coincident with the proposed location of the Munsiari thrust (Kohn, 2008; Corrie & Kohn, 2011). This thrust was originally described in the Kumaun Himalaya in NW India (Valdiya, 1980) but has since been extrapolated along strike into the central Himalaya (e.g. Srivastava & Mitra, 1994; Khanal *et al.*, 2014; Robinson & Martin, 2014). Whilst no discrete thrust plane

coincident with the expected location of the Munsiari thrust was observed in the Annapurna-Dhaulagiri field area, the localised low temperature deformation at the top of the LGHS may be evidence of such a structure as a wider zone of distributed shear.

The localisation of strain during this final stage of ductile deformation is likely to reflect a positive feedback between strain partitioning into weaker lithologies, followed by localised strain softening (e.g. through phyllonitisation) and further strain partitioning. This feedback is strengthened if deformation occurs through decreasing temperatures, as strain is allowed to migrate and accumulate in mechanically weaker rock layers. These processes would result in a series of rigid thrust sheets separated by narrow, weak shear zones, comparable to processes associated with duplexing and underplating (e.g. Srivastava & Mitra, 1994; Robinson *et al.*, 2006; He *et al.*, 2014). This final stage of deformation (Figure 3.23c) is assumed to occur synchronously with development of the Lesser Himalayan Duplex (e.g. Decelles *et al.*, 2001; Paudel & Arita, 2006; Robinson & Martin, 2014).

The evolution of deformation through stage 2 to stage 3 is comparable to findings of similar studies from elsewhere in the Himalaya that record deformation temperature gradients in LGHS- and STDS-equivalent stratigraphy that decrease away from the UGHS, (Bouchez & Pêcher, 1981; Law *et al.*, 2004; Law *et al.*, 2011; Yakymchuk & Godin, 2012; Law *et al.*, 2013; Larson & Cottle, 2014). The evolution between stage 2 and 3 is also compatible with geochronological studies in the Bhutanese Himalaya that reveal a migrating deformation front in LGHS-equivalent strata that moves down-section over several million years (Mottram *et al.*, 2014a). It is possible that stage 2 and 3 were active simultaneously at different structural positions, stage 2 being at a deeper hinterland position and stage 3 being at a shallower foreland position.

3.6. Summary of interpretations

Detailed optical and electron microscopy of deformation microstructures and CPO fabrics of samples from the Greater Himalayan Sequence (GHS) and bounding units in the Annapurna-Dhaulagiri region, provide insights into the microstructural behaviour of these rocks in their orogenic setting. In summary, quartz, feldspar, calcite and dolomite microstructures and CPO fabrics have been analysed in 43 samples from the Modi Khola transect and 56 samples in the Kali Gandaki transect. A range of deformation mechanisms have been identified along the transects, including intracrystalline deformation (e.g. deformation twins, undulose extinction, subgrains), dynamic recrystallisation (e.g. BLG, SGR, GBM) and diffusive mass transfer. Active crystal slip systems have been determined from CPO fabrics, and verified by microstructural and petrological observations.

Comparing these observations with published natural, experimental and computational microstructural studies also provides a means to determine the temperatures at which rocks were deformed. Temperatures of metamorphism are derived from previously published data and from new grt-bt thermometry (3 samples) and Zr-in-titanite thermometry (4 samples) from the UGHS and STDS in the Kali Gandaki transect. The interpretations made from the deformation temperature profiles for the Modi Khola and Kali Gandaki transects are summarised below:

1) In the Modi Khola transect, deformation at the base of the transect in the LHS occurred between <280 ^{o}C and 300-400 ^{o}C. Deformation temperatures in the overlying LGHS increase up-section from 280-490 ^{o}C to 420-600 ^{o}C. A distinct step in peak metamorphic and deformation temperatures is observed up-section across the CT from the LGHS (~500-600 ^{o}C) into the UGHS (~700-800 ^{o}C). In the UGHS, the dominant deformation occurred between 500-700 ^{o}C and >650 ^{o}C, but did not exceed 750-850 ^{o}C, based on metamorphic constraints. At lower ambient temperatures (300-400 ^{o}C), deformation concentrated in the immediate hangingwall of the CT at the base of the UGHS. A subdued, low-strain, low to intermediate temperature (280-500 ^{o}C) deformation overprint is also observed across the whole of the UGHS. Deformation temperatures in the STDS range from 280-500 ^{o}C to >650 ^{o}C. A low strain overprint produced at <300 ^{o}C is also observed. In the THS, deformation temperatures range from <300 to 600 ^{o}C.
2) At the base of the Kali Gandaki transect, deformation temperatures in the LGHS increase up-section from 280-420 ^{o}C to 390-490 in the lower 2 km, ~400-550 ^{o}C at structural levels between ~2-4 km above the MCT, and <300 ^{o}C to 600 ^{o}C in the top 2 km. Additionally, a few samples at structural levels ~2-3 km above the MCT also contain the remnants of an older, high temperature deformation (>650 ^{o}C), probably produced under a different differential stress regime. As in the Modi Khola transect, a distinct step in peak metamorphic and deformation temperatures is observed up-section across the CT in the kali Gandaki transect from the LGHS (~500-600 ^{o}C) into the UGHS (~700-800 ^{o}C). Based on constraints from metamorphic mineral assemblages, peak deformation temperatures in the UGHS did not exceed 700-825 ^{o}C. Minimum deformation temperatures increase up-section from 350-500 ^{o}C in the lower ~0.1 km vertical section of the UGHS, to 600-700 ^{o}C at structural levels between ~0.1-2 km above the CT to ~700 ^{o}C and ~3-5 km above the CT. Above this structural level, deformation temperature in the UGHS decrease up-section to 500-700 ^{o}C at structural levels between ~5-6.5 km above the CT and 300-400 ^{o}C in the uppermost 0.1 km of vertical section. In the STDS, the lower margin experienced deformation at 500-600 ^{o}C to 250-300 ^{o}C, whilst the upper margin experienced deformation above 550 ^{o}C, which continued to temperatures as low as

(*a*) STAGE 1: Mid-crustal channel flow

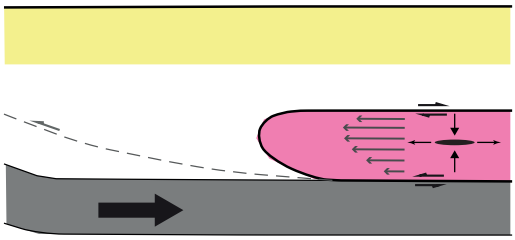

(*b*) STAGE 2: Wedge extrusion

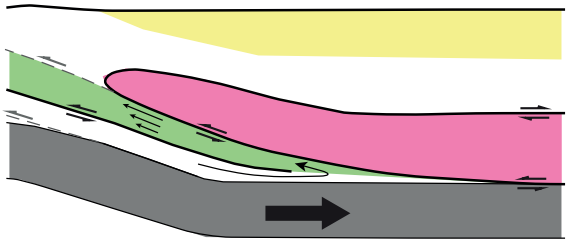

(*c*) STAGE 3: Duplexing / Underplating

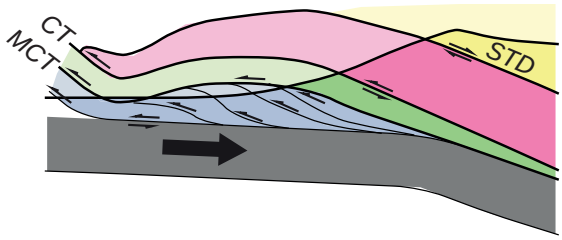

Figure 3.23. Kinematic evolution of the GHS. Schematic cross sectional models of the GHS in the Annapurna-Dhaulagiri region. (*a*) Stage 1: Mid crustal channel flow of the UGHS. (*b*) Stage 2: Wedge extrusion of rigid UGHS (pink) facilitated by pervasive non-coaxial shearing in the LGHS (green). (*c*) Stage 3: Duplexing / underplating of LHS beneath the LGHS facilitates the exhumation of the GHS. Not to scale. *UGHS + STDS – pink; LGHS – green; LHS – blue; THS – yellow; Indian lower crust – grey*

300 °C. The THS in the Kali Gandaki transect experienced deformation temperatures from 300-400 °C to <280 °C.

The trends in these deformation temperature profiles have implications for models of Himalayan orogenesis. Both deformation temperature profiles mimic the inverted metamorphic profile and overlying right-way-up metamorphic profile observed in the GHS along the length of the central and eastern Himalaya. Overprinting relationships indicate that the recorded microstructural evolution reflects deformation on a retrograde path from close to peak metamorphic conditions. By considering the regional tectonic framework and known metamorphic constraints, the deformation temperature profiles can provide information relating to the thermo-kinematic evolution of the GHS and bounding units in the Annapurna-Dhaulagiri Himalaya.

3.6.1 Thermo-kinematic evolution of the Annapurna-Dhaulagiri Himalaya

Three distinct deformation stages are identified from trends in the distribution and migration of deformation through an evolving thermal regime:

Stage 1 (Figure 3.23a) is characterised by high temperature coaxial and non-coaxial deformation in the UGHS and base of the STDS in both profiles. This stage occurred during partial melting and is consistent with the required criteria for mid-crustal channel flow (*Section 1.3.5*). Pervasive ductile deformation (i.e. crustal flow) is maintained in the UGHS down to temperatures of ~550-650 °C, below which the threshold viscosity (i.e. maximum viscosity) for flow is exceeded. Transition through this threshold

viscosity is marked by a rheological transformation from pervasive ductile flow to rigid body behaviour of the UGHS and defines the end of deformation stage 1.

Stage 2 (Figure 3.23b) occurs between ~400-600 ^{o}C and corresponds to exhumation of the UGHS as a rigid block, facilitated by non-coaxial ductile shearing in the LGHS. During this stage, the UGHS deforms only at its margins, whilst the LGHS behaves as a crustal-scale shear zone. This stage is comparable to previously proposed wedge extrusions models and extrusion and exhumation of a frozen channel-plug.

Stage 3 (Figure 3.23c) corresponds to localised ductile deformation on the MCT and CT and in the upper portion of the LGHS due to a positive feedback between strain partitioning and strain softening during cooling. The localisation of low temperature deformation in the upper LGHS may represent the lateral continuation of the Munsiari Thrust reported elsewhere in Nepal at similar structural levels. This deformation stage is comparable to previously proposed duplexing and underthrusting models and is assumed to occur synchronously with development of the Lesser Himalayan Duplex.

3.7 Conclusions

The data presented here provide insights into the thermo-kinematic evolution of the GHS in the Annapurna-Dhaulagiri region. The three orogenic stages defined by distinct tectonic processes correspond to the early mid-crustal (Stage 1) and late upper-crustal (Stage 3) kinematic evolution of the GHS. Stage 2 forms a transition stage between the mid and upper crust and may reflect the migration of the UGHS through the brittle-ductile transition zone. Each of these tectonic processes has been presented as a possible model of Himalayan orogenesis. In some circumstances, these models are interpreted as mutually exclusive end-members and used as evidence against the occurrence of any of the other two processes (e.g. Robinson *et al.*, 2006; Kohn, 2008; Carosi *et al.*, 2010; Martin *et al.*, 2010). In contrast, the findings of this chapter are comparable to recent studies that have proposed composite tectonic models for the Himalayan orogeny, which involve elements of two or more of the 'end-member' models (Beaumont *et al.*, 2004; Jamieson *et al.*, 2006; Larson *et al.*, 2010; Spencer *et al.*, 2012; Jamieson & Beaumont, 2013; Mukherjee, 2013a; Wang *et al.*, 2013; He *et al.*, 2014; Larson & Cottle, 2014). These models demonstrate that channel flow, wedge extrusion and duplexing/underplating processes are not incompatible and instead, reflect spatial and temporal variations in rheological boundary conditions (Larson *et al.*, 2010; Jamieson & Beaumont, 2013). It is demonstrated here that at least in the case of the Annapurna-Dhaulagiri region, channel flow, wedge extrusion and duplexing/underplating all played an integral part in the evolution of the Himalaya. Importantly, this study indicates that these processes are not incompatible end-

members when the development of the Himalayan orogen is considered in terms of an evolving rheology.

3.8 Appendix

Figure A.3.24. Quartz CPO. (*a*) LHS & LGHS – Modi Khola. (*b*) UGHS, STDS & THS – Modi Khola. (*c*) LGHS – Kali Gandaki. (*d*) UGHS – Kali Gandaki. (*e*) STDS – Kali Gandaki. (*f*) THS – Kali Gandaki. Pole figures are constructed for *a, m, c, r,* and *z* axes and plotted with equal area antipodal projection. Pole figures are presented in *XZ* plane of kinematic reference frame. Contours show multiples of uniform distribution.

Figure A.3.25. Calcite & dolomite CPO. (*a*) LGHS & STDS – Modi Khola. (*b*) LGHS & UGHS – Kali Gandaki. (*c*) STDS – Kali Gandaki. (*d*) THS – Kali Gandaki. Pole figures are constructed for *a, m, c, e, f, r,* and *z* axes and D1, D2 and D3 slip directions and are plotted with equal area antipodal projection. Pole figures are presented in *XZ* plane of kinematic reference frame. Contours show multiples of uniform distribution.

Figure A.3.26. Feldspar CPO. (*a*) Modi Khola. (*b*) Kali Gandaki. Pole figures are constructed for (100), (010) and (001) pole to planes and <100>, <010> and <001> directions. Pole figures are plotted with equal area projection for both lower and upper hemispheres. Pole figures are presented in *XZ* plane of kinematic reference frame. Contours show multiples of uniform distribution.

Figure A.3.27. Universal stage-based quartz c-axis fabric opening angle thermometry. All data collected using a universal-stage and optical microscope by the author except for P12/027 (RDL) and P12/030 (RDL) which were completed by Richard D. Law and included for completeness. Opening angles are measured from the red lined fabric 'skeletons', which are drawn on top of the quartz *c*-axis pole figures. Temperatures are determined from the average best-fit opening angle of each fabric skeleton using the Kruhl (1998) thermometer. All temperatures have a ±50 ^{o}C uncertainty.

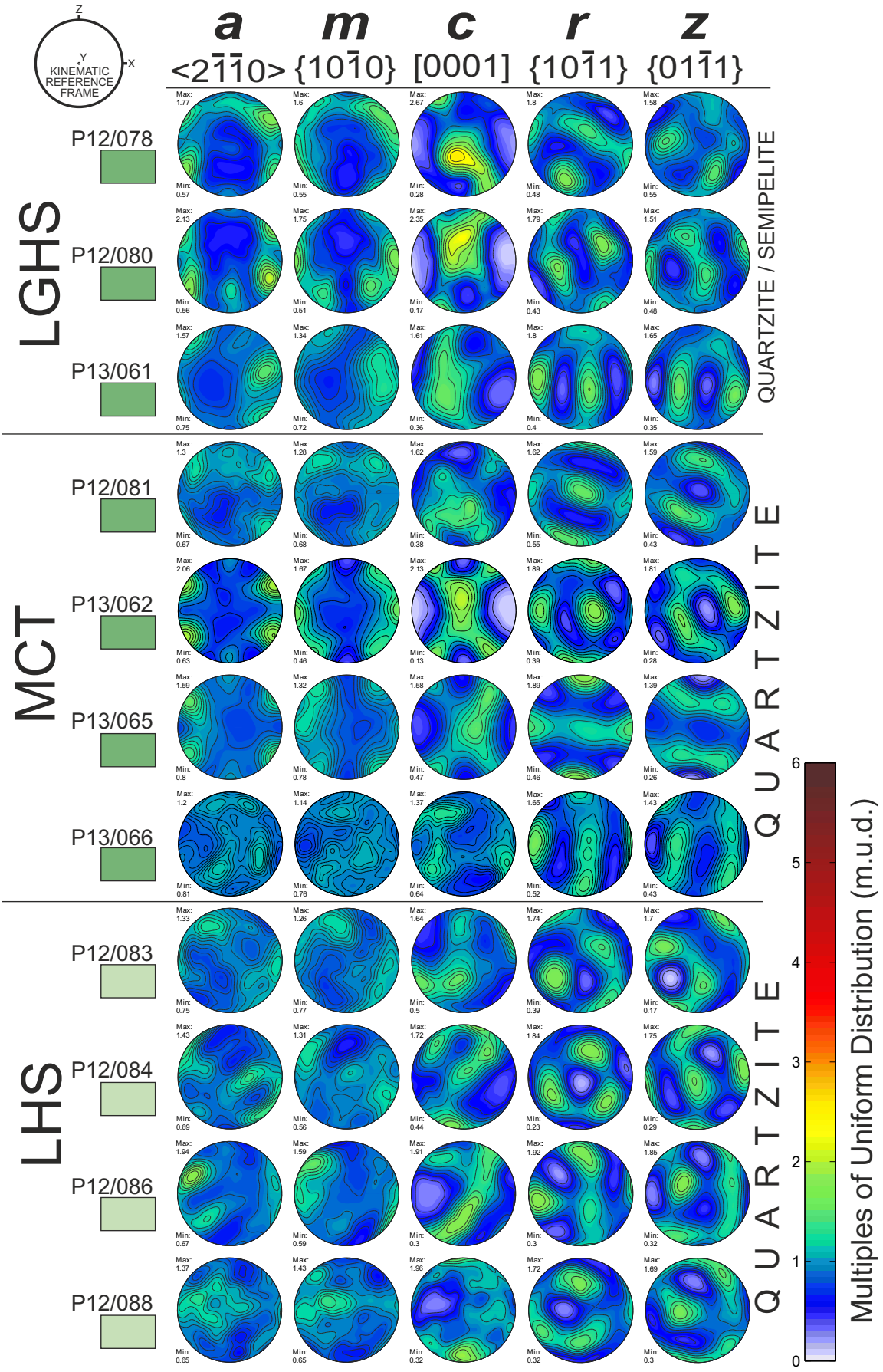

Figure A.3.24a. Quartz CPO.

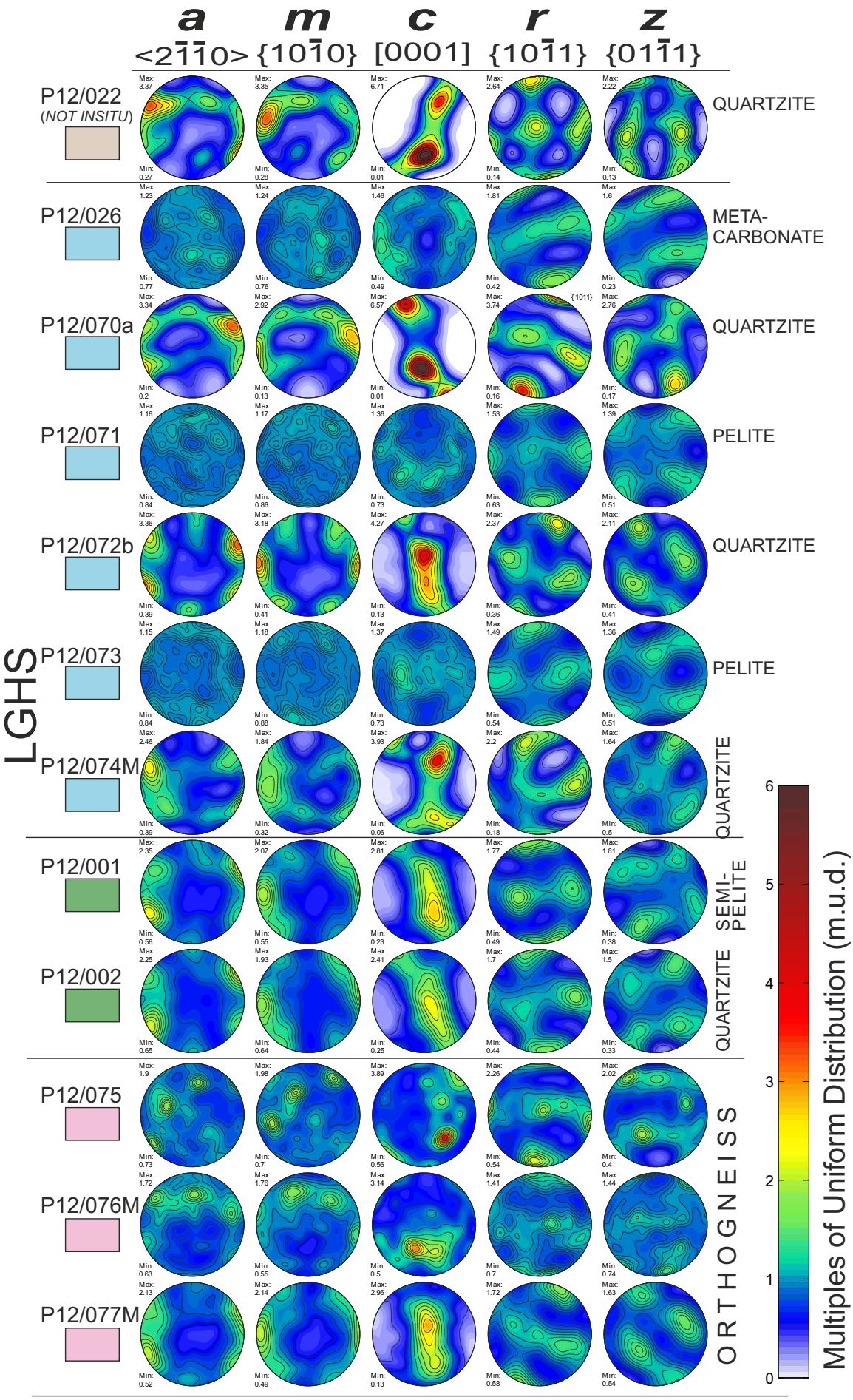

Figure A.3.24a. Quartz CPO cont.

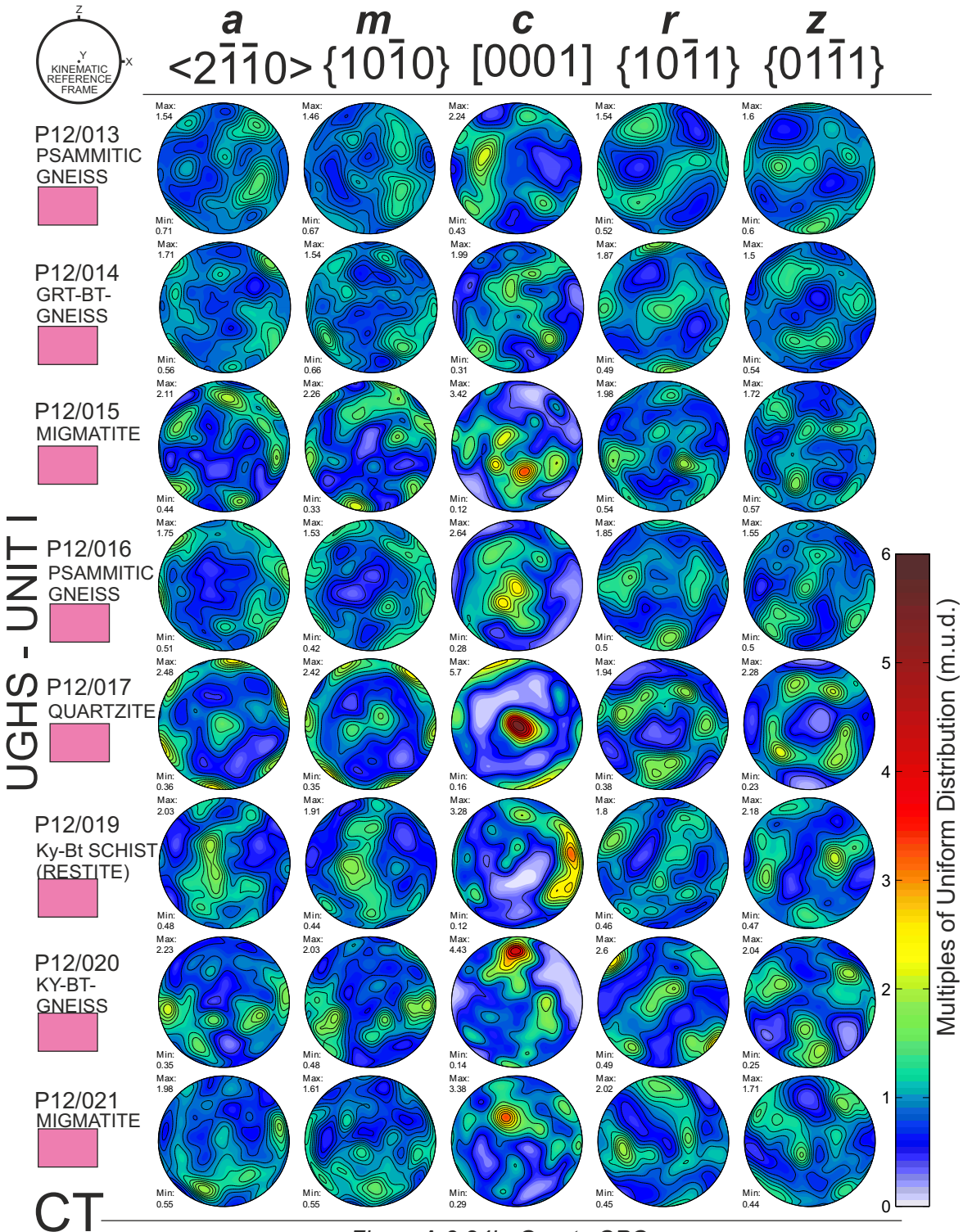

Figure A.3.24b. Quartz CPO.

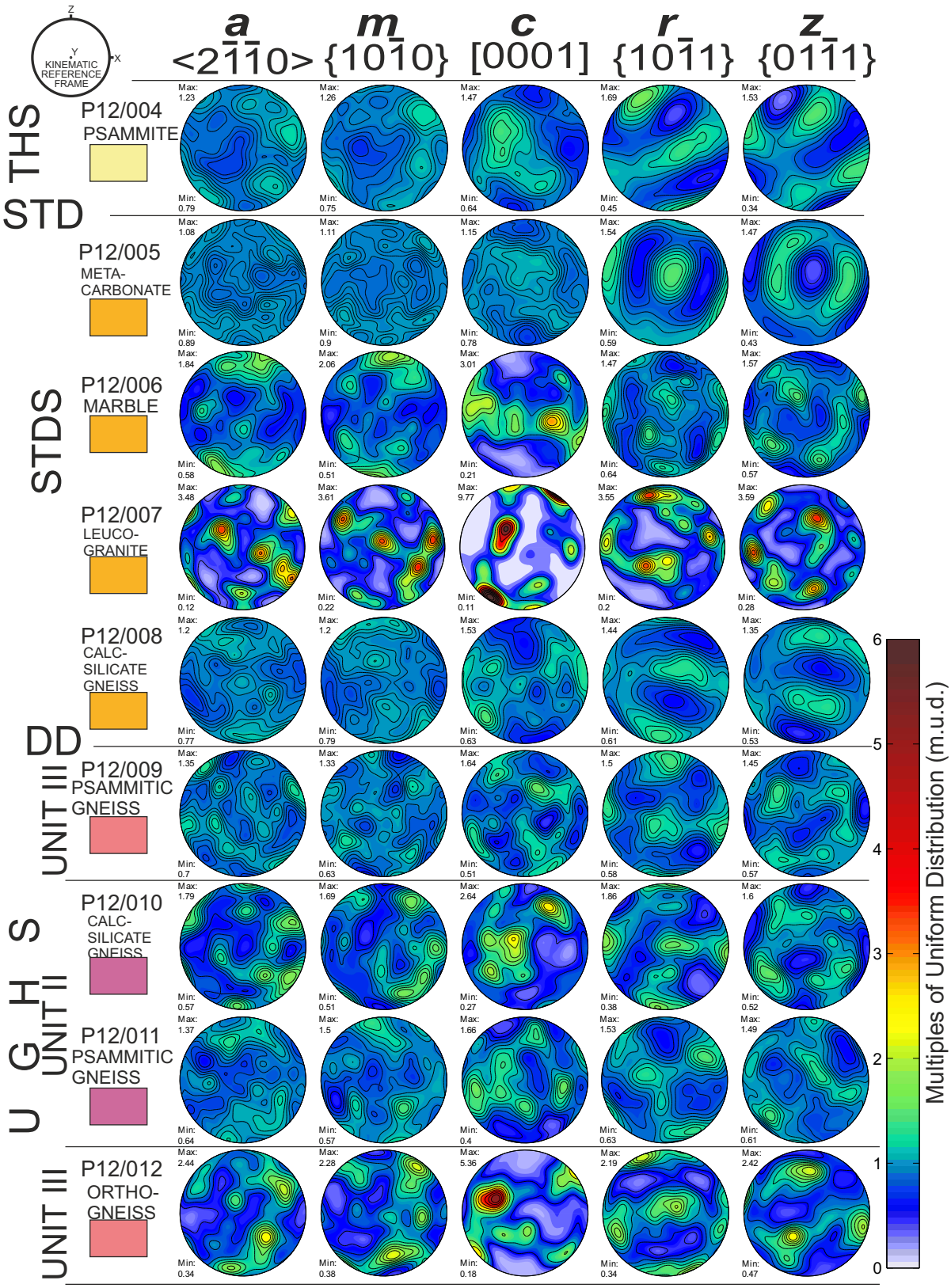

Figure A.3.24b. Quartz CPO cont.

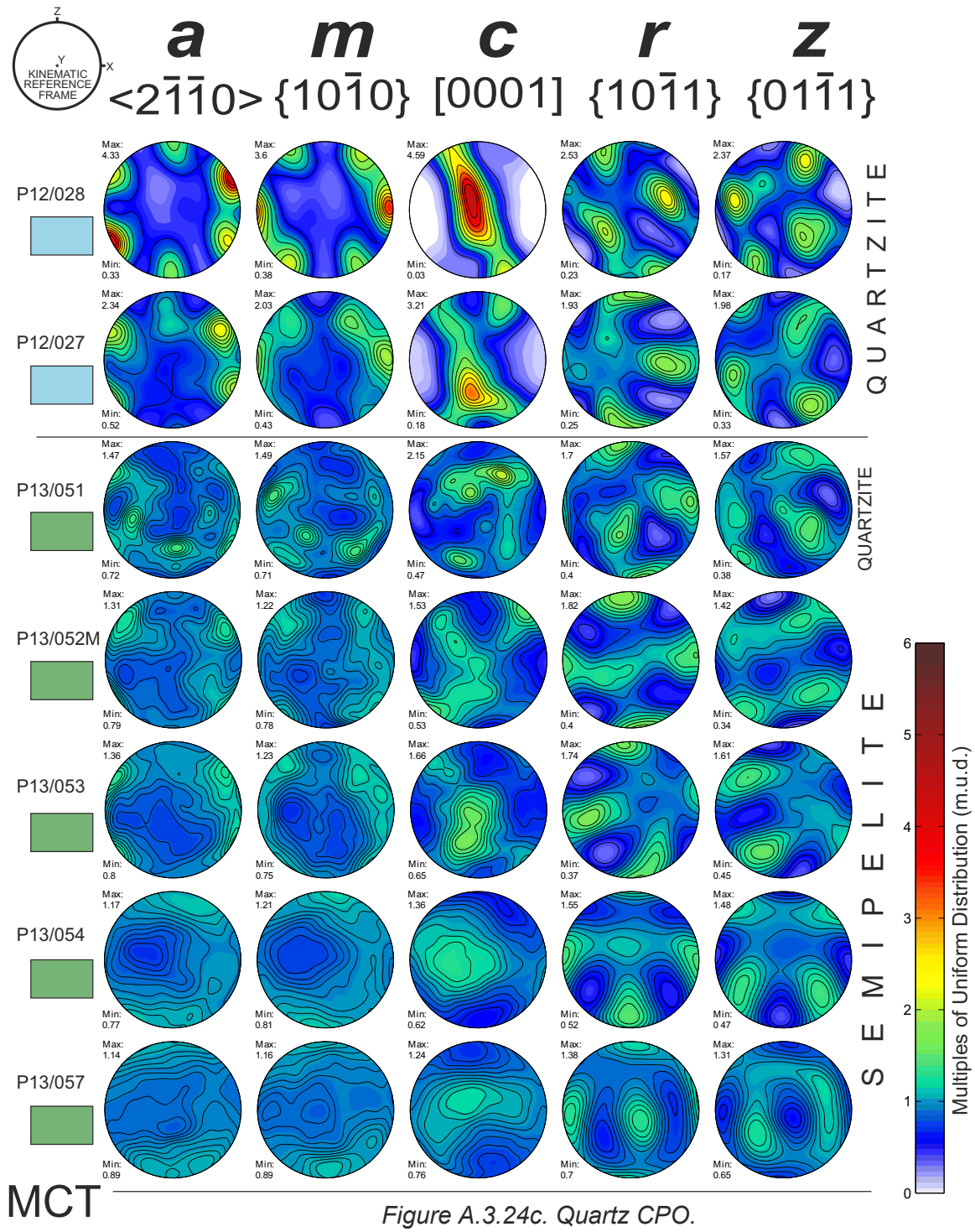

Figure A.3.24c. Quartz CPO.

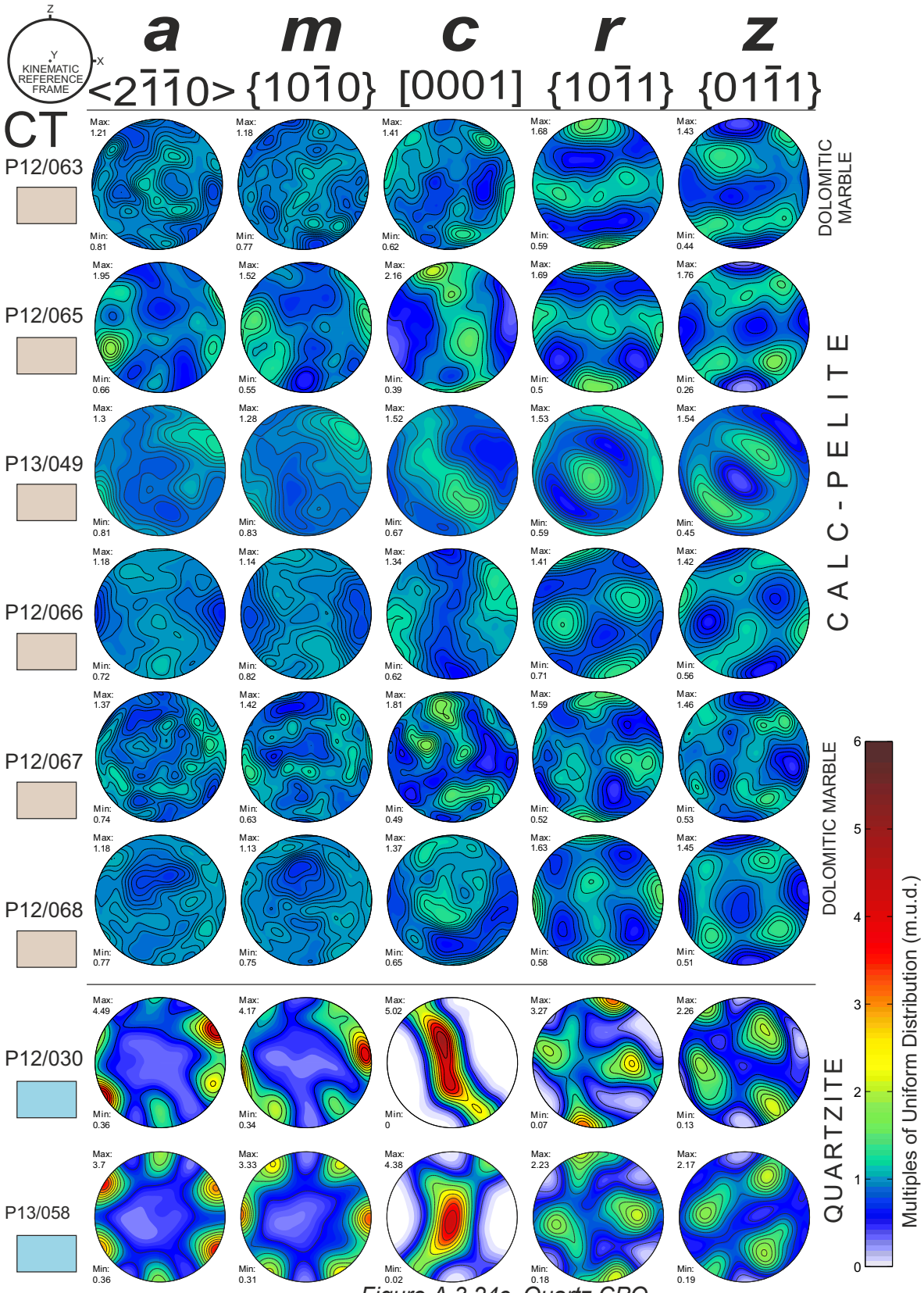

Figure A.3.24c. Quartz CPO

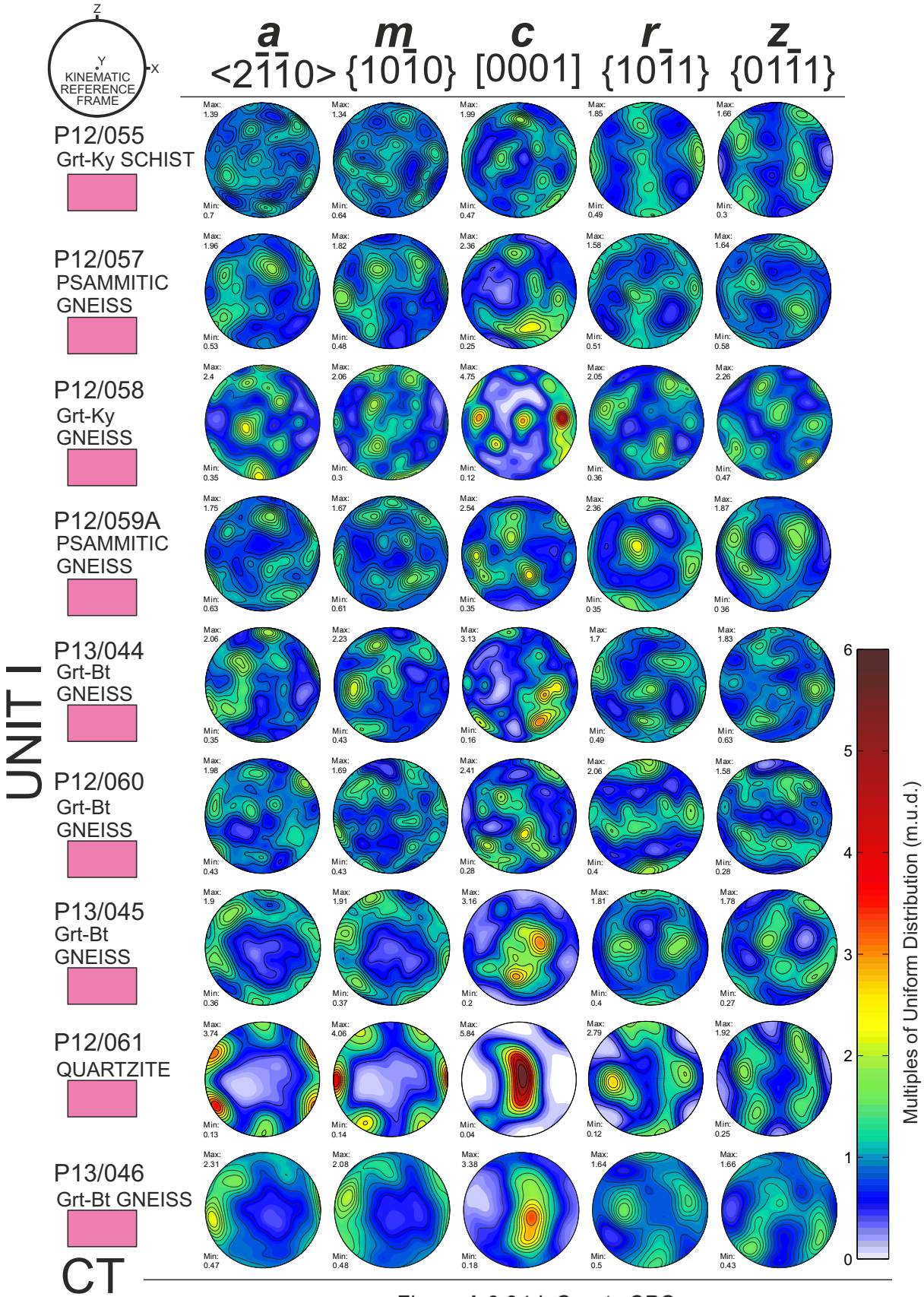

Figure A.3.24d. Quartz CPO.

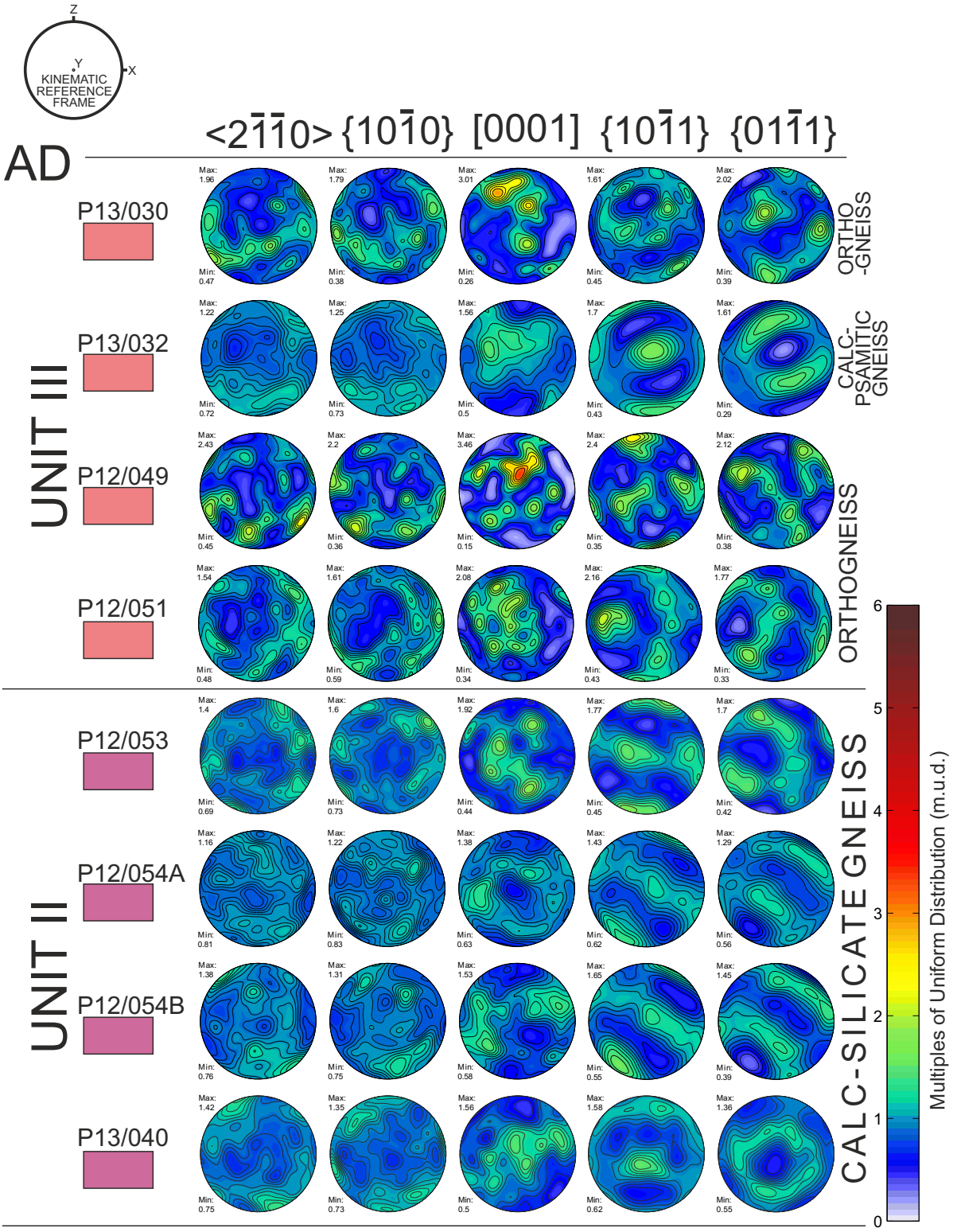

Figure A.3.24d. Quartz CPO cont.

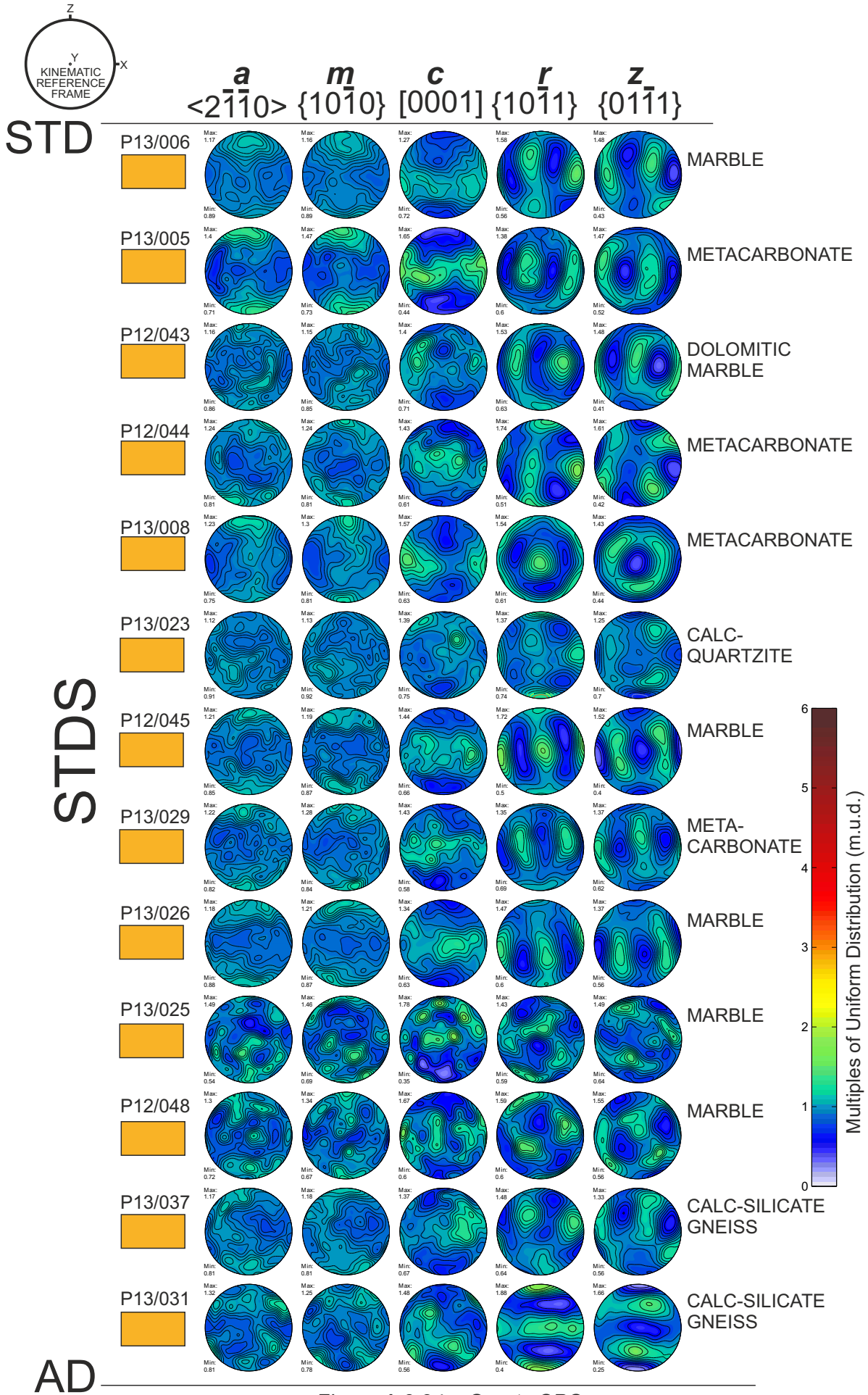

Figure A.3.24e. Quartz CPO.

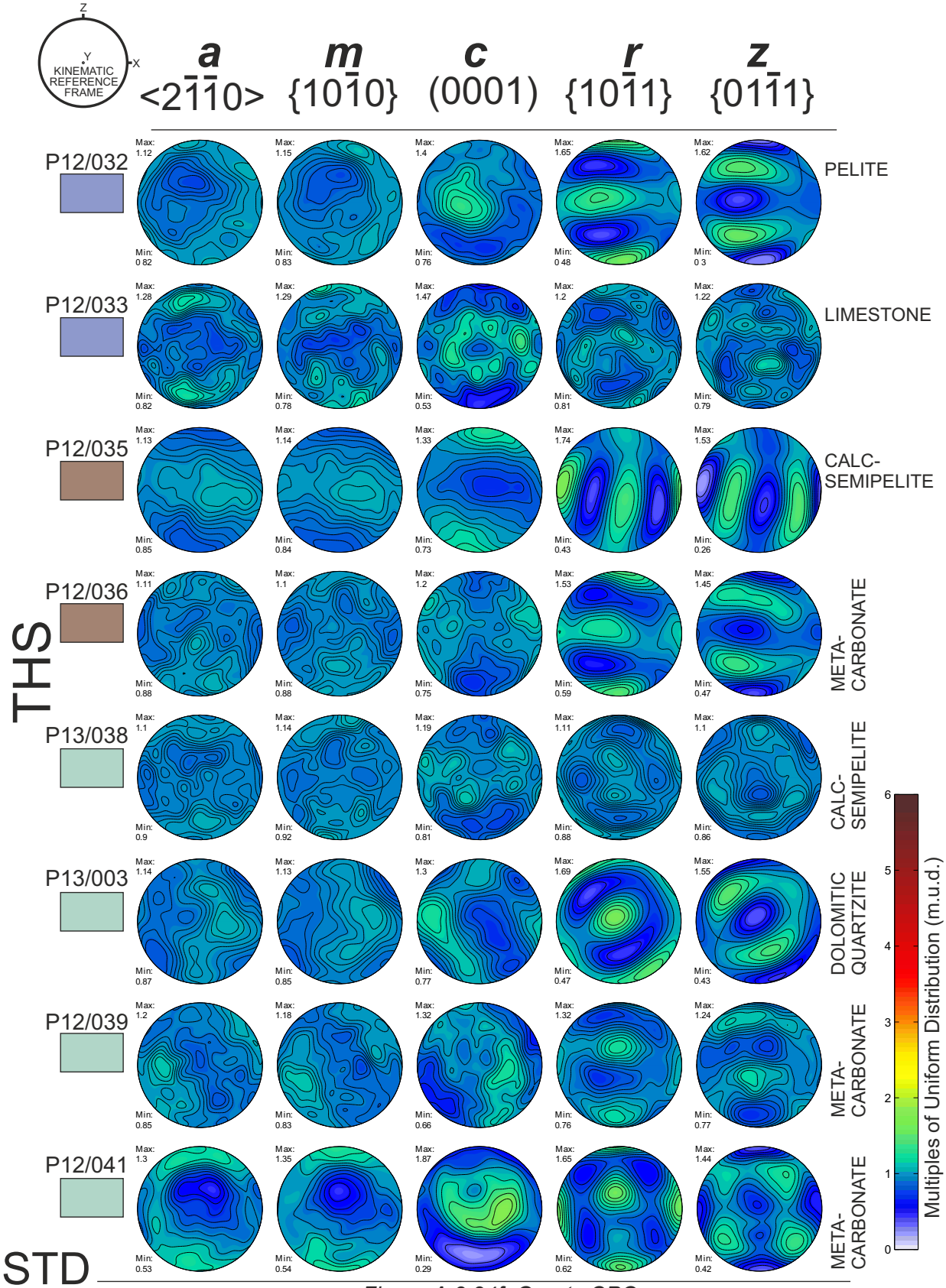

Figure A.3.24f. Quartz CPO.

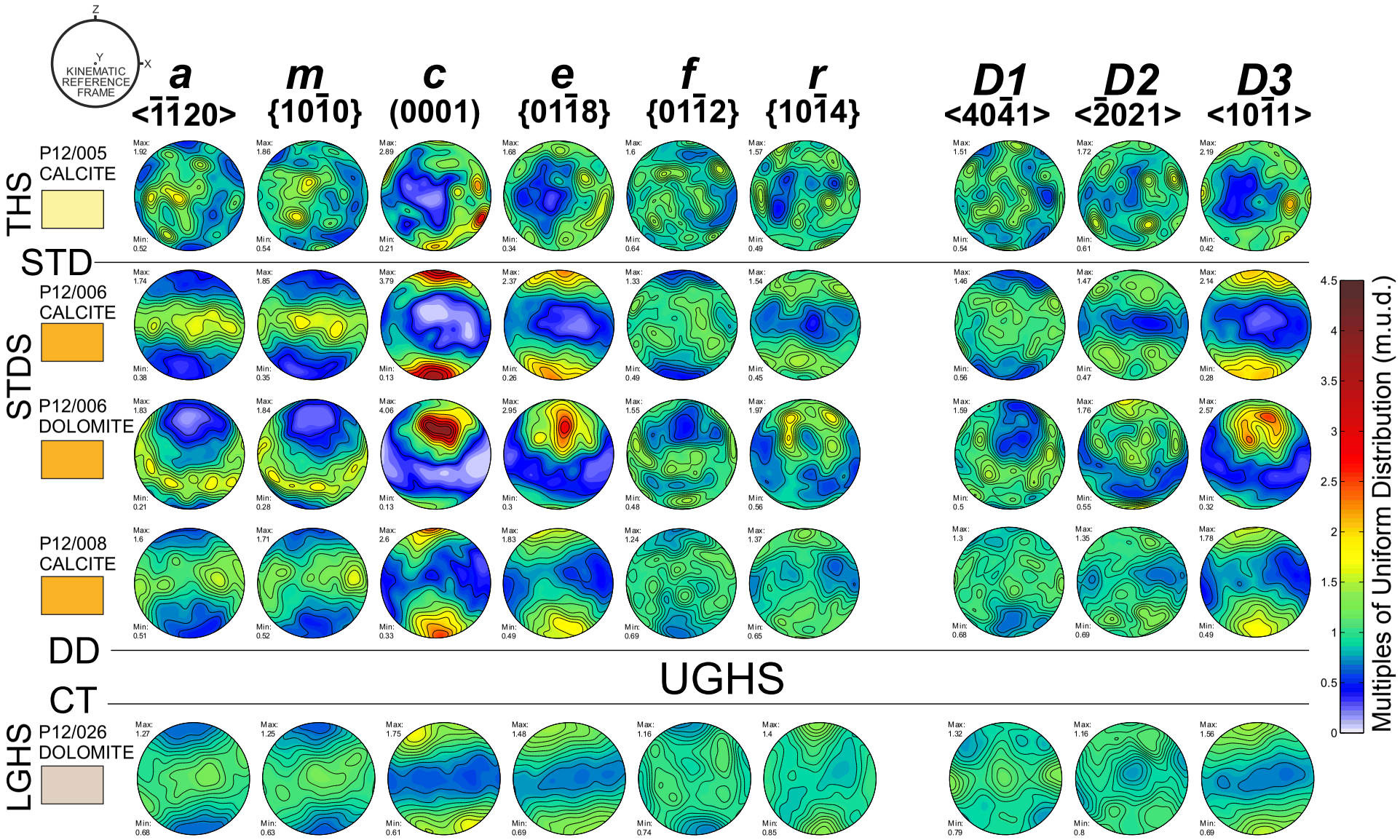

Figure A.3.25a. Calcite & Dolomite CPO.

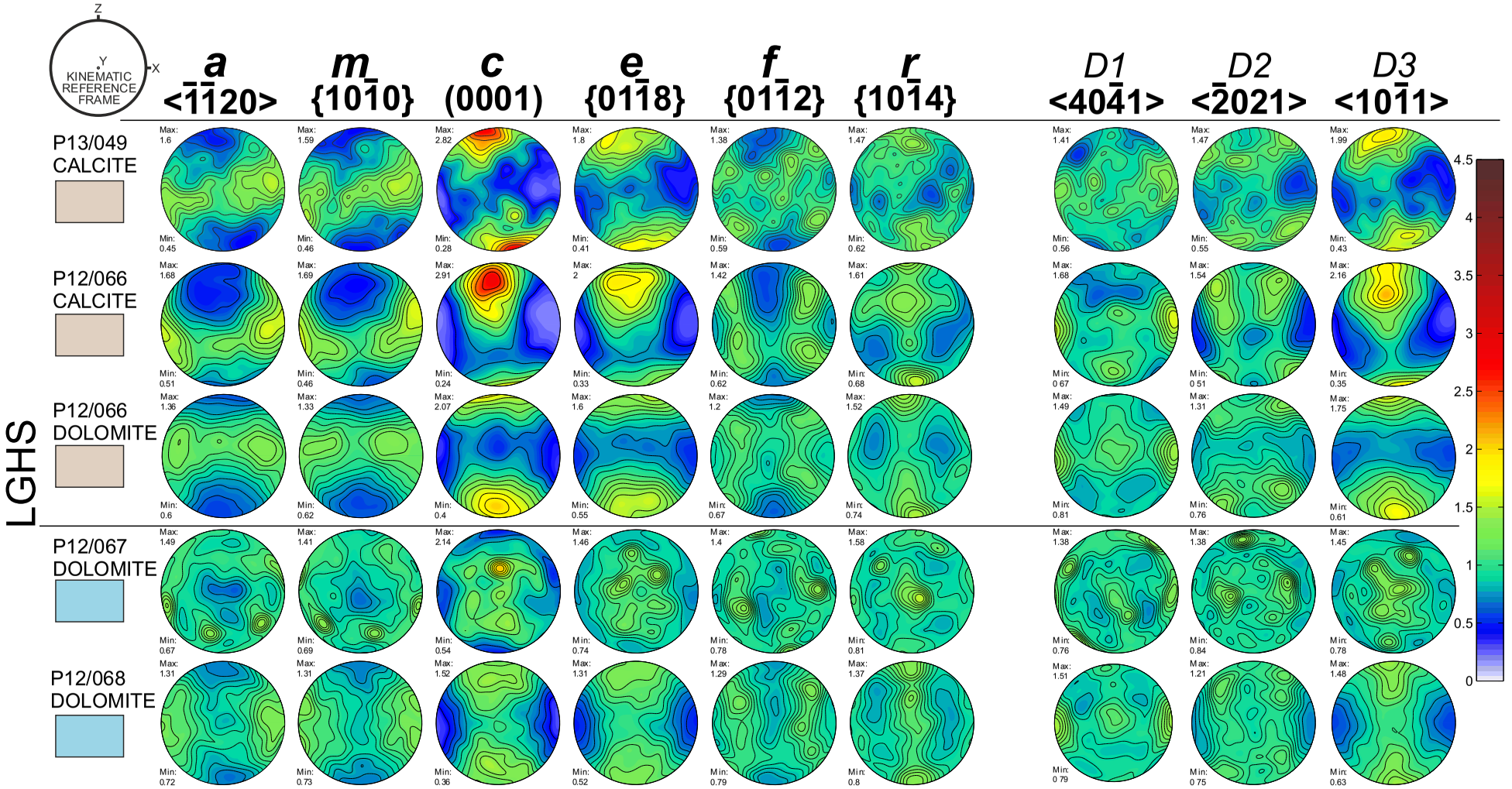

Figure A.3.25b. Calcite & dolomite CPO.

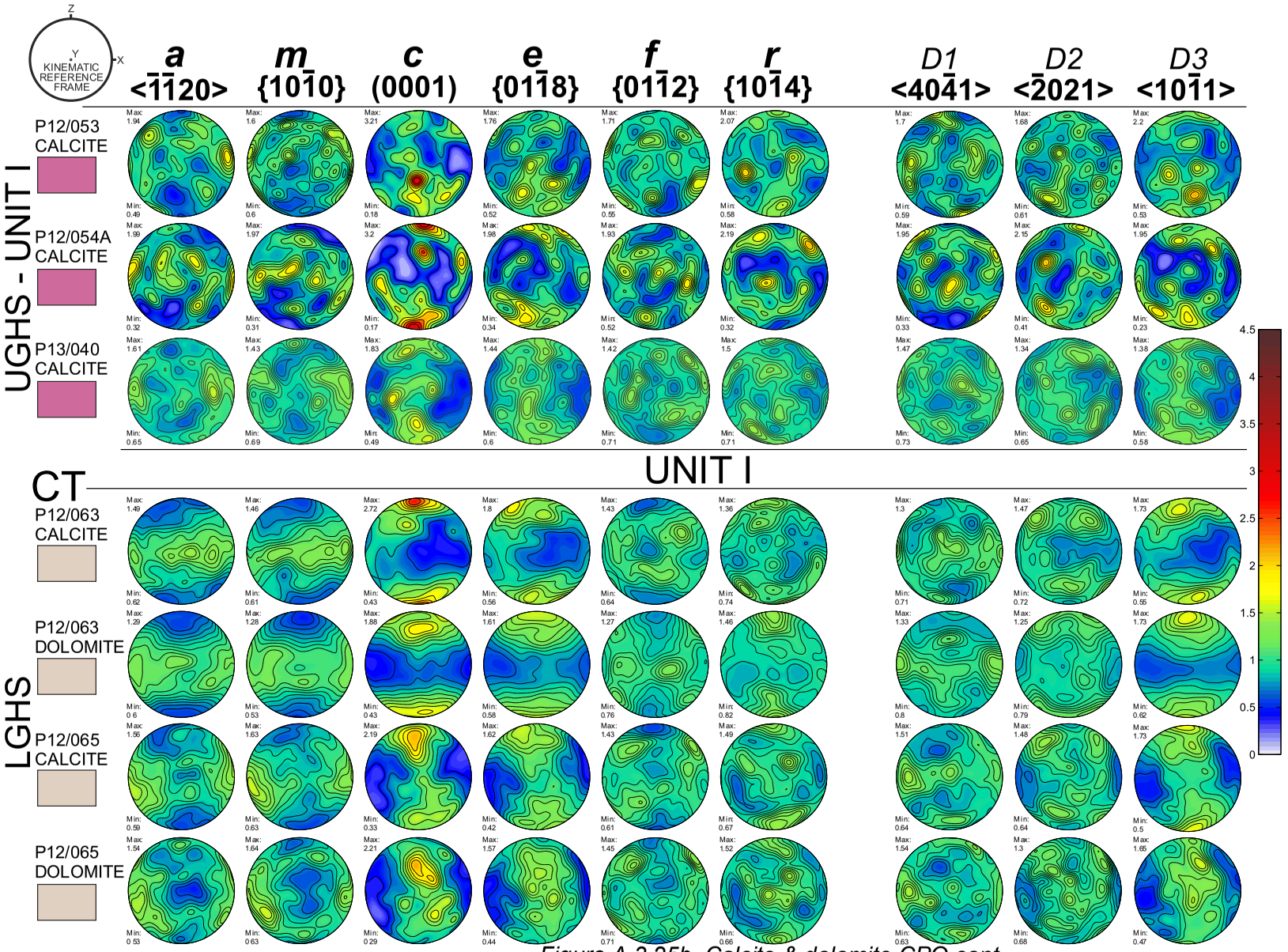

Figure A.3.25b. Calcite & dolomite CPO cont.

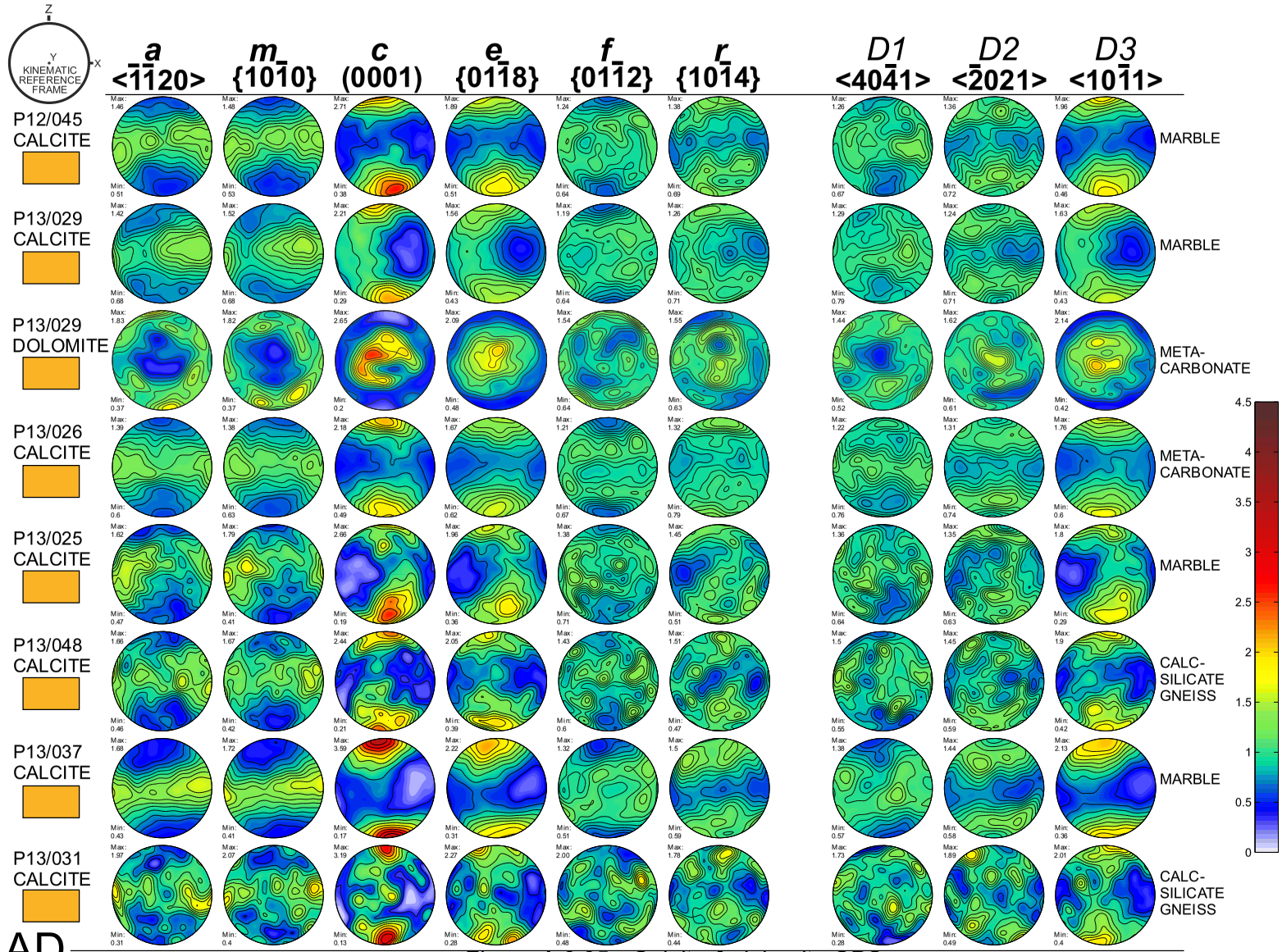

Figure A.2.25c. Calcite & dolomite CPO.

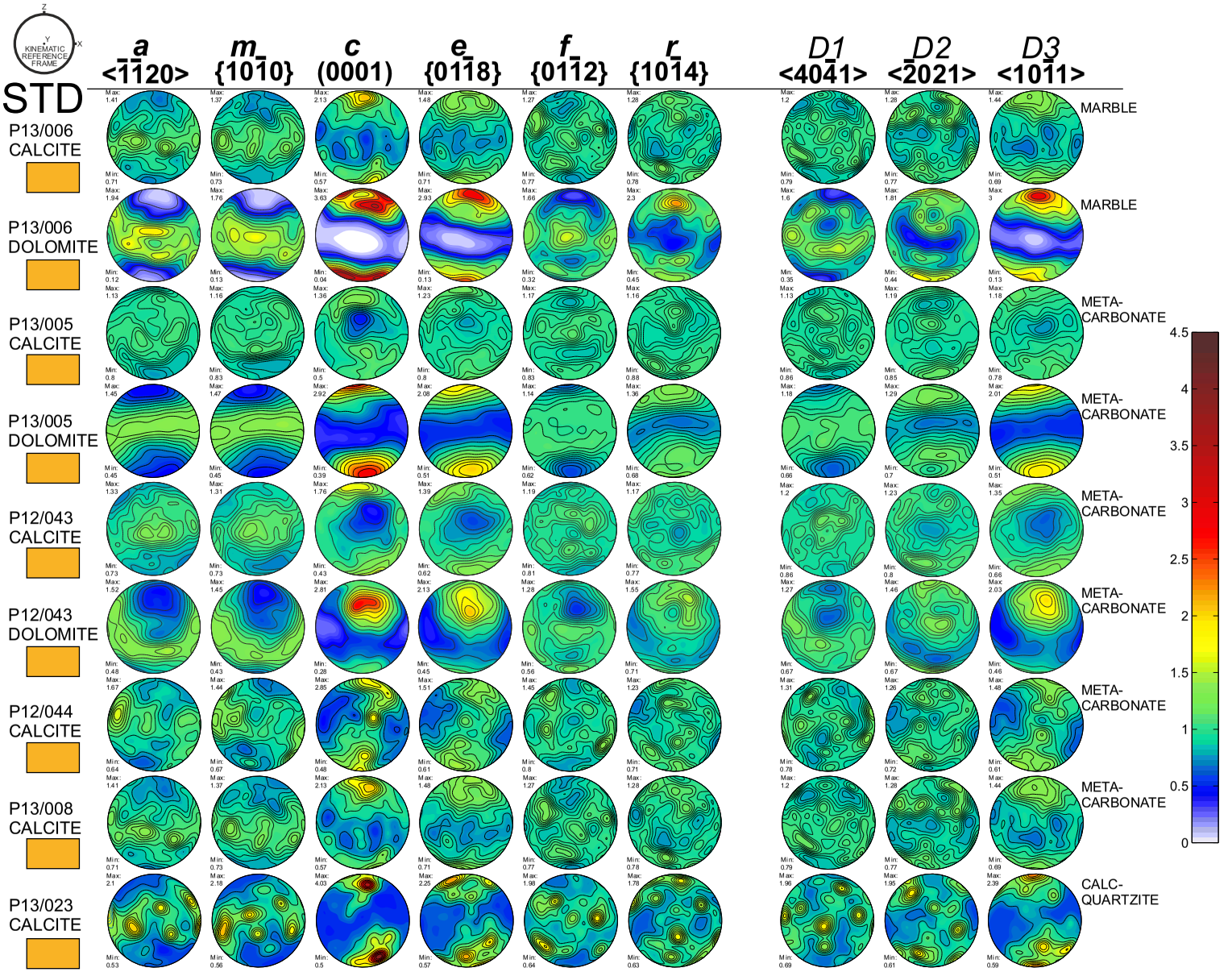

Figure A.2.25c. Calcite & dolomite CPO cont.

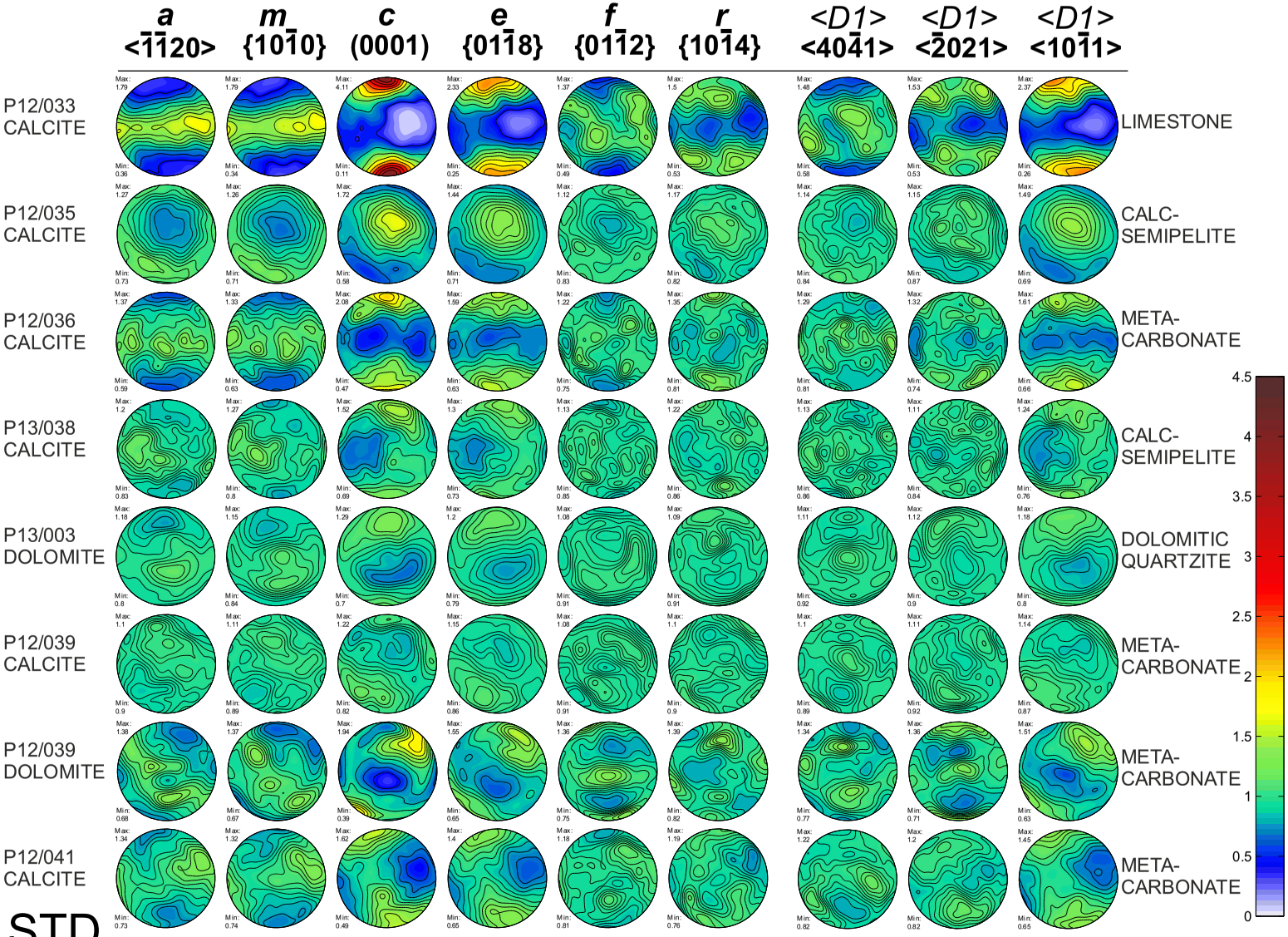

FigureA.3.25d. Calcite & dolomite CPO.

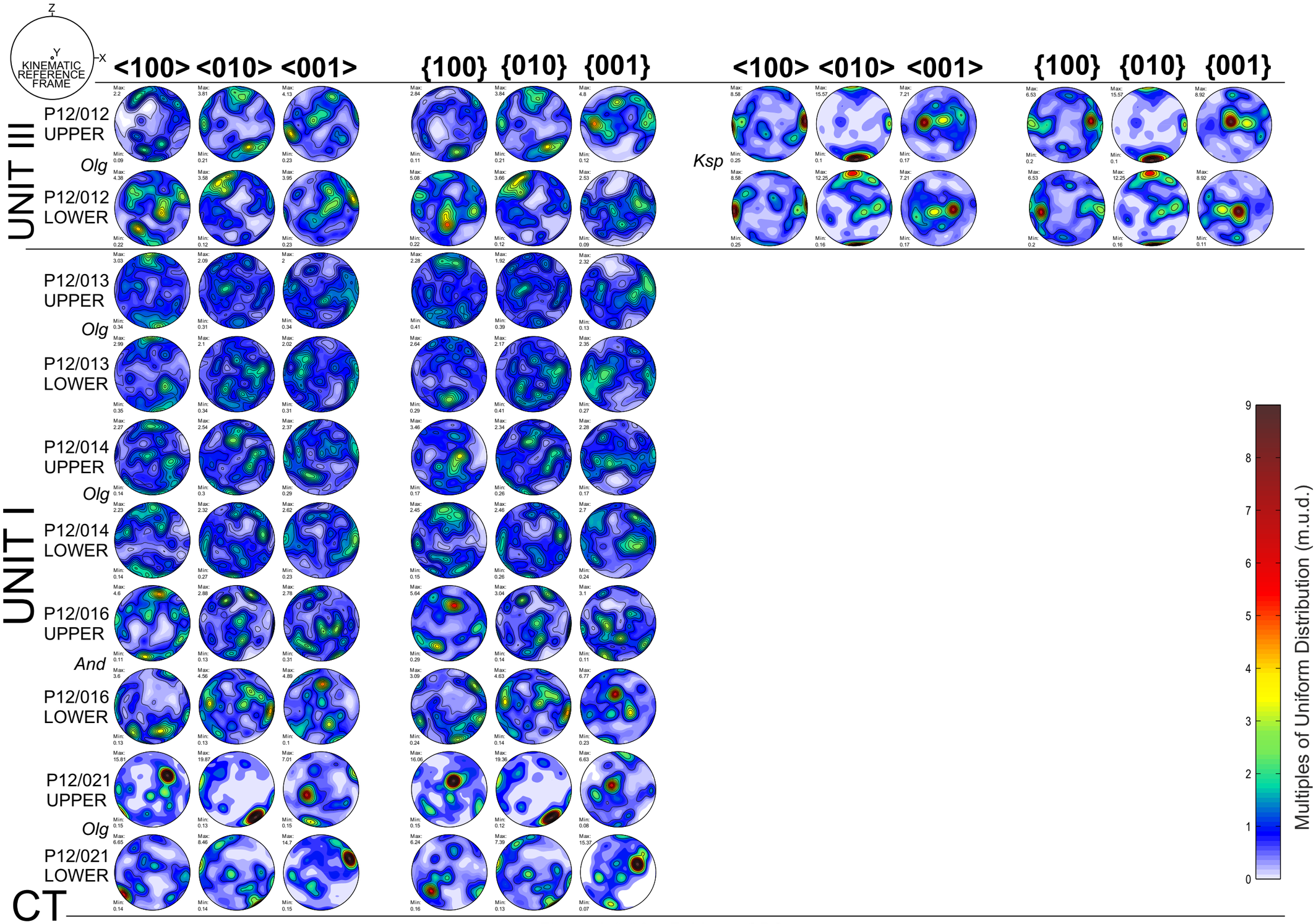

Figure A.3.26a. Feldspar CPO.

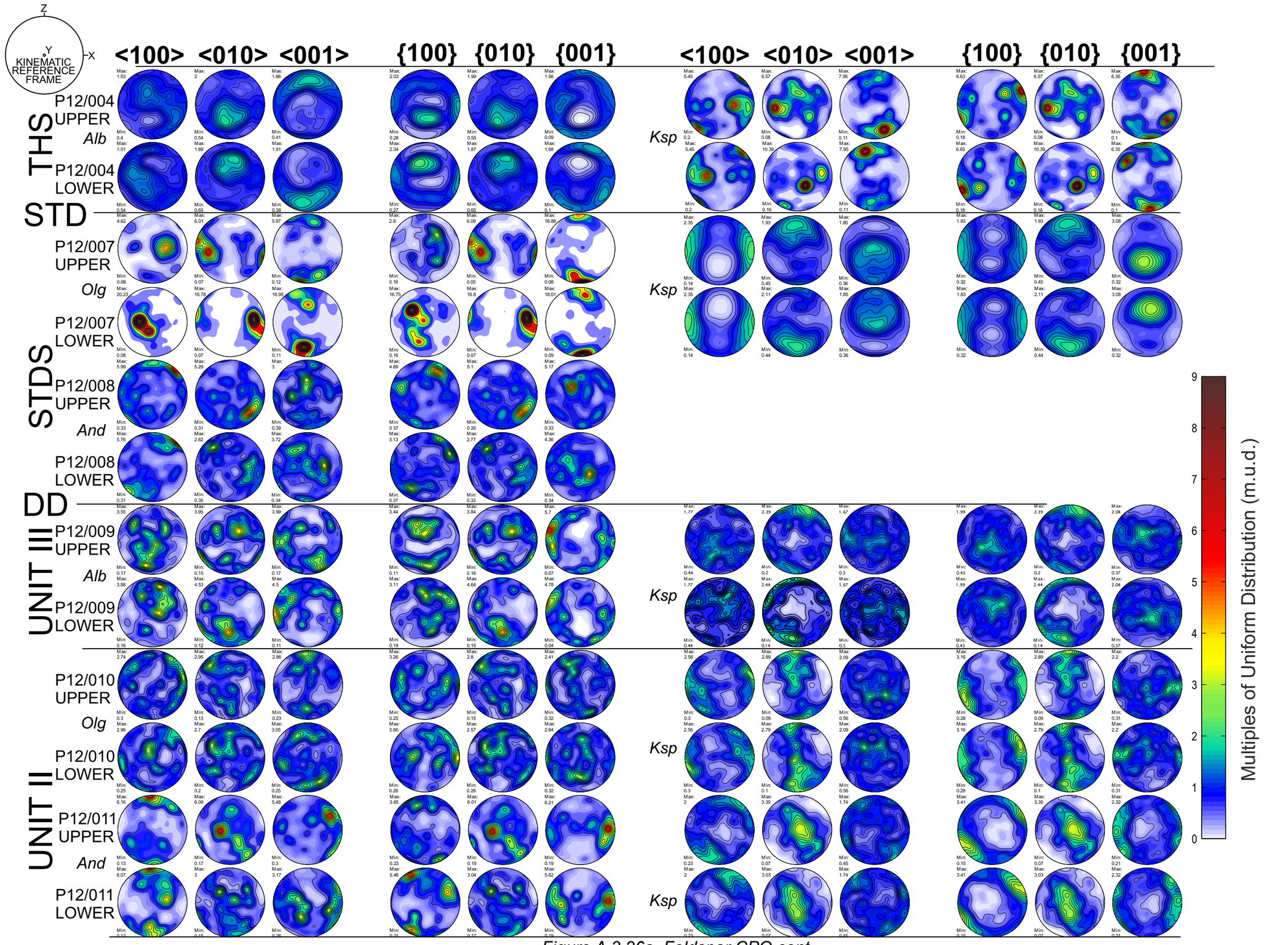

Figure A.3.26a. Feldspar CPO cont.

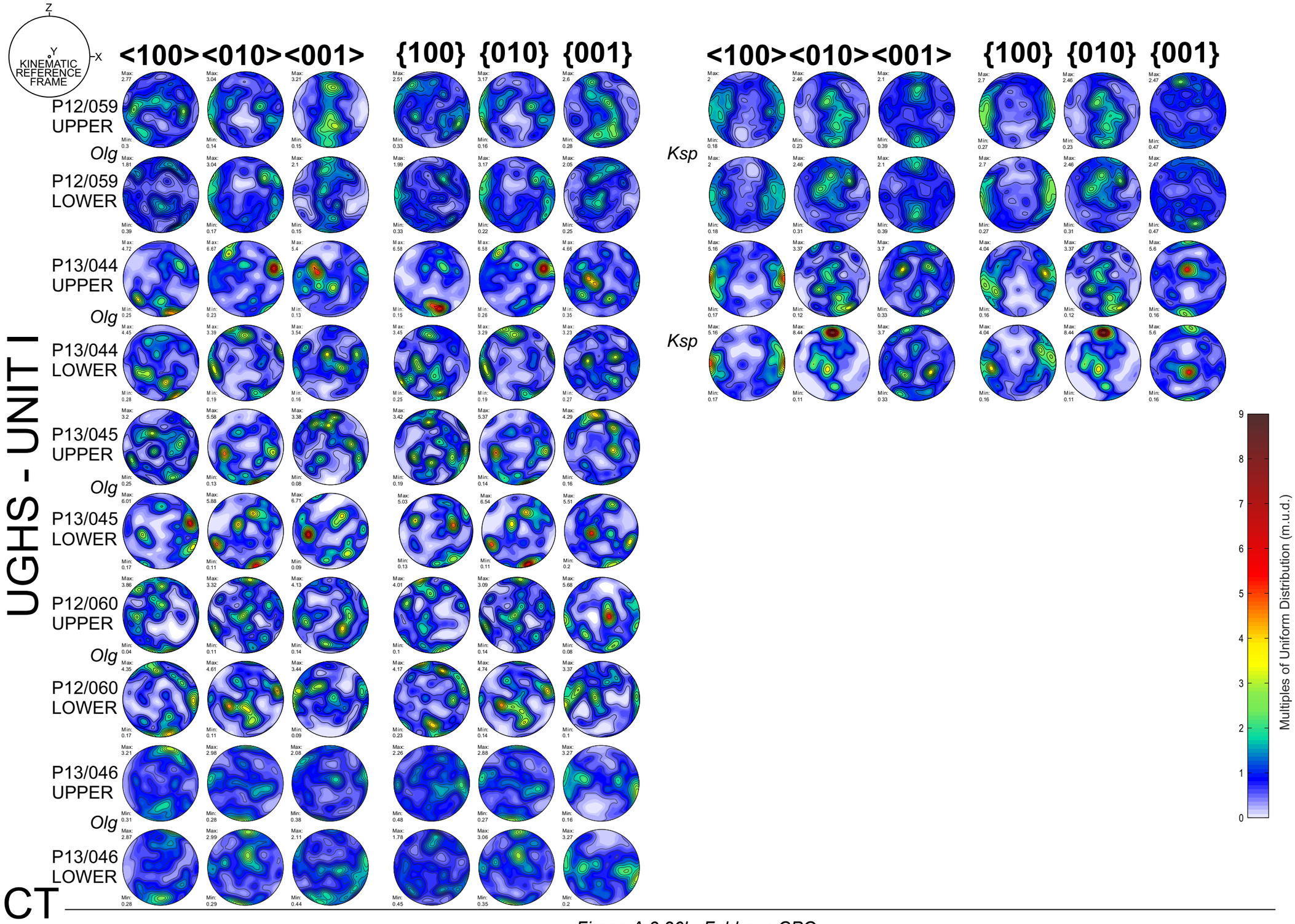

Figure A.3.26b. Feldspar CPO.

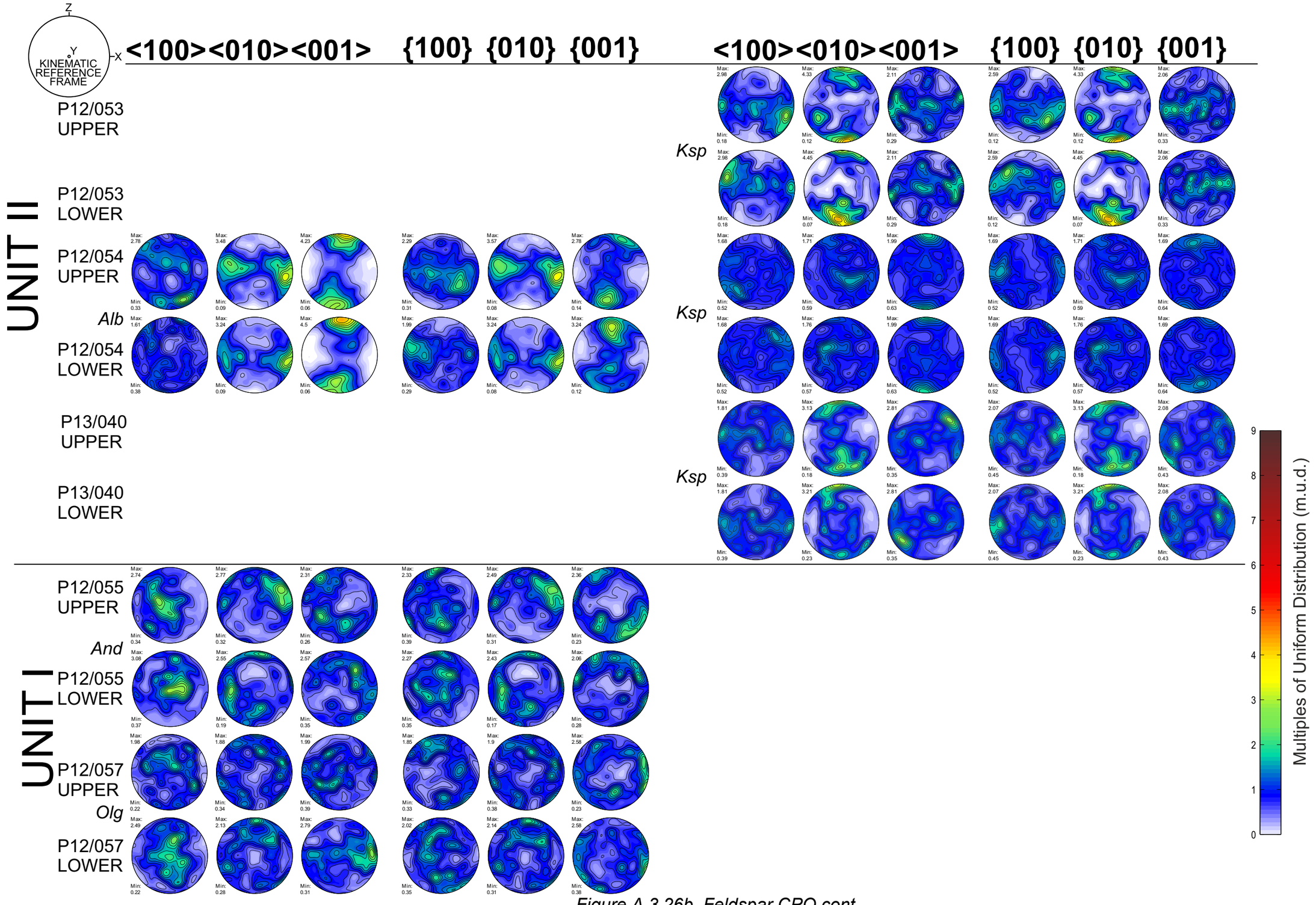

Figure A.3.26b. Feldspar CPO cont.

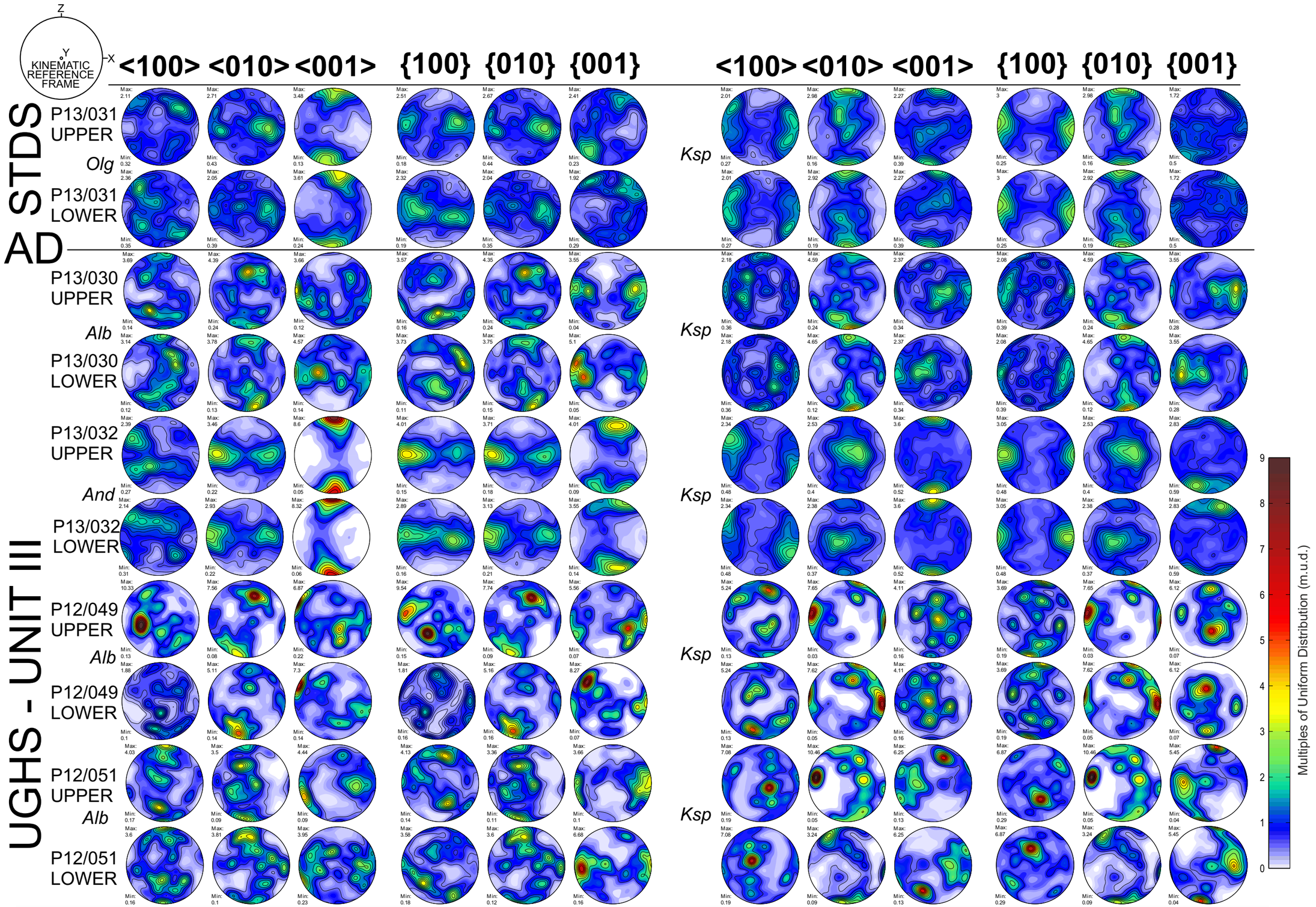

Figure A.3.26b. Feldspar CPO cont.

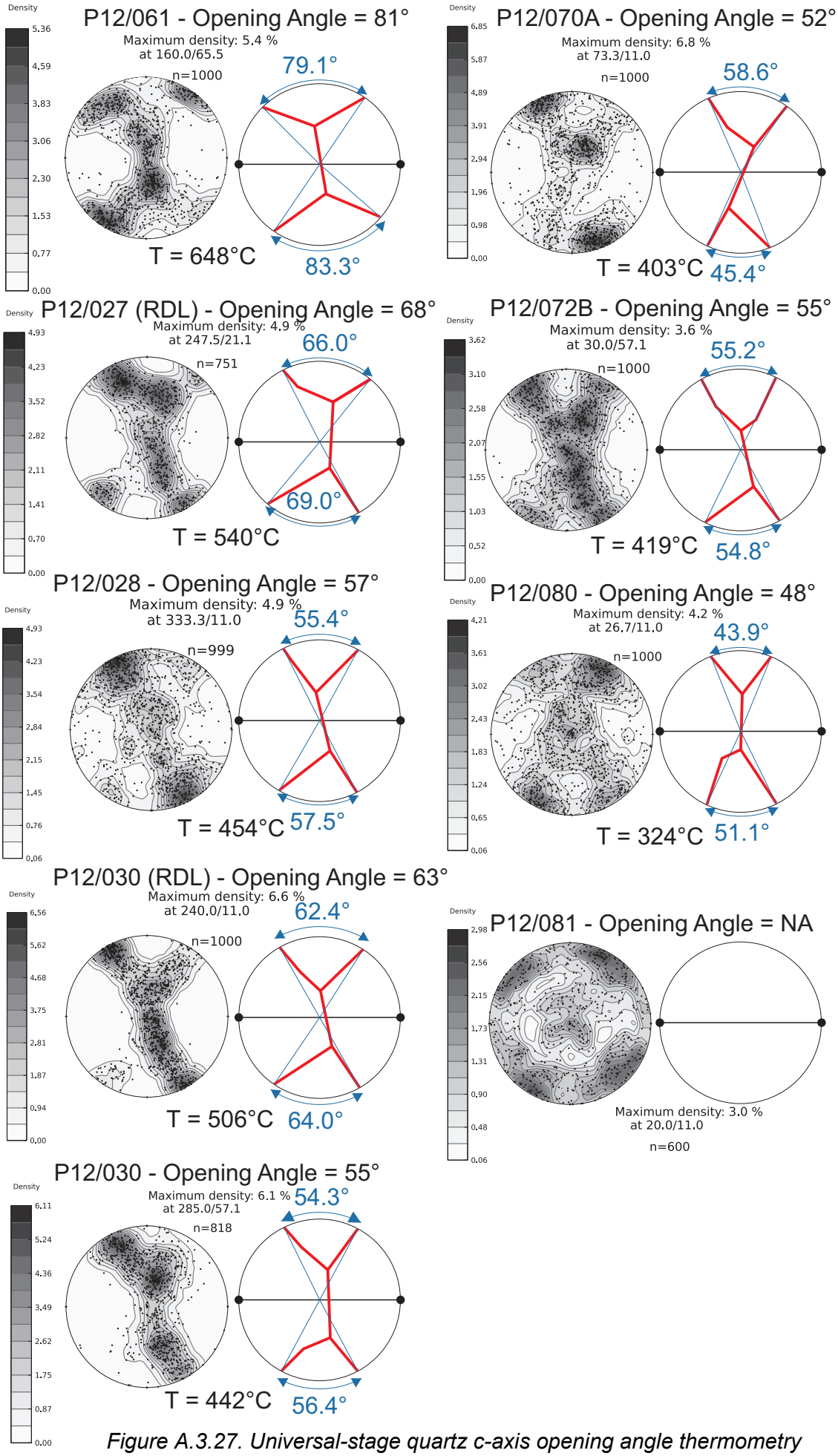

Figure A.3.27. Universal-stage quartz c-axis opening angle thermometry

- CHAPTER 4 -
ANISOTROPY OF MAGNETIC SUSCEPTIBILITY (AMS) ANALYSIS OF THE GHS: KINEMATICS & STRAIN GEOMETRY

4.1. Introduction

Typically, structural and microstructural strain analyses of deformed rocks require local strain markers to be preserved (e.g. Bouchez & Pêcher, 1981; Law *et al.*, 2004; Carosi *et al.*, 2007; Larson & Godin, 2009). Such analyses are not always possible in exhumed metamorphic rocks where strain markers are commonly overprinted by smaller scale structural heterogeneities or late stage static recrystallization. Analysis of the anisotropy of magnetic susceptibility (AMS) can be used to quantify relative magnitudes of strain when classic structural and microstructural techniques are not applicable (Housen *et al.*, 1995; Borradaile & Jackson, 2004; Ferré *et al.*, 2014).

AMS describes the directional-dependent anisotropic magnitude of an induced magnetic field around an object (Tarling & Hrouda, 1993; Borradaile & Jackson, 2010). In rocks, AMS is controlled by deformation, mineral content and crystallographic fabric. In the case of a metamorphic rock, AMS measurements can relate to deformation fabrics and may correlate directly with both structural and crystallographic orientation data (Tarling & Hrouda, 1993; Borradaile & Jackson, 2010). Furthermore, AMS data can serve as a proxy for both the relative magnitudes of strain and strain geometry (Tarling & Hrouda, 1993; Borradaile & Jackson, 2010; Ferré *et al.*, 2014).

In this chapter, AMS analysis is utilized to interrogate the kinematics and strain geometry of the GHS in the Annapurna-Dhaulagiri region. Firstly, the theoretical controls of AMS and its relation to deformation are presented in detail as a proof of concept. Following this, the results of AMS analyses of samples from the Kali Gandaki transect and southern portion of the Modi Khola transect are presented. Through multiple magnetic fabric analysis techniques, the controls on the measured AMS fabrics are tested to determine whether or not they record information related to deformation. It is shown that for almost all samples, the AMS data presented in this chapter are genetically linked to the deformation fabrics described in Chapter 3**.** Finally, the AMS data are used to determine the kinematics and strain geometries of the recorded deformation in the GHS and bounding units.

Importantly, this chapter forms the basis for development of an AMS-derived strain proxy profile for the GHS and bounding units, which is presented in Chapter 5. The analyses presented in this chapter and the resulting strain-proxy profile in Chapter 5

are independent of the macro- and microstructural data presented in Chapters 2 and 3 and provide an additional data set to test the kinematic predictions of channel flow models (e.g. Turcotte & Schubert, 2002; Beaumont *et al.*, 2004; Jamieson *et al.*, 2004; Grujic, 2006; Harris, 2007). The following results reveal a significant component of mid-crustal orogen-parallel deformation of the GHS; a process which is unaccounted for by most models of Himalayan orogenesis, including thermo-mechanical simulations of channel flow (Beaumont *et al.*, 2001; Beaumont *et al.*, 2004). The implications of these data for the development of the Himalayan orogen are not yet fully understood and are discussed in further detail in Chapter 7.

4.2. Magnetisation and anisotropy of magnetic susceptibility

4.2.1. Magnetisation

The axial spin and orbit of electrons produces a magnetic moment, m (Am^2). A magnetic moment at an angle θ to a magnetic field vector, H, has a magnetostatic energy of $m.\mu_0.H.\cos\theta$, where μ_0 is the permeability of free space (Tauxe, 2002). Magnetisation, M is defined as the magnetic moment per unit volume (Am^{-1}) or mass (Am^2kg^{-1}) (Tauxe, 2002). The magnetic properties of any material represent the summation of magnetic moments produced by electron spins and orbits (Tarling & Hrouda, 1993; Tauxe, 2002).

Magnetisation can be split into two categories: *induced magnetisation*, which represents the combined magnetic responses of electrons to an external magnetic field, H, and *remnant magnetisation*, which occurs due to the alignment of electron spins and orbits that exists without an external magnetic field (Tauxe, 2002).

The magnitude of induced magnetization is a function of the original electron spin and orbit configuration prior to the application of an external field, temperature, stress state and external field strength and orientation (Tarling & Hrouda, 1993; Tauxe, 2002). At a fixed state of environmental conditions, the magnitude of induced magnetisation (M) for a given object is proportional to the external field strength (H). This proportionality is defined as the magnetic susceptibility (K) and is a distinct property of any material (Tarling & Hrouda, 1993),

$$M = K\,H \qquad \textit{Equation 4.1}$$

For most materials, the direction of induced magnetisation will be parallel to the external field (except for ferromagnetic grains; *Section 4.2.3.1.*) (Tarling & Hrouda, 1993; Tauxe, 2002). The maximum magnetization occurs in the direction that requires the least energy to realign the electron spins. This direction is termed the “easy

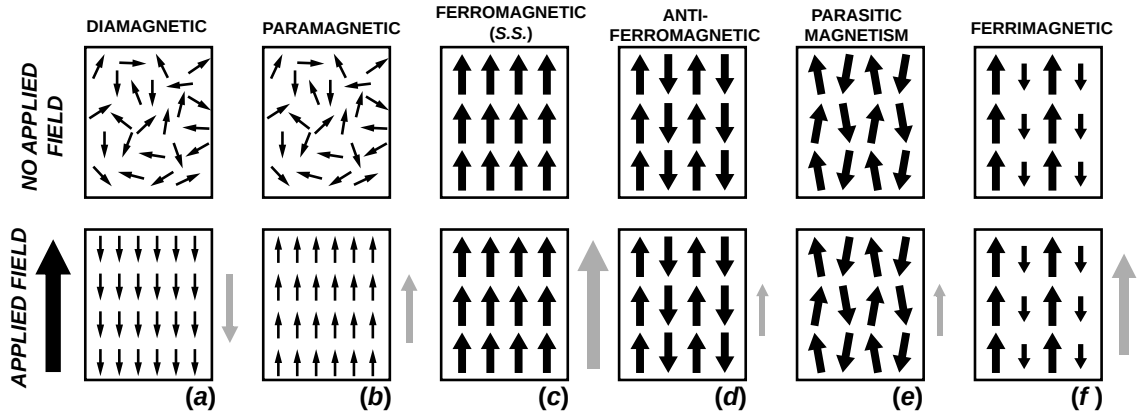

Figure 4.1. Magnetic behaviour classifications (Modified from Tarling & Hrouda, 1993). The magnetisation of different types of materials is show (grey arrows) both in the absence (top row) and presence (bottom row) of an externally applied field. The direction of the applied field is shown by the large black arrow to the left of the bottom row. The direction and relative magnitude of the magnetisation is represented by the direction and size of the grey arrows relative to the applied field arrow. Small black arrows within boxes show the variations in the internal magnetisation of the material, which correspond to the alignment of electron spins. See text for complete explanations (*a*) diamagnetism, (*b*) paramagnetism, (*c*) ferromagnetism (*sensu stricto*), (*d*) antiferromagnetism, (*e*) parasitic magnetism, (*f*) ferrimagnetism.

direction", which runs along an "easy axis" (Tauxe, 2002). Typically, the easy axis of a single grain is parallel to its long axis. The direction which requires the most energy to realign the electron spins (i.e. minimum magnetization) is the "hard direction". The energy required to switch the direction of the magnetization from one easy direction, through the hard direction to an opposite easy direction (i.e. to switch polarities) is the anisotropy energy, also known as the coercivity (H_c) and is a distinct characteristic of each grain (Tauxe, 2002). Most grains have only one easy axis and thus produce a strongly anisotropic magnetisation (uniaxial anisotropy). For small equant grains, with no obvious long axis, it is possible to have multiple easy axes that produce a less anisotropic magnetisation due to the reduced angle between easy direction, so-called cubic anisotropy (Tarling & Hrouda, 1993; Tauxe, 2002).

4.2.2. Classification of magnetic materials

Materials can be classified into one of three behavioural groups (diamagnetic, paramagnetic and ferromagnetic) based on how they respond to an externally applied magnetic field and whether or not they possess a remnant magnetisation (Figure 4.1) (Tarling & Hrouda, 1993).

Diamagnetic materials (Figure 4.1a) do not possess a remnant magnetisation and produce the weakest induced magnetisation in response to an external magnetic field. The induced magnetisation is lost instantaneously upon removal of the external field. These materials have complete electron shells (i.e. even atomic numbers) that produce

an induced magnetisation in the opposite direction to that of the applied magnetic field. As a result, diamagnetic materials produce negative values of magnetic susceptibility at the lowest order of magnitude out of the three magnetic material classifications (Tarling & Hrouda, 1993). Quartz, calcite and dolomite are examples of diamagnetic minerals with susceptibilities on the order of -10^{-5}-10^{-6} [*SI*] (*SI - Système International* standard of units) (Tarling & Hrouda, 1993).

Paramagnetic materials (Figure 4.1b) have incomplete electron shells and produce an induced magnetisation with the same direction as the applied magnetic field (*K* is positive). As with diamagnetic materials, paramagnetic materials do not possess a remnant magnetism and lose an induced magnetisation instantaneously upon removal of the external field. At room temperature, most rock-forming minerals are paramagnetic, including all phyllosilicates, amphiboles and pyroxenes. Paramagnetic minerals typically exhibit magnetic susceptibilities of the order of 10^{-3} to 10^{-4} [*SI*] (Tarling & Hrouda, 1993).

Ferromagnetic materials (Figure 4.1c-f) possess a spontaneous coupling and parallel or antiparallel alignment of electron spins without the presence of an external field (Tarling & Hrouda, 1993; Tauxe, 2002). Ferromagnetic materials contain elements that have unpaired electrons in the *3d* electron shell, the most common of which are the first transition series elements; iron, nickel, cobalt and chromium (Tauxe, 2002). Typically, these materials produce the strongest induced positive magnetisation ($K > 0$) of all three material classes and some can retain a remnant magnetisation after the removal of an external field. More specifically, ferromagnetic materials, *sensu lato* (*s.l.*) can be subdivided into three categories with different magnetic properties; ferromagnetic *sensu stricto* (*s.s.*), antiferromagnetic and ferrimagnetic (Tarling & Hrouda, 1993; Tauxe, 2002). Electron spins in ferromagnetic (*s.s.*) materials (Figure 4.1c), such as iron have a unidirectional parallel alignment. The summation of the spin magnetizations produced by each electron spin adds up to produce a positive net remnant magnetization (Tarling & Hrouda, 1993; Tauxe, 2002). Antiferromagnetic materials (Figure 4.1d) such as chromium and ilmenite have antiparallel electron spins (opposed directions) that cancel each other out to produce zero net remnant magnetisation (Tarling & Hrouda, 1993; Tauxe, 2002). If there is a very small difference in the opposing magnetic moments or if the electron spins are slightly misaligned, then a small positive net remnant magnetisation may be produced. This weak magnetisation is known as parasitic magnetisation (Figure 4.1e) and is a property of hematite (Tarling & Hrouda, 1993; Tauxe, 2002). Ferrimagnetic materials (Figure 4.1f), such as magnetite, have antiparallel electron spins with one direction producing a greater

magnetic moment than the other due to an uneven distribution of first transition elements within the compound. Ferrimagnetic materials have a positive net remnant magnetization (Tarling & Hrouda, 1993; Tauxe, 2002). For the rest of the chapter, the term 'ferromagnetic' referrers to the *sensu lato* definition, unless otherwise stated.

4.2.2.1. Magnetic domains and ferromagnetic grain size

An additional control on the magnetisation of ferromagnetic minerals is grain size, which determines the number of magnetic domains within the grain. A magnetic domain represents a volume of material with a dipole magnetisation (i.e. two poles, north and south), across which the direction of magnetisation is uniform.

The smallest ferromagnetic grains (typically ~1 μm in diameter) are made up of only one magnetic domain (i.e. grain and magnetic domain are the same) (Tarling & Hrouda, 1993). These grains are termed single domain (SD) grains and they possess a uniform magnetisation (Tarling & Hrouda, 1993; Tauxe, 2002).

As grain size increases it becomes more energetically favourable to divide a single domain into multiple domains, separated by domain walls aligned into the most energetically stable configuration with the lowest magnetostatic energy. Construction of domains occurs through changes in electron spin configurations rather than changes to the crystal lattice, although their development is influenced by lattice defects, stress state and grain shape (Tauxe, 2002). Multiple domains are typically arranged antiparallel or orthogonal depending on grain shape and crystal symmetry. Such grains are termed multidomain (MD) grains (Tarling & Hrouda, 1993; Tauxe, 2002). Small ferromagnetic grains with approximately 2 to 4 magnetic domains are termed pseudo-single domain (PSD) grains as they display a magnetic behaviour more similar to SD grains rather than larger MD grains (Tarling & Hrouda, 1993; Tauxe, 2002).

The remnant magnetisation of all ferromagnetic grains decays with time (Tarling & Hrouda, 1993). For SD and PSD grains, this decay, defined as the relaxation time (τ), takes place over geological time scales (~10^9 years). MD grains have relaxation times of hundreds to thousands of years (Tauxe, 2002). However, for the smallest SD grains (≤ 0.05 μm) relaxation times are on the scale of minutes to almost instantaneous. Such ferromagnetic grains are termed superparamagnetic (SP) as they lose their magnetism (Tarling & Hrouda, 1993; Tauxe, 2002). Determining the grain size of ferromagnetic grains (i.e. SP, SD, PSD or MD) is important as different grain sizes have different responses to an external magnetic field, which affects the overall magnetisation of a sample (S*ection 4.2.3.*).

4.2.3. Magnetic hysteresis analysis

4.2.3.1. Hysteresis loops

A plot of induced magnetisation, M, against the corresponding high field strength, H, responsible for the magnetisation produces a hysteresis loop that provides information on the type of magnetic carriers present (Figure 4.2.). The hysteresis loop measured from a rock sample represents the summation of every hysteresis loop produced by every grain within that rock. Magnetic hysteresis loops can be used to determine the composite magnetic behaviour of a rock (i.e. diamagnetic, paramagnetic or ferromagnetic), which reflects the combined magnetic responses of the most dominantly magnetic minerals, and the composition and grain size of any ferromagnetic minerals present (Tauxe *et al.*, 1996; Pike *et al.*, 1999; Tauxe *et al.*, 2002).

Hysteresis loops are produced by measuring the induced magnetisation of a sample in an external high magnetic field of varying magnitude (Figure 4.2.). The external field is first increased from 0 to $+H_{max}$, (typically ≥ 1 T). Saturation magnetisation, M_s, is measured at the point where the hysteresis loop becomes horizontal, by which point, the easy axes of all constituent minerals have realigned parallel to the applied field. M_s is the maximum magnetisation of the sample. The saturation field, H_s, is the field strength at which M_s is achieved and is measured from the point at which the hysteresis loop closes (Tauxe *et al.*, 2002). Changes in the induced magnetization are then measured as the external field decreases from $+H_{max}$ through $H = 0$, to $-H_{max}$ and then increases back to $+H_{max}$. The value of M recorded at $H = 0$, is the remnant magnetisation, M_r; $M_r>0$ reflects the remnant magnetisation of any ferromagnetic minerals present. The value of H recorded at $M = 0$ is the bulk coercivity, H_c, which reflects that strength of field required to change the direction of magnetisation along the easy axis. The coercivity of remnance H_{cr} is the field strength needed to irreversibly change the direction of M_r and is measured by incrementally increasing the high field magnitude in the opposite direction to M_r until the field is strong enough to reduce M_r to 0 (Tauxe *et al.*, 2002). Note the difference between H_{cr} and H_c. The latter is the field strength needed to reduce the net magnetization parallel to the field to 0 and does not need to permanently change the direction of M_r (Tauxe *et al.*, 2002). Figure 4.3 shows a variety of hysteresis loops produced by different magnetic materials.

When considering the hysteresis parameters of ferromagnetic materials, both grain size and grain orientation will influence the hysteresis loop-shape (Tauxe *et al.*, 2002). Ferromagnetic grains have high coercivities (H_c) due to their energetically stable arrangement of electron spins (Tarling & Hrouda, 1993). In low external magnetic fields (<300 A/m, as typically used in AMS analysis, Pokorný *et al.*, 2004), the magnitude of

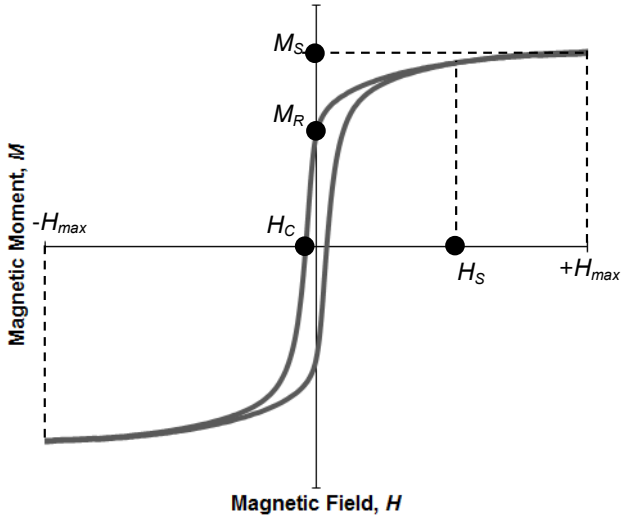

Figure 4.2. Schematic hysteresis curve for a ferromagnetic material. $M_{s,}$ saturation magnetisation; $M_{r,}$ remnant magnetisation; $H_{s,}$ saturation field; $H_{c,}$ bulk coercivity. $+H_{max}$ and $-H_{max}$ defines the range of field magnitude.

the applied field is typically lower than that needed to overcome the coercivity of ferromagnetic grains. As a result, in low magnetic fields, the direction of induced magnetisation in ferromagnetic grains is parallel to the easy axis of that grain, rather than parallel to the external field direction. It is only in high magnetic fields (typically >1 T) that the applied field is greater than the saturation field (H_s) of ferromagnetic grains and is able, therefore, to re-align the orientation of the easy axis into parallelism with the applied field. The re-orientated easy axis will maintain its new orientation until subjected to another high external field ($H \geq H_s$). (Tarling & Hrouda, 1993; Tauxe, 2002; Tauxe *et al.*, 2002).

Figure 4.4 shows the theoretical hysteresis loops of a single uniaxial SD grain (USD – one easy axis) produced by an external field applied at an angle, Φ, to the easy axis (Tauxe *et al.*, 2002). The hysteresis loops record the magnetisation parallel to the applied field vectors. Due to the effect of coercivity, when $\Phi = 0^o$ (external field parallel to the easy axis), a square hysteresis loop is produced (Figure 4.4), as the magnetization along the easy axis does not change direction until field strength is equal or greater than the bulk coercivity of the USD grain (Tauxe, 2002). For angles of $90^o > \Phi > 0^o$ the external field is able to bend the magnetization away from the easy axis by an angle θ, which lowers the measured M_r and H_{cr}. As Φ increases, the opposing magnetisation decreases. Consequently, for $\Phi > 0^o$ incremental changes in the external field will incrementally increase the strength of the induced magnetic moment parallel to the applied field, thus producing a curved hysteresis loop (Figure 4.4) (Tauxe, 2002). For $\Phi = 90^o$ the magnetic moment is bent into parallelism with the external field when $H \geq H_s$, but will bend back into parallelism with the easy axis as the external field is reduced. In such cases, the hysteresis loop forms a straight line through the origin (Tauxe *et al.*, 1996; Tauxe, 2002; Tauxe *et al.*, 2002). The squareness ratio, M_r / M_s is used to describe the shape of the hysteresis loop, ranging

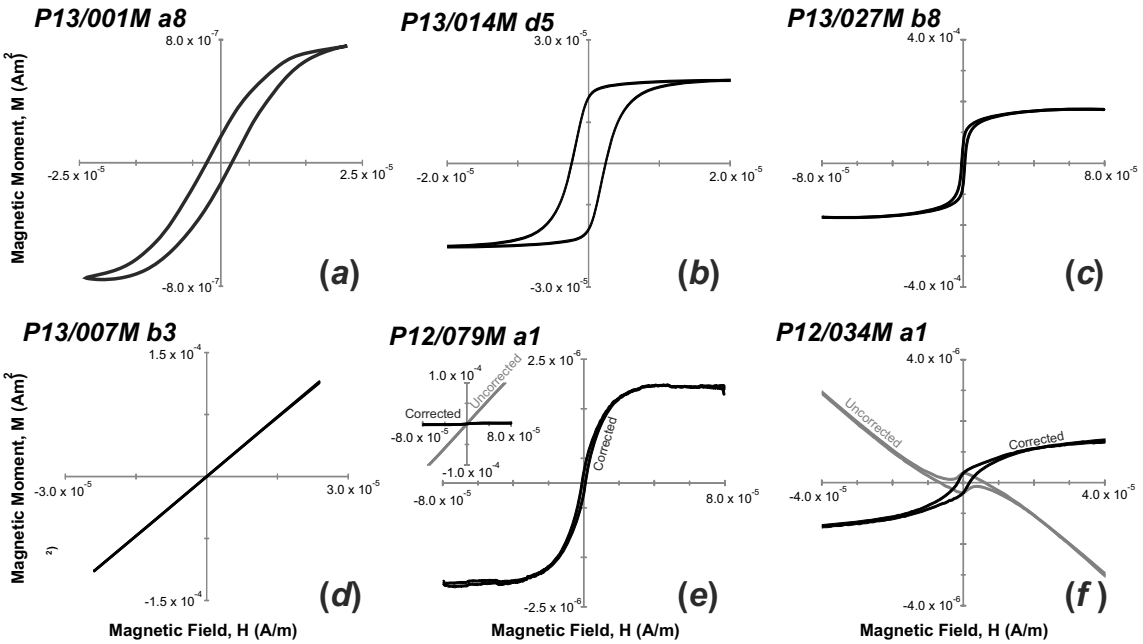

Figure 4.3. Magnetic hysteresis loops of different magnetic materials measured from samples analysed in this study. (*a*) Uniaxial SD magnetite (P13/001M a8); (*b*) magnetocrystalline SD magnetite (P13/014M d5); (*c*) PSD magnetite (P13/027M b8); (*d*) biotite (paramagnetic – P13/007M b3); (*e-f)* show 'uncorrected' curves (grey), which contain both paramagnetic/diamagnetic and ferromagnetic components of magnetisation, and 'corrected' curves (black), which show only the ferromagnetic component of magnetisation. (*e*) 'Uncorrected' curve produced by chlorite (paramagnetic) and 'corrected' curve produced by MD magnetite (P12/079M a1), (*f*) 'Uncorrected' diamagnetic curve produced by quartz and 'corrected' curve produced by SD-SP magnetite mix (P12/034M a1). The full magnetic hysteresis data set for all samples can be found in the appendix (Figure A.4.17.).

from a square (M_r / M_s = 1, Φ = 0^o) to a line (M_r / M_s = 0, Φ = 90^o) . In reality, ferromagnetic grains within a single rock have a range of orientations. A population of randomly orientated USD grains produces a hysteresis loop with a squareness ratio of approximately 0.5 (Figure 4.3a) (Tauxe et al., 2002).

An important distinction is made between the hysteresis loops produced from a population of randomly orientated USD grains and a population of randomly orientated SD grains with a cubic anisotropy (i.e. multiple easy axes), commonly referred to as Magnetostatic Single Domain (MSD) grains. An equant grain of magnetite with cubic crystal symmetry has four easy axes with body diagonal directions (i.e. parallel to [111]) and a maximum Φ of 55^o (Tauxe, 2002). It is not possible for a grain with cubic anisotropy to produce a single line hysteresis loop through the origin (Tauxe, 2002). As a result, a hysteresis loop produced by a population of randomly orientated cubic SD grains is more square in appearance than that produced by the same population randomly orientated USD grains and has a squareness ratio of approximately 0.8-0.9 (Figure 4.3b) (Tauxe *et al.*, 2002).

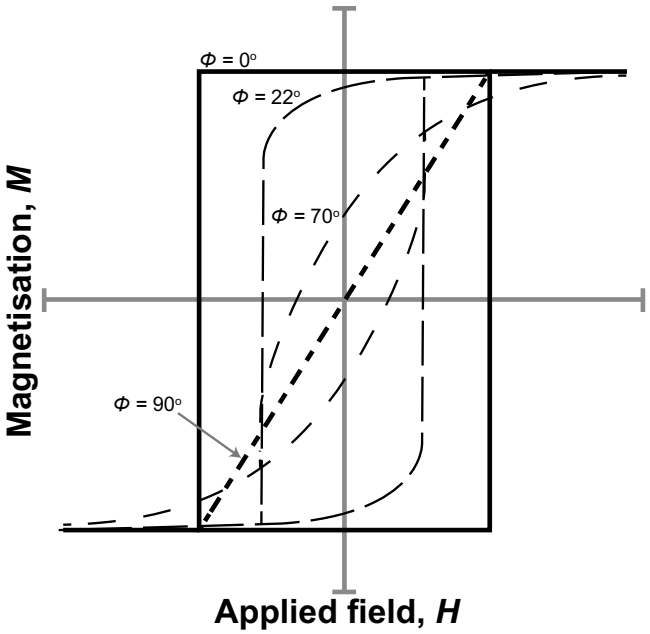

Figure 4.4. USD hysteresis loops. Modelled hysteresis curves for the induced magnetisation parallel to an external field in a single USD magnetite grain (after Tauxe *et al.*, 1996). Magnetisation varies with angle, Φ between the applied field vector and the grain's easy axis. See text for a full explanation.

PSD and MD hysteresis loops (Figure 4.3c,e) are generally thinner as they have lower coercivities than SD grains (Tauxe, 2002). This is due to the opposing exchange forces between multiple domains in a single grain that reduce the overall magnetisation (Tauxe, 2002). As a result, MD and PSD grains respond immediately to an external magnetic field in any orientation, even if the field is weak. As the strength of the external field increases, the number of individual domains that will align their internal field orientation with the external field increases. When the external field is removed, all domains will revert to their original orientation (Tarling & Hrouda, 1993).

Rocks with less than 0.1% volume of ferromagnetic grains produce hysteresis loops controlled by the paramagnetic minerals within that sample. In the absence of paramagnetic minerals, diamagnetic minerals control the hysteresis loop. As diamagnetic and paramagnetic minerals do not have a remnant magnetism, they produce a straight line loop through the origin. Diamagnetic minerals produce a negative slope as the magnetisation is antiparallel to the external field (Figure 4.3f). Paramagnetic minerals produce a magnetisation parallel to the external field and so produce a hysteresis loop with a positive slope (Figure 4.3e) (Tarling & Hrouda, 1993; Tauxe, 2002). In most cases, rocks that produce a diamagnetic or paramagnetic hysteresis loop can still contain some ferromagnetic phases. In these situations it is possible to subtract the paramagnetic or diamagnetic slope from the hysteresis loop to leave behind a ferromagnetic hysteresis loop (Figure 4.3e-f). This procedure, known as 'paramagnetic slope correction', is possible because it is assumed that H_{max} is greater than H_{sat} of the ferromagnetic phases, which implies that the slope of the hysteresis loop at H_{max} is produced only from the magnetisation of paramagnetic or diamagnetic phases (Tauxe, 2002).

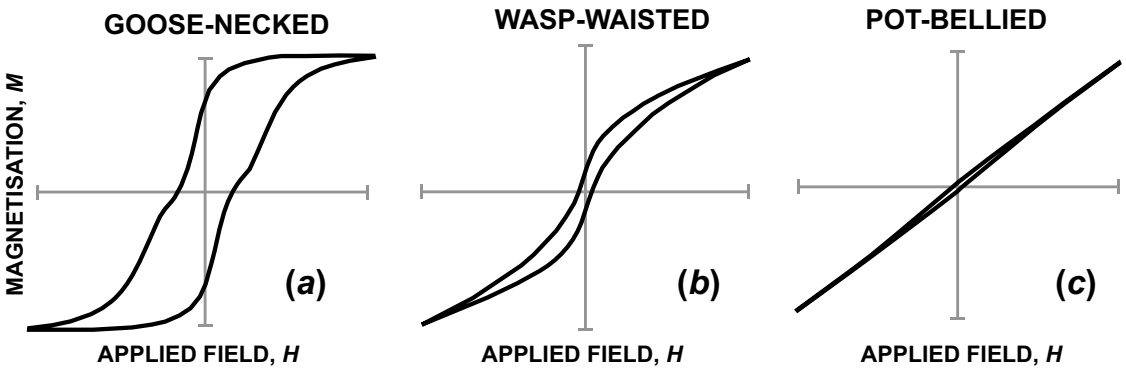

Figure 4.5. Hysteresis loops of ferromagnetic mixtures (from Tauxe et al., 1996). Distorted hysteresis loops modelled for mixtures of ferromagnetic grain sizes and mixtures of ferromagnetic phases. (*a*) '*Goose-necked'* hysteresis loop produced from a mix of hematite and magnetite. (*b*) '*Wasp-waisted'* hysteresis loop produced from a mix of SD and large (~20-30 nm) SP grains. (*c*) '*Pot-bellied'* hysteresis loop produced for a mix of SD and small (<10 nm) SP grains.

For mixed populations of SD and SP grains or mixed populations of different ferromagnetic phases, the resulting hysteresis loops are often distorted with kinks or bulges, categorised as *'goose-necked'*, *'wasp-waisted'* and *'pot-bellied'* (Figure 4.5) (Tauxe et al., 1996). *Goose-necked* hysteresis loops (Figure 4.5a) are typically formed by a mix of two ferromagnetic phases (Wasilewski, 1973; Roberts *et al.*, 1995; Tauxe *et al.*, 1996), whilst *wasp-waisted* (Figure 4.5b) and *pot-bellied* (Figure 4.5c) loops are typically formed by a mix of SD and large SP grains (~20-30 nm) and SD and small SP grains (<10 nm), respectively (Pick & Tauxe, 1994; Tauxe *et al.*, 1996). Whilst the shape of ferromagnetic hysteresis loops can indicate the presence of mixed grain size populations, they cannot distinguish the ratios of such mixtures. For this information, it is useful to plot the hysteresis parameters on a Day plot (Day *et al.*, 1977; Dunlop, 2002a, b).

4.2.3.2. Day (Dunlop) plots

By plotting the squareness ratio, M_r / M_s, against H_{cr} / H_c, it is possible to determine the magnetic grain size (in terms of domains) of ferromagnetic grains in a rock. The original Day plot (Day et al., 1977) outlines regions of M_r / M_s vs. H_{cr} / H_c that correspond to populations of SD, PSD or MD ferromagnetic grains. The plot was calibrated against titanomagnetite grains of known grain size although it can still be used for determining the grain size populations of other ferromagnetic materials if careful consideration is given to their distinct magnetic properties (Dunlop & Özdemir, 2001). In some cases, M_r / M_s and H_{cr} / H_c values that fall in or near to the PSD region may correspond to mixtures of different grain sizes (Tauxe *et al.*, 1996; Dunlop & Özdemir, 2001; Dunlop, 2002b). Calculations of M_r / M_s and H_{cr} / H_c values of modelled mixtures of SD and MD grains (Dunlop, 2002b) and SD and SP grains (Tauxe *et al.*, 1996) give rise to

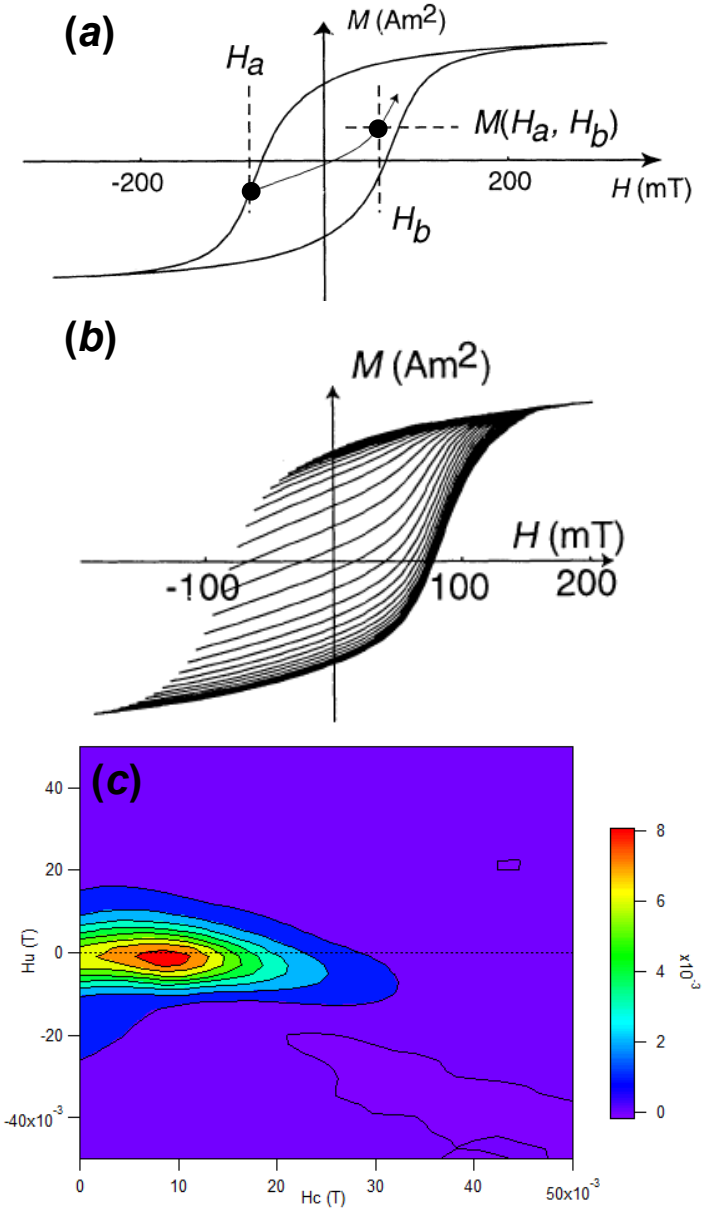

Figure 4.6. Graphical explanation of magnetic hysteresis loop and FORC analysis. (*a*) Magnetic hysteresis loops display changes in the strength of an object's induced magnetic field (*M*) caused by changes in the strength of the applied field (*H*). H_a, initial field strength of a FORC; H_b, field strength at any point along a FORC between H_a and M_S; $M(H_a, H_b)$, magnetisation of sample at H_b, of a FORC with an initial field strength of H_a (after Roberts *et al.*, 2000). (*b*) FORC analysis requires multiple FORC measurements with variable values of H_a. Each line represents a single FORC (after Roberts *et al.*, 2000). (*c*) FORC diagram for a single sample. $H_u = (H_a + H_b)/2$, $H_c = (H_b - H_a)/2$. Colour contouring represents density of (H_u, H_c).

theoretical mixing curves that can be used to work out the percentage of MD or SP grains in an MD-SD mix or a SP-SD or SP-PSD mix (see *Section 4.5.3.* for a worked example) (Dunlop, 2002b).

4.2.3.3. Magnetostatic grain interaction and FORC analysis

In certain arrangements it is possible for SD grains to magnetically interact with each other (Pike *et al.*, 1999; Muxworthy *et al.*, 2004). Such interaction can affect the magnetic behaviour of a rock and must be investigated if the magnetic carriers are suspected to be ferromagnetic (Tarling & Hrouda, 1993; Borradaile & Jackson, 2004). First order reversal curve (FORC) analysis is used to measure magnetostatic interactions occurring between ferromagnetic grains. FORCs describes the magnetisation, *M*, of a sample in a variable magnetic field, H_b, with an initial field strength H_a (Pike *et al.*, 1999; Roberts *et al.*, 2006). H_b ranges between H_a and the magnetic saturation point, M_s, of the sample (Figure 4.6a). The magnetisation curve between H_a and M_s represents a single FORC. The magnetisation of a sample at any point along the FORC is described

as $M(H_a, H_b)$. By varying the strength of H_a, multiple FORCs are measured with different trends in $M(H_a, H_b)$ (Figure 4.6b). A FORC diagram represents the density distribution of $M(H_a, H_b)$ produced from multiple FORCs with differing values of H_a (Figure 4.6c). Graphical presentation of the variable concentrations of $M(H_a, H_b)$ is plotted in the coordinate system of $H_u = (H_a + H_b) / 2$ against $H_c = (H_b - H_a) / 2$, where H_c represents the coercivity distribution and H_u represents the interaction field distribution (Muxworthy *et al.*, 2004).

The shape and size of the concentration(s) of $M(H_a, H_b)$ displayed on a FORC diagram varies with ferromagnetic mineral phase and grain size (e.g., Pike *et al.*, 1999; Roberts *et al.*, 2000; Roberts *et al.*, 2006). SD grains typically produce a maxima along $H_u = 0$ mT with a value of H_c greater than 0 at the centre of the maxima that corresponds to the H_c of the magnetic carrier (Pike *et al.*, 1999). A flat elongate maxima along $H_u = 0$ mT, is representative of a non-interacting population of SD grains (Pike *et al.*, 1999). If SP grains are present, the centre of the maxima moves to $H_c = 0$ mT (Roberts *et al.*, 2000). A population of MD grains also has a maximum at $H_c = 0$ mT, plus considerable vertical and horizontal spreading of contours along $H_u = 0$ mT to values of $H_u = \pm 50$ to 100 mT and along $H_c = 0$ mT to values of $H_c = \sim 20$ to 100 mT (Roberts *et al.*, 2000). When the volume of ferromagnetic grains drops below negligible concentration, no maxima are observed.

On a FORC diagram, magnetostatic interactions between SD grains are identified by the spreading of contours around a maximum horizontally towards the H_u axis and vertically beyond ~ ±20 mT (Pike et al., 1999; Muxworthy et al., 2004). Asymmetries may also develop and the centre of the maximum may be moved above or below the $H_u = 0$ line (Pike *et al.*, 1999). When interaction is significant, multiple maxima are observed (Muxworthy *et al.*, 2004). Care must be taken when interpreting AMS data from samples with interacting SD grains as such interactions can influence the orientation and shape of the resulting AMS fabric (S*ection 4.3.1.2*).

4.3. Anisotropy of magnetic susceptibility

Magnetic susceptibility (K) describes the proportionality of the magnitude of induced magnetisation (M) to the strength of the external magnetic field (H) in which it is induced (Tarling & Hrouda, 1993) (*See Equation 4.1*). The anisotropy of magnetic susceptibility (AMS) describes the variation of K with direction and is modelled as a 2nd rank tensor, represented by the magnetic susceptibility ellipsoid. This ellipsoid is defined by mutually orthogonal principal magnetic susceptibility axes, K_1 (maximum), K_2 (intermediate) and K_3 (minimum) (Tarling & Hrouda, 1993). K_1 is commonly referred

to as the magnetic lineation, whilst K_3 represents the pole to the magnetic foliation (K_1-K_2 plane). Bulk susceptibility (K_m) is the mean of K_1, K_2 and K_3 (Janák, 1965). The corrected degree of anisotropy (P' – referred to simply as the degree of anisotropy from here after) describes the strength of the AMS in terms of the deviation of the susceptibility ellipsoid from a sphere (P' = 1) to an ellipsoid (P' > 1) (Jelínek, 1981),

$$P' = exp\sqrt{2\sum(lnK_i - lnK_m)^2} \qquad \textit{Equation 4.2}$$

where K_i refers to the three susceptibility axes, K_1, K_2 and K_3. The shape parameter (-1 ≥ T ≥ 1) describes the shape of the magnetic susceptibility ellipsoid in terms of prolate (T = -1; $K_1 > K_2 = K_3$) and oblate (T = 1; $K_1 = K_2 > K_3$) end members (Jelínek, 1981).

$$T = \frac{\ln(F) - \ln(L)}{\ln(F) + \ln(L)} \quad where \quad L = \frac{K_1}{K_2} \quad and \quad F = \frac{K_2}{K_3} \qquad \textit{Equation 4.3}$$

4.3.1. The controls of AMS

In order to make valid interpretations from AMS data, the controls of AMS of the rocks being studied must be investigated (e.g. Wallis *et al.*, 2014). AMS of a rock is controlled by the individual magnetic properties of its constituent minerals and by the degree of mineral alignment as defined by the shape preferred orientation (SPO) and crystallographic preferred orientation (CPO) of its most dominantly magnetic phase(s) (Borradaile & Jackson, 2004). When ferromagnetic phases are present, the effects of variable grain sizes (i.e. number of magnetic domains) (e.g. Dunlop, 2002a; Tauxe *et al.*, 2002) and magnetic interactions between grains must also be investigated (e.g. Pike *et al.*, 1999).

4.3.1.1. Grain-scale anisotropy energy & ferromagnetic grain size

Anisotropy energy of a single grain is controlled by the combined effects of *magnetostatic* anisotropy, *magnetocrystalline* anisotropy and *magnetostrictive* anisotropy (Tarling & Hrouda, 1993; Tauxe, 2002).

Magnetostatic anisotropy, also known as shape anisotropy, is controlled by grain shape. In order to minimize the magnetic moment produced by the externally applied field, grains with an elongate shape will align the easy direction parallel to the long axis of the grain (i.e. uniaxial anisotropy). In such cases, magnetostatic anisotropy will dominate the magnetic response of a grain to an external field (Tarling & Hrouda, 1993; Tauxe, 2002). The magnetic behaviour of uniaxial SD (USD) magnetite is dominated by magnetostatic anisotropy (Tarling & Hrouda, 1993).

Magnetocrystalline anisotropy is controlled by crystal symmetry. In such cases, the most energetically favourable electron spin configuration (i.e. lowest magnetic moment, greatest magnetisation) is controlled by the crystal structure, such that the easy axis aligns parallel or sub-parallel to one of the crystal axes (Tarling & Hrouda, 1993; Tauxe, 2002). When magnetocrystalline anisotropy dominates over magnetostatic anisotropy, certain crystal symmetries (e.g. cubic) can allow a single grain to have multiple easy axes. Grains with cubic crystal symmetry and no magnetostatic anisotropy (i.e. equant magnetite grains) have four body-diagonal (parallel to [111]) easy axes (i.e. cubic anisotropy) (Tauxe, 2002). The magnetic behaviour of hematite (rhombohedral symmetry) is most typically dominated by magnetocrystalline anisotropy (Tarling & Hrouda, 1993).

Magnetostrictive anisotropy, also known as magnetostriction refers to the stress-induced grain length changes produced the reconfiguration of electron spins in the presence of an external magnetic field (Tauxe, 2002). Magnetostriction has a negligible effect on the AMS of a rock relative to the influence of magnetostatic and magnetocrystalline anisotropy and is not considered further (Tauxe, 2002).

In summary, the competing roles of magnetostatic and magnetocrystalline anisotropy vary in dominance with both mineralogy and grain size. As such, both of these variables must be considered when interpreting the grain-scale contribution to AMS fabrics (Tarling & Hrouda, 1993).

4.3.1.2. Mineral alignment and interaction

AMS of a rock reflects the summation of anisotropy energies of all constituent grains (Borradaile & Jackson, 2004). Rocks with a strong SPO and/or CPO, which align the “easy” directions of the most magnetically dominant grains, produce strong magnetic lineations and foliations that mimic mineral fabrics (Borradaile, 1991; Borradaile & Jackson, 2004; Borradaile & Jackson, 2010).

The effects of grain-scale anisotropy and mineral alignment must be considered together. Strong alignment of grains with weak anisotropy energies may produce an AMS fabric indistinguishable from weakly aligned grains with strong anisotropy energies (Tarling & Hrouda, 1993). Likewise, when the AMS of a rock is influenced by the SPO or CPO of USD ferromagnetic grains, the orientation of K_1 is likely to be orthogonal, rather than parallel to, the mineral lineation (*Section 4.2.3.1.*) (Tarling & Hrouda, 1993). In such situations it is more appropriate to use K_3 as the magnetic lineation in order to make correlations between AMS and deformation fabrics.

The spatial distribution of magnetic carriers throughout a rock must also be considered (Tarling & Hrouda, 1993; Borradaile & Jackson, 2004). Magnetostatic interaction between SD grains becomes significant when the distance between SD grains is two diameter lengths or less from centre-to-centre and one diameter length or less from edge-to-edge (Stephenson, 1994). Magnetostatic interactions between a population of evenly spread SD grains produces a stable mean interaction field that mimics, and may strengthen the anisotropy energies of the rest of the sample (Roberts *et al.*, 2000; Muxworthy *et al.*, 2004). In contrast, local concentrations of magnetostatic interacting SD grains may produce a local interaction field (Muxworthy *et al.*, 2004) that differs in direction to the magnetisation produced by the rest of the sample (Borradaile & Jackson, 2004). If strong enough, these local interaction fields produce a *'distribution anisotropy*' (Hargraves *et al.*, 1991) that can interfere or dominate over the AMS fabric produced by the rest of the rock (Borradaile & Jackson, 2004; Muxworthy *et al.*, 2004). For example, a localised concentration of SD grains with a linear or planar arrangement can magnetically interact to produce an AMS fabric with a strong prolate or oblate symmetry respectively that bares no relation to their individual grain shape, crystallography or SPO/CPO (Tarling & Hrouda, 1993). Such factors are particularly important for weathered or altered rocks in which secondary mineral phases such as hematite and goethite may preferentially grow in pore spaces or fractures (Borradaile & Jackson, 2010).

4.3.1.3. Mineral assemblages

Minerals that control the magnetic behaviour of a rock are known as magnetic carriers (Tarling & Hrouda, 1993). A rock with more than 0.1% volume of ferromagnetic minerals produces a magnetic response that is governed by the ferromagnetic phase(s) (Tarling & Hrouda, 1993). The most common ferromagnetic phases are magnetite and hematite.

Magnetite has a high M_s (92 Am^2 kg^{-1}) and H_c (10-100 mT, 8-80 kA/m) (O'Reilly, 1984), and has a high K_m (mass susceptibility of 578 x 10^{-8} *SI/kg*) (Tarling & Hrouda, 1993). Magnetite is a ferrimagnetic mineral with cubic crystal symmetry. Undeformed equant grains have no magnetostatic anisotropy and only a weak magnetocrystalline anisotropy with 4 easy axes parallel to the body diagonals (Tarling & Hrouda, 1993; Tauxe, 2002). Magnetostatic anisotropy dominates for grains with ≥10% deviation from an equant to elongate grain shape (Tauxe, 2002). In most natural cases, SD magnetite has a uniaxial rather than cubic anisotropy, which when isolated produces an '*inverse*' AMS fabric where K_3 represents the magnetic lineation (Rochette *et al.*, 1999; Ferré, 2002). Where '*normal*' and '*inverse*' fabrics mix, an '*intermediate'* fabric can form, in

which K_2 represents the magnetic lineation and *P'* is significantly reduced (<1.05) (Ferré, 2002). Magnetite readily includes titanium into its crystal structure to form titanomagnetite, which has similar properties to magnetite but with a lower M_s (24 Am^2 kg^{-1}) and H_c (~8 mT, 6.3 kA/m) (Tauxe, 2002). Due to the relatively high susceptibility of magnetite compared to other ferromagnetic phases, the ferromagnetic signature of a rock is controlled by magnetite when present as ≥ 0.5% of the ferromagnetic mineral content (Tarling & Hrouda, 1993).

Hematite is characterised by low M_s (0.4 Am^2 kg^{-1}) and variable H_c, which can be as high as 10^2 T (~80000 kA/m) (O'reilly, 1984). K_m of hematite is low compared to magnetite (mass susceptibility of 25 x 10^{-8} *SI/kg*) (Tarling & Hrouda, 1993) but still higher than paramagnetic phases (Hrouda & Kahan, 1991). Hematite has rhombohedral crystal symmetry, which produces magnetic lattices of equal strength that are sub-antiparallel to each other, resulting in a parasitic ferromagnetism. The AMS of hematite is dominated by magnetocrystalline anisotropy. Consequently, SD hematite grains do not produce an inverse AMS fabric (Tarling & Hrouda, 1993). Other ferromagnetic minerals include pyrrhotite, maghaemite, gregite and goethite. Based on the results of this study, there is no evidence to suggest that these other ferromagnetic phases form the dominant magnetic carriers of the samples analysed. Consequently, the magnetic properties of these minerals is not discussed but can be found in Tarling and Hrouda (1993), Dunlop and Özdemir (2001) and Tauxe (2002).

A lower volume of ferromagnetic minerals results in a magnetic response controlled by the combined effects of both ferromagnetic and paramagnetic mineral phases. In the absence of ferromagnetic minerals, paramagnetic minerals become the next dominant mineral phase to control the magnetic behaviour. Diamagnetic minerals are the least magnetically dominant and only control rock magnetism when the volume of ferromagnetic and paramagnetic minerals approaches 0 (Tarling & Hrouda, 1993; Tauxe, 2002). In general, the magnetic susceptibility and anisotropy of rocks with K_m > 5 x 10^{-3} and ≥10% volume of paramagnetic minerals is controlled by a ferromagnetic phase. In rocks with K_m < 5 x 10^{-4} and ≥10% volume of paramagnetic minerals, the susceptibility and anisotropy is controlled by a paramagnetic phase. In rocks with K_m between 5 x 10^{-3} and 5 x 10^{-4} and ≥10% volume of paramagnetic minerals, AMS is controlled by both ferromagnetic and paramagnetic components (Tarling & Hrouda, 1993).

4.3.2. AMS analysis as a proxy for strain

As deformation is generally responsible for SPO and CPO development, and as SPO and CPO can control AMS, it follows that the magnitude and orientation of AMS can serve as a proxy for relative strain magnitudes and 3D strain geometry and kinematics (Borradaile, 1991; Borradaile & Jackson, 2004; Borradaile & Jackson, 2010; Ferré *et al.*, 2014). In such situations, the finite strain axes ($X \geq Y \geq Z$) and principal magnetic susceptibility axes ($K_1 \geq K_2 \geq K_3$) are respectively parallel (e.g. Borradaile, 1991; Guillot *et al.*, 1993; Kruckenberg *et al.*, 2011). Correlations may also exist between *P'* and finite strain magnitudes (e.g. Borradaile, 1991; Benn, 1994; Tripathy, 2009) and *T* and strain ellipsoid shape (e.g. Sidman *et al.*, 2005; Molina Garza *et al.*, 2009). Whilst a correlation between AMS fabric orientations and deformation kinematics is a widely accepted phenomenon (Borradaile & Jackson, 2010; Ferré *et al.*, 2014), strain related interpretations of *P'* and *T* should be made with caution as these parameters are also strongly controlled by mineralogy (Borradaile & Jackson, 2010; Borradaile *et al.*, 2011; Haerinck *et al.*, 2013; Ferré *et al.*, 2014). Such interpretations are hard to validate when comparing the AMS of rocks with differing magnetic carriers and lithologies (Wallis *et al.*, 2014).

Magnetic carriers must be identified and the competing factors that control or influence AMS must be investigated (e.g. Kruckenberg *et al.*, 2010) before any correlation between deformation and AMS fabrics can be made (Borradaile & Jackson, 2010; Ferré *et al.*, 2014). Deformation related AMS studies should include complimentary magnetic analyses, such as hysteresis and FORC analysis, and where necessary, be combined with petrological analysis of mineral assemblages, CPO and SPO fabrics and ferromagnetic mineral spatial distributions (Ferré *et al.*, 2014; Wallis *et al.*, 2014).

4.4. Analytical methods

4.4.1. AMS samples

41 field-orientated samples were collected along a N-S transect through the Kali Gandaki valley and Modi Khola valley in central Nepal (Figure 4.7). Sample lithology, stratigraphic affiliation and location are summarised in Table 4.1. The samples were cut into 17-18 mm cubes, depending on the size of the original sample (total of 628 cubes from 41 samples). AMS measurements were performed on each cube with an AGICO KLY-4S Kappabridge susceptometer at 300 A/m (a small minority of low magnetic susceptibility samples were run at 450 A/m) (Pokorný *et al.*, 2004) at the Department of Geology, Southern Illinois University. AMS data were acquired using SUFAR 1.2 and Anisoft 4.2 software (Chadima & Jelínek, 2008). The mean magnitude and orientation

Sample	Lithology	Tectonic Unit	Longitude	Latitude	Altitude (m)
P12/034M	Marl / Micaceous Limestone	THS	83.67948041	28.74004017	2703.33
P12/037M	Marl / Micaceous Limestone	THS	83.66810072	28.7221676	2703.33
P12/042M	Metacarbonate	STDS	83.62629883	28.69993788	2595.18
P12/046M	Marble	STDS	83.59729946	28.67225966	2545.68
P12/050M	Orthogneiss	Unit III - Upper GHS	83.59325058	28.65373892	2515.88
P12/052M	Calc-silicate gneiss	Unit II - Upper GHS	83.62248355	28.62549568	2329.62
P12/056M	Ky-Grt-Bt-Schist	Unit I - Upper GHS	83.64503054	28.58614273	1885.98
P12/062M	Quartzite	Unit I - Upper GHS	83.64533874	28.54509462	1468.53
P12/064M	Calc-Phyllite	Lower GHS	83.65177051	28.5281242	1405.32
P12/069M	Quartzite	Lower GHS	83.6498073	28.49130309	1228.20
P12/074M	Quartzite	Lower GHS	83.71106904	28.38403962	2455.8
P12/076M	Augen orthogneiss	Lower GHS	83.71737256	28.37695666	2401.00
P12/077M	Augen orthogneiss	Lower GHS	83.73614962	28.3544546	1951.83
P12/079M	Quartzite	Lower GHS	83.73930138	28.35091312	1924.43
P12/082M	Quartzite	MCT - Lower GHS	83.75881839	28.32030681	1262.09
P12/085M	Quartzite	LHS	83.7586966	28.28786063	1034.02
P12/087M	Quartzite	LHS	83.72209476	28.26262096	859.78
P13/001M	Marl / Micaceous Limestone	THS	83.6868668	28.75452183	2688.672
P13/003M	Dolomitic Quartzite	THS	83.6438134	28.71782393	2663.678
P13/004M	Metacarbonate	THS	83.63271752	28.70487297	2614.65
P13/007M	Porphyritic Biotite-metacarbonate	STDS	83.620635	28.694594	2600
P13/011M	Marble	THS	83.61991894	28.68310316	2581.967
P13/014M	Marble	THS	83.61221648	28.67285092	2540.15
P13/021M	Calc-sandstone / metacarbonate	STDS	83.58892719	28.68603288	2764.616
P13/024M	Calc-silicate gneiss	STDS	83.59037584	28.66704360	2531.26
P13/027M	Calc-silicate gneiss	STDS	83.59655774	28.67096055	2488.96
P13/028M	Basin Sediment Fill	Recent	83.59765904	28.6715876	2536.785
P13/033M	Orthogneiss	Unit III - Upper GHS	83.59475404	28.64640786	2565.63
P13/036M	Marble	STDS	83.62667249	28.65039706	2668.485
P13/038M	Calc-silicate gneiss	Unit II - Upper GHS	83.63005903	28.64170645	2522.606
P13/039M	Calc-silicate gneiss	Unit II - Upper GHS	83.63825871	28.61593486	2161.63
P13/041M	Calc-silicate	Unit II - Upper GHS	83.64798792	28.59030124	1945.099
P13/042M	Migmatite	Unit I - Upper GHS	83.64402463	28.57709438	1863.15
P13/043M	Migmatite	Unit I - Upper GHS	83.63931802	28.56712092	1698.522
P13/048M	Metacarbonate	Lower GHS	83.65177051	28.52812420	1405.32
P13/050M	Calc-Phyllite	Lower GHS	83.65662103	28.51106745	1333.70
P13/052M	Semipelite	Lower GHS	83.633737	28.471542	1200
P13/055M	Semipelite	Lower GHS	83.61679082	28.44751686	1096.501
P13/059M	Semipelite	Lower GHS	83.74481701	28.33036635	1351.73
P13/067M	Quartzite	LHS	83.77168537	28.31084507	1108.76
P13/068M	Quartzite	LHS	83.74486336	28.27654758	901.60

Table 4.1. Sample list. AMS sample lithology, tectonic unit classification and location (latitude and longitude given in decimal degrees).

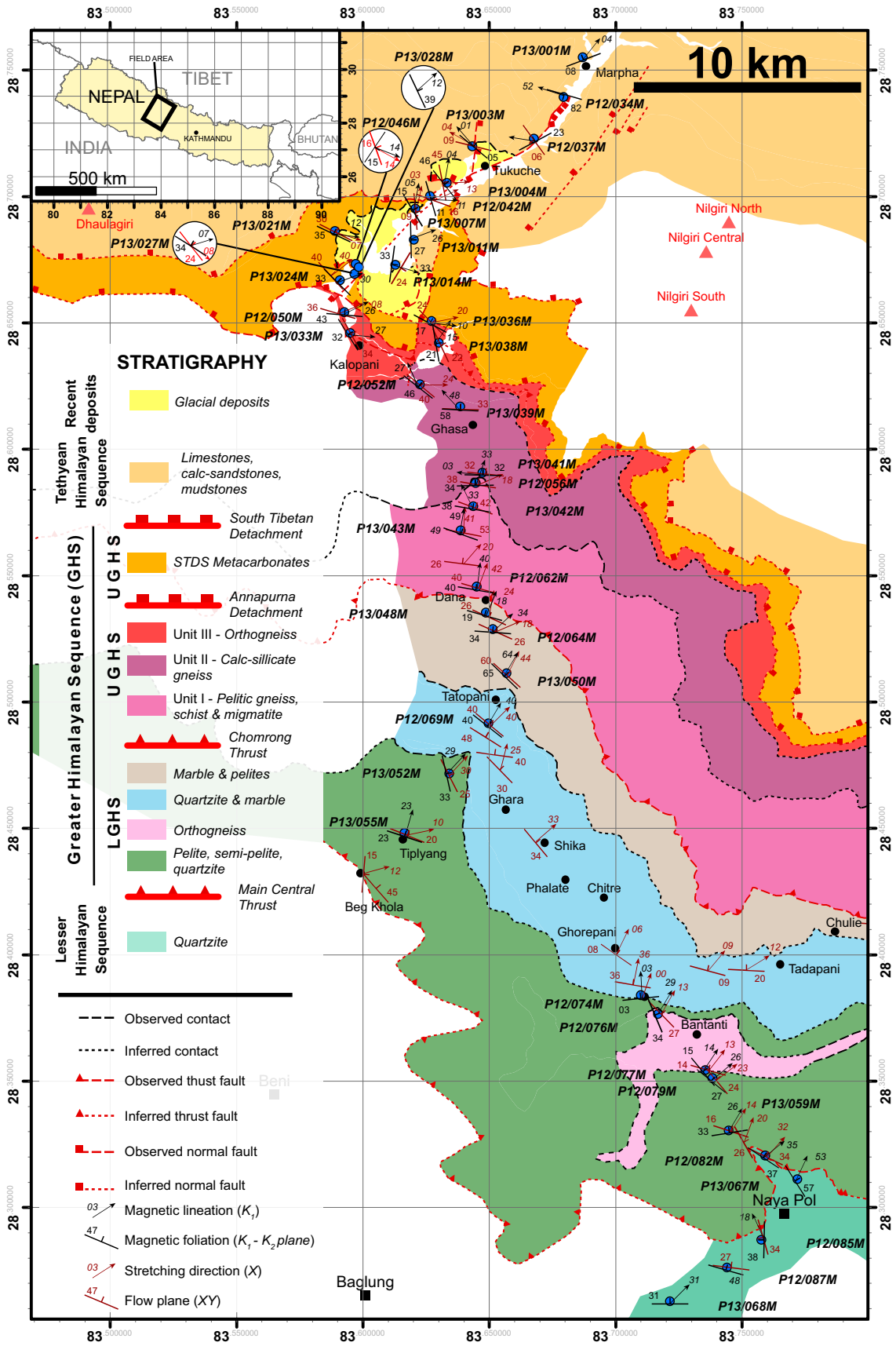

Figure 4.7 Geological map of the Kali Gandaki valley and surrounding regions. Modified after Parsons *et al.* (2014). AMS sample locations are represented by blue dots, with sample number labels. Magnetic lineation and foliation orientations measured from each sample are also plotted. Inset map shows the locations of the field area (black box).

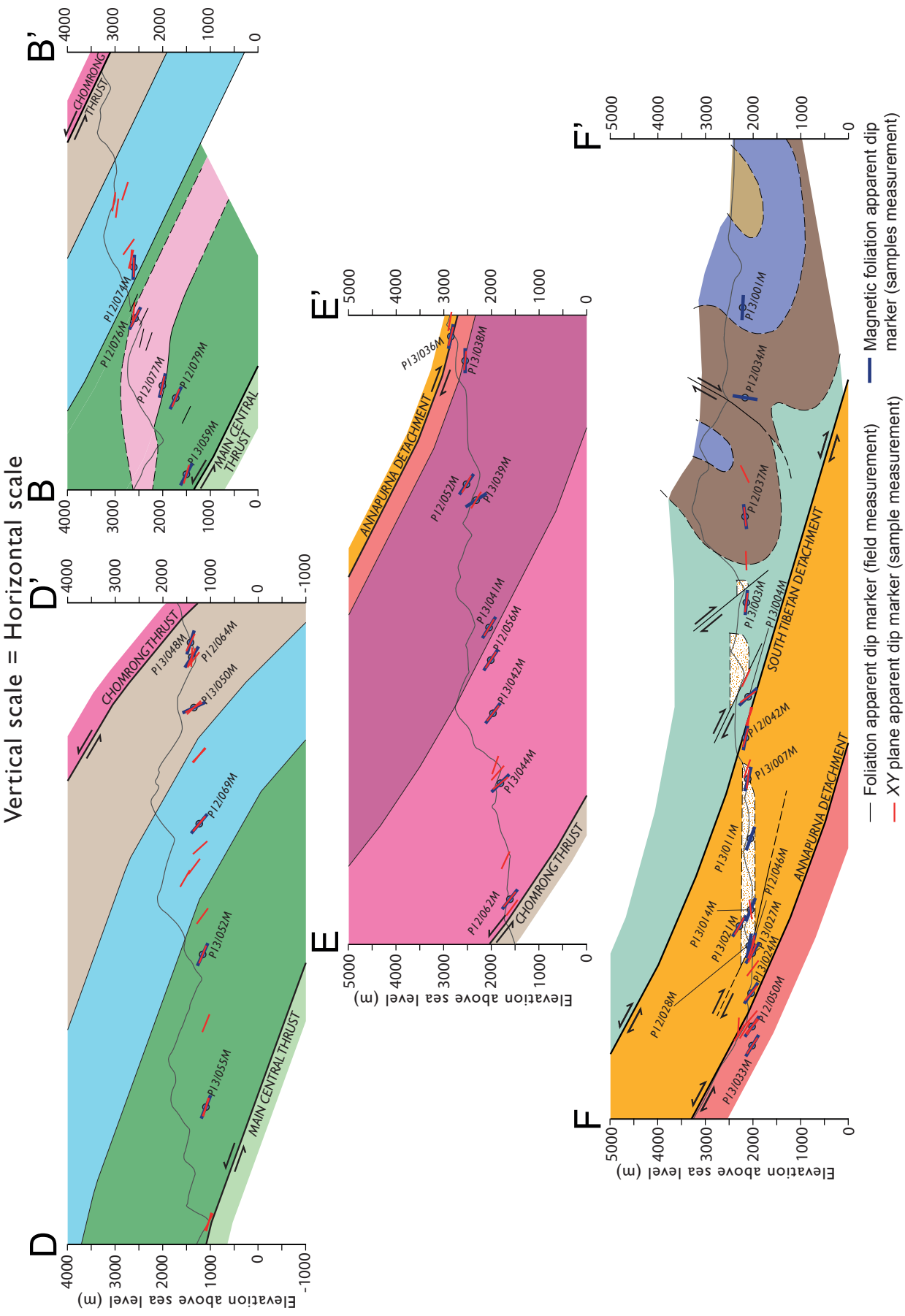

Figure 4.7 Magnetic & kinematic (XY) foliation dips.

of the magnetic susceptibility axes and their 95% confidence ellipse angles were calculated with Anisoft 4.2 (Chadima & Jelínek, 2008), in accordance with methods proposed by Jelínek (1978). The magnetic hysteresis and FORC analyses were conducted with a Princeton 3900-04 vibrating sample magnetometer up to a field of 7.94 x 10^5 A/m (1 *T*) also at Southern Illinois University in order to identify magnetic carriers and assess the extent of magnetic grain interaction within each sample. FORC data were processed using FORCinel 1.21 (Harrison & Feinberg, 2008). All procedures were in accordance with those used by Ferré *et al.* (2003; 2004) and Kruckenberg *et al.* (2010).

Between 1 and 3 cubes were selected from each sample for hysteresis parameter analysis. Comparison with experimental and modelled hysteresis loop end members allows the dominant magnetic response of each sample to be categorised as either diamagnetic, paramagnetic or ferromagnetic (e.g., Tauxe, 2002) and in some cases allows for positive identification of ferromagnetic mineral phases (e.g., Pike *et al.*, 1999; Roberts *et al.*, 2000; Tauxe *et al.*, 2002; Roberts *et al.*, 2006).

4.4.2. Electron microscopy

Back Scattered Electron (BSE) microscopy and Electron Dispersive Spectrometry (EDS) was used to image and identify ferromagnetic phases and determine their origin (e.g. primary or secondary, inclusions or interstitial material). Electron Back Scattered Diffraction (EBSD) was used to measure the crystallographic preferred orientations (CPO) of phyllosilicates, which typically form the magnetic carriers of paramagnetic samples. Comparison of CPO with AMS fabrics helps to assess the control of mineral alignment on AMS fabric. 12 paramagnetic samples were selected for CPO analysis via EBSD. SEM/EBSD analyses were carried out on a FEI Quanta 650 FEGESEM environmental SEM with an Oxford Instruments INCA 350 EDX system/80mm X-Max SDD detector and KE Centaurus EBSD system at the School of Earth & Environment, University of Leeds. Most EBSD data were collected via large area EBSD mapping, although some were collected via manual control of sample stage movement and electron beam positioning. Samples were prepared in resin blocks and polished with colloidal silica (Lloyd, 1987). Oxford Instruments Channel5 software was used for data acquisition, whilst MTEX open source software toolbox (Bachmann *et al.*, 2010) for MATLAB (MathWorks, Inc.) was used for processing and pole figure plotting.

4.5. Results

4.5.1. AMS parameters (K_m, P', T)

The mean AMS parameters for each sample are given in Table 4.2. Average bulk susceptibility (K_m) of each sample varies between 3.70 x 10^{-6} to 3639.41 x 10^{-6} [*SI*] (Figure 4.9a), reflecting a variety of diamagnetic, paramagnetic and ferromagnetic carriers. In general, the lowest values of K_m (~10^{-5} – 10^{-6} [*SI*]) are measured in the lowest grade metamorphic samples in the LHS and THS, whilst the highest values of K_m (~10^{-3} – 10^{-5} [*SI*]) are measured in the high-grade metamorphic samples from the UGHS.

The mean corrected degree of anisotropy of magnetic susceptibility (P') of each sample ranges between 1.01 and 3.43 (Figure 4.9a). Mean P' is calculated for each tectonic unit as 1.15 for the THS, 1.69 for the STDS, 1.48 for the UGHS, 1.56 for the LGHS and 1.27 for the LHS. Figure 4.9a demonstrates a positive correlation between K_m and P'.

The mean shape parameter of the susceptibility ellipsoid (T) of each sample ranges between -0.85 (prolate – $K_1 > K_2 = K_3$) to 0.92 (oblate – $K_1 = K_2 > K_3$) (Figure 4.9b). Mean T is calculated for each tectonic unit as -0.06 for the THS, 0.41 for the STDS, 0.73 for the UGHS, 0.44 for the LGHS and 0.32 for the LHS. Figure 4.9b shows no obvious correlation between K_m and T. The full AMS data set can be found in the supplementary data CD.

4.5.2. AMS orientations

All samples, except P12/087M, produced a coherent AMS fabric with a magnetic foliation and in most cases a magnetic lineation. The full AMS orientation data set is displayed in the appendix (Figure A.4.16). Mean orientations (Table 4.2) were calculated from the eigenvectors of each data set. Stereographic projection of the mean magnetic lineation (K_1), and magnetic foliation (K_1-K_2 great circle) of each sample (Figure 4.10a,b) shows that there is a general trend towards the NE. P13/001M, P13/003M and P13/048M, have an '*inverse*' AMS fabric, where K_3 forms the magnetic lineation due to the presence of USD magnetite (Table 4.2). P12/052M is suspected to have an '*intermediate*' (*'Intermediate A2 fabric' - see* Ferré, 2002) AMS fabric due to the close correlation between the orientation of the mineral lineation and K_2 and the anomalously low value of P' (1.01) (Table 4.2). AMS orientation data are grouped by the tectonic unit (THS, STDS, UGHS, LGHS, LHS) to show how the mean orientations of the magnetic foliation and lineation vary across the transect. From the bottom to top

- Red rows indicate samples with an inverse AMS (K3 = Magnetic lineation)

- Blue rows indicate samples with an intermediate (A2) AMS (K2 = Magnetic lineation)

Sample	Lithology	Number of cubes, *n*	Mean *Km* (x10-6)	Mean *P'*	Mean *T*	Mean structural foliation/bedding	Mean Structural Lineation	Magnetic foliation	Magnetic lineation
P12/034M	Marl / Micaceous Limestone	9	4.01	1.535	0.225	174/36 W	28/289	106/82 SW	52/288
P12/037M	Marl / Micaceous Limestone	15	277.09	1.118	-0.085	144/06 S	15/211	062/23 N	14/279
P12/042M	Metacarbonate	15	969.60	3.184	0.149	110/16 N	13/076	164/11 E	11/092
P12/046M	Calc-Mylonite	14	339.07	1.578	0.279	165/14 E	17/073	155/15 E	14/073
P12/050M	Orthogneiss	16	57.95	1.253	0.880	112/11 N	08/069	095/43 N	26/064
P12/052M	Calc-silicate gneiss	16	117.19	1.017	0.098	138/45 N	27/079	128/46 NE	34/087
P12/056M	Ky-Grt-Bt-Schist	16	1955.63	1.953	0.690	098/36 E		089/34 N	33/019
P12/062M	Quartzite	19	220.05	1.897	0.714	106/40N	53/010	100/40 N	40/007
P12/064M	Calc-Phyllite	15	947.47	1.905	0.218	117/24 N	18/067	106/ 34 N	34/047
P12/069M	Quartzite	12	6.49	1.918	0.681	134/40 N	40/043	128/40 N	40/031
P12/074M	Quartzite	14	11.92	1.862	0.850	172/00	00/199	084/03 N	03/357
P12/076M	Augen orthogneiss	15	91.65	1.107	0.337	135/32 N	19/024	157/34 N	29/031
P12/077M	Augen orthogneiss	14	49.89	1.131	0.269	118/10 N	12/036	140/15 N	14/034
P12/079M	Quartzite	15	54.18	1.076	0.048	140/24N	23/052	129/27 N	26/050
P12/082M	Quartzite	14	34.73	1.386	0.812	114/36 N	32/042	123/37 N	35/051
P12/085M	Quartzite	18	80.83	1.203	0.465	156/45 W	23/202	001/38 W	18/336
P12/087M	Quartzite	16	8.10	1.082	-0.032	148/38 W	-	-	48/045
P13/001M	Marl / Micaceous Limestone	16	88.83	1.054	-0.854	127/24 NE	-	069/08 NW	04/039
P13/003M	Dolomitic Quartzite	16	29.14	1.037	0.034	129/18 NE	03/295	130/05 NE	01/319
P13/004M	Metacarbonate	15	90.20	1.113	0.106	142/38 NE	-	142/46 NE	04/010

Table 4.2. Mean AMS Parameters

Sample	Lithology	Number of cubes, *n*	Mean *Km* (x10-6)	Mean *P'*	Mean *T*	Mean structural foliation/bedding	Mean Structural Lineation	Magnetic foliation	Magnetic lineation
P13/007M	Porphyritic Biotite-metacarbonate	14	102.38	1.043	0.483	166/09 NE	06/101	149/15 NE	15/073
P13/011M	Marble	11	20.85	1.080	-0.396	061/51 SE	28/110	179/27 E	26/070
P13/014M	Marble	21	179.86	1.231	0.004	030/26 SE	22/087	008/33 E	33/106
P13/021M	Calc-sandstone / metacarbonate	14	26.31	1.112	0.549	118/34 N	07/107	115/35 N	12/097
P13/024M	Calc-silicate gneiss	19	99.67	1.211	0.902	134/32 NE	40/052	135/33 NE	30/070
P13/027M	Calc-silicate gneiss	14	609.09	2.108	0.230	143/23 NE	07/120	122/34 NE	07/111
P13/028M	Glacial Sediment	13	32.79	1.028	0.474	149/13 NE	-	034/39 SE	12/048
P13/033M	Orthogneiss	23	40.92	1.206	0.914	148/33 NE	28/085	148/32 NE	27/095
P13/036M	Calc-mylonite	15	545.75	1.618	0.283	126/24 NE	28/082	118/17 N	10/097
P13/038M	Calc-silicate gneiss	15	203.23	1.297	0.785	143/20 NE	22/022	170/21 E	15/033
P13/039M	Calc-silicate gneiss	15	455.25	1.481	0.782	096/06 N	22/331	093/58 N	48/317
P13/041M	Calc-silicate	15	88.20	1.134	0.777	096/31 N	26/338	091/32 N	03/276
P13/042M	Migmatite	17	3639.41	2.434	0.916	110/42 N	-	100/38 N	33/335
P13/043M	Migmatite	16	81.44	1.107	0.762	110/48 N	41/003	110/49 N	49/010
P13/048M	Metacarbonate	13	66.91	1.047	-0.333	109/27 N	20/352	094/19 N	18/023
P13/050M	Calc-Phyllite	14	909.93	3.430	0.035	128/54 NE	60/046	134/65 NE	64/031
P13/052M	Semipelite	13	44.27	1.215	0.745	158/23 NE	16/030	167/33 NE	29/043
P13/055M	Semipelite	15	120.84	1.376	0.924	102/24 N	-	108/23 N	23/016
P13/059M	Semipelite	20	41.01	1.205	0.721	112/13 N	14/033	081/33 N	26/031
P13/067M	Quartzite	17	3.70	1.328	0.284	143/53 NE	-	148/57 NE	53/025
P13/068M	Quartzite	13	10.88	1.447	0.543	094/19 N	21/024	106/31 N	31/014

Table 4.2. Mean AMS parameters. Mean magnetic properties of each sample and the orientation of the resulting magnetic fabrics and magnetic lineations, plus the locally measured structural foliation and mineral lineation are listed. Red highlighted rows indicate samples with an inverse AMS fabric. Blue highlighted rows indicate samples with an intermediate AMS fabric. K_m, bulk susceptibility; *P'*, corrected degree of anisotropy; *T*, shape parameter - see section 4.3 for explanation and derivation of parameters. Tectonic unit affiliations are given in Table 4.1. See the supplementary data CD for the full AMS data set.

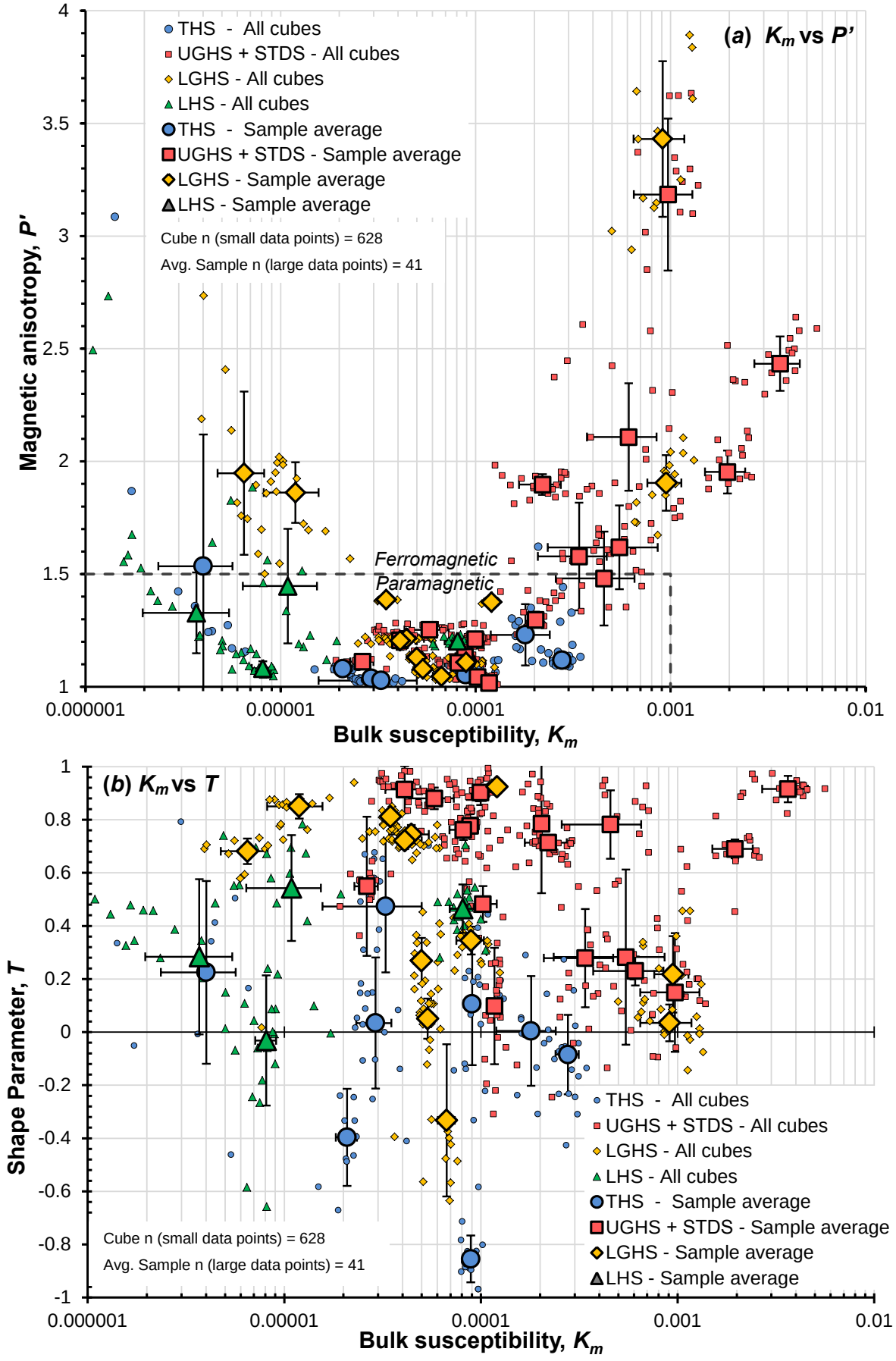

Figure 4.8. AMS results.

of the transect there is a general rotation of magnetic foliation and lineation dip and plunge direction from NNE to E. In the LHS, magnetic foliations and lineations display no trend and so no mean orientations have been calculated. Magnetic foliation varies in dip direction between 271° clockwise to 058°, with dips of 31° to 58°. Magnetic lineations vary in azimuth between 336° clockwise to 045° and dips of 18° to 53°. Within the LGHS, samples have a mean magnetic foliation of 125/38 N varying with dip directions between 351° to 077° and dips of 03° to 65°. Magnetic lineations in the LGHS have a mean orientation of 29/032 and vary in azimuths between 357° to 051°, with dips of 03° to 64°. Samples in the UGHS have a mean magnetic foliation of 108/37 N, varying in dip direction between 359° to 080° with dips of 21° to 58°. Magnetic lineations in the UGHS, have a mean orientation of 39/010 and variable azimuths of 335° to 095° and dips of 15° to 49° except for sample P13/041M, which has a lineation oriented 03/276. Samples in the STDS have a mean magnetic foliation of 131/22 NE, varying individually in dip direction between 025° to 074° and dip between 11° to 35°. Magnetic lineations in the STDS have a mean orientation of 14/088 and vary in azimuths between 070° to 111° with dips of 07° to 30° except for sample P13/007M, which has a lineation oriented 05/011. At the top of the transect, the THS has a mean magnetic foliation of 163/18 NE, with individual magnetic foliations varying in dip direction from 332° to 196° and dip between 05° to 82°. Magnetic lineations in the THS have no clear trend so a mean lineation has not been calculated. In this unit, magnetic lineations vary widely with azimuths ranging from 279° clockwise to 106° and plunges ranging from 01° to 52°.

4.5.3. Hysteresis results

Magnetic hysteresis curves are presented in the appendix (Figure A.4.17). Magnetic hysteresis analysis reveals a wide variety of hysteresis loop shapes and hysteresis parameters, typical of diamagnetic, paramagnetic and ferromagnetic behaviour (Table 4.3). Paramagnetic slope correction of most paramagnetic and diamagnetic hysteresis

---

Figure 4.9. AMS results. Bulk susceptibility (K_m), magnetic anisotropy (*P'*) and susceptibility ellipsoid shape parameter (*T*). (*a*) Plot of magnetic anisotropy (*P'*) versus bulk susceptibility (K_m [*SI*]) of all measured cubes (small data points) and mean *P'* versus mean K_m of each whole sample (large data points). Error bars represent one standard deviation of mean *P'* and K_m. Data point shape and colour corresponds to tectonic unit: *Blue circle, THS; red square, UGHS + STDS; yellow diamond, LGHS; green triangle, LHS*. Dashed lines define a typical range of *P'* and K_m for paramagnetic samples (Tarling and Hrouda, 1993). (*b*) Plot of bulk susceptibility (K_m), versus shape parameter (*T*) of all measured cubes (small data points) overlain by mean K_m versus mean *T* of each whole sample (large data points). Error bars represent one standard deviation of mean *T* and K_m. Data point shape and colour follow same symbology as (*a*). See *section 4.3* for the derivation of AMS parameters.

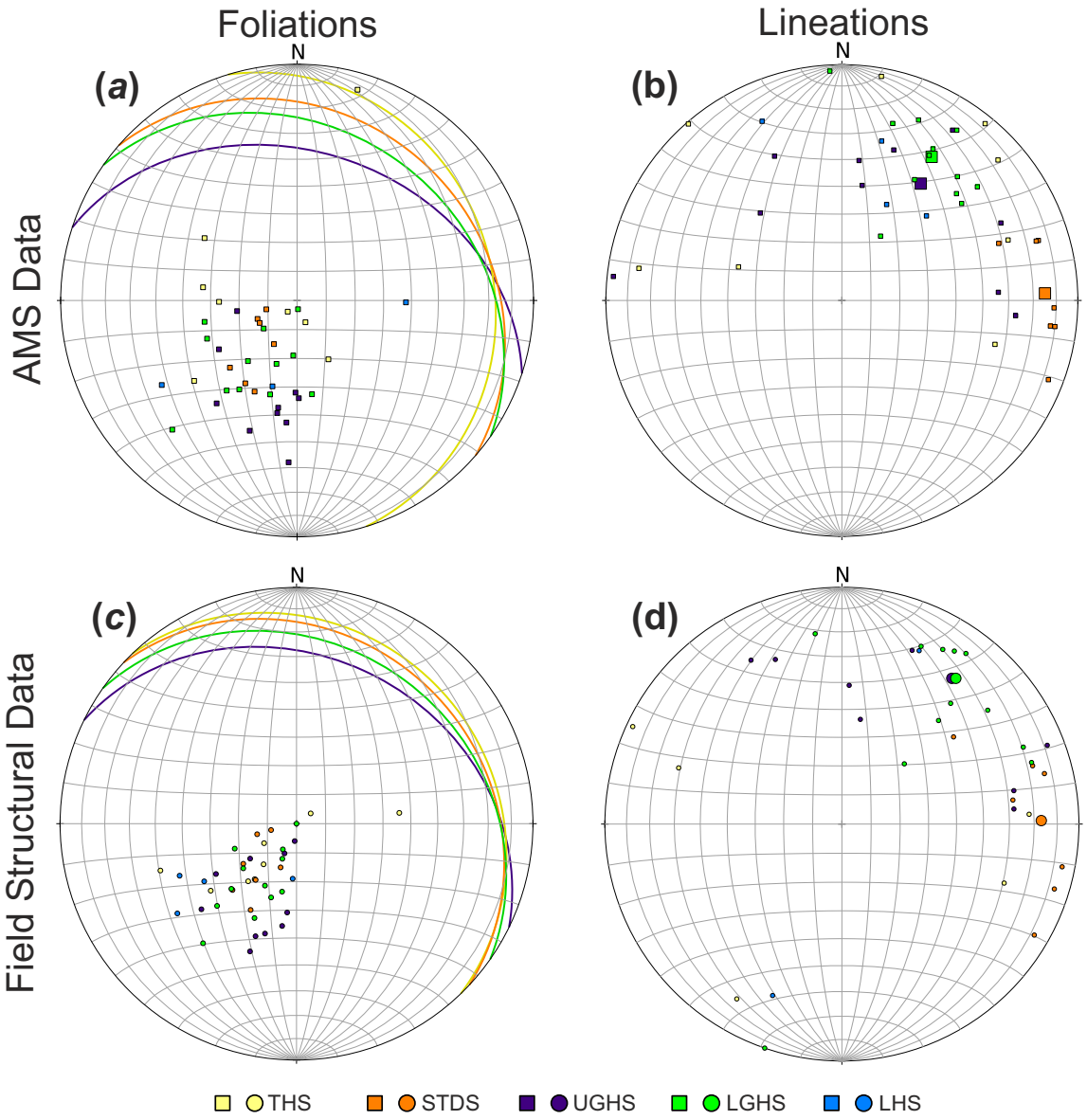

Figure 4.10. Equal area stereographic projection of mean AMS and field structural fabrics. Orientation data is grouped into tectonic units (see figure for key). (*a*) Mean magnetic foliations – small squares are the poles to magnetic foliations of each sample, great circles are the mean magnetic foliations of each tectonic unit. (*b*) Mean magnetic lineations – small squares are the magnetic lineations of each sample, large squares are the mean magnetic lineations of each tectonic unit. (*c*) Mean structural foliations – small circular data points are the poles to structural foliations of each sample measured in the field, great circles are the mean structural foliations of each tectonic unit. (*d*) Mean mineral lineations – small circular data points are the mineral lineations of each sample measured in the field, large circular data points are the mean mineral lineations of each tectonic unit. Mean foliations are not calculated for LHS and mean lineations are not calculated for the THS and LHS due to a poor spread of data from this unit with no visible trends. All stereonets are geographically oriented and plotted using Stereonet 8.0 (Allmendinger *et al.*, 2012).

loops commonly revealed the presence of a minor ferromagnetic phase. Ferromagnetic loops indicate variability in ferromagnetic grain size between samples, which include both USD, MSD, PSD, MD and SP grain sizes. Some hysteresis loops have loop

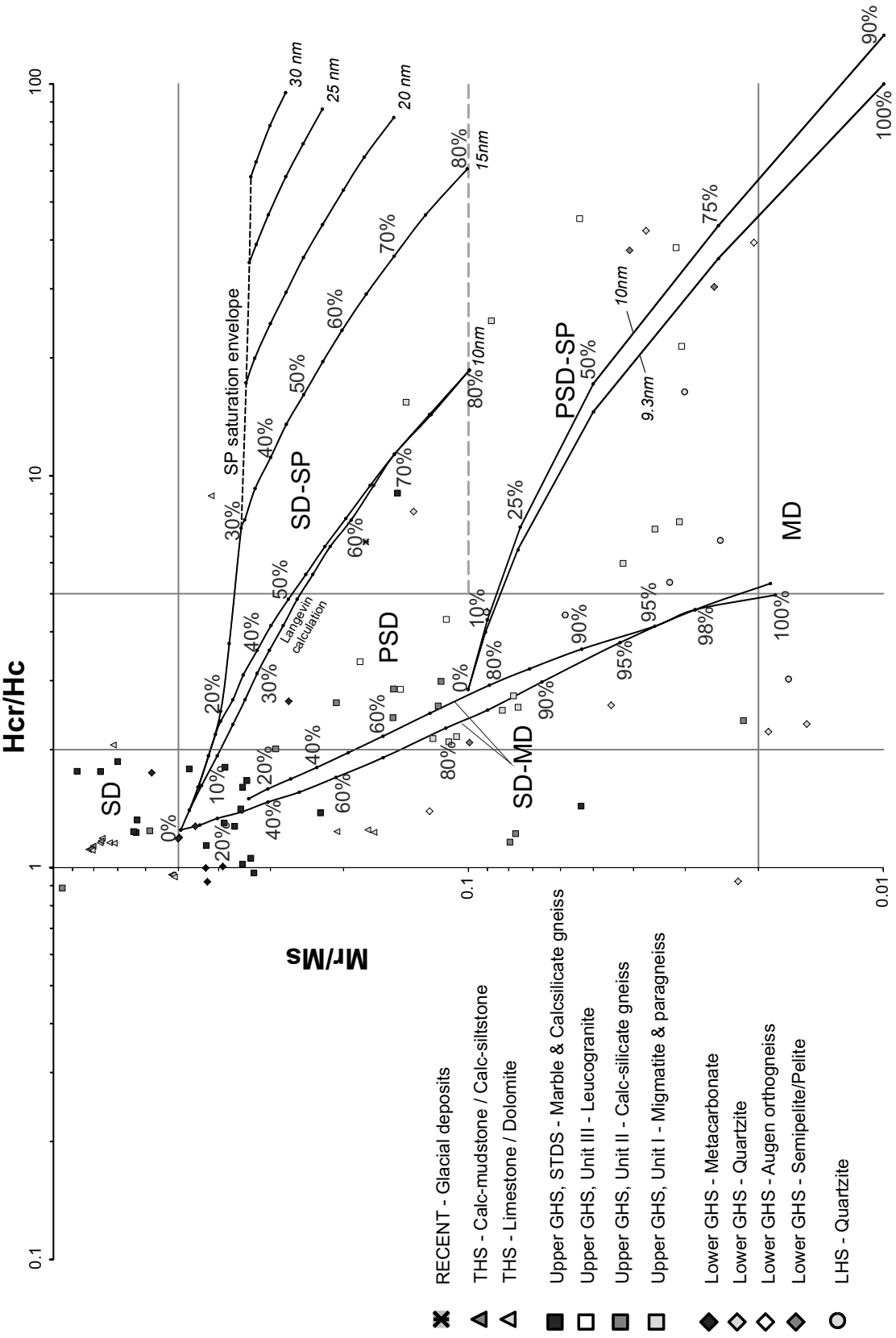

Figure 4.11. Day plot of magnetic hysteresis parameters reveals grain size populations of ferromagnetic grains.

defects, including wasp-waists, pot-bellies and goose-necks (*Section 4.2.3.1.*) that are indicative of both variable grain size mixes and poly-ferromagnetic phase mixes.

Variable ferromagnetic grain size mixes are also suggested by a Day plot of the hysteresis parameters with grain size mixing curves that show that some samples may contain mixes of SD-MD, SD-SP and PSD-SP grains (Figure 4.11). FORC analysis, used to detect magnetostatic interactions between ferromagnetic grains revealed a range of responses (Table 4.3). In all cases, either no interaction or only minor interaction is detected, as indicated by a small amount of vertical spreading of contours from the density maxima (*Section 4.2.3.3.*). In no cases were multiple density maxima observed. All FORC analyses are presented in Figure A.4.18.

In general, the results produced by multiple specimen cubes of the same sample were consistent, suggesting a homogenous distribution of ferromagnetic phases and grain size distributions. A few samples produced non-self-consistent results that suggest an uneven spatial distribution of ferromagnetic phases and grain sizes across the sample (Table 4.3).

4.5.4. Magnetic carriers

Through careful consideration of both the AMS and magnetic hysteresis results, the magnetic carrier(s) of each sample have been identified. Table 4.3 summarises the magnetic carrier(s) of each sample along with the magnetic hysteresis results used to identify them. Details of additional ferromagnetic phases and the most dominant paramagnetic phases that do not represent the magnetic carriers, but may still affect the overall AMS are also displayed.

Three samples display a diamagnetic behaviour (P12/034M, P12/087M, P13/067M, Table 4.3), as indicated by negatively sloped hysteresis loops (Figure A.4.17) and low bulk susceptibilities (~10^{-6} [*SI*]) (Table 4.2). Quartz and calcite form the magnetic carriers in these samples.

22 samples display a paramagnetic behaviour (Table 4.3), as indicated by positively

Figure 4.11. Day plot of magnetic hysteresis parameters reveals grain size populations of ferromagnetic grains. M_r, magnetic remanence (Am^2); M_s, magnetic saturation (Am^2); H_{cr}, coercivity of remanence (A/m); H_c, coercivity (A/m). Boxes surround grains of same domain size – SD, single domain; PSD, pseudo-single domain; MD, multidomain; SP, superparamagnetic. Black lines represent theoretical mixing curves that show % of MD and SP grains in an MD-SD or SP-SD mixed population. Use of the Day plot is explained in *Section 2.3.2.* For a more detailed explanation of the theory and mathematics behind the Day plot and derivation of the mixing curves, see Dunlop (2002ab).

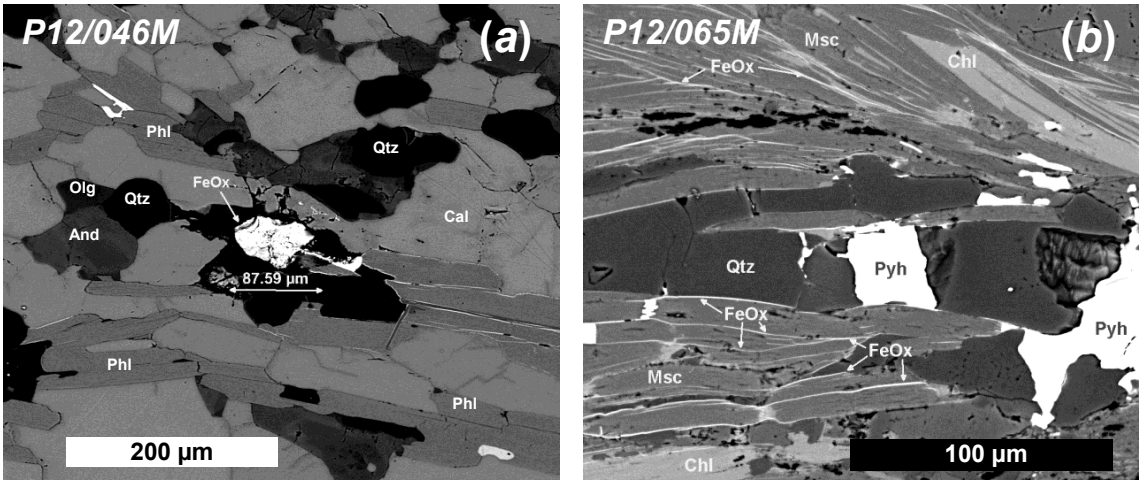

Figure 4.12. Back Scattered Electron (BSE) images of ferromagnetic phases. (*a*) Iron oxide (magnetite) grain surrounded by quartz grains within P12/046M. (*b*) Iron oxide (magnetite or hematite) along the basal cleavages on muscovite grains within P12/065M. Iron oxides and pyrrhotite are often found close to each other. Mineral abbreviations: *And, andesine; Cal, calcite; Chl, chlorite; FeOx, iron oxide; Msc, muscovite; Olg, oligoclase; Phl, phlogopite; Pyh, pyrrhotite; Qtz, quartz*.

sloped straight-line hysteresis loops that intersect the origin (i.e. no remnant magnetism) and low to intermediate values of bulk susceptibilities (~10^{-4} to 10^{-5} [*SI*]). Phyllosilicate is identified as the magnetic carrier in all of these samples, expect for samples P12/052M and P13/041M (calc-silicate gneisses) in which diopside and/or phyllosilicate form the carrier. Biotite, chlorite and phlogopite have similar susceptibilities (Tarling & Hrouda, 1993) and cannot be distinguished between each other. However, all of these phyllosilicate are more magnetically dominant than muscovite (Tarling & Hrouda, 1993).

Paramagnetic slope correction of samples that display paramagnetic / diamagnetic behaviour typically reveal the presence of a minor (<0.1% volume, Tarling & Hrouda, 1993) ferromagnetic phase. In most cases, hematite is likely to be a secondary phase related to late stage alteration. Pyrrhotite is also present in some samples.

16 samples display a dominant ferromagnetic behaviour (Table 4.3), as indicated by well-defined hysteresis loops. Magnetite ± Ti-magnetite is identified as the magnetic

Table 4.3. Hysteresis results and magnetic carriers. Table displays the magnetic hysteresis properties of each sample plus details of the identified magnetic carriers. Additional data used to identify the magnetic carriers is also displayed. These include the hysteresis loop shape, FORC analysis results and ferromagnetic grain size populations and interactions. Where identified, all ferromagnetic grains and the most dominant paramagnetic phase(s) in each sample are also listed. Note that these additional phases are not necessarily the same as the magnetic carriers of each sample, but may affect the samples' AMS fabrics. M_S, magnetic saturation; M_R, magnetic remanence; H_C, coercivity; H_{CR}, coercivity of remanence. See the Appendix for the full hysteresis and FORC analyses (Figure A.4.17 & A.4.18).

Sample	Lithology	Number of cubes analysed for Hysteresis	Dominant Hysteresis Curve Behavior	Dominant Magnetic Carrier	Corrected hysteresis curve	Mean Ms (µAm2)	Mean Ms/mass (µAm2/kg)	Mean Hcr (kA/m)	Mean Mr/Ms	Mean Hcr/Hc	FORC results: Ferromagnetic grain interaction	Hcr derived from FORC diagram (kA/m)	Normal (K1) Inverse (K3) or Intermediate A2 (K2) magnetic lineation	Ferromagnetic phases	Magnetite grain size mix	Dominant paramagnetic phases	Comments
P12/034M	Marl / Micaceous Limestone	3	Diamagnetic	Quartz and/or Calcite	SD-SP ferromagnetic	1.51	111.29	21.50	0.184	1.24	-	-	NORMAL	SD-SP magnetite (negligible)	50-70% MD in SD-MD mix	Muscovite	
P12/037M	Marl / Micaceous Limestone	3	Ferromagnetic	SD magnetite	MSD ferromagnetic	145.30	9871.41	22.70	0.515	0.95	Minor interaction	14.30	POSSIBLY INVERSE	USD magnetite	USD ± MSD	Biotite	
P12/042M	Metacarbonate	3	Ferromagnetic	SD-MD magnetite	PSD / SD-MD ferromagnetic	273.93	20190.49	9.47	0.306	1.55	No interation	3.97	NORMAL	SD-MD±SP magnetite ± hematite / hemo-ilmenite	10-40% MD in SD-MD±SP mix	Biotite, Muscovite, Ilmenite	
P12/046M	Calc-Mylonite	3	Ferromagnetic	SD-MD magnetite	SD-SP / SD-MD ferromagnetic	259.28	16359.70	12.36	0.338	1.02	Minor interaction	6.36	NORMAL	SD-MD / PSD magnetite + pyrrhotite ± hematite / hemo-ilmenite	30-40% MD in SD-MD mix	Biotite, Muscovite, Ilmenite	
P12/050M	Orthogneiss	3	Paramagnetic	Biotite	WEAK - PSD / SD-SP ferromagnetic	1.40	122.82	188.25	0.039	34.97	Negligible ferromagnetism	n/a	NORMAL	PSD-SP magnetite, pyrrhotite ± hematite / hemo-ilmenite (negligible)	50-75% SP in SP-PSD mix	Biotite, Muscovite ± Tourmaline	
P12/052M	Calc-silicate gneiss	3	Paramagnetic	Diopside and/or phlogopite	USD ferromagnetic	3.48	276.58	141.47	0.059	1.59	Negligible ferromagnetism	n/a	INTERMEDIATE A2	PSD / USD-MD magnetite, phyrrotite ± hematite (negligible)	85-99% MD in USD-MD mix	Diopside, Phlogopite, Olivine	Non-self-consistent results
P12/056M	Ky-Grt-Bt-Schist	3	Ferromagnetic	SD-MD / PSD magnetite ± minor SP magnetite	PSD / SD-MD ferromagnetic	802.00	62603.60	14.69	0.113	2.13	No interaction	< 3.97	NORMAL	SD-MD magnetite ± minor SP magnetite ± hematite	80% MD in SD-MD mix OR PSD	Biotite, Muscovite	
P12/062M	Quartzite	3	Ferromagnetic	SD-MD magnetite ± minor SP magnetite	MD / SD-SP ferromagnetic Polyphase ferromagnetic mix or SD-SP ferromagnetic mix	97.00	8114.18	11.84	0.079	2.61	No interaction	< 3.97	NORMAL	SD-MD magnetite ± minor SP magnetite	85% MD in SD-MD mix	Muscovite	
P12/064M	Calc-Phyllite	3	Ferromagnetic	SD-MD / PSD magnetite ± hematite		804.40	65253.81	18.99	0.415	0.98	-	7.94	NORMAL	SD-MD magnetite, pyrrhotite ± hematite / hemo-ilmenite	10-20% MD in SD-MD mix OR PSD	Biotite, Muscovite, Chlorite	
P12/069M	Quartzite	3	Paramagnetic	Biotite ± Muscovite	PSD / SD-MD ferromagnetic	0.82	77.69	29.16	0.034	1.76	-	-	NORMAL	PSD / SD-MD magnetite (negligible)	90-95% MD in MD-SD mix OR PSD	Muscovite, minor Biotite, minor Chlorite	Non-self-consistent results
P12/074M	Quartzite	3	Paramagnetic	Chlorite	PSD / SD-SP ferromagnetic	0.75	69.39	131.63	0.024	15.59	No interaction	n/a	NORMAL	SD-MD / SP-PSD magnetite ± hematite / hemo-ilmenite (negligible)	MD-PSD mix / 50-75% SP in SP-PSD mix	Chlorite, minor Muscovite, Ilmenite ± Tourmaline	Non-self-consistent results
P12/076M	Augen orthogneiss	1	Paramagnetic	Chlorite	WEAK - SD / PSD ferromagnetic	1.41	42.67	18.64	0.124	1.39	-	-	NORMAL	PSD / SD-MD magnetite and/or hematite (negligible)	70-80% MD in SD-MD mix OR PSD	Chlorite, Muscovite, minor Biotite	
P12/077M	Augen orthogneiss	1	Paramagnetic	Biotite	WEAK - bad data	1.22	34.56	172.28	0.021	39.38	-	-	NORMAL	PSD-SP / MD magnetite and/or hematite (negligible)	75-80% SP in SP-PSD mix	Biotite, Muscovite, minor Chlorite	
P12/079M	Quartzite	3	Paramagnetic	Chlorite	WEAK - MD ferromagnetic	1.30	87.97	148.50	0.055	23.35	Negligible ferromagnetism	n/a	NORMAL	SD-SM + PSD-SP magnetite and/or hematite (negligible)	80% MD in SD-MD mix + 60-75% SP in SP-PSD mix	Chlorite ± muscovite	Non-self-consistent results
P12/082M	Quartzite	1	Paramagnetic	Muscovite	WEAK - PSD ferromagnetic	1.27	33.66	180.59	0.030	16.37	-	-	NORMAL	PSD-SP magnetite (negligible)	60-70% SP in SP-PSD mix	Muscovite, tourmaline	
P12/085M	Quartzite	1	Paramagnetic	Chlorite	WEAK - bad data	2.94	81.14	37.07	0.033	5.35	Negligible ferromagnetism	n/a	NORMAL	SD-MD / PSD magnetite and/or hematite / hemo-ilmenite (negligible)	98% MD in SD-MD mix OR PSD	Chlorite	
P12/087M	Quartzite	1	Diamagnetic	Quartz	WEAK - PSD / MD ferrmagnetic	1.33	41.80	21.07	0.017	3.03	-	-	NORMAL	MD magnetite (negligible)	100% MD	None	
P13/001M	Marl / Micaceous Limestone	1	Paramagnetic	Biotite ± Muscovite	USD ferromagnetic	0.72	42.87	177.44	0.416	8.89	-	-	INVERSE	USD-SP magnetite mix (negligible)	30% SP in SD-SP mix	Biotite and/or Muscovite	
P13/003M	Dolomitic Quartzite	1	Paramagnetic	Muscovite	Polyphase ferromagnetic mix or SD-SP ferromagnetic mix	0.41	27.75	29.84	0.717	2.06	-	-	INVERSE	USD + MSD magnetite and/or hematite (negligible)	100% SD	Muscovite	Hematite is probably a secondary phase
P13/004M	Metacarbonate	3	Ferromagnetic	MSD magnetite	MSD ferromagnetic	36.48	2670.78	35.36	0.785	1.15	Minor interaction	15.9	NORMAL	MSD magnetite	100% MSD	Muscovite	
P13/007M	Porphyritic Biotite-metacarbonate	2	Paramagnetic	Biotite	Polyphase ferromagnetic mix or SD-SP ferromagnetic mix	0.63	40.53	63.28	0.309	5.41	Negligible ferromagnetism	n/a	NORMAL	SD-SP magnetite and/or hematite/hemo-ilmenite (negligible)	10-70% SP in SD-SP mix	Biotite, Muscovite, minor Chlorite, Ilmenite	Non-self-consistent results
P13/011M	Marble	3	Ferromagnetic	MSD magnetite	MSD ferromagtic	4.41	411.74	42.59	0.795	1.14	No interaction	26.2	NORMAL	MSD magnetite	100% MSD	Unknown	Hematite is probably a secondary phase
P13/014M	Marble	3	Ferromagnetic	MSD magnetite	MSD ferromagnetic	88.32	5259.22	24.61	0.751	1.14	Minor interaction	13.5	NORMAL	MSD magnetite	100% MSD	Unknown	
P13/021M	Calc-sandstone / metacarbonate	3	Paramagnetic	Phlogopite	USD ferromagnetic	0.67	45.47	156.62	0.783	1.80	Negligible ferromagnetism	n/a	NORMAL	SD hematite (negligible)	MSD	Phlogopite, Muscovite	Hematite is probably a secondary phase
P13/024M	Calc-silicate gneiss	3	Ferromagnetic	MSD-SP magnetite	SD-SP ferromagnetic	5.99	337.13	20.11	0.634	1.26	Minor interaction	12.7	NORMAL	MSD-SP magnetite	MSD + minore SP	Biotite, Muscovite	

Table 4.3. Hysteresis parameters and magnetic carriers

Sample	Lithology	Number of cubes analysed for Hysteresis	Dominant Hysteresis Curve Behavior	Dominant Magnetic Carrier	Corrected hysteresis curve	Mean Ms (μAm2)	Mean Ms/mass (μAm2/kg)	Mean Hcr (kA/m)	Mean Mr/Ms	Mean Hcr/Hc	FORC results: Ferromagnetic grain interaction	Hcr derived from FORC diagram (kA/m)	Normal (K1) Inverse (K3) or Intermediate A2 (K2) magnetic lineation	Ferromagnetic phases	Magnetite grain size mix	Dominant paramagnetic phases	Comments
P13/027M	Calc-silicate gneiss	3	Ferromagnetic	SD-MD magnetite	MD / PSD ferromagnetic	316.14	17734.02	10.65	0.369	1.33	Minor interaction	5.16	NORMAL	SD-MD magnetite + minor pyrrhotite	20-30% MD in SD-MD mix	Phlogopite, Muscovite ± Hornblende	
P13/028M	Glacial Sediment	1	Paramagnetic	Muscovite	SD-SP ferromagnetic	0.75	68.53	29.19	0.177	6.78	-	-	NORMAL	SD-SP magnetite or hematite (negligable)	60% SP in SD-SP mix	Muscovite	
P13/033M	Orthogneiss	3	Paramagnetic	Biotite	SD-SP ferromagnetic	0.30	22.35	33.86	0.147	3.50	-	-	NORMAL	PSD / SD-MD magnetite (negligable)	60-80% MD in SD-MD mix OR PSD	Biotite, Muscovite, Tourmaline	
P13/036M	Calc-mylonite	3	Ferromagnetic	SD-MD-SP / PSD magnetite	MD / PSD ferromagnetic	208.69	14430.25	17.55	0.289	1.46	No interaction	5.16	NORMAL	PSD / SD-MD / SD-SP magnetite	10-20% MD in SD-MD mix OR PSD + 15% SP in SD-SP mix	Biotite, Muscovite	Non-self-consistant results
P13/038M	Calc-silicate gneiss	3	Ferromagnetic	SD-MD±SP magnetite	SD-MD ferromagnetic	34.08	2006.94	14.29	0.610	1.38	Minor interaction	5.96	NORMAL	SD-MD±SP magnetite	20-30% MD ± SP in SD-MD±SP mix	Diopside ± Mica ± Olivine	Non-self-consistant results
P13/039M	Calc-silicate gneiss	3	Ferromagnetic	SD-MD / PSD magnetite	SP ferromagnetic or SD-SP ferromagnetic	97.99	7620.88	17.91	0.129	2.66	No interaction	~0	NORMAL	SD-MD magnetite + hematite	60-75% MD in SD-MD mix OR PSD	Biotite, Muscovite	Magnetite grains with hematite rims observed via electron microscopy
P13/041M	Calc-silicate	2	Paramagnetic	Biotite and/or Diopside	WEAK - USD / SD-SP ferromagnetic	0.92	72.19	28.99	0.180	2.75	Negligable ferromagnetism	n/a	NORMAL	SD-MD / PSD magnetite (negligable)	50-70% MD in SD-MD mix OR PSD	Biotite ± Diopside	
P13/042M	Migmatite	3	Ferromagnetic	MD (Ti-)magnetite plus minor SD (Ti-)magnetite	SD-MD / PSD-SP ferromagnetic	1012.08	53209.98	16.45	0.036	6.97	No interaction	~0	NORMAL	MD plus minor SD (Ti-)magnetite	95-98% MD in SD-MD mix / 50-75% SP in PSD-SP mix	Biotite, Muscovite, Ilmentie	Ti-magnetite observed with electron microscopy
P13/043M	Migmatite	2	Paramagnetic	Biotite	WEAK - USD ferromagnetic	0.28	15.26	116.49	0.115	20.14	Negligable ferromagnetism	n/a	NORMAL	SD-SP / PSD-SP hematite (negligable)	Not applicable to hematite	Biotite, Muscovite	
P13/048M	Metacarbonate	2	Paramagnetic	Muscovite	WEAK - USD / SD-SP ferromagnetic	0.66	46.07	43.21	0.425	2.20	-	-	INVERSE	USD magnetite and/or hematite / hemo-ilmenite + minor pyrrhotite (negligable)	SD / PSD	Biotite / Phlogopite, Muscovite ± Chlorite	Non-self-consistant results
P13/050M	Calc-Phyllite	3	Ferromagnetic	SD-MD magnetite	SD-MD ferromagnetic	453.61	27632.33	12.91	0.484	1.22	Minor interaction	7.94	NORMAL	SD-MD magnetite	0-10% MD in SD-MD mix	Phlogopite, Chlorite	
P13/052M	Semipelite	1	Paramagnetic	Muscovite	WEAK - USD ferromagnetic	0.25	17.93	34.89	0.090	4.50	-	-	NORMAL	SD-MD magnetite and/or hematite / hemo-ilmenite (negligable)	80-85 % MD in SD-MD mix	Biotite, Muscovite, Imenite	
P13/055M	Semipelite	2	Paramagnetic	Chlorite	-	0.60	32.74	-	0.112	-	-	-	NORMAL	n/a	n/a	Muscovite, Chlorite, Tourmaline	Poor quailty hysteresis data could not produced a corrected curve
P13/059M	Semipelite	1	Paramagnetic	Chlorite	WEAK - PSD ferromagnetic	0.18	11.64	56.77	0.136	8.11	-	-	NORMAL	SD-SP magnetite and/or hematite/hemo-ilmenite (negligable)	60-65% SP in SD-SP mix	Chlorite, Muscovite, Ilmenite	
P13/067M	Quartzite	1	Diamagnetic	Quartz	WEAK - PSD / MD-SP ferromagnetic	0.73	38.76	23.45	0.025	6.84	Negligable ferromagnetism	n/a	NORMAL	MD magnetite (negligable)	98-100% MD in SD-MD±SP mix	None	
P13/068M	Quartzite	2	Paramagnetic	Chlorite ± Muscovite	WEAK - PSD / MD-SP ferromagnetic	0.48	39.37	24.48	0.074	4.45	Negligable ferromagnetism	n/a	NORMAL	SD-MD / PSD-SP magnetite (negligable)	80-90% MD in SD-MD mix OR 10 % SP in PSD-SP mix	Chlorite and/or Muscovite	

Table 4.3. Hysteresis parameters and magnetic carriers

carrier in all of these samples, as suggested by large values of M_s ($10^3 – 10^5$ $\mu Am^2 kg^{-1}$) and intermediate values of H_{cr} ($10^2 – 10^3$ kA/m). Electron microscopy reveals that iron oxides are often present as both interstitial grains and as inclusions (Figure 4.12). Comparison of hysteresis loops and hysteresis parameters of ferromagnetic samples indicate that a variety of grain sizes and/or additional ferromagnetic phases may contribute to the magnetic behaviour of these samples. The goose-necked defects in the hysteresis loops of samples P12/034M, P13/003M, P13/007M and P13/048M suggest that an additional ferromagnetic phase, possibly hematite, may control the magnetic behaviour of these samples. Samples P12/064M, P13/028M and P13/050M have wasp-waisted loop defects, indicative of a mixed population of SD-SP ferromagnetic grains. Hysteresis parameters and loops of the other ferromagnetic samples show variability in magnetite grain size. Most samples have a PSD or SD-MD mix of magnetite grain size (e.g. P12/056M, P12/062M, P13/039M), with the percentage of MD varying from across the range from 10% to 98% (Figure 4.11). In some cases, a population of MSD magnetite grains formed the magnetic carriers (e.g. P13/004M, P13/014M), as identified by high squareness ratios (M_r / M_s> 0.7) (Figure 4.11) and an angular shaped hysteresis loop (Figure A.4.17). High values of H_{cr} / H_c (>5) produced by some ferromagnetic samples indicate the presence of SP magnetite grains in an SD-SP or PSD-SP mix, varying in percentage of SP grains between 15-75% (Figure 4.11). USD magnetite grains form a portion of the magnetic carriers of some samples (P12/034M, P13/039M, P13/050) as indicated by a squareness ratio of ~0.5 (Figure 4.11).

4.5.5. Phyllosilicate CPOs

The AMS of paramagnetic samples is typically controlled by the CPO of the paramagnetic carriers (Borradaile & Jackson, 2010). As phyllosilicates are identified as the carrier of all paramagnetic samples in this study, it is useful to compare these AMS

Figure 4.13. Phyllosilicate CPOs and AMS fabrics of paramagnetic samples. Phyllosilicate CPOs were measured using EBSD for a selection of paramagnetic samples. The left column displays the stereographic projection of AMS fabrics and mean magnetic and structural foliations and mineral lineation orientations. Phyllosilicate CPO pole figures are displayed for the <100> (*a-axis*) and <010> (*b-axis*) directions and the [001] axis (*c-axis*). In most cases CPOs were measured from an additional sample collected at the same locality as the AMS samples. The phyllosilicate phase is listed for each pole figure next to the sample number (*Msc, muscovite; Bt, biotite; Chl, chlorite; Phl, phlogopite*). Contouring on the pole figures shows the multiples of uniform distribution. *n* denotes the number of measurements made for each pole figure. Most CPOs were measured via automate EBSD mapping (labelled, '*Automated*'), whilst some were measured via manual control of the stage and beam positioning (labelled, '*Manual*'). All pole figures and AMS stereonets are plotted with an equal area projection in a geographic reference frame.

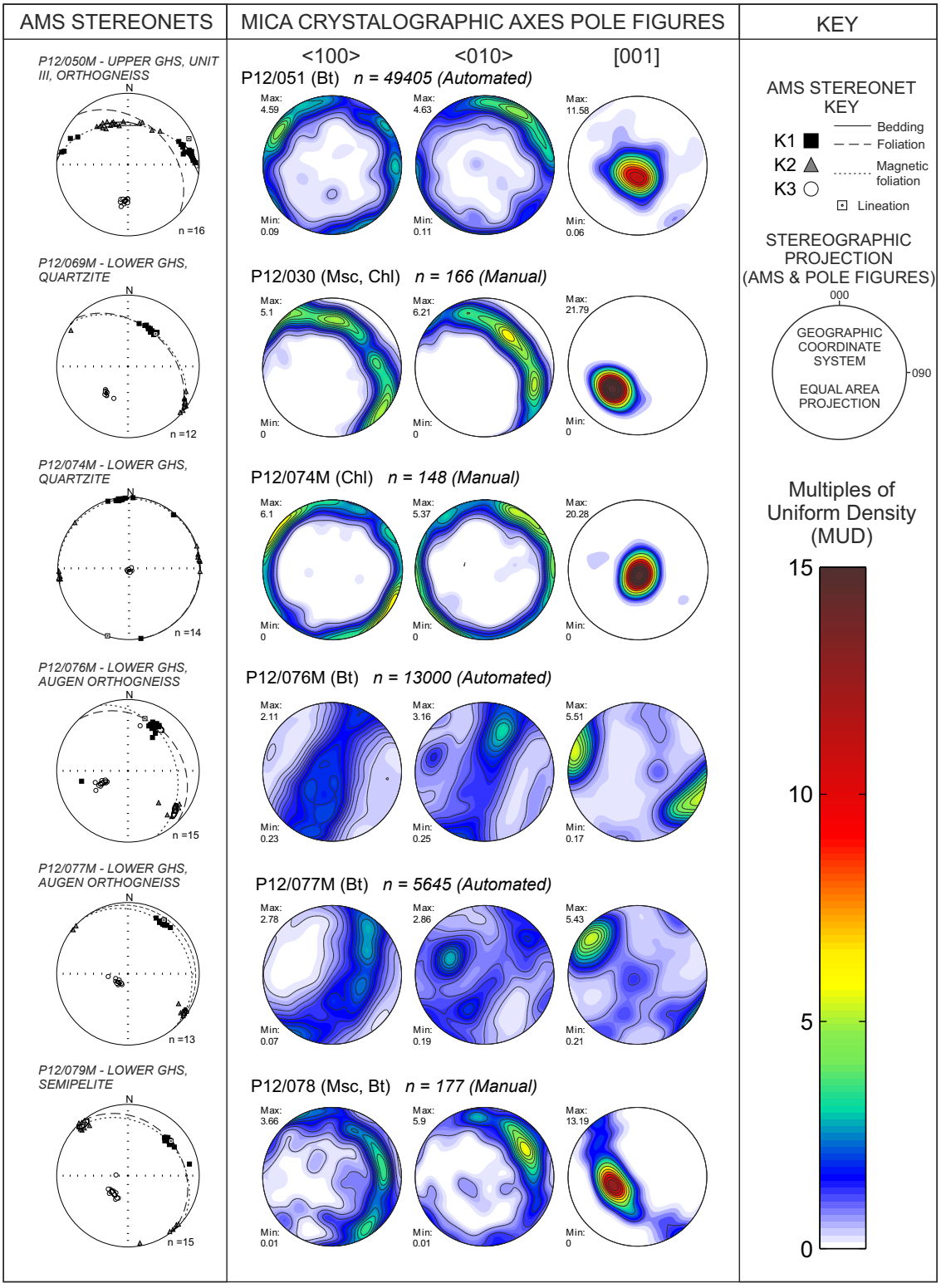

Figure 4.13. Phyllosilicate CPOs and AMS fabrics of paramagnetic samples

fabrics with phyllosilicate CPOs of the same samples. All measured samples show a good correlation between phyllosilicate CPOs and magnetic fabric orientations (Figure 4.13). In all cases except for samples P12/076M and P12/077M, the orientations of the [001] axis (*c-axis*) and pole to the magnetic foliation neatly overlap. Excluding P12/076M and P12/077M, the <100> (*a-axis*) and <010> (*b*-axes) directions of all

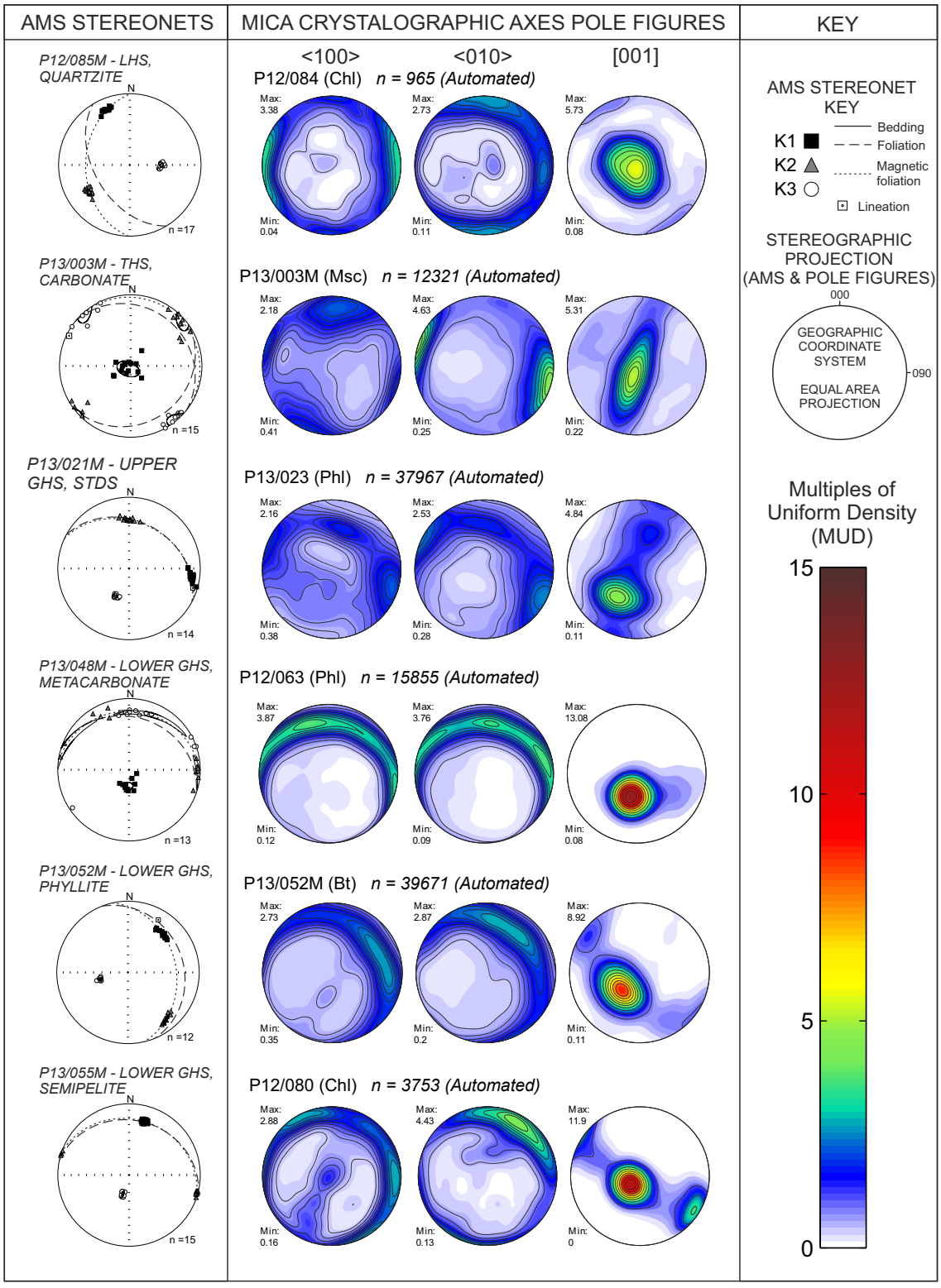

Figure 4.13. continued...

samples form girdle or cluster distributions that overlap the magnetic foliation. In some cases there is also a strong correlation between the orientations of the magnetic lineation and <010> direction. P12/076M and P12/077M show good correlation between the [001] axis and K_2 cluster. The <100> and <010> directions form a girdle that intersects the magnetic lineation and pole to the magnetic foliation. These samples have coherent AMS fabrics that correlate with the local structural foliations and mineral

lineations (Figure 4.13) but very poorly defined hysteresis loops (Figure A.4.17). Thus, whilst a correlation between deformation and magnetic fabrics exists for samples P12/076M and P12/077M, the mismatch between the pole to the magnetic foliation and the [001] axis suggests that these samples may have an additional magnetic carrier that has not been identified.

4.6. Discussion

4.6.1. Correlation between AMS fabrics and deformation of the GHS

Plots of K_m vs *P'* and K_m vs *T* with data points categorised in terms of diamagnetic, paramagnetic and ferromagnetic carriers (Figure 4.14) show strong variation in *P'* and *T* between samples of the same classification. This indicates that mineralogy is not the only controlling factor of the measured AMS fabrics. Additionally, there is a close fit between the local orientation of magnetic foliations and lineations with local structural foliations and mineral lineations (Figures 4.7 & 4.8). This correlation extends to the regional scale, as orientations of mean magnetic foliation and lineation and mean structural foliation and mineral lineation of the THS, STDS, UGHS and LGHS are similar (Figure 4.10). As such, a positive correlation between AMS and deformation fabrics has been determined for most samples (except P12/034M, P12/087M, and P13/011M*;* see Figures 4.10, 4.13 & A.4.16).

For diamagnetic samples (P12/034M, P12/087M, P13/067M) it is assumed that the CPO of quartz (± calcite for P12/034M) defines the AMS fabric (Table 4.3). The magnetic foliation of sample P12/034M from the THS does not correlate with the locally recorded foliation. However, there are several cross cutting structural foliations in the THS that may relate to this fabric (Chapter 2). P12/087M from the LHS, does not have a well-defined magnetic foliation and this may reflect the relatively undeformed state of the LHS that would results in a random quartz CPO (Figure A.3.24).

All paramagnetic samples (Table 4.3) produce a positive correlation between magnetic and deformation fabrics. CPO of phyllosilicates appears to be responsible for the AMS in all of these samples except P12/052M and P13/041M (Figure 4.13)*,* in which the CPOs of diopside and/or phyllosilicate control AMS. The <010> direction (*b-axis*) of phyllosilicates are commonly aligned with magnetic lineations (Figure 4.13).

All ferromagnetic samples (except P13/011M) produce a positive correlation between magnetic and deformation fabrics. For samples with MSD magnetite magnetic carriers (P13/004M, P13/011M, P13/014M and P13/024M) it is probable that the spatial

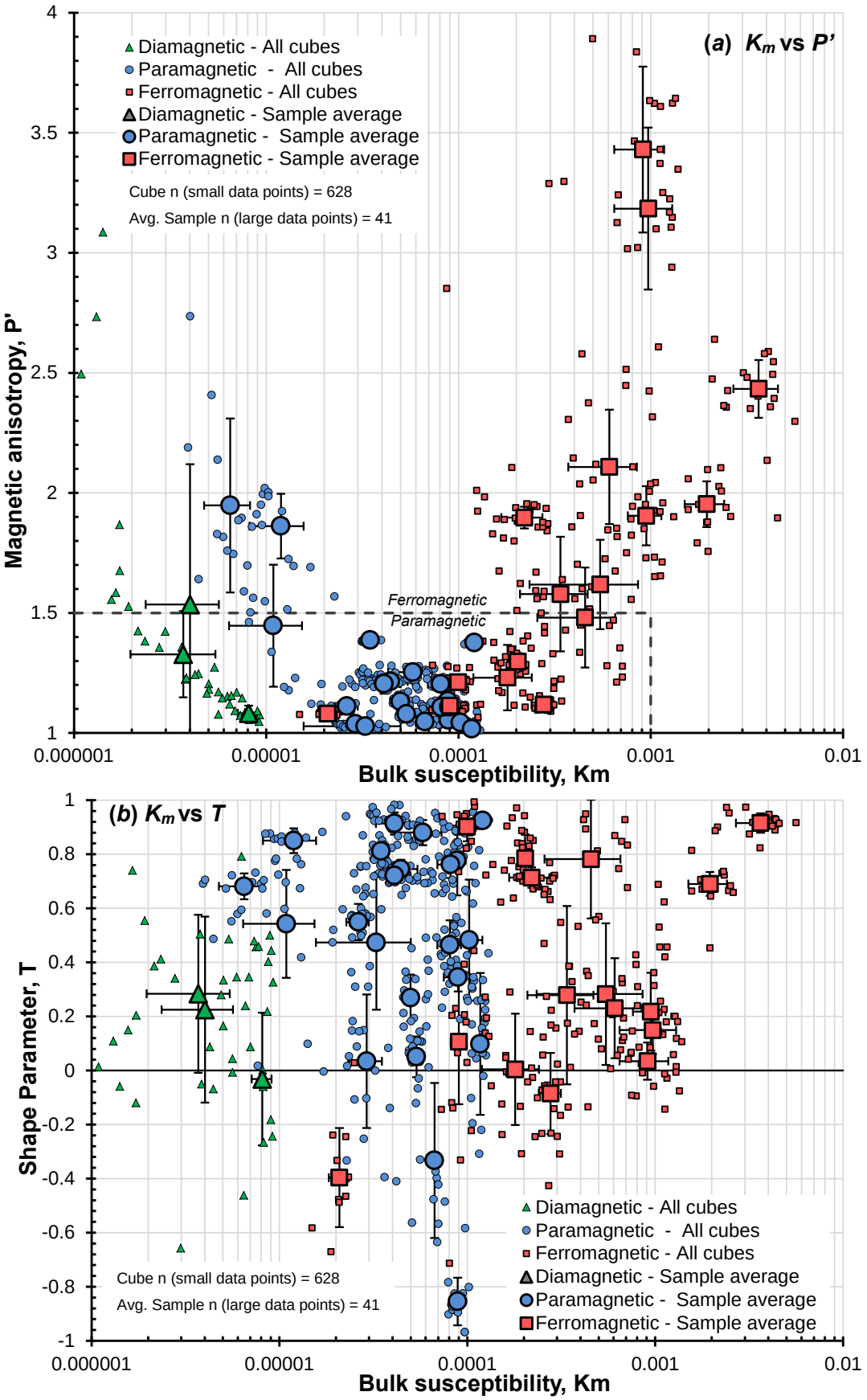

Figure 4.14. K_m, P' & T of Dia- Para- and Ferromagnetic samples. Bulk susceptibility (K_m), magnetic anisotropy (*P'*) and susceptibility ellipsoid shape parameter (*T*). (*a*) Same as *Figure 4.9a* but with new symbology. (*b*) Same as *Figure 4.9b* but with new symbology. *Red squares, ferromagnetic samples; blue circles, paramagnetic samples; green triangles, diamagnetic samples.*

distribution of magnetite is responsible for the AMS as individually, these grains should have a close-to-isotropic AMS. In all other ferromagnetic samples, magnetite SPO appears to control the AMS *(*Table 4.3). FORC analysis (Figure A.4.18) revealed only minor magnetostatic interactions in half of the ferromagnetic samples and no magnetostatic interactions in the remaining half (Table 4.3). With the exception of P13/011M, the close correlations between structural and magnetic fabrics suggest that where interactions have been detected, any resulting distribution anisotropy does do not conflict with SPO and CPO derived anisotropy (*Section 4.3.1.2*.). As such, a correlation between AMS and deformation fabrics remains valid.

The correlation between structural and magnetic foliations suggest that AMS fabrics record the deformation that occurred during the extrusion and exhumation of the GHS. More significantly, the correlations between magnetic and mineral stretching lineations suggest that AMS fabrics record the kinematics of extrusion (Figure 4.10).

As magnetostatic (i.e. uniaxial) anisotropy controls the AMS of magnetite in all ferromagnetic samples from the UGHS (except P13/004M, P13/011M, P13/014M and P13/024M*,* which have cubic anisotropy), it can be assumed that dislocation creep of magnetite, which occurs typically at amphibolite facies conditions is responsible for the AMS of these samples (Housen *et al.*, 1995; Ferré *et al.*, 2003; Ferré *et al.*, 2014). Additionally, ferromagnetic AMS fabrics derived from leucosomes in the UGHS record deformation during partial melting. As such, these AMS fabrics record deformation at or close to peak metamorphic conditions of the GHS under sub-solidus conditions.

4.6.2. AMS ellipsoid shape as a proxy for strain geometry

The shape parameter of the magnetic susceptibility ellipsoid, *T*, is plotted against vertical structural height above to the MCT (Figure 4.15) to provide a proxy for strain ellipsoid shape. Many authors warn against the use of *T* as a proxy for strain ellipsoid shape as *T* often reflects the properties of the magnetic carriers rather than the strain ellipsoid (Borradaile & Jackson, 2010; Ferré *et al.*, 2014). This is certainly an issue when AMS is controlled by phyllosilicates, which typically align in planes and naturally possess a highly oblate intrinsic AMS (Borradaile & Werner, 1994; Martin-Hernandez & Hirt, 2003; Kruckenberg *et al.*, 2010). Despite this problem, there is good evidence to support the use of *T* as a proxy of strain ellipsoid shape in this study. Firstly it has already been demonstrated that for this sample suite, AMS fabrics are controlled by deformation fabrics and a clear correlation exists between the orientation of the kinematic axes *X*, *Y* and *Z* of the finite strain ellipsoid and the magnetic lineations and

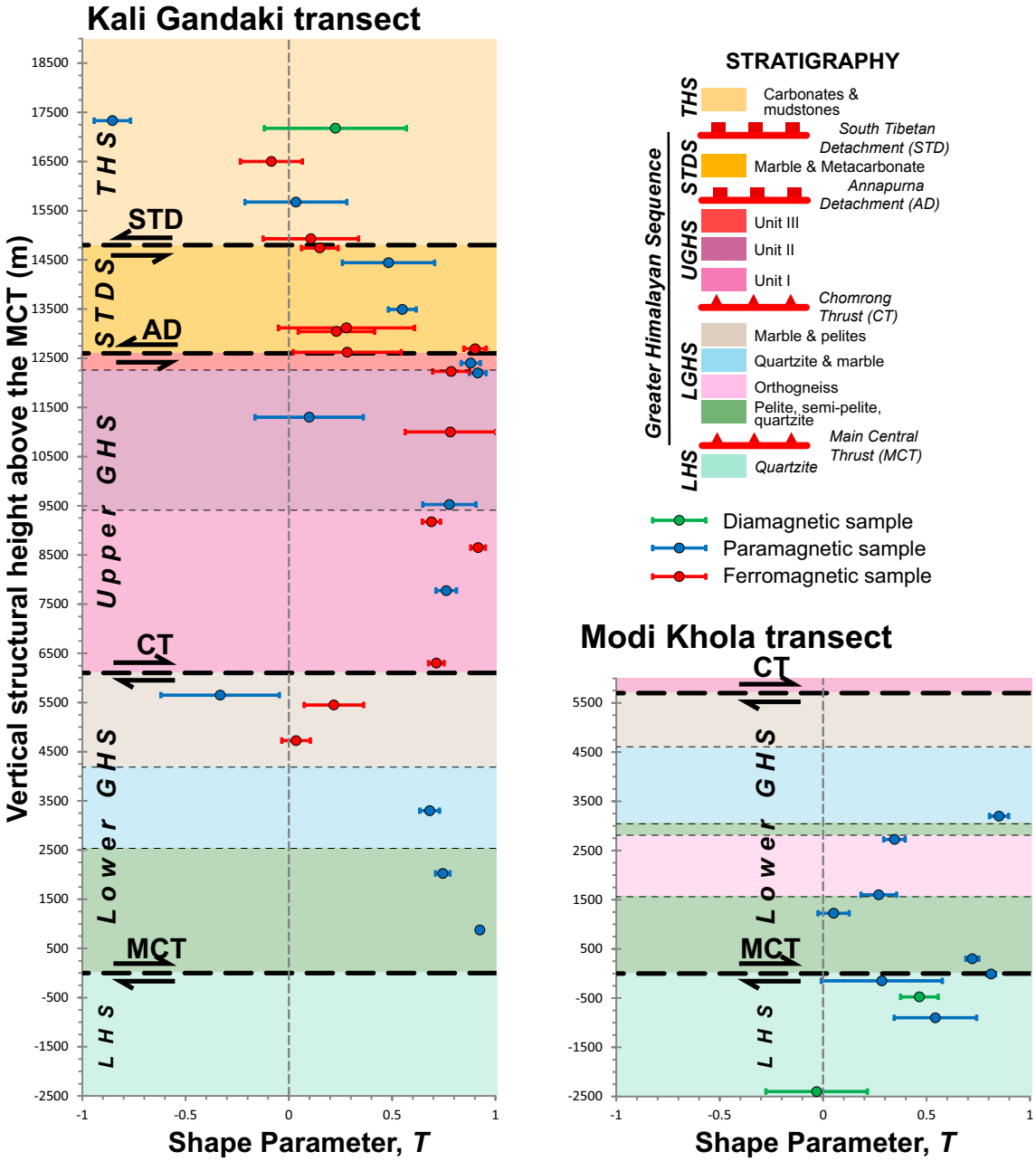

Figure 4.15. Shape parameter (T) profile for the GHS and bounding units. AMS ellipsoid shape parameter, *T,* against relative structural height above the MCT. Error bars display 1 standard deviation of *T.* Data points are categorised as diamagnetic (green circles), paramagnetic (blue circles) and ferromagnetic (red circles). Data points overlay a stratigraphic column of the local geology, plotted to scale. Major shear zones and their relative shear senses are also displayed and labelled in the plots and the accompanying stratigraphic key. See text for discussion.

foliations (Figure 4.10). Secondly, a plot of K_m vs. T in which diamagnetic, paramagnetic and ferromagnetic samples are grouped together (Figure 4.14b) shows no trend between T and K_m, which suggests that T varies independently of mineralogy. Most importantly, both ferromagnetic and paramagnetic samples produce trends in T that agree with each other over a range of T = 0 to T = 0.90 across the THS and UGHS. This agreement is significant as single crystals of magnetite have an intrinsic T

of -0.3 (Tarling & Hrouda, 1993) whilst single crystals of phyllosilicate have an intrinsic *T* ranging from 0.73 to 0.91 for muscovite, 0.93 to 1.00 for biotite, 0.87 to 0.99 for chlorite (Martin-Hernandez & Hirt, 2003) and 0.95 for phlogopite (Tarling & Hrouda, 1993). Thus, it is justifiable to assume that for this particular study, variations in *T*, at least within the UGHS, STDS and THS, describe variations in the strain ellipsoid shape under which the AMS fabric was produced.

Along the transect a clear trend is seen across the boundary between the STDS and underlying UGHS. The THS has a mean *T* of -0.11 (neutral ellipsoid), the STDS has a mean *T* of 0.41 (weakly oblate) whilst Units I, II and III below have a mean *T* of 0.75 (highly oblate) (Figure 4.15). *T* is much more variable in the LGHS and LHS, making it difficult to identify clear trends. In the LGHS there are only two ferromagnetic samples found at the top of this unit to compare with *T* for paramagnetic samples. Therefore, it is not appropriate, to use *T* as a proxy for strain ellipsoid shape in the LGHS below the position of these ferromagnetic samples as the oblate values of *T* in the paramagnetic samples could be attributed to the intrinsic properties of the phyllosilicate magnetic carriers rather than the strain ellipsoid shape.

4.6.3. Evidence for orogen-parallel deformation and 3D flattening of the GHS

Both AMS fabric orientations and ellipsoid shapes highlight the occurrence of orogen-parallel deformation within the GHS of the Annapurna-Dhaulagiri Himalaya. Within the LGHS, mean mineral and magnetic lineations plunge approximately 30-50^{o} towards NE (Figure 4.10). This is typical for the GHS and matches closely with lineation measurements made elsewhere along the Himalayan orogen (e.g. Hodges *et al.*, 1996; Searle *et al.*, 2003; Law *et al.*, 2004; Law *et al.*, 2013). In the lower portion of the UGHS (Unit I and Unit II) mineral and magnetic lineations vary in azimuth between NW to E, with a slight concentration in azimuths between N to NE. In contrast, mineral and magnetic lineations in Unit III of the UGHS and in the STDS have azimuths ranging between N and SE with a distinct concentrations of E plunging azimuths. Elsewhere in the Himalaya, this distinctly orogen-parallel orientation is not typical for the STDS (e.g. Cottle *et al.*, 2011; Law *et al.*, 2011), however, similar E-W orientated lineations have been documented both locally and up to 80 km east of the Kali Gandaki in the Marsyandi valley of the Manaslu Himalaya, from both field structural observations and AMS data (Pêcher, 1991; Guillot *et al.*, 1993).

Direct correlation between the AMS ellipsoid and the strain ellipsoid suggests that the UGHS records deformation under an oblate strain regime. These contrast markedly with the STDS, THS, and upper LGHS near to the CT, which produce neutral AMS

ellipsoids indicative of deformation under a plane strain regime (Figure 4.15). The dominance of oblate strain proxies in the UGHS reflects a larger component of flattening relative to the over- and underlying sequences. It is necessary to consider whether the oblate strain ellipsoid proxies determined from AMS fabrics in the UGHS record a true flattening with out-of-section movement of material. If dilation (Δ_v) during the recorded deformation is 0 (i.e. no volume change), then an oblate strain ellipsoid reflects 'true flattening', whereby extension must occur in all directions normal to the shortening axis (Ramsey & Huber, 1983). However, when volume loss has occurred ($\Delta_v < 0$) an oblate strain ellipsoid can be produced by plane strain or even constrictional deformation and reflects only an 'apparent flattening' (Ramsey & Huber, 1983). When using AMS fabrics as a proxy for strain geometry, volume loss of the magnetic carriers during deformation (i.e. due to metamorphic reactions) could result in the production of oblate fabric under a plan strain or constrictional deformation. In the case of the UGHS, it is not clear whether the magnetic carriers have undergone dilation during deformation. However, the prevalence of planar over linear fabrics observed in the UGHS and the scatter of lineation azimuths recorded across the sequence supports the interpretation that the oblate strain proxies reflect a 'true flattening' with out-of-plane (i.e. orogen-parallel) stretching.

Correlation between AMS fabrics and high temperature deformation microstructures and metamorphic mineral assemblages imply that three dimensional horizontal stretching occurred within the UGHS at temperatures greater than ~550 ^{o}C (Chapter 3). Furthermore, oblate AMS fabrics measured from migmatitic leucosomes record deformation under sub-solidus conditions (T = 0.7-0.9, P13/042M, P13/043M). Consideration of the distribution of migmatites and leucogranites across the profile suggests that the dominance of oblate fabrics in the UGHS may be due to the reduction in rheological strength relative to the bounding sequences. The sharp discontinuities between oblate strain proxies and plane strain proxies that occur across the CT and AD, coincident with lower temperature deformation microstructures (Chapter 3) suggest that non-coaxial shearing on these structures may have continued during the early stages of extrusion and exhumation after high-temperature flattening of the UGHS.

4.6.4. Tectonic implications

A correlation of oblate fabrics (Figure 4.15) with high temperature deformation across the whole of the UGHS in the Kali Gandaki transect (Figure 3.21) supports the field and microstructural evidence that the UGHS has was subjected to pervasive horizontal stretching and vertical thinning, synchronous with partial melting during its mid-crustal

evolution. This is in close agreement with the geological criteria for channel flow, presented in *Section 1.3.5.* Additionally, in the footwall of the CT and hangingwall of the AD, which bound the margins of the UGHS, the reduction in shape parameter, *T* to *T* = ~0 and *T* = 0.41, respectively indicates a transition from oblate to plane strain (although still weakly oblate in the STDS) deformation from the UGHS to bounding unit. This may reflect an increase in the ratio of coaxial to non-coaxial deformation from the centre of the UGHS to its margins, as indicated from microstructural observations and CPO fabrics (Chapter 3). Such findings are also consistent with the criteria for mid-crustal channel flow. Importantly, the thermo-mechanical simulations on which much of the understanding of channel flow is derived, simulate deformation under a plane strain regime (Beaumont *et al.*, 2001; Beaumont *et al.*, 2004). The authors of these models suggest that in nature, orogen-parallel mid-crustal flow may occur and should have an import influence on the kinematic evolution of the system (Beaumont *et al.*, 2004; Culshaw *et al.*, 2006). In particular, where orogen-parallel flow occurs, rates of exhumation may be reduced as surface directed pressure gradients should be weaker as material can escape laterally.

Additionally, E-W directed AMS and mineral lineations in the STDS also suggests that at least the upper portions of the GHS have been subjected orogen-parallel stretching (Figure 4.10). It is known that the THS in the Kali Gandaki valley has undergone E-W extension during the opening of the Thakkhola Graben since the late Miocene (Hurtado *et al.*, 2001; Garzione *et al.*, 2003) and some authors suggest that this deformation also effected the STDS and UGHS (Godin *et al.*, 2001; Hurtado *et al.*, 2001). However, the correlation between E-W lineations and high temperature (>550 ^{o}C) deformation suggests that E-W extension could have affected the GHS during its mid-crustal evolution. These findings are similar to AMS data from the Manaslu leucogranite pluton and surrounding UGHS, ~80 km east of the Kali Gandaki valley (Guillot *et al.*, 1993; Coleman, 1998). Here, magmatic lineations in the leucogranite and stretching lineations in the surrounding country rock, identified from both field structural observations and AMS analyses, record an E-W stretching and magmatic flow direction (Guillot *et al.*, 1993; Coleman, 1998). Elsewhere in the Himalaya, other authors have presented additional evidence of high temperature orogen-parallel deformation of the GHS (Pêcher, 1991; Pêcher *et al.*, 1991; Guillot *et al.*, 1993; Scaillet *et al.*, 1995; Vannay & Steck, 1995; Coleman, 1996; Argles & Edwards, 2002; Hurtado, 2002; Jessup & Cottle, 2010; Xu *et al.*, 2013). Similar observations are made from the Gangotri granite in the Garhwal Himalaya which forms km-scale tabular laccoliths, interpreted as crustal scale boudins formed during oblate coaxial deformation with a component of orogen-parallel stretching (Scaillet *et al.*, 1995). The cause and

mechanism of apparent high-temperature orogen-parallel deformation of the GHS in the Annapurna-Dhaulagiri region and elsewhere in the Himalaya is yet to be fully understood. However, the numerous reports of this phenomenon suggest that it may have played an important role during its kinematic evolution and requires further attention.

The significance of these processes and their implications for the kinematic evolution of the GHS and the Himalaya is discussed further in Chapter 7. Importantly, the occurrence of orogen-parallel deformation are unaccounted for by current models of Himalayan orogenesis (e.g. Beaumont *et al.*, 2001; Bollinger *et al.*, 2006; Grujic, 2006; Webb *et al.*, 2007; Kohn, 2008; Robinson, 2008; Larson *et al.*, 2010), yet may have important implications for the rheological properties of the GHS.

4.7. Conclusions

When a genetic link between AMS and deformation fabrics is identified, AMS fabrics can provide an insight into the strain distribution and kinematics of a sequence of tectonically deformed rocks. 41 samples have been collected for AMS analysis from the GHS and bounding units along the Kali Gandaki transect in the Annapurna-Dhaulagiri Himalaya. Through detailed magnetic analyses, the controls of all AMS fabrics have been determined, as follows:

1) The magnetic carriers of diamagnetic, paramagnetic and ferromagnetic samples are identified as quartz and/or calcite, phyllosilicate and magnetite respectively.
2) Grain size populations of magnetite vary between samples, and are populated by SD, PSD or MD ± SP grains or SD-MD, SD-SP or PSD-SP mixes.
3) SD magnetite populations are most commonly dominated by uniaxial SD (USD) grains; a minority of samples contain magnetocrystalline SD (MSD) magnetite grains
4) For diamagnetic and paramagnetic samples, the AMS fabric is controlled by the CPO of quartz and/or calcite, and phyllosilicate respectively.
5) For ferromagnetic samples, the AMS fabric is controlled by the SPO of magnetite, except for samples P13/004M, P13/011M, P13/014M and P13/024M which have near-isotropic AMS fabrics controlled by the CPO of magnetite (cubic anisotropy).
6) A positive correlation is observed between the orientation of structural and magnetic foliations and mineral and magnetic lineations, demonstrating a genetic link between AMS and deformation fabrics, enabling AMS fabrics to provide information on the kinematics of deformation.

7) In the THS, STDS UGHS and top of the LGHS, a close fit between the shape parameter (*T*) of AMS ellipsoids of ferromagnetic and paramagnetic samples and the absence of correlation between *T*, K_m and the mineralogy of magnetic carriers suggests that *T* reflects the shape of the strain ellipsoid under which the AMS fabrics were developed; in the LGHS and LHS, where only paramagnetic samples are present, it is not possible to evaluate the contribution of mineralogical controls on *T*. Consequently, strain-related interpretations are not made from *T* for samples in the LGHS and LHS below the lowest ferromagnetic sample.

Following the identification of a genetic link between AMS and deformation fabrics, it has been possible to extract information regarding the distribution and characterisation of deformation across the GHS and bounding units along the sample transect. The orientation of the kinematic axes is derived from both structural and magnetic fabrics. Additionally, the shape parameter, *T* is used as a proxy for strain ellipsoid shape, which is plotted along a stratigraphic column to produce a strain geometry proxy profile for the GHS and bounding units. The following conclusions regarding the structural evolution of the GHS have been made from these data:

1) The orientation of mineral and magnetic lineations indicate stretching in the UGHS occurred in a NE-SW direction with a plunge of 30-40^o NE, whilst in the STDS stretching occurred in an E-W direction with a plunge of 10-20^o E.
2) Variations in *T* imply that deformation recorded by the AMS fabrics in the STDS and top of the LGHS occurred under a plane strain regime, whilst deformation in the UGHS occurred under an oblate strain regime.
3) Oblate strain proxies in the UGHS reflect a three dimensional flattening deformation that occurred at mid-crustal conditions, possibly due to the reduction in rheological strength caused by the higher temperatures and presence of migmatites and leucogranites. These fabrics imply that the UGHS underwent pervasive vertical shortening and horizontal stretching and are supportive evidence of mid-crustal channel flow of the UGHS.
4) The sharp discontinuity between plane strain and oblate strain proxies across the AD and CT, correlated with lower temperature deformation microstructures and CPO fabrics, suggest that non-coaxial deformation on these structures continued after a cessation of internal flattening of the UGHS. These observations may also reflect an increase in the ratio of non-coaxial to coaxial deformation from the centre of the UGHS to its margins. This fulfils an additional criterion of the channel flow model.

5) Oblate strain ellipsoids in the UGHS and E-W magnetic and mineral lineations in the UGHS and STDS correlate with high temperature (>550 °C) deformation microstructures and the deformation of migmatitic leucosomes at sub solidus conditions. This implies that the GHS was affected by a component of orogen-parallel deformation during its mid-crustal evolution. Similar observations of orogen-parallel deformation of the GHS are documented elsewhere across the Himalaya but their occurrence is not yet fully understood.
6) Most models of Himalayan orogenesis assume deformation occurred under a plane strain regime and are unable to account for orogen parallel deformation; more attention is needed to understand the role of orogen-parallel deformation in the GHS and its compatibility with current models of Himalayan orogenesis.

The results and interpretations described in this chapter provide an insight into the distribution and characterisation of deformation across the GHS. Three dimensional flattening and orogen-parallel stretching of the GHS is yet to be fully understood but appears to be an important phenomenon. The findings of this chapter and their implications for the kinematic evolution of the Annapurna-Dhaulagiri Himalaya will be discussed explored in further detail in Chapter 7 and used to interrogate the predictions of models of Himalayan orogenesis.

4.8 Appendix

Figure A.4.16. AMS fabric orientations. Equal area stereographic projection of AMS and structural fabrics. The orientations of the three susceptibility axes (K_1, black squares; K_2, grey triangles; K_3, white circles) measured from all cubes of each sample are plotted in lower hemisphere equal area stereographic projection. Dotted grey-lined great circles represent the mean magnetic foliation. Dashed grey-lined great circles represent structural foliations and solid grey-lined great circles represent bedding orientations. White squares represent the mineral lineations measured locally to each sample. N = the number of cubes measured per sample. All stereonets are geographically oriented and plotted using Anisort 4.2 (Chadima & Jelínek, 2008).

Figure A.4.17. Complete magnetic hysteresis data set. Uncorrected (grey) and corrected (black) magnetic hysteresis loops for all samples. Sample cube number is given for each plot. Corrected hysteresis loops have had paramagnetic contributions to the magnetic susceptibility removed to show the ferromagnetic hysteresis properties of that sample (Martin-Hernandez & Ferré, 2007). P12/076M, P12/077M, P12/082M, P12/085M, P12/087M, P13/033M, P13/043M, P13/052M, P13/055M and P13/059M produce poorly defined corrected hysteresis loops that do not produce neat closures at

each end. The poor quality of these data is likely to reflect the weakness of the ferromagnetic signal and they are included only for completeness and should only be interpreted in a qualitative manner as the data is too poor to use quantitatively.

Figure A.4.18. Complete FORC data set. FORC diagrams for samples indicate that magnetostatic interactions between grains are minor or negligible. $H_u = (H_a + H_b)/2$, $H_c = (H_b - H_a)/2$. Coloured contouring shows density distributions of ρ (H_u, H_c). SF = smoothing factor. See text for explanation of axis units. See Harrison and Feinberg (2008) for a description of the graphical methods used to produce FORC diagrams. See Figure 4.6 for an explanation of FORC curves. P12/050M b2, P12/052M a1, P12/074M a5, P12/079M a1, P12/085M a16, P13/007M b3, P13/021M b2, P13/041M b1, P13/043M b1, P13/067M a2 and P13/068M a2 do not show any ferromagnetic response and are included only for completeness.

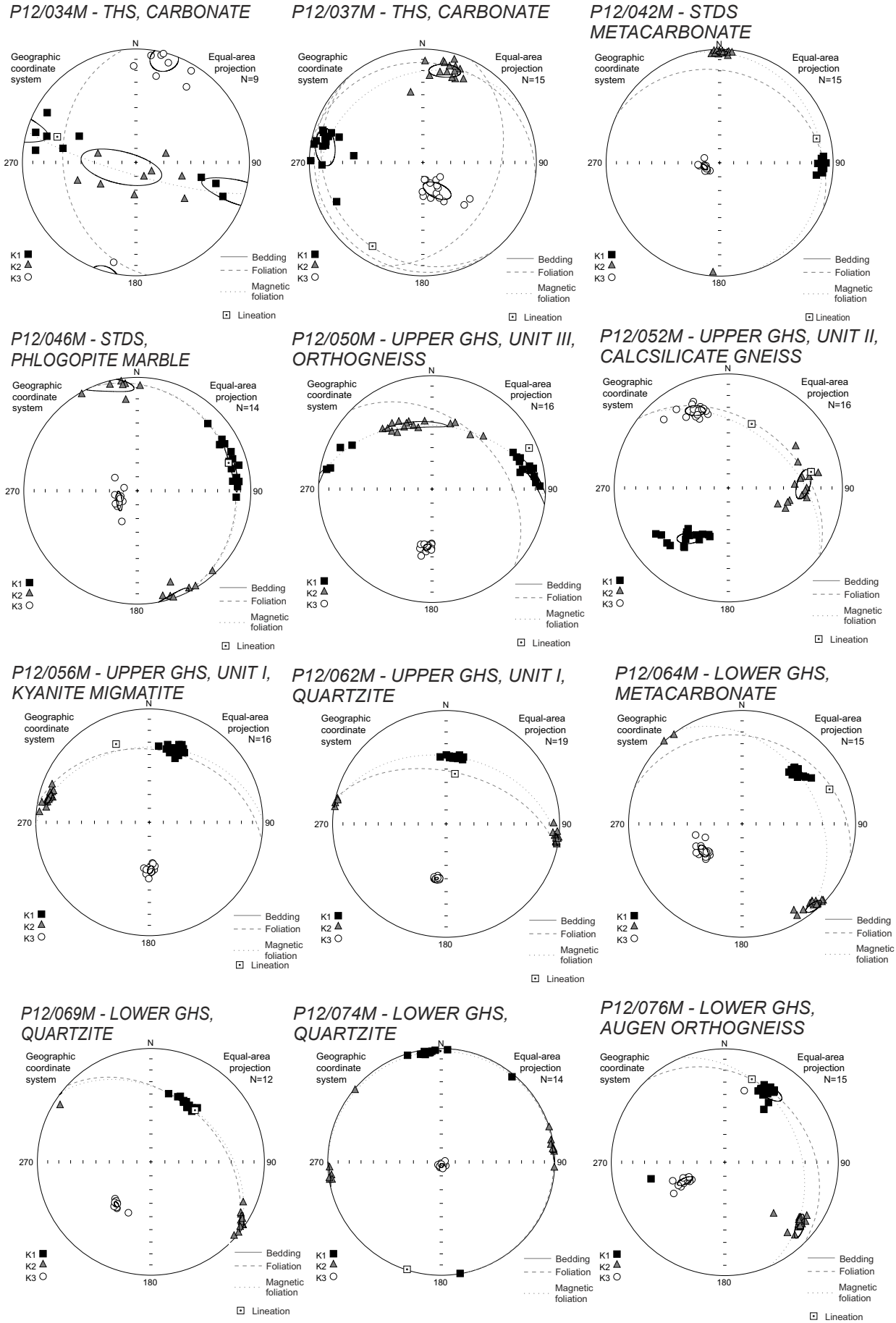

Figure A.4.16. AMS fabric orientations

P12/077M - LOWER GHS, AUGEN ORTHOGNEISS

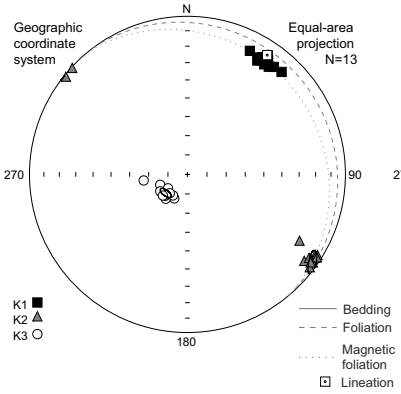

P12/079M - LOWER GHS, SEMIPELITE

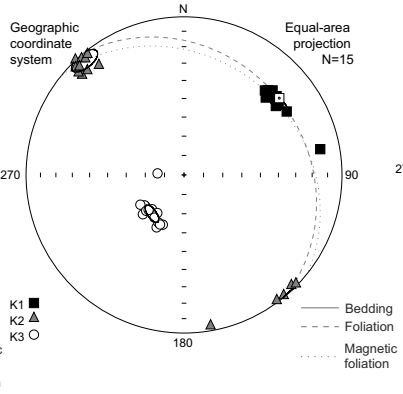

P12/082M - LHS, QUARTZITE

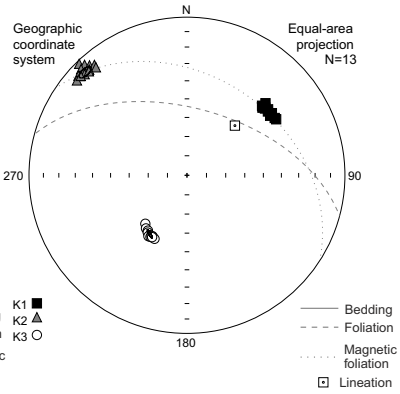

P12/087M - LHS, QUARTZITE

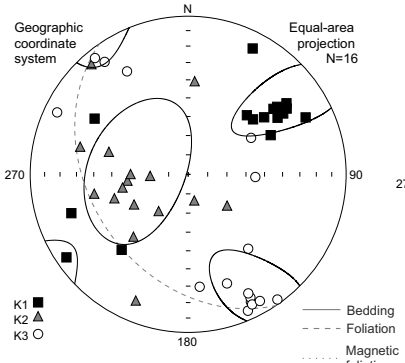

P12/085M - LHS, QUARTZITE

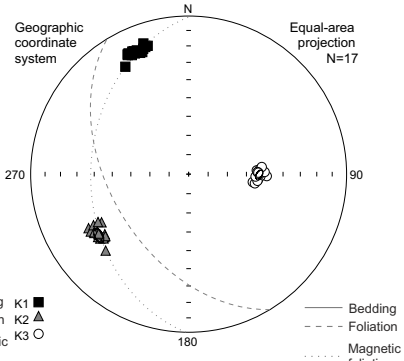

P13/001M - THS, CARBONATE

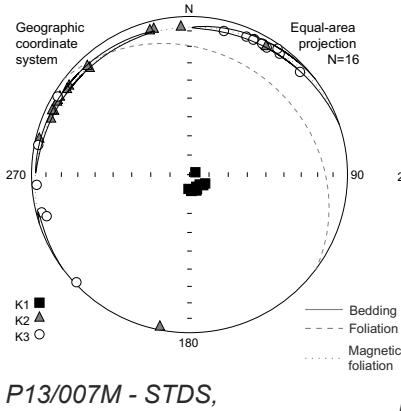

P13/003M - THS, CARBONATE

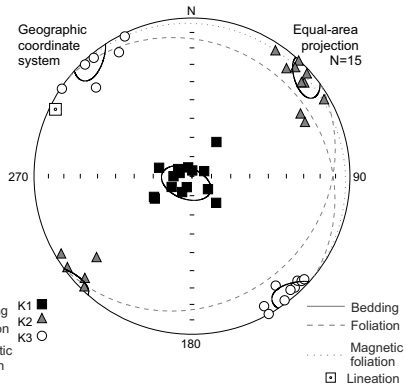

P13/004M - THS, CARBONATE

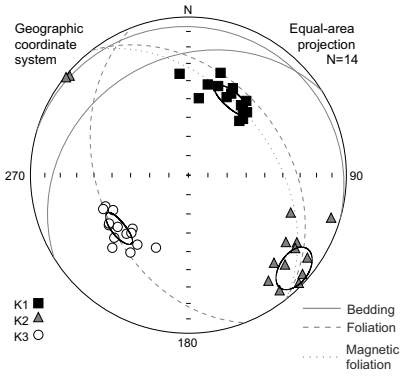

P13/007M - STDS, METACARBONATE

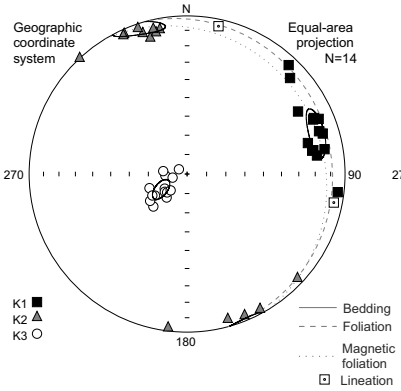

P13/011M - THS, CARBONATE

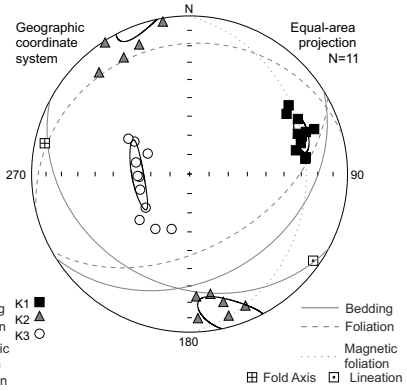

P13/014M - THS, CARBONATE

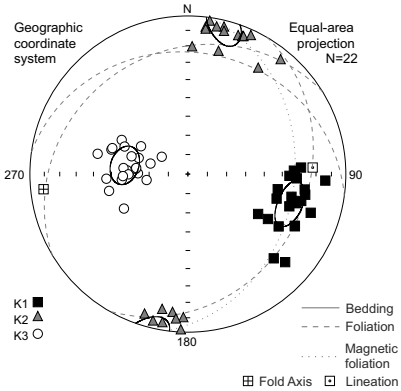

Figure A.4.16. continued...

P13/021M - STDS METACARBONATE

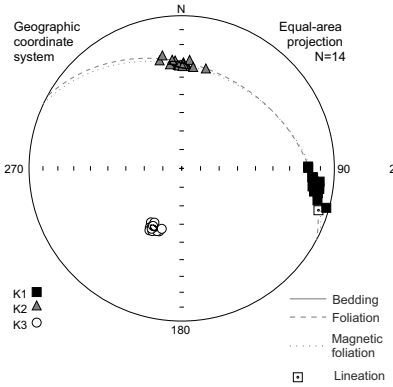

P13/024M - STDS, CALC-SILICATE GNEISS

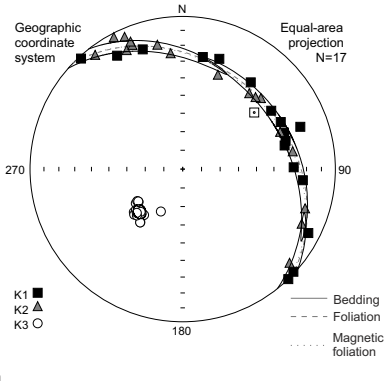

P13/027M - STDS, PHLOGOPITE MARBLE

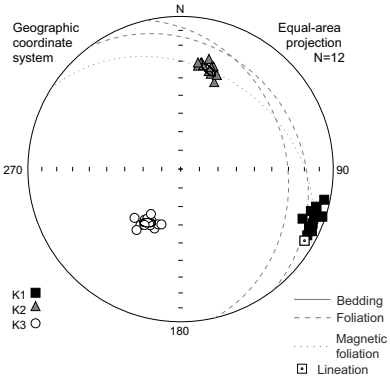

P13/028M - RECENT, GLACIAL DEPOSIT

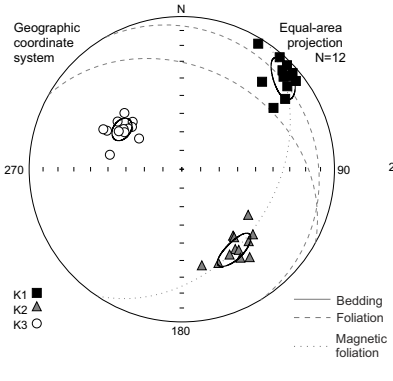

P13/033M - UPPER GHS, UNIT III, ORTHOGNEISS

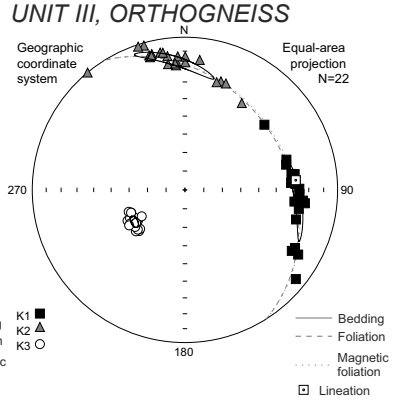

P13/036M - STDS,CALC-SILICATE GNEISS

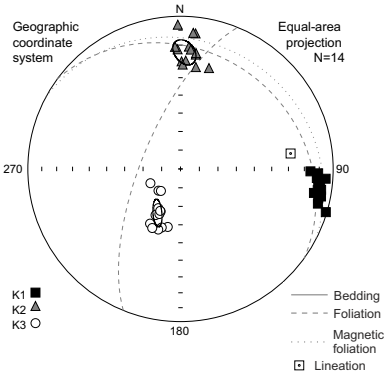

P13/038M - UPPER GHS, UNIT II, CALCSILICATE GNEISS

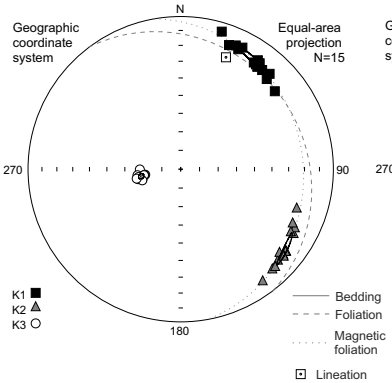

P13/039M - UPPER GHS, UNIT II, CALCSILICATE GNEISS

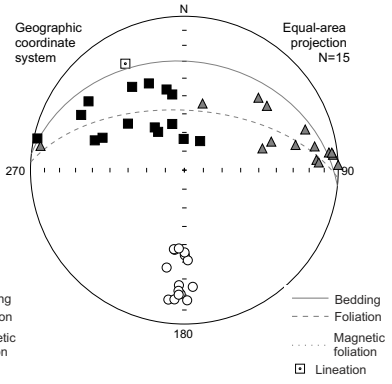

P13/041M - UPPER GHS, UNIT II, CALCSILICATE GNEISS

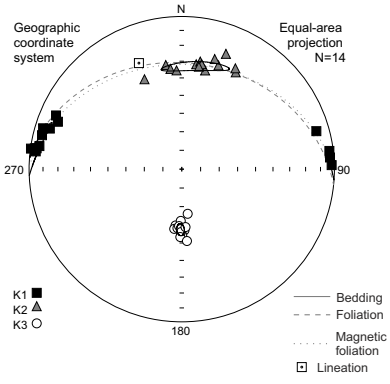

P13/042M - UPPER GHS, UNIT I, KYANITE PARAGNEISS

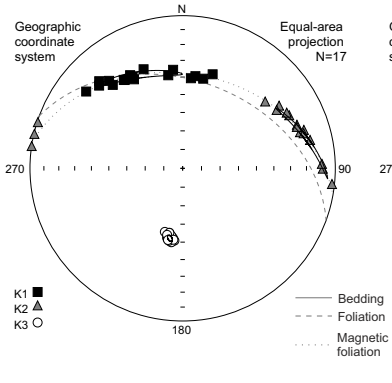

P13/043M - UPPER GHS, UNIT I, KYANITE MIGMATITE

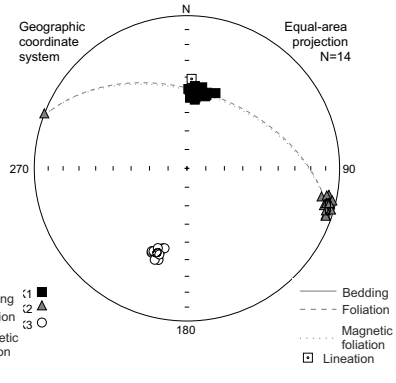

P13/048M - LOWER GHS, METACARBONATE

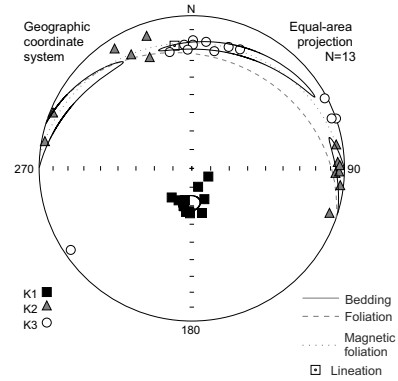

Figure A.4.16. continued...

P13/050M - LOWER GHS, METACARBONATE

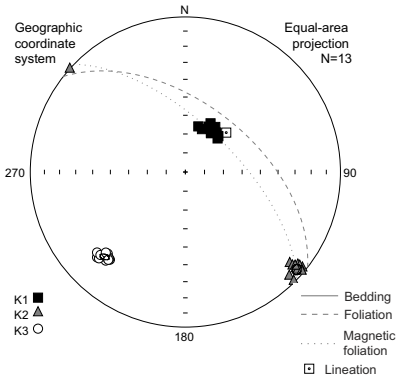

P13/052M - LOWER GHS, PHYLLITE

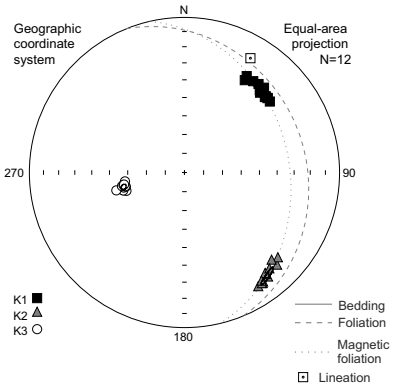

P13/055M - LOWER GHS, SEMIPELITE

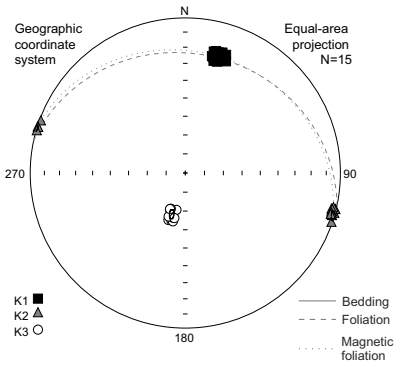

P13/059M - LOWER GHS, SEMIPELITE

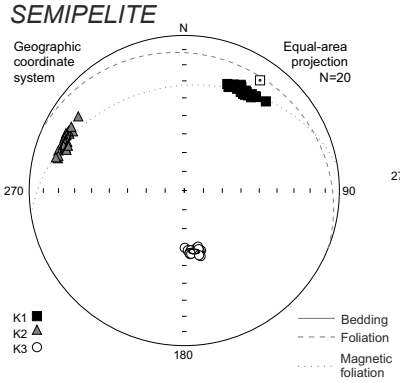

P13/068M - LHS, QUARTZITE

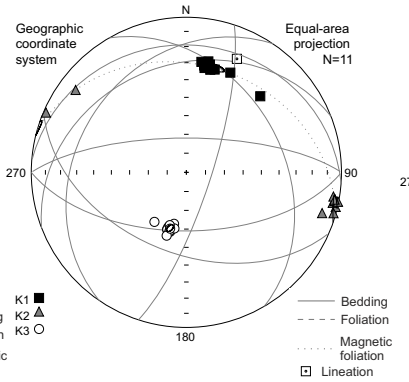

P13/067M - LHS, QUARTZITE

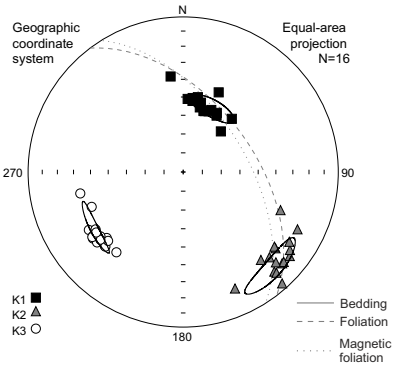

Figure A.4.16. continued...

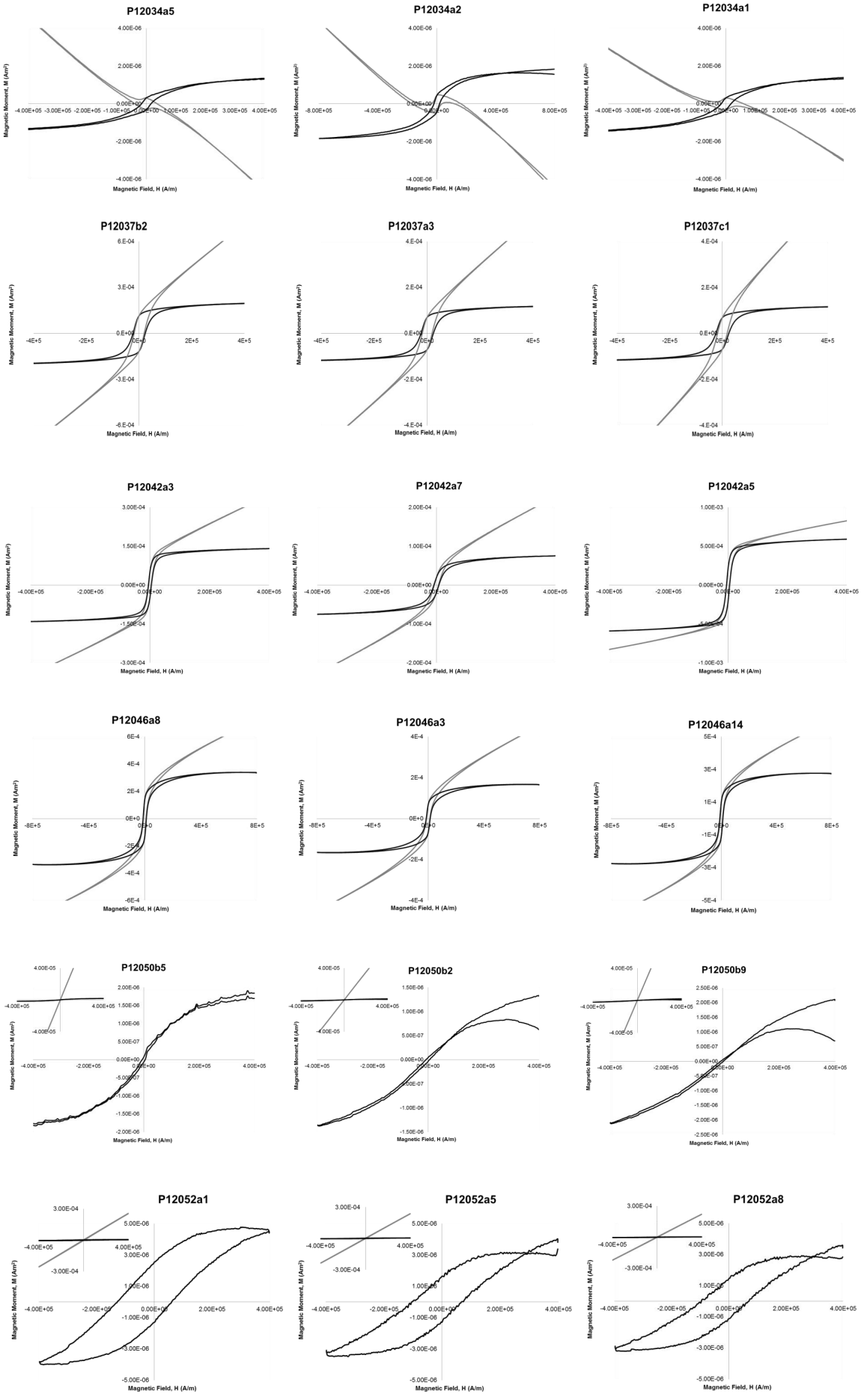

Figure A.4.17. Complete magnetic hysteresis data set.

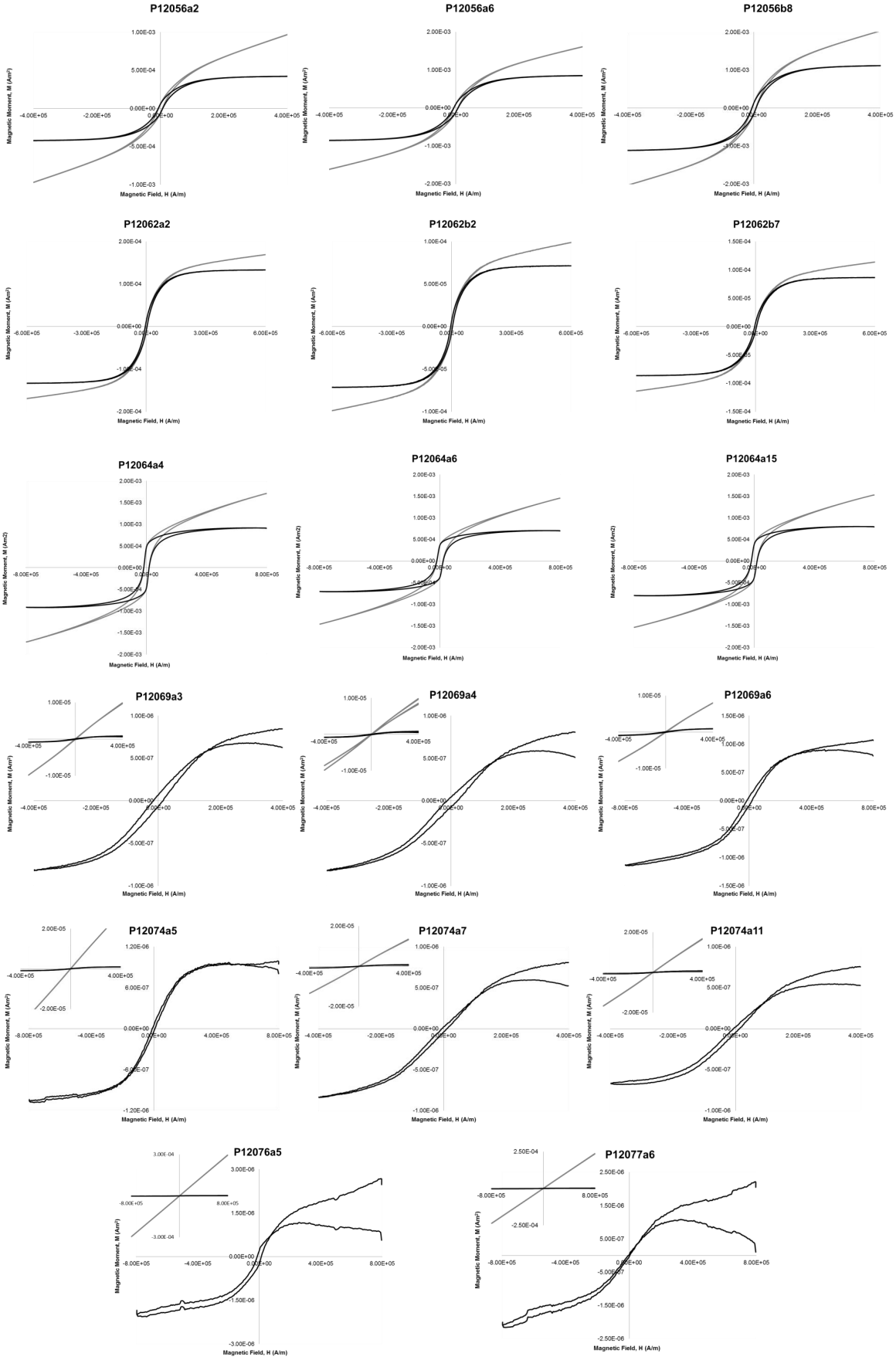

Figure A.4.17. continued…

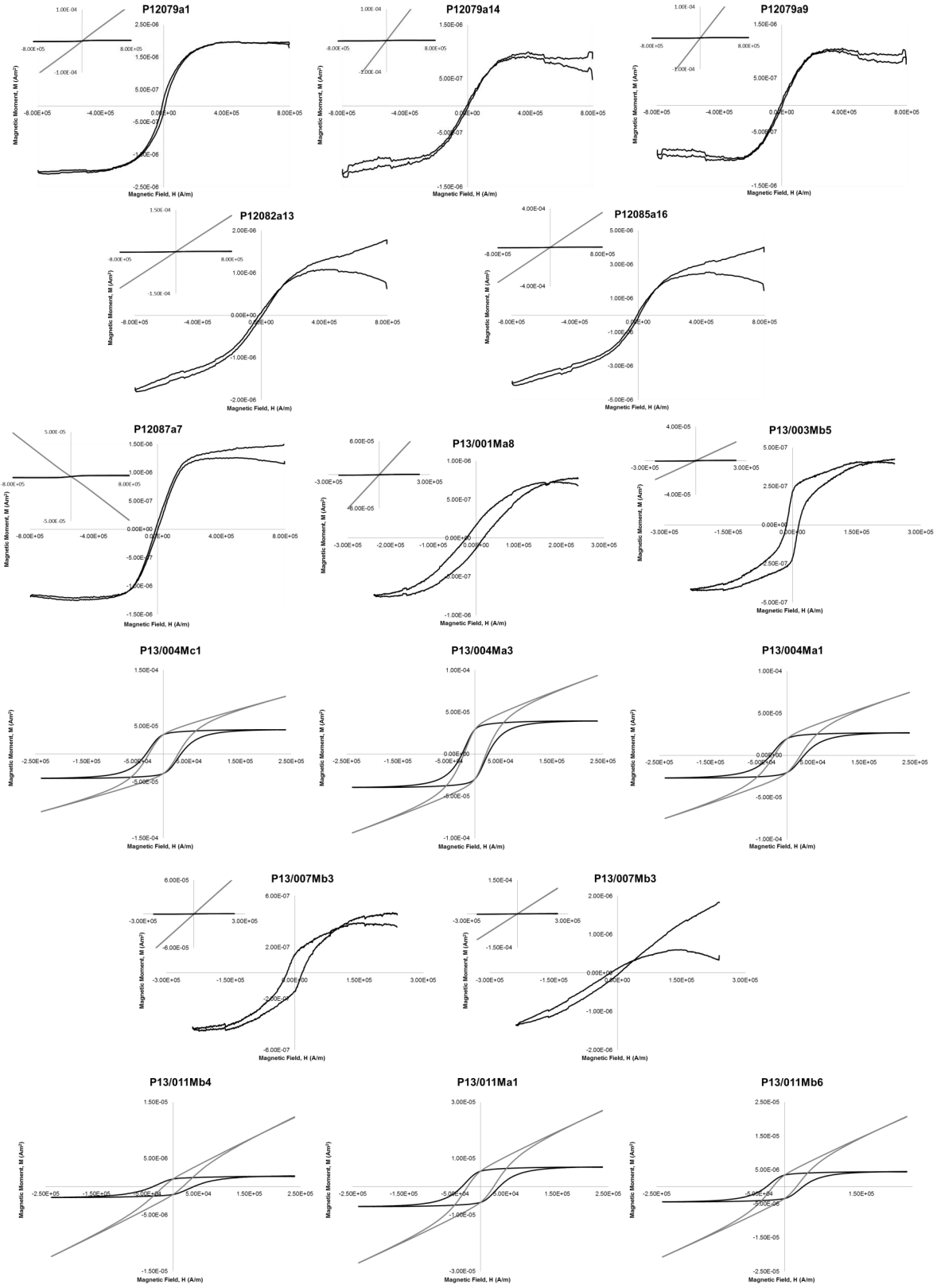

Figure A.4.17. continued…

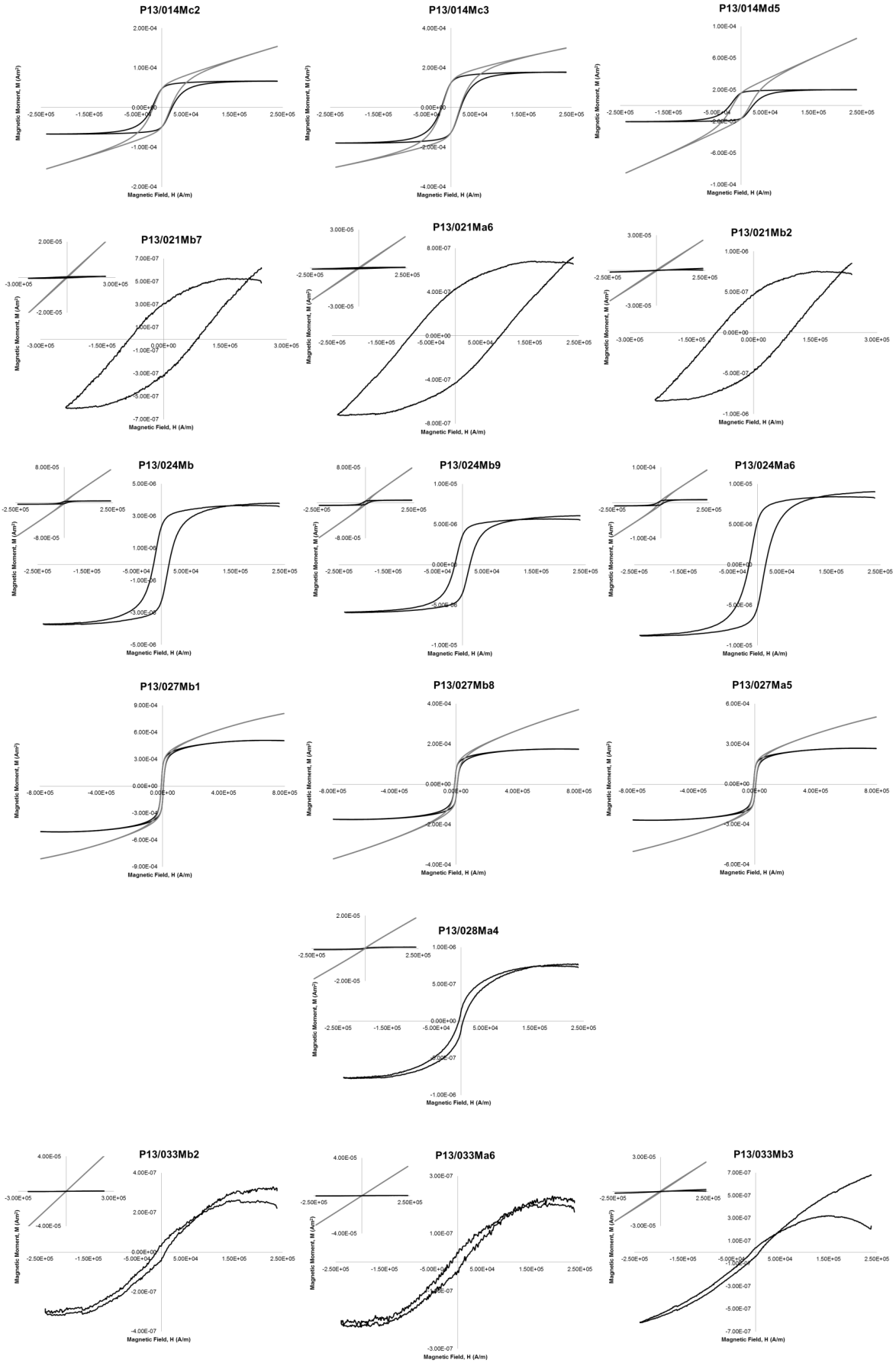

Figure A.4.17. continued…

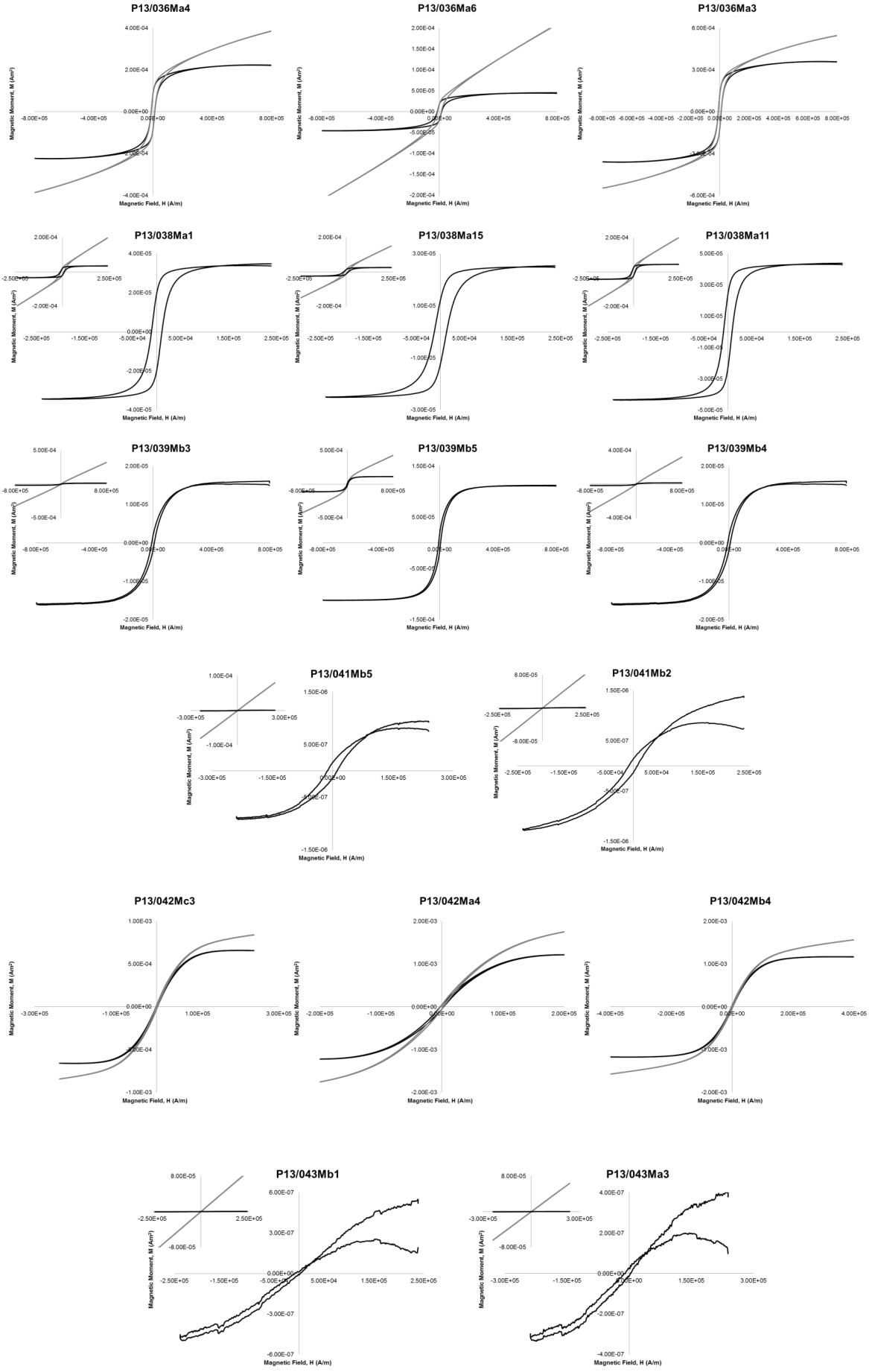

Figure A.4.17. continued…

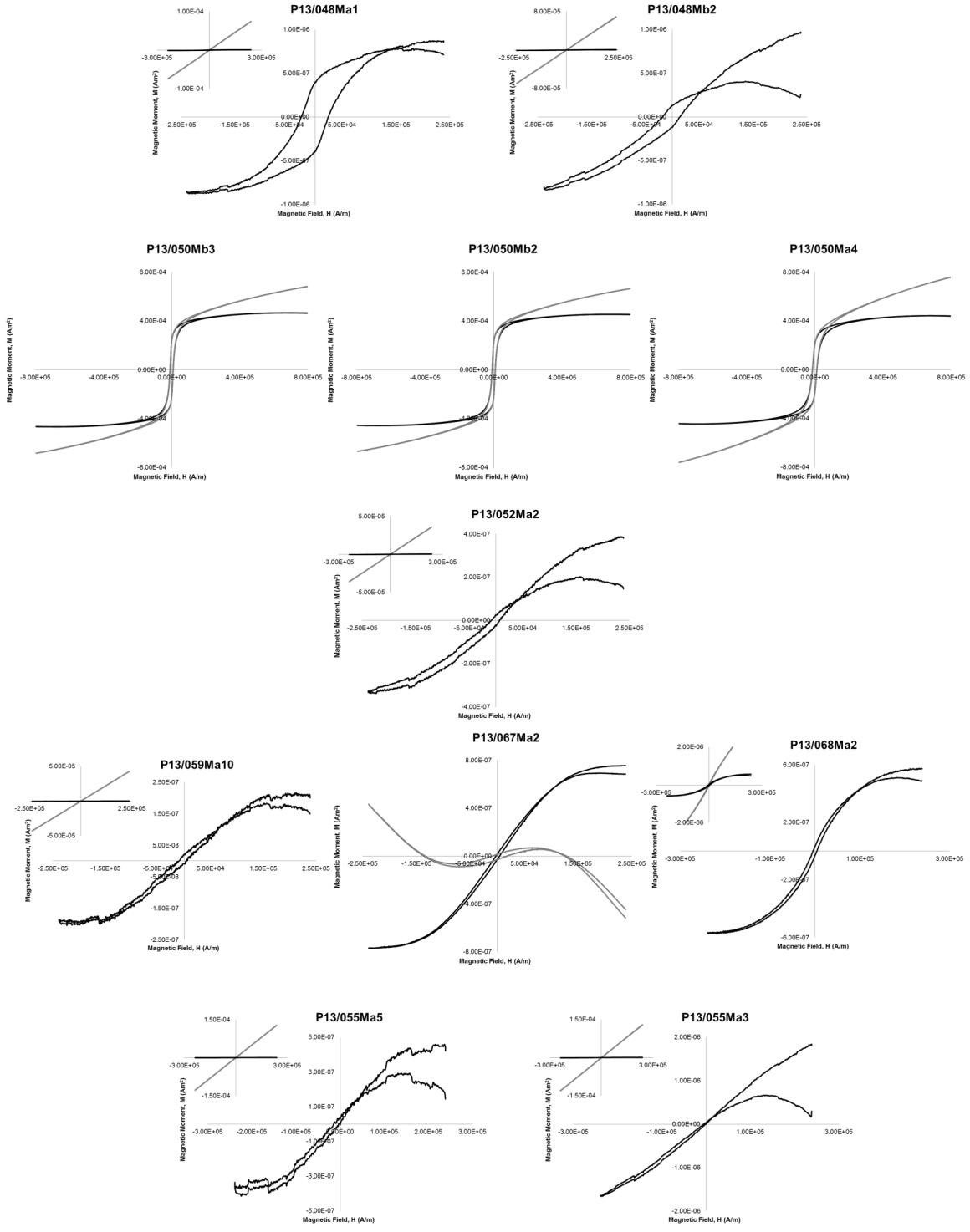

Figure A.4.17. continued…

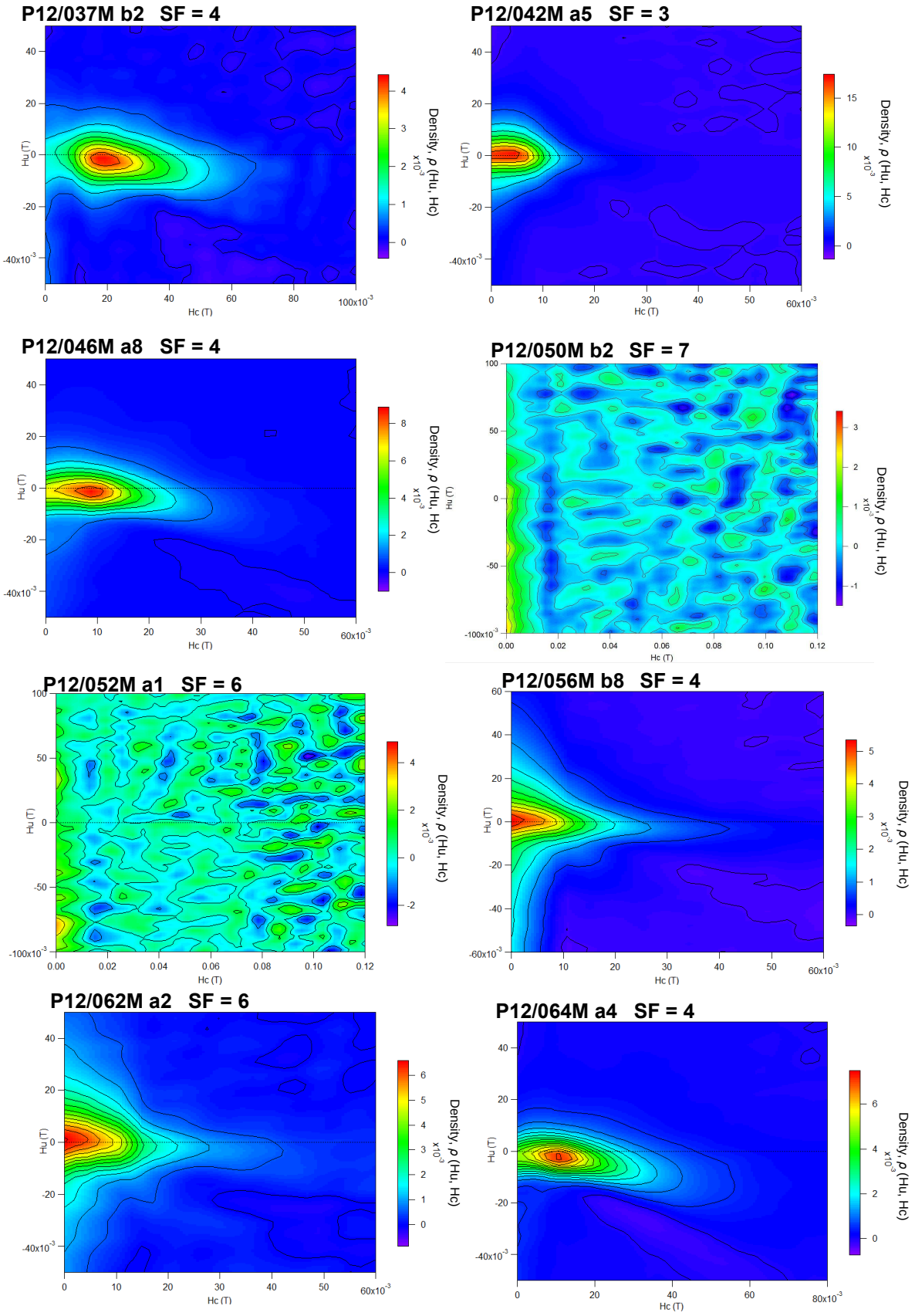

Figure A.4.18. Complete FORC dat a set.

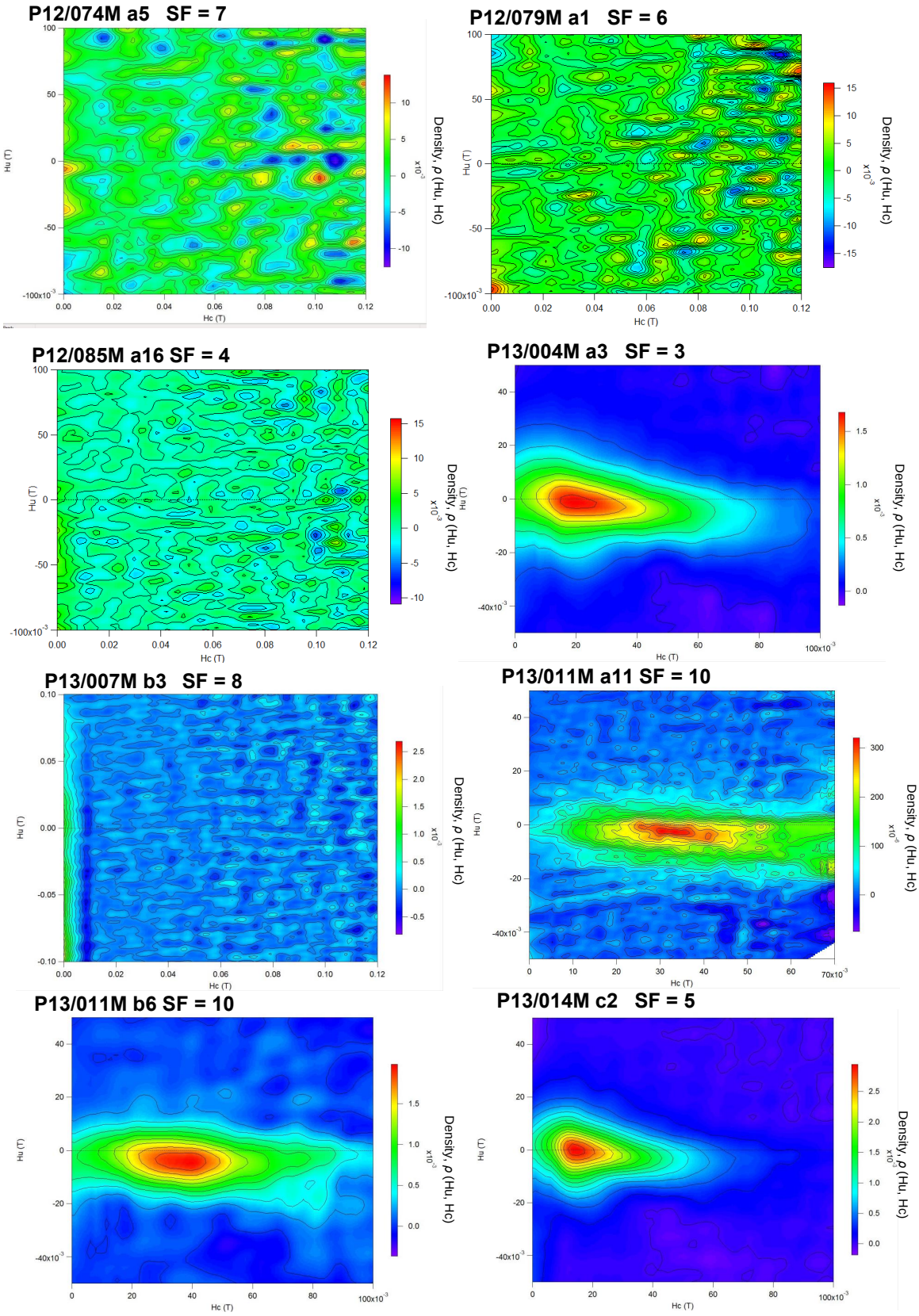

Figure A.4.18. continued…

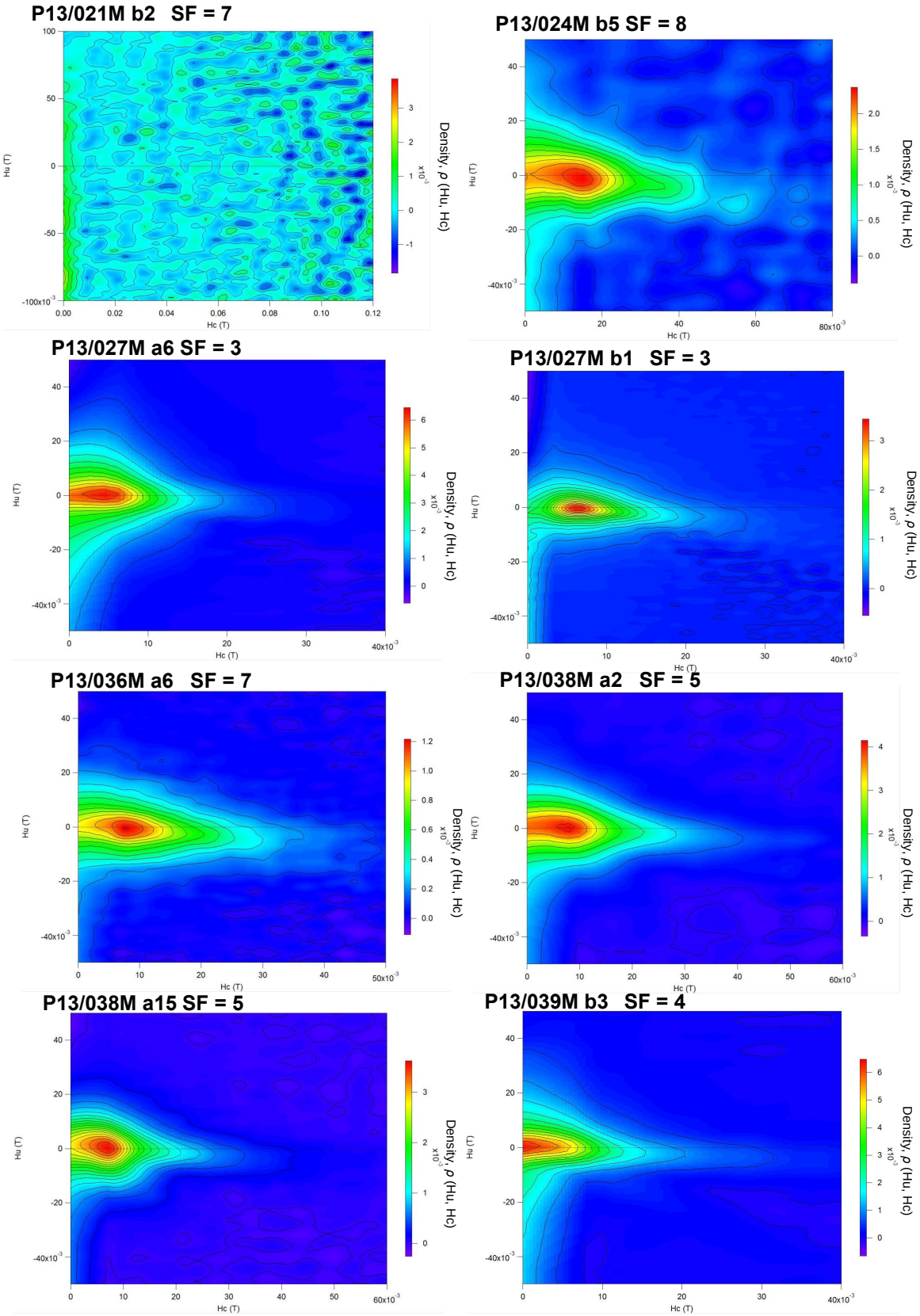

Figure A.4.18. continued…

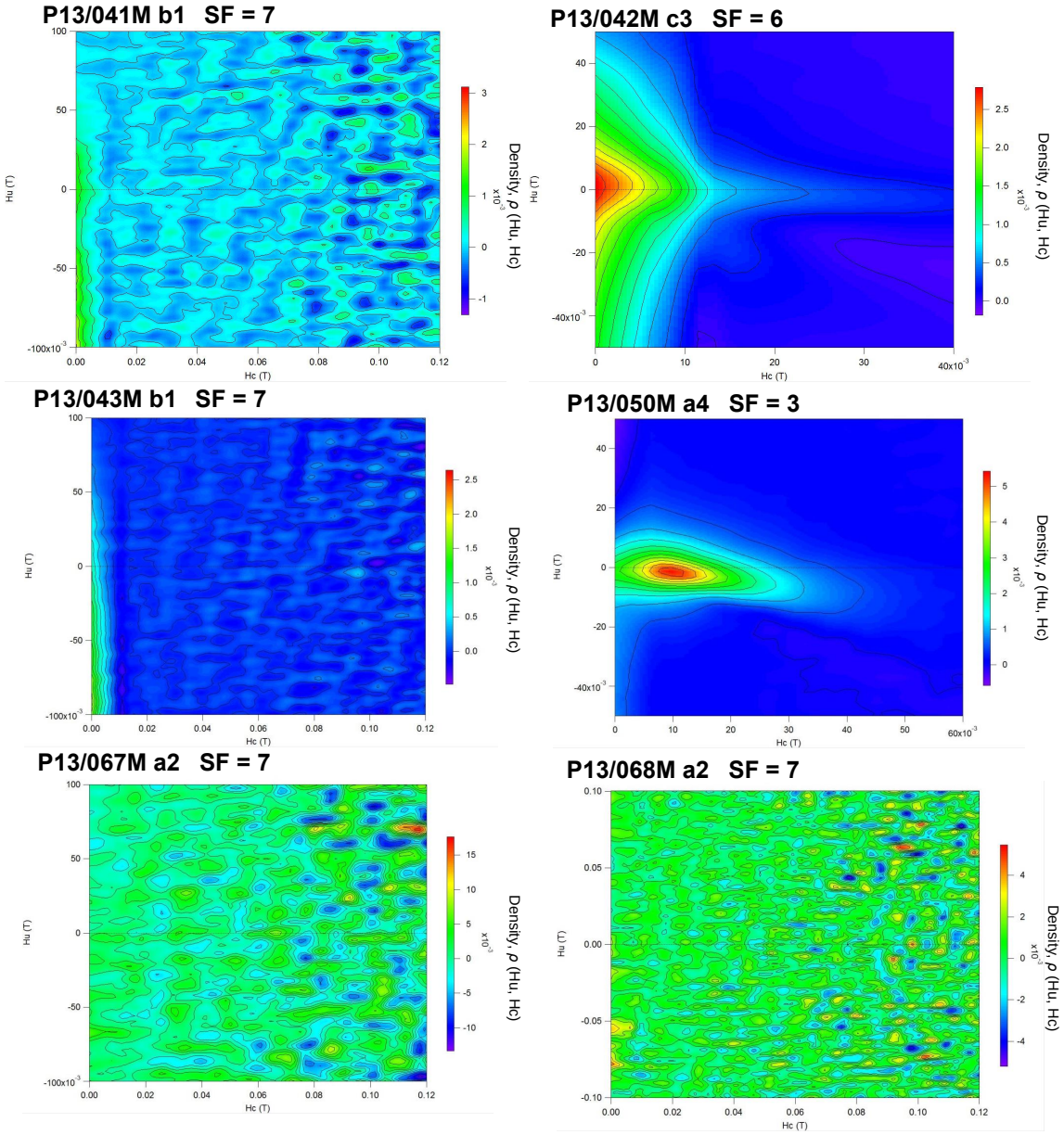

Figure A.4.18. continued…

- CHAPTER 5 -

RELATIVE STRAIN MAGNITUDE PROFILES FOR THE ANNAPURNA-DHAULAGIRI HIMALAYA

5.1. Introduction

In order to fully understand the kinematic evolution of large metamorphic terranes and shear zones, quantitative analysis of regional-scale trends in deformation is required. This chapter presents a new method for quantitatively assessing the distribution and magnitude of strain across deformed regions. Two independent data sources derived from Crystallographic Preferred Orientation (CPO) and Anisotropy of Magnetic Susceptibility (AMS) analyses are used to construct relative strain proxy profiles for the Annapurna-Dhaulagiri Himalaya. Whilst these methods have been used in previously published studies of other terranes, this is the first study to combine quantified analysis of CPO and AMS data to construct regional strain profiles. The combination of crystallographic and magnetic fabric analyses produces a robust data set and the ability to correlate between observed trends in CPO and AMS data greatly strengthens the resulting interpretations. The profiles identify high and low strain zones and regional strain gradients across the GHS and bounding units. When combined with the deformation temperature profiles derived from Chapter 3, these data provide information on the kinematic evolution of the GHS. Furthermore, they provide a means to test models of Himalayan orogenesis, specifically the channel flow model.

5.2.1. CPO development

CPO fabrics can develop and evolve through a variety of deformation mechanisms, including rigid body rotation (Stallard & Shelley, 1995; Díaz Aspiroz *et al.*, 2007; Wallis *et al.*, 2011), dissolution-precipitation creep (Hippertt, 1994; Bons & Den Brok, 2000; Bestmann & Prior, 2003), and dislocation creep (Sylvester & Christie, 1968; Tullis, 1977; Schmid & Casey, 1986; Rosenberg & Stünitz, 2003; Barnhoorn *et al.*, 2004; Heilbronner & Tullis, 2006). Additionally, post-deformation static annealing has been shown to weaken CPO strength slightly, without altering CPO topology (Heilbronner & Tullis, 2002; Barnhoorn *et al.*, 2005).

In the case of quartz, calcite and dolomite, where dislocation creep is shown to be the dominant mechanism for crystal plastic deformation (Baëta & Ashbee, 1969; Tullis, 1977; Barber *et al.*, 1981; Schmid & Casey, 1986; De Bresser & Spiers, 1997), CPO development occurs in response to the preferential activation of specific slip systems that are governed by temperature, differential stress and additionally in the case of quartz, hydraulic weakening (Nicolas & Poirier, 1976; Lister & Williams, 1979;

Mainprice *et al.*, 1986; Okudaira *et al.*, 1995; De Bresser & Spiers, 1997; Heilbronner & Tullis, 2006). Natural, experimental and numerical deformation studies have shown that when these factors are held constant, a positive correlation between strain magnitude and CPO strength may be recorded (Sylvester & Christie, 1968; Bouchez, 1977; Lister & Hobbs, 1980; Law, 1986; Schmid & Casey, 1986; Dell'angelo & Tullis, 1989; Barnhoorn *et al.*, 2004; Heilbronner & Tullis, 2006; Oesterling *et al.*, 2007; Delle Piane *et al.*, 2008; Morales *et al.*, 2011; Morales *et al.*, 2014). It is on this basis that quantified variations in CPO strength are used to construct strain proxy profiles through the Annapurna-Dhaulagiri Himalaya.

Whilst the dominating control behind CPO development is strain, there are many other factors that contribute to the strength of CPO fabrics. These factors described below, do not prevent the use of CPO strength as a strain proxy, but must be considered when interpreting the relative CPO strengths of different samples. Of greatest importance to CPO development are the effects of pre-existing fabrics (whether sedimentary, magmatic or tectonic) and strain partitioning in polymineralic rocks.

The strength of a polymineralic rock at a given set of conditions is controlled in part by the volumetric ratio of the strongest to weakest minerals (Handy, 1990; Czaplińska *et al.*, 2015). Three strength domains can be considered: (*1*) a load-bearing framework constructed from an interconnected network of the strongest phase, separating isolated pockets of a weaker phase; (*2*) a deformed matrix (weaker phase) with interspersed stretched porphyroclasts (stronger phase); and (*3*) a deformed matrix (weaker phase) and undeformed clasts (stronger phase) (Handy, 1990). In domain 1, the strongest phase controls the strength of the rock and hinders the development of foliation, grain Shape Preferred Orientation (SPO) and CPO (e.g. Herwegh *et al.*, 2011). In domain 3, there is a high strength contrast between the strong and weak phases and all the strain is accommodated by the weaker phase. Thus, domain 3 is essentially monomineralic in behaviour and develops a strong CPO in the weak phase (Herwegh *et al.*, 2011) and either weak or no CPO in the strong phase (Handy, 1990; Herwegh *et al.*, 2011). Polymineralic rocks with a mechanical behaviour akin to domain 2 fall along a sliding spectrum of variable mineral strengths and to a degree, the relative CPO strengths reflect the proportion of strain accommodated by each phase (Herwegh *et al.*, 2011). Additionally, the distribution of the stronger phases may hinder CPO development of the weaker phase through grain boundary pinning (Herwegh *et al.*, 2011). As a consequence, the individual rheological behaviour of all minerals in a polymineralic rock must be considered when interpreting their CPOs. Crucially, a low strength CPO is not necessarily indicative of a low strain rock if the mineral analysed is not the weakest phase.

Micro-scale variations in CPO fabrics can also be observed across a single thin section, through the development of microstructural heterogeneities (Garcia Celma, 1982; Lister & Williams, 1983; Knipe & Law, 1987; Larson *et al.*, 2014). Anisotropic fabrics can promote flow partitioning of coaxial and non-coaxial deformation into differing microstructural domains (Lister & Williams, 1983). Additionally, grain size variations and the presence of large, strong porphyroclasts in weaker matrix material affect the distribution of deformation, also leading to the development of microstructural domains (Garcia Celma, 1982; Lloyd *et al.*, 1992; Czaplińska *et al.*, 2015). Where present, these microstructural domains can preserve different CPO fabrics (e.g. Knipe & Law, 1987; Larson *et al.*, 2014).

Pre-existing fabrics, relating either to an original undeformed state or to an earlier deformation, can affect CPO development during subsequent deformations (Lister & Williams, 1979, 1983; Wilson, 1984; Knipe & Law, 1987; Czaplińska *et al.*, 2015). During deformation, grain shape and fabric anisotropies ideally develop into parallelism with stretching directions (Lister & Williams, 1983) and the ease at which this can occur is controlled to some extent by the orientation of the original fabric with respect to the externally applied deviatoric stress field (Lister & Williams, 1983; Wilson, 1984). At the grain scale, the ease at which intracrystalline deformation can occur depends on the orientation of slip systems relative to the applied stress field (i.e. the resolved shear stress) and the relative strengths of each slip system (i.e. the critical resolved shear stress). Thus, for a given stress regime, some grain orientations are weaker than others (e.g. Knipe & Law, 1987; Law *et al.*, 1990). For example, Toy *et al.* (2008) demonstrated an inheritance of a pre-existing high temperature quartz CPO fabric in a subsequent lower temperature CPO quartz fabric. This was attributed to the relative ease of continuing deformation on a favourably orientated ‘high temperature’ slip system, compared to the difficultly of rotating a grain into the orientation required for slip on a ‘low temperature’ slip system (Toy *et al.*, 2008).

Strain paths and deformation states must also be considered when interpreting CPO strengths. Investigation of fabric development during steady state deformation suggests that once a steady state has been achieved, CPO strength remains constant even if strain continues to increase (Lister & Hobbs, 1980; Wenk & Christie, 1991; Pennacchioni *et al.*, 2010). However, preservation of truly steady-state deformation fabrics is improbable as this requires an almost instantaneous removal of deformation conditions (Means, 1981; Knipe & Law, 1987). Instead, it is likely that preserved microstructures are modified during a final stage of ‘quenching’ as strain rate and differential stress decrease (Knipe & Law, 1987). The timing and conditions at which this ‘quenching’ occurs throughout a single package of rock are not necessarily uniform

(Knipe & Law, 1987), and the distribution of deformation is not necessarily homogeneous (Lloyd *et al.*, 1992). The implications of these factors are that the bulk CPO of a rock represents a time-averaged, heterogeneously deforming medium with zones of both grain growth and grain size reduction (Knipe & Law, 1987; Wenk & Christie, 1991).

Additionally, Wenk and Christie (1991) suggest that CPO strength may relate to the strain path (i.e. strain magnitude), rather than finite strain. Cyclic experimental deformation of limestone that first extended and then compressed the sample back to its original shape resulted in a CPO attributed to the final stage of compression (Wenk *et al.*, 1986). In this example, the finite strain ellipsoid is essentially spherical, yet the CPO records a deformation. Furthermore, the CPO showed no indication of an earlier extensional phase, indicating that the CPOs do not always record the entire strain history (Wenk *et al.*, 1986). In a similar experiment, a cube of aluminium alternately compressed in three orthogonal directions developed a strong CPO, but exhibited approximately zero finite strain (Takeshita *et al.*, 1989). Whilst these observations may seem problematic, they do imply that CPOs may preserve more information on deformation histories than strain analysis data derived from microstructural observations (e.g. Rf/ϕ method, SPO measurements, Flinn plot; etc. Ramsay & Huber, 1983).

To account for the outlined complexities of CPO development, CPO analysis should always be accompanied with microstructural and petrological analysis of thin sections. Whilst high strength CPOs are often simply related to high strain magnitudes, low strength CPOs can be derived from a number of factors and are not necessarily indicative of low strain. In polymineralic rocks, consideration should always be given to the relative strengths of each phase and how they are likely to affect CPO development. Additionally, and when possible, the nature of any pre-existing fabric(s) should be investigated and its influence on the overprinting CPO determined. Finally, the observed fabrics should always be interpreted as a dynamic system that may or may not have attained a steady state (Means, 1981; Lister & Williams, 1983; Knipe & Law, 1987) and the possibility of non-linear strain paths should be recognised (Takeshita *et al.*, 1989; Wenk & Christie, 1991). Consideration of these factors leads to better understanding of CPO development and allows for a more meaningful use of CPO strength as a proxy for relative strain magnitudes.

5.2.2. Quantified CPO analysis

There are several numerical methods by which CPO strength may be quantified (*e.g. strength parameter, C* - Woodcock, 1977; *J index* - Bunge, 1982; *Intensity parameter, I*

- Lisle, 1985; *Point-Girdle-Random index (PGR)* - Vollmer, 1990; *Misorientation index (M)* - Skemer *et al.*, 2005). The *J*-index (Bunge, 1982) is derived from the Orientation Distribution Function (ODF), which describes the volume fraction of crystals with orientation **g**, where **g** is the orientation matrix, defined by a set of Euler angles that describe the rotation of a crystal from a referenced orientation to the measured orientation (e.g. Mainprice *et al.*, 1993). The *J*-index is defined as,

$$J = \int f(\mathbf{g})^2 \, dg \qquad \textit{Equation 5.1}$$

where *f*(**g**) defines the density of the ODF with orientation **g** and,

$$dg = 1/8\pi^2 \sin\varphi \, d\Phi_1 \, d\varphi \, d\Phi_2 \qquad \textit{Equation 5.2}$$

where Φ_1, φ *and* Φ_2 are the Euler angles. *J* ranges from 1 for a random fabric to infinity for a single crystal. Whilst several publications have shown the *J*-index to be a useful parameter for fabric analysis, (e.g. Mainprice *et al.*, 1993; Ismaïl & Mainprice, 1998; Barth *et al.*, 2010; Mainprice *et al.*, 2014), it has been demonstrated to be highly sensitive to sample size and to the arbitrary choice of smoothing factors required to handle ODFs with multiple orientation density peaks (Skemer *et al.*, 2005).

The *M*-index (Skemer *et al.*, 2005) is based on the distribution of misorientation angles, determined from the smallest angle of rotation around a common axis needed to crystallographically align two grains (Randle & Ralph, 1986; Mainprice *et al.*, 1993; Randle, 1993). *M* is defined as

$$M = \frac{1}{2}\int \left| R_i^T(\theta) - R_i^0(\theta) \right| \mathrm{d}\theta \qquad \textit{Equation 5.3}$$

and quantifies the difference between the normalised distribution of measured misorientations, R_i^0, with a misorientation angle *θ,* and the theoretical distribution of misorientations in a random fabric, R_i^T, with a misorientation angle *θ.* The *M*-index, which ranges from 0 (random) to 1 (single crystal), is less sensitive to sample size than the *J*-index and has been used in several studies for quantitative analysis (e.g. Mehl & Hirth, 2008; Skemer *et al.*, 2010; Hansen *et al.*, 2012).

As an alternative to the *J*- and *M*-index, CPO strength can be quantified using eigenvalue analysis (where $\lambda_1 \geq \lambda_2 \geq \lambda_3$ are the maximum, intermediate and minimum eigenvalues of a spherical dataset). In addition to fabric strength, eigenvalue analysis of spherical data may also be used to describe fabric shape. The most basic of these approaches is the strength parameter, *C* (Woodcock, 1977),

$$C = \ln(S_1/S_3) \qquad \textit{Equation 5.4}$$

where $S_1 \geq S_2 \geq S_3$ are the normalised eigenvalues. *C* ranges from 0 (random) to infinity (single crystal) and is often used in conjunction with a plot of $\ln(S_2/S_3)$ (*x*-axis) against $\ln(S_1/S_2)$ (*y*-axis). On this plot, lines of *k* describe the symmetry of the eigenvalue distribution,

$$k = \frac{\ln(S_1/S_2)}{\ln(S_2/S_3)} \qquad \textit{Equation 5.5}$$

where $k < 1$ represents a oblate (flattening) strain (i.e. girdle distribution), $k = 1$ represents a plane strain and $k \rightarrow \infty$ represents a prolate (constrictional) strain (i.e. point maxima distribution) (i.e. Flinn plots, Ramsay & Huber, 1983).

Whilst the simplicity of *C* makes it an appealing option for fabric analysis, Lisle (1985) noted that on a plot of $\ln(S_2/S_3)$ against $\ln(S_1/S_2)$, contours of *C* are straight, but the distribution of eigenvalue ratios either side of the line, $k = 1$, which distinguishes girdle from point maxima fabrics, is asymmetric. This dichotomy implies that *C* behaves differently for girdle and point maxima distributions (Lisle, 1985). It was also noted that the critical value of *C* used to distinguish ordered fabrics from random fabrics varies with sample size (Woodcock & Naylor, 1983; Lisle, 1985). Consequently, Lisle (1985) proposed an alternative eigenvalue-based method of fabric analysis, the intensity parameter, *I* (Lisle, 1985),

$$I = 7.5\left[\left({S_1}^2 + {S_2}^2 + {S_3}^2\right) - {}^1/_3\right] \qquad \textit{Equation 5.6}$$

I ranges from 0 to 5 for point maxima distributions and 0 to 3.75 for girdle distributions. Unlike the strength parameter, *I* is independent of sample size and relates simply to the uniformity statistic, S_u (Mardia, 1975),

$$S_u = In \qquad \textit{Equation 5.7}$$

where *n* is the sample size. Fabrics with $S_u > 11.07$ and $S_u > 15.09$ suggest a deviations from uniformity with 95% and 99% confidence levels, respectively (Mardia, 1975). Additionally, it may be demonstrated graphically (see Figure 2 of Lisle, 1985) that *I* is less biased towards certain fabric shapes than *C* due to the curved nature of the contours of *I* on a plot of $\ln(S_2/S_3)$ against $\ln(S_1/S_2)$, which compensates for the asymmetry of eigenvalue ratios across the $k = 1$ line (Lisle, 1985). The Intensity parameter has been used to investigate the distribution of deformation strain with CPO analysis in a variety of tectonic settings (e.g. Tagami & Takeshita, 1998; Baratoux *et al.*, 2005; Okudaira *et al.*, 2010; Wallis, 2014).

Vollmer (1990) suggested the Point-Girdle-Random index (PGR) as a means to statistically quantify the shape of a fabric in terms of three fabric end members, point maxima (P), girdle (G) and random (R).

$$P = (\lambda_1 - \lambda_2)/N \qquad \textit{Equation 5.8}$$

$$G = 2(\lambda_2 - \lambda_3)/N \qquad \textit{Equation 5.9}$$

$$R = 3(\lambda_3)/N \qquad \textit{Equation 5.10}$$

where,

$$N = \lambda_1 + \lambda_2 + \lambda_3 \qquad \textit{Equation 5.11}$$

and,

$$P + G + R = 1 \qquad \textit{Equation 5.12}$$

The PGR index can be used more simply to measure the strength of a fabric by calculating (1 – *R*), where 0 represents a random fabric and 1 represents a perfect girdle or point maxima and produces similar trends to *C* and *J* (Vollmer, 1990; Barth *et al.*, 2010; Mainprice *et al.*, 2014).

5.2.3. Evaluation of CPO parameters

The CPO fabrics presented in Chapter 3 display a range of fabrics, including point maxima, girdles and random fabrics. Additionally some fabrics have multiple point maxima or partially formed girdles that have no relevance to the single crystal structure or deformation kinematics. In order to quantify the CPO in terms of relative strain magnitude, the chosen method must be able to distinguish well-ordered fabrics representative of a particular set of slip systems and strain geometries from fabrics with strong, but kinematically anomalous configurations. To determine the most appropriate parameter for describing CPO strength, 10 quartz *c*-axis pole figures (*PF1-10*) with a range of fabric shapes and strengths have been selected (Figure 5.1a) for analysis with all 5 parameter presented above.

Figure 5.1b-f presents the *J*, *M*, *C*, *I* and (1 – *R*) values of the *c*-axis distributions. The *c*-axes are selected for analysis as the multiplicity of all other axes prevents them from developing statistically recognisable single point maxima (Mainprice *et al.*, 2014). *J* was calculated using a built-in function in the MTEX textural analysis software (Bachmann *et al.*, 2010) for MATLAB (MathWorks, Inc.). *M, C, I* and (1 – *R*) were calculated using MTEX scripts provided by D. Mainprice, at the University of Montpellier (see Mainprice *et al.*, 2014 for examples). The pole figures are qualitatively (visually) arranged in

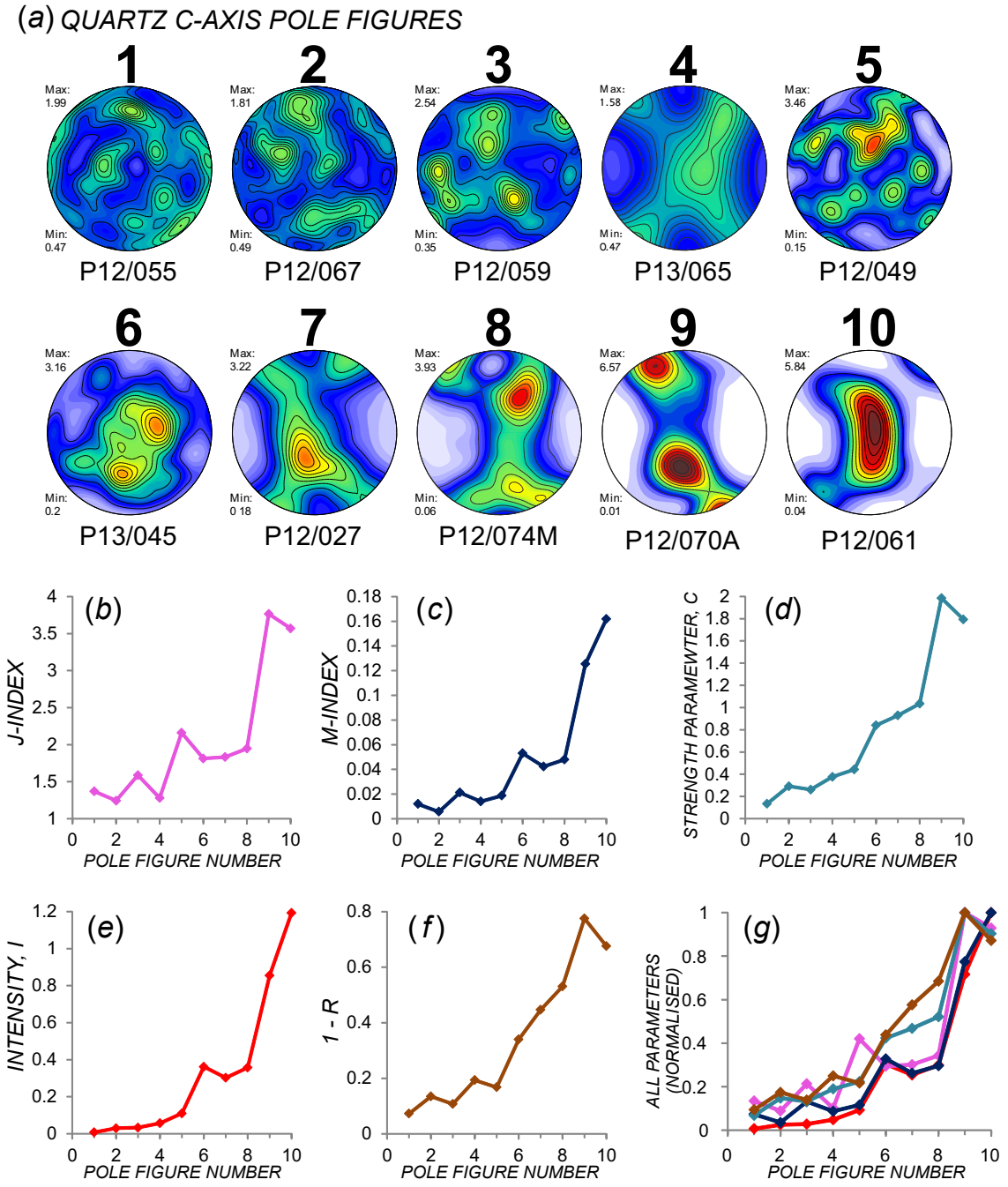

Figure 5.1. CPO fabric strength parameters. (*a*) A range of quartz *c*-axis CPO fabrics, plotted with antipodal projection in the *XZ* plane of the kinematic reference frame (*X* – parallel to lineation, *Z* – normal to foliation). Contours display multiples of uniform distribution. Maximum and minimum values of multiples of uniform distribution are presented next to each pole figure. Corresponding sample numbers are displayed below each pole figure. Pole figures are arranged qualitatively in order of least (1) to most (10) ordered fabric, determined through comparison with published examples of quartz CPO (see text). (*b-g*) Correlations between fabrics (indicated by pole figure number) and various statistical estimates of fabric attributes: (*b*) *J*-index, (*c*) *M*-index, (*d*) strength parameter, *C*, (*e*) intensity, *I*, (*f*) 1 – *R* (*g*) All parameters normalised to 1.

order, from 'random' to 'well-ordered', as determined from comparison with known examples of deformed quartz CPOs (e.g. Lister & Williams, 1979; Schmid & Casey, 1986; Law, 1990; Barth *et al.*, 2010).

Figure 5.1g displays the results of all five parameters on a single graph, normalised to 1 for comparison and reveals some important differences in behaviour. All parameters except *I* record noticeable differences between *PF1-3*, yet these fabrics have low strength (<2.5 m.u.d.) and no recognisable fabric. Qualitatively these fabrics are indistinguishable and the variations recorded by *J, M, C* and (1 – *R*) may carry no significance. *PF4* displays a recognisable cross-girdle fabric but has a low strength (1.6 m.u.d.). Importantly, *I, C* and (1 – *R*) classifies *PF4* as a stronger fabric than *PF1-3*. *J* classifies *PF4* as a weaker fabric than *PF1-3* (Figure 5.1b). *M* classifies *PF4* as a weaker fabric than *PF3* (Figure 5.1b). *PF5* displays a strong point maxima (3.5 m.u.d.) surrounded by several weaker point maxima. *I, M* and *C* classify *PF5* as a slightly stronger fabric than *PF4*. *PF5* is classified as a slightly weaker fabric than *PF4* by (1 – *R*) (Figure 5.1f). In contrast, *J* classifies *PF5* as a significantly stronger fabric than all other fabrics, except for *PF9-10*, and yet graphically *PF6-8* have similar strengths but better-defined structures than *PF5*. *PF6-8* have intermediate strengths (3.2-3.9 m.u.d.). *PF6* displays a broad but well defined point maximum parallel to *Y*, whilst *PF7* and *PF8* display well defined crossed-girdles. All parameters show little variation between these fabrics except for (1 – *R*), which produces a significant gradient between *PF6-8*. *I* and *M* classify *PF6* (a broad point maximum with two subsidiary maxima) as a slightly stronger fabric than *PF7-8.* However, this may be insignificant as qualitatively *PF6-8* appear similar in strength and definition. *PF9-10* display the visibly strongest fabrics. *PF9* (6.6 m.u.d.) displays a single girdle fabric with two strong point maxima. *C, J* and (1 – *R*), classify *PF9* as the strongest fabric and this may be in response to the density of the strongest point maximum. *PF10* (5.8 m.u.d.) displays a single point maximum with a weaker crossed-girdle fabric. *I* and *M* classify *PF10* as the strongest fabric of the data set, which suggests that they give more weight to fabric structure than the other parameters. *PF10* displays a more ‘classic’ quartz fabric structure than *PF9*. However, it is not clear which of these fabrics is representative of the highest strain.

All parameters clearly distinguish the strongest fabrics from the weakest (Figure 5.1g). However, the outlined trends reveal some important biases that control the behaviour of these parameters. *J* is highly sensitive to point maxima, and gives less weight to well-formed girdles (Figure 5.1b). Based on these findings, it is suggested that *J* should not be used to compare the strength of fabrics with variable geometries. Additionally, *M, C* and 1 - *R*, (Figure 5.1c,d,f) record noticeably different fabric strengths between fabrics that are visibly indistinguishable in appearance. In contrast, *I* (Figure 5.1e) statistically groups *PF1-5* (weak), *PF6-8* (intermediate) and *PF9-10* (strong) together and most closely matches the qualitative assessment of the fabric strengths (the arrangement from *PF1-10*). Based on these grounds, *I* has been chosen as the most

suitable parameter to quantify CPO strength as a proxy for relative strain magnitudes. The trends in Figure 5.1 suggest that (1 – *R*) may also be a suitable parameter to quantify CPO strength as a proxy for relative strain magnitudes.

5.3. AMS-based strain analysis

As discussed in Chapter 4, where AMS fabrics are controlled by deformation fabrics, the three-dimensional nature of AMS data allows for a direct correlation with the strain ellipsoid (e.g. Borradaile & Jackson, 2010; Ferré *et al.*, 2014). In Chapter 4 (*Section 4.6.1.*) a strong correlation between deformation and AMS fabrics is demonstrated and forms the basis for the use of AMS data as a proxy for strain with this data set. Previous AMS studies have used the degree of anisotropy, *P'*, as a proxy for finite strain (e.g. Borradaile, 1991; Benn, 1994; Tripathy, 2009). However, such correlations are warned against by many authors (e.g. Borradaile & Jackson, 2010; Ferré *et al.*, 2014), particularly when used with AMS data derived from differing rock types. In such cases, variations in *P'* more commonly reflect variations in magnetic carriers. The following section demonstrates why *P'* cannot be used as a strain proxy for this data set and outlines an alternative method for using AMS data as a strain proxy based on fabric orientations.

5.3.1. Argument against the use of *P'* as a proxy for strain

P' can only be used as a proxy for relative strain when all other parameters (mineral assemblage, grain size, magnetostatic grain interaction) remain constant between different samples (Borradaile, 1991; Borradaile & Jackson, 2010; Ferré *et al.*, 2014). Figure 5.2 demonstrates that *P'* cannot be used as a strain proxy for the samples analysed in this study, by regrouping the recorded values of *P'* vs K_m into diamagnetic, paramagnetic and ferromagnetic samples. Both *P'* and K_m vary between samples with the same type of magnetic carrier. For ferromagnetic samples, much of this variability is likely to reflect variations in grain size populations of magnetite, as detected in Chapter 4 (Table 4.3). An important observation worth highlighting is the distribution of ferromagnetic and paramagnetic samples, which cluster together. Whilst the low values

Figure 5.2. AMS parameters categorised by magnetic carrier. Bulk susceptibility (K_m), magnetic anisotropy (*P'*) and susceptibility ellipsoid shape parameter (*T*); same graphical convention used as in Figure 4.8, but with new symbol system. (*a*) Plot of magnetic anisotropy (*P'*) versus bulk susceptibility (K_m [*SI*]) of all measured sample cubes (small data points) and mean *P'* versus mean K_m of each whole sample (large data points). Error bars represent one standard deviation of mean *P'* and K_m. Dashed lines define a typical range of *P'* and K_m for paramagnetic samples (Tarling and Hrouda, 1993). (*b*) Plot of bulk susceptibility (K_m), versus shape parameter (*T*) of all measured sample cubes (small data points) overlain by mean K_m versus mean *T* of each whole sample (large data points). Error bars represent one standard deviation of mean *T* and K_m. See Chapter 4, *Section 4.3* for explanation of AMS parameters.

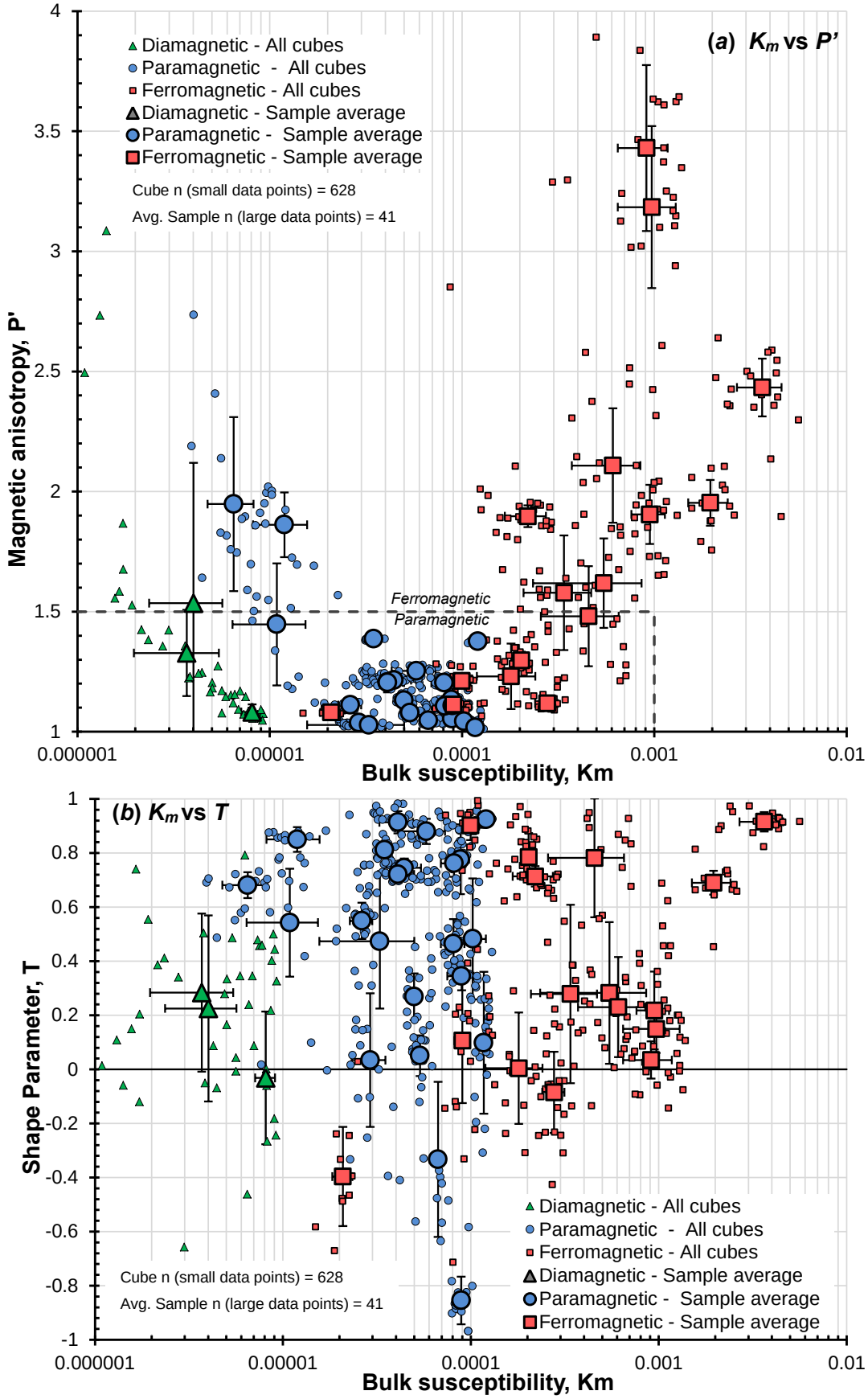

Figure 5.2. AMS parameters categorised by magnetic carrier

of *P'* and K_m of the former are more typical of the latter, hysteresis and FORC analyses (Chapter 4) identify magnetostatic single domain (MSD) magnetite as the magnetic carrier (Table 4.3). Without such additional analyses, these ferromagnetic samples with low *P'* – low K_m would have been misinterpreted as paramagnetic. This highlights the problem that for this data set, it is not possible to distinguish between changes in *P'* due to variations in strain and variations in magnetic carriers. This study does not, therefore, interpret variations in *P'* in terms of strain. An alternative approach to using AMS as a proxy for relative strain magnitude is presented below.

5.3.2. AMS fabric orientation as a proxy for shear strain

The angle φ', measured between the magnetic foliation and shear plane can be used to calculate a shear strain proxy, γ (Figure 5.3), for each sample using the equation (Ramsay & Huber, 1983):

$$\gamma = 2/\tan 2\varphi' \qquad \textit{Equation 5.13}$$

This approach was used by Housen *et al.* (1995) to quantify the shear strain of mylonites and granitic plutons. The calculation assumes that deformation occurred under a simple shear regime. In this study, the orientation of the regional foliation (S3 – *see Chapter 2*) is used as an approximation of the shear plane orientation, based on the parallelism between S3 transpositional fabrics and bounding shear zones of the UGHS. The angle φ' is measured between the poles of the magnetic and structural foliations. The angle between the stretching lineation and magnetic lineation is not used because in some situations the former is controlled by mineral SPO but the latter is controlled by mineral CPO (or vice-versa). In such a case, the magnetic and mineral lineations can become misorientated with respect to each other, whilst a close alignment between the magnetic and structural foliations is maintained. Consequently, φ' is calculated from the angle between the poles to the magnetic and structural foliations. Samples with an angle of $\varphi' > 45^{o}$ produce negative values of γ and are discarded on the grounds that their AMS fabric does not closely resemble the observed deformation fabrics and are, therefore, misrepresentative of the strain ellipsoid.

Previous studies found that magnetite AMS fabrics continue to rotate towards the shear plane up to shear strains of $\gamma = 13$ (Housen *et al.*, 1995; Ferré *et al.*, 2014). No further change in AMS fabric orientation was recorded above these strains. Additionally, AMS fabric orientation has only been used to calculate a shear strain proxy from ferromagnetic fabrics (Housen *et al.*, 1995; Djouadi *et al.*, 1997). In this study, the shear strain proxy is also used with paramagnetic samples. In order to account for

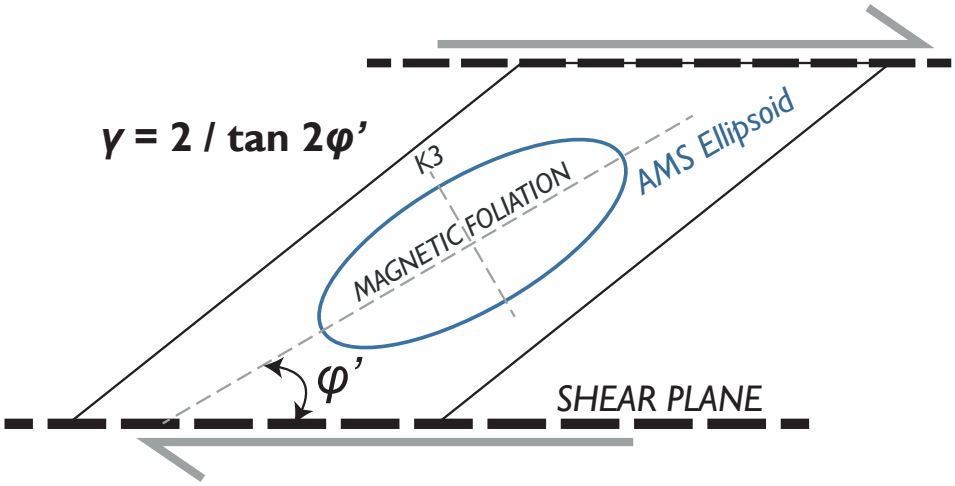

Figure 5.3. AMS shear strain proxy, γ (After Housen et al. 1995). γ is calculated from the equation shown. φ' is the angle between the magnetic foliation and the shear plane. This is calculated from angle between K_3 and the pole to the shear plane, which is approximated from the regional S3 foliation orientation.

differing magnetic properties, shear strain proxies calculated from paramagnetic and ferromagnetic samples must be interpreted separately. As the relationship between paramagnetic fabric orientation and shear strain has not been tested, relative variations in γ are more meaningful than the absolute values.

5.4. CPO & AMS strain proxy profiles

Based on the criteria outlined above, variations in CPO intensity (*I*) and AMS shear strain proxy (γ) can be used together as a proxy for relative strain magnitude. These parameters are calculated for each sample and plotted against their structural height above the MCT (Figures 5.4 & 5.5). The relative positions of unit boundaries and shear zones are also plotted on these profiles so that changes in *I* and γ can be correlated with changes in lithology and structure of the GHS and bounding units. These profiles are described below and form the basis for determining the vertical strain profile of the GHS in the Annapurna-Dhaulagiri Himalaya (*Section 5.5.1*).

5.4.1. CPO intensity profiles

Figure 5.4 displays the CPO intensity profiles for the Kali Gandaki and Modi Khola transects calculated for quartz, calcite and dolomite *c*-axis CPOs. The full data set for each of these profiles may be found in the supplementary materials CD. For clarity, quartz CPO intensity from the Kali Gandaki transect is presented on a separate plot (Figure 5.4a) to the calcite and dolomite CPO intensity (Figure 5.4b). For the Modi Khola transect the smaller sample size allows all CPO intensities to be plotted on a single profile (Figure 5.4d). Quartz CPO intensities are colour coded by lithology so that monomineralic and polymineralic assemblages can be distinguished to assess the effects of multiple mineralogy content on CPO development. Calcite and dolomite CPO

intensities are not grouped into lithologies as for each sample, calcite and/or dolomite are the volumetrically dominant mineral phase and/or the weakest phase, thereby negating the effects of multiple mineralogy content on CPO development. Deformation temperature profiles for each transect, determined in Chapter 3, are also presented (Figure 5.4c,e).

Structural variations in *I* reveal high and low intensity zones and intensity gradients. In the Kali Gandaki transect (Figure 5.4a-c), semipelitic samples and a single quartzite sample from the lower portion of the LGHS record very low quartz CPO intensities (<0.1). A significant peak in quartz CPO intensity (up to *I* = 1.1) is produced by quartzites in the Massive quartzite & marble unit in the middle of the LGHS. Above this, marble and semipelitic samples from the Metacarbonate & pelite unit produce low intensity (<0.2) quartz CPOs. From the top of the Massive quartzite & marble unit to the CT, calcite and dolomite CPO increase from low (<0.2) to intermediate (0.2-0.4) intensities. The strongest CPO intensity from the study (~1.2) is produced by a quartzite sample at the base of the UGHS close to the CT. Quartz CPO intensities from gneisses and schists in Unit I gradually decrease up-section from intermediate (0.5) to very low values (<0.1), most of which plot along a constant gradient. In Unit II, quartz CPO intensities are very low (<0.1), whilst calcite CPO intensities are low to intermediate (0.1-0.2). In Unit III, a slight increase in quartz CPO intensity is recorded in the gneisses in the footwall of the AD (~0.2). Within the STDS, quartz CPO intensities remain consistently very low (<0.1), with the exception of a small but noticeable increase in intensity (~0.2) in the immediate footwall of the STD. Calcite and dolomite CPO intensities decrease up-section from intermediate (~0.3) to low (~0.1) values, with noticeable spikes coincident with the positions of the AD (0.5) and STD (0.5-1.0). At the base of the THS in the immediate hangingwall of the STD, quartz CPO intensity has a noticeable spike that is similar to the adjacent spike recorded in the immediate STD footwall (~0.2). Above this, quartz CPO intensity remains very low (<0.1). Calcite and dolomite CPO intensities in the THS remain at low levels (0.1-0.2), with the exception of the uppermost sample, which produces a strong calcite CPO intensity (~0.6).

Figure 5.4. CPO intensity (I) profiles. CPO intensity, *I,* plotted at structural height above the MCT for each sample. (*a*) Quartz *c*-axis CPO intensity – Kali Gandaki. (*b*) Calcite and dolomite *c*-axis CPO intensity – Kali Gandaki (*d*) Quartz, calcite and dolomite *c*-axis CPO intensity – Modi Khola. (*a, d*) Coloured quartz CPO data points correspond to different rock types. (*b, d*) Calcite and dolomite CPO data points distinguished by yellow (calcite) and red (dolomite) circles. Data points overlay tectono-stratigraphic columns for each transect, plotted to scale. Major shear zones and their relative shear senses are also labelled. (*c, e)* Simplified deformation temperature profiles (to scale) for each transect showing zones of equal maximum and minimum deformation temperatures (determined from Chapter 3). (*f*) Key for the tectono-stratigraphic columns constructed for each profile.

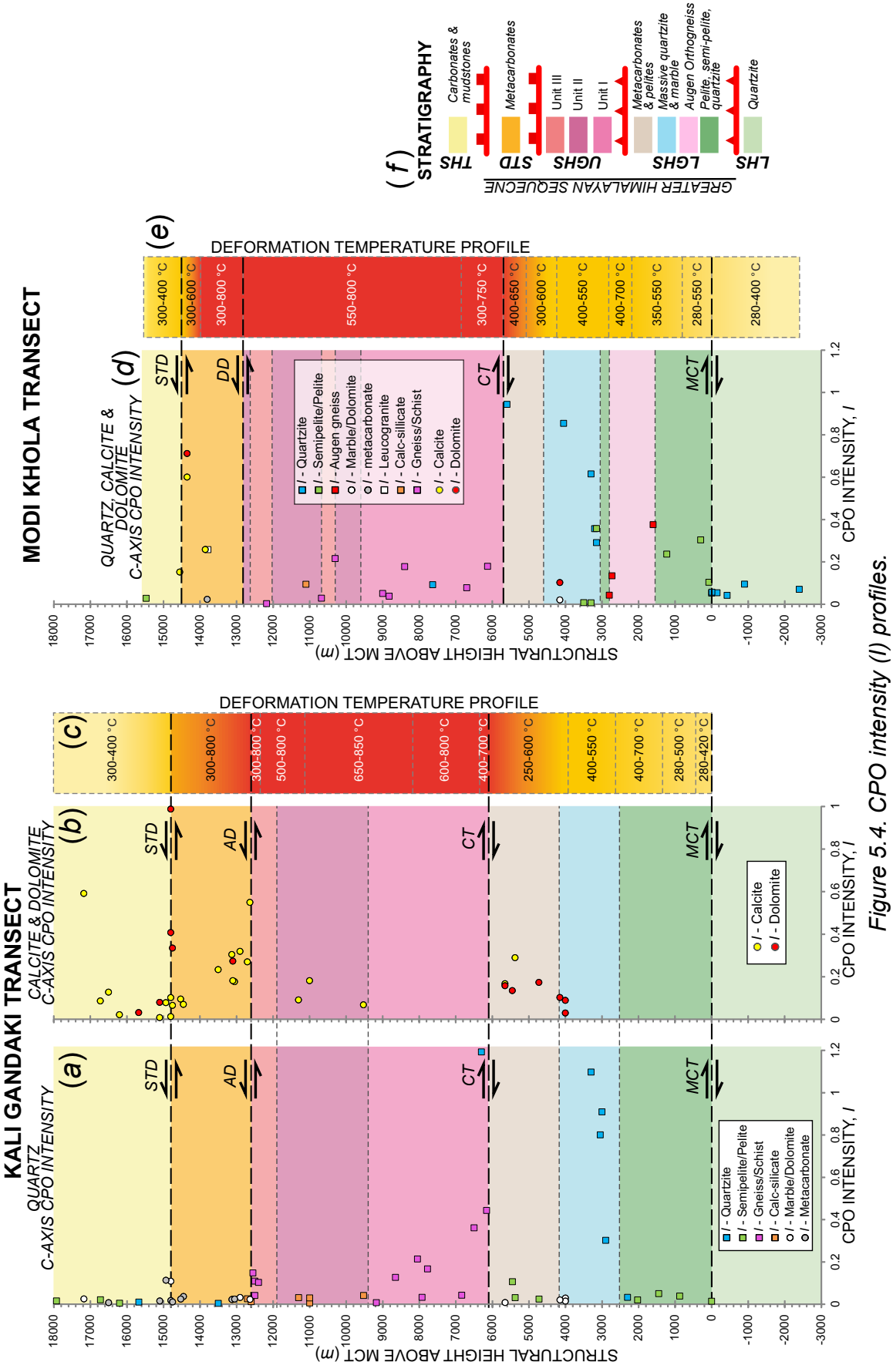

Figure 5.4. CPO intensity (I) profiles.

In the Modi Khola transect (Figure 5.4d,e), quartz CPOs from quartzites in the LHS have low CPO intensities (~0.1). In the LGHS, quartz CPO intensities show an approximately linear up-section increase (0.1 to ~1.0). Within the augen orthogneiss layer, quartz CPO has an intermediate intensity at the base (0.4) and low intensity at the top (0.1-0.2). Above this, quartzites from the Massive quartzite & marble unit show an up-section increase in CPO intensity (0.3 to 0.8), similar to the Kali Gandaki section. The strongest CPO intensity (~1.0) is produced by a quartzite at the top of the LGHS from the footwall of the CT. This is similar to the high quartz intensity recorded in the hangingwall of the CT in the Kali Gandaki transect. In the UGHS, quartz CPO intensities have low to intermediate values (~0.1-0.3) and have no discernible correlation with structural position or lithology. The STDS in the Modi Khola is poorly sampled. At the top of the GHS, quartz, calcite and dolomite CPOs, increase from intermediate intensity (~0.3) in the middle of the STDS to high intensities (0.6-0.7) in the footwall of the STD. In the THS, calcite, and quartz CPO intensities decrease to low values (<0.2).

5.4.2. AMS shear strain proxy profiles

Figure 5.5 shows a plot of γ against structural height above the MCT for AMS samples collected across the whole of the Kali Gandaki transect (Figure 5.5a) and from across the LHS and LGHS of the Modi Khola transect (Figure 5.5c). The deformation temperature profiles for both transects are also presented (Figure 5.5b,d). Values of γ are calculated from AMS data presented in Chapter 4. AMS samples P13/011M, P13/014M, and P13/028M are not shown on these profiles as the first two are believed to be faulted out of section by an unknown but potentially significant distance and the third is a younger sedimentary rock sample that post-dates Himalayan metamorphism. The dashed line at γ = 13 represents the limit at which previous studies have shown magnetite AMS fabrics to show no further decrease in φ' (Housen *et al.*, 1995; Ferré *et al.*, 2014). Many of the paramagnetic samples have γ >> 13 and this probably reflects the ease at which strong phyllosilicate CPOs develop (Borradaile, 1991; Housen *et al.*, 1995; Ferré *et al.*, 2014).

In the Kali Gandaki transect (Figure 5.5a), paramagnetic AMS fabrics produce relatively low values of γ in the Quartzite, semipelite and pelite unit and Metacarbonate and pelite unit (~5-20) and relatively high values of γ in the Massive quartzite and marble unit (~40). At the top of the LGHS, ferromagnetic AMS fabrics record γ of ~5. Sample density is insufficient to determine the magnitude of the lithological control on this trend. In the UGHS, both paramagnetic and ferromagnetic AMS samples record a peak value of γ = ~45 and γ = ~15, respectively at the base of the sequence. From this

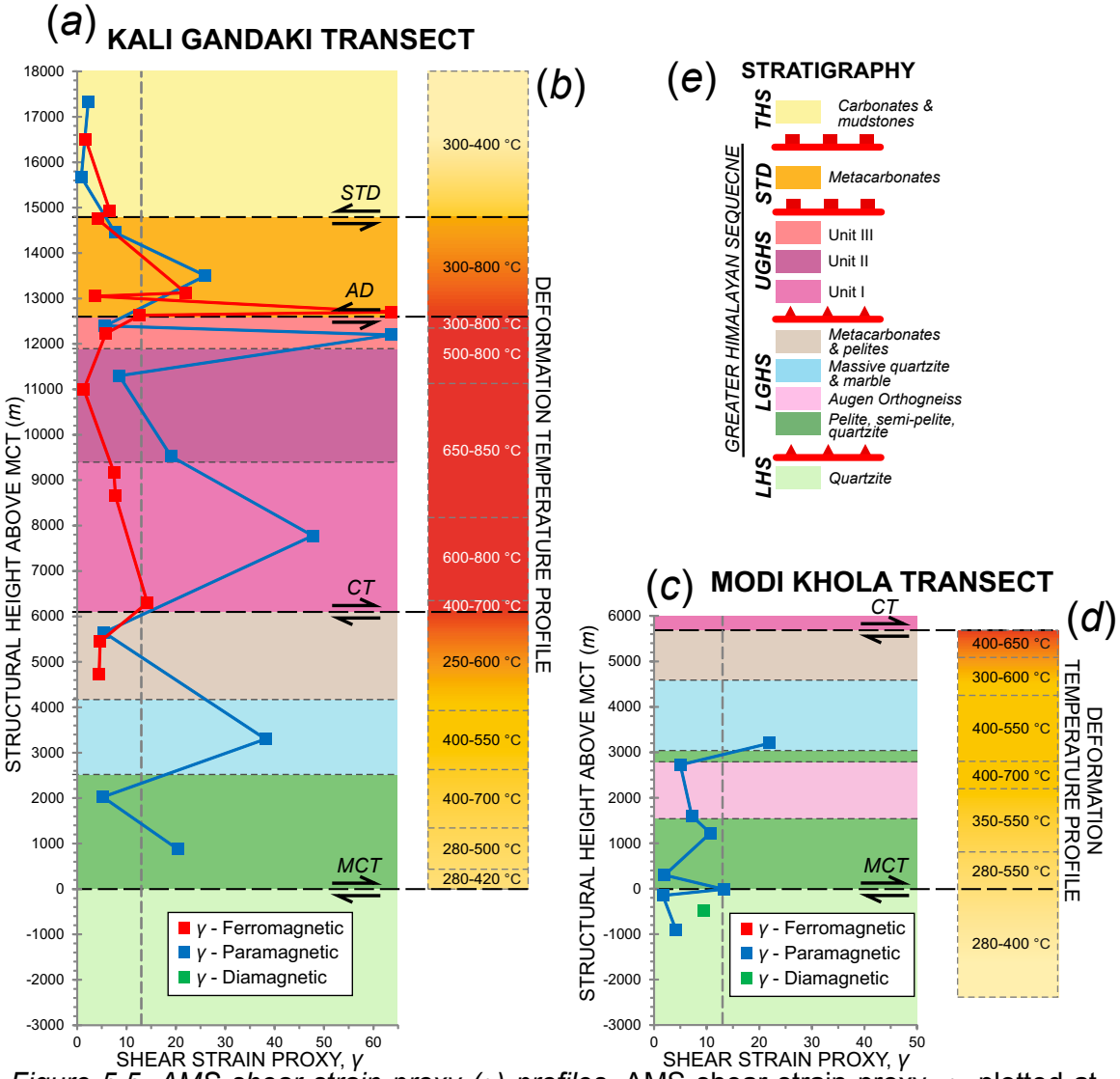

Figure 5.5. AMS shear strain proxy (γ) profiles. AMS shear strain proxy, γ, plotted at structural height above the MCT for each sample. (*a*) Kali Gandaki, (*c*) Modi Khola. γ is plotted against relative structural height above the MCT for each sample. Data points are distinguished as diamagnetic (green squares), paramagnetic (blue squares) and ferromagnetic (red squares) carriers. Vertical dashed grey line of γ = 13 represents the previously proposed maximum value of γ that can be measured for ferromagnetic AMS fabrics (Djouadi *et al.* 1997). Data points overlay a tectono-stratigraphic column for each transect plotted to scale. Major shear zones and their relative shear senses are also labelled. (*b, d*) Simplified deformation temperature profiles (to scale) for each transect showing zones of equal maximum and minimum deformation temperatures (determined from Chapter 3). (*e*) Key for the tectono-stratigraphic columns constructed for each profile.

position, paramagnetic and ferromagnetic γ decreases up-section to <10 and <5 respectively in Unit II. Above Unit II, ferromagnetic fabrics in Unit III increase to γ = ~12 in the footwall of the AD. Paramagnetic fabrics increase in γ, up-section sharply in Unit III (~65) and then decrease below the AD (<10). In the STDS, paramagnetic fabrics decrease up-section from γ = ~25 to γ <10. Ferromagnetic fabrics record a sharp increase in γ to ~65 in the hangingwall of the AD followed by a decrease to ~5 and then another increase to ~20. At the top of the STDS, γ is low for both paramagnetic (<5) and ferromagnetic (<7) fabrics.

In the Modi Khola transect (Figure 5.5c), AMS samples were only collected from the LHS and LGHS. Of these samples, one from the LHS is identified as diamagnetic, whilst the others are all identified as paramagnetic (Chapter 4). Low γ is recorded by both diamagnetic (<10) and paramagnetic (<5) fabrics in the LHS. A small, but noticeable spike in γ is recorded at the position of the MCT (~13). In the LGHS, γ increases up-section from ~2-10 in the Quartzite, semipelite and pelite unit to ~20 at the base of the Massive quartzite and marble unit. Between these samples, the augen orthogneiss unit records γ of ~5-7.

It is acknowledged that the calculated shear strain values are large, and yet many of the accompanying microstructures observed in these samples do not reflect such high strain conditions (*Chapter 3*). Firstly, the assumption that the regional foliation orientation defines the shear plane orientation needs evaluating. If, in fact, shear plane and regional foliation orientations are not parallel then the calculated shear strains are over-estimates. However, based on the field and fabric relationships between the regional S3 foliation and the orientation of the bounding shear zones, such an assumption is not unreasonable. In samples and field locations with well-defined S-C fabrics, the regional S3 foliation is parallel to the C-plane orientation. Additionally, the dichotomy between high shear strain values and apparently low strain microstructures in the GHS may be the result of continuous dynamic recrystallisation during deformation, which prevented the development of well-defined grain shape fabrics and fabric anisotropies, in a manner comparable to the development of a 'steady-state' foliation (Means, 1981). In this case, the regional S3 foliation may have developed parallel to the shear plane, which would require less shear strain than that needed to rotate an existing fabric into parallelism with the shear plane. Based on these considerations, and on those presented in *Section 5.3.2.*, it is reiterated that the AMS shear strain proxy is best interpreted in terms of its relative trends across the profiles rather than in terms of absolute values of shear strain.

5.5.1. Vertical strain profile through the GHS, Annapurna-Dhaulagiri Himalaya

Through cross correlation of the trends displayed by *I* (Figure 5.4) and γ (Figure 5.5) it is possible to construct a relative strain magnitude proxy profile for the Kali Gandaki and Modi Khola transects (Figure 5.6). The thick dark grey lines on each profile represent changes in relative strain magnitude (RSM). Dashed horizontal lines show the positions of the major shear zones (thick lines) and unit boundaries (thin lines). The RSM curves are derived through qualitative assessment of the relative changes in both *I* and γ, which are also plotted on the RSM profiles (Figure 5.6). The overall shape of the RSM curve is determined from the common trends displayed by both *I* and γ. When drawing the strain profile curve, CPO intensities for monomineralic quartzites (light grey

squares) were ascribed the most importance, followed by calcite and dolomite CPO intensities (light and dark grey circles). These CPOs are expected to have the closest correlation to strain magnitudes as they have not been influenced by the presence of a second phase (*see Section 5.2.1.*), and are used to determine the relative amplitude of the peaks and troughs of the RSM curves. Values of *I* determined from polymineralic samples are useful for determining relative trends in RSM but record less strain than monomineralic samples, due to the weakening effect of poly-mineral assemblages on CPO strength. As such, the amplitude of the RSM curve against the horizontal axis (relative strain) is always relative to the position of polymineralic *I* data points. Where it is possible to draw different trends in RSM through the same tectono-stratigraphic unit, the simplest trend is chosen (solid thick grey line). The more complex trends in RSM (dashed thick grey line) are drawn as possible deviations from the simplest trend. It is not possible to determine the significance of these more complicated RSM profiles (dashed lines) due to the various types of data used on the profile. As such, both should be considered as possible representatives of the distribution of strain across the GHS and bounding units. To the right of each strain profile in Figure 5.6 is the corresponding deformation temperature profile showing structural variations in maximum and minimum deformation temperatures. It is important to acknowledge that the construction of these RSM curves is a qualitative process and the absolute amplitudes of the peaks and troughs are subjective. However, the *relative* size and shape of peaks, troughs and gradients are more accurately constrained as the use of two independently determined data sets allows for a robust evaluation of variations in RSM. As such, these profiles (Figure 5.6a,b) provide the first detailed assessment of the relative distribution of strain across the whole of the GHS and its bounding units.

5.5.1.1. Kali Gandaki transect

In the Kali Gandaki transect (Figure 5.6a) a small peak in RSM coincident with the MCT is inferred from a down-section extrapolation of γ and from an intensification in foliation intensity observed in the field. RSM increases up-section through the LGHS towards the CT and correlates with an increase in peak deformation temperatures from ~420 ^{o}C to ~600 ^{o}C. The simplest RSM profile displays a linear up-section increase through the LGHS. It is possible that RSM may deviate from this linear trend, in sympathy with changes in rock type and may be greater in the Massive quartzite and marble unit than in the other units above and below. However, the apparent increase in RSM in the Massive quartzite and marble unit also correlates with the position of high intensity monomineralic quartz CPO (Figure 5.4). Furthermore, samples from below the Massive quartzite and marble unit contained relict porphyroclasts with well-developed Chess Board Subgrain (CBS) textures, indicating the presence of older (possibly pre-

Himalaya) fabrics which may hinder subsequent (i.e. S3) CPO development (Chapter 3, Figure 3.1). Similarly, samples at the top of the LGHS in the Metacarbonate and pelite unit are dominated by a mix of carbonate and phyllosilicate phases and contain multiple deformation fabrics (e.g. S-C fabrics, crenulation cleavage, etc. Figures 3.2 & 3.3). Recognition of these features indicates that that the low values of *I* and γ could have been influenced by factors other than relative strain magnitude. As such, the simple linear gradient of RSM is the most appropriate profile for the LGHS, although local variations in RSM due to lithology-driven mechanical anisotropies may occur.

In the UGHS, peak RSM is coincident with the location of the CT. Both *I* and γ record an up-section decrease in RSM through Unit I, with a relatively linear gradient. Minimum RSM is recorded in Unit II. At the top of the UGHS, RSM increases up-section towards the footwall of the AD. Additionally, paramagnetic AMS fabrics record a localised spike in RSM in Unit III, coincident with the location of the Kalopani Shear Zone (Figure 2.4). The low RSM in the UGHS is supported by observations of large grain sizes and high temperature deformation microstructures with no SPO (Figure 3.5), which suggest that differential stresses were low. Peaks in RSM at the margins of the UGHS also correlate with zones of lower minimum deformation temperatures. In the STDS, a spike in *I* and γ correlate with the high strain zone across the AD. From the AD, RSM decreases up-section through the STDS, and produces a localised spike coincident with the position of the STD. In the THS, both deformation temperature and RSM are low, although an increase in RSM towards the top of the section may be due to deformation on the Dangardzong fault during extension of the Thakkhola graben (*Section 2.5.6.*).

5.5.1.2. Modi Khola transect

The Modi Khola transect (Figure 5.6b) displays similar trends in RSM to the Kali Gandaki transect. At the base of the transect, low RSM is recorded in the LHS, coincident with low deformation temperatures. Paramagnetic AMS fabrics record a spike in RSM coincident with the position of the MCT, whilst CPO intensities remain unchanged. This may reflect the partitioning of deformation into phyllosilicate phases. In the LGHS, an up-section increase in RSM is recorded. The simplest RSM profile for the LGHS displays a linear increase. However, minor variations in *I* and γ suggest that RSM may deviate from this linear trend due to changes in lithology. Across the Augen orthogneiss unit RSM appears to remain relatively constant. RSM in the Massive quartzite and marble increases up-section. Above the Massive quartzite and marble unit, RSM is poorly constrained by a single sample from the footwall of the CT that indicates that RSM is greatest at the top of the LGHS. As with the Kali Gandaki transect, variations of *I* and γ in the LGHS of the Modi Khola transect also correlate

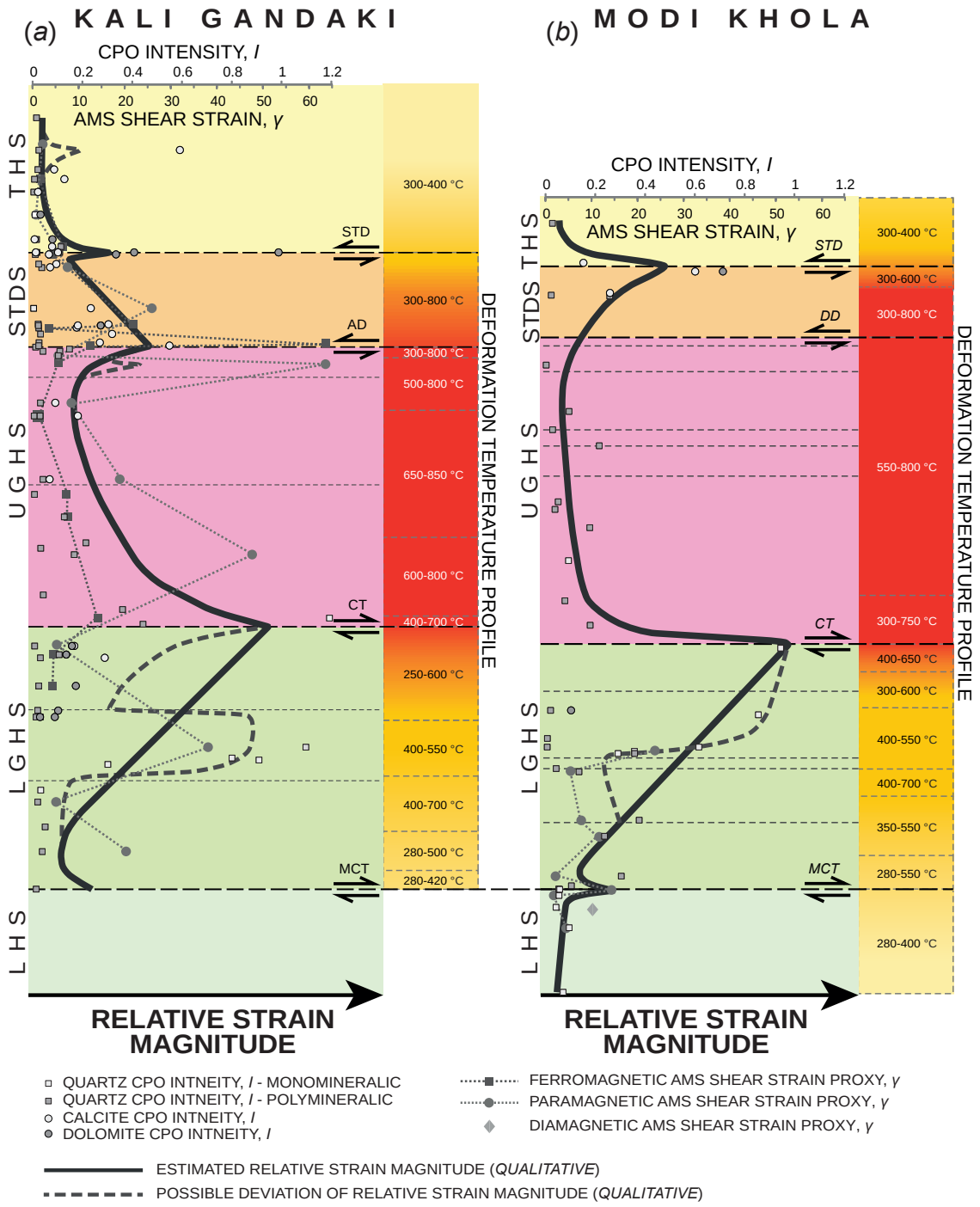

Figure 5.6. Relative strain magnitude (RSM) profiles. (*a*) Kali Gandaki, (*b*) Modi Khola. Thick solid dark grey line represents RSM, determined through qualitative assessment of the observed trends in *I* and γ. Thick *dashed* dark grey line represents possible deviations in RSM suggested by small scale variations in *I* and γ (see text for discussion). *I* and γ are plotted together to scale. Horizontal dashed lines represent unit bounding shear zones (thick) and lithological boundaries (thin). Right of each profile is a summarised deformation temperature profile (to scale) for each transect showing zones of equal maximum and minimum deformation temperatures (determined from Chapter 3).

with changes in sample lithology and mineral content and as such, the strain-related significance of these small scale trends is unclear. Consequently, a linear profile is the most appropriate approximation of RSM in the LGHS, although the possibility of strain localisation due to lithology-driven mechanical anisotropy is acknowledged.

In the UGHS, RSM decreases sharply up-section of the CT to a constant low level. This correlates with a homogenous distribution of deformation temperatures (relative to the Kali Gandaki transect). As with the Kali Gandaki transect, low RSM in the UGHS of the Modi Khola transect is supported by the large grain sizes and high temperature deformation microstructures with no SPO (Figure 3.5), which may be indicative of low differential stresses. Whilst minor fluctuations in *I* are recorded, it is not clear whether these have any strain-related significance as the spatial coverage of CPO data and absence of AMS data are insufficient for such interpretations. At the top of the UGHS and within the STDS, an increase in RSM might be expected in response to deformation on the DD but data from this section are too sparse for testing this hypothesis. At the top of the STDS, RSM is high, presumably due to deformation on the STD. In the THS, at the top of the Modi Khola transect, RSM decreases to a low level, coincident with an up-section decrease in deformation temperature.

5.5.2. Strain types

Strain types across each profile are estimated from field structural (*Chapter 2*) and microstructural (*Chapter 3*) observations. Shear bands, S-C fabrics, sheared and folded quartz veins and rotated porphyroclasts observed throughout the LGHS are indicative of a dominantly non-coaxial deformation. Quartz and calcite CPO geometries from the LGHS also suggest that the recorded deformation is dominantly non-coaxial. Within the UGHS S-C fabrics, rotated porphyroblasts and quartz CPO geometries from the hangingwall of the CT record non-coaxial deformation. Above this, field and microstructural observations from the UGHS record both coaxial and non-coaxial deformation (i.e. general shear). Where present, deformed leucosomes show signs of both coaxial and non-coaxial shearing, folding and stretching. In thin section, grain shape fabrics from the UGHS rarely display any shear sense and porphyroblast do not record any rotation, suggesting that the ratio of non-coaxial to coaxial deformation (i.e. vorticity) is low. Quartz and feldspar CPO geometries from the UGHS are dominantly indicative of coaxial deformation, although non-coaxial fabrics are sometimes observed. In the STDS, shear bands and folded leucosomes observed in the field and grain shape fabrics, rotated porphyroblasts and calcite CPO geometries suggest that the recorded deformation is dominantly non-coaxial. However, subordinate boudinaged leucosomes and porphyroblasts suggests that this deformation was accompanied by a minor component of coaxial deformation (i.e. general shear with a large vorticity).

5.5.3. Kinematic implications

Spikes in RSM are coincident with the major sequence-bounding shear zones, reflecting the high degree of deformation localised on these structures (Figure 5.6). The

CT displays the highest peak in RSM and the largest range of deformation temperatures (700-750 ^{o}C to 300-400 ^{o}C). This implies that the CT was a long-lived structure that accommodated a significant amount of deformation (relative to the other shear zone) from high temperatures during mid-crustal extrusion through to lower temperatures during upper-crustal exhumation. The MCT and STD produce smaller and also narrower spikes of RSM, indicative of more discrete structures. In the case of the MCT, this may reflect the lower minimum temperature down to which this structure was active compared with the other shear zones on these transects (Figure 5.6).

The RSM profiles also reveal zones of low (relative) strain and strain gradients. The lowest RSM is interpreted in the LHS and THS. In the LHS, this correlates with relatively undeformed field structural and microstructural observations (Chapters 2 & 3). In the THS, field structural observations indicate that this sequence has been deformed on a regional-scale (Chapter 2). However, on a microstructural scale, deformation is largely accommodated by phyllosilicate phases during cleavage development, with little or no crystal-plastic deformation in other phases and the intensity of deformation is low relative to microstructures observed from the GHS (Chapter 3). A strong calcite CPO at the top of the Kali Gandaki transect (Figure 5.6a) relates to localised deformation on the Dangardzong fault during E-W extension of the Thakkhola graben (*Section 2.5.6.*).

In both the Kali Gandaki (Figure 5.6a) and Modi Khola (Figure 5.6b) transects, RSM decreases down-section from the top of the LGHS to its base, indicative of a zone of pervasive deformation. Localised peaks and troughs in RSM may also exist within the LGHS, possibly correlating with changes in lithology. Correlation with maximum and minimum deformation temperatures in the LGHS suggests that this zone of deformation expanded down-section towards the MCT as the overlying UGHS exhumed through lower and lower temperatures. The localised low temperature deformation microstructures at the top and bottom of the LGHS reflect a late stage localisation of strain in the weaker metacarbonate, pelitic and semipelitic units. This late stage deformation, accommodated on mechanically weak phyllosilicate- and calcite-rich layers could serve to disrupt deformation fabrics in mechanically stronger quartz- and dolomite-rich layers (e.g. through development of a crenulation cleavage), thus explaining the reductions in I and γ without need for reduction in RSM. A gradient of up-section decreasing RSM in the STDS on the Kali Gandaki transect (Figure 5.6a) is also observed, which correlates with an up-section decrease in peak temperatures (*Chapters 2 & 3*). Given the scarcity of data from the STDS of the Modi Khola transect, no reliable geological interpretations can be made from the differences in RSM in the STDS between the two transect.

Low RSM in the middle of the UGHS may suggest that high temperature deformation was not intense, although continuous dynamic recrystallisation may also be responsible to a certain degree for the reduced intensity of fabrics across the UGHS (e.g. Means, 1981). The gradual up-section decrease in RSM through Unit I from the CT in the Kali Gandaki transect (Figure 5.6a) may reflect the occurrence of strain partitioning at high temperature, as proposed in Chapter 3, based on the observed reduction in minimum deformation temperatures towards the margins of the UGHS. This high temperature strain partitioning is not recorded in the UGHS of the Modi Khola transect, which may account for the constant level of RSM interpreted in the UGHS along this transect (Figure 5.6b) and suggests a more homogeneous distribution of high temperature deformation relative to the Kali Gandaki transect (Figure 5.6a). Importantly, a concentration of deformation at the margins of the UGHS relative to its centre is compatible with the geological criteria for channel flow (*Section 1.3.5.*). Additionally, in the Kali Gandaki transect, AMS fabrics at the top of the UGHS suggest a localised peak in RSM in Unit III that is coincident with the location of the Kalopani Shear Zone (*see Section 2.5.3*). The discrete nature of this spike suggests that it may be an overprint on the otherwise smooth RSM curve, which supports evidence that the Kalopani shear zone is a syn- to post-peak metamorphic structure (e.g. Vannay & Hodges, 1996).

Trends in RSM reveal structurally distinct strain domains that correlate with changes in deformation temperatures and may correspond to distinct stages in development of the Himalayan orogen, as proposed in Chapter 3. The identification of these domains and different tectonic stages has implications for models of Himalayan orogenesis and provide the focus of discussion for Chapter 7.

5.6. Conclusions

Consideration of the factors that control CPO and AMS fabric development have aided the use of CPO and AMS data as proxies for strain. The resulting RSM profiles are the first of their kind for the GHS and the Himalayan orogen. The following conclusions have been made from this study:

1) Graphical comparisons of parameters, *C*, *I*, *M*, *J* and (1 – *R*) used to describe the strength of CPO data indicate that *I* is the most suitable parameter for quantifying CPO strength as a proxy for relative strain magnitude. The parameter (1 – *R*) was also found to be a suitable parameter for quantifying CPO strength. The *J*-index was the least suitable parameter due to its bias to point maxima over girdles.
2) Chapter 4 demonstrated a genetic link between AMS and deformation fabrics and validates the use of this AMS dataset for strain analysis. It is demonstrated

graphically that the degree of anisotropy, *P'*, is not an appropriate parameter for strain analysis with AMS data due to the inability to distinguish the relative contributions of mineral content from strain. Assuming that deformation was produced by simple shear, the AMS shear strain proxy, γ, calculated from the angle between the magnetic foliation and the shear plane is recommended.

3) Trends in *I* and γ are compared and cross-correlated to construct relative strain magnitude (RSM) profiles for the Modi Khola and Kali Gandaki transect. The independent methods from which *I* and γ are derived add weight to interpretations made from trends identified by the two parameters.
4) The RSM profiles identify high strain zones coincident with the location of the MCT, STD, CT and AD. The highest peak in RSM is produced by the CT, which also has the largest range of deformation temperatures. This suggests that the CT is a long lived structure that remained active from high to low temperatures during cooling/exhumation.
5) Low RSM recorded in the LHS and THS reflects a significant reduction in deformation relative to the GHS. A peak in calcite *I* at the top of the Kali Gandaki transect correlates to deformation on the Dangardzong fault during E-W extension of the Thakkhola graben.
6) Trends in RSM in the LGHS are indicative of a zone of pervasive deformation. Correlation with deformation temperature gradients suggests that a zone of active deformation broadened as a deformation front migrated down-section from the CT during exhumation of the overlying UGHS with decreasing temperatures. Reductions in *I* and γ at the top and bottom of the LGHS may relate to strain localisation into weaker rock units at low temperatures causing a disruption to CPO and AMS fabrics.
7) High temperature deformation in the UGHS is concentrated towards the margins of this tectonic unit. The intensity of deformation in the middle of the UGHS is low. An isolated peak in γ in Unit III of the Kali Gandaki transect may reflect syn- to post-peak-metamorphic deformation on the Kalopani Shear Zone.
8) The gradual up-section decrease in RSM recorded through Unit I in the UGHS of the Kali Gandaki transect coincides with lower minimum deformation temperatures recorded towards the margins of the UGHS. This gradual decrease in RSM may reflect strain partitioning at high temperatures. RSM and deformation temperatures are approximately homogeneous through the UGHS in the Modi Khola transect, suggesting that high temperature strain partitioning did not occur on this transect.
9) An increase in RSM from the centre of the UGHS to its margins fulfils one of the criteria for mid-crustal channel flow (*Section 1.3.5.*).

10) Correlation of RSM and deformation temperatures suggests that the Annapurna-Dhaulagiri Himalaya can be divided into distinct orogenic domains. These domains may correlate to specific stages in the development of the Himalayan orogen that occurred at different crustal depths and temperatures.

- CHAPTER 6 -

RELATIVE VELOCITY PROFILES FOR THE GHS AND BOUNDING UNITS

The relative strain profiles determined from CPO and AMS strain proxies (Figure 5.6) provide valuable insights into the distribution of deformation across the GHS and bounding units. These profiles present an opportunity to test the kinematic predictions of channel flow models (e.g. Beaumont *et al.*, 2001; Grujic *et al.*, 2002; Beaumont *et al.*, 2004; Jamieson *et al.*, 2004; Grujic, 2006; Jamieson *et al.*, 2006). The model predictions can be tested further by considering the velocity structures of 1-dimensional channel flows and how these relate to strain distributions.

In this chapter the basic controls of channel flow are explored via a series of simple mechanical models. Following this, the relative strain profiles for the GHS and bounding units are converted into relative velocity profiles based on the numerical relationship between velocity and strain rate. The relative velocity profiles for the GHS and bounding units are then compared to the mechanical models to explore their rheological behaviours. Finally, kinematic interpretations of the relative velocity profiles for the GHS and bounding units are presented and their implications for the channel flow model for the Himalayan orogen are discussed.

6.1. The mechanics of channel flow

Flow of a viscous fluid between parallel-sided channel walls can be driven by shear stresses relating to channel-parallel motion of the channel walls (Couette flow) and/or channel-parallel pressure gradients within the channel (Poiseuille flow). These end-member flow models can be distinguished by their resulting velocity profiles (Figure 6.1) (Turcotte & Schubert, 2002; Grujic, 2006; Mukherjee, 2013b, 2014). Where channel wall motion and a pressure gradient are applied in opposing directions, a Hybrid flow is formed with a velocity structure resulting from a composite of both Couette flow and Poiseuille flow (Figure 6.1c) (Turcotte & Schubert, 2002; Grujic, 2006). If the relative contribution of Poiseuille flow is great enough, return-flow of channel material can occur in the opposite direction to the moving channel wall (Turcotte & Schubert, 2002; Grujic, 2006). It is under these conditions that channel flow during the Himalayan orogeny is proposed to have occurred (Beaumont *et al.*, 2001; Beaumont *et al.*, 2004; Jain *et al.*, 2005; Grujic, 2006).

In order to better understand the basic mechanical controls of channel flow, several analytical velocity models of a 1-dimensional laminar flow between parallel sided channel walls are constructed based on well-established principles of fluid mechanics (Turcotte & Schubert, 2002). Models with divergent channel walls (e.g. Mukherjee &

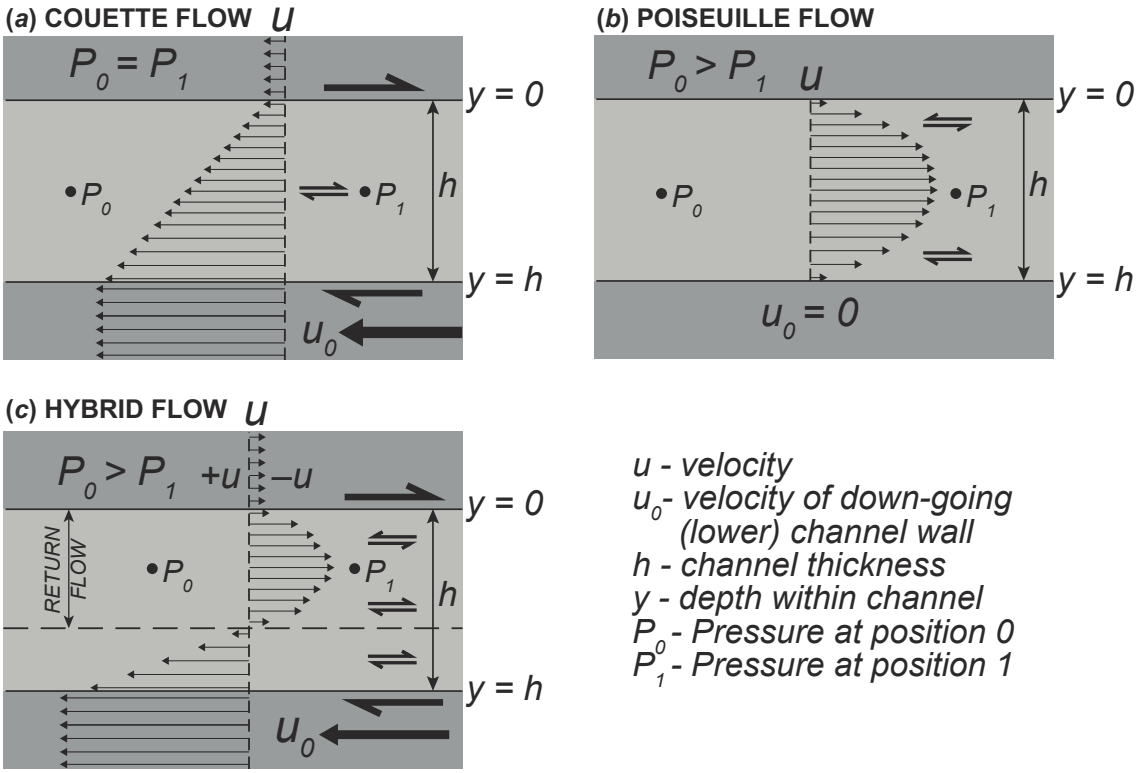

Figure 6.1. Simplified 1-Dimensional channel flow velocity profiles. After Grujic 2006. All models follow same key, displayed in figure. Channel defined by light grey rectangle. Rigid channel walls defined by dark grey rectangles. No slip boundary conditions apply (see text for discussion) (*a*) Couette flow – due to dextral shear between channel walls. Pressure gradient between P_0 and P_1 = 0. (*b*) Poiseuille flow – due to positive pressure gradient between P_0 and P_1. Channel walls are stationary. (*c*) Hybrid flow. Due to combined effects of dextral shear between channel walls plus a positive pressure gradient between P_0 and P_1. Return flow occurs in the opposite direction to the down going (bottom) channel wall.

Koyi, 2010) are not considered as these are based on the exhumed structure of the GHS exposed at the surface. Geophysical observations and thermo-mechanical simulations suggest that at mid-crustal depths the rheological boundaries to a weak, partially molten mid-crustal layer (i.e. the proposed channel) are (sub)-parallel (Nelson *et al.*, 1996; Beaumont *et al.*, 2001; Unsworth *et al.*, 2005; Nábelek *et al.*, 2009). The models are designed to show how velocity profiles vary under different boundary conditions, rather than to replicate settings comparable to the Himalayan-Tibetan orogenic system (e.g. Beaumont *et al.*, 2001). Crucially, the derivative of the velocity profile represents the strain rate profile (Turcotte & Schubert, 2002). Understanding how strain rate varies between these flow models provides an opportunity to compare the relative strain profiles presented in Chapter 5 (Figure 5.6) to a laminar viscous flow. First, the basic controls of Couette and Poiseuille flows are explored. All equations below are taken from Turcotte and Schubert (2002).

For a Couette flow of a homogeneous linear viscous fluid, channel velocity (u_c), is driven by the shear stress produced from channel-parallel motion of one of the channel walls, with a velocity, (u_0),

$$u_c = u_0(y^2 - hy) \qquad \textit{Equation 6.1.}$$

with channel thickness (h), and vertical distance from the moving plate (y). Additionally, the velocity is related to the shear stress (τ) and viscosity (μ), through the equation,

$$\frac{\tau}{\mu} = \frac{du}{dy} \qquad \textit{Equation 6.2.}$$

This and all subsequent models assume no-slip boundary conditions; $u_c = 0$ at $y = h$ and $u_c = u_0$ at $y = 0$ (Turcotte & Schubert, 2002). Figure 6.2 demonstrates how the velocity profile of a Couette flow varies with increasing, τ and μ. The derivation of a Couette velocity profile defines a uniform strain rate profile (Figure 6.2c).

Poiseuille flow is driven by a lateral pressure gradient defined as,

$$\frac{dp}{dx} = -\frac{(p_1 - p_0)}{L} \qquad \textit{Equation 6.3.}$$

where p_1 and p_0 represent the pressure at either end of a channel of length *L* and $p_1 > p_0$ produces a pressure gradient in the channel-parallel direction (x) (Turcotte & Schubert, 2002). For a linear viscous homogeneous channel with $u_0 = 0$, and $dp/dx \neq 0$, the velocity of a Poiseuille flow (u_p) is defined as,

$$u_p = \frac{1}{2\mu}\frac{dp}{dx}(y^2 - hy) \qquad \textit{Equation 6.4.}$$

For a given channel thickness, h, the shape of a linear viscous Poiseuille flow is controlled by viscosity, μ, and pressure gradient, dp/dx (Figure 6.3). An increase in pressure gradient and/or decrease in viscosity increases the maximum velocity at the centre of the channel and the velocity gradient from the channel walls to the channel centre (Figure 6.3). The resulting strain rate profiles display maximum strain rate at the channel walls and zero strain rate at the channel centre (Figure 6.3c). Larger velocity at the centre of the channel produces larger strain rate at the margin, whilst the rate of change in strain rate remains constant for each profile (Figure 6.3c).

Deformation experiments have shown that natural rocks tend to behave as non-Newtonian materials with a power law rheology (e.g. Gleason & Tullis, 1995; Rutter, 1999; Hirth ***et al.***, 2001). In such situations, the shear stress and velocity gradient (i.e. strain rate) are defined as,

$$\frac{du}{dy} = C_1\tau^n \qquad \textit{Equation 6.5.}$$

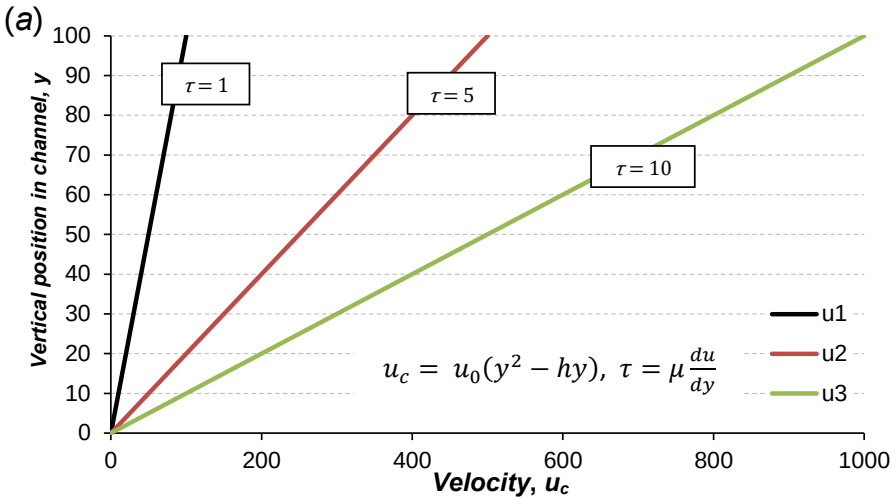

	τ	μ	u_0	h
u1	1	1	100	100
u2	5	1	500	100
u3	10	1	1000	100

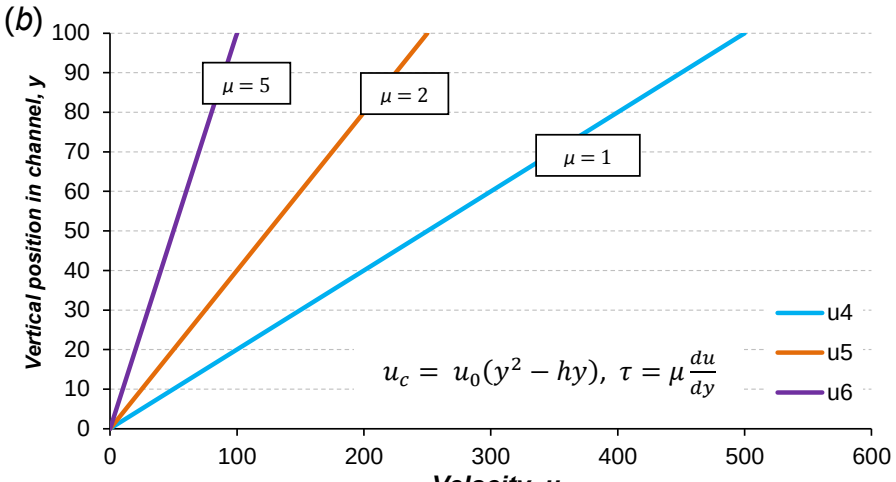

	τ	μ	u_0	h
u4	5	5	500	100
u5	5	2	500	100
u6	5	1	500	100

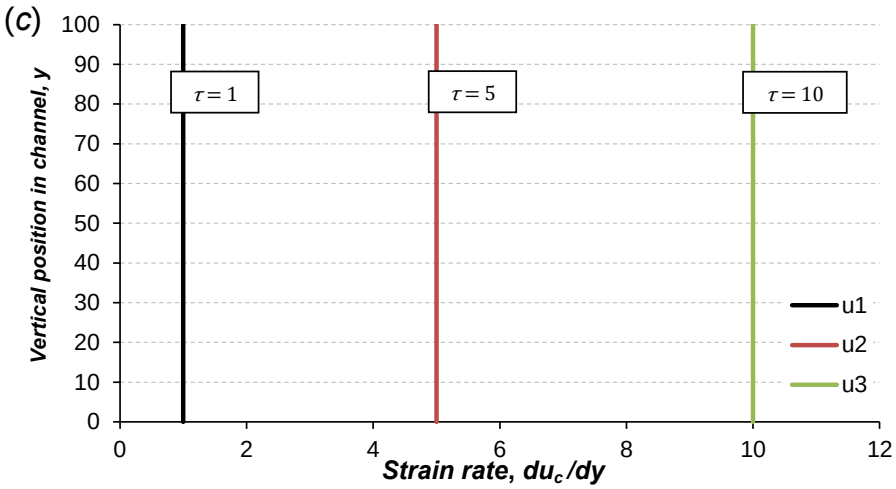

Figure 6.2. Couette flow velocity and strain rate profiles. (*a*) Couette flow velocity profiles for variable shear stress, τ. (*b*) Couette flow velocity profiles for variable viscosity, μ. (*c*) Corresponding strain rate profile calculated from (*a*). Velocity equations presented on each plot. Parameters used in calculations are listed below each plot. See text for full discussion.

C_1 is a positive constant and n is the power law exponent (Turcotte & Schubert, 2002). Linear viscous materials have $n=1$, whereas materials with a power-law rheology have $n>1$. *Equation 6.4* may be modified to calculate the velocity, $\bar{\mu}_p$, of a non-Newtonian Poiseuille flow (Turcotte & Schubert, 2002) such that,

$$\bar{u}_p = \frac{C_1}{(n+1)}\left\{\frac{p_1 - p_0}{L}\right\}^n \left\{\left(\frac{h}{2}\right)^{n+1} - y^{n+1}\right\} \qquad \textit{Equation 6.6.}$$

where n is a positive integer. Figure 6.4a,b presents the velocity profiles of a Poiseuille flow for $n = 1, 3$, and 5. As n increases, the velocity profiles develop a plateau of equal velocity at the centre of the flow. The width of this central plateau increases with n. This behaviour reflects the vertical change in the effective viscosity, μ_{eff}, of the channel, which is low at the channel margins where τ is high and high at the channel centre where τ is low (Turcotte & Schubert, 2002). Thus,

$$\mu_{eff} \equiv \frac{\tau}{du/dy} = \left(\frac{p_1 - p_0}{L}\right)\frac{h^2}{4(n+2)\bar{u}}\left(\frac{2y}{h}\right)^{1-n} \qquad \textit{Equation 6.7.}$$

where $\bar{u}$ is the average channel velocity. With increasing n, the stress dependency of the effective viscosity increases, resulting in a larger contrast in effective viscosity between the channel margins and centre (Turcotte & Schubert, 2002). Consequently, the core of a flow with a power-law rheology behaves as a rigid plug whilst strain is partitioned to the channel margins (Figure 6.4). The corresponding strain rate profiles display high strain rate at the channel margins and zero strain rate in the rigid core (Figure 6.4c). As n increases, so does the rate of change of strain rate between the margins and core (Figure 6.4c). Additionally, the relative velocities of flows with different values of n change as a function of lateral pressure gradient (E*quation 6.4*) due to the relationship between the pressure gradient in the x direction and the and stress distribution in the y direction (Figure 6.4b) (Turcotte & Schubert, 2002),

$$\frac{d\tau}{dy} = \frac{dp}{dx} = -\frac{(p_1 - p_0)}{L} \qquad \textit{Equation 6.8.}$$

At the lowest values of dp/dx, a flow with $n = 1$ has a larger maximum velocity than a flow with $n > 1$ (Figure 6.4a). Above a threshold value of dp/dx, determined by the ratio between h and dp/dx, this relationship switches and flows with $n = 1$ have a lower maximum velocity than flows with $n > 1$ (Figure 6.4b).

When both a lateral pressure gradient and a channel-parallel motion of one of the channel walls are applied to a channel flow (i.e. $dp/dx \neq 0$ and $u_0 \neq 0$), a Hybrid flow (Figure 6.1c) is produced (Grujic, 2006). If the lateral pressure gradient operates in the

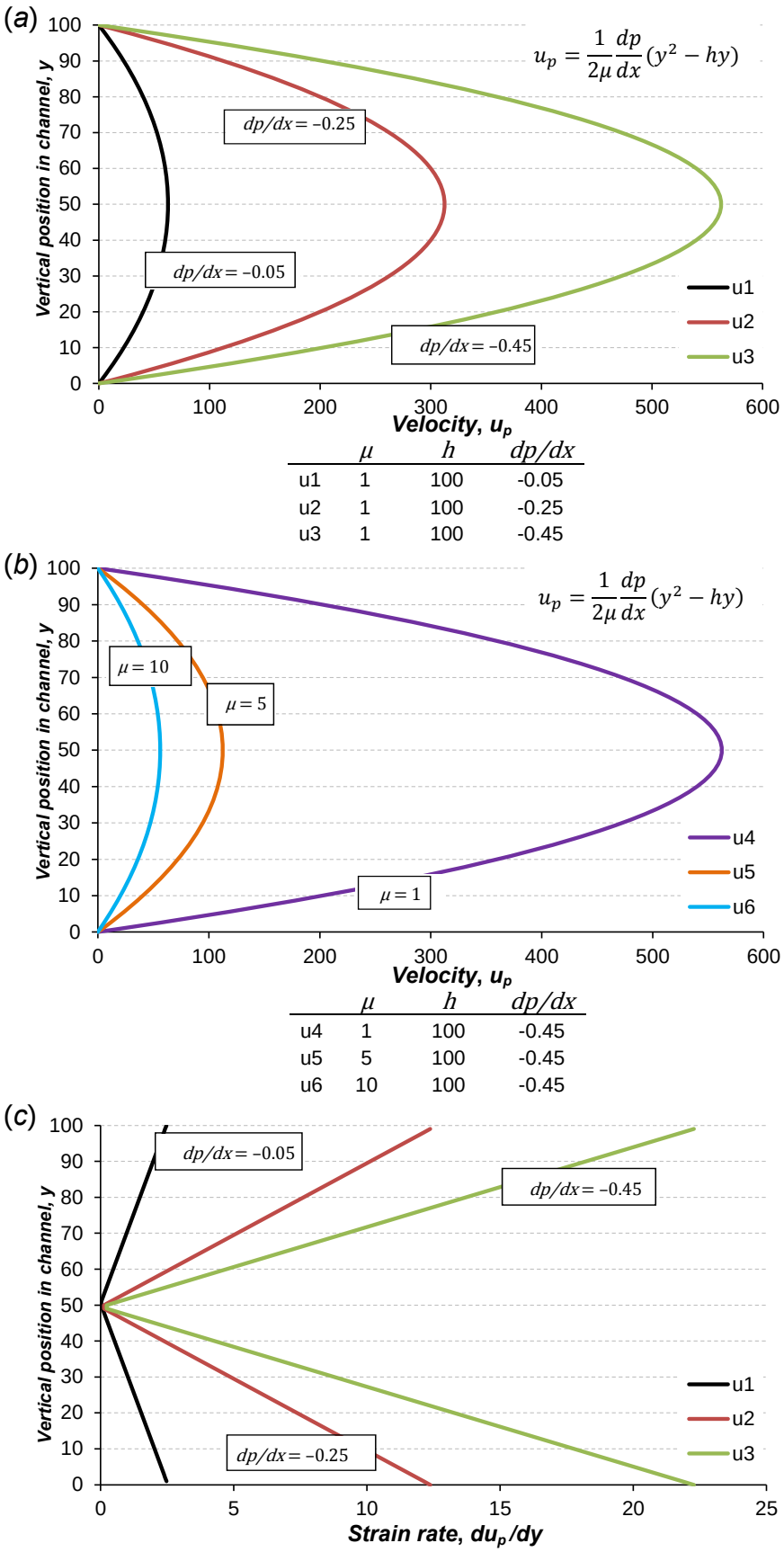

	μ	h	dp/dx
u1	1	100	-0.05
u2	1	100	-0.25
u3	1	100	-0.45

	μ	h	dp/dx
u4	1	100	-0.45
u5	5	100	-0.45
u6	10	100	-0.45

Figure 6.3. Poiseuille flow velocity and strain rate profiles. (*a*) Poiseuille flow velocity profiles for variable pressure gradient, dp/dx. (*b*) Poiseuille flow velocity profiles for variable viscosity, μ. (*c*) Corresponding strain rate profile calculated from (*a*). Velocity equations presented on each plot. Parameters used in calculations are listed below each plot. See text for full discussion.

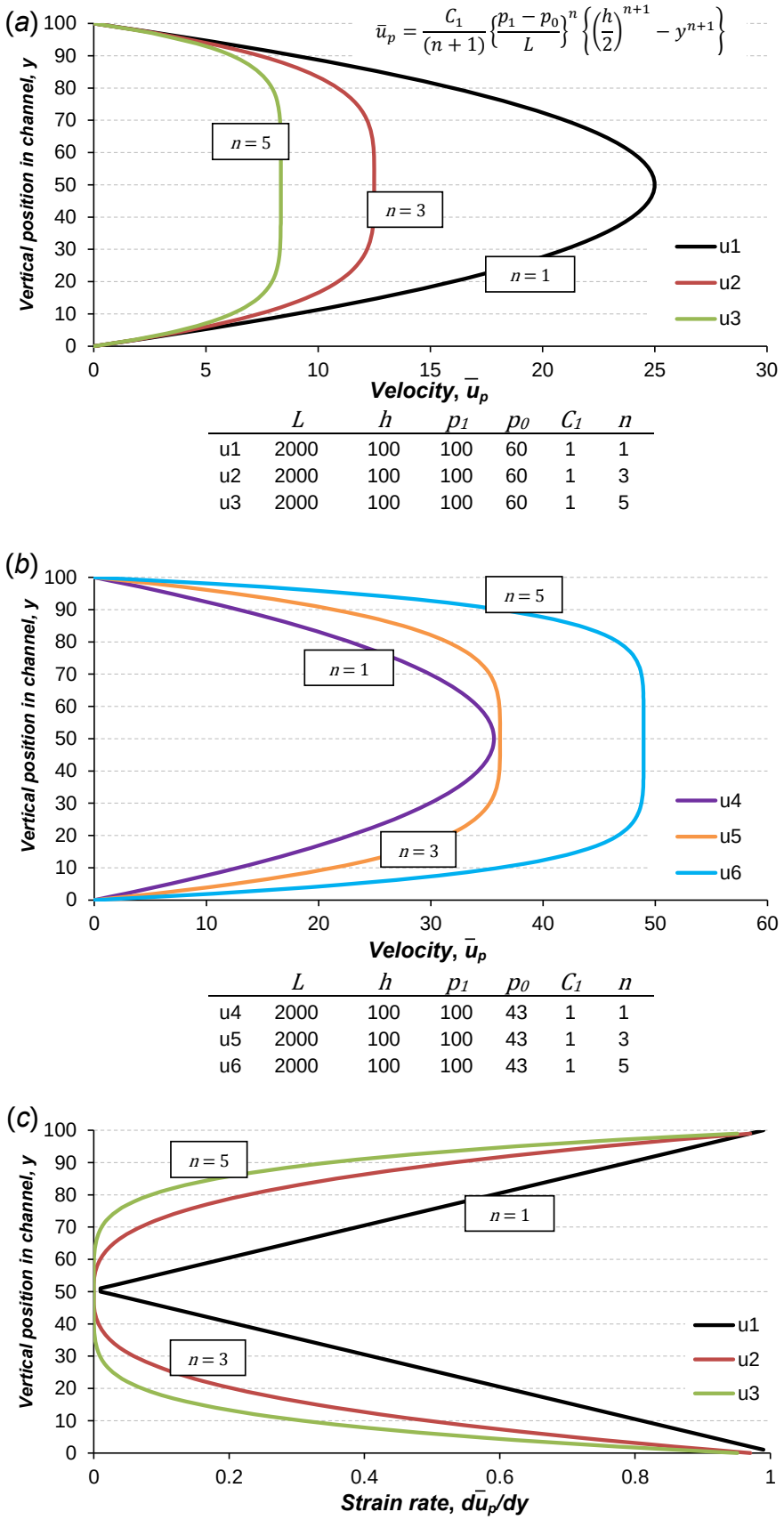

Figure 6.4. Poiseuille flow velocity and strain rate profiles for a stress dependant power-law channel rheology. (*a*) Poiseuille flow velocity profiles for variable power-law exponent, n below dp/dx threshold (see text for explanation). (*b*) Poiseuille flow velocity profiles for variable power-law exponent, n above dp/dx threshold (see text for explanation). (*c*) Corresponding strain rate profile calculated from (*a*). Velocity equations presented on plot (*a*). Parameters used in calculations are listed below each plot. See text for full discussion.

opposite direction to the channel wall motion, return-flow may occur in the opposite direction to the channel wall motion (Mancktelow, 1995; Turcotte & Schubert, 2002). The velocity of a hybrid flow, $u_h$may be determined from the following equation (Mancktelow, 1995),

$$u_h = u_c - u_p \qquad \textit{Equation 6.9}$$

Figure 6.5 shows the velocity profiles for a hybrid flow where the pressure gradient acts in the opposite direction to the channel wall motion. The shapes of the profiles are controlled by the proportionality between u_c and u_p. As $u_p$increases, the profiles become more 'bow-like'. Above a threshold level of u_p, part of the channel has a negative velocity that produces a return-flow in the opposite direction to u_0 (Figure 6.5). This threshold level is controlled by the relative values of h, dp/dx, μ and u_0 (Figure 6.5). An increase in h, dp/dx or μ increases the value of u_p, whilst an increase in u_0 increases u_c (Figure 6.5a,d,e). The strain rate profiles show a decreasing gradient to the point of minimum velocity (Figure 6.5b,d,f). As return-flow becomes more dominant, the locus of maximum return-flow velocity and minimum strain rate migrates down-section towards the centre of the channel. The rate of change of strain rate also increases with an increased component of return-flow (Figure 6.5b,d,f).

With respect to models of channel flow for the Himalayan orogen, the occurrence of return-flow results in southwards exhumation in the upper portion of the channel and northwards burial in the lower portion of the channel (Beaumont *et al.*, 2004; Grujic, 2006). This implies that different parts of the channel can have different PTt paths (Jamieson *et al.*, 2004; Jamieson *et al.*, 2006). Substitution of $\bar{u}_p$ for u_p into *Equation 6.9* produces the velocity, $\bar{u}_h$, of a Hybrid flow with a power-law rheology (Figure 6.6). Where $n > 1$, the plateau of constant velocity at the core of the channel, displayed in Figure 6.4 is now deformed by the additional shear stress produced by the moving channel wall (Figure 6.6). This locates the point of maximum return-flow velocity of a power law material closer towards the stationary channel wall than for an equivalent flow of linear viscous material. The power-law Hybrid flow is governed by the same controls as the linear viscous hybrid flow and power-law Poiseuille flow. An increase in h or dp/dx increases the amount of return-flow, whilst an increase in u_0 decreases the amount of return-flow (Figure 6.6a,c,d). An increase in n either increases or decreases the amount of return-flow depending on the relative values of h and dp/dx. The lowest values of h and dp/dx produce a negative correlation between n and the return-flow velocity, whilst larger values of h and dp/dx produce a positive correlation between n and the return-flow velocity.

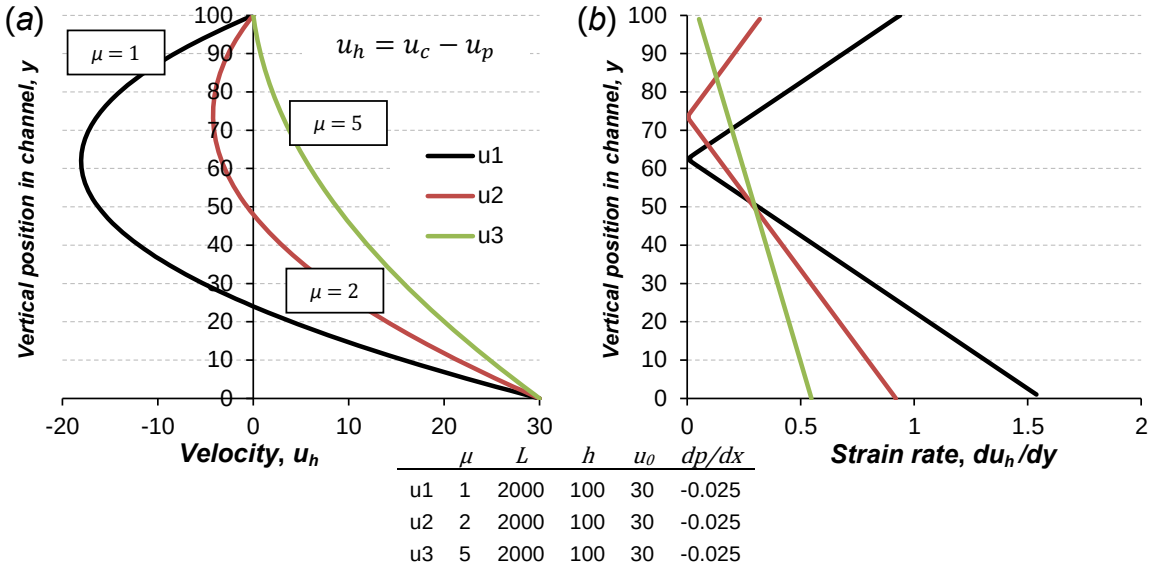

	μ	L	h	u_0	dp/dx
u1	1	2000	100	30	-0.025
u2	2	2000	100	30	-0.025
u3	5	2000	100	30	-0.025

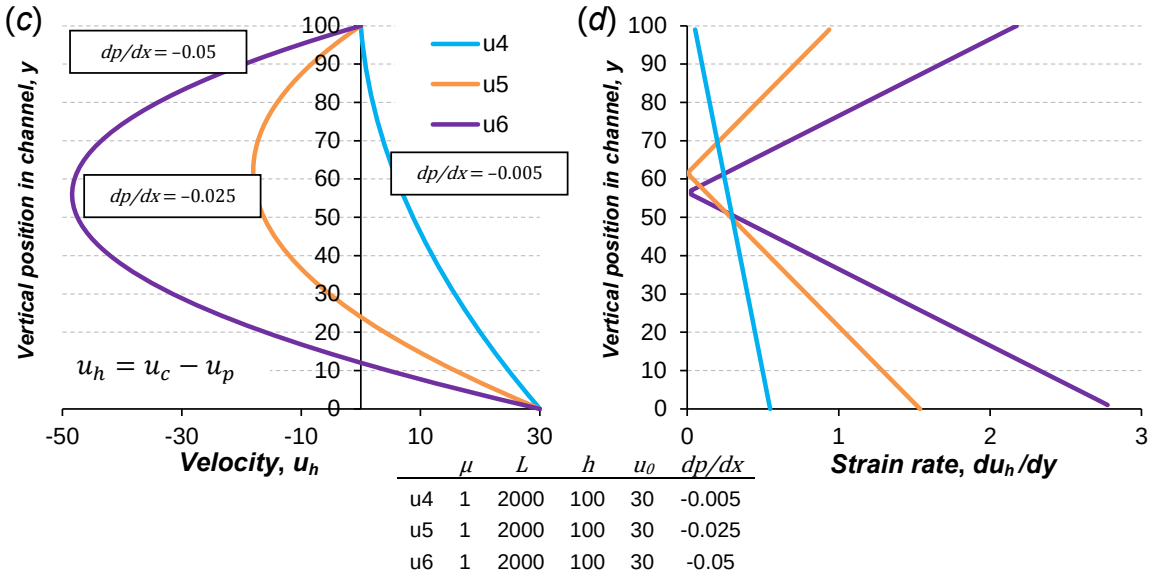

	μ	L	h	u_0	dp/dx
u4	1	2000	100	30	-0.005
u5	1	2000	100	30	-0.025
u6	1	2000	100	30	-0.05

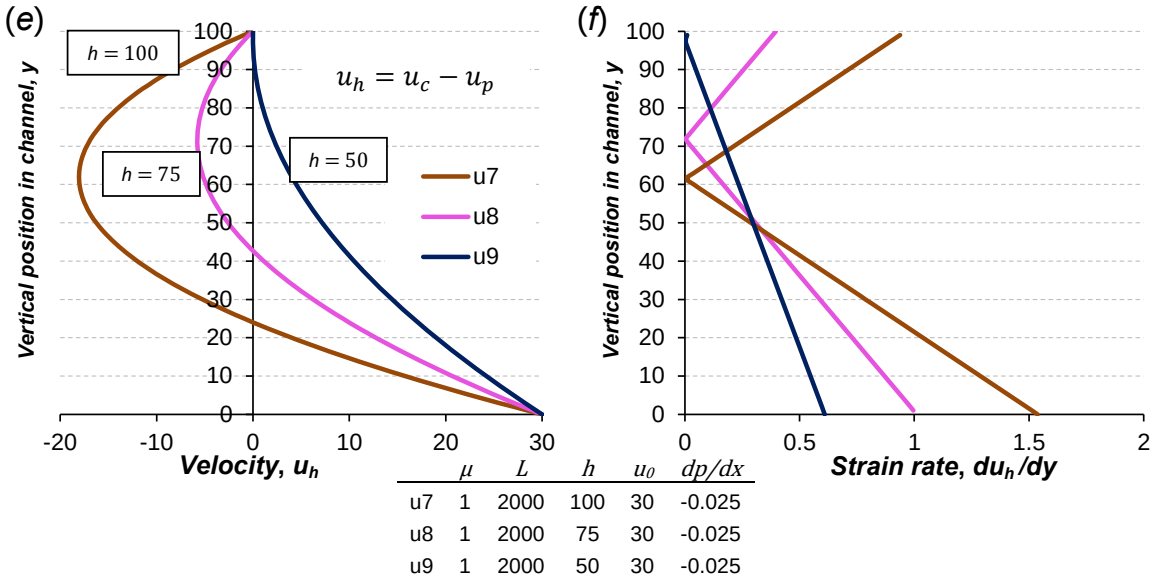

	μ	L	h	u_0	dp/dx
u7	1	2000	100	30	-0.025
u8	1	2000	75	30	-0.025
u9	1	2000	50	30	-0.025

Figure 6.5. Hybrid flow velocity and strain rate profiles. (*a*) Hybrid flow velocity profiles for variable viscosity, μ. (*b*) Strain rate profile for (*a*). (*c*) Hybrid flow velocity profiles for variable pressure gradient, dp/dx. (*d*) Strain rate profile for (*c*). (*e*) Hybrid flow velocity profiles for variable channel thickness, h. (*f*) Strain rate profile for (*e*). Parameters used in calculations are listed below each plot. See text for full discussion.

Hybrid flow of a power-law material produces a more complex strain rate profile (Figure 6.6b,d,f). If return-flow occurs, the point of minimum strain rate is towards the top of the channel in the middle of the return-flow (Figure 6.6b,d,f). Increasing the amount of return-flow drives the position of minimum strain rate down-section towards the channel centre. Below the strain rate minimum, a zone of constant strain rate exists, corresponding to the core of the channel, where only motion of the channel wall affects the flow (Figure 6.6b,d,f). Increasing the value of n increases the width of this zone of constant strain rate without increasing the magnitude (Figure 6.6b). An increase in dp/dx increases the maximum strain rate at the margins without changing the value of low strain rate in the core (Figure 6.6d). In contrast, increasing h or u_0 increases the maximum strain rate and decreases the low strain rate at the core (Figure 6.6f).

The effective viscosity of a power-law material can also be temperature dependent (Turcotte & Schubert, 2002). This factor becomes important when considering the velocity structure of channel flow with a non-uniform temperature field (Turcotte & Schubert, 2002). As a simple example, a temperature dependant channel viscosity, μ_T, can be simulated for a Couette flow with a vertical temperature gradient parallel to y (Turcotte & Schubert, 2002). Temperature, T, at position y, is defined as,

$$T = T_0 + (T_1 - T_0)\frac{y}{h} \qquad \textit{Equation 6.10.}$$

where T_0 and T_1 define the temperature of the upper and lower channel walls respectively (Turcotte & Schubert, 2002). If the effects of shear heating are assumed negligible, μ_T may be defined with reference to the upper channel wall viscosity, μ_0, as,

$$\mu_T = \mu_0 \exp\left\{\frac{E_a}{RT_0}\left(\left[1 + \left(\frac{T_1 - T_0}{T_0}\right)\right]\frac{y}{h}^{-1} - 1\right)\right\} \qquad \textit{Equation 6.11.}$$

in which E_a defines the activation energy for viscous flow and R is the universal gas constant (Turcotte & Schubert, 2002). Substituting μ for μ_T in *Equation 6.2* provides the means to produce a velocity profile for a temperature dependant shear driven flow with a non-uniform temperature field (Figure 6.7). The upper wall has $u = u_0$, the lower wall has $u = 0$ and $dp/dx = 0$. The gradient of the resulting velocity profile decreases in the direction of decreasing temperature. Consequently, the resulting strain rate profiles (Figure 6.7b) show a down-section decrease in strain rate. Increasing the temperature gradient between the top and bottom walls results in a lower maximum velocity and greater rate of change in strain rate across the channel (Figure 6.7). This behaviour can be explained by a greater contrast in effective viscosity in flows with a larger temperature gradient, which causes the cold lower portion of the channel to behave

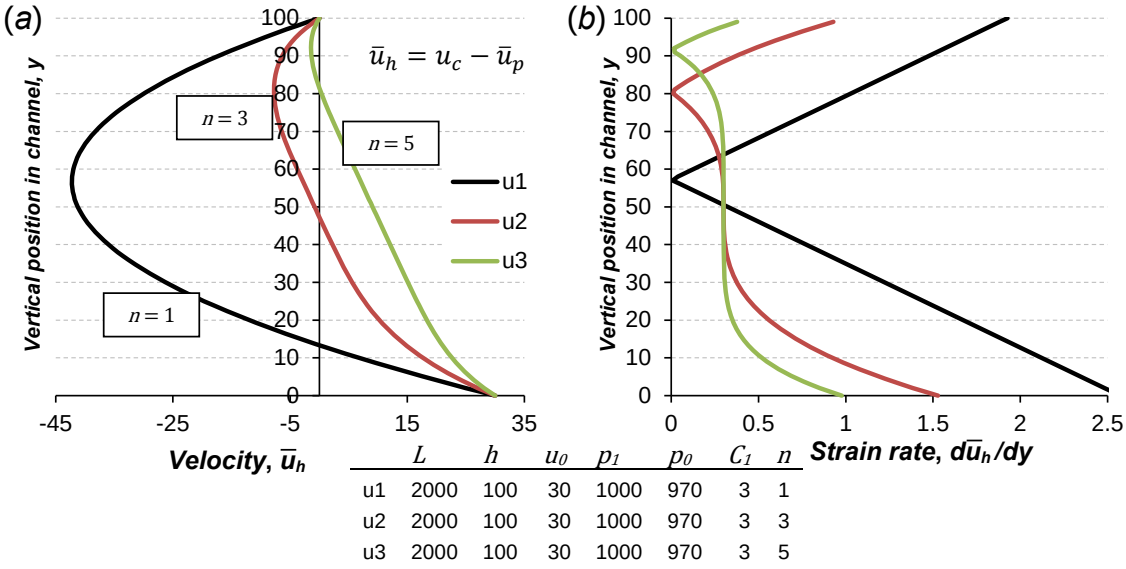

	L	h	u_0	p_1	p_0	C_1	n
u1	2000	100	30	1000	970	3	1
u2	2000	100	30	1000	970	3	3
u3	2000	100	30	1000	970	3	5

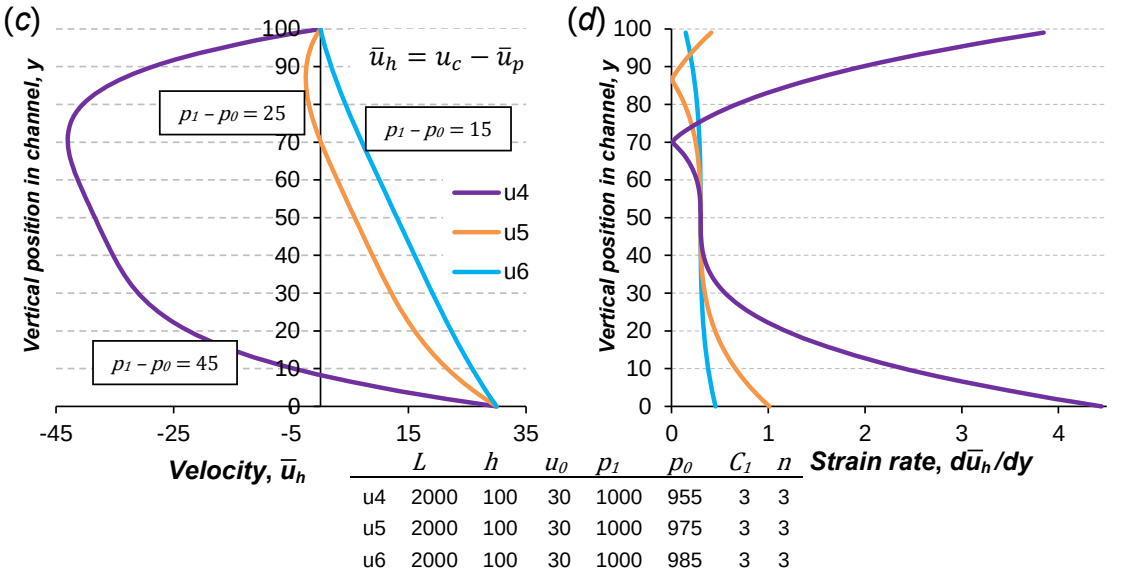

	L	h	u_0	p_1	p_0	C_1	n
u4	2000	100	30	1000	955	3	3
u5	2000	100	30	1000	975	3	3
u6	2000	100	30	1000	985	3	3

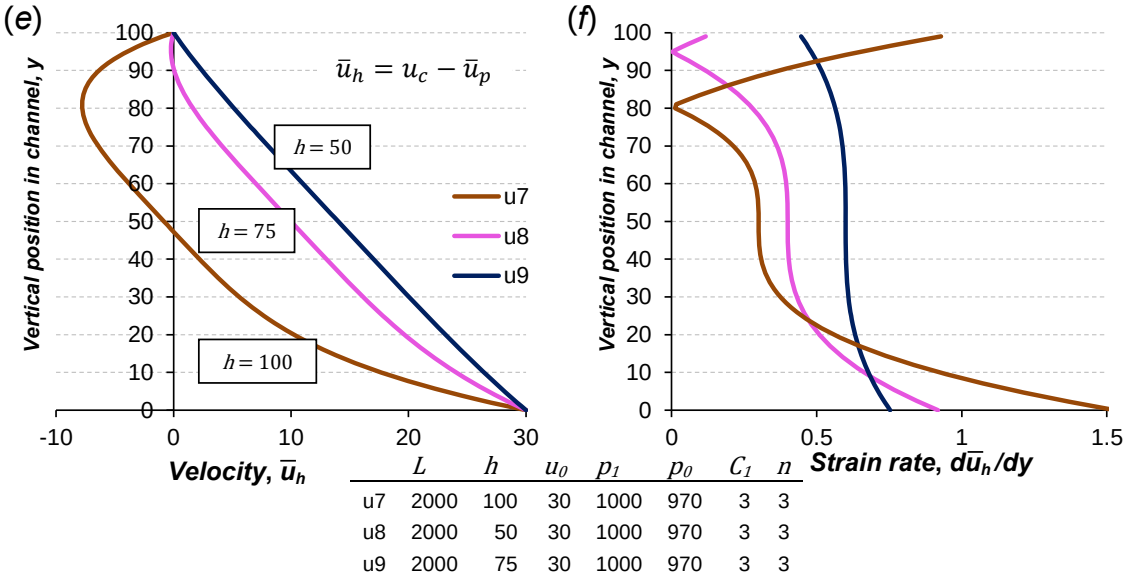

	L	h	u_0	p_1	p_0	C_1	n
u7	2000	100	30	1000	970	3	3
u8	2000	50	30	1000	970	3	3
u9	2000	75	30	1000	970	3	3

Figure 6.6. Hybrid flow velocity and strain rate profiles for a stress dependant power-law channel rheology. (*a*) Hybrid flow velocity profiles for variable power-law exponent, n. (*b*) Strain rate profile for (*a*). (*c*) Hybrid flow velocity profiles for variable pressure difference, $p_1 - p_0$. (*d*) Strain rate profile for (*c*). (*e*) Hybrid flow velocity profiles for variable channel thickness, h. (*f*) Strain rate profile for (*e*). Parameters used in calculations are listed below each plot. See text for full discussion.

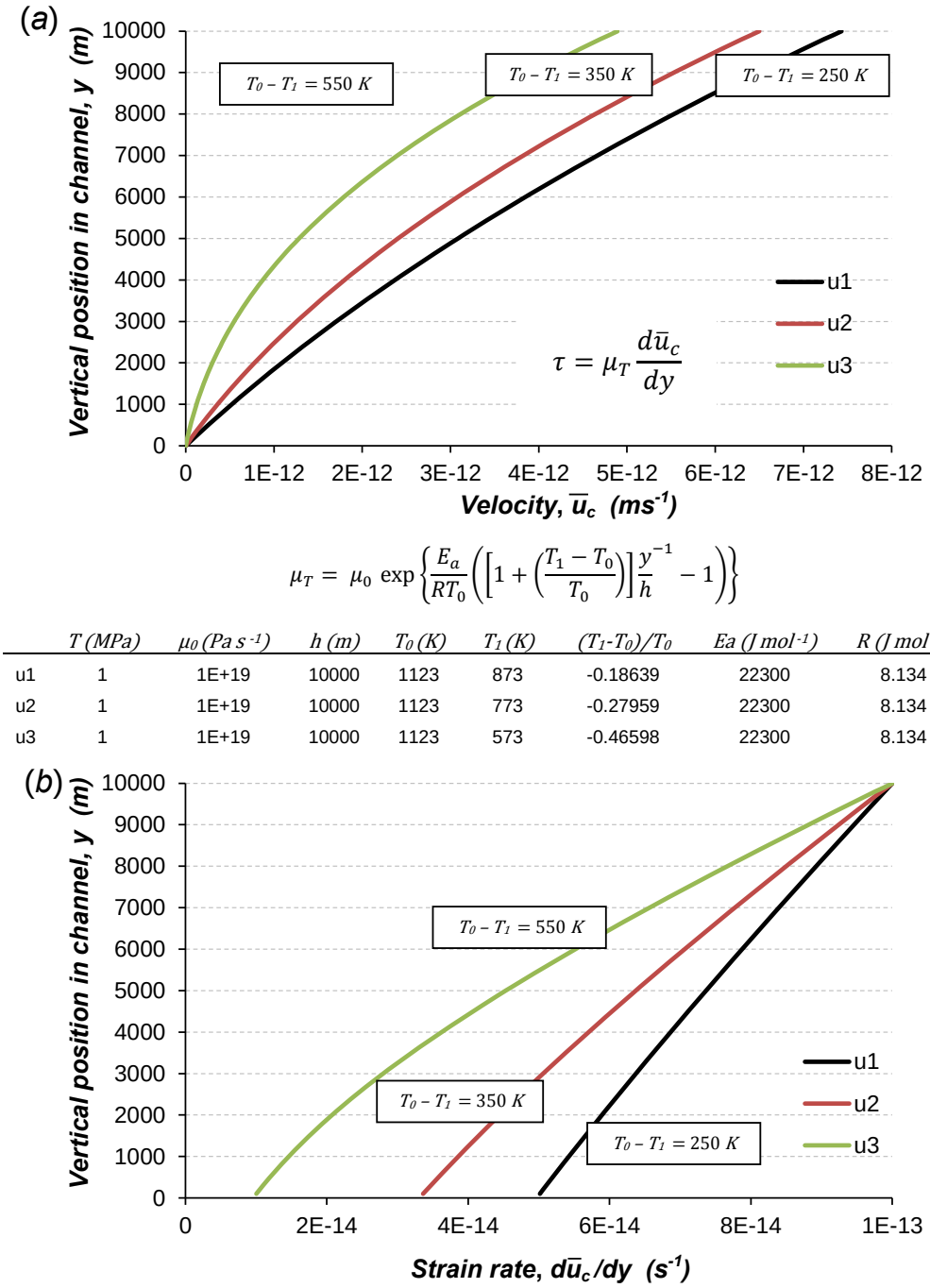

$$\mu_T = \mu_0 \exp\left\{\frac{E_a}{RT_0}\left(\left[1 + \left(\frac{T_1 - T_0}{T_0}\right)\right]\frac{y}{h}^{-1} - 1\right)\right\}$$

	T (MPa)	μ_0 (Pa s^{-1})	h (m)	T_0 (K)	T_1 (K)	$(T_1-T_0)/T_0$	Ea (J mol^{-1})	R (J mol^{-1})	Ea/RT_0
u1	1	1E+19	10000	1123	873	-0.18639	22300	8.134	4.984084
u2	1	1E+19	10000	1123	773	-0.27959	22300	8.134	4.984084
u3	1	1E+19	10000	1123	573	-0.46598	22300	8.134	4.984084

Figure 6.7. Couette flow velocity and strain rate profiles for a temperature dependant power-law channel rheology. (*a*) Couette flow velocity profiles for variable temperature gradient, $T_0 - T_1$. (*b*) Corresponding strain rate profile calculated from (*a*). Velocity equations presented on plot (*a*). Parameters used in calculations are listed below each plot. Activation energy, E_a based on wet Black Hills flow law (Gleason & Tullis, 1995). See text for full discussion.

more rigidly than the hot upper portion of the channel. The situation simulated in Figure 6.7 maybe comparable to the sheared inverted metamorphic sequence of the LGHS in the Annapurna-Dhaulagiri region described in *Chapter 3* and similar sections often referred to as the Main Central Thrust Zone (MCTZ) (e.g. Grasemann *et al.*, 1999; Law *et al.*, 2013) elsewhere in the Himalaya.

6.2. Relative velocity profiles for the Annapurna-Dhaulagiri Himalaya

The results derived from the mechanical models presented above provide an insight into the first order controls of a 1-dimensional channel flow. Furthermore, the accompanying strain rate profiles provide a data set that is more readily comparable with macro- and microstructural geological observations. In the same way that the derivative of the velocity profiles provides a means to calculate strain rate profiles, the integral of the relative strain profiles of the GHS and bounding units presented in Chapter 5 (Figure 5.6) can be converted into relative velocity profiles.

$$v = \int_{h=y}^{h=0} \dot{e}\ dy$$

The relative velocity v, at vertical position y, along the vertical transect with length h, is the integral of the relative strain rate proxy $\dot{e}$ (determined from the RSM profiles), between $h = 0$ and $h = y$. This requires that relative strain and relative strain rate maintain the same proportionality across each profile. This criterion requires the assumptions that; (*1*) the duration of deformation for each profile is uniform; (*2*) whilst strain rates may vary across each profile, the strain rate at any given position must either remain constant throughout the duration of deformation *or* if strain rate changes through time at a single given position, strain rate at all other potions must also change by the same factor; and (*3*) the conversion from relative strain rate to relative velocity assumes that the recorded deformation occurred via simple shear.

Figure 6.8 presents the relative velocity profiles for the GHS and bounding units in the Annapurna-Dhaulagiri region. To construct the relative velocity profiles the relative strain magnitude profiles (Figure 5.6) were scaled graphically so that any point along the profile may be defined in terms of an *x*-*y* coordinate system. Structural height was assigned to the *y*-axis. Relative strain ranging from 0 to 1 was assigned to the *x*-axis, corresponding to the minimum and maximum relative strain magnitudes of each profile, respectively. Next, following the assumptions outlined above, the integral of each profile was calculated to determine the relative velocity profiles (Figure 6.8). The velocity at the top of each profile is zero. This corresponds to the THS and represents a stationary upper channel wall against which relative velocity is measured. The calculated velocities were normalised against the largest positive velocity of the two transects. Positive velocity equates to southwards motion, negative velocity equates to northwards motion. Solid and dashed velocity profiles for each transect correspond to the solid and dashed relative strain magnitude profiles, respectively in Figure 5.6.

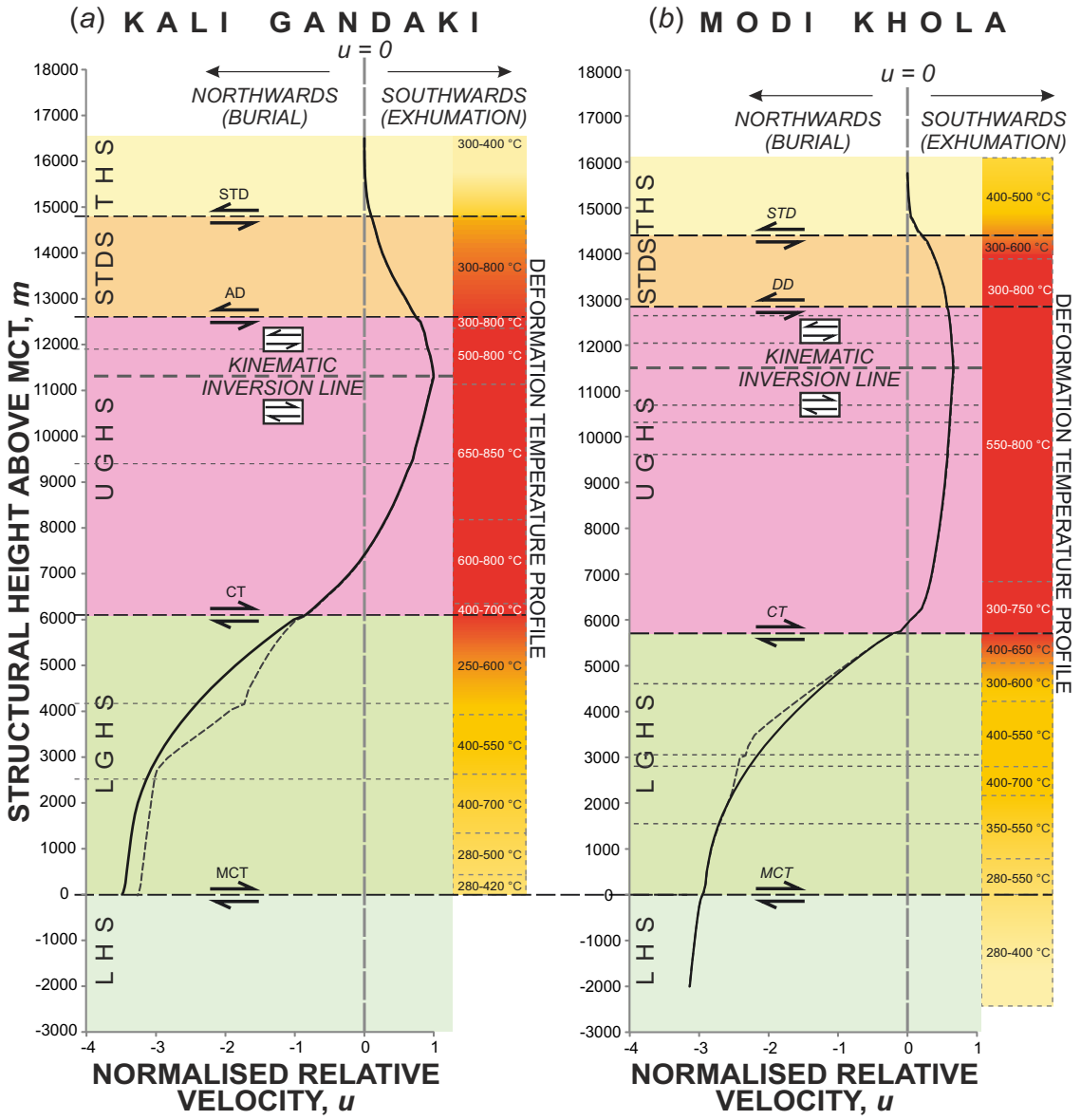

Figure 6.8. Normalised relative velocity profiles for the GHS and bounding units. (*a*) Kali Gandaki transect, (*b*) Modi Khola transect. THS represents fixed reference point, with $u = 0$. Positive velocity = southwards motion (exhumation), negative velocity = northwards motion (burial). Solid and dashed velocity curves correspond to solid and dashed relative strain magnitude profiles, respectively in Figure 5.6. Kinematic inversion line represent point at which shear sense changes from top-to-south to top-to-north. Relative velocity profiles are plotted to scale over a simplified stratigraphic column. Horizontal dashed lines represent unit bounding shear zones (thick) and lithological boundaries (thin). Right of each profile is a summarised deformation temperature profile (to scale) for each transect showing zones of equal maximum and minimum deformation temperatures (determined from Chapter 3).

The mechanical models presented in *Section 6.1* represent a snap shot of deformation occurring at a single moment in time and assume the same rheological boundary conditions (i.e. same flow laws and same stress- and temperature-dependencies of effective viscosity) to the entire channel. In contrast, the different temperature domains in which different sections of the profile deformed (determined in Chapter 3; Figures 3.20 & 3.21) imply that the velocity profile of the GHS for the Kali Gandaki and Modi Khola transects (Figure 6.8) should be considered as a composite velocity profile

composed of distinct velocity structures with different rheological boundary conditions relating to the different tectono-stratigraphic units. As such, the velocity profiles are interpreted as composite profiles built from discrete velocity profiles (segments) corresponding to the LHS, LGHS, UGHS, STDS and THS. This approach also helps to satisfy assumption (*1*), which now becomes: *the duration of deformation within each individual segment (i.e. the LGHS) is uniform*.

In the LHS of the Modi Khola transect (Figure 6.8b), negative velocities (i.e. northwards directed) are roughly constant and of the greatest magnitude in the transect. This corresponds to a uniform zone of low relative strain (Figure 5.6b). In the LGHS, both transects show an up-section decrease in negative velocity that steepens in gradient towards the CT. This behaviour reflects an up-section increase in relative strain (Figure 5.6). The dashed-lined velocity profiles in the LGHS are not as smooth as the solid-lined profiles, but still show an overall up-section increase in relative velocity. The stepped nature of these dashed-lined profiles corresponds to relative changes in strain magnitude proxy (Figure 5.6) between different lithologies in the LGHS. At the base of the UGHS, negative (i.e. northwards) velocities are recorded in both profiles (Figure 6.8), which decrease up-section to a point of zero relative velocity. In the Kali Gandaki profile (Figure 6.8a), the relative magnitude of negative velocity at the base of the UGHS is greater than at the equivalent position in the Modi Khola profile (Figure 6.8b). Consequently, the point of zero velocity in the UGHS of the Kali Gandaki section is structurally higher than in the Modi Khola section. Above these structural levels, velocities increase up-section with a positive (i.e. southwards) direction.

In the Kali Gandaki transect (Figure 6.8a), the velocity gradient in the UGHS decreases up-section gradually to a point of maximum positive velocity close to the top of the UGHS. In contrast, the velocity gradient in the UGHS of the Modi Khola transect (Figure 6.8b) changes rapidly from steep to shallow, close to the base of the sequence. Above this level, the changes in velocity gradient are relatively small. These differences correspond to the gradual up-section decrease in relative strain in the Kali Gandaki transect (Figure 5.6a) and the rapid decrease in relative strain in the Modi Khola transect (Figure 5.6b). Maximum positive velocities are recorded close to the top of UGHS for both transects (Figure 6.8). Above this point and into the STDS, velocity in the Kali Gandaki transect decreases with a relatively constant gradient towards the STD (Figure 6.8a). In contrast, velocity in the Modi Khola transect remains high in the STDS and decreases with a much shallower gradient towards the STD (Figure 6.8). This behaviour reflects differences in the relative strain profiles across the STDS between both profiles (Figure 5.6). In the Kali Gandaki transect (Figure 5.6a), relative strain decreases towards the STD, whilst in the Modi Khola transect (Figure 5.6b)

relative strain increases towards the STD. At the top of the velocity profiles, relative positive velocity at the base of the THS decreases to zero (Figure 6.8). Above this point, relative velocity remains at zero, corresponding to a uniform zone of low relative strain (Figure 5.6).

6.3. Kinematic interpretations

Both the Kali Gandaki and Modi Khola velocity profiles (Figure 6.8) show a number of features comparable to the modelled velocity profiles presented above (Figures 6.2-6.7) and suggest that the GHS can be interpreted in terms of a laminar viscous flow. Additionally, the gradient of relative velocity provides an indication of vorticity, with steep gradients being indicative of high vorticity (i.e. simple shear dominated deformation) and shallow to flat gradients indicative of low vorticity (i.e. pure shear dominated deformation) (Grujic, 2006).

In both the LHS and THS, velocity and strain profiles are uniform (Figures 5.6 & 6.8). This implies that that these units behaved as coherent blocks with little or no internal deformation (i.e. rigid). The relative magnitude and direction of velocity in these units imply that the LHS moved northwards relative to a stationary THS. This behaviour is comparable to the channel walls of a Couette or Hybrid flow, where the upper wall has a velocity $u = 0$ (i.e. the THS) and the lower plate has a velocity $u = u_0$ (i.e. the LHS).

When considered as a distinct velocity structure, the UGHS and STDS (Figure 6.8) represent a Hybrid flow with an upper portion of return-flow, driven by the northwards motion of the lower channel wall (i.e. the LGHS), and a southwards directed pressure gradient (e.g. Figure 6.5 & 6.6). Strata within the return-flow represent the southwards extruding and exhuming portion of the channel on a retrograde (exhumation) path, whilst strata in the lower northwards flowing portion are on a prograde (burial) path.

Steep velocity gradients at the margins of the UGHS and STDS and shallow velocity gradients in the middle of the return-flow are suggestive of a power-law rheology (Figure 6.4 & 6.6). This suggestion is also supported by the location of maximum return-flow velocity (Figure 6.8), which is positioned close to the top of the return-flow rather than in the middle of the return-flow (e.g. Figure 6.6). This peak in return-flow velocity represents the position at which shear sense indicators should switch from top-to-the-south to top-to-the-north. The implication is that only the upper 500-1000 m of the UGHS should display top-to-the-north shear sense indicators in the Annapurna-Dhaulagiri region. Velocity gradients also suggest a decrease in the ratio of simple shear to pure shear from the margins to the centre. Notably, the modelled strain rate profiles produce a localised trough in the upper portion of the flow coincident with the peak return-flow velocity (Figure 6.6), which is not observed in either of the relative

strain profiles from the Annapurna-Dhaulagiri region (Figure 5.6). This trough in the modelled profiles can be removed if the power-law constant, C_1 (*Equation 6.6*) is increased. Absence of these troughs in the relative strain profiles of the GHS (Figure 6.8) reflects differences in the rheological boundary conditions between the mechanical models and the actual rheological properties of the GHS.

Following comparison with the modelled hybrid flows (Figure 6.6), the differences in velocity profile curvature in the lower portions of the UGHS of each transect (Figure 6.8) may have several explanations. For example, an increase in u_0 and/or decrease in dp/dx for the UGHS in the Kali Gandaki, relative to the Modi Khola transect may account for this difference. A change in rheological boundary conditions relating to the stress- or temperature-dependency of effective viscosity could also be responsible. Such differences between transects may be achieved through variations in temperature, melt content and/or lithology (e.g. Rosenberg & Handy, 2005; Grujic, 2006; Rutter *et al.*, 2006). Alternatively, or additionally, the difference between the two transects may correspond to a gradual increase in strain localisation towards the lower margin of the UGHS of the Kali Gandaki during decreasing deformation temperatures, which did not occur in the Modi Khola section (Figures 3.20 & 3.21). Such a situation does not fit with assumption *1* (i.e. uniform duration of deformation) used to construct the velocity profiles. Consequently, the shallower velocity gradient at the base of the UGHS in the Kali Gandaki may reflect a longer duration of deformation at the lower margin of the UGHS relative to its centre. Nevertheless, with or without adhering to assumption 1, the UGHS in the Kali Gandaki would still produce a comparable velocity profile to the Modi Khola transect, characterised by return-flow in the middle and upper sections. Removing the additional duration of deformation at the lower margin would only decrease the amount of northwards directed flow at the base of the UGHS in the Kali Gandaki transect (Figure 6.8a).

The relative strain and velocity structures of the UGHS and STDS in the Modi Khola transect (Figures 5.6b & 6.8b) appear conformable, which suggests that boundary conditions governing viscous flow remained the same between these units. However, data coverage from this section is sparse (Figure 2.5) and it is possible that with a denser suite of samples differences in relative strain and velocity may become apparent. Interpretations made from the equivalent strata in the Kali Gandaki transect (Figure 6.8a) are more reliable due to the greater density of sampling (Figure 2.5). Here, a localisation of high relative strain is observed on the AD, followed by an up-section decrease in relative strain through the STDS (Figure 5.6a). The resulting velocity profile (Figure 6.8a) produces a short section of decreasing velocity with a steep velocity gradient in the footwall of the AD, followed by an up-section decrease in

velocity with a shallower velocity gradient in the STDS that flattens towards the STD. The composite velocity profile of the STDS and UGHS in the Kali Gandaki transect differs from the power-law Hybrid flow models (Figure 6.6), which show that velocity gradient and strain rate should increase towards the channel boundary, as opposed to the observed up-section decrease in velocity gradient and relative strain recorded in the STDS of the Kali Gandaki transect. A plausible explanation is that the rheological boundary conditions of flow differ between the UGHS and STDS. This interpretation is likely as melt content, lithology and deformation temperatures differ sufficiently between the UGHS and STDS, so that their rheological properties should also differ (e.g. Rosenberg & Handy, 2005; Grujic, 2006; Rutter *et al.*, 2006). In this situation, the AD represents a rheological discontinuity between the UGHS and STDS. When considered in isolation, the velocity profile of the STDS in the Kali Gandaki is comparable to a temperature-dependant Couette flow (Figure 6.7) driven by the relative motion between the UGHS and THS. The curvature in the velocity profile in the STDS may indicate the presence of an up-section decrease in temperature (e.g. Figure 6.7), as observed in the Annapurna-Dhaulagiri region and elsewhere in the Himalaya (e.g. Cottle *et al.*, 2011), causing an up-section increase in effective viscosity (*Equation 6.11*).

The velocity structures of the LGHS in both transects show down-section increases in northwards relative velocity indicative of a wide zone of top-to-the-south shear (Figure 6.8). It is possible that localised fluctuations in velocity occur within the LGHS coincident with lithology boundaries, if potential deviations from the relative strain profiles are considered (Figure 5.6**;** *see Section 5.5.1*). However, the resulting velocity profile would still show an overall down-section increase in northwards velocity. The down-section decrease in relative strain (Figure 5.6) is responsible for the curvature in the velocity profile. This is comparable to a Couette flow with a temperature dependant effective viscosity and a down section decrease in temperature (Figure 6.7), which fits the inverted metamorphic and deformation temperature profile recorded in this portion of the GHS (Chapters 2 & 3) and in equivalent strata elsewhere in the Himalaya (e.g. Le Fort, 1975; Grasemann *et al.*, 1999; Law *et al.*, 2013; Rolfo *et al.*, 2014). Additionally, the down-section reduction in the gradients of the relative velocity profiles in the LGHS may indicate a reduction in the ratio of simple shear to pure shear. This behaviour is also suggested by the down-section transition from quartz single to crossed girdle *c*-axis fabrics (*Section 3.3.1.*) and correlates with observations made by Grasemann *et al.* (1999) in equivalent strata in the Bhutanese Himalaya. The change in velocity structure between the UGHS and LGHS suggests that the CT represents a rheological discontinuity in a similar fashion to the AD.

6.4. Conclusions

The observation-based relative velocity profiles (Figure 6.8) display many features that can be compared directly to the 1-dimensional laminar flow models (Figures 6.2 to 6.7**)** presented in *Section 6.1*. The velocity structure of the UGHS is comparable to a Hybrid flow driven by northwards motion of the underlying LGHS and LHS and a southward-directed lateral pressure gradient. The inferred pressure gradient is strong enough to overcome some of the northwards-directed shear and produce a southwards-directed return-flow in the middle to upper portions of the UGHS. The shape of the curve is indicative of a power-law flow rheology. This velocity structure suggests that most of the UGHS is exhuming southwards on a retrograde path, whilst the base of the UGHS is buried on a prograde path. The STDS of the Kali Gandaki transect displays a velocity profile that is comparable to Couette flow driven by southwards motion of the underlying return-flow. The LGHS shows a similar profile indicative of Couette flow driven by northwards motion of the LHS and/or southwards motion of the UGHS. Curvature of these velocity structures may relate to a decrease in deformation temperature up-section in the STDS and down-section in the LGHS. At the margins of the profiles, the LHS and THS have uniform velocity structures comparable to a lower northwards moving channel wall and a stationary upper channel wall, respectively. This suggests that the LGHS, UGHS and STDS can all be interpreted as channel material. However, the distinct differences in velocity structure between these sequences, combined with differences in deformation temperatures, suggests that they deformed in different temperature domains with different rheological boundary conditions and perhaps at different times. This implies that the CT and AD represent rheological as well as structural and lithological discontinuities. Most notably, the return-flow velocity structure and relative strain profile for the UGHS fit the kinematic predictions made by channel flow models for the Himalayan orogen (e.g. Beaumont *et al.*, 2001; Grujic *et al.*, 2002; Beaumont *et al.*, 2004; Jain *et al.*, 2005; Grujic, 2006; Mukherjee, 2013b, 2014). These interpretations are explored further in Chapter 7.

- CHAPTER 7 -

CHANNEL FLOW, EXTRUSION AND EXHUMATION OF THE GHS, ANNAPURNA-DHAULAGIRI, NEPAL

In this chapter, the different models of Himalayan orogenesis are critically assessed, based on a synthesis of new data presented in this thesis with existing constraints. In doing so, it is shown that these models should not be considered as mutually exclusive and that in 'Large Hot Orogens' such as the Himalayan-Tibetan orogen (Beaumont *et al.*, 2006; Jamieson & Beaumont, 2013), elements relating to different models can be found within a single system. Following this critical assessment, geological conditions required for channel flow in the Himalayan orogen (*Section 1.3.5.*) are evaluated based on the findings of this thesis. Results indicate that the mid-crustal evolution of the GHS in the Annapurna-Dhaulagiri Himalaya is coherently explained by southwards directed channel flow within a hot, partially molten and rheologically weak mid-crustal channel. Additionally, previously unexplained features, such as reduced leucogranite volumes, late-stage reversal of motion on the STDS and orogen-parallel deformation of the GHS, are considered and reconciled with the channel flow model. Finally, the kinematic evolution of the Annapurna-Dhaulagiri region is discussed based on a synthesis of this research with previously published work. Notably, it will be shown that the Himalayan orogenic system developed as a composite orogen with rheologically contrasting orogenic domains. The GHS evolved through these domains governed by spatially and temporally evolving rheological boundary conditions.

7.1. Tectonic processes operating during formation of the Himalayan orogen

Structural, metamorphic, geochronological and geodynamic studies of the Himalayan orogen have all been used as supporting evidence for the occurrence of: (*a*) channel flow (e.g. Beaumont *et al.*, 2001; Grujic *et al.*, 2002; Searle & Godin, 2003; Beaumont *et al.*, 2004; Jamieson *et al.*, 2004; Grujic, 2006; Spencer *et al.*, 2012; Rolfo *et al.*, 2014; Larson & Cottle, 2015); (*b*) wedge extrusion (e.g. Burchfiel & Royden, 1985; Burchfiel *et al.*, 1992; Hodges *et al.*, 1993; Hodges *et al.*, 1998; Grasemann *et al.*, 1999); (*c*) duplexing and underplating (e.g. Robinson *et al.*, 2006; Kohn, 2008; Carosi *et al.*, 2010; Corrie & Kohn, 2011; Montomoli *et al.*, 2014; Robinson & Martin, 2014); and (*d*) tectonic wedging (Yin, 2006; Webb *et al.*, 2007; Webb *et al.*, 2011a; Webb *et al.*, 2013; He *et al.*, 2014) (Figure 7.1).

These orogenic processes have dominantly been envisaged as being mutually exclusive and have often been presented as contradictory evidence for or against the occurrence of different processes, particularly when considering the role of channel flow versus critical wedge tectonics (e.g. Robinson *et al.*, 2006; Kohn, 2008; Carosi *et*

(*a*) CHANNEL FLOW

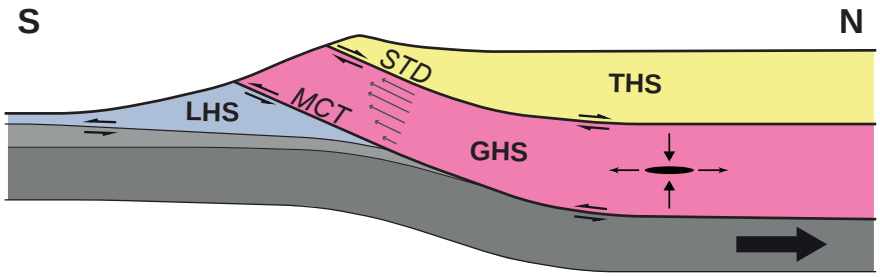

(*b*) WEDGE EXTRUSION

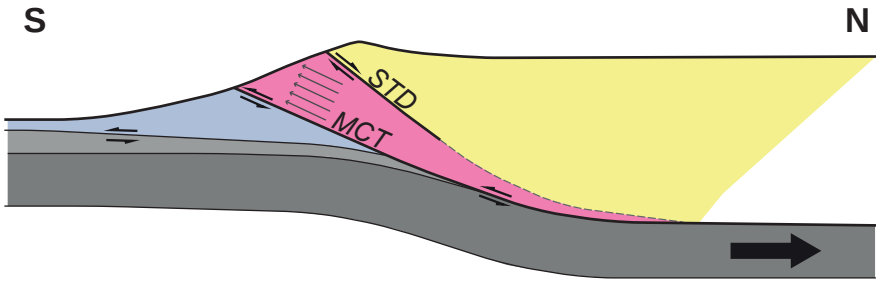

(*c*) DUPLEX (*Single Thrust Sheet*)

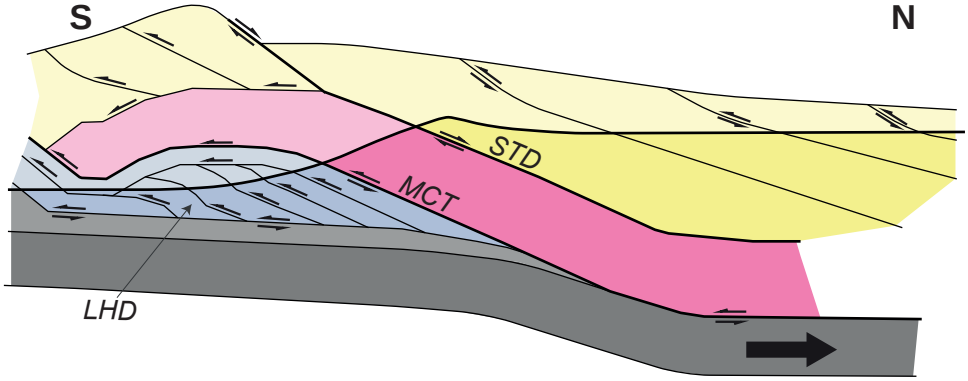

(*d*) DUPLEX/UNDERPLATING (*Internal Thrusting*)

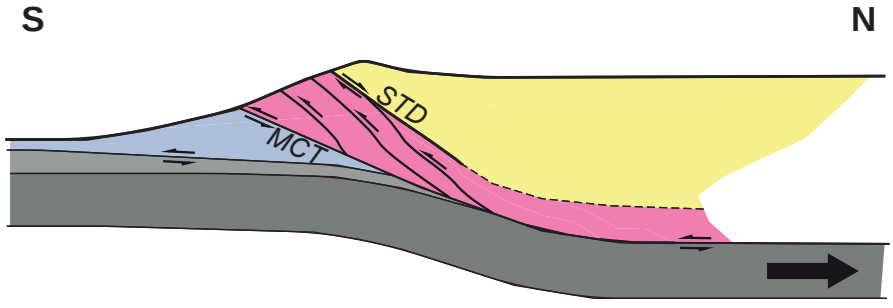

(*e*) TECTONIC WEDGING

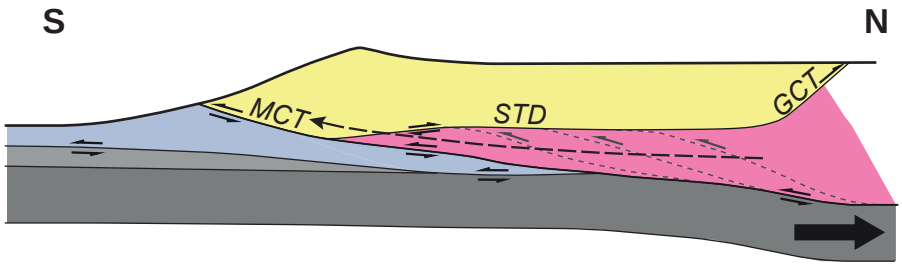

Figure 7.1 Models of Himalayan orogenesis

al., 2010; Martin *et al.*, 2010; Webb *et al.*, 2011a). However, more recent studies have shown that for orogens as large and long lived as the Himalayan-Tibetan orogenic system, spatial and temporal variations in tectonic processes are to be expected and reflect changes in rheological boundary conditions (Beaumont *et al.*, 2004; Gleeson & Godin, 2006; Godin *et al.*, 2006a; Larson *et al.*, 2010b; Spencer *et al.*, 2012; Jamieson & Beaumont, 2013; Mukherjee, 2013a; Wang *et al.*, 2013; He *et al.*, 2014; Larson & Cottle, 2014). Firstly, claims that proposed models are mutually exclusive are assessed, via a consideration of the adherence of each model to concepts of the Superstructure-Infrastructure Association (Wegmann, 1935; Fyson, 1971; Culshaw *et al.*, 2006) or to concepts of 'classic' crustal scale thrust stacking and duplex development (e.g. Boyer & Elliott, 1982; Davis *et al.*, 1983; Butler, 1986; Cook & Varsek, 1994).

7.2. The Superstructure-Infrastructure Association (SIA)

The Superstructure-Infrastructure Association (SIA - Wegmann, 1935; Fyson, 1971; Culshaw *et al.*, 2006; Williams *et al.*, 2006) has been used to account for differing styles of deformation (Figure 7.2) observed in high grade mid- to lower-crustal orogenic cores (infrastructure) and their lower grade upper-crustal carapace (superstructure) in continental collisions such as the Pyrenean, Caledonian, Hercynian and Cordilleran orogens (e.g. Haller, 1956; Fyson, 1971; Zwart, 1979; Snoke, 1980; Murphy, 1987; Higgins, 1988). Typically, the infrastructure (Figure 7.2a) comprises amphibolite facies and/or higher grade metamorphic rocks and migmatites, deformed by vertical shortening and associated shallow dipping transpositional foliation, sub-horizontal stretching and recumbent folding at all scales that may become isoclinal (Fyson, 1971; Culshaw *et al.*, 2006; Williams *et al.*, 2006). Above this, the superstructure (Figure 7.2a) is typically characterised by horizontal shortening and associated upright folds, thrust faults and steep foliation deforming greenschist facies and lower grade rocks

Figure 7.1. Models for Himalayan orogenesis. Schematic cross sections of the Himalaya (not to scale) show different model end-members. All cross sections follow same key; *Yellow – THS; Purple – GHS; Blue – LHS; Light Grey – Indian Upper crust; Dark Grey – Indian Lower Crust.* Thick black arrow shows northwards motion of Indian Lower Crust. (*a*) Channel flow – grey arrows in GHS represent velocity relative to the down going slab. Black arrows and ellipse show vertical shortening + horizontal stretching of GHS. (*b*) Wedge extrusion - grey arrows in GHS represent velocity of a rigid wedge relative to the down going slab. Dashed line of STD reflects model's uncertainty of structure at depth (e.g. Burchfield *et al.* 1992). (*c*) Duplex – GHS deforms as a single thrust sheet within a duplex. *LHD – Lesser Himalayan Duplex.* Modified from Robinson *et al.,* 2006. (*d*) Duplex/Underplating – GHS deforms internally as a thrust stack. Dashed line of STD reflects model's uncertainty of structure at depth. (*e*) Tectonic wedging – Wedge may form as a thrust stack (e.g. grey dashed lines – Webb *et al.* 2013). Tectonic wedging occurs at depth and does not involve exhumation. Dashed black arrow shows exhumation path of wedge during subsequent duplexing of LHS. *GCT – Great Counter Thrust.* Modified from He *et al.,* 2014.

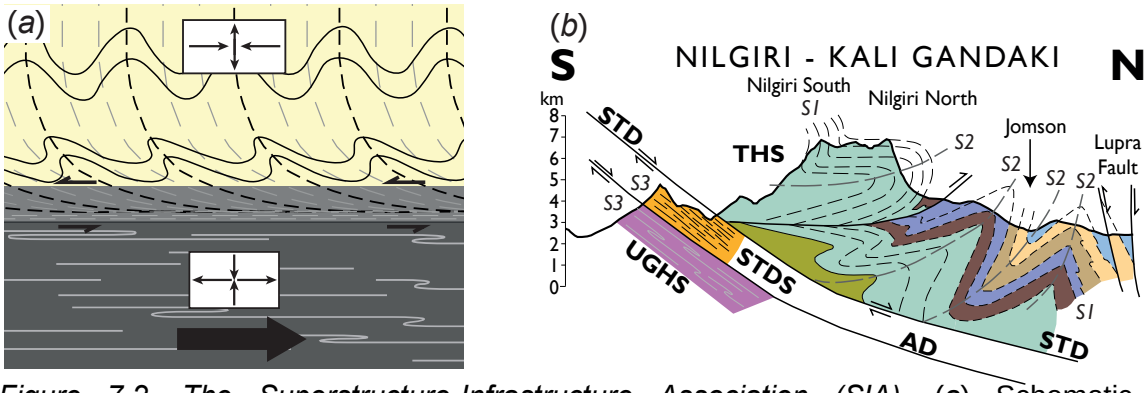

Figure 7.2. The Superstructure-Infrastructure Association (SIA). (*a*) Schematic structural model of the SIA. Superstructure – beige; Infrastructure – dark grey; Abscherungszone (shear zone) – light grey. (*b*) North-south sketch cross section through the eastern margin of Kali Gandaki valley demonstrating the SIA between the THS and GHS. Stratigraphy of THS uses same symbols as Figure 2.4. Modified from Parsons *et al.*, 2014; after Searle, 2010.

(Fyson, 1971; Culshaw *et al.*, 2006; Williams *et al.*, 2006). In some areas, the boundary between the infrastructure and superstructure known as the 'Abscherungszone' (shearing zone; Haller, 1956) forms a transitional zone where upright fold axial surfaces and associated foliation in the superstructure are transposed into parallelism with the underlying infrastructure (e.g. Murphy, 1987). An important feature of the SIA, is the relative timing of deformation, whereby development of the SIA occurs through an early period of crustal shortening and thickening, followed by thermal relaxation, rheological weakening and ductile flow at mid- to lower-crustal depths (Fyson, 1971; Beaumont *et al.*, 2006; Culshaw *et al.*, 2006). Recently, thermo-mechanical modelling has demonstrated that the SIA is a defining feature in large, hot orogens where crustal thickening leads to the development of a rheologically weak middle or lower crust that subsequently flows laterally through horizontal stretching and vertical thinning (Beaumont *et al.*, 2006; Culshaw *et al.*, 2006; Jamieson & Beaumont, 2013).

In the Himalayan orogen, the SIA is clearly replicated by the structural relationship between the GHS and THS (Figure 7.2b) (e.g. Godin, 2003; Kellett & Godin, 2009; Searle, 2010; Kellett & Grujic, 2012). The high grade mid-crustal GHS represents the orogenic infrastructure (Figure 7.2b), characterised by vertical shortening, well defined transpositional fabrics showing signs of both coaxial and non-coaxial deformation and sub horizontal stretching (e.g. Grujic *et al.*, 1996; Grasemann *et al.*, 1999; Grujic *et al.*, 2002; Law *et al.*, 2004; Jessup *et al.*, 2006; Larson & Godin, 2009; Mukherjee & Koyi, 2010). The low grade upper crustal THS represents the superstructure (Figure 7.2b), characterised by horizontal shortening with km-scale upright folds and thrust faults (e.g. Ratschbacher *et al.*, 1994; Godin, 2003; Kellett & Godin, 2009; Searle, 2010). At the boundary between the GHS and THS, fold axial surfaces and axial planar cleavage in the THS are transposed into parallelism with the GHS, through horizontal shearing along the STDS (Figure 7.2b), which behaves as a stretching fault (Means, 1989)

between the THS and GHS (Law *et al.*, 2004; Kellett & Godin, 2009; Searle, 2010; Kellett & Grujic, 2012). Timing constraints based on deformation fabric relationships indicate that crustal thickening and shortening in the THS occurred prior to sub-horizontal stretching in the GHS (Godin, 2003; Kellett & Godin, 2009; Searle, 2010), thereby replicating the SIA. In this respect, the high temperature mid-crustal development of the GHS occurred through infrastructural processes (e.g. channel flow; Grujic *et al.*, 2002; Law *et al.*, 2004; Beaumont *et al.*, 2006; Culshaw *et al.*, 2006; Searle *et al.*, 2006; Larson & Godin, 2009; Searle, 2010; Kellett & Grujic, 2012; Jamieson & Beaumont, 2013).

7.3. Crustal-scale thrust stacking and duplex development

Models of thrust stacking and duplexing are used to explain the tectonic development of some mountain belts such as the European Alps, Canadian Rockies and Spanish Pyrenees (e.g. Boyer & Elliott, 1982; Davis *et al.*, 1983; Butler, 1986; Cook & Varsek, 1994). Duplex development implies crustal thickening and horizontal shortening and occurs through the exploitation of mechanically weak horizons that form basal decollements, combined with progressive stacking of thrust slices (Boyer & Elliott, 1982; Cook & Varsek, 1994). Shortening is accommodated through strain localisation along the detachments and thrust slices undergo little internal deformation (Boyer & Elliott, 1982; Davis *et al.*, 1983). Thrust propagation typically occurs in-sequence, commonly towards the foreland (Boyer & Elliott, 1982). In such situations, deformation 'youngs' down-section (Boyer & Elliott, 1982). These features contrast with those of the SIA and may be used to distinguish 'classic' thrust stacking and duplex development (e.g. Boyer & Elliott, 1982) from infrastructural deformation processes (e.g. Williams *et al.*, 2006).

Deformation in the LHS and Siwaliks, exposed along the Himalayan foreland, is characterised by thrust stacking and duplex development (e.g. Paudel & Arita, 2000; Decelles *et al.*, 2001; Pearson & Decelles, 2005; Robinson & Martin, 2014). Additionally, timing constraints show that thrust stacking within the Lesser Himalayan Duplex occurred in-sequence, propagating towards the foreland (Paudel & Arita, 2000; Pearson & Decelles, 2005). These deformation features, driven by horizontal shortening and vertical thickening, are based on balanced cross sections (Paudel & Arita, 2000; Robinson, 2008; Robinson & Martin, 2014) that provide a robust explanation for the exhumation and upward warping of the GHS during development of the underlying LHD.

More recently, metamorphic and structural discontinuities identified within the GHS, and associated deformation that *youngs* down-section towards the foreland have led

some authors to suggest that in-sequence thrust stacking and duplex development were also responsible for mid-crustal emplacement of the GHS (Carosi *et al.*, 2010; Corrie & Kohn, 2011; He *et al.*, 2014; Montomoli *et al.*, 2014). Whilst such observations fit with the expectations of crustal scale duplex development (e.g. Soper & Barber, 1982; Butler, 1986), they do not provide a means to explain the vertical thinning, horizontal stretching and associated transpositional fabrics and isoclinal folding observed throughout the GHS that are diagnostic features of infrastructural deformation processes (e.g. Grujic *et al.*, 1996; Grasemann *et al.*, 1999; Grujic *et al.*, 2002; Law *et al.*, 2004; Jessup *et al.*, 2006; Larson & Godin, 2009; Mukherjee & Koyi, 2010). Additionally, thrust stacking requires that thrust slices maintain their mechanical strength, whilst failure occurs on the bounding detachments. Thermochronology from the UGHS in the Annapurna-Dhaulagiri Himalaya indicates that it was subjected to high temperatures (>700 ^{o}C) and partial melting over a period of ~30 Myr (Kohn & Corrie, 2011; Larson & Cottle, 2015). The associated drop in strength with increasing temperature and melt production would prevent the UGHS from moving as a coherent block (Rosenberg & Handy, 2005; Rutter *et al.*, 2006; Rosenberg *et al.*, 2007; Jamieson *et al.*, 2011). As a final caveat, models of thrust stacking and duplex development for the GHS are yet to provide a working mechanical explanation for formation of the STDS (Jamieson & Beaumont, 2013).

7.4. The role of the STDS

Kinematic evolution of the STDS provides a critical distinction between channel flow and thrust stacking models for mid-crustal evolution of the GHS (Godin *et al.*, 2006b; Searle, 2010; Kellett & Grujic, 2012). Exposures of the STDS along the Himalaya record either a composite shear zone built from an upper brittle detachment and a lower ductile detachment (e.g. Searle *et al.*, 2003) or an entirely ductile detachment (e.g. Cottle *et al.*, 2007). Additionally, whilst the majority of field and microstructural observations record top-to-the-north sense shearing, top-to-the-south shear sense indicators are also recorded in the STDS (Hodges *et al.*, 1996; Carosi *et al.*, 1998; Godin *et al.*, 1999a; Grujic *et al.*, 2002; Law *et al.*, 2004). In different locations, the top-to-the-south microstructures in the STDS has (relative to top-to-the-north shearing) been interpreted as: (*a*) an earlier fabric relating to southwards thrusting of the THS over the GHS during crustal thickening, (Hodges *et al.*, 1996; Grujic *et al.*, 2002); (*b*) a contemporaneous fabric, indicating a pure shear flattening component of deformation developed during southwards flow of the UGHS beneath the THS (Law *et al.*, 2004); and (*c*) a later fabric developed during late-stage reversal of shear on the STDS, and associated with southward thrusting of the THS over the GHS (Hodges *et al.*, 1996; Godin *et al.*, 1999a).

Channel flow models require that the STDS undergoes kinematic inversion due to a switch from northwards Couette-dominated flow of the GHS to southwards Poiseuille-dominated return-flow (Beaumont *et al.*, 2004; Grujic, 2006; Kellett & Grujic, 2012), thereby accounting for an early reversal in shear sense. In such cases, the ductile portion of the STDS forms a stretching fault (Means, 1989) with a fixed hangingwall (Searle, 2010) that accommodates large amounts of vertical thinning and horizontal stretching (e.g. Law *et al.*, 2004; Law *et al.*, 2011). Later brittle faults can develop within the STDS if it is utilized during exhumation of the GHS (Searle & Godin, 2003; Beaumont *et al.*, 2004; Searle, 2010; Kellett & Grujic, 2012). However, this is not a necessity of the channel flow model, which can exhume the GHS during crustal scale folding or upwarping during duplex development in the underlying LHS with no need for brittle faulting at the top of the STDS (Beaumont *et al.*, 2004; Godin *et al.*, 2006a; Kellett & Grujic, 2012).

In a thrust stacking and duplex system without channel flow, top-to-the-north normal sense shearing above the GHS may still occur in response to focused erosion and exhumation (Kellett & Grujic, 2012). Importantly, in this setting, the STDS is an extensional structure related to exhumation of the GHS and can exist as either a brittle fault or as a composite shear zone with an upper brittle fault and lower ductile shear zone. This latter model for the STDS cannot explain the reported occurrence of earlier top-to-the-south shearing within the STDS, nor can it explain the observed examples of entirely ductile portions of the STDS (Godin *et al.*, 2006b; Kellett & Grujic, 2012). Furthermore, achieving an estimated N-S displacement of 100-200 km along the STDS through extension-related exhumation alone is unfeasible given the lack of additional extensional deformation features to support such claims (Searle *et al.*, 2006; Searle, 2010; Law *et al.*, 2011).

In summary, the observed kinematic features of the STDS and the infrastructural style of internal deformation within the GHS indicate that mid-crustal emplacement and subsequent extrusion and exhumation of the GHS cannot be explained through thrust stacking and crustal scale duplexing alone (Searle, 2010; Kellett & Grujic, 2012). In the case of the Kali Gandaki valley, the STDS is an almost entirely ductile feature, with only minor amounts of brittle deformation towards its top. The STD marks the upper limit of intense pervasive shearing and does not have a discrete principal slip surface. Top-to-the-south sense shearing on the STDS in the Kali Gandaki valley post-dates top-to-the-north sense shearing.

7.5. Tectonic wedging

In acknowledgement of the problems associated with models that only consider thrust stacking and duplex development, some researchers have proposed that the mid crustal evolution of the GHS can be explained by models that invoke tectonic wedging (Figure 7.1e) (Yin, 2006; Webb *et al.*, 2013; He *et al.*, 2014). These models are based upon a variant of the standard duplex system, in which the roof thrust to the duplex (i.e. the STDS) behaves as a passive backthrust (Banks & Warburton, 1986; Price, 1986). The application of the tectonic wedging model to the Himalaya is largely based on the inferred merger of the MCT and STD towards the foreland, interpreted from field observations along the northern margin of the Kathmandu Klippe (Webb *et al.*, 2007; Webb *et al.*, 2011a), and the assumption that the STD forms the southward continuation of the Great Counter Thrust (GCT) (Figure 7.3), which represents a passive roof backthrust to an underlying tectonic wedge (the GHS) (Yin, 2006; Webb *et al.*, 2007). Reversal in shear within the STDS is accounted for by varying the relative motions of the GHS and THS through time, whilst maintaining a southwards motion on the basal detachment (the MCT) (Yin, 2006; Webb *et al.*, 2007).

The tectonic wedging model for the Himalayan orogen proposes that the merger of the STD and MCT occurs in other Himalayan crystalline nappes (Figure 7.3a), although this is based on inferences and cross sectional extrapolation of boundaries (Yin, 2006; Webb *et al.*, 2011a; Webb *et al.*, 2011b; He *et al.*, 2014). It has also been proposed that no other model can explain the suggested merging of the STD and MCT exposed along the Kathmandu Klippe (Figure 7.3c,d) (Webb *et al.*, 2011a; Webb *et al.*, 2013; He *et al.*, 2014). However, this interpretation hangs on the assumption that the two faults are indeed the MCT and STD, which remains highly controversial (e.g. Khanal *et al.*, 2014; Robinson *et al.*, 2014; Khanal *et al.*, 2015). Given the large collection of evidence for out-of-sequence thrusting of the GHS (Hodges *et al.*, 1996; Vannay & Hodges, 1996; Grujic *et al.*, 2002; Larson *et al.*, 2010a; Mukherjee, 2013a; Larson & Cottle, 2014), it is entirely possible that the exposed section along the Kathmandu Klippe, interpreted as the tip of the GHS, could be a thrust slice cut from the GHS (e.g. Khanal *et al.*, 2015), in which case, the faults bounding the tip cannot represent the merger of the STD and MCT. In this situation, tectonic wedging fits the development of the Kathmandu Klippe. However, there is no supporting evidence to warrant extrapolation of these observations to explain emplacement of the entire GHS. This caveat is compounded by the absence of evidence (geological or geophysical) for a structural link between the STDS and GCT (one of the main stimuli for proposing the model; Yin, 2006). Based on these shortcomings, the tectonic wedging model for the Himalaya as

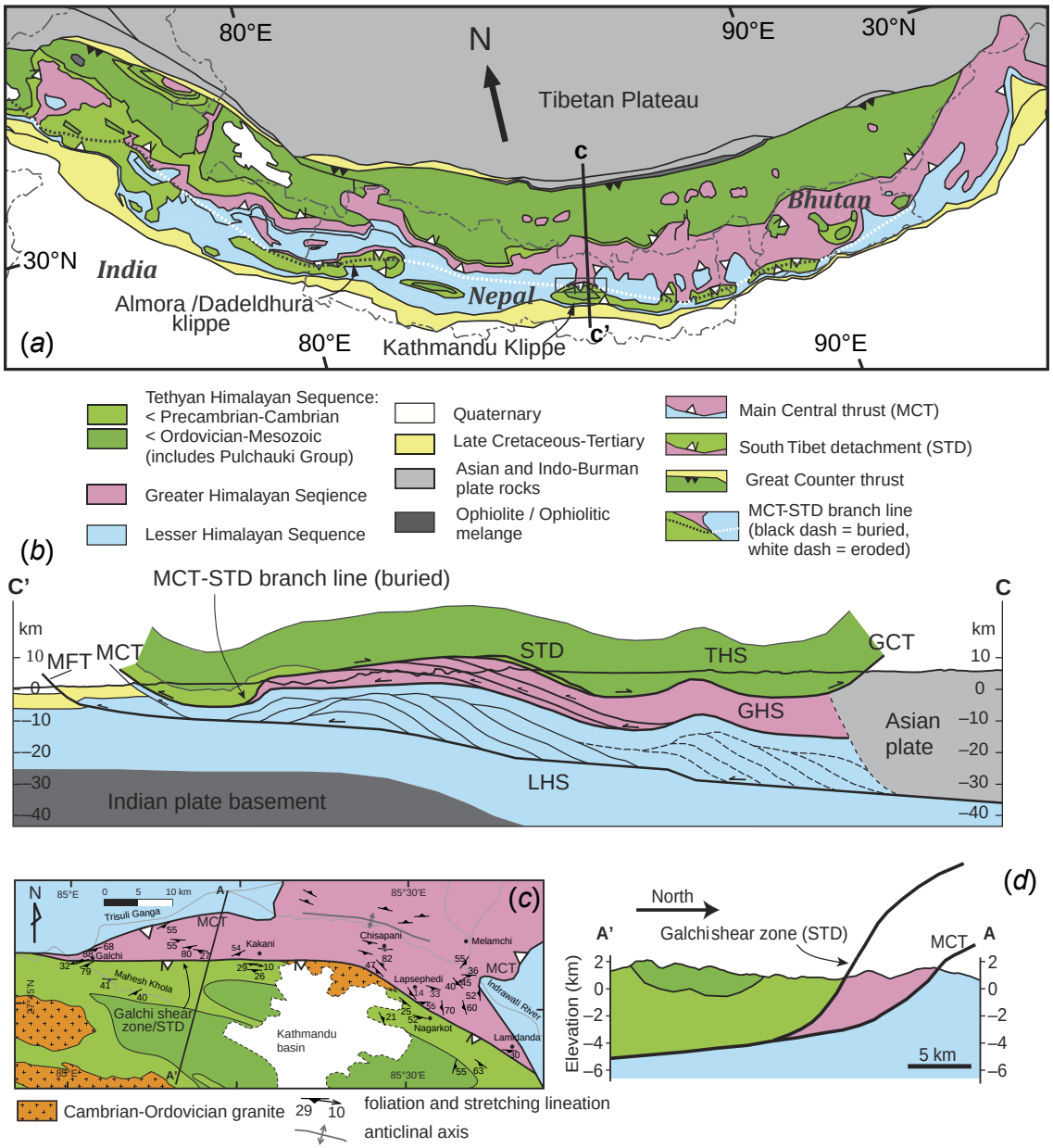

Figure 7.3. Structural basis for the tectonic wedging model applied to the Himalayan orogen (After He et al., 2014). (*a*) Simplified tectonic map of the Himalayan orogen showing proposed location of the MCT-STD merger (branch line) and the mapped location of the GCT. Small black box shows the extent of Figure 7.3c. (*b*) Schematic cross section through central Himalaya in Kathmandu region. (*c*) Geological map of the Kathmandu Klippe. Galchi shear zone is the proposed foreland exposure of the STD. (*d*) Simplified cross section through the Kathmandu Klippe showing the proposed MCT-STD merger. All figures after He *et al.*, 2014.

proposed by Yin (2006) and Webb (2007) does not provide a viable model for kinematic evolution of the GHS.

7.6. The composite orogenic system

Thus far, it has been shown that models of thrust stacking, duplex development and tectonic wedging, cannot in isolation, explain the kinematic evolution of the GHS and mid-crustal channel flow must have played an important role during development of the observed SIA (Godin *et al.*, 1999b; Beaumont *et al.*, 2006; Culshaw *et al.*, 2006;

Williams *et al.*, 2006; Kellett & Godin, 2009; Searle, 2010; Jamieson & Beaumont, 2013). Similarly, it is also acknowledged that some observations made from the GHS and bounding units cannot be explained without the occurrence of thrust stacking, duplex development or possibly tectonic wedging (Kellett & Grujic, 2012; Wang *et al.*, 2013; Webb *et al.*, 2013; He *et al.*, 2014; Larson & Cottle, 2014; Mottram *et al.*, 2014a,b). This dichotomy may be overcome if the rheological boundary conditions that govern the structural development of an orogen vary both spatially and temporally (Beaumont *et al.*, 2004; Larson *et al.*, 2010b; Jamieson & Beaumont, 2013).

When channel flow and critical taper wedge models are considered together, a variety of orogenic processes, commonly perceived as mutually exclusive 'end-member' models may operate as distinct orogenic domains that form the modular components of a composite orogenic system (Godin *et al.*, 2006a; Larson *et al.*, 2010b; Spencer *et al.*, 2012; Jamieson & Beaumont, 2013; Mukherjee, 2013a; Wang *et al.*, 2013; Larson & Cottle, 2014). For 'Large Hot Orogens' such as the Himalayan-Tibetan system (Beaumont *et al.*, 2006; Jamieson & Beaumont, 2013), the initial stages of rapid crustal thickening and heating lead to melt-driven rheological weakening of mid-crustal levels and subsequent plateau development (Jamieson *et al.*, 2011; Kohn & Corrie, 2011; Searle *et al.*, 2011; Jamieson & Beaumont, 2013; Larson & Cottle, 2015). Thermo-mechanical models demonstrate that gravity driven mid-crustal lateral flow from beneath the plateau to its margins then occurs in response to the topographic gradient between the plateau and orogenic foreland (Beaumont *et al.*, 2001; Beaumont *et al.*, 2004; Jamieson *et al.*, 2011; Jamieson & Beaumont, 2013). This two-stage development of crustal thickening, followed by lateral flow typifies the SIA, referred to here as 'orogenic domain 1' (Figure 7.4) (Wegmann, 1935; Beaumont *et al.*, 2006; Culshaw *et al.*, 2006). Contemporaneously, out on the flanks of the plateau, colder, thinner upper crustal rocks form a foreland propagating coulomb thrust wedge (Platt, 1986; Willett *et al.*, 1993), with a critical taper (referred to as the thrust wedge from herein) balanced by convergence and erosion rates (Decelles *et al.*, 2002; Beaumont *et al.*, 2004; Pearson & Decelles, 2005; Jamieson & Beaumont, 2013). These wedges (orogenic domain 2) are characterised by thrust stacking and duplex development and are distinct from orogenic domain 1 (Figure 7.4) (Paudel & Arita, 2000; Pearson & Decelles, 2005). Thermo-mechanical simulations (Beaumont *et al.*, 2001; Beaumont *et al.*, 2004; Jamieson & Beaumont, 2013) have demonstrated that during southwards extrusion of a mid crustal channel beneath the Himalaya (orogenic domain 1), horizontal tunnelling of the channel stops upon contact with the cold, strong Indian continental crust in the thrust wedge, which develops in the LHS and Siwaliks (orogenic domain 2) of the Himalayan foreland (Beaumont *et al.*, 2001; Beaumont & Jamieson,

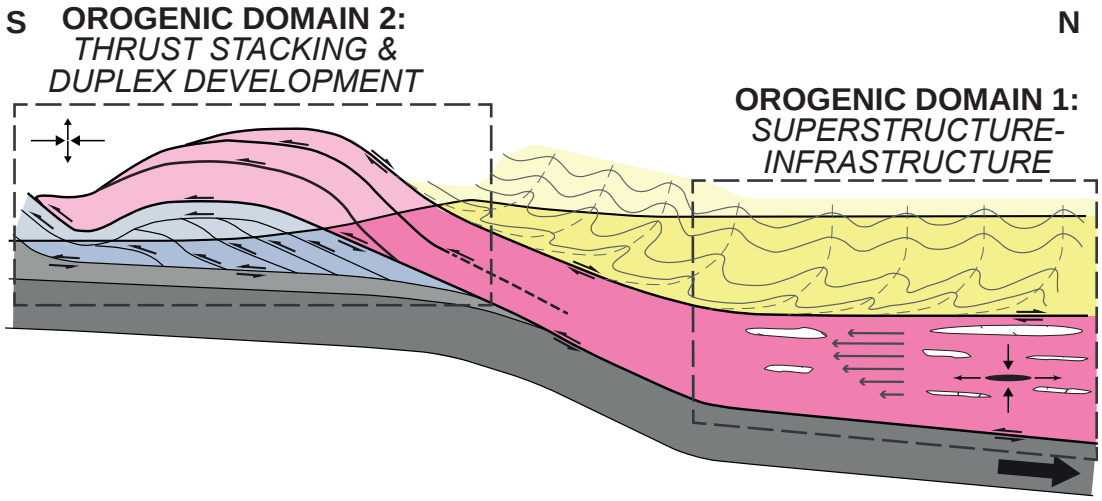

Figure 7.4. The composite orogenic system. Schematic cross sectional model of the Himalayan orogen comprising multiple 'orogenic domains' characterised by distinct tectonic processes. Structure of Orogenic Domain 2 based on Robinson *et al.,* 2006. *Yellow – THS; Purple – GHS; White – mid-crustal partial melting; Blue – LHS; Light grey – Indian Upper Crust; Dark grey – Indian lower crust.*

2010). In this sense, orogenic domain 1 is responsible for the mid-crustal deformation of the GHS, driven by a gravitational pressure gradient and convergence, whilst orogenic domain 2 is responsible for the upper-crustal extrusion and exhumation of the GHS driven by erosion and convergence (Figure 7.4).

If all three forces (gravity, convergence, erosion) are in equilibrium, the channel will extrude and exhume towards the surface as an '*active channel*' (Beaumont *et al.*, 2001; Beaumont *et al.*, 2004), which may replicate the final kinematic stages of a rigid wedge extrusion model as the exhuming channel cools and strengthens (Grujic, 2006). If erosion rates drop significantly, the '*active channel*' is no longer exhumed along the Himalayan front and instead, retreats towards the plateau (Beaumont *et al.*, 2004; Jamieson & Beaumont, 2013). This retreat does not reflect northward motion of channel material but, relates to the rheological boundary between the low viscosity '*active channel*' and higher viscosity '*channel plug*' (Beaumont *et al.*, 2004). Contemporaneous to channel retreat, deformation in the overlying thrust wedge migrates to the hinterland as the thrust wedge expands and builds upwards towards a new critical angle (Beaumont *et al.*, 2001; Beaumont *et al.*, 2004; Godin *et al.*, 2006a; Larson *et al.*, 2010b; Jamieson & Beaumont, 2013). Naturally observed hinterland uplift of a sub-critical thrust wedge, coinciding with reduced erosion rates in the early to mid Miocene (White *et al.*, 2002), is suggested to be the driving force behind development of the gneissic domes in the North Himalayan Antiform (see Figure 2.1) of southern Tibet (e.g. Beaumont *et al.*, 2004; Lee *et al.*, 2004; Larson *et al.*, 2010a; Yan *et al.*, 2011) and crustal scale buckling of the GHS (e.g. Gleeson & Godin, 2006; Godin *et al.*, 2006a).

If channel retreat occurs before the *active channel* is extruded and exhumed to the surface, the STD will not intersect the thrust wedge and the STDS will be an entirely ductile (i.e. no upper brittle component) infrastructural shear zone (Jamieson & Beaumont, 2013). Uplift in the hinterland then continues until the thrust wedge reaches a critical taper angle, and/or erosion rates at the Himalayan front increase to efficient levels, at which point out-of-sequence thrusting occurs along the Himalayan front, and the foreland fold thrust belt begins to build again (Beaumont *et al.*, 2004; Hodges, 2006; Larson *et al.*, 2010b; Jamieson & Beaumont, 2013). This late-orogenic stage rejuvenation of deformation along the Himalayan front is suggested to be responsible for out-of-sequence thrusting in the GHS and Lesser Himalayan Duplex (Jamieson *et al.*, 2006; Larson *et al.*, 2010b; Kellett & Grujic, 2012) and reactivation of the MCT (Wobus *et al.*, 2003; Huntington *et al.*, 2006).

Together, this sequence of geological events determined from first order observations and subsequently reproduced by working mechanical models, demonstrate that in large hot orogens, channel flow and critical (coulomb) wedge tectonics need not be mutually exclusive processes and should in fact be dynamically linked within the same system (Beaumont *et al.*, 2001; Beaumont *et al.*, 2004; Godin *et al.*, 2006a; Hodges, 2006; Beaumont & Jamieson, 2010; Larson *et al.*, 2010b; Spencer *et al.*, 2012; Jamieson & Beaumont, 2013; Mukherjee, 2013a; Wang *et al.*, 2013). Applying this concept to previous studies that argued for the occurrence of one tectonic process over another (Robinson *et al.*, 2006; Kohn, 2008) suggests that these apparently contradictory studies may actually reflect spatial or temporal differences in orogenic domains. Thus, channel flow and critical wedge tectonics are entirely compatible if the rheological boundary conditions for orogenesis are considered to be mobile through time and space. It is through this holistic view that the kinematic evolution of the GHS in the Annapurna-Dhaulagiri region and the role of channel flow in the evolution of the Himalayan orogen is now assessed.

7.7. Validating models of channel flow for the Himalayan orogen

In Chapter 1 a suite of required geological criteria for the operation of channel flow during the formation of the Himalayan orogen are listed. These criteria will now be discussed in light of the research presented in this thesis, and in combination with previously published constraints, in order to assess the applicability of the channel flow model to the GHS exposed in the Annapurna-Dhaulagiri region.

7.7.1. High grade metamorphic rocks bound above and below by sub-parallel syn-metamorphic ductile shear zones with opposite shear senses and coeval activities.

Following the definitions of Searle *et al.* (2008) and Searle (2010), the GHS in the Annapurna-Dhaulagiri region is bound above by the STD and below by the MCT. These structures have a top-to-the-north and top-to-the-south shear sense, respectively. Deformation temperatures associated with these structures indicate that the MCT was active between ~300-500 ^{o}C, whilst the STD is less well constrained between <300-600 ^{o}C (Figures 3.20 & 3.21). The UGHS is bound above by the AD and DD in the Kali Gandaki and Modi Khola valleys, respectively and below by the CT in both valleys. The AD and DD are top-to-the-north ductile shear zones and the CT is a top-to-the-south ductile shear zone. Deformation temperatures from these structures indicate that the CT, AD and DD were active above 650 ^{o}C and between 300-650 ^{o}C (Figures 3.20 & 3.21). Within the UGHS high temperature deformation occurred between ~550-850 ^{o}C and was synchronous with partial melting (Figure 2.9). Monazite growth indicates that early prograde metamorphism in the UGHS in the Kali Gandaki transect occurred during 48-30 Ma (Larson & Cottle, 2015). Peak temperatures in Unit III were attained between 35-31.5 Ma (Godin *et al.*, 2001). The earliest melt production occurred during 41-35 Ma within the kyanite stability field (Godin *et al.*, 2001; Carosi *et al.*, 2014). Following this, monazite growth recorded continued crustal melting between 28-18 Ma (Larson & Cottle, 2015). In Unit II of the Kali Gandaki valley, a deformed leucogranite produced a crystallisation age of ~22.5 Ma (Nazarchuk, 1993) providing a minimum age for penetrative deformation. In the Modi Khola valley, titanite geothermometry from Unit II records a prolonged period of increasing temperatures from 700-725 ^{o}C between 35-40 Ma to 775-800 ^{o}C between 20-25 Ma (Kohn & Corrie, 2011). The earliest melt production in the Modi Khola transect is recorded at ~36 Ma from inherited monazites in Unit III (Hodges *et al.*, 1996), which correlates with the earliest prograde metamorphism recorded in Unit III between 38-30 Ma (Corrie & Kohn, 2011). Monazite growth in Unit I of the Modi Khola transect records prograde metamorphism and partial melting between ~33 and 21 Ma (Corrie & Kohn, 2011). Deformed migmatitic leucosomes in Unit I have a crystallisation age of 21.5 to 22.5 Ma (Hodges *et al.*, 1996). An undeformed leucogranite dyke that cross cuts the AD in the Kali Gandaki valley, indicates that deformation on the AD ended before ~22 Ma (Godin *et al.*, 2001). In the Modi Khola valley, a boudinaged leucogranite in the STDS has a crystallisation age of ~22 Ma, providing a minimum age for motion on the DD (Hodges *et al.*, 1996). Along the CT, the crystallisation age of a cross-cutting undeformed leucogranite in the Kali Gandaki valley indicates that penetrative shearing on the CT occurred before ~21 Ma (Nazarchuk, 1993). The age of an undeformed dyke in Unit II

in the Modi Khola indicates that deformation stopped sometime between 22.5 and 18.5 Ma (Hodges *et al.*, 1996).

Considered together, these constraints imply that the UGHS in the Annapurna-Dhaulagiri region was subjected to high temperatures deformation (>700 ^{o}C) for as much as ~30 Myr and underwent partial melting for at least ~15 Myr (Kohn & Corrie, 2011; Carosi *et al.*, 2014; Larson & Cottle, 2015). Top-to-the-north shearing on the AD and DD and top-to-the-south shearing on the CT occurred during this time, with a recorded overlap of activity at least at ~22 Ma and probably earlier than this (Nazarchuk, 1993; Hodges *et al.*, 1996; Godin *et al.*, 2001). These constraints indicate that the UGHS in the Annapurna-Dhaulagiri region has had a long history of high grade syn-metamorphic and syn-migmatitic deformation relating to internal shearing and deformation on the CT and AD/DD. The sustained period of high temperatures and partial melting suggest that the UGHS should have been subjected to significant melt-driven rheological weakening that would ultimately lead to the initiation of mid-crustal channel flow (Jamieson *et al.*, 2004; Kohn & Corrie, 2011; Jamieson & Beaumont, 2013; Larson & Cottle, 2015). Lower crystal-plastic deformation temperatures (280-500 ^{o}C) and brittle structures associated with shearing on the MCT indicate that this structure facilitated the late stage extrusion and exhumation of the GHS, perhaps as a rigid wedge, and was not involved during mid-crustal extrusion. It is possible that the STD was also active during this low temperature, late-stage exhumation, based on poorly constrained deformation temperatures of ~300-600 ^{o}C.

7.7.2. An inverted metamorphic profile at the base of the channel and a right-way-up metamorphic profile at the top of the channel.

Petrological observations of the GHS in the Annapurna region record an inverted metamorphic sequence increasing up-section form biotite-chlorite to garnet grade in the LGHS. Kyanite and in-situ partial melting is observed throughout Unit I of the UGHS. In Unit II and Unit III, kyanite is sometimes observed, whilst partial melting is common. Other authors report the occurrence of sillimanite in isolated pelitic pods in the top portion of the UGHS (Unit III) (Hodges *et al.*, 1996; Godin, 2003; Larson & Godin, 2009). In the STDS a right-way-up sequence is recorded by an up-section decrease from diopside to biotite grade. Peak metamorphic temperatures of ~700-850 ^{o}C are recorded in the UGHS of both transects (this study, Section 3.4.2.; Le Fort *et al.*, 1987; Kaneko, 1995; Martin *et al.*, 2010; Corrie & Kohn, 2011; Kohn & Corrie, 2011) and peak pressures of 10-16 Kbar and 6-10 Kbar are recorded in the Modi Khola transect (Martin *et al.*, 2010; Corrie & Kohn, 2011) and Kali Gandaki transect (Le Fort *et al.*, 1987; Vannay & Hodges, 1996), respectively. Such high temperature are consistent with the metamorphic conditions required for development

of a partially-molten and rheologically-weakened mid-crustal layer (Rosenberg & Handy, 2005; Rutter *et al.*, 2006; Harris, 2007; Rosenberg *et al.*, 2007; Jamieson *et al.*, 2011) and fall within the range of temperatures and pressures required by current working thermo-mechanical models of mid-crustal channel flow for the Himalayan orogen (Jamieson *et al.*, 2004; Jamieson *et al.*, 2006).

7.7.3. Significant syn-tectonic partial melting, capable of sustaining channel flow through a reduction in rock strength relative to stronger over- and underlying crustal layers.

PTt constraints indicate that the UGHS underwent partial-melting and high temperature metamorphism (>700 ^{o}C) from ~48 to 18 Ma (Le Fort *et al.*, 1987; Nazarchuk, 1993; Kaneko, 1995; Hodges *et al.*, 1996; Godin *et al.*, 2001; Martin *et al.*, 2010; Corrie & Kohn, 2011; Kohn & Corrie, 2011; Carosi *et al.*, 2014; Larson & Cottle, 2015). However, it is noted here and by others (e.g. Nazarchuk, 1993; Larson & Godin, 2009) that melt volumes in the UGHS of the Annapurna-Dhaulagiri region are substantially lower than in equivalent strata elsewhere (e.g. Garhwal - Scaillet *et al.*, 1990; Langtang - Inger & Harris, 1992; Manaslu - Harrison *et al.*, 1999; Zanskar - Walker *et al.*, 1999; Bhutan - Grujic *et al.*, 2002; Everest - Searle *et al.*, 2003; Sikkim - Searle & Szulc, 2005; Makalu - Streule *et al.*, 2010a). Additionally, in the Annapurna-Dhaulagiri region, sillimanite is almost entirely absent from the UGHS (Nazarchuk, 1993; Hodges *et al.*, 1996; Carosi *et al.*, 2014) and only reported from the very top of the sequence (Larson & Godin, 2009; Carosi *et al.*, 2014) and rarely and sporadically through the rest of the UGHS (Arita, 1983; Carosi *et al.*, 2014). In a migmatitic sample from Unit I in the Kali Gandaki valley, Carosi *et al.* (2014) observed rare fibrolitic sillimanite needles within fractures in kyanite and sometimes at the rims of biotite, muscovite and garnet. These microstructural relationships were interpreted as indicating that the rock had equilibrated within the kyanite-biotite-garnet-melt field, before crossing into the sillimanite field (Carosi *et al.*, 2014). Accordingly, the pertinent question to ask when considering models of channel flow is *'was the viscosity of the UGHS low enough for crustal flow?'*

An additional consideration when assessing the viscosity of UGHS in terms of models of crustal flow is channel thickness (Beaumont *et al.*, 2004; Jamieson *et al.*, 2004; Mukherjee, 2013b). In order to maintain a constant velocity, a reduction in channel thickness must be accompanied by a reduction in viscosity (Turcotte & Schubert, 2002; Grujic, 2006). The numerically modelled thickness required for channel flow in the Himalayan orogen is 10-20 km (Beaumont *et al.*, 2004; Jamieson *et al.*, 2004; Godin *et al.*, 2006b) and in most regions the UGHS matches or exceeds this (e.g. *10-15 km – Bhutan, Manaslu*, *Garhwal*; Grujic *et al.,* 2002; Searle & Godin, 2003; Webb *et al,.*

	– Log A (MPa^{-n} s^{-1})	error	Q ($kJ\ mol^{-1}$)	error	n	error	Source
Quartzite with melt	– 7.75	±2	137	±34	4	±0.9	Gleason & Tullis 1995
Quartz-diorite	7.3		219		2.4		Hansen & Carter 1982
Granite	4.6		139		3.4		Hansen & Carter 1982
Plagioclase-Diopside Agg.	– 1.53	+1.25, – 1.24	454	±34	1		Dimanov & Dresden 2005

Table 7.1. Flow law parameters for selected geological materials. A – pre-exponent constant, *Q* – activation energy, *n* – power law exponent.

2011b; *20 km – Langtang, Sikkim*; Inger & Harris, 1992; Searle & Szulc, 2005; *30 km – Everest-Makalu*; Searle *et al.*, 2003; Jessup *et al.*, 2006; Streule *et al.,* 2010a). The UGHS of the Annapurna-Dhaulagiri region has a structural thickness of ~7 km so it is necessary to consider whether this reduced thickness would hinder or even prevent channel flow (Godin *et al.*, 2006b).

If the average velocity of a channel, (u_m) is known, then the viscosity, (μ) of that channel is defined as,

$$\mu = -\left[\frac{1}{12}\left\{\frac{h^2}{\left(\frac{u_m - (u_0/2)}{dp/dx}\right)}\right\}\right] \qquad \textit{Equation 7.1}$$

where h is channel thickness, u_0 is the velocity of the down-going channel wall and dp/dx is the pressure gradient, with dp being the difference in channel pressure over the horizontal channel distance dx (Turcotte & Schubert, 2002). Suitable parameters may be derived from the return-flow portion of particle pathways (Figure 7.5) taken from thermo-mechanical channel flow model HT1 of Beaumont *et al.* (2004) and Jamieson *et al.* (2004; their figure 4). Over an 18 Myr period of return-flow with a convergence rate of 50 mm yr^{-1}, the four particle pathways shown in Figure 7.5 have a velocity of 0.019-0.020 m yr^{-1} and undergo a 2.25-8.50 Kbar reduction in pressure over a distance of 345-360 km. Based on these parameters, a channel flow of 7 km thickness has a viscosity of 1.6-5.4 x 10^{19} Pa s. Therefore, with these constraints as boundary conditions, the thermo-mechanical channel flow models (Beaumont *et al.*, 2001; Beaumont *et al.*, 2004), which assign a '*Melt Weakened*' rheology of 10^{19} Pa s to material at >700 ^{o}C, should produce an effective southwards return-flow.

A comparison of the above calculated channel viscosity with experimentally derived flow laws provides another means to assess the rheological weakness of the UGHS (e.g. Mukherjee & Mulchrone, 2012; Mukherjee, 2013b). Stress (σ^n) and temperature (T) dependant flow laws for a variety of experimentally deformed rocks (Table 7.1), provide a means to determine the strain rate, $(\dot{\varepsilon})$ of visco-plastic creep (e.g. Passchier & Trouw, 2005),

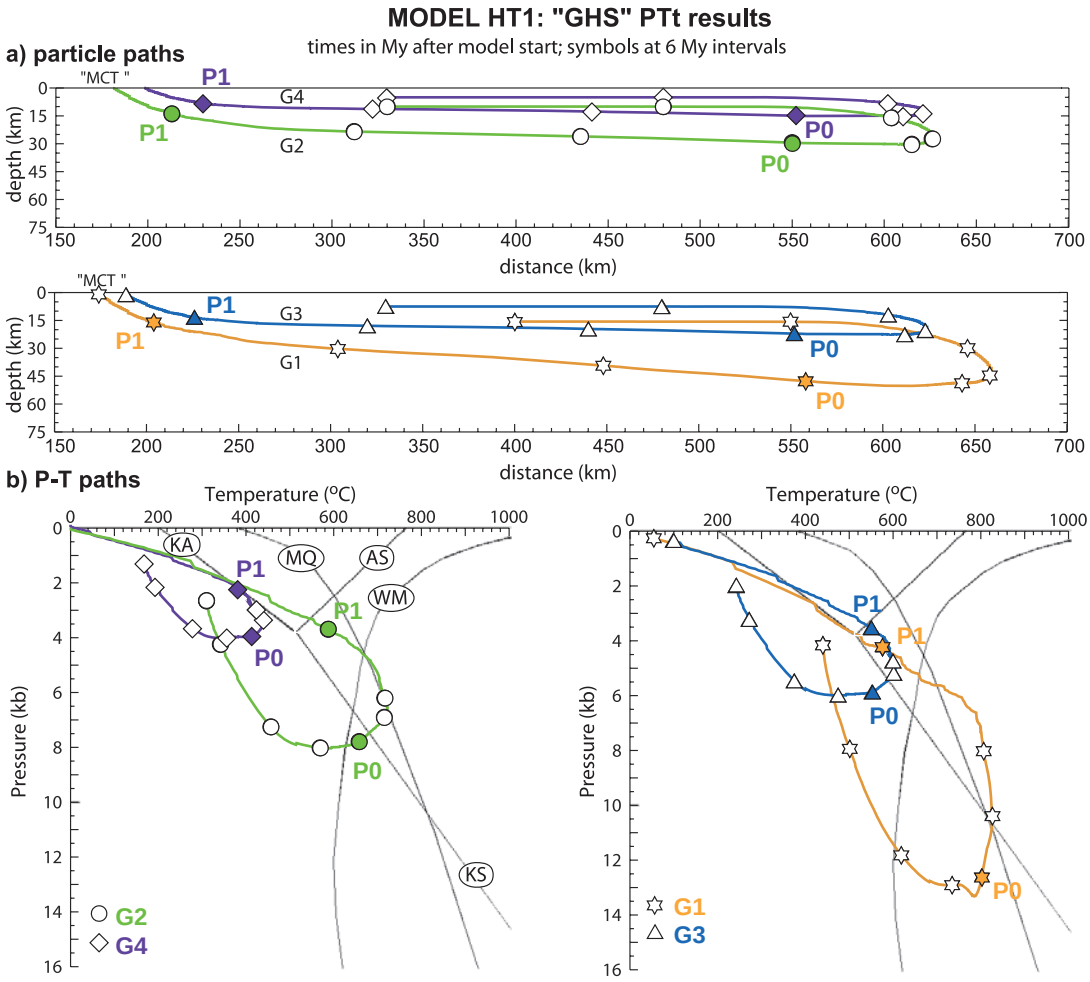

Figure 7.5. GHS particle pathways from channel flow model HT1 (Jamieson et al., 2004). (*a*) Paths for particles G1, G2, G3 and G4 through crust (*x* = horizontal distance, *y* = crustal depth) from channel flow model HT1. Pairs of points separated for clarity. Total model duration = 54 million years (Myr). Symbols on pathway show 6 Myr intervals. Coloured symbols P0 and P1 show interval of southwards return flow used to determine estimated channel pressure gradients for *Equations 7.1* and *7.3.* (*b*) Pressure-temperature time paths for particles G1, G2, G3 and G4. Coloured symbols P0 and P1 show interval of southwards return flow used to determine estimated channel pressure gradients for *Equations 7.1* and *7.3.* Reaction boundaries defined as, *KA – kyanite-andalusite; KS – kyanite-sillimanite; AS – andalusite-sillimanite; MQ – muscovite + quartz = Al-silicate + K-feldspar + H_2O; WM – fluid present melting of granitoid rocks.* All figures after Jamieson *et al.*, 2004.

$$\dot{\varepsilon} = A\sigma^{n}\exp(-Q/RT) \qquad \textit{Equation 7.2}$$

where A is a pre-exponential constant (MPa^{-n} s^{-1}), n is the power law stress exponent, Q is activation energy (kJ mol^{-1}) and R is the gas constant. Flow laws have been selected for dry quartzite with small amounts (1-2%) of melt (Gleason & Tullis, 1995), a dry quartz-diorite and dry granite (Hansen & Carter, 1982; Kirby, 1985), and a synthetic dry aggregate of plagioclase (75% volume) and clinopyroxene (25% volume) (Dimanov & Dresen, 2005). The quartz-diorite and granite flow laws are used as a proxy for a feldspathic gneiss rheology, whilst the plagioclase-clinopyroxene aggregate is used as a proxy for a calc-silicate gneiss rheology. A channel temperature of T = 750 °C, is based on metamorphic temperatures from the UGHS of the Annapurna-Dhaulagiri

region. Shear stress (τ), provides an estimate for flow stress (σ), and is determined from the previously calculated pressure gradient (dp/dx), for a channel of 7 km thickness from the equation (Turcotte & Schubert, 2002),

$$\tau = \frac{1}{2}\frac{dp}{dx}(2y - h) - \mu\frac{u_0}{h} \qquad \textit{Equation 7.3}$$

Based on the pressure gradients derived from the four channel material pathways measured from Jamieson ***et al.*** (2004) (Figure 7.5), shear stress, in the central part of a 7 km thick channel (y = $h/2$ = 3.5 km) ranges between 3.6 and 12.3 MPa.

At T = 750 ^{o}C and σ^n = 3.6-12.3 MPa, strain rates calculated from the four flow laws (Table 7.2) are of the order of 10^{-11} s^{-1} to 10^{-14} s^{-1}. Using the equation,

$$\mu = \dot{\varepsilon}\sigma \qquad \textit{Equation 7.4}$$

the selected flow laws produce estimated viscosities of 10^{17}–10^{19} Pa s for dry quartzite with melt, 10^{18}–10^{19} Pa s for dry quartz-diorite, 10^{19}–10^{20} Pa s for dry granite and 10^{18} Pa s for the plagioclase-clinopyroxene aggregate (Table 7.2). The majority of these values equate to, or fall below, the previously estimated viscosity required for a 7 km thick channel (1.6-5.4 x 10^{19} Pa s). They also match or fall below the chosen viscosity of the '***Melt Weakened***' rheology of the thermo-mechanical channel flow models (Beaumont ***et al.***, 2001; Beaumont ***et al.***, 2004). Notably, with the exception of the quartzite flow law, these viscosities are for rocks that have not undergone partial melting. The proposed driving force for rheological weakening of mid-crustal rocks is the addition of melt (Rosenberg & Handy, 2005; Grujic, 2006; Rosenberg ***et al.***, 2007; Jamieson ***et al.***, 2011), with an order of magnitude drop in rock strength during an increase in melt fraction from 0% to 8% (Rosenberg & Handy, 2005).

The effect of partial melting on rock rheology may be considered with a modified flow law derived from partially molten synthetic granite (Rutter ***et al.***, 2006),

$$\varepsilon = A\, exp(B\Phi^m)\, exp(-Q/RT)\sigma^n \qquad \textit{Equation 7.5}$$

Where Φ is the melt fraction, which ranges from 0 (0% melt) to 1 (100% melt), Q is the activation energy (220 ± 65 kJ mol^{-1}), and A, B, m and n are material constants ($\log A$ = -1.39 MPa^{-n} s^{-1}; B = 192; m = 3; and n = 1.8). This flow law provides a potential proxy for migmatite rheology in the UGHS. Observations from migmatitic sections in the UGHS of the Annapurna-Dhaulagiri Himalaya typically record melt fractions of approximately 0.1-0.3 (Chapter 3). Based on this equation, the viscosities of partially molten feldspathic rocks from the UGHS with $\Phi = 0.1$, 0.2 and 0.3 are of the order of 10^{17} to 10^{18} Pa s, 10^{17} Pa s and 10^{15} Pa s, respectively (Table 7.3).

	σ (*MPa*)	$\dot{\varepsilon}$ (s^{-1})	μ (*Pa s*)	*Source*
Quartzite with melt	3.6	3.2×10^{-13}	1.1×10^{19}	Gleason & Tullis 1995
	4.4	6.6×10^{-13}	6.6×10^{18}	
	6.4	3.0×10^{-12}	2.2×10^{18}	
	12.3	4.2×10^{-11}	3.0×10^{17}	
Quartz-diorite	3.6	1.8×10^{-13}	2.0×10^{19}	Hansen & Carter 1982
	4.4	2.9×10^{-13}	1.5×10^{19}	
	6.4	7.0×10^{-13}	9.1×10^{18}	
	12.3	3.4×10^{-12}	3.6×10^{18}	
Granite	3.6	1.6×10^{-14}	2.3×10^{20}	Hansen & Carter 1982
	4.4	3.0×10^{-14}	1.5×10^{20}	
	6.4	1.1×10^{-13}	5.9×10^{19}	
	12.3	1.0×10^{-12}	1.2×10^{19}	
Plagioclase-Diopside Agg.	3.6	7.1×10^{-13}	5.1×10^{18}	Dimanov & Dresden 2005
	4.4	8.5×10^{-13}	5.1×10^{18}	
	6.4	1.2×10^{-12}	5.1×10^{18}	
	12.3	2.4×10^{-12}	5.1×10^{18}	

Table 7.2. Strain rate and viscosity of a 7 km thick channel determined from experimental flow laws. σ – Flow stress (determined from model derived pressure gradients – s*ee Figure 7.5*), $\dot{\varepsilon}$ – strain rate, μ – viscosity. See Table 7.1 for flow law parameters.

Φ	σ (*MPa*)	$\dot{\varepsilon}$ (s^{-1})	μ (*Pa s*)
0.1	3.6	3.0×10^{-12}	1.2×10^{18}
	4.4	4.1×10^{-12}	1.1×10^{18}
	6.4	8.1×10^{-12}	7.9×10^{17}
	12.3	2.7×10^{-11}	4.6×10^{17}
0.2	3.6	1.1×10^{-11}	3.2×10^{17}
	4.4	1.6×10^{-11}	2.8×10^{17}
	6.4	3.1×10^{-11}	2.1×10^{17}
	12.3	1.1×10^{-10}	1.2×10^{17}
0.3	3.6	4.3×10^{-10}	8.4×10^{15}
	4.4	6.0×10^{-10}	7.2×10^{15}
	6.4	1.2×10^{-09}	5.4×10^{15}
	12.3	3.9×10^{-09}	3.2×10^{15}

Table 7.3. Strain rate and viscosity of a 7 km thick channel determined from experimental flow law for a partially molten granite with variable melt fractions. Parameters derived from flow law of Rutter *et al.*, 2006. Φ – Melt fraction, σ – flow stress (determined from model derived pressure gradients – s*ee Figure 7.5*), $\dot{\varepsilon}$ – strain rate, μ – viscosity. See Table 7.1 for flow law parameters.

The results presented above suggest that at peak metamorphic temperatures, the UGHS in the Annapurna-Dhaulagiri region was weak enough to form a southwards directed return channel flow, despite its lower than typical structural thickness and melt volume. This is also supported by 'Model 3' of the thermo-mechanical channel flow simulations, which did not impose a '*Melt Weakened*' rheology at high temperatures (Beaumont *et al.*, 2004). During this simulation, in which deformation was governed by power-law creep flow laws (e.g. Gleason & Tullis, 1995) regardless of temperature, mid-crustal channel flow occurred at 850 ^{o}C, albeit at a more 'sluggish' pace than that produced by the '*Melt Weakened*' rheology (Beaumont *et al.*, 2004). Additionally, in this simulation, there is no development of an upper detachment to the channel (i.e. no STDS equivalent structure) and the upper and middle crust remain coupled (Beaumont *et al.*, 2004).

Whilst it is shown that the UGHS in the Annapurna-Dhaulagiri Himalaya may have been weak enough for mid-crustal flow, the relationships between channel thickness, melt volume and viscosity still holds. Thus, the UGHS in the Annapurna-Dhaulagiri Himalaya must have been relatively stronger than UGHS-equivalent units elsewhere in the Himalaya that are thicker (10-30 km) and had higher melt fractions ($\Phi = 0.2$-0.4). Lateral variations in viscosity

should result in orogen-parallel pressure gradients, which suggests that the UGHS may have flowed both perpendicular and parallel to the orogenic front.

7.7.4. Pervasive general shear throughout the channel with concentration of deformation on the channel margins. Deformation at the margins has a larger component of non-coaxial strain relative to deformation in the channel centre.

The GHS of the Annapurna-Dhaulagiri region is pervasively sheared (Figures 2.8-2.13 & 3.1-3.7). Field observations throughout the GHS record a strong transpositional foliation and associated coaxial (e.g. boudinage) and non-coaxial (e.g. drag folds, rotated augen) deformation features. Within the UGHS, migmatites are commonly layered in response to shear driven melt migration (Figure 2.9). Whilst these deformation features are observed throughout the GHS, relative changes in CPO intensity and AMS shear strain proxy across the sample transects (Figure 5.6) indicate that strain was concentrated on the bounding shear zones at the margins of the UGHS, LGHS and STDS. This interpretation is supported by field observations of mylonites localised along the shear zones. Deformation temperature estimates determined from microstructures and CPO fabrics (Figures 3.20 & 3.21) indicate that deformation within the UGHS and its bounding shear zones occurred at temperatures consistent with thermo-mechanical models of mid-crustal channel flow (>700 ^{o}C**;** Grujic *et al.*, 1996; Beaumont *et al.*, 2001; Beaumont *et al.*, 2004; Jamieson & Beaumont, 2013).

Deformation microstructures from the UGHS are consistent with a dominance of non-coaxial strain at the channel margins relative to the channel centre (Figure 3.4). This is supported by the relative velocity and strain profiles which predict a dominance of non-coaxial deformation at the channel margins and coaxial deformation in the channel centre (Figures 5.6 & 6.8). Microstructures and CPO fabrics in the lower STDS and upper LGHS are characteristic of non-coaxial deformation (Figures 3.1-3.3 & 3.7) at temperatures close to those within the UGHS (500-600 ^{o}C). Additionally, measurements of AMS ellipsoid shape parameter from the UGHS of the Kali Gandaki transect are indicative of oblate strain (T > 0.5), accommodated through vertical thinning and horizontal stretching (Figure 4.14).

These findings are consistent with observations from equivalent strata elsewhere in the Himalaya (e.g. Grujic *et al.*, 1996; Grasemann *et al.*, 1999; Searle & Godin, 2003; Searle *et al.*, 2006; Carosi *et al.*, 2007; Law *et al.*, 2013) and are compatible with models in which the UGHS represents a mid-crustal channel, internally flowing through non-coaxial general shear and bounded by simple shear dominated margins (Beaumont *et al.*, 2001; Beaumont *et al.*, 2004).

7.7.5. Hybrid velocity profiles indicative of combined northwards Couette flow (shear driven) and southwards Poiseuille flow (pressure gradient driven).

Quantification of CPO strengths and AMS fabric orientation and shape provides a means to construct relative strain proxy profiles for the GHS and bounding units in the Annapurna-Dhaulagiri region (Figure 5.6). Following the arguments presented in Chapter 6, these profiles are mathematically converted to relative velocity profiles (Figure 6.8). These can be directly correlated with the velocity and strain rate profiles from analytical models of 1-dimensional laminar channel flows (Figures 6.2-6.7).

At the upper and lower margins of the transect, the THS and LHS have a uniform relative velocity structure with low relative strain (Figure 6.8). These sequences are comparable to hypothetical rigid channel walls with little or no internal deformation that are displaced relative to each other with a top-to-the south motion.

Comparison with the analytical model velocity profiles indicates that the relative velocity profiles for the UGHS best represents hybrid flow of a viscous channel with a stress-dependant power law rheology (Figure 7.6a). The flow is driven by northwards motion of the underlying LGHS and LHS and a southwards directed pressure gradient (Figure 7.6a). The middle to upper portions of the UGHS form a southwards exhuming return-flow, whilst the lowermost portion of the UGHS is buried northwards (Figure 7.6a). According to the shape of the return-flow velocity profile, the UGHS is dominated by top-to-the-south shearing, except for the uppermost 0.5-1.0 km that is characterised by top-to-the-north shearing.

In the STDS and LGHS velocity profiles are characteristic of Couette flow within a viscous channel with a temperature-dependant power-law rheology (Figure 6.7). Changes in the velocity and strain profiles across these sequences (Figure 5.6 & 6.8) are consistent with decreasing deformation temperatures up- and down-section from the UGHS and towards the STD and MCT (Figures 3.20 & 3.21). In the LGHS, the relative strain profiles and field- and microstructural observations, suggest that the entire sequence behaved as a large shear zone dominated by pervasive non-coaxial top-to-the-south deformation. A correlation between the minimum deformation temperatures in the UGHS and the maximum deformation temperatures in the LGHS (~500-600 ^{o}C) indicates that pervasive shearing in the LGHS activated at the same temperature at which, internal deformation of the UGHS stopped (Figures 3.20 & 3.21). This temperature may correspond to the threshold viscosity above which, channel flow stops due to an increase in strength. Deformation continued in the LGHS to relatively low temperatures (~300 ^{o}C). When considered together, the relative strain, relative

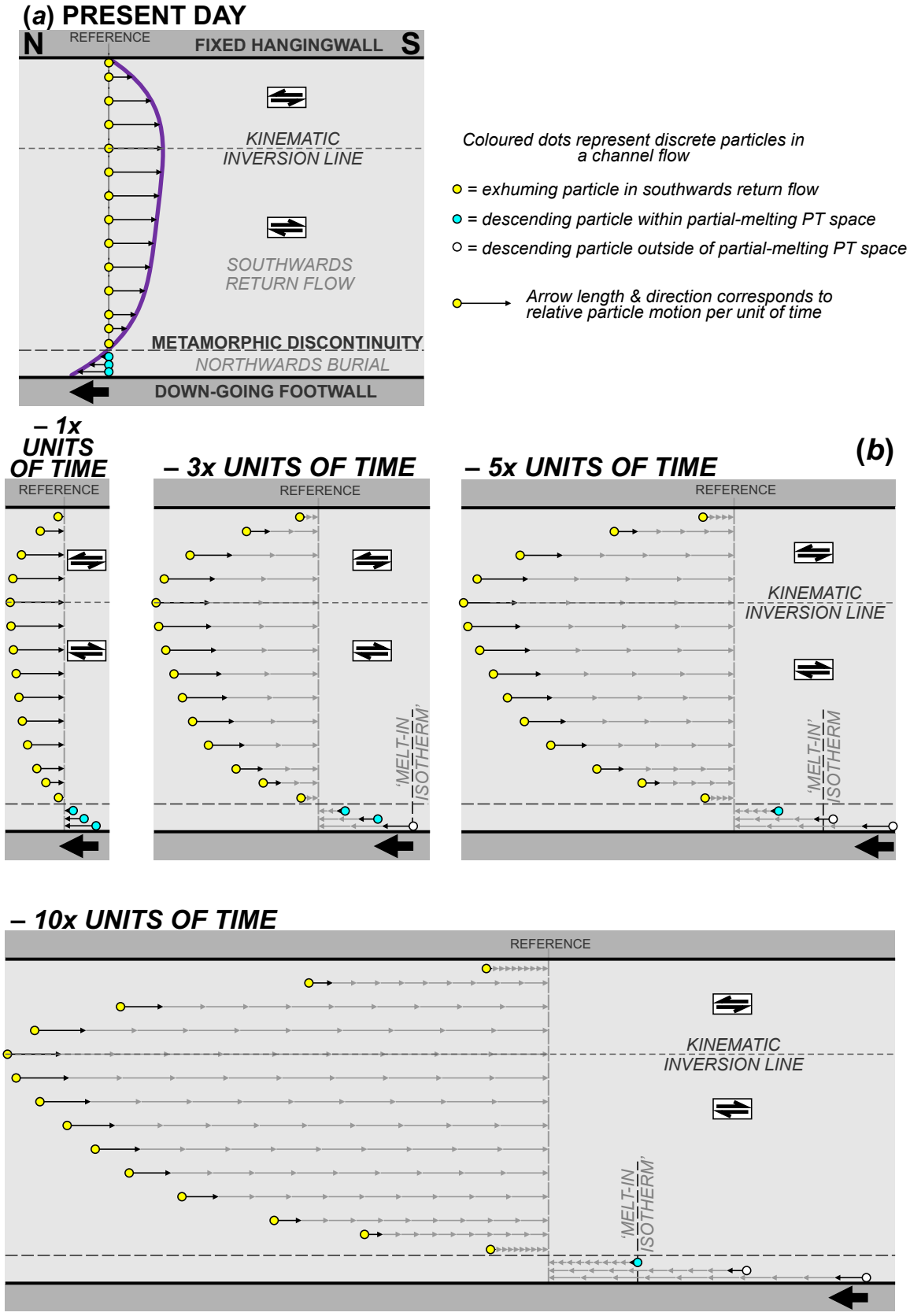

Figure 7.6 Relative particle motion of a Hybrid channel flow.

velocity and deformation temperature profiles suggest that after high temperature ductile flow of the UGHS shut down, mid to low temperature extrusion was concentrated in the LGHS and this was responsible for exhumation of the overlying UGHS. Under these conditions, the UGHS exhumed as a coherent block, comparable

to an exhumed rigid *channel plug* (Beaumont *et al.*, 2004; Godin *et al.*, 2006a; Grujic, 2006). This interpretation fits with many authors classification of LGHS-equivalent strata as the Main Central Thrust Zone (e.g. Bouchez & Pêcher, 1981; Arita, 1983; Hubbard & Harrison, 1989; Metcalfe, 1993; Grasemann *et al.*, 1999).

It is not possible to interpret the STDS in as much detail as the LGHS due to the lack of deformation temperature constraints. However, this kinematic interpretation of the LGHS is compatible with the known constraints from the STDS in the Annapurna-Dhaulagiri region, although the lack of brittle deformation in the STDS of the Kali Gandaki transect suggests that it did not operate down to the same low temperatures as the LGHS. Additionally, these observations are similar to the better-constrained kinematic evolution of the STDS in the Everest region of southern Tibet (Cottle *et al.*, 2011; Law *et al.*, 2011).

Synthesis of these interpretations indicates that the flow structure of the UGHS is consistent with the expected velocity profile of an exhuming mid-crustal channel beneath the Himalaya and Tibetan Plateau, deforming by pervasive general shear (Beaumont *et al.*, 2004; Grujic, 2006; Jamieson *et al.*, 2006). The LGHS and STDS represent pervasively sheared portions of the crust responsible for the extrusion and exhumation of a rigid *channel plug* through non-coaxial shearing at medium to low temperatures. As such, the difference in velocity structures between the STDS, UGHS and LGHS can be explained by a difference in rheological boundary conditions. In this sense, the CT and AD and DD represent rheological discontinuities, as well as structural and lithological discontinuities.

7.7.6. Kinematic inversion of STDS, relating to a switch from northwards Couette-flow to southwards Poiseuille–dominated return-flow.

Deformation within the STDS in the Annapurna-Dhaulagiri region is dominated by a top-to-the-north shear fabric (S3) relating to the southwards extrusion of the underlying UGHS. Within the Kali Gandaki valley, S3 foliation in the STDS is often deformed by

Figure 7.6. Relative particle motion in a Hybrid channel flow. (*a*) Relative velocity profile (purple line) for a hybrid channel flow with a stress-dependant power law rheology (derived from *Figure 6.6*). Upper channel wall is stationary, lower channel wall moves northwards (left). Flow driven by lower channel wall motion and lateral pressure gradient within channel. Velocity profile drawn relative to stationary upper channel wall. Adjacent particles (coloured dots) in an exhumed channel section are derived from different crustal positions due to differences in individual particle pathways. Blue particles have northwards burial pathways. Yellow particles have southwards exhumation pathways. (*b*) Relative particle positions after -1, -3, -5 and -10 units of time. Variations in relative velocity can result in metamorphic discontinuities between exhuming and burying particles. Within burial section, timing of initial partial melting decreases down-section from earliest to latest (i.e. *youngs* down-section).

later top-to-the-south ductile shearing (S4) and steep N-S striking brittle fractures (S5). Earlier top-to-the south shearing within the STDS is not observed. This may reflect the high strain nature of fabric transposition recorded by earlier S1 and S2 foliation and associated F2 fold hinge surfaces in the THS which are folded into parallelism with the S3 foliation with increasing proximity to the STDS (Figure 7.2b). This transpositional relationship indicates that S3 is an older deformation fabric than S1 and S2. Within the THS, F2 folds closest to the STDS are north verging and often overturned. North of the STDS, F2 folds within the THS gradually rotate from north verging to south verging (Godin *et al.*, 1999a; Godin, 2003; Searle, 2010). This implies that the original vergence of the F2 folds, prior to transposition by S3 deformation was north verging. A south-verging structural arrangement of F2 folds is consistent with a top-to-the-south shear sense at the base of the THS, prior to S3 deformation. Thus, whilst there is no record of an earlier top-to-the-south shear within the STDS in the Annapurna-Dhaulagiri Himalaya, fold architecture in the overlying THS is supportive of such a shear sense along the STDS, followed by kinematic inversion to top-to-the-north shearing at the on-set of southwards return-flow of the GHS.

7.7.7. Identification of the STDS as a stretching fault with a fixed hangingwall, separating an overlying low metamorphic grade *superstructure* with upright folds, thrust faults, steep foliation from an underlying high metamorphic grade *infrastructure* of horizontal shearing and recumbent folding produced during non-coaxial flow

Deformation within the STDS of the Annapurna-Dhaulagiri region is indicative of top-to-the-north, non-coaxial general shear (e.g. boudinage, drag folds), reflecting vertical thinning and horizontal stretching. As described above, the associated mylonitic fabric (S3) is transpositional, and deforms earlier foliations in the THS (S1 and S2) into parallelism with the STDS. Deformation within the UGHS is also indicative of vertical thinning and horizontal stretching whereas regional scale folding in the THS is indicative of horizontal shortening and crustal thickening. Additionally, the STDS in the Annapurna-Dhaulagiri region represents a major metamorphic discontinuity between the amphibolite facies (diopside grade) UGHS and the lower greenschist facies (chlorite grade) THS. These findings are consistent with other observations from the same region (Brown & Nazarchuk, 1993; Godin *et al.*, 1999a; Godin, 2003; Kellett & Godin, 2009; Searle, 2010) and from equivalent strata elsewhere in the Himalaya (Law *et al.*, 2004; Kellett *et al.*, 2010; Cottle *et al.*, 2011; Law *et al.*, 2011). Additionally, the STDS in the Kali Gandaki valley is a ductile structure with no upper brittle detachment. Based on the criteria discussed in *Section 7.4*, the STDS in the Kali Gandaki valley is not related to the final stages of exhumation of the GHS and cannot be produced by

thrust stacking, duplex development and wedge extrusion (Beaumont *et al.*, 2004; Kellett & Grujic, 2012). In this respect, the structural relationship between the THS, STDS and UGHS replicates the SIA (Wegmann, 1935; Culshaw *et al.*, 2006), which forms in response to mid-crustal channel flow (Beaumont *et al.*, 2006; Culshaw *et al.*, 2006; Kellett & Godin, 2009; Jamieson & Beaumont, 2013).

7.7.8. Progressive variations in metamorphic histories across the channel thickness and metamorphic discontinuities across channel boundaries.

In the Annapurna-Dhaulagiri Himalaya, metamorphic discontinuities are recorded across the MCT, CT and AD and STD (Chapter 2). The MCT and STD separate chlorite grade and unmetamorphosed rocks in the LHS and THS from the upper greenschist to amphibolite facies rocks of the GHS. At the base of the UGHS, in the Kali Gandaki transect, a jump from garnet grade to kyanite + melt grade is observed between the footwall and hangingwall, respectively, of the CT. Across the AD, an up-section decrease in metamorphic grade is also observed, although it is more of a diffuse zone of decreasing metamorphic grade rather than a sharp discontinuity like the CT. This is also reflected by the presence of melt within the STDS, which is absent in the LGHS. Low temperature deformation microstructures from the CT indicate that this structure continued to be active after the UGHS had cooled to temperatures too low for mid-crustal flow. This continued deformation on the CT may explain why it forms a sharper discontinuity than the AD. Prior to localised low temperature deformation on the CT, these discontinuities could be considered to be the walls of a mid crustal channel flow and represent rheological as well as structural and metamorphic discontinuities between the hot, weak UGHS and the stronger, lower and upper continental crust.

Internally, the UGHS in the Annapurna-Dhaulagiri Himalaya contains additional structural and metamorphic discontinuities. In the Kali Gandaki transect, the Kalopani shear zone deforms strata from Unit II and Unit III (Vannay & Hodges, 1996; Godin *et al.*, 1999a; Larson & Godin, 2009). Thermobarometric data from across this structure suggests it forms a top-to-the-south reverse sense structure that places higher grade over lower grade material (Vannay & Hodges, 1996). Deformation and petrological associations suggest that motion on the shear zone was synchronous with peak to post-peak metamorphism, whilst $^{40}Ar/^{39}Ar$ muscovite ages record no change in the timing of exhumation across this structure, indicating that it was not related to upper-crustal exhumation of the UGHS (Vannay & Hodges, 1996). A similar structure is reported towards the top of the UGHS in the Modi Khola transect, identified as the Modi Khola shear zone (Hodges *et al.*, 1996). Structural relationships between deformation fabrics suggest that the Modi Khola shear zone also developed during peak to post-

peak metamorphism of the UGHS (Hodges *et al.*, 1996). In both shear zones, deformation is characterised by non-coaxial shearing and horizontal stretching (Hodges *et al.*, 1996; Vannay & Hodges, 1996).

Similarly, metamorphic discontinuities in Unit I of the UGHS in the Modi Khola valley have been interpreted as discrete faults, defined as the Sinuwa thrust and Bhanuwa fault (Martin *et al.*, 2010; Corrie & Kohn, 2011; Martin *et al.*, 2014). These structures are identified solely on contrasting thermobarometric and geochronological data from across Unit I (Martin *et al.*, 2005; Corrie & Kohn, 2011) and have not been identified anywhere in the field. Moving down-section through Unit I, peak temperatures decrease and the onset of prograde metamorphism, partial melting and peak metamorphism gets younger (Corrie & Kohn, 2011). Three fault bound crustal slices are identified in this section, based on stepped changes in the PTt history (Corrie & Kohn, 2011). An up-section decrease in peak pressure and an increase in $^{40}Ar/^{39}Ar$ muscovite cooling ages from 10-13 Ma to 16-18 Ma led Martin *et al.* (2010, 2014) to interpret the Bhanuwa fault as a normal sense structure. Corrie and Kohn (2011) recorded equal pressure and an up-section increase in peak temperature across the same transect, leading them to interpret the discontinuity as a reverse sense structure.

The discontinuities recorded in the UGHS of the Annapurna-Dhaulagiri Himalaya are similar to other intra-GHS shear zones reported elsewhere along the Himalaya that separate rocks with distinct and sometimes contrasting metamorphic histories (e.g. Grujic *et al.*, 2002; Carosi *et al.*, 2010; Montomoli *et al.*, 2013; Khanal *et al.*, 2014; Larson & Cottle, 2014). Post-peak metamorphic structural discontinuities such as the Kakhtang thrust in Bhutan (Grujic *et al.*, 2002) and an unnamed discontinuity in the Tama Kosi region of east central Nepal (Larson *et al.*, 2013; Larson & Cottle, 2014) are regarded as out-of-sequence shear zones. These structures are interpreted to have formed after mid-crustal channel flow and therefore, their presence does not affect the validity of the channel flow model (Grujic *et al.*, 2002; Larson & Cottle, 2014).

Not all discontinuities within the UGHS can be interpreted as out-of-sequence thrusts. The Tiojem shear zone, Lower Dolpo region, western Nepal (Carosi *et al.*, 2010), Mangri shear zone, Mugu-Karnali region , western Nepal (Montomoli *et al.*, 2013) and the High Himalayan Thrust in far-eastern Nepal (Goscombe *et al.*, 2006; Imayama *et al.*, 2012) all form intra-UGHS shear zones that separate sections of the UGHS with contrasting metamorphic histories. Motion on these structures occurred during pre-peak to syn-peak metamorphism, and typically the hangingwalls record sillimanite grade decompression, whilst the footwalls record kyanite grade metamorphism at similar temperatures but higher pressures (Carosi *et al.*, 2010; Imayama *et al.*, 2012; Montomoli *et al.*, 2013; Montomoli *et al.*, 2014). More commonly, these structures are

interpreted as mid-crustal in-sequence shear zones responsible for the emplacement and early extrusion of the GHS, and are presented as evidence against the channel flow model (Carosi *et al.*, 2010; He *et al.*, 2014; Montomoli *et al.*, 2014).

However, an important feature of the channel flow model is the contrasting PTt paths experienced by different sections of the channel (Jamieson *et al.*, 2004; Jamieson *et al.*, 2006; Jamieson & Beaumont, 2013). Consideration of how individual material trajectories vary across the channels reveals how over time, points originally separated by large distances (>100 km) and differing initial PT conditions can be transported and positioned adjacent to each other (Figure 7.5) (Jamieson *et al.*, 2004; Jamieson & Beaumont, 2013). The typical Hybrid flow velocity profile (Figure 7.6) required for southwards return-flow of channel material beneath the Tibetan Plateau implies that the base of the channel should be transported northwards on a prograde burial path, whilst channel material in the return-flow is transported southwards on a retrograde exhumation path. The transition between the northwards and southwards moving portions of the channel is characterised by a steep velocity gradient, indicative of high strain rates and is, therefore, likely to form a high strain shear zone within the channel. The contrast in metamorphic histories above and below this transition line then becomes a function of channel velocity and time with faster and/or older channels displacing material across much larger distances (Figure 7.6b). The position of this burial-exhumation transition relative to the channel walls can vary, based upon the relative strengths of the southwards pressure gradient, and northwards drag of the lower channel wall (Figure 7.6). As such, the identification of metamorphic discontinuities across intra-GHS shear zones is entirely compatible with channel flow models for the Himalayan orogen (Jamieson *et al.*, 2004; Jamieson *et al.*, 2006; Jamieson & Beaumont, 2013).

With respect to the intra-UGHS shear zones reported from the Annapurna-Dhaulagiri Himalaya, it is unclear exactly when the Modi Khola and Kalopani shear zones formed. However, timing constraints based on deformation and petrofabric associations (Hodges *et al.*, 1996; Vannay & Hodges, 1996) suggest that these structures are out-of-sequence thrusts. With respect to the channel flow model, out-of-sequence thrusting can be explained by a reorganisation of the thrust wedge in response to changes in rates of uplift and erosion (Beaumont *et al.*, 2004; Jamieson *et al.*, 2004; Kellett & Grujic, 2012; Jamieson & Beaumont, 2013). The Sinuwa thrust and Bhanuwa fault in Unit I of the UGHS in the Modi Khola transect (Martin *et al.*, 2010; Corrie & Kohn, 2011) require a different interpretation. Previously, the down-section decrease in peak temperatures and younging of prograde metamorphism, partial melting and peak metamorphism led authors to interpret these discontinuities as evidence against

channel flow and for mid-crustal in-sequence thrusting (Corrie & Kohn, 2011). However, the metamorphic and geochronological trends fit the modelled particle pathways of the channel flow model (Jamieson *et al.*, 2004). Figure 7.6 demonstrates how a down-section increase in northwards channel velocity can align material points with successively younger ages of partial melting and prograde metamorphism. The PTt data from Corrie and Kohn (2011) support the interpretation that the lower portion of the UGHS in the Modi Khola transect is flowing northwards as the lower burial section of a Hybrid flow. The up-section increases in $^{40}Ar/^{39}Ar$ muscovite ages across the Bhanuwa fault relate to lower temperature exhumation processes and do not affect the validity of the channel flow model (Martin *et al.*, 2014). However, the absence of supporting structural evidence for the Bhanuwa fault means that kinematic interpretation of these data remains problematic (Martin *et al.*, 2014).

In summary, the metamorphic gradients across the MCT, CT, and STDS and the structural and metamorphic discontinuities within the UGHS are all supportive of models of mid-crustal channel flow for the Himalayan orogen. Previous interpretation of intra-UGHS discontinuities, which state that such structures are incompatible with the channel flow model, should be reassessed.

7.8. Outstanding issues

Whilst most of the findings derived from this project are compatible and often supportive of channel flow of the UGHS in the Annapurna-Dhaulagiri Himalaya, some observations are harder to reconcile with the model predictions. Of most importance is an explanation for the lower-than-typical volumes of sillimanite and leucogranite, the cause of the late reversal of the STDS in the Kali Gandaki transect, and the role of orogen-parallel deformation in the UGHS. These issues are discussed below, and supplemented with previously published findings in order to determine their cause and assess their role in the kinematic evolution of the GHS in the Annapurna-Dhaulagiri region.

7.8.1. Leucogranite & sillimanite volumes

It has been shown that the low volumes of leucogranite and sillimanite grade material do not appear to have prevented the UGHS forming a southwards return-flow (*Section 7.7.3.*), the question remains as to why these volumes are lower than elsewhere in the Himalaya.

Leucogranites are found along the length of the central-eastern Himalaya in the GHS and are most commonly the product of fluid-absent muscovite dehydration and, at higher temperatures, biotite dehydration reactions (Harris & Massey, 1994; Harris *et*

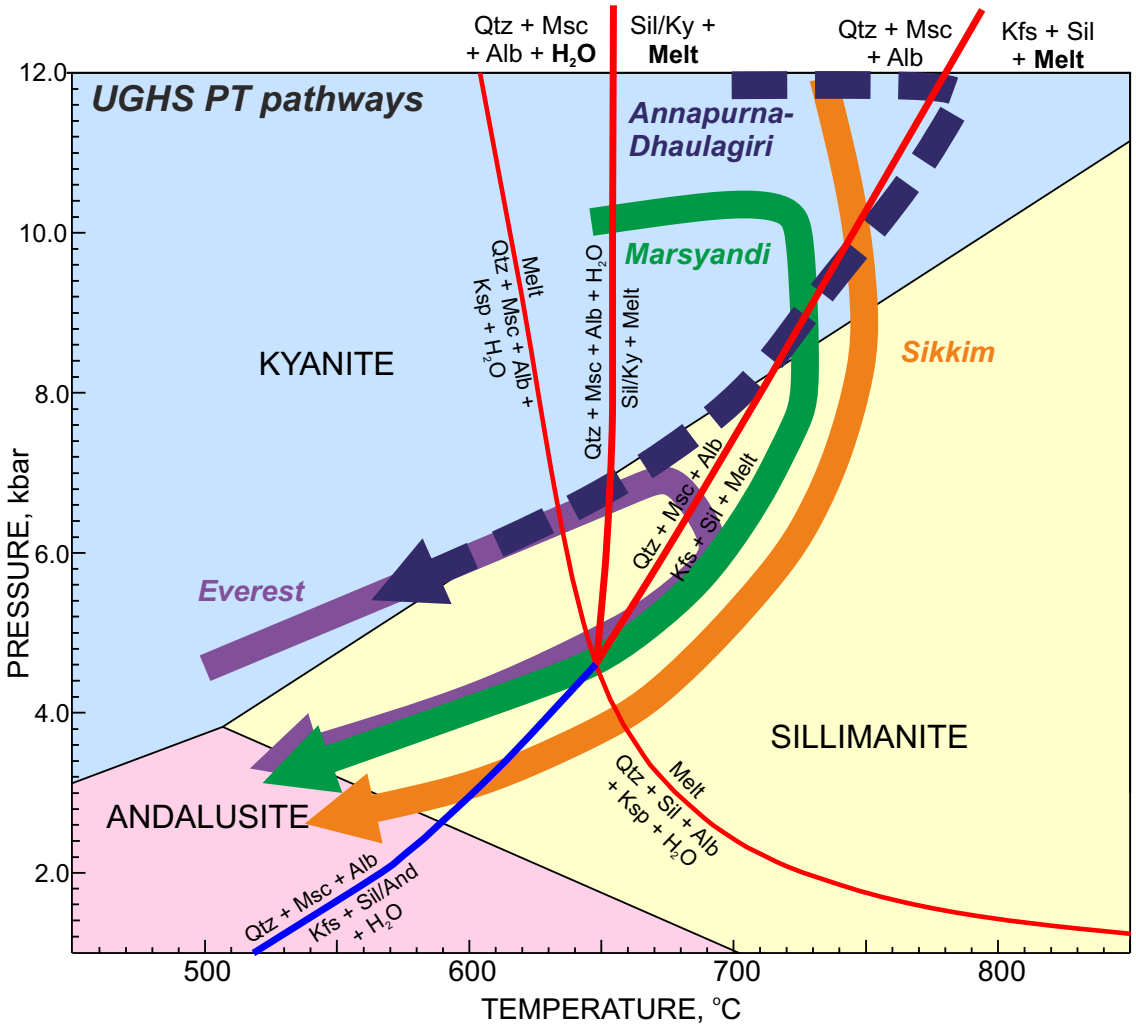

Figure 7.7. PT pathways for the UGHS. Purple – Everest section, Searle *et al.,* 2003; Orange – Sikkim section, Harris *et al.,* 2004; Green – Marsyandi section, Caddick, 2005. Dashed blue line represents proposed PT pathway for the UGHS of the Annapurna-Dhaulagiri region based on petrological observations and thermometry constraints from this study, plus thermobarometric constraints from Le Fort *et al.,* 1987, Pêcher, 1989, Hodges *et al.*, 1996, Godin *et al.*, 2001, Corrie & Kohn, 2011, Kohn & Corrie, 2011 and Carosi *et al.*, 2014. Reaction curves based on White *et al.*, 2001.

al., 1995; Streule *et al.*, 2010a; Searle, 2013). The earliest recorded partial-melting (Eocene-Oligocene) in the GHS occurred within the kyanite stability field, as observed in the Annapurna-Dhaulagiri region (Nazarchuk, 1993; Hodges *et al.*, 1996; Carosi *et al.*, 2014; Larson & Cottle, 2015) and is typically associated with a large radiogenic heat source and thermal relaxation during crustal thickening (Zhang *et al.*, 2004). However, the largest volumes of leucogranites along the Himalaya were produced at lower pressures in the sillimanite stability field, during the Early Miocene (Streule *et al.*, 2010a; Jamieson *et al.*, 2011; Searle, 2013). This transition from initial high pressures and temperatures (750 ^{o}C, 10-14 kbar; Corrie & Kohn, 2011; Martin *et al.*, 2010) to intermediate to low pressures and high temperatures (>700 ^{o}C, 4-6 kbar; Streule *et al.,* 2010a; Searle, 2013) represents a migration of PTt trajectories (Figure 7.7) along a near isobaric heating path from the kyanite stability field, into the sillimanite stability field accompanied by fluid-absent muscovite dehydration melting during near-

isothermal exhumation (White *et al.*, 2001; Searle, 2013; Kohn, 2014). Once within this stability field, melting can be sustained through lower pressures (Figure 7.7) as long as temperatures remain high (White *et al.*, 2001; Kohn, 2014). As such, the Himalayan leucogranites are mostly interpreted as a consequence of rapid exhumation at 23-20 Ma, coincident with activity on the MCT and STD (Harris & Massey, 1994; Jamieson *et al.*, 2011; Searle, 2013).

This PTt evolution of the GHS has been replicated by the thermo-mechanical channel flow models, which identify three distinct stages of metamorphic evolution, describing: (*1*) burial and heating at kyanite grade conditions; (*2*) melt production leading to near isobaric southward return-flow of the GHS, initiating in the kyanite stability field usually ending in the sillimanite field; and (*3*) cooling and decompression within the sillimanite field during late stage exhumation and erosion of the channel (Jamieson *et al.*, 2004).

PTt constraints for the Annapurna-Dhaulagiri Himalaya (Nazarchuk, 1993; Kaneko, 1995; Hodges *et al.*, 1996; Godin *et al.*, 2001; Martin *et al.*, 2010; Corrie & Kohn, 2011; Kohn & Corrie, 2011; Carosi *et al.*, 2014; Larson & Cottle, 2015) suggest that the UGHS in this region was not subjected to a final stage of melt production during sillimanite retrograde metamorphism relating to cooling, exhumation and erosion of the GHS. Instead, the PTt constraints and petrological observations suggest that the UGHS in this region only underwent an early stage of burial and heating at kyanite grade conditions, followed by the initial stages of southwards channel flow almost entirely within the kyanite grade stability field (Nazarchuk, 1993; Kaneko, 1995; Hodges *et al.*, 1996; Godin *et al.*, 2001; Martin *et al.*, 2010; Corrie & Kohn, 2011; Kohn & Corrie, 2011; Carosi *et al.*, 2014).

Consequently, the UGHS was not subjected to high temperature metamorphism during exhumation (i.e. exhumation of an '*active channel*'; Beaumont *et al.*, 2001; Beaumont *et al.*, 2004) but instead cooled and 'froze' at depth to form a rigid *channel plug* that would be exhumed later through crustal-scale buckling and thrust stacking within the underlying LGHS and LHS (Vannay & Hodges, 1996; Godin *et al.*, 2001; Gleeson & Godin, 2006; Godin *et al.*, 2006a; Larson *et al.*, 2010b). This interpretation is supported by the lack of brittle structures in the STDS in the Kali Gandaki valley, implying that this structure was not active during low temperature exhumation (Beaumont *et al.*, 2004; Kellett & Grujic, 2012). Furthermore, $^{40}Ar/^{39}Ar$ cooling ages of hornblende, biotite and muscovite show no variation across the UGHS, indicating that the sequence was exhumed as a coherent rigid block during late stage erosion and denudation (Vannay & Hodges, 1996; Godin *et al.*, 2001; Godin *et al.*, 2006a). Importantly, this interpretation does not imply that leucogranite and partial melts in the UGHS of the Annapurna-

Dhaulagiri Himalaya were *always* low in volume. Syn-migmatitic deformation drives melt migration (Vanderhaeghe, 2009), as is evident from field observations in the UGHS in the Annapurna-Dhaulagiri region (Figure 2.9). Large kilometre scale accumulations of leucogranite, such as: (*a*) the Mugu granite dome ~50 km north of the STDS in the Kali Gandaki valley (Krummenacher, 1971; Sorkhabi & Stump, 1993; Harrison *et al.*, 1997; Hurtado, 2002) and (*b*) the Manaslu leucogranite, ~80 km east of the Kali Gandaki valley are testaments to this melt migration (Le Fort, 1981; Guillot *et al.*, 1993; Harrison *et al.*, 1999).

If rates of melt migration exceed rates of melt production then with continued deformation the volume of melt within the UGHS should decrease. A decrease in melt volume should be accompanied by an increase in viscosity (Rosenberg & Handy, 2005; Rutter *et al.*, 2006) and the channel velocity and subsequent rate of exhumation should decrease (Beaumont *et al.*, 2004; Beaumont *et al.*, 2006). Consequently the PTt trajectory of exhumation is unlikely to follow a near-isothermal path as rates of exhumation decrease relative to rates of cooling and strengthening. Thus, the apparently premature shut down of channel flow before exhumation of an *active channel*, is the proposed cause of the reduced leucogranite volumes and sillimanite retrograde metamorphism in the UGHS of the Annapurna-Dhaulagiri region. Based on these interpretations, it is unlikely that the PTt trajectory of the UGHS in the Annapurna-Dhaulagiri region followed a near-isothermal exhumation path. Instead, it is suggested that the UGHS began to cool prior to and/or during exhumation, probably outside of the fluid-absent melting field (Figure 7.7). This interpretation has also been proposed by Pêcher (1989) for the UGHS in the Annapurn-Dhaulagiri region.

7.8.2. Late-stage top-to-the-south reversal of the STDS

Within the Kali Gandaki valley, field structural observations from the STDS record late stage top-to-the-south shearing that deforms earlier top-to-the-north shear related fabrics and leucogranites (Figure 2.13 & 3.7). This late stage reversal has been reported by other authors (Hodges *et al.*, 1996; Godin *et al.*, 1999a; Godin, 2003; Larson & Godin, 2009), and correlated with D4 deformation in the THS and syn- to post-peak metamorphism in the UGHS along the Kalopani shear zone in the Kali Gandaki valley (Vannay & Hodges, 1996; Godin *et al.*, 1999a) and the Modi Khola shear zone in the Modi Khola valley (Hodges *et al.*, 1996). Late stage top-to-the-south shearing on the STDS is suggested to have occurred at ~18 Ma based on an $^{40}Ar/^{39}Ar$ muscovite cooling age from the lowermost THS (Godin *et al.*, 2001). Therefore, it must have occurred after top-to-the-north shearing and crystallisation of leucogranites (<22 Ma) (Godin *et al.*, 2001) and prior to the wholesale exhumation of the UGHS between 16-13 Ma (Vannay & Hodges, 1996; Godin *et al.*, 2001; Martin *et al.*, 2014). This timing

implies that the reversal occurred after or during the final stages of mid-crustal channel flow and before exhumation and erosion at the topographic surface. Late-stage top-to-the-south reversal of the STDS is unique to the Annapurna-Dhaulagiri region and is yet to be fully explained.

As previously demonstrated in *Section 7.4.,* top-to-the-north ductile motion on the STDS along the length of the Himalayan orogen is best explained with models of mid-crustal channel flow in the context of a Superstructure-Infrastructure Association (Beaumont *et al.*, 2004; Culshaw *et al.*, 2006; Grujic, 2006; Kellett & Grujic, 2012; Jamieson & Beaumont, 2013). In this interpretation, the top-to-the-north motion on the STDS forms in response to a change in the rheological properties of the underlying infrastructure (UGHS), which results in a reduction of viscosity relative to the overlying superstructure (THS), followed by southwards return-flow of the mid crust beneath the Himalaya and southern Tibet (Beaumont *et al.*, 2004; Grujic, 2006; Jamieson & Beaumont, 2013). Additionally, thermo-mechanical channel flow simulations without a significant contrast in rheology between mid and upper crustal levels were unable to produce an STDS-equivalent structure (Model 3, Beaumont *et al.*, 2004). Thus, it follows that a later reversal in shear sense on the STDS, occurring after initiation of southwards return-flow is likely to reflect a change in the relative rheological properties of the GHS or THS.

In *Section 7.8.1.* it is postulated that channel flow of the UGHS ended prior to exhumation and extrusion to the topographic surface. This was accompanied by an increase in viscosity that reduced the rheological contrast between the UGHS and THS. It is suggested that post-flow, top-to-the-south thrusting on the STDS occurred in response to continued convergence after the viscosity increase, resulting in southwards motion of the THS over the now stronger UGHS. Timing constraints suggest that this occurred synchronously to thrusting on the Kalopani shear zone and Modi Khola shear zone (Hodges *et al.*, 1996; Vannay & Hodges, 1996; Godin *et al.*, 2001). Deformation structures associated with this top-to-the-south shearing (Figure 2.13) indicate that whilst the UGHS may not have been weak enough for flow, it was still hot and weak enough to deform via pervasive ductile shearing.

A premature shut down of channel flow prior to extrusion and exhumation of an *active channel*, followed by top-to-the-south thrusting on the STDS and Kalopani and Modi Khola shear zones could be explained by the following sequence: (*1*) a reduction in the rate of exhumation of the UGHS; (*2*) development of a rigid *channel plug* beneath the Annapurna-Dhaulagiri Himalaya and retreat of the '*active channel*' towards the hinterland (southern Tibet); (*3*) propagation and expansion of the thrust wedge towards the hinterland, resulting in hinterland doming of the GHS and uplift to a critical angle;

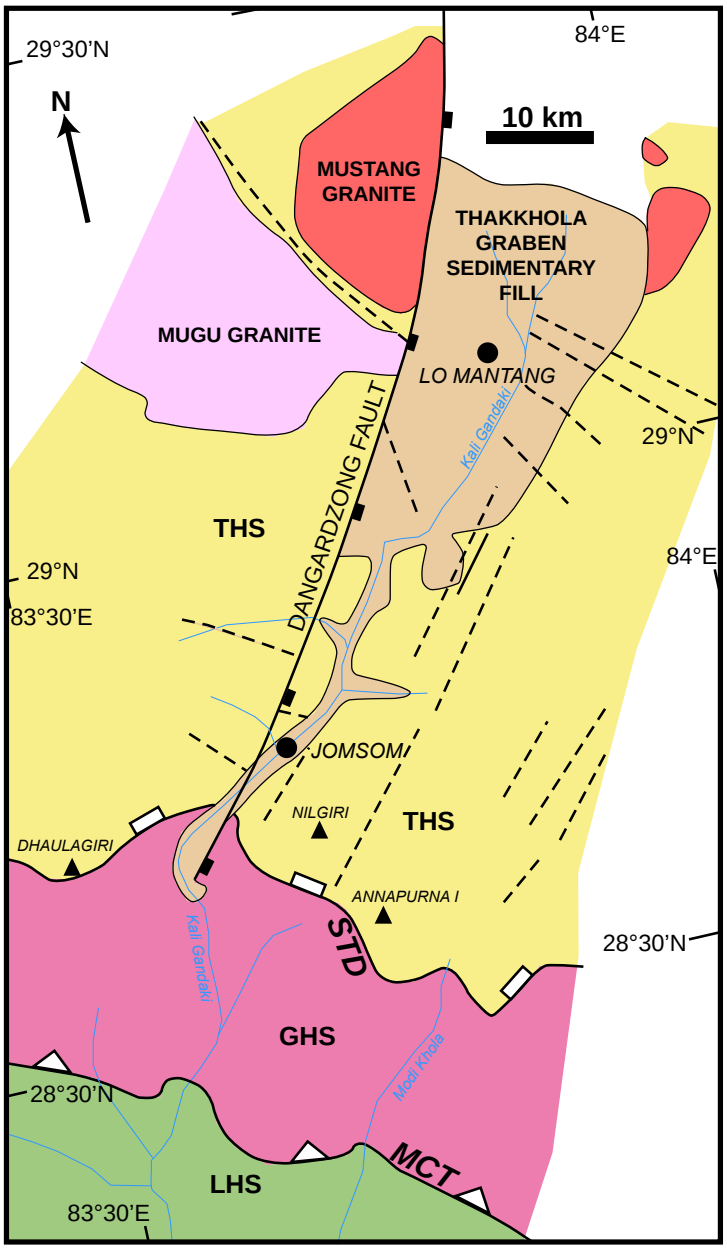

Figure 7.8. Simplified geological map of the Thakkhola graben and Mustang and Mugu granite domes. All units and major structures are labelled on the map. Unnamed normal faults are indicated by dashed lines. Modified after Hurtado *et al.*, 2001 and Hurtado, 2002.

and (*4*) subsequent propagation of out-of-sequence thrusting towards the foreland (i.e. reversal of the STDS and thrusting on the Kalopani and Modi Khola shear zones) during structural reorganisation of the thrust wedge (Beaumont *et al.*, 2004; Godin *et al.*, 2006a; Jamieson *et al.*, 2006; Larson *et al.*, 2010b; Jamieson & Beaumont, 2013; Larson & Cottle, 2014). According to thermo-mechanical simulations, dome formation may result in instability of the upper plate (THS), and initiate localised upper-crustal extension and propagation of the upper crust south of the uplifted dome towards the foreland (Beaumont *et al.*, 2004). If the ascension of the hinterland domes is driven by buoyancy or an underlying ramp-flat geometry, dome uplift can become coupled with extension, alleviating the need for surface denudation and may even result in subsidence and sedimentation of the hinterland (Beaumont *et al.*, 2004).

Both hinterland dome formation and upper crustal extension have occurred in the Annapurna-Dhaulagiri region. North of the Kali Gandaki transect, the Mustang-Mugu granite domes form the hangingwalls to basin bounding faults on either side of the E-W extended Thakkhola graben (Figure 7.8) (Krummenacher, 1971; Sorkhabi & Stump, 1993; Le Fort & France-Lanord, 1995; Harrison *et al.*, 1997; Guillot *et al.*, 1999; Hurtado, 2002; Garzione *et al.*, 2003). U-Pb and Th-Pb crystallisation ages indicate

that the Mustang granite formed at ~23-24 Ma (Hurtado, 2002), whilst the Mugu granite had a protracted history of emplacement from ~21-17 Ma (Harrison *et al.*, 1997; Hurtado, 2002; Hurtado *et al.*, 2007). These ages indicate that mid-crustal partial melting beneath southern Tibet continued: (*1*) after the youngest leucogranites exposed in the Modi Khola and Kali Gandaki valleys had crystallised and (*2*) during or before out-of-sequence thrusting on the STDS and Kalopani and Modi Khola shear zones (Nazarchuk, 1993; Hodges *et al.*, 1996; Vannay & Hodges, 1996; Godin *et al.*, 2001; Corrie & Kohn, 2011). Such timing constraints support the hypothesis of retreat of the '*active channel*' towards the hinterland after ~22 Ma. Muscovite and biotite $^{40}Ar/^{39}Ar$ cooling ages of 15-17 Ma from the Mustang and Mugu granites indicate that these domes cooled quickly as a result of rapid exhumation and denudation (Guillot *et al.*, 1999; Hurtado, 2002). These timing constraints are consistent with: (*1*) initial southwards flow of the UGHS with associated melt production and top-to-the-north shearing on the STDS (35-22 Ma); (*2*) a cessation of flow before exhumation of an '*active channel*' can be achieved, followed by channel retreat no further north than the Mustang and Mugu granite domes which were emplaced between 24 and 17 Ma; (*3*) rapid exhumation of the Mustang and Mugu granites and out-of-sequence, top-to-the-south shearing on the STDS and Kalopani and Modi Khola shear zones (22-15 Ma); and finally (*4*) wholesale uplift of the UGHS (16-13 Ma) (Hodges *et al.*, 1996; Vannay & Hodges, 1996; Harrison *et al.*, 1997; Guillot *et al.*, 1999; Godin *et al.*, 2001; Hurtado, 2002; Hurtado *et al.*, 2007; Corrie & Kohn, 2011; Martin *et al.*, 2014). This sequence of events is compatible with those described by Godin *et al.* (2006a) and Larson *et al.* (2010b) for the Annapurna-Manaslu Himalaya, whereby hinterland uplift of the thrust wedge to a critical angle results in the foreland-ward propagation of out-of-sequence deformation. Thus, late stage top-to-the-south reversal of sense of motion on the STDS can be explained by a change in the relative rheological properties of the UGHS and THS, accompanied by northwards retreat and subsequent southwards advancement of the locus of deformation during structural reorganisation of the thrust wedge (Beaumont *et al.*, 2004; Godin *et al.*, 2006a; Larson *et al.*, 2010b; Jamieson & Beaumont, 2013).

7.8.3. Orogen-parallel deformation of the Annapurna-Dhaulagiri Himalaya

Orogen-parallel deformation has affected the UGHS, STDS and THS in the Kali Gandaki valley. At the top of the UGHS and in the STDS of the Kali Gandaki valley, mineral elongation and magnetic lineations plunge eastwards, whilst foliation surfaces strike NNW-SSE (Figures 2.10 & 4.9). These lineation and foliation orientations are roughly parallel to several brittle low-angle normal faults that contain STDS or THS rocks in their footwall and more recent (Mid Miocene to Pleistocene) sedimentary rocks

in their hanging wall (Chapter 3) (Brown & Nazarchuk, 1993; Hurtado *et al.*, 2001; Garzione *et al.*, 2003). E-plunging lineations and NNE-SSW striking foliation surfaces in the STDS and top of the UGHS may relate to E-W upper crustal extension since the Mid Miocene, during and after exhumation of the GHS. Similar observations of orogen-parallel deformation in STDS and UGHS-equivalent strata are reported elsewhere in the Himalaya (e.g. Brun *et al.*, 1985; Pêcher *et al.*, 1991; Gapais *et al.*, 1992; Guillot *et al.*, 1993; Scaillet *et al.*, 1995; Vannay & Steck, 1995; Coleman, 1996; Xu *et al.*, 2013). Muscovite $^{40}Ar/^{39}Ar$ ages of ~12 Ma from the AD have been interpreted to reflect a hydrothermal event after the exhumation of the GHS (Vannay & Hodges, 1996; Godin *et al.*, 2001). This observation led some authors to suggest that the STDS formed a southern basin bounding structure to the Thakkhola graben and was kinematically linked to its opening and extension (Godin *et al.*, 2001; Hurtado *et al.*, 2001). However, the E-plunging lineations have not been dated and it is possible that they formed prior to ~12 Ma.

Additionally, in the UGHS, AMS samples consistently record a high AMS shape parameter ($T > 0.5$), which is indicative of an oblate strain geometry (Figure 4.14). This requires an orogen-parallel component of horizontal stretching, implying that the UGHS in the Annapurna-Dhaulagiri region underwent 3-dimensional flattening.

Orogen-parallel extension has affected the upper crust of the Himalayan orogen since late Miocene times through to the present day (e.g., Mccaffrey & Nabelek, 1998; Hurtado *et al.*, 2001; Murphy & Copeland, 2005; Jessup & Cottle, 2010; Lee *et al.*, 2011; Styron *et al.*, 2011; Murphy *et al.*, 2014). Within the THS of the Kali Gandaki valley, E-W extension of the Thakkhola graben is well documented and has deformed the upper crust since at least 11 Ma (Hurtado *et al.*, 2001; Garzione *et al.*, 2003). The occurrence of late-Miocene to recent orogen-parallel deformation in the THS is easily reconciled with present day deformation occurring across the Tibetan Plateau (Styron *et al.*, 2011). Models of strain partitioning into reverse-sense faulting and strike-slip faulting due to oblique convergence between the Indian plate and the arcuate Himalayan orogen provide a favourable explanation for this phenomenon (e.g. Mccaffrey & Nabelek, 1998; Styron *et al.*, 2011; Murphy *et al.*, 2014; Whipp *et al.*, 2014). However, extension may have occurred earlier than 17 Ma (Hurtado, 2002). $^{40}Ar/^{39}Ar$ muscovite ages from the footwall and hangingwall of the northern end of Dangardzong fault, which forms the western margin of the Thakkhola Graben, produce indistinguishable ages of ~17-18 Ma (Hurtado, 2002). The metamorphic discontinuity between the amphibolite facies Lo Mantang gneiss in the footwall and the unmetamorphosed hanging wall rocks leads to the conclusion that the footwall and hangingwall were exhumed together at ~17-18 Ma and that motion on the

Dangardzong fault must have initiated before this time (Hurtado, 2002). This age correlates roughly with the earliest time of E-W normal faulting and fracture development in the Marsyandi region (14-17.5 Ma; Coleman & Hodges, 1998). Given the timing of emplacement of the Mugu granite at ~21-17 Ma (Harrison *et al.*, 1997; Hurtado, 2002; Hurtado *et al.*, 2007) and the Manaslu leucogranite at 22-19 Ma, it is possible that early E-W extension and granitic dome emplacement were kinematically linked (Guillot *et al.*, 1993; Hurtado, 2002). Similar observations are made from the Gangotri granite in the Garhwal Himalaya which forms km-scale tabular laccoliths, interpreted as crustal scale boudins formed during oblate coaxial deformation with a component of orogen-parallel stretching (Scaillet *et al.*, 1995).

It is unclear whether the oblate AMS fabrics and the E-plunging mineral and magnetic lineations recorded in the UGHS and STDS of the Annapurna-Dhaulagiri region formed during the same deformation event. Some of the oblate AMS fabrics are recorded in the leucosomes of migmatitic rocks and suggests that flattening occurred during partial melting of the UGHS. This would imply that a component of orogen-parallel deformation affected the UGHS during its mid-crustal evolution. Given the timing constraints on final crystallisation of leucogranites in the UGHS (~22-18 Ma; Nazarchuk, 1993; Hodges *et al.*, 1996; Godin *et al.*, 2001; Larson & Cottle, 2015), this suggests that the oblate fabrics formed before the earliest extension occurred (~17 Ma) in the Thakkhola graben.

Mid crustal orogen-parallel deformation has not yet been simulated by thermo-mechanical channel flow models as these all assume plane strain geometries (Beaumont *et al.*, 2001; Beaumont *et al.*, 2004; Jamieson & Beaumont, 2013). However, the possibility of orogen-parallel stretching during channel flow has been suggested in some situations, perhaps where along-strike variations in structure exist (Beaumont *et al.*, 2004; Beaumont *et al.*, 2006; Culshaw *et al.*, 2006). Orogen parallel flow would have significant implications for melt migration and may be responsible for the accumulation of large leucogranite bodies such as the Manaslu and Mugu leucogranites (Guillot *et al.*, 1993; Harrison *et al.*, 1997; Guillot *et al.*, 1999; Harrison *et al.*, 1999; Hurtado, 2002). E-W trending magmatic mineral lineations and magnetic lineations in the Manaslu pluton and E-W trending mineral lineations in the surrounding country rock, support the occurrence of orogen-parallel deformation driving magma migration and emplacement in the GHS (Guillot *et al.*, 1993).

Orogen-parallel mid crustal flow also has implications for exhumation of the UGHS. When subjected to oblate flattening, the UGHS should flow both perpendicular and parallel to the orogen. As a consequence, the amount of southwards propagating material in the channel is reduced as some of this material now flows parallel to the

orogen. Such behaviour may slow extrusion and hinder exhumation of an active channel. If the orogen-perpendicular pressure gradient is less than the orogen-parallel pressure gradient then exhumation of an 'active channel' may be prevented (*c.f. Leigh Royden, pers comms to A. Parsons. 2014*). This may provide the stimulus for the premature shut down of channel flow beneath the Annapurna-Dhaulagiri region hypothesised in *Section 7.8.2.*

In summary, the low volumes of leucogranite and sillimanite retrograde material in the UGHS, together with the late reversal of the STDS and orogen-parallel deformation of the UGHS and STDS, all have implications for the kinematic evolution of the GHS and the role of channel flow during its mid-crustal evolution. The rheological consequences of these features indicate that channel flow may have been hindered or subdued in this region.

7.9. Summary: Channel flow in the Annapurna-Dhaulagiri Himalaya

Through testing the kinematic, metamorphic and geochronological criteria for the channel flow model, it has been shown that channel flow of the UGHS played an important role in the Himalayan orogen and was responsible for mid-crustal evolution of the GHS in the Annapurna-Dhaulagiri Himalaya. Additionally, it has been shown that previous examples of evidence against channel flow, such as the identification of syn-metamorphic and geochronological discontinuities, are entirely consistent with the channel flow model. Furthermore, by addressing the atypical observations of the GHS from the Annapurna-Dhaulagiri region, such as the late reversal of the STDS, relatively low melt volumes and orogen-parallel deformation, it has been demonstrated how variations in crustal rheology place a dominant control on orogenic processes. Importantly, the GHS has been subjected to a protracted and varied progressive deformation pathway, from mid-crustal flow in a superstructure-infrastructure setting, through to out-of-sequence thrusting, underplating and upper-crustal exhumation within a thrust wedge setting. Consequently the preserved deformation history is both detailed and complex. Through synthesis of the results and interpretations of this research, combined with previously published constraints, the kinematic evolution of the GHS in the Annapurna-Dhaulagiri Himalaya is now described.

7.9.1. Mid-crustal channel flow of the UGHS (~40-22 Ma)

Following initial collision between India and Eurasia at ~50 Ma (Searle *et al.*, 1987; Green *et al.*, 2008; Najman *et al.*, 2010), high temperature (>700 ^{o}C) prograde metamorphism began at ~48 Ma (Larson & Cottle, 2015). The earliest partial melting occurred between 41 and 36 Ma (Carosi *et al.*, 2014). Crystallisation ages of deformed leucogranites and migmatites and metamorphic monazite ages indicate that peak

metamorphism and partial melting was sustained during southwards return-flow of the UGHS and coeval shearing on the CT and AD and DD between 40 and 22 Ma (Figure 7.9a) (Nazarchuk, 1993; Hodges *et al.*, 1996; Godin *et al.*, 2001; Larson & Godin, 2009; Corrie & Kohn, 2011; Kohn & Corrie, 2011; Carosi *et al.*, 2014; Larson & Cottle, 2015). Flow was most-likely driven by the overburden and south-sloping topographic gradient of the already-thickened Tibeatan Plateau, which by had attained a surface elevation of >4000 m by the Eocene (Searle *et al.*, 2011; Guillot & Replumaz, 2013; Wang *et al.*, 2014). During this time, the UGHS deformed internally via pervasive general shear with an increased component of non-coaxial deformation at the margins relative to the centre. AMS fabrics indicate that the UGHS was subjected to oblate flattening, involving a component of orogen-parallel stretching. Across the UGHS, the timing of initial prograde and peak metamorphism decreases down-section. At the top of the UGHS in Unit III, the earliest prograde metamorphism is recorded at ~38 to 30 Ma and reached peak conditions at ~30 Ma (Godin *et al.*, 2001; Corrie & Kohn, 2011). In Unit II, titanite geothermometry, from the Modi Khola transect records a continuous increase in temperature from 700-725 ^{o}C between 35 and 40 Ma to peak temperatures of 775-800^{o}C between 20 and 25 Ma (Kohn & Corrie, 2011). In Unit I in the Modi Khola transect, the timing of initial prograde and peak metamorphism decrease down-section from 33 to 26 Ma and 25 to 22 Ma, respectively (Corrie & Kohn, 2011). At the base of Unit I in the Modi Khola transect, exhumation related partial-melting is not recorded by monazite growth (Corrie & Kohn, 2011). This temporal trend in initiation of prograde and peak metamorphism is consistent with the largest relative velocities occurring towards the top of the UGHS in a southwards directed return-flow and smaller velocities related to northwards directed burial occurring in the lowermost portions of the UGHS in Unit I (Figure 7.6). Petrological observations and thermobarometric constraints indicate that during this time, the UGHS equilibrated within the kyanite stability field except for the uppermost portion of Unit III, which contains isolated pods of sillimanite-biotite schist (Nazarchuk, 1993; Hodges *et al.*, 1996; Godin *et al.*, 2001; Larson & Godin, 2009; Martin *et al.*, 2010; Corrie & Kohn, 2011; Carosi *et al.*, 2014). This early mid-crustal deformation correlates with ‘Stage 1’ of the kinematic evolution of the GHS (*Section 3.5.1.*) as determined from microstructural and crystal fabric observations and deformation temperatures estimates in Chapter 3.

7.9.2. Channel retreat and hinterland dome formation (24-18 Ma)

The absence of sillimanite retrograde metamorphism and associated decompression melting and the lack of brittle structures in the STDS (excluding E-dipping structures associated with the Thakkhola graben), indicates that the UGHS was not extruded to the surface as an ‘*active channel*’. Instead, crystallisation ages of undeformed

leucogranites that cut across top-to-the-south deformation fabrics in the CT and top-to-the-north fabrics in the AD indicate channel flow of the UGHS ended prematurely, some time between 22 and 18 Ma (Figure 7.9b) (Nazarchuk, 1993; Hodges *et al.*, 1996; Godin *et al.*, 2001). There are two likely explanations for this premature shut down of channel flow: (*1*) reduction in erosion rates, resulting in reduction in exhumation rates and southwards extrusion; and (*2*) orogen-parallel stretching of the UGHS during mid-crustal flow and/or orogen-parallel melt migration, which reduces the southwards flux of material, which must, therefore, also reduce rates of southwards exhumation. If melt migration exceeds melt production, then below a threshold rate of southwards extrusion, the frontal portion of the '*active channel*' may cool and strengthen at depth into a solid '*channel plug*' before it can exhume (Beaumont *et al.*, 2001; Jamieson & Beaumont, 2013). Subsequently, the frontal tip of the *active channel* retreats northwards to beneath the Tibetan Plateau (Beaumont *et al.*, 2004). A reduction in erosion of UGHS rocks in Nepal is recorded between 20 and 17 Ma from provenance analysis and low temperature geochronology of sediments in the Himalayan foreland (White *et al.*, 2002). Additionally, ~80 km east of the Kali Gandaki valley, E-W oriented magmatic lineations in the Manaslu leucogranite and associated E-W trending mineral stretching lineations in the surrounding host rocks suggest that orogen-parallel extrusion and melt migration occurred in the region between 22 and 19 Ma (Guillot *et al.*, 1993; Harrison *et al.*, 1999). Therefore, it is possible that both orogen-parallel flow and reduced erosion rates may be responsible for the stagnation and subsequent shut down of channel flow of the UGHS of the Annapurna-Dhaulagiri Himalaya between 22 and 18 Ma. Microstructures and CPO fabrics indicate that internal deformation of the UGHS persisted down to temperatures of 550-650 ^{o}C (Figures 3.20 & 3.21). This temperature may correspond to the threshold viscosity at which the UGHS transformed from an '*active channel*' to an inactive '*channel plug*'.

Prior to, and during the shutdown of channel flow beneath the Annapurna-Dhaulagiri region between 24 and 17 Ma, the Mustang and Mugu granite domes were emplaced ~80 km and ~50 km, respectively, north of the STDS in the Kali Gandaki valley (Harrison *et al.*, 1997; Hurtado, 2002; Hurtado *et al.*, 2007). Contemporaneously, between 23.5 and 22 Ma, the Changgo dome was emplaced ~150 km NE of the STDS in the Kali Gandaki valley (Larson *et al.*, 2010a). Emplacement of these domes may correspond to the position to which the frontal part of the *active channel* retreated (Hodges, 2006; Larson *et al.*, 2010b; Jamieson & Beaumont, 2013). This is supported by mid crustal zones of low resistivity beneath the Himalaya and Tibetan Plateau recorded by magnetotelluric surveys (Figure 7.9g,h), which are interpreted as present day *active channels* (Unsworth *et al.*, 2005; Rippe & Unsworth, 2010; Jamieson & Beaumont, 2013). ~100 km east of the Annapurna-Dhaulagiri region, the 800 Line

(*a*) Mid-crustal channel flow (40-22 Ma)

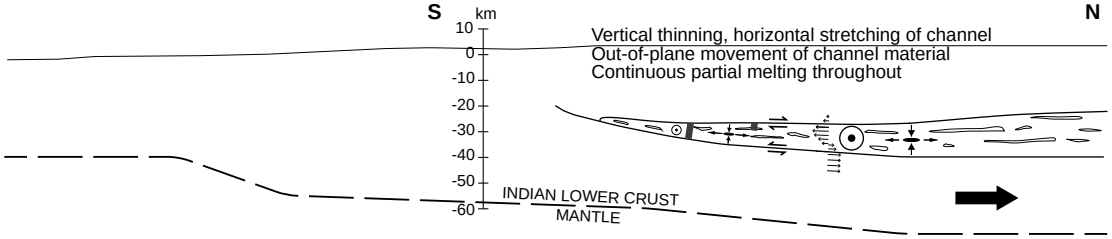

(*b*) Channel retreat and hinterland granite emplacment (24-18 Ma)

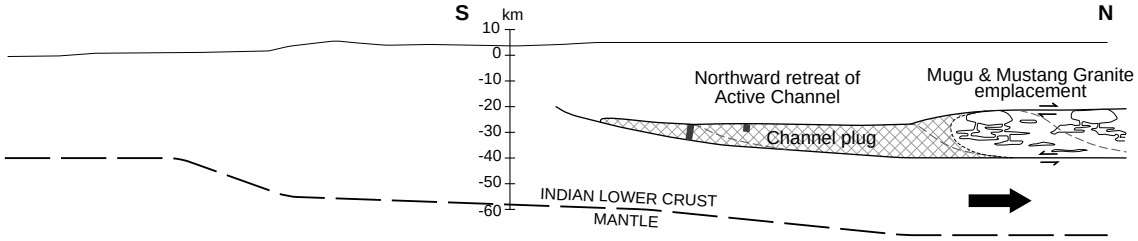

(*c*) Hinterland uplift and out-of-sequence thrusting (18-15 Ma)

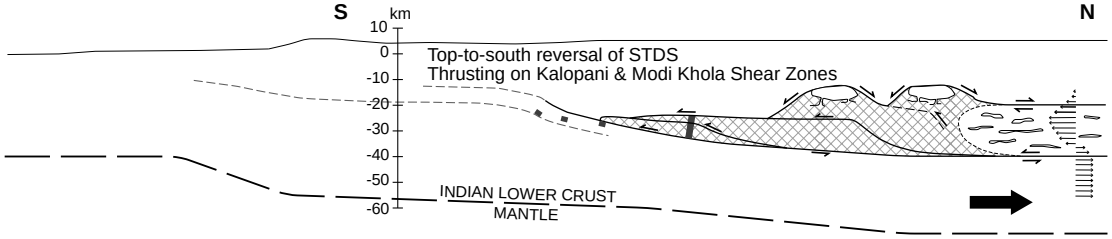

(*d*) Exhumation of the channel plug (16-10 Ma)

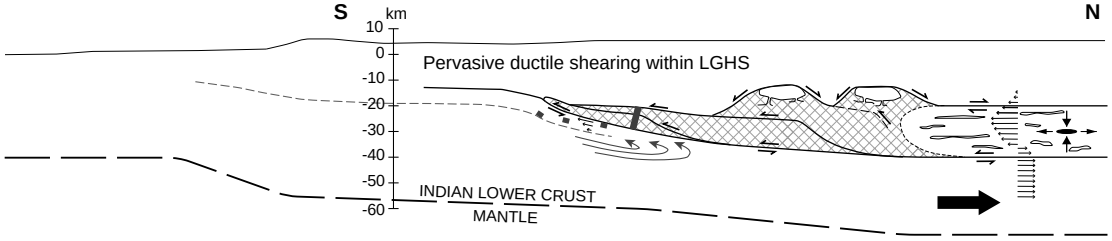

(*e*) Exhuamtion of the channel plug (continued) (16-10 Ma)

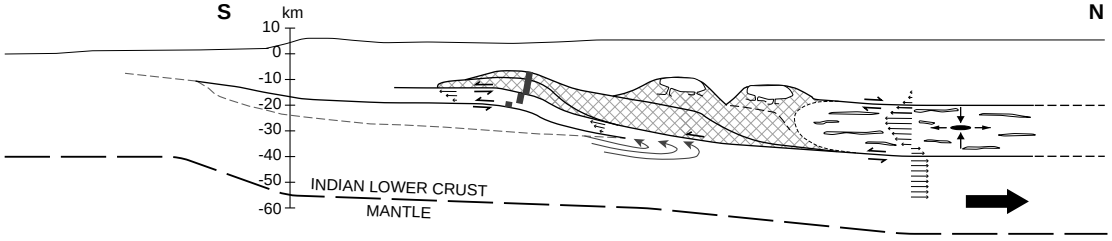

Figure 7.9 Tectonic evolution of the Annapurna Dhaulagiri Himalaya.

(*f*) Uplift and exhumation of the GHS during thrust stacking in the Lesser Himalayan Duplex (<12 Ma)

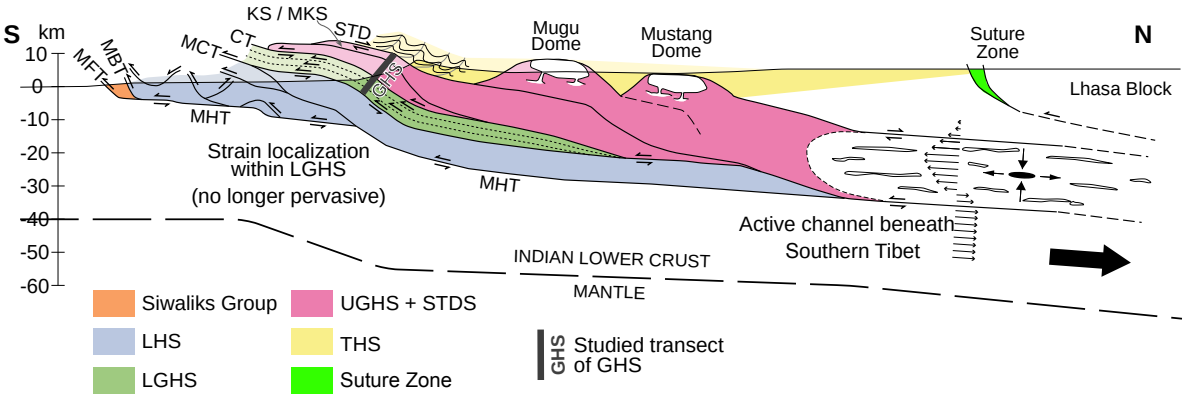

(*g*) 800 Line magnetotelluric survey through equivalent local section

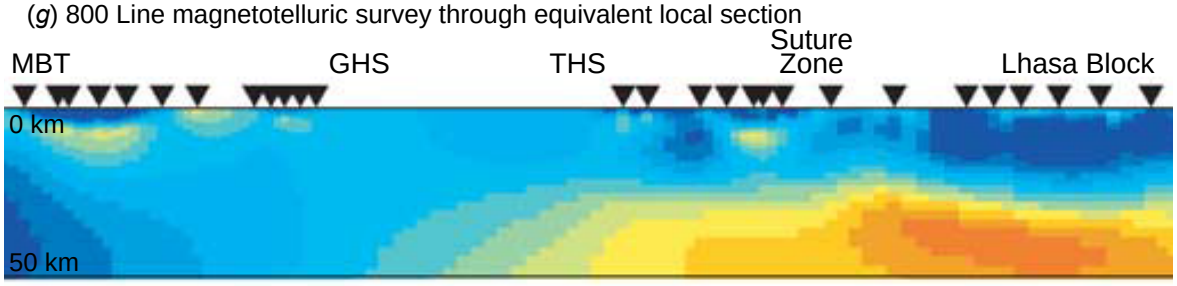

(*h*) Magnetotelluric surveys through the Himalayan & Southern Tibet

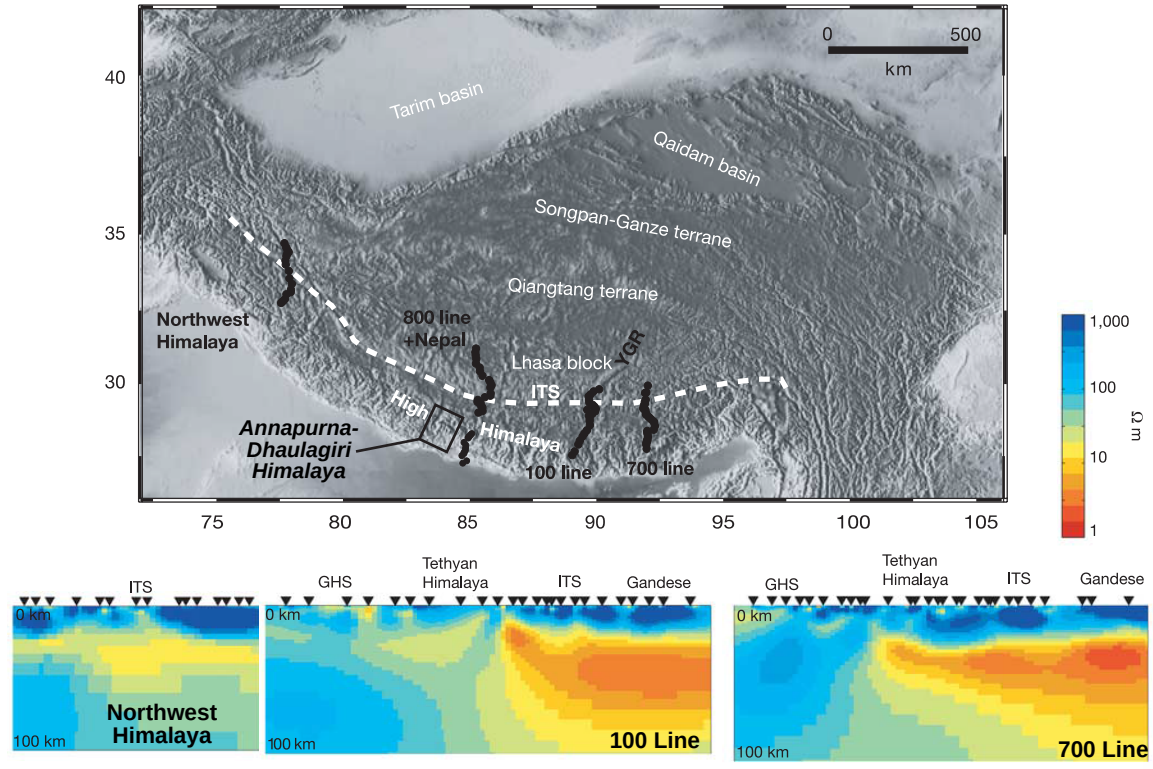

Figure 7.9 Continued.

magnetotelluric profile (Figure 7.9g) indicates that the mid crustal low resistivity zone is 50-100 km further north than positions measured elsewhere (Unsworth *et al.*, 2005). It has been suggested that the more northerly position of the low resistivity zone, north of the central Himalaya, may be due to localised retreat of the *active channel* towards the hinterland (Jamieson & Beaumont, 2013).

7.9.3. Hinterland uplift and out-of-sequence thrusting (18-15 Ma)

Hinterland retreat of the '*active channel*' was accompanied by hinterland advancement of the thrust wedge (Hodges, 2006; Jamieson *et al.*, 2006; Larson *et al.*, 2010b; Jamieson & Beaumont, 2013). Subsequently, $^{40}Ar/^{39}Ar$ muscovite and biotite cooling ages record uplift of the Mustang and Mugu granites between 15 and 17 Ma (Guillot *et al.*, 1999; Hurtado, 2002) and uplift of the Changgo culmination at 18.4 Ma (Larson *et al.*, 2010a). This phase represents a reorganisation of the thrust wedge (Figure 7.9c) as deformation migrates to the hinterland resulting in rapid uplift of the domes (Gleeson & Godin, 2006; Godin *et al.*, 2006a; Hodges, 2006; Larson *et al.*, 2010b; Jamieson & Beaumont, 2013). During and/or subsequent to dome uplift in the hinterland, top-to-the-south thrusting on the STDS and Kalopani and Modi Khola shear zones occurred prior to wholesale exhumation of the UGHS at 16-13 Ma (Vannay & Hodges, 1996; Godin *et al.*, 2001; Martin *et al.*, 2014). Low temperature deformation (300-400 ^{o}C) in the hangingwall of the AD (Figure 3.21) correlates approximately with the muscovite closure temperature for Ar loss (Harrison *et al.*, 2009) and may record this reverse-sense reactivation of the STDS. This is interpreted as out-of-sequence thrusting during southwards propagation of the deformation front after the thrust wedge attained a critical taper (Larson *et al.*, 2010b). It also suggests that by this time the rheological contrast between the UGHS and THS, which formed the stimulus for southwards-

Figure 7.9. Tectonic evolution of the Annapurna-Dhaulagiri Himalaya. (*a*-*e*) Schematic cross sectional evolution of the GHS and bounding units of the Annapurna-Dhaulagiri region based on thermobarometric and geochronological constraints (*see text for discussion*). Thick grey bars show migration and amalgamation of portions of present day exposed section of the GHS. Depth of muscovite closure temperature depth assumed to be 15 km, based on a geothermal gradient of 30 ^{o}C km^{-1}. Moho depth based on Huang *et al.*, 2009 and Nábelek *et al.*, 2009. (*f*) Sketch cross section of the present day structure of the Annapurna-Dhaulagiri Himalaya. LHS duplex structure based on Paudel & Arita, 2000, 2006. GHS thickness and position based on this study. Granite dome position based approximately on Hurtado, 2002. Suture zone and Moho structure based on Huang *et al.*, 2009, Nábelek *et al.*, 2009 and Godin & Harris 2014. (*g*) The 800 Line magnetotelluric profile measured ~100-120 km east of the Annapurna-Dhaulagiri Himalaya through the Manaslu region (*see 7.9h for profile location*). After Unsworth *et al.*, 2005. Orange-yellow colours and blue colours highlight low and high resistivity regions, respectively. Low resistivity zone is interpreted as a fluid rich, partially molten crustal layer, indicative of a present day active channel, beneath southern part of Tibetan Plateau (Unsworth *et al.,* 2005; Jamieson & Beaumont, 2013). (*h*) Additional magnetotelluric surveys through the Himalaya and southern Tibet. Map shows location of all profiles. After Unsworth *et al.*, 2005.

directed channel flow, no longer existed as the STDS translated the THS southwards over the now stronger UGHS. Additionally, indistinguishable $^{40}Ar/^{39}Ar$ muscovite cooling ages of ~18-17 Ma from the amphibolite facies footwall and unmetamorphosed hangingwall of the Dangardzong fault suggest that the earliest E-W extension of the Thakkhola graben began before this time (Hurtado, 2002). Thermo-mechanical channel flow models suggest that extension during or prior to 17 Ma may have occurred in response to upper-crustal instability above the hinterland '*active channel*' due to variations in topographic loading and/or tectonic or buoyancy driven dome uplift (Beaumont *et al.*, 2004). The initiation of E-W extension by ~17 Ma in the upper Kali Gandaki valley is approximately synchronous with the earliest E-W extension recorded in the Marsyandi valley at 17.5-14 Ma (Coleman, 1996; Coleman & Hodges, 1998).

7.9.4. Exhumation of the rigid *channel plug* (16-10 Ma)

Uniform $^{40}Ar/^{39}Ar$ muscovite cooling ages of 16-13 Ma from the UGHS indicate that the sequence was extruded and exhumed to the surface as a coherent single block (Figure 7.9d,e) (Vannay & Hodges, 1996; Godin *et al.*, 2001; Martin *et al.*, 2014), similar to models of an exhumed *channel plug* (Beaumont *et al.*, 2004; Grujic, 2006; Hodges, 2006). Medium to low temperature deformation (550-300 ^{o}C) in the LGHS (Figures 3.20 & 3.21) indicate that exhumation was facilitated by non-coaxial top-to-the-south pervasive shearing across the whole unit. Trends in deformation temperatures suggest that the zone of shearing within the LGHS either expanded or migrated down section as the cooling UGHS was exhumed. In the Modi Khola transect, 10 Ma $^{40}Ar/^{39}Ar$ muscovite cooling ages from the Unit I of the UGHS have been interpreted to represent NE-extension on the Bhanuwa fault between 15 and 10 Ma (Martin *et al.*, 2014). However, this fault is only identified on a geochemical basis and there is no field evidence to support such a structure (Martin *et al.*, 2010; Corrie & Kohn, 2011; Martin *et al.*, 2014). Localised low deformation temperature estimates of 300-450 ^{o}C on the CT that correlate with the closure temperature of muscovite (380-450 ^{o}C; Harrison *et al.*, 2009), suggest that focused deformation on the CT may have continued up until 10 Ma. Low temperature deformation (300-400 ^{o}C) recorded in the STDS suggests that this structure may have also been involved during the low temperature ductile extrusion and exhumation of the UGHS. This phase of intermediate to low temperature ductile extrusion correlates with 'Stage 2' of the kinematic evolution of the GHS (*Section 3.5.1.*) as determined from microstructural and crystal fabric observations and deformation temperatures estimates in Chapter 3.

Additionally, during this stage, E-W extension and syn-rift sedimentation in the Thakkhola graben continued. E-dipping low angle normal faults and hydrothermally produced $^{40}Ar/^{39}Ar$ muscovite ages of 12 Ma from within the STDS suggest that the

STDS and the Thakkhola graben may have been kinematically linked (Godin *et al.*, 2001; Hurtado *et al.*, 2001).

7.9.5. Strain localisation in the LGHS during thrust stacking and development of the Lesser Himalayan Duplex (Post-12 Ma)

Following exhumation of the UGHS through the muscovite closure temperature by 12-10 Ma (Vannay & Hodges, 1996; Godin *et al.*, 2001; Martin *et al.*, 2014), deformation focused into the LGHS and underlying LHS (Figure 7.9f) (Paudel & Arita, 2000; Martin *et al.*, 2014). In the LGHS, a single $^{40}Ar/^{39}Ar$ muscovite cooling age of 7 Ma is recorded in the Modi Khola transect (Martin *et al.*, 2014). A comparison of deformation temperature estimates and the muscovite closure temperature indicates that pervasive deformation in the LGHS of the Modi Khola transect was still on-going at 7 Ma. The recorded low temperature (<400 ^{o}C) strain localisation onto the MCT and into the proposed location of the Munsiari thrust (Martin *et al.*, 2010; Corrie & Kohn, 2011) near the top of the LGHS must have occurred after this time. After 12 Ma, strain localisation and thrust stacking and duplex development in the LHS became prevalent as the thrust wedge built outwards (Paudel & Arita, 2000; Pearson & Decelles, 2005; Larson *et al.*, 2010b). Thrusting within the Lesser Himalayan duplex began as earlier as 14 Ma (Paudel & Arita, 2000), although erosion of the duplex is reported at 11-12 Ma (Pearson & Decelles, 2005). Thrusting within the duplex south of the Annapurna-Dhaulagiri region is estimated to have continued to ~ 5 Ma (Paudel & Arita, 2000; Pearson & Decelles, 2005) and this is also likely to be the final stage of deformation within the LGHS (Pearson & Decelles, 2005). In the UGHS, a final stage of brittle faulting and hydrothermal activity is recorded between 5 and 2 Ma (Vannay & Hodges, 1996). Apatite fission track ages and apatite-helium ages from the UGHS and uppermost LGHS in the Modi Khola valley record wholesale exhumation through the 140 ^{o}C and 90 ^{o}C isotherms at ~1 Ma and 0.5-0.8 Ma, respectively, with no evidence of faulting during this time (Nadin & Martin, 2012). At the base of the duplex, thrusting on the MBT at the front of the thrust wedge initiated sometime between 11 and 5 Ma (Burbank *et al.*, 1996; Pearson & Decelles, 2005) and may have continued to as late as 1 Ma (Paudel & Arita, 2000). This final stage of upper-crustal deformation correlates with ‘Stage 3’ of the kinematic evolution of the GHS (*Section 3.5.1.*) as determined from microstructural and crystal fabric observations and deformation temperatures estimates in Chapter 3. The present day structure of the Annapurna-Dhaulagiri region (Figure 7.9f) is characterised by thrust stacking and duplex development, whilst magnetotelluric surveys suggest that a mid-crustal *active channel flow* currently resides further north beneath the southern part of the Tibetan Plateau (Figure 7.9g). This

typifies the composite orogenic system, described in Figure 7.4, built from multiple orogenic domains.

7.10. Summary of discussion

In this chapter, it has been demonstrated that composite models of channel flow and critical wedge tectonics best reflect the geological features of the Annapurna-Dhaulagiri Himalaya (Figure 7.9). The apparent dichotomy between channel flow, wedge extrusion and thrust stacking and duplex development has been shown to be misleading. It is demonstrated that large hot orogens such as the Himalaya-Tibetan orogenic system can develop different crustal-scale orogenic domains (Figure 7.4) characterised either by the Superstructure-Infrastructure Association or by thrust stacking and duplex development in a thrust wedge. The penetrative deformation and metamorphic history of the GHS records a progressive kinematic evolution through both of these domains. Based on the findings of this research and synthesis with previously published constraints, the mid-crustal evolution of the GHS may be explained consistently by the channel flow model. Seemingly incompatible features, such as the lower than typical structural thickness of the UGHS and the metamorphic and geochronological discontinuities recorded across the UGHS, may be reconciled with the channel flow model. Additionally, the effects of features such as the low volume of leucogranite, lack of sillimanite retrograde metamorphism, reversal of motion on the STDS and orogen-parallel deformation, have been considered. It is postulated that these features reflect the premature shutdown of channel flow beneath the Annapurna-Dhaulagiri Himalaya and subsequent channel retreat towards the hinterland before exhumation of an '*active channel*' could be achieved.

Finally, the kinematic evolution of the GHS in the Annapurna-Dhaulagiri Himalaya has been described, based on research presented in this thesis and previously published PTt constraints. The early evolution of the GHS involved a protracted period of prograde metamorphism and anatexis during southward-propagating mid-crustal channel flow. Following the premature shut down of the channel beneath the Annapurna-Dhaulagiri region, channel retreat towards the hinterland, possibly accompanied by reduced erosion rates, resulted in northwards expansion of the thrust wedge. Subsequent uplift and exhumation of the Mustang, Mugu and Changgo domes in southern Tibet built the wedge to a critical taper. This was proceeded by propagation of deformation towards the foreland, resulting in out-of-sequence top-to-the-south thrusting on the STDS and the Kalopani and Modi Khola shear zones in the UGHS. E-W extension of the Thakkhola graben occurred during or before this time, possibly in response to dome uplift and upper-crustal instabilities. Shortly after this, the deformation front of the thrust wedge continued to propagate southwards. The UGHS

was subsequently exhumed as a rigid block, facilitated by pervasive non-coaxial shearing in the LGHS. The final stages of deformation involved low temperature strain localisation on to the MCT and Munsiari thrust within the LGHS, as the Lesser Himalayan Duplex uplifted and eroded.

The complex kinematic history exhibited by the Annapurna-Dhaulagiri Himalaya demonstrates that channel flow, wedge extrusion and thrust stacking and duplex development may occur within a single orogen. In such cases, the dominant control on the spatial and temporal evolution of the metamorphic core is rheology. Spatial differences in rheological controls, such as temperature, melt volume and pressure gradients, are likely to account for many of the structural, metamorphic and geochronological variations observed in the GHS along the length of the orogen. In 'Large Hot Orogens' (Beaumont *et al.*, 2006; Jamieson & Beaumont, 2013) such as the Himalayan-Tibetan system, the structural architecture of the orogen is assembled from multiple orogenic domains, each driven by different controls and processes. Significantly, the recorded transfer of crustal material through and between these domains indicates that the rheological boundary conditions that control orogenesis are dynamic and mobile, and must vary both spatially and temporarily.

- CHAPTER 8 –

CONCLUSIONS & FUTURE WORK

8.1. Conclusions

The kinematic evolution of the Greater Himalayan Sequence (GHS) forms the central focus of all models of Himalayan orogenesis. Models of mid-crustal channel flow proposed for the Himalayan orogen by numerous authors over the last two decades, are frequently contested by contradictory studies that favour models of wedge extrusion, underplating, duplex development and/or tectonic wedging. The aim of this thesis has been to test a set of geological criteria required for validation of the channel flow model. The Annapurna-Dhaulagiri Himalaya was chosen as a suitable region to test the model and a decision was made to focus on the kinematic and strain related criteria for channel flow, through geological mapping, field structural and microstructural and magnetic fabric analyses. The following conclusions have been made from this research.

1) The geological framework of the Annapurna-Dhaulagiri region contains many of the salient structural and lithological features recorded from the GHS and bounding units along the length of the central Himalaya. These include: (*1*) an inverted metamorphic sequence at the base of the GHS overlain by a right-way up metamorphic sequence; (*2*) coeval motion on high strain shear zones at the top and bottom of the GHS with top-to-the-north and top-to-the-south shear senses, respectively; and (*3*) a core of amphibolite facies, kyanite to sillimanite grade schists, gneisses, migmatites and syn- and post-tectonic leucogranite intrusions, bound above and below by low grade metasedimentary rocks (i.e. the Lesser Himalayan Sequence, LHS and Tethyan Himalayan Sequence, THS). Additionally, the Annapurna-Dhaulagiri region possesses several atypical features that are not readily conformable with the channel flow model. These include: (*1*) a lower-than-typical volume of partial melt and sillimanite grade material in the GHS; (*2*) a lower-than-typical structural thickness (~7 km) of the amphibolite facies Upper Greater Himalayan Sequence (UGHS); (*3*) late-stage top-to-the-south shearing in the South Tibetan Detachment System (STDS); and (*4*) orogen-parallel stretching lineations and magnetic lineations in the UGHS and STDS.

2) Microstructural and Crystallographic Preferred Orientation (CPO) analyses indicate that the GHS has been subjected to pervasive ductile shearing and is characterised by a transpositional shear fabric. Microstructures and CPO fabrics show a dominance of non-coaxial deformation in the Lower Greater Himalayan Sequence (LGHS) and STDS. Deformation in the UGHS has an increased component of coaxial deformation. Anisotropy of Magnetic Susceptibility (AMS) ellipsoid shape fabrics record an oblate strain in the UGHS indicative of vertical thinning and horizontal orogen-parallel and orogen-perpendicular stretching synchronous with partial melting.
3) CPO intensity (*I*) and AMS fabric shear strain proxy (γ) calculated from samples from across the GHS and bounding units provide a means of constructing relative strain magnitude (RSM) profiles for the Annapurna-Dhaulagiri Himalaya. The profiles identify high strain zones coincident with the location of the Main Central Thrust (MCT), South Tibetan Detachment (STD), Chomrong Thrust (CT), Annapurna Detachment (AD) and Deurali Detachment (DD). Low RSM in the LHS and THS reflects a significant reduction in deformation relative to the GHS. In the LGHS and STDS, the RSM profiles record a zone of pervasive deformation that increases in intensity with proximity to the UGHS. Within the UGHS, deformation is concentrated towards the margins of the sequence. The intensity of deformation in the middle of the UGHS is low.
4) Relative velocity profiles were calculated from the integrals of the RSM profiles and are comparable to 1-dimensional laminar flow models. The velocity structure of the UGHS is comparable to a Hybrid flow with a portion of southwards return-flow, driven by northwards motion of the underlying LGHS and LHS, and a southward-directed lateral pressure gradient. The shape of the curve is indicative of a stress-dependent power-law flow rheology. The STDS and LGHS have similar velocity structures indicative of temperature-dependant power law Couette flow driven by the relative motions of the LHS, UGHS and THS. At the margins of the profiles the LHS and THS have uniform velocity structures, comparable to a northwards moving lower channel wall and a stationary upper channel wall, respectively. Velocity gradients indicate an increase in the ratio of non-coaxial to coaxial deformation from the centre of the UGHS towards its margins. In the LGHS and STDS, velocity gradients are indicative of non-coaxial deformation.

5) Trends in RSM, relative velocity and deformation temperatures indicate that the Annapurna-Dhaulagiri Himalaya can be divided into distinct orogenic domains that correlate to specific stages of development of the Himalayan orogen governed by different rheological boundary conditions. The observed deformation records a spatial and temporal transition from mid-crustal ductile flow of the UGHS (>550 ^{o}C; Orogenic Domain 1) to lower temperature extrusion and exhumation of the UGHS as a rigid body (<550 ^{o}C). Extrusion and exhumation of the UGHS occurred firstly by pervasive ductile shearing in the LGHS and possibly in the STDS (~400-550 ^{o}C; Orogenic Domain 2); and secondly by localised low temperature shearing on the MCT and CT (<400 ^{o}C; Orogenic Domain 3). The CT and AD represent rheological as well as structural and lithological discontinuities between these domains.
6) Geological criteria for channel flow during the Himalayan orogeny have been tested and evaluated. The UGHS in the Annapurna-Dhaulagiri Himalaya has been subjected to high temperature (>700 ^{o}C) metamorphism and partial melting for at least 20 Myr following collision of India with Eurasia (~50 Ma) (*see Section 7.7.1 and references therein*). During this time, syn-metamorphic pervasive shearing is recorded throughout the UGHS, with a concentration of top-to-the-south and top-to-the-north non-coaxial deformation at its lower and upper margins, respectively. Deformation in the centre of the UGHS is of a lower intensity and has an increased component of coaxial deformation relative to its margins. Viscosity estimates from experimental flow laws suggest that at peak temperatures of 750-850 ^{o}C, the UGHS in the Annapurna-Dhaulagiri Himalaya was mechanically weak (viscosity $\leq 10^{19}$ Pa s) despite its lower-than-typical structural thickness (~7 km) and partial melt volume. The relative velocity structure of the UGHS is indicative of a Hybrid flow, dominated by a pressure-gradient-driven southwards return-flow with a minor amount of northwards burial at its base relating to subduction of the lower Indian crust. Fold structures and associated axial-planar cleavage in the THS are folded into parallelism with the UGHS transpositional foliation via horizontal stretching on the STDS, typical of a Superstructure-Infrastructure Association (SIA). Fold vergence north of the STDS suggests that UGHS material originally underthrusted the THS with a top-to-the-south motion, before extruding southwards via

top-to-the-north motion on the STDS. These findings satisfy the geological criteria for channel flow during the Himalayan orogen and indicate that the channel flow model provides a likely explanation for the mid-crustal evolution of the UGHS.

7) The atypical geological features of the Annapurna-Dhaulagiri Himalaya have been shown to be compatible with the channel flow model if rheological boundary conditions are allowed to evolve. The lower-than-typical volumes of leucogranite and sillimanite grade material suggest that high temperature deformation (>550 ^{o}C) of the UGHS occurred almost entirely within the kyanite stability field and the sequence was not subjected to a final stage of melt production during sillimanite retrograde metamorphism relating to cooling, exhumation and erosion of the GHS. Instead, the UGHS cooled and 'froze' at depth to form a rigid channel plug that would later be exhumed through crustal-scale buckling and thrust stacking within the underlying LGHS and LHS in a manner similar to that described by Gleeson and Godin (2006), Godin *et al.* (2006a) and Larson *et al.* (2010b). It is possible that the low volumes of leucogranite in the UGHS may be the result of melt migration to one or more of the large leucogranite plutons close to the Annapurna-Dhaulagiri Himalaya (e.g. the Mugu and Manaslu leucogranites).

   Late stage top-to-the-south shearing in the STDS and within the UGHS on the Kalopani and Modi Khola Shear Zones (KSZ, MKSZ) reflects a change in the relative rheological strengths of the UGHS and THS. Following cessation of channel flow and development of a rigid *channel plug* beneath the Annapurna-Dhaulagiri Himalaya, the increased strength of the UGHS removed the rheology contrast between the THS and GHS, thereby promoting top-to-the-south out-of-sequence thrusting between the THS and GHS, localised in the STDS and on the KSZ and MKSZ.

8) Orogen-parallel stretching affected the GHS during its mid-crustal evolution. Timing constraints suggest that initiation of E-W extension of the Thakkhola graben may have been responsible for orogen-parallel deformation in the UGHS and STDS (*see Section 7.8.3. and references therein*). Orogen-parallel stretching in the UGHS may also correlate with similar solid-state and magmatic deformation features observed by other authors in the Marsyandi valley of the Manaslu Himalaya, ~80 km east of the Annapurna-Dhaulagiri Himalaya. It is possible that orogen-parallel mid-crustal flow may

be responsible for the ponding of large leucogranite bodies such as the Manaslu and Mugu leucogranites. Additionally, orogen-parallel flow may have reduced southwards extrusion and hindered exhumation. This may provide the stimulus for the premature shut down of channel flow beneath the Annapurna-Dhaulagiri Himalaya. Mid-crustal orogen-parallel flow has not been numerically simulated by any of the channel flow models and its role during mid-crustal evolution of the GHS requires further investigation.

9) Research presented in this thesis indicates that the GHS in the Annapurna-Dhaulagiri Himalaya evolved through an early stage of mid-crustal channel flow and ductile extrusion and a later stage of thrust stacking and underplating during exhumation. Similar composite models for the Himalayan orogen have been proposed by other authors and reflect the migration of the GHS between different orogenic domains, governed by different rheological boundary conditions (*see Section 7.6. and references therein*). A synthesis of all available thermobarometric and geochronological constraints for the Annapurna-Dhaulagiri Himalaya reveals the kinematic evolution of the GHS through these domains and demonstrates interplay between crustal flow, thrust wedge development and exhumation. Following a prolonged period of mid-crustal flow of the UGHS, a reduction in the rate of southward extrusion and/or rates of erosion and exhumation led to the cessation of channel flow beneath the Annapurna-Dhaulagiri Himalaya. The UGHS ‘froze’ to form a channel plug beneath the Annapurna-Dhaulagiri Himalaya and the active channel retreated northwards, where the Mugu and Mustang granite domes developed. Mid-crustal channel retreat was accompanied by northwards thrust wedge expansion in the upper crust, in response to reduced exhumation and erosion rates, which triggered the uplift and exhumation of the Mustang and Mugu domes. Dome uplift was proceeded by southward migration of deformation during reorganisation of the thrust wedge to a new critical taper, possibly due to increased erosion rates along the Himalayan front. This final stage resulted in out-of-sequence thrusting in the STDS and UGHS, followed by extrusion and exhumation of the rigid UGHS, during underplating, thrust stacking and duplex development in the underlying LGHS and LHS (*see Section 7.9 and references therein for geochronological constraints*).

8.2. Future work

The data and new findings presented in this thesis provide scope for several additional studies and highlight critical areas of research that are required in order to further our understanding of both the Himalayan orogen, and orogenic processes in general. Future work based on this thesis should focus on the following topics.

1) *PTt evolution of the GHS in the Annapurna-Dhaulagiri region.* The findings of this research combined with available thermobarometric constraints suggest that the UGHS in the Annapurna-Dhaulagiri region did not undergo isothermal decompression and sillimanite grade retrogression and associated decompression melting. Instead, the data suggest that the UGHS cooled and strengthened at depth, resulting in a slower exhumation path that occurred after peak metamorphism, with a reduction in temperature as the UGHS exhumed through lower pressures. The timing and magnitude of peak pressures and temperatures experienced by the UGHS in the Annapurna-Dhaulagiri region are relatively well constrained (*see Section 7.7.1 and references therein*). However, the retrograde PTt path experienced by the UGHS needs more detailed study through targeted geochronometry and thermobarometry. Relevant approaches include: (*a*) phase equilibrium (e.g. Grt-Bt Fe/Mg exchange) and multi-equilibrium thermobarometry (e.g. THERMOCALC), pseudosection analysis (see Kohn, 2014 for a review of techniques); (*b*) garnet element zonation analysis (Kohn *et al.*, 2001; Jessup *et al.*, 2008; Caddick & Kohn, 2013); (*c*) Raman spectroscopy of carbonaceous material (RSCM) thermometry (Beyssac *et al.*, 2004; Bollinger *et al.*, 2004; Cottle *et al.*, 2011); (*d*) titanite thermochronology (Cottle *et al.*, 2011; Kohn & Corrie, 2011); and (*e*) monazite and zircon geochronology (Kohn *et al.*, 2001; Caddick *et al.*, 2007; Jessup *et al.*, 2008; Corrie & Kohn, 2011; Cottle *et al.*, 2011; Larson & Cottle, 2015). Such approaches should validate the PT path proposed for the UGHS in this thesis. An important feature of the proposed evolution of the GHS in the Annapurna-Dhaulagiri region is that the UGHS cooled and strengthened at depth and was exhumed as a rigid plug via pervasive shearing in the LGHS. Validation of this sequence of events also requires PTt data from the LGHS and STDS of which there are currently few. Low

temperature thermochronology studies, such as $^{40}Ar/^{39}Ar$ chronology of muscovite, biotite and amphibole (e.g. Godin *et al.*, 2001; Martin *et al.*, 2014) and apatite and zircon fission track dating (e.g. Blythe *et al.*, 2007; Nadin & Martin, 2012), would also provide further information on late stage exhumation of the GHS during thrust stacking and underplating in the Lesser Himalayan duplex. Combining the data presented in this thesis with the proposed techniques listed above would provide a comprehensive and detailed account of the kinematic evolution of the GHS in the Annapurna-Dhaulagiri Himalaya.

2) *Calibration of CPO and AMS strain proxies.* The use of CPO and AMS data as proxies for strain provide a valuable opportunity to study the distribution of strain across metamorphic terranes and shear zone of differing lithologies. These techniques should be applied in other settings to test their use and applicability. Of most significance would be the calibration of these techniques to produce quantified strain gauges. With regards to the CPO strain proxy, recent advances in the Visco-Plastic Self Consistent (VPSC) modelling of crystal-plastic deformation (Lebensohn & Tomé, 1993; Morales *et al.*, 2011; Galán *et al.*, 2014; Morales *et al.*, 2014; Nie & Shan, 2014) may provide the best opportunity to determine the quantified relationship between CPO strength and strain. One of the major challenges for this technique is to understand the effects of multiple mineral phase content and pre-existing crystal fabrics on CPO development. Recent microstructural analyses (e.g. Herwegh *et al.*, 2011; Czaplińska *et al.*, 2015) and numerical simulations of crystal fabric development (e.g. Jessell *et al.*, 2001; Piazolo *et al.*, 2010; Montési, 2013; Cook *et al.*, 2014) provide some insight into these controls. In addition to the suggested computation techniques, deformation experiments of geological materials continue to improve our understanding of the relationships between crystal fabric development and strain (e.g. Heilbronner & Tullis, 2006; Barreiro *et al.*, 2007; Delle Piane *et al.*, 2008). A combined study utilizing all of these techniques would provide the best opportunity to develop a calibrated CPO strength strain gauge. Calibrating the AMS strain proxy is more difficult. Calibration would require that all other controls of AMS (e.g. mineral content, grain size and magnetostatic grain interaction) for a given sample are known and can be negated, so as to consider only the deformation fabric-related AMS signal. Calibration of the

AMS strain proxy might be achievable through AMS analysis of experimentally deformed materials. However, due to the variability of controls on AMS between different lithologies and geological settings, this strain proxy is probably most affective as a relative proxy. As such, the development of this technique would benefit greatly from further application to other geological settings, perhaps with fewer lithologies and deformation phases

3) *The role of mid-crustal flow in other orogenic systems*. Models of crustal flow have been proposed for several other orogens, including the Grenville (Jamieson & Beaumont, 2011), Canadian Cordillera (Brown & Gibson, 2006), Variscan (Schulmann *et al.*, 2008), Appalachians (Hatcher & Merschat, 2006) and Hellenides (Xypolias & Kokkalas, 2006). A relatively simple but useful study would be to compare the known PTt and deformation histories (e.g. St-Onge *et al.*, 2006; Streule *et al.*, 2010b) to assess whether the geology of these other orogens meets the requirements for channel flow processes. The thermo-mechanical models used to simulate channel flow in the Himalayan orogen have been modified to simulate continental collision and mid-crustal flow in other orogens, such as the Western Superior Province, Grenville and European Alps (e.g. Culshaw *et al.*, 2006; Jamieson & Beaumont, 2011; Butler *et al.*, 2013; Jamieson & Beaumont, 2013; Butler *et al.*, 2014). The results of these models require testing and it would be useful to study these other orogens in detail, employing the same techniques used in this study.
4) *The role of orogen-parallel deformation during orogenesis*. There is growing evidence for orogen-parallel deformation during the Himalayan orogen, which in some cases may have affected the mid-crustal evolution of the GHS (*see Section 7.8.3. and references therein*). Orogen-parallel deformation requires further study, ranging from field observations to numerical simulations. Current models of Himalayan orogenesis do not account for this phenomenon, yet it may have had significant influence on development of the mountain belt. The variability in the lithological and structural framework of the GHS along the length of the orogen is testament to the variability of rheological controls present during the Himalayan orogeny. In order to understand this orogen-parallel variability and the role of

orogen-parallel deformation, large (≥100 km) orogen-parallel transects through the GHS should be studied in detail.

5) *Petrofabric-derived seismic properties of the GHS.* One of the long standing questions surrounding the development of the Himalayan-Tibetan orogenic system is by how much and to what lateral extent is the mid crust beneath the Tibetan Plateau partially molten (*see Section 1.3.1. and references therein*). One of the difficulties in answering this question is making robust geological interpretations from geophysical data. EBSD data can be used to calculate seismic velocities and anisotropies of a sample using computational textural analysis software (Mainprice & Nicolas, 1989; Mainprice, 1990; Lloyd & Kendall, 2005; Lloyd *et al.*, 2011b; Mainprice *et al.*, 2011). These data can be compared directly to the seismic parameters derived from surveys across the Himalaya and Tibet (e.g. Nelson *et al.*, 1996; Shapiro *et al.*, 2004; Schulte-Pelkum *et al.*, 2005; Guo *et al.*, 2009; Huang *et al.*, 2009; Nábelek *et al.*, 2009). Additionally, petrofabric-derived seismic properties can be used to forward model the seismic response of large tectono-stratigraphic units (e.g. Lloyd *et al.*, 2011a; Lloyd *et al.*, 2011b). Using software packages such as One-way (Audet *et al.*, 2007) and A-TRAK (Guest *et al.*, 1993), synthetic seismic sections based on modelled crustal sections populated with the petrofabric-derived seismic properties can be developed and compared directly to the seismic sections output by geophysical surveys of the Himalaya and Tibet. Such studies may help to assess ambiguous features of geophysical surveys and assess the control exerted by crystal fabric and lithology on the seismic properties of the Tibetan crust (e.g. Shapiro *et al.*, 2004; Schulte-Pelkum *et al.*, 2005; Nábelek *et al.*, 2009).

List of References

Adhikari, B. R., Wagreich, M. 2011. Provenance evolution of collapse graben fill in the Himalaya—The Miocene to Quaternary Thakkhola-Mustang Graben (Nepal). *Sedimentary Geology,* 233, 1-14, DOI: 10.1016/j.sedgeo.2010.09.021.

Altenberger, U., Wilhelm, S. 2000. Ductile deformation of K-feldspar in dry eclogite facies shear zones in the Bergen Arcs, Norway. *Tectonophysics,* 320, 107-121, DOI: 10.1016/S0040-1951(00)00048-2.

Argles, T. W., Edwards, M. A. 2002. First evidence for high-grade, Himalayan-age synconvergent extension recognised within the western syntaxis—Nanga Parbat, Pakistan. *Journal of Structural Geology,* 24, 1327-1344, DOI: 10.1016/S0191-8141(01)00136-5.

Arita, K. 1983. Origin of the inverted metamorphism of the Lower Himalayas, Central Nepal. *Tectonophysics,* 95, 43-60, DOI: 10.1016/0040-1951(83)90258-5.

Audet, P., Bostock, M. G., Mercier, J.-P. 2007. Teleseismic waveform modelling with a one-way wave equation. *Geophysical Journal International,* 171, 1212-1225, DOI: 10.1111/j.1365-246X.2007.03586.x.

Bachmann, F., Hielscher, R., Schaeben, H. 2010. Texture Analysis with MTEX – Free and Open Source Software Toolbox. *Solid State Phenomena,* 160, 63-68, DOI: 10.4028/www.scientific.net/SSP.160.63.

Baëta, R., Ashbee, K. 1969. Slip Systems in Quartz. 1. Experiements. *American Mineralogist,* 54, 1551-1573.

Baltz, T., Murphy, M. A. Structural evolution of the Thakkhola graben and implications on the architecture of the central Himalaya. *Fall Meeting 2009*, American Geophysical Union, San Francisco, CA.

Banks, C. J., Warburton, J. 1986. 'Passive-roof' duplex geometry in the frontal structures of the Kirthar and Sulaiman mountain belts, Pakistan. *Journal of Structural Geology,* 8, 229-237, DOI: 10.1016/0191-8141(86)90045-3.

Baratoux, L., Schulmann, K., Ulrich, S., Lexa, O. 2005. Contrasting microstructures and deformation mechanisms in metagabbro mylonites contemporaneously deformed under different temperatures (c. 650 °C and c. 750 °C). *In:* Gapais, D., Brun, J. P., Cobbold, P. R. (eds.), *Deformation Mechanisms, Rheology and Tectonics: from Minerals to the Lithosphere.* Geological Society of London Special Publications*,* 243, 97-125, DOI: 10.1144/gsl.sp.2005.243.01.09.

Barber, D. J., Heard, H. C., Wenk, H. R. 1981. Deformation of dolomite single crystals from 20–800° C. *Physics and Chemistry of Minerals,* 7, 271-286, DOI: 10.1007/bf00311980.

Barber, D. J., Wenk, H.-R., Heard, H. C. 1994. The plastic deformation of polycrystalline dolomite: comparison of experimental results with theoretical predictions. *Materials Science and Engineering: A,* 175, 83-104, DOI: 10.1016/0921-5093(94)91048-0.

Barber, D. J., Wenk, H.-R. 2001. Slip and dislocation behaviour in dolomite. *European Journal of Mineralogy,* 13, 221-243, DOI: 10.1127/0935-1221/01/0013-0221.

Barnhoorn, A., Bystricky, M., Burlini, L., Kunze, K. 2004. The role of recrystallisation on the deformation behaviour of calcite rocks: large strain torsion experiments on Carrara marble. *Journal of Structural Geology,* 26, 885-903, DOI: 10.1016/j.jsg.2003.11.024.

Barnhoorn, A., Bystricky, M., Burlini, L., Kunze, K. 2005. Post-deformational annealing of calcite rocks. *Tectonophysics,* 403, 167-191, DOI: 10.1016/j.tecto.2005.04.008.

Barreiro, J. G., Lonardelli, I., Wenk, H. R., Dresen, G., Rybacki, E., Ren, Y., Tomé, C. N. 2007. Preferred orientation of anorthite deformed experimentally in Newtonian creep. *Earth and Planetary Science Letters,* 264, 188-207, DOI: 10.1016/j.epsl.2007.09.018.

Barth, N. C., Hacker, B. R., Seward, G. G. E., Walsh, E. O., Young, D., Johnston, S. 2010. Strain within the ultrahigh-pressure Western Gneiss region of Norway recorded by quartz CPOs. *In:* Law, R. D., Butler, R. W. H., Holdsworth, R. E., Krabbendam, M. Strachan, R. A. (eds.), *Continental Tectonics and Mountain Building: The Legacy of Peach and Horne.* Geological Society of London Special Publications, 335, 663-685, DOI: 10.1144/Sp335.27.

Beaumont, C., Jamieson, R. A., Nguyen, M. H., Lee, B. 2001. Himalayan tectonics explained by extrusion of a low-viscosity crustal channel coupled to focused surface denudation. *Nature,* 414, 738-742, DOI: 10.1038/414738a.

Beaumont, C., Jamieson, R. A., Nguyen, M. H., Medvedev, S. 2004. Crustal channel flows: 1. Numerical models with applications to the tectonics of the Himalayan-Tibetan orogen. *Journal of Geophysical Research: Solid Earth,* 109, B06406, DOI: 10.1029/2003JB002809.

Beaumont, C., Nguyen, M. H., Jamieson, R. A., Ellis, S. 2006. Crustal flow modes in large hot orogens. *In:* Law, R. D., Searle, M. P. Godin, L. (eds.), *Channel Flow, Ductile Extrusion and Exhumation in Continental Collision Zones.* Geological Society of London Special Publications, 268, 91-145, DOI: 10.1144/GSL.SP.2006.268.01.05.

Beaumont, C., Jamieson, R. A. 2010. Himalayan-Tibetan orogeny: Channel flow versus (critical) wedge models, a false dichotomy? *In:* Leech, M. L. Others, A. (eds.), *Proceedings for the 25th Himalaya-Karakoram-Tibet Workshop.* San Francisco, CA.

Behrmann, J. H., Platt, J. P. 1982. Sense of nappe emplacement from quartz c-axis fabrics; an example from the Betic Cordilleras (Spain). *Earth and Planetary Science Letters,* 59, 208-215, DOI: 10.1016/0012-821X(82)90126-1.

Benn, K. 1994. Overprinting of magnetic fabrics in granites by small strains: numerical modelling. *Tectonophysics,* 233, 153-162, DOI: 10.1016/0040-1951(94)90238-0.

Berthé, D., Choukroune, P., Jegouzo, P. 1979. Orthogneiss, mylonite and non coaxial deformation of granites: the example of the South Armorican Shear Zone. *Journal of Structural Geology,* 1, 31-42, DOI: 10.1016/0191-8141(79)90019-1.

Bestmann, M., Prior, D. J. 2003. Intragranular dynamic recrystallization in naturally deformed calcite marble: diffusion accommodated grain boundary sliding as a result of subgrain rotation recrystallization. *Journal of Structural Geology,* 25, 1597-1613, DOI: 10.1016/S0191-8141(03)00006-3.

Beyssac, O., Bollinger, L., Avouac, J. P., Goffe, B. 2004. Thermal metamorphism in the Lesser Himalaya of Nepal determined from Raman spectroscopy of carbonaceous material. *Earth and Planetary Science Letters,* 225, 233-241, DOI: 10.1016/j.espl.2004.05.023.

Blythe, A. E., Burbank, D. W., Carter, A., Schmidt, K., Putkonen, J. 2007. Plio-Quaternary exhumation history of the central Nepalese Himalaya: 1. Apatite and zircon fission track and apatite [U-Th]/He analyses. *Tectonics,* 26, TC3002, DOI: 10.1029/2006tc001990.

Bodenhausen, J. W. A., Egeler, C. 1971. On the geology of the upper Kali Gandaki valley, Nepalese Himalayas*. I: Akademie van Wetenschappen Proceedings,* Koninklijke Nederlandse, 74, 526–538.

Bollinger, L., Avouac, J. P., Beyssac, O., Catlos, E. J., Harrison, T. M., Grove, M., Goffe, B., Sapkota, S. 2004. Thermal structure and exhumation history of the Lesser Himalaya in central Nepal. *Tectonics,* 23, TC5015, DOI:10.1029/2003tc001564.

Bollinger, L., Henry, P., Avouac, J. P. 2006. Mountain building in the Nepal Himalaya: Thermal and kinematic model. *Earth and Planetary Science Letters,* 244, 58-71 DOI: 10.1016/j.epsl.2006.01.045.

Bons, P. D., Den Brok, B. 2000. Crystallographic preferred orientation development by dissolution–precipitation creep. *Journal of Structural Geology,* 22, 1713-1722 DOI: 10.1016/S0191-8141(00)00075-4.

Bordet, P., Coichen, M., Krummenacher, D., Le Fort, P., Mouterde, R., Remy, M. 1971. Recherches Géologiques dans l'Himalaya du Népal, Région de la Thakkhola. *Centre National de la Recherche Scientifique*, Paris*,* 279*,* 1-86.

Borradaile, G. J. 1991. Correlation of Strain with Anisotropy of Magnetic-Susceptibility (AMS). *Pure and Applied Geophysics,* 135, 15-29, DOI: 10.1007/BF00877006.

Borradaile, G. J., Werner, T. 1994. Magnetic anisotropy of some phyllosilicates. *Tectonophysics,* 235, 223-248, DOI: 10.1016/0040-1951(94)90196-1.

Borradaile, G. J., Jackson, M. 2004. Anisotropy of magnetic susceptibility (AMS): magnetic petrofabrics of deformed rocks. *In:* Martin-Hernandez, F., Luneburg, C. M., Aubourg, C. Jackson, M. (eds.), *Magnetic fabric: Methods and Applications.* Geological Society of London Special Publication, 238, 299-360, DOI: 10.1144/GSL.SP.2004.238.01.18.

Borradaile, G. J., Jackson, M. 2010. Structural geology, petrofabrics and magnetic fabrics (AMS, AARM, AIRM). *Journal of Structural Geology,* 32, 1519-1551, DOI: 10.1016/j.jsg.2009.09.006.

Borradaile, G. J., Almqvist, B. S. G., Geneviciene, I. 2011. Anisotropy of magnetic susceptibility (AMS) and diamagnetic fabrics in the Durness Limestone, NW Scotland. *Journal of Structural Geology,* 34, 54-60, DOI: 10.1016/j.jsg.2011.10.008.

Bouchez, J.-L. 1977. Plastic deformation of quartzites at low temperature in an area of natural strain gradient. *Tectonophysics,* 39, 25-50, DOI: 10.1016/0040-1951(77)90086-5.

Bouchez, J.-L., Pêcher, A. 1981. The Himalayan Main Central Thrust pile and its quartz-rich tectonites in central Nepal. *Tectonophysics,* 78, 23-50, DOI: 10.1016/0040-1951(81)90004-4.

Boyer, S. E., Elliott, D. 1982. Thrust systems. *American Association of Petroleum Geologists Bulletin,* 66, 1196-1230.

Brown, L. D., Zhao, W. J., Nelson, D. K., Hauck, M., Alsdorf, D., Ross, A., Cogan, M., Clark, M., Liu, X. W., Che, J. K. 1996. Bright spots, structure, and

magmatism in southern Tibet from INDEPTH seismic reflection profiling. *Science,* 274, 1688-1690, DOI: 0.1126/science.274.5293.1688.

Brown, R. L., Gibson, H. D. 2006. An argument for channel flow in the southern Canadian Cordillera and comparison with Himalayan tectonics. *In:* Law, R. D., Searle, M. P. Godin, L. (eds.), *Channel Flow, Ductile Extrusion and Exhumation in Continental Collision Zones.* Geological Society of London Special Publications, 268, 543-559, DOI: 10.1144/GSL.SP.2006.268.01.25.

Brown, R. L., Nazarchuk, J. H. 1993. Annapurna Detachment Fault in the Greater Himalaya of Central Nepal. *Himalayan Tectonics,* 74, 461-473, DOI: 10.1144/GSL.SP.1993.074.01.31.

Brun, J.-P., Burg, J.-P., Ming, C. G. 1985. Strain trajectories above the Main Central thrust (Himalaya) in southern Tibet. *Nature,* 313, 388-390, DOI: 10.1038/313388a0.

Bunge, H. 1982. *Texture analysis in materials science*. Butterworths, London.

Burbank, D., Beck, R. A., Mulder, T. 1996. The Himalayan foreland basin. *In:* Yin, A., Harrison, T.M., (eds.), *The Tectonic Evolution of Asia,* 149–188. Cambridge University Press, Cambridge.

Burchfiel, B. C., Royden, L. H. 1985. North-south extension within the convergent Himalayan region. *Geology,* 13, 679-682, DOI: 10.1130/0091-7613(1985) 13<679:NEWTCH>2.0.CO;2.

Burchfiel, B. C., Zhiliang, C., Hodges, K. V., Yuping, L., Royden, L. H., Changrong, D., Jiene, X. 1992. The South Tibetan detachment system, Himalaya orogen: Extension contemporaneous with and parallel to shortening in a collisional mountain belt. *Geological Society of America Special Papers,* 269, 1-41, DOI: 10.1130/SPE269-p1.

Burg, J. P., Brunel, M., Gapais, D., Chen, G. M., Liu, G. H. 1984. Deformation of leucogranites of the crystalline Main Central Sheet in southern Tibet (China). *Journal of Structural Geology,* 6, 535-542, DOI: 10.1016/0191-8141(84)90063-4.

Burkhard, M. 1993. Calcite twins, their geometry, appearance and significance as stress-strain markers and indicators of tectonic regime: a review. *Journal of Structural Geology,* 15, 351-368, DOI: 10.1016/0191-8141(93)90132-T.

Butler, J. P., Beaumont, C., Jamieson, R. A. 2013. The Alps 1: A working geodynamic model for burial and exhumation of (ultra)high-pressure rocks in Alpine-type orogens. *Earth and Planetary Science Letters,* 377–378, 114-131, DOI: 10.1016/j.epsl.2013.06.039.

Butler, J. P., Beaumont, C., Jamieson, R. A. 2014. The Alps 2: Controls on crustal subduction and (ultra)high-pressure rock exhumation in Alpine-type orogens. *Journal of Geophysical Research: Solid Earth,* 119, 2013JB010799, DOI: 10.1002/2013jb010799.

Butler, R. W. H. 1986. Thrust tectonics, deep structure and crustal subduction in the Alps and Himalayas. *Journal of the Geological Society,* 143, 857-873, DOI: 10.1144/gsjgs.143.6.0857.

Caddick, M. J. 2005. *Tectono-metamorphic Evolution of the Central and Western Himalaya [Ph.D. Thesis]*. University of Cambridge.

Caddick, M. J., Bickle, M. J., Harris, N. B. W., Holland, T. J. B., Horstwood, M. S. A., Parrish, R. R., Ahmad, T. 2007. Burial and exhumation history of a Lesser Himalayan schist: Recording the formation of an inverted metamorphic sequence in NW India. *Earth and Planetary Science Letters,* 264, 375-390, DOI: 10.1016/j.epsl.2007.09.011.

Caddick, M. J., Kohn, M. J. 2013. Garnet: Witness to the Evolution of Destructive Plate Boundaries. *Elements,* 9, 427-432 DOI: 10.2113/gselements.9.6.427.

Carosi, R., Lombardo, B., Molli, G., Musumeci, G., Pertusati, P. C. 1998. The south Tibetan detachment system in the Rongbuk valley, Everest region. Deformation features and geological implications. *Journal of Asian Earth Sciences,* 16, 299-311, DOI: 10.1016/S0743-9547(98)00014-2.

Carosi, R., Montomoli, C., Visona, D. 2007. A structural transect in the Lower Dolpo: Insights on the tectonic evolution of Western Nepal. *Journal of Asian Earth Sciences,* 29, 407-423, DOI: 10.1016/j.jseaes.2006.05.001.

Carosi, R., Montomoli, C., Rubatto, D., Visonà, D. 2010. Late Oligocene high-temperature shear zones in the core of the Higher Himalayan Crystallines (Lower Dolpo, western Nepal). *Tectonics,* 29, TC4029, DOI: 10.1029/2008tc002400.

Carosi, R., Montomoli, C., Langone, A., Turina, A., Cesare, B., Iaccarino, S., Fascioli, L., Visonà, D., Ronchi, A., Rai, S. M. 2014. Eocene partial melting recorded in peritectic garnets from kyanite-gneiss, Greater Himalayan Sequence, central Nepal. *In:* Mukherjee, S., Carosi, R., Van Der Beek, P. K., Mukherjee, B. K. Robinson, D. M. (eds.), *Tectonics of the Himalaya.* Geological Society London Special Publications, 412, DOI: 10.1144/SP412.1.

Carreras, J., Estrada, A., White, S. 1977. The effects of folding on the C-axis fabrics of a quartz mylonite. *Tectonophysics,* 39, 3-24, DOI: 10.1016/0040-1951(77)90085-3.

Cattin, R., Martelet, G., Henry, P., Avouac, J. P., Diament, M., Shakya, T. R. 2001. Gravity anomalies, crustal structure and thermo-mechanical support of the Himalaya of Central Nepal. *Geophysical Journal International,* 147, 381-392, DOI: 10.1046/j.0956-540x.2001.01541.x.

Chadima, M., Jelínek, V. Anisoft 4.2.–Anisotropy data browser. *Paleo, Rock and Environmental Magnetism, 11th Castle Meeting, Contribution to Geophysics and Geodesy, Special issue.* , 2008 Geophysical Institute of the Slovak Academy of Sciences, Bojnice Castle, Slovac Republic.

Chemenda, A. I., Mattauer, M., Malavieille, J., Bokun, A. N. 1995. A mechanism for syn-collisional rock exhumation and associated normal faulting - Results from physical modeling. *Earth and Planetary Science Letters,* 132, 225-232, DOI: 10.1016/0012-821X(95)00042-B.

Colchen, M., Le Fort, P., Pêcher, A. 1986. *Recherches géologiques dans l'Himalaya du Népal: Annapurna-Manaslu-Ganesh Himal.* Editions du Centre national de la recherche scientifique, Paris, 1-136.

Coleman, M. E. 1996. Orogen-parallel and orogen-perpendicular extension in the central Nepalese Himalayas. *Geological Society of America Bulletin,* 108, 1594-1607, DOI: 10.1130/0016-7606(1996)108<1594:OPAOPE>2.3.CO;2.

Coleman, M. E. 1998. U-PB constraints on oligocene-miocene deformation and anatexis within the central Himalaya, Marsyandi valley, Nepal. *American Journal of Science,* 298, 553-571, DOI: 10.2475/ajs.298.7.553.

Coleman, M. E., Hodges, K. V. 1998. Contrasting Oligocene and Miocene thermal histories from the hanging wall and footwall of the South Tibetan detachment in the central Himalaya from Ar-40/Ar-39 thermochronology, Marsyandi Valley, central Nepal. *Tectonics,* 17, 726-740, DOI: 10.1029/98TC02777.

Cook, A. C., Vel, S. S., Gerbi, C., Johnson, S. E. 2014. Computational analysis of nonlinear creep of polyphase aggregates: Influence of phase morphology. *Journal of Geophysical Research: Solid Earth*, 119, 6877-6906, DOI: 10.1002/2014jb011197.

Cook, F. A., Varsek, J. L. 1994. Orogen-scale decollements. *Reviews of Geophysics,* 32, 37-60, DOI: 10.1029/93rg02515.

Corrie, S. L., Kohn, M. J. 2011. Metamorphic history of the central Himalaya, Annapurna region, Nepal, and implications for tectonic models. *Geological Society of America Bulletin,* 123, 1863-1879, DOI: 10.1130/B30376.1.

Cottle, J. M., Jessup, M. J., Newell, D. L., Searle, M. P., Law, R. D., Horstwood, M. S. A. 2007. Structural insights into the early stages of exhumation along an orogen-scale detachment: The South Tibetan Detachment System, Dzakaa Chu section, Eastern Himalaya. *Journal of Structural Geology,* 29, 1781-1797, DOI: 10.1016/j.jsg.2007.08.007.

Cottle, J. M, Searle, M. P., Horstwood, M. S. A., Waters, D. J. 2009. Timing of Midcrustal Metamorphism, Melting, and Deformation in the Mount Everest Region of Southern Tibet Revealed by U(-Th)-Pb Geochronology. *The Journal of Geology,* 117, 643-664, DOI: 10.1086/605994.

Cottle, J. M., Waters, D. J., Riley, D., Beyssac, O., Jessup, M. J. 2011. Metamorphic history of the South Tibetan Detachment System, Mt. Everest region, revealed by RSCM thermometry and phase equilibria modelling. *Journal of Metamorphic Geology,* 29, 561-582, DOI: 10.1111/j.1525-1314.2011.00930.x.

Culshaw, N. G., Beaumont, C., Jamieson, R. A. 2006. The orogenic superstructure-infrastructure concept: Revisited, quantified, and revived. *Geology,* 34, 733-736, DOI: 10.1130/g22793.1.

Czaplińska, D., Piazolo, S., Zibra, I. 2015. The influence of phase and grain size distribution on the dynamics of strain localization in polymineralic rocks. *Journal of Structural Geology,* 72, 15-32, DOI: 10.1016/j.jsg.2015.01.001.

Dasgupta, S., Ganguly, J., Neogi, S. 2004. Inverted metamorphic sequence in the Sikkim Himalayas: crystallization history, P-T gradient and implications. *Journal of Metamorphic Geology,* 22, 395-412, DOI: 10.1111/j.1525-1314.2004.00522.x.

Davis, D., Suppe, J., Dahlen, F. A. 1983. Mechanics of fold-and-thrust belts and accretionary wedges. *Journal of Geophysical Research: Solid Earth,* 88, 1153-1172, DOI: 10.1029/JB088iB02p01153.

Day, R., Fuller, M., Schmidt, V. A. 1977. Hysteresis properties of titanomagnetites: Grain-size and compositional dependence. *Physics of the Earth and Planetary Interiors,* 13, 260-267, DOI: 10.1016/0031-9201(77)90108-X.

De Bresser, J. H. P., Spiers, C. J. 1997. Strength characteristics of the r, f, and c slip systems in calcite. *Tectonophysics,* 272, 1-23, DOI: 10.1016/S0040-1951(96)00273-9.

Decelles, P. G., Gehrels, G. E., Quade, J., Lareau, B., Spurlin, M. 2000. Tectonic implications of U-Pb zircon ages of the Himalayan orogenic belt in Nepal. *Science,* 288, 497-499, DOI: 10.1126/science.288.5465.497.

Decelles, P. G., Robinson, D. M., Quade, J., Ojha, T. P., Garzione, C. N., Copeland, P., Upreti, B. N. 2001. Stratigraphy, structure, and tectonic evolution of the Himalayan fold-thrust belt in western Nepal. *Tectonics,* 20, 487-509, DOI: 10.1029/2000TC001226.

Decelles, P. G., Robinson, D. M., Zandt, G. 2002. Implications of shortening in the Himalayan fold-thrust belt for uplift of the Tibetan Plateau. *Tectonics,* 21, 1062, DOI: 10.1029/2001tc001322.

Dell'angelo, L. N., Tullis, J. 1989. Fabric development in experimentally sheared quartzites. *Tectonophysics,* 169, 1-21, DOI: 10.1016/0040-1951(89)90180-7.

Dell`Angelo, L. N., Tullis, J., Yund, R. A. 1987. Transition from dislocation creep to melt-enhanced diffusion creep in fine-grained granitic aggregates. *Tectonophysics,* 139, 325-332, DOI: 10.1016/0040-1951(87)90107-7.

Delle Piane, C., Burlini, L., Kunze, K., Brack, P., Burg, J. P. 2008. Rheology of dolomite: Large strain torsion experiments and natural examples. *Journal of Structural Geology,* 30, 767-776, DOI: 10.1016/j.jsg.2008.02.018.

Delle Piane, C., Burlini, L., Kunze, K. 2009. The influence of dolomite on the plastic flow of calcite: Rheological, microstructural and chemical evolution during large strain torsion experiments. *Tectonophysics,* 467, 145-166, DOI: 10.1016/j.tecto.2008.12.022.

Dézes, P. J., Vannay, J.-C., Steck, A., Bussy, F., Cosca, M. 1999. Synorogenic extension: Quantitative constraints on the age and displacement of the Zanskar shear zone (northwest Himalaya). *Geological Society of America Bulletin,* 111, 364-374, DOI: 10.1130/0016-7606(1999)111<0364:seqcot>2.3.co;2.

Díaz Aspiroz, M., Lloyd, G. E., Fernández, C. 2007. Development of lattice preferred orientation in clinoamphiboles deformed under low-pressure metamorphic conditions. A SEM/EBSD study of metabasites from the Aracena metamorphic belt (SW Spain). *Journal of Structural Geology,* 29, 629-645, DOI: 10.1016/j.jsg.2006.10.010.

Dimanov, A., Dresen, G. 2005. Rheology of synthetic anorthite-diopside aggregates: Implications for ductile shear zones. *Journal of Geophysical Research: Solid Earth,* 110, B07203, DOI: 10.1029/2004jb003431.

Djouadi, M. T., Gleizes, G., Ferré, E., Bouchez, J. L., Caby, R., Lesquer, A. 1997. Oblique magmatic structures of two epizonal granite plutons, Hoggar, Algeria: late-orogenic emplacement in a transcurrent orogen. *Tectonophysics,* 279, 351-374, DOI: 10.1016/S0040-1951(97)00123-6.

Dunlop, D. J., Özdemir, Ö. 2001. *Rock magnetism: fundamentals and frontiers,* Cambridge University Press, Cambridge, 1-575.

Dunlop, D. J. 2002a. Theory and application of the Day plot (Mrs/Ms versus Hcr/Hc), 2, Application to data for rocks, sediments, and soils. *Journal of Geophysical Research: Solid Earth,* 107, EPM 5-1–EPM 5-15, DOI: 10.1029/2001JB000487.

Dunlop, D. J. 2002b. Theory and application of the Day plot (Mrs/Ms versus Hcr/Hc) 1. Theoretical curves and tests using titanomagnetite data. *Journal of Geophysical Research: Solid Earth,* 107, EPM 4-1–EPM 4-22, DOI: 10.1029/2001JB000486.

England, P., Molnar, P. 1993. Cause and effect among thrust and normal faulting, anatectic melting and exhumation in the Himalaya. *In:* Treloar, P. J. Searle, M. P. (eds.), *Himalayan Tectonics.* Geological Society of London Special Publications, 74, 401-411, DOI: 10.1144/gsl.sp.1993.074.01.27.

Evans, M. A., Dunne, W. M. 1991. Strain factorization and partitioning in the North Mountain thrust sheet, central Appalachians, U.S.A. *Journal of Structural Geology,* 13, 21-35, DOI: 10.1016/0191-8141(91)90098-4.

Ferré, E. C. 2002. Theoretical models of intermediate and inverse AMS fabrics. *Geophysical Research Letters,* 29, 1127, DOI: 10.1029/2001GL014367.

Ferré, E. C., Teyssier, C., Jackson, M., Thill, J. W., Rainey, E. S. G. 2003. Magnetic susceptibility anisotropy: A new petrofabric tool in migmatites. *Journal of Geophysical Research: Solid Earth,* 108, 2086, DOI:10.1029/2002jb001790.

Ferré, E. C., Martin-Hernandez, F., Teyssier, C., Jackson, M. 2004. Paramagnetic and ferromagnetic anisotropy of magnetic susceptibility in migmatites: measurements in high and low fields and kinematic implications. *Geophysical Journal International,* 157, 1119-1129, DOI: 10.1111/j.1365-246X.2004.02294.x.

Ferré, E. C., Gébelin, A., Till, J. L., Sassier, C., Burmeister, K. C. 2014. Deformation and magnetic fabrics in ductile shear zones: A review. *Tectonophysics,* 629, 179-188, DOI: 10.1016/j.tecto.2014.04.008.

Ferrill, D. A., Morris, A. P., Evans, M. A., Burkhard, M., Groshong Jr, R. H., Onasch, C. M. 2004. Calcite twin morphology: a low-temperature deformation geothermometer. *Journal of Structural Geology,* 26, 1521-1529, DOI: 10.1016/j.jsg.2003.11.028.

Ferry, J. M., Spear, F. S. 1978. Experimental calibration of the partitioning of Fe and Mg between biotite and garnet. *Contributions to Mineralogy and Petrology,* 66, 113-117, DOI: 10.1007/bf00372150.

Fitz Gerald, J. D., Stünitz, H. 1993. Deformation of granitoids at low metamorphic grade. I: Reactions and grain size reduction. *Tectonophysics,* 221, 269-297, DOI: 10.1016/0040-1951(93)90163-E.

Fleet, M. E. 2003. *Rock Forming Minerals, Vol. 3A Sheet Silicates: Micas,* Geological Society of London, London.

Fuchs, G. 1973. On the geology of the karnali and Dolpo regions, west Nepal. *Mitteilungen der Geologischen Gesellschaft in Wien, 66,* 67, 21-32.

Fuchs, G. 1977. *The geology of the Karnali and Dolpo regions, western Nepal,* Jahrbuch der Geologischen Bundesanstalt, 120, 165–217.

Fukuda, J.-I., Okudaira, T., Satsukawa, T., Michibayashi, K. 2012. Solution–precipitation of K-feldspar in deformed granitoids and its relationship to the distribution of water. *Tectonophysics,* 532–535, 175-185, DOI: 10.1016/j.tecto.2012.01.033.

Fyson, W. K. 1971. Fold attitudes in metamorphic rocks. *American Journal of Science,* 270, 373-382, DOI: 10.2475/ajs.270.5.373.

Galán, J., Verleysen, P., Lebensohn, R. A. 2014. An improved algorithm for the polycrystal viscoplastic self-consistent model and its integration with implicit finite element schemes. *Modelling and Simulation in Materials Science and Engineering,* 22, 055023, DOI: 10.1088/0965-0393/22/5/055023.

Gandais, M., Willaime, C. 1984. Mechanical Properties of Feldspars. *In:* Brown, W. (ed.), *Feldspars and Feldspathoids.*Springer Netherlands, 137, 207-246, DOI: 10.1007/978-94-015-6929-3_6.

Gapais, D., Pêcher, A., Gilbert, E., Ballèvre, M. 1992. Synconvergence spreading of the higher Himalaya crystalline in Ladakh. *Tectonics,* 11, 1045-1056, DOI: 10.1029/92tc00819.

Garcia Celma, A. 1982. Domainal and fabric heterogeneities in the Cap de Creus quartz mylonites. *Journal of Structural Geology,* 4, 443-455, DOI: 10.1016/0191-8141(82)90035-9.

Garzanti, E. 1999. Stratigraphy and sedimentary history of the Nepal Tethys Himalaya passive margin. *Journal of Asian Earth Sciences,* 17, 805-827, DOI: 10.1016/S1367-9120(99)00017-6.

Garzione, C. N., Decelles, P. G., Hodkinson, D. G., Ojha, T. P., Upreti, B. N. 2003. East-west extension and Miocene environmental change in the southern Tibetan plateau: Thakkhola graben, central Nepal. *Geological Society of America Bulletin,* 115, 3-20, DOI: 10.1130/0016-7606(2003)115<0003:eweame>2.0.co;2.

Gleason, G. C., Tullis, J. 1995. A flow law for dislocation creep of quartz aggregates determined with the molten-salt cell. *Tectonophysics,* 247, 1-23, DOI: 10.1016/0040-1951(95)00011-B.

Gleeson, T. P., Godin, L. 2006. The Chako antiform: A folded segment of the Greater Himalayan sequence, Nar Valley, Central Nepal Himalaya. *Journal of Asian Earth Sciences,* 27, 717-734, DOI: 10.1016/j.jseaes.2005.06.011.

Godin, L., Brown, R. L., Hanmer, S. 1999a. High strain zone in the hanging wall of the Annapurna detachment, central Nepal Himalaya. *In:* Macfarlane, A., Sorkhabi, R. B. Quade, J. (eds.), *Himalaya and Tibet: Mountain Roots to Mountain Tops.* Geological Society of America Special Papers, Boulder, CO, 328, 199-210, DOI: 10.1130/0-8137-2328-0.199.

Godin, L., Brown, R. L., Hanmer, S., Parrish, R. 1999b. Back folds in the core of the Himalayan orogen: An alternative interpretation. *Geology,* 27, 151-154, DOI: 10.1130/0091-7613(1999)027<0151:BFITCO>2.3.CO;2.

Godin, L., Parrish, R. R., Brown, R. L., Hodges, K. V. 2001. Crustal thickening leading to exhumation of the Himalayan metamorphic core of central Nepal: Insight from U-Pb geochronology and Ar-40/Ar-39 thermochronology. *Tectonics,* 20, 729-747, DOI: 10.1029/2000TC001204.

Godin, L. 2003. Structural evolution of the Tethyan sedimentary sequence in the Annapurna area, central Nepal Himalaya. *Journal of Asian Earth Sciences,* 22, 307-328, DOI: 10.1016/S1367-9120(03)00066-X.

Godin, L., Gleeson, T. P., Searle, M. P., Ullrich, T. D., Parrish, R. R. 2006a. Locking of southward extrusion in favour of rapid crustal-scale buckling of the Greater Himalayan sequence, Nar valley, central Nepal. *In:* Law, R. D., Searle, M. P. Godin, L. (eds.), *Channel Flow, Ductile Extrusion and Exhumation in Continental Collision Zones.* Geological Society of London Special Publications, 268, 269-292, DOI: 10.1144/GSL.SP.2006.268.01.13.

Godin, L., Grujic, D., Law, R. D., Searle, M. P. 2006b. Channel flow, ductile extrusion and exhumation in continental collision zones: an introduction. *In:* Law, R. D., Searle, M. P. Godin, L. (eds.), *Channel Flow, Ductile Extrusion and Exhumation*

in Continental Collision Zones. Geological Society of London Special Publications, 268, 1-23, DOI: 10.1144/GSL.SP.2006.268.01.01.

Godin, L., Yakymchuk, C., Harris, L. B. 2011. Himalayan hinterland-verging superstructure folds related to foreland-directed infrastructure ductile flow: Insights from centrifuge analogue modelling. *Journal of Structural Geology,* 33, 329-342 DOI: 10.1016/j.jsg.2010.09.005.

Godin, L., Harris, L. B. 2014. Tracking basement cross-strike discontinuities in the Indian crust beneath the Himalayan orogen using gravity data – relationship to upper crustal faults. *Geophysical Journal International,* 198, 198-215, DOI: 10.1093/gji/ggu131.

Goscombe, B., Gray, D., Hand, M. 2006. Crustal architecture of the Himalayan metamorphic front in eastern Nepal. *Gondwana Research,* 10, 232-255, DOI: 10.1016/j.gr.2006.05.003.

Gradstein, F. M. von Rad, U., Gibling, M. R., Jansa, L. F., Kaminski, M. A., Kristiansen, I. L.,Ogg, J. G., Roehl, U., Sarti, M., Thurow, J. W.,Westermann, G. E. G., Wiedmann, J. 1992. Stratigraphy and depositional history of the Mesozoic continental margin of central Nepal. *Geologisches Jahrbuch, Reihe B: Regionale Geologie Ausland*, 77, 1–141.

Grasemann, B., Fritz, H., Vannay, J. C. 1999. Quantitative kinematic flow analysis from the Main Central Thrust Zone (NW-Himalaya, India): implications for a decelerating strain path and the extrusion of orogenic wedges. *Journal of Structural Geology,* 21, 837-853, DOI: 10.1016/S0191-8141(99)00077-2 .

Grasemann, B., Vannay, J. C. 1999. Flow controlled inverted metamorphism in shear zones. *Journal of Structural Geology,* 21, 743-750, DOI: 10.1016/S0191-8141(99)00071-1.

Grasemann, B., Edwards, M. A., Wiesmayr, G. 2006. Kinematic dilatancy effects on orogenic extrusion. *In:* Law, R. D., Searle, M. P. Godin, L. (eds.), *Channel Flow, Ductile Extrusion and Exhumation in Continental Collision Zones.* Geological Society of London Special Publications, 268, 183-199, DOI: 10.1144/Gsl.Sp.2006.268.01.08.

Green, O. R., Searle, M. P., Corfield, R. I., Corfield, R. M. 2008. Cretaceous-tertiary carbonate platform evolution and the age of the India-Asia collision along the Ladakh Himalaya (northwest India). *Journal of Geology,* 116, 331-353, DOI: 10.1086/588831.

Grujic, D., Casey, M., Davidson, C., Hollister, L. S., Kundig, R., Pavlis, T., Schmid, S. 1996. Ductile extrusion of the Higher Himalayan Crystalline in Bhutan: Evidence from quartz microfabrics. *Tectonophysics,* 260, 21-43, DOI: 10.1016/0040-1951(96)00074-1.

Grujic, D., Hollister, L. S., Parrish, R. R. 2002. Himalayan metamorphic sequence as an orogenic channel: insight from Bhutan. *Earth and Planetary Science Letters,* 198, 177-191, DOI: 10.1016/S0012-821X(02)00482-X.

Grujic, D. 2006. Channel flow and continental collision tectonics: an overview. *In:* Law, R. D., Searle, M. P. Godin, L. (eds.), *Channel Flow, Ductile Extrusion and Exhumation in Continental Collision Zones.* Geological Society of London Special Publications, 268, 25-37, DOI: 10.1144/GSL.SP.2006.268.01.02.

Guest, W. S., Thomson, C. J., Spencer, C. P. 1993. Anisotropic reflection and transmission calculations with application to a crustal seismic survey from the

East Greenland Shelf. *Journal of Geophysical Research: Solid Earth,* 98, 14161-14184 DOI: 10.1029/93jb01156.

Guillot, S., Pêcher, A., Rochette, P., Le Fort, P. 1993. The emplacement of the Manaslu Granite of Central Nepal - field and magnetic-susceptibility constraints. *In:* Treloar, P. J., Searle, M. P. (eds.), *Himalayan Tectonics.* Geological Society of London Special Publications*,* 74, 413-428, DOI: 10.1144/GSL.SP.1993.074.01.28.

Guillot, S., Cosca, M., Allemand, P., Le Fort, P. 1999. Contrasting metamorphic and geochronologic evolution along the Himalayan belt. *In:* Macfarlane, A., Sorkhabi, R. B. Quade, J. (eds.), *Himalaya and Tibet: Mountain Roots to Mountain Tops.*Geological Society of America Special Paper, Boulder, CO, 328, 117-128.

Guillot, S., Replumaz, A. 2013. Importance of continental subductions for the growth of the Tibetan plateau. *Bulletin de La Societe Geologique de France,* 184, 199-223, DOI: 10.2113/gssgfbull.184.3.199

Guo, Z., Gao, X., Yao, H. J., Li, J., Wang, W. M. 2009. Midcrustal low-velocity layer beneath the central Himalaya and southern Tibet revealed by ambient noise array tomography. *Geochemistry Geophysics Geosystems,* 10, Q05007, DOI: 10.1029/2009gc002458.

Hacker, B. R., Ritzwoller, M. H., Xie, J. 2014. Partially melted, mica-bearing crust in Central Tibet. *Tectonics,* 33, 2014TC003545, DOI: 10.1002/2014tc003545.

Haerinck, T., Adriaens, R., Debacker, T. N., Hirt, A. M., Sintubin, M. 2013. Paramagnetic metamorphic mineral assemblages controlling AMS in low-grade deformed metasediments and the implications with respect to the use of AMS as a strain marker. *Journal of the Geological Society, Lonndon,* 170, 263-280, DOI: 10.1144/jgs2012-062.

Hagen, T. 1959. Geologie des Thakkhola (Nepal). *Eclogae Geologicae Helveticae,* 52, 709-720.

Haller, J. 1956. Probleme der Tiefentektonik Bauformen im Migmatit Stockwerk der Ostgrönländischen Kaledoniden. *Geologische Rundschau,* 45, 159-167, DOI: 10.1007/bf01802002.

Handy, M. R. 1990. The solid-state flow of polymineralic rocks. *Journal of Geophysical Research: Solid Earth,* 95, 8647-8661, DOI: 10.1029/JB095iB06p08647.

Hansen, F., Carter, N. 1982. Creep of selected crustal rocks at 1000 MPa. *EOS, Trans. AGU,* 63, 437.

Hansen, L. N., Zimmerman, M. E., Kohlstedt, D. L. 2012. The influence of microstructure on deformation of olivine in the grain-boundary sliding regime. *Journal of Geophysical Research: Solid Earth,* 117, B09201, DOI: 10.1029/2012jb009305.

Hargraves, R. B., Johnson, D., Chan, C. Y. 1991. Distribution anisotropy: The cause of AMS in igneous rocks? *Geophysical Research Letters,* 18, 2193-2196, DOI: 10.1029/91gl01777.

Harris, N., Massey, J. 1994. Decompression and anatexis of Himalayan metapelites. *Tectonics,* 13, 1537-1546, DOI: 10.1029/94TC01611.

Harris, N., Ayres, M., Massey, J. 1995. Geochemistry of granitic melts produced during the incongruent melting of muscovite - Implications for the extraction of

Himalayan leucogranite magmas. *Journal of Geophysical Research-Solid Earth,* 100, 15767-15777, DOI: 10.1029/94JB02623.

Harris, N. 2007. Channel flow and the Himalayan-Tibetan orogen: a critical review. *Journal of the Geological Society, London,* 164, 511-523, DOI: 10.1144/0016-76492006-133.

Harris, N. B. W., Caddick, M., Kosler, J., Goswami, S., Vance, D., Tindle, A. G. 2004. The pressure-temperature-time path of migmatites from the Sikkim Himalaya. *Journal of Metamorphic Geology,* 22, 249-264, DOI: 10.1111/j.1525-1314.2004.00511.x.

Harrison, R. J., Feinberg, J. M. 2008. FORCinel: An improved algorithm for calculating first-order reversal curve distributions using locally weighted regression smoothing. *Geochemistry Geophysics Geosystems,* 9, Q05016, DOI: 10.1029/2008GC001987.

Harrison, T. M., Lovera, O. M., Grove, M. 1997. New insights into the origin of two contrasting Himalayan granite belts. *Geology,* 25, 899-902, DOI: 10.1130/0091-7613(1997)025<0899:NIITOO>2.3.CO;2.

Harrison, T. M., Grove, M., Mckeegan, K. D., Coath, C. D., Lovera, O. M., Le Fort, P. 1999. Origin and episodic emplacement of the Manaslu intrusive complex, central Himalaya. *Journal of Petrology,* 40, 3-19, DOI: 10.1093/petroj/40.1.3.

Harrison, T. M., Célérier, J., Aikman, A. B., Hermann, J., Heizler, M. T. 2009. Diffusion of ^{40}Ar in muscovite. *Geochimica Et Cosmochimica Acta,* 73, 1039-1051, DOI: 10.1016/j.gca.2008.09.038.

Hatcher, R. D., Merschat, A. J. 2006. The Appalachian Inner Piedmont: an exhumed strike-parallel, tectonically forced orogenic channel. *In:* Law, R. D., Searle, M. P. Godin, L. (eds.), *Channel flow, ductile extrusion and exhumation in continental collision zones.* Geological Society of London Special Publications, 268, 517-541, DOI: 10.1144/gsl.sp.2006.268.01.24.

Hauck, M. L., Nelson, K. D., Brown, L. D., Zhao, W. J., Ross, A. R. 1998. Crustal structure of the Himalayan orogen at ~90^{o} east longitude from Project INDEPTH deep reflection profiles. *Tectonics,* 17, 481-500, DOI: 10.1029/98TC01314.

Hayden, L., Watson, E. B., Wark, D. 2008. A thermobarometer for sphene (titanite). *Contributions to Mineralogy and Petrology,* 155, 529-540, DOI: 10.1007/s00410-007-0256-y.

He, D., Webb, A. a. G., Larson, K. P., Martin, A. J., Schmitt, A. K. 2014. Extrusion vs. duplexing models of Himalayan mountain building 3: duplexing dominates from the Oligocene to Present. *International Geology Review,* 57, 1-27, DOI: 10.1080/00206814.2014.986669.

Heidelbach, F., Post, A., Tullis, J. 2000. Crystallographic preferred orientation in albite samples deformed experimentally by dislocation and solution precipitation creep. *Journal of Structural Geology,* 22, 1649-1661, DOI: 10.1016/S0191-8141(00)00072-9.

Heilbronner, R., Tullis, J. 2002. The effect of static annealing on microstructures and crystallographic preferred orientations of quartzites experimentally deformed in axial compression and shear. *In:* De Meer, S., Drury, M. R., De Bresser, J. H. P., Pennock, G. M. (eds.), *Deformation mechanisms, rheology and tectonics: Current status and future perspectives*. Geological Society of London Special Publications*,* 200, 191-218, DOI: 10.1144/gsl.sp.2001.200.01.12.

Heilbronner, R., Tullis, J. 2006. Evolution of c axis pole figures and grain size during dynamic recrystallization: Results from experimentally sheared quartzite. *Journal of Geophysical Research: Solid Earth,* 111, B10202, DOI: 10.1029/2005jb004194.

Herwegh, M., Linckens, J., Ebert, A., Berger, A., Brodhag, S. H. 2011. The role of second phases for controlling microstructural evolution in polymineralic rocks: A review. *Journal of Structural Geology,* 33, 1728-1750, DOI: 10.1016/j.jsg.2011.08.011.

Higgins, A. K. 1988. The Krummedal supracrustal sequence in East Greenland. *In:* Winchester, J. A. (ed.), *Later Proterozoic Stratigraphy of the Northern Atlantic Regions.*Springer, 86-96, DOI: 10.1007/978-1-4615-7344-9_7.

Hippertt, J. F. 1994. Microstructures and c-axis fabrics indicative of quartz dissolution in sheared quartzites and phyllonites. *Tectonophysics,* 229, 141-163, DOI: 10.1016/0040-1951(94)90026-4.

Hirth, G., Teyssier, C., Dunlap, J. 2001. An evaluation of quartzite flow laws based on comparisons between experimentally and naturally deformed rocks. *International Journal of Earth Sciences,* 90, 77-87, DOI: 10.1007/s005310000152.

Hodges, K., Bowring, S., Davidek, K., Hawkins, D., Krol, M. 1998. Evidence for rapid displacement on Himalayan normal faults and the importance of tectonic denudation in the evolution of mountain ranges. *Geology,* 26, 483-486, DOI: 10.1130/0091-7613(1998)026<0483:efrdoh>2.3.co;2.

Hodges, K. V., Burchfiel, B. C., Royden, L. H., Chen, Z., Liu, Y. 1993. The metamorphic signature of contemporaneous extension and shortening in the central Himalayan orogen: data from the Nyalam transect, southern Tibet. *Journal of Metamorphic Geology,* 11, 721-737, DOI: 10.1111/j.1525-1314.1993.tb00183.x.

Hodges, K. V., Parrish, R. R., Searle, M. P. 1996. Tectonic evolution of the central Annapurna Range, Nepalese Himalayas. *Tectonics,* 15, 1264-1291, DOI: 10.1029/96TC01791.

Hodges, K. V. 2006. A synthesis of the channel flow-extrusion hypothesis as developed for the Himalayan-Tibetan orogenic system. *In:* Law, R. D., Searle, M. P. Godin, L. (eds.), *Channel Flow, Ductile Extrusion and Exhumation in Continental Collision Zones.* Geological Society of London Special Publication, 268, 71-90, DOI: 10.1144/GSL.SP.2006.268.01.04.

Hollister, L. S., Grujic, D. 2006. Pulsed channel flow in Bhutan. *In:* Law, R. D., Searle, M. P. Godin, L. (eds.), *Channel Flow, Ductile Extrusion and Exhumation in Continental Collision Zones.* Geological Society of London Special Publications, 268, 415-423, DOI: 10.1144/GSL.SP.2006.268.01.19.

Housen, B. A., Van Der Pluijm, B. A., Essene, E. J. 1995. Plastic behavior of magnetite and high strains obtained from magnetic fabrics in the Parry Sound shear zone, Ontario Grenville Province. *Journal of Structural Geology,* 17, 265-278, DOI: 10.1016/0191-8141(94)E0045-Z.

Hrouda, F., Kahan, Š. 1991. The magnetic fabric relationship between sedimentary and basement nappes in the High Tatra Mountains, N. Slovakia. *Journal of Structural Geology,* 13, 431-442, DOI: 10.1016/0191-8141(91)90016-C.

Huang, G.-C., Wu, F. T., Roecker, S. W., Sheehan, A. F. 2009. Lithospheric structure of the central Himalaya from 3-D tomographic imaging. *Tectonophysics,* 475, 524-543, DOI: 10.1016/j.tecto.2009.06.023.

Hubbard, M. S., Harrison, T. M. 1989. Ar-40/Ar-39 age constraints on deformation and metamorphism in the Main Central Thrust Zone and Tibetan Slab, Eastern Nepal Himalaya. *Tectonics,* 8, 865-880, DOI: 10.1029/TC008i004p00865.

Huntington, K. W., Blythe, A. E., Hodges, K. V. 2006. Climate change and Late Pliocene acceleration of erosion in the Himalaya. *Earth and Planetary Science Letters,* 252, 107-118, DOI: 10.1016/j.epsl.2006.09.031.

Hurtado, J. M., Hodges, K. V., Whipple, K. X. 2001. Neotectonics of the Thakkhola graben and implications for recent activity on the South Tibetan fault system in the central Nepal Himalaya. *Geological Society of America Bulletin,* 113, 222-240, DOI: 10.1130/0016-7606(2001)113<0222:NOTTGA>2.0.CO;2.

Hurtado, J. M. 2002. *Tectonic Evolution of the Thakkahola Graben and Dhaulagiri Himalaya, Central Nepal [PhD Thesis].* Department of Earth, Atmospheric, and Planetary Sciencesy, Massachusetts Institute of Technology.

Hurtado, J. M., Chatterjee, N., Ramezani, J., Hodges, K. V., Bowring, S. A. 2007. Electron microprobe chemical dating of uraninite as a reconnaissance tool for leucogranite geochronology (Unpublished work). *Available from Nature Precedings.*

Ihinger, P. D., Zink, S. I. 2000. Determination of relative growth rates of natural quartz crystals. *Nature,* 404, 865-869, DOI: 10.1038/35009091.

Imayama, T., Takeshita, T., Arita, K. 2010. Metamorphic P-T profile and P-T path discontinuity across the far-eastern Nepal Himalaya: investigation of channel flow models. *Journal of Metamorphic Geology,* 28, 527-549, DOI: 10.1111/j.1525-1314.2010.00879.x.

Imayama, T., Takeshita, T., Yi, K., Cho, D.-L., Kitajima, K., Tsutsumi, Y., Kayama, M., Nishido, H., Okumura, T., Yagi, K., Itaya, T., Sano, Y. 2012. Two-stage partial melting and contrasting cooling history within the Higher Himalayan Crystalline Sequence in the far-eastern Nepal Himalaya. *Lithos,* 134–135, 1-22, DOI: 10.1016/j.lithos.2011.12.004.

Inger, S., Harris, N. B. W. 1992. Tectonothermal Evolution of the High Himalayan Crystalline Sequence, Langtang Valley, Northern Nepal. *Journal of Metamorphic Geology,* 10, 439-452, DOI: 10.1111/j.1525-1314.1992.tb00095.x.

Ishii, K., Kanagawa, K., Shigematsu, N., Okudaira, T. 2007. High ductility of K-feldspar and development of granitic banded ultramylonite in the Ryoke metamorphic belt, SW Japan. *Journal of Structural Geology,* 29, 1083-1098, DOI: 10.1016/j.jsg.2007.02.008.

Ismaïl, W. B., Mainprice, D. 1998. An olivine fabric database: an overview of upper mantle fabrics and seismic anisotropy. *Tectonophysics,* 296, 145-157, DOI: 10.1016/S0040-1951(98)00141-3.

Jain, A., Manickavasagam, R., Singh, S., Mukherjee, S. 2005. Himalayan collision zone: new perspectives-its tectonic evolution in a combined ductile shear zone and channel flow model. *Himalayan Geology,* 26, 1-18.

Jamieson, R. A., Beaumont, C., Nguyen, M. H., Lee, B. 2002. Interaction of metamorphism, deformation and exhumation in large convergent orogens.

Journal of Metamorphic Geology, 20, 9-24, DOI: 10.1046/j.0263-4929.2001.00357.x.

Jamieson, R. A., Beaumont, C., Medvedev, S., Nguyen, M. H. 2004. Crustal channel flows: 2. Numerical models with implications for metamorphism in the Himalayan-Tibetan orogen. *Journal of Geophysical Research: Solid Earth,* 109, B06407, DOI: 10.1029/2003jb002811.

Jamieson, R. A., Beaumont, C., Nguyen, M. H., Grujic, D. 2006. Provenance of the Greater Himalayan Sequence and associated rocks: predictions of channel flow models. *In:* Law, R. D., Searle, M. P. Godin, L. (eds.), *Channel Flow, Ductile Extrusion and Exhumation in Continental Collision Zones.* Geological Society of London Special Publications, London, 268, 165-182, DOI: 10.1144/GSL.SP.2006.268.01.07.

Jamieson, R. A., Beaumont, C. 2011. Coeval thrusting and extension during lower crustal ductile flow – implications for exhumation of high-grade metamorphic rocks. *Journal of Metamorphic Geology,* 29, 33-51, DOI: 10.1111/j.1525-1314.2010.00908.x.

Jamieson, R. A., Unsworth, M. J., Harris, N. B. W., Rosenberg, C. L., Schulmann, K. 2011. Crustal melting and the flow of mountains. *Elements,* 7, 253-260, DOI: 10.2113/gselements.7.4.253.

Jamieson, R. A., Beaumont, C. 2013. On the origin of orogens. *Geological Society of America Bulletin,* 125, 1671-1702, DOI: 10.1130/b30855.1.

Janák, F. 1965. Determination of anisotropy of magnetic susceptibility of rocks. *Studia geophysica et geodaetica,* 9, 290-301.

Jelínek, V. 1978. Statistical processing of anisotropy of magnetic susceptibility measured on groups of specimens. *Studia geophysica et geodaetica,* 22, 50-62.

Jelínek, V. 1981. Characterization of the magnetic fabric of rocks. *Tectonophysics,* 79, T63-T67, DOI: 10.1016/0040-1951(81)90110-4.

Jessell, M., Bons, P., Evans, L., Barr, T., Stüwe, K. 2001. Elle: the numerical simulation of metamorphic and deformation microstructures. *Computers & Geosciences,* 27, 17-30, DOI: 10.1016/S0098-3004(00)00061-3.

Jessup, M. J., Law, R. D., Searle, M. P., Hubbard, M. S. 2006. Structural evolution and vorticity of flow during extrusion and exhumation of the Greater Himalayan Slab, Mount Everest Massif, Tibet/Nepal: implications for orogen-scale flow partitioning. *In:* Law, R. D., Searle, M. P. Godin, L. (eds.), *Channel Flow, Ductile Extrusion and Exhumation in Continental Collision Zones.* Geological Society of London Special Publications, 268, 379-413, DOI: 10.1144/GSL.SP.2006.268.01.18.

Jessup, M. J., Cottle, J. M., Searle, M. P., Law, R. D., Newell, D. L., Tracy, R. J., Waters, D. J. 2008. P-T-t-D paths of Everest Series schist, Nepal. *Journal of Metamorphic Geology,* 26, 717-739, DOI: 10.1111/j.1525-1314.2008.00784.x.

Jessup, M. J., Cottle, J. M. 2010. Progression from south-directed extrusion to orogen-parallel extension in the southern margin of the Tibetan Plateau, Mount Everest Region, Tibet. *Journal of Geology,* 118, 467-486, DOI: 10.1086/655011.

Ji, S., Jiang, Z., Rybacki, E., Wirth, R., Prior, D., Xia, B. 2004. Strain softening and microstructural evolution of anorthite aggregates and quartz–anorthite layered

composites deformed in torsion. *Earth and Planetary Science Letters,* 222, 377-390, DOI: 10.1016/j.epsl.2004.03.021.

Jin, Y., Mcnutt, M. K., Zhu, Y. S. 1996. Mapping the descent of Indian and Eurasian plates beneath the Tibetan Plateau from gravity anomalies. *Journal of Geophysical Research-Solid Earth,* 101, 11275-11290, DOI: 10.1029/96JB00531.

Kaneko, Y. 1995. Thermal structure in the Annapurna region, central Nepal Himalaya: implication for the inverted metamorphism. *Journal of Mineralogy, Petrology and Economic Geology,* 90, 143-154, DOI: 10.2465/ganko.90.143.

Kellett, D. A., Godin, L. 2009. Pre-Miocene deformation of the Himalayan superstructure, Hidden valley, central Nepal. *Journal of the Geological Society, London,* 166, 261-275, DOI: 10.1144/0016-76492008-097.

Kellett, D. A., Grujic, D., Warren, C., Cottle, J., Jamieson, R., Tenzin, T. 2010. Metamorphic history of a syn-convergent orogen-parallel detachment: The South Tibetan detachment system, Bhutan Himalaya. *Journal of Metamorphic Geology,* 28, 785-808, DOI: 10.1111/j.1525-1314.2010.00893.x.

Kellett, D. A., Grujic, D. 2012. New insight into the South Tibetan detachment system: Not a single progressive deformation. *Tectonics,* 31, TC2007 DOI: 10.1029/2011tc002957.

Khanal, S., Robinson, D. M., Mandal, S., Simkhada, P. 2014. Structural, geochronological and geochemical evidence for two distinct thrust sheets in the 'Main Central thrust zone', the Main Central thrust and Ramgarh–Munsiari thrust: implications for upper crustal shortening in central Nepal. *In:* Mukherjee, S., Carosi, R., Van Der Beek, P. K., Mukherjee, B. K. Robinson, D. M. (eds.), *Tectonics of the Himalaya.* Geological Society of London Special Publications, 412, DOI: 10.1144/sp412.2.

Khanal, S., Robinson, D. M., Kohn, M. J., Mandal, S. 2015. Evidence for a far-traveled thrust sheet in the Greater Himalayan thrust system, and an alternative model to building the Himalaya. *Tectonics,* 34, 2014TC003616, DOI: 10.1002/2014tc003616.

Kirby, S. H. 1985. Rock mechanics observations pertinent to the rheology of the continental lithosphere and the localization of strain along shear zones. *Tectonophysics,* 119, 1-27, DOI: 10.1016/0040-1951(85)90030-7.

Klemperer, S. L. 2006. Crustal flow in Tibet: geophysical evidence for the physical state of Tibetan lithosphere, and inferred patterns of active flow. *In:* Law, R. D., Searle, M. P. Godin, L. (eds.), *Channel Flow, Ductile Extrusion and Exhumation in Continental Collision Zones.* Geological Society of London Special Publications, 268, 39-70, DOI: 10.1144/GSL.SP.2006.268.01.03.

Knipe, R. J., Law, R. D. 1987. The influence of crystallographic orientation and grain boundary migration on microstructural and textural evolution in an S-C mylonite. *Tectonophysics,* 135, 155-169, DOI: 10.1016/0040-1951(87)90158-2.

Kohn, M. J., Orange, D. L., Spear, F. S., Rumble, D., Harrison, T. M. 1992. Pressure, Temperature, and Structural Evolution of West-Central New Hampshire: Hot Thrusts over Cold Basement. *Journal of Petrology,* 33, 521-556, DOI: 10.1093/petrology/33.3.521.

Kohn, M. J., Catlos, E. J., Ryerson, F. J., Harrison, T. M. 2001. Pressure-temperature-time path discontinuity in the Main Central thrust zone, central

Nepal. *Geology,* 29, 571-574, DOI: 10.1130/0091-7613(2001) 029<0571:PTTPDI>2.0.CO;2.

Kohn, M. J. 2008. P-T-t data from central Nepal support critical taper and repudiate large-scale channel flow of the Greater Himalayan Sequence. *Geological Society of America Bulletin,* 120, 259-273, DOI: 10.1130/B26252.1.

Kohn, M. J., Corrie, S. L. 2011. Preserved Zr-temperatures and U–Pb ages in high-grade metamorphic titanite: Evidence for a static hot channel in the Himalayan orogen. *Earth and Planetary Science Letters,* 311, 136-143, DOI: 10.1016/j.epsl.2011.09.008.

Kohn, M. J. 2014. Himalayan metamorphism and Its tectonic implications. *Annual Review of Earth and Planetary Sciences,* 42, 381-419, DOI: 10.1146/annurev-earth-060313-055005.

Kruckenberg, S. C., Ferré, E. C., Teyssier, C., Vanderhaeghe, O., Whitney, D. L., Seaton, N. C. A., Skord, J. A. 2010. Viscoplastic flow in migmatites deduced from fabric anisotropy: An example from the Naxos dome, Greece. *Journal of Geophysical Research,* 115, B09401, DOI: 10.1029/2009JB007012.

Kruckenberg, S. C., Vanderhaeghe, O., Ferré, E. C., Teyssier, C., Whitney, D. L. 2011. Flow of partially molten crust and the internal dynamics of a migmatite dome, Naxos, Greece. *Tectonics,* 30, TC3001, DOI: 10.1029/2010tc002751.

Kruhl, J. H. 1996. Prism- and basal-plane parallel subgrain boundaries in quartz: a microstructural geothermobarometer. *Journal of Metamorphic Geology,* 46, 581-586, DOI: 10.1046/j.1525-1314.1996.00413.x.

Kruhl, J. H. 1998. Reply: Prism- and basal-plane parallel subgrain boundaries in quartz: a microstructural geothermobarometer. *Journal of Metamorphic Geology,* 16, 142-146, DOI: 10.1111/j.1525-1314.1998.00063.x.

Krummenacher, D. 1971. Géochronométrie des roches de l'Himalaya. *In:* Bordet, P., Colchen, M., Krummenacher, D. Le Fort, P. (eds.), *Recherches géologiques dans l'Himalaya du Népal, région de la Takkhola.* Edition du Centre Nationale de la Recherche Scientifique, Paris, 6, 187-202.

Lafrance, B., White, J. C., Williams, P. F. 1994. Natural calcite c-axis fabrics: An alternate interpretation. *Tectonophysics,* 229, 1-18, DOI: 10.1016/0040-1951(94)90002-7.

Larson, K. P., Godin, L. 2009. Kinematics of the Greater Himalayan sequence, Dhaulagiri Himal: implications for the structural framework of central Nepal. *Journal of the Geological Society, London,* 166, 25-43, DOI: 10.1144/0016-76492007-180.

Larson, K. P., Godin, L., Davis, W. J., Davis, D. W. 2010a. Out-of-sequence deformation and expansion of the Himalayan orogenic wedge: insight from the Changgo culmination, south central Tibet. *Tectonics,* 29, TC4013, DOI: 10.1029/2008tc002393.

Larson, K. P., Godin, L., Price, R. A. 2010b. Relationships between displacement and distortion in orogens: Linking the Himalayan foreland and hinterland in central Nepal. *Geological Society of America Bulletin,* 122, 1116-1134, DOI: 10.1130/B30073.1.

Larson, K. P., Gervais, F., Kellett, D. A. 2013. A P–T–t–D discontinuity in east-central Nepal: Implications for the evolution of the Himalayan mid-crust. *Lithos,* 179, 275-292, DOI: 10.1016/j.lithos.2013.08.012.

Larson, K. P., Cottle, J. M. 2014. Midcrustal discontinuities and the assembly of the Himalayan midcrust. *Tectonics,* 33, 2013TC003452, DOI: 10.1002/2013tc003452.

Larson, K. P., Lamming, J. L., Faisal, S. 2014. Microscale strain partitioning? Differential quartz lattice preferred orientation development in micaceous phyllite, Hindu Kush, northwestern Pakistan. *Solid Earth Discussions,* 6, 2735-2758, DOI: 10.5194/sed-6-2735-2014.

Larson, K. P., Cottle, J. M. 2015. Initiation of crustal shortening in the himalaya. *Terra Nova,* 00, 1-6, DOI: 10.1111/ter.12145.

Law, R. D. 1986. Relationships between strain and quartz crystallographic fabrics in the Roche Maurice quartzites of Plougastel, western Brittany. *Journal of Structural Geology,* 8, 493-515, DOI: 10.1016/0191-8141(86)90001-5.

Law, R. D. 1990. Crystallographic fabrics: a selective review of their applications to research in structural geology. *In:* Knipe, R. J., Rutter, E. H. (eds.), *Deformation mechanisms, rheology and tectonics*. Geological Society of London Special Publications*,* 54, 335-352, DOI: 10.1144/gsl.sp.1990.054.01.30.

Law, R. D., Schmid, S. M., Wheeler, J. 1990. Simple shear deformation and quartz crystallographic fabrics: a possible natural example from the Torridon area of NW Scotland. *Journal of Structural Geology,* 12, 29-45, DOI: 10.1016/0191-8141(90)90046-2.

Law, R. D., Searle, M. P., Simpson, R. L. 2004. Strain, deformation temperatures and vorticity of flow at the top of the Greater Himalayan Slab, Everest Massif, Tibet. *Journal of the Geological Society, London,* 161, 305-320, DOI: 10.1144/0016-764903-047.

Law, R. D., Jessup, M. J., Searle, M. P., Francsis, M. K., Walters, D. J., Cottle, J. M. 2011. Telescoping of isotherms beneath the South Tibetan Detachment System, Mount Everest Massif. *Journal of Structural Geology,* 33, 1569-1594, DOI: 10.1016/j.jsg.2011.09.004.

Law, R. D., Stahr Iii, D. W., Francsis, M. K., Ashley, K. T., Grasemann, B., Ahmad, T. 2013. Deformation temperatures and flow vorticities near the base of the Greater Himalayan Series, Sutlej Valley and Shimla Klippe, NW India. *Journal of Structural Geology,* 54, 21-53, DOI: 10.1016/j.jsg.2013.05.009.

Law, R. D. 2014. Deformation thermometry based on quartz c-axis fabrics and recrystallization microstructures: A review. *Journal of Structural Geology,* 66, 129-161, DOI: 10.1016/j.jsg.2014.05.023.

Le Fort, P. 1975. Himalayas: the collided range. Present knowledge of the continental arc. *American Journal of Science,* 275-A, 1-44.

Le Fort, P. 1981. Manaslu Leucogranite - a collision signature of the himalaya: a model for Its genesis and emplacement. *Journal of Geophysical Research,* 86, 545-568, DOI: 10.1029/JB086iB11p10545.

Le Fort, P., Pêcher, A., Upreti, B. N. 1987. A section through the Tibetan Slab in Central Nepal (Kali Gandaki valley): mineral chemistry and thermobarometry of the Main Central Thrust zone. *In:* Le Fort, P., Colchen, M. Montenat, C. (eds.), *Orogenic Evolution of Southern Asia (from Turkey to Indonesia).*Sciences de la Terre, Nancy, France, 211–228.

Le Fort, P., France-Lanord, C. 1995. Granites from Mustang and surrounding regions (central Nepal). *Journal of Nepal Geological Society,* 11, 53-57.

Lebensohn, R. A., Tomé, C. N. 1993. A self-consistent anisotropic approach for the simulation of plastic deformation and texture development of polycrystals: Application to zirconium alloys. *Acta Metallurgica et Materialia,* 41, 2611-2624, DOI: 10.1016/0956-7151(93)90130-K.

Lee, J., Hacker, B., Wang, Y. 2004. Evolution of North Himalayan gneiss domes: structural and metamorphic studies in Mabja Dome, southern Tibet. *Journal of Structural Geology,* 26, 2297-2316, DOI: 10.1016/j.jsg.2004.02.013.

Lee, J., Mcclelland, W., Wang, Y., Blythe, A., Mcwilliams, M. 2006. Oligocene-Miocene middle crustal flow in southern Tibet: geochronology of Mabja Dome. *In:* Law, R. D., Searle, M. P. Godin, L. (eds.), *Channel Flow, Ductile Extrusion and Exhumation in Continental Collision Zones.* Geological Society of London Special Publications, 268, 445-469, DOI: 10.1144/GSL.SP.2006.268.01.21 .

Lee, J., Hager, C., Wallis, S. R., Stockli, D. F., Whitehouse, M. J., Aoya, M., Wang, Y. 2011. Middle to late Miocene extremely rapid exhumation and thermal reequilibration in the Kung Co rift, southern Tibet. *Tectonics,* 30, TC2007, DOI: 10.1029/2010TC002745.

Leiss, B., Barber, D. J. 1999. Mechanisms of dynamic recrystallization in naturally deformed dolomite inferred from EBSP analyses. *Tectonophysics,* 303, 51-69, DOI: 10.1016/S0040-1951(98)00258-3.

Leiss, B., Molli, G. 2003. 'High-temperature' texture in naturally deformed Carrara marble from the Alpi Apuane, Italy. *Journal of Structural Geology,* 25, 649-658, DOI: 10.1016/S0191-8141(02)00148-7.

Li, H., Shen, Y., Huang, Z., Li, X., Gong, M., Shi, D., Sandvol, E., Li, A. 2014. The distribution of the mid-to-lower crustal low-velocity zone beneath the northeastern Tibetan Plateau revealed from ambient noise tomography. *Journal of Geophysical Research: Solid Earth,* 119, 2013JB010374, DOI: 10.1002/2013jb010374.

Linker, M. F., Kirby, S. H., Ord, A., Christie, J. M. 1984. Effects of compression direction on the plasticity and rheology of hydrolytically weakened synthetic quartz crystals at atmospheric pressure. *Journal of Geophysical Research: Solid Earth,* 89, 4241-4255, DOI: 10.1029/JB089iB06p04241.

Lisle, R. J. 1985. The Use of the Orientation Tensor for the Description and Statistical Testing of Fabrics. *Journal of Structural Geology,* 7, 115-117, DOI: 10.1016/0191-8141(85)90119-1.

Lister, G. S. 1977. Discussion: Crossed-girdle c-axis fabrics in quartzites plastically deformed by plane strain and progressive simple shear. *Tectonophysics,* 39, 51-54, DOI: 10.1016/0040-1951(77)90087-7.

Lister, G. S., Paterson, M. S., Hobbs, B. E. 1978. The simulation of fabric development in plastic deformation and its application to quartzite: The model. *Tectonophysics,* 45, 107-158, DOI: 10.1016/0040-1951(78)90004-5.

Lister, G. S., Williams, P. F. 1979. Fabric development in shear zones: theoretical controls and observed phenomena. *Journal of Structural Geology,* 1, 283-297, DOI: 10.1016/0191-8141(79)90003-8.

Lister, G. S., Hobbs, B. E. 1980. The simulation of fabric development during plastic deformation and its application to quartzite: the influence of deformation history. *Journal of Structural Geology,* 2, 355-370, DOI: 10.1016/0191-8141(80)90023-1.

Lister, G. S., Williams, P. F. 1983. The partitioning of deformation in flowing rock masses. *Tectonophysics,* 92, 1-33, DOI: 10.1016/0040-1951(83)90083-5.

Lloyd, G. E. 1987. Atomic number and crystallographic contrast images with the SEM: a review of backscattered electron techniques. *Mineralogical Magazine,* 51, 3-19, DOI: 10.1180/minmag.1987.051.359.02.

Lloyd, G. E., Kendall, J. M. 2005. Petrofabric-derived seismic properties of a mylonitic quartz simple shear zone: implications for seismic reflection profiling. *In:* Harvey, P. K., Brewer, T. S., Pezard, P. A., Petrov, V. A. (eds), *Petrophysical Properties of Crystalline Rocks.* Geological Society of London Special Publications, 240, 75-94, DOI: 10.1144/GSL.SP.2005.240.01.07.

Lloyd, G. E., Law, R. D., Mainprice, D., Wheeler, J. 1992. Microstructural and crystal fabric evolution during shear zone formation. *Journal of Structural Geology,* 14, 1079-1100, DOI: 10.1016/0191-8141(92)90037-W.

Lloyd, G. E., Freeman, B. 1994. Dynamic recrystallization of quartz under greenschist conditions. *Journal of Structural Geology,* 16, 867-881, DOI: 10.1016/0191-8141(94)90151-1.

Lloyd, G. E., Butler, R. W. H., Casey, M., Tatham, D. J., Mainprice, D. 2011a. Constraints on the seismic properties of the middle and lower continental crust. *In:* Prior, D. J., Rutter, E. H. Tatham, D. J. (eds.), *Deformation mechanisms, rheology and tectonics: Microstructures, mechanics and anisotropy.* Geological Society of London Special Publications, 360, 7-32, DOI: 10.1144/SP360.2.

Lloyd, G. E., Halliday, J. M., Butler, R. W. H., Casey, M., J.-M., K., Wookey, J., Mainprice, D. 2011b. From crystal to crustal: petrofabric-derived seismic modelling of regional tectonics. *In:* Prior, D. J., Rutter, E. H. Tatham, D. J. (eds.), *Deformation mechanisms, rheology and tectontics: Microstructures, mechanics and anisotropy.* Geological Society of London Special Publicaitons, 360, 49-78, DOI: 10.1144/SP360.4.

Mainprice, D., Bouchez, J.-L., Blumenfeld, P., Tubià, J. M. 1986. Dominant c slip in naturally deformed quartz: Implications for dramatic plastic softening at high temperature. *Geology,* 14, 819-822, DOI: 10.1130/0091-7613(1986)14<819:dcsind>2.0.co;2.

Mainprice, D., Nicolas, A. 1989. Development of shape and lattice preferred orientations: application to the seismic anisotropy of the lower crust. *Journal of Structural Geology,* 11, 175-189, DOI: 10.1016/0191-8141(89)90042-4.

Mainprice, D. 1990. An efficient Fortran program to calculate seismic anisotropy from the lattice preferred orientation of minerals. *Computers and Geosciences*, 16, 385-393, DOI: 10.1016/0098-3004(90)90072-2.

Mainprice, D., Lloyd, G. E., Casey, M. 1993. Individual orientation measurements in quartz polycrystals: advantages and limitations for texture and petrophysical property determinations. *Journal of Structural Geology,* 15, 1169-1187, DOI: 10.1016/0191-8141(93)90162-4.

Mainprice, D., Hielscher, R., Schaeben, H. 2011. Calculating anisotropic physical properties from texture data using the MTEX open-source package. *In:* Prior, D. J., Rutter, E. H. Tatham, D. J. (eds.), *Deformation mechanisms, rheology and tectonics: Microstructures, mechanics and anisotropy.* Geological Society of London Special Publications, 360, 175-192, DOI: 10.1144/sp360.10.

Mainprice, D., Bachmann, F., Hielscher, R., Schaeben, H. 2014. Descriptive tools for the analysis of texture projects with large datasets using MTEX: strength,

symmetry and components. *In:* Faulkner, D. R., Mariani, E., Mecklenburgh, J., *Rock deformation from field, experiments and theory: A volume in honour of Ernie Rutter.* Geological Society of London Special Publications, 409, DOI: 10.1144/sp409.8.

Makovsky, Y., Klemperer, S. L., Huang, L. Y., Lu, D. Y. 1996. Structural elements of the southern Tethyan Himalaya crust from wide-angle seismic data. *Tectonics,* 15, 997-1005, DOI: 10.1029/96TC00310.

Mancktelow, N. S. 1995. Nonlithostatic pressure during sediment subduction and the development and exhumation of high pressure metamorphic rocks. *Journal of Geophysical Research: Solid Earth,* 100, 571-583, DOI: 10.1029/94jb02158.

Mardia, K. V. 1975. Statistics of directional data. *Journal of the Royal Statistical Society. Series B (Methodological),* 37, 349-393, DOI: 10.2307/2984782.

Martin-Hernandez, F., Hirt, A. M. 2003. The anisotropy of magnetic susceptibility in biotite, muscovite and chlorite single crystals. *Tectonophysics,* 367, 13-28, DOI: 10.1016/S0040-1951(03)00127-6.

Martin, A. J., Decelles, P. G., Gehrels, G. E., Patchett, P. J., Isachsen, C. 2005. Isotopic and structural constraints on the location of the Main Central thrust in the Annapurna Range, central Nepal Himalaya. *Geological Society of America Bulletin,* 117, 926-944, DOI: 10.1130/B25646.1.

Martin, A. J., Ganguly, J., Decelles, P. G. 2010. Metamorphism of Greater and Lesser Himalayan rocks exposed in the Modi Khola valley, central Nepal. *Contributions to Mineralogy and Petrology,* 159, 203-223, DOI: 10.1007/s00410-009-0424-3.

Martin, A. J., Copeland, P., Benowitz, J. A. 2014. Muscovite $^{40}Ar/^{39}Ar$ ages help reveal the Neogene tectonic evolution of the southern Annapurna Range, central Nepal. *In:* Mukherjee, S., Carosi, R., Van Der Beek, P. K., Mukherjee, B. K. Robinson, D. M. (eds.), *Tectonics of the Himalaya.* Geological Society of London Special Publications, 412, DOI: 10.1144/SP412.5.

Mccaffrey, R., Nabelek, J. 1998. Role of oblique convergence in the active deformation of the Himalayas and southern Tibet plateau. *Geology,* 26, 691-694, DOI: 10.1130/0091-7613(1998)026<0691:ROOCIT>2.3.CO;2.

Means, W. D. 1981. The concept of steady-state foliation. *Tectonophysics,* 78, 179-199, DOI: 10.1016/0040-1951(81)90013-5.

Means, W. D. 1989. Stretching Faults. *Geology,* 17, 893-896, DOI: 10.1130/0091-7613(1989)017<0893:SF>2.3.CO;2.

Mehl, L., Hirth, G. 2008. Plagioclase preferred orientation in layered mylonites: Evaluation of flow laws for the lower crust. *Journal of Geophysical Research: Solid Earth,* 113, B05202, DOI: 10.1029/2007jb005075.

Menegon, L., Pennacchioni, G., Spiess, R. 2008. Dissolution-precipitation creep of K-feldspar in mid-crustal granite mylonites. *Journal of Structural Geology,* 30, 565-579, DOI: 10.1016/j.jsg.2008.02.001.

Metcalfe, R. P. 1993. Pressure, temperature and time constraints on metamorphism across the Main Central Thrust zone and High Himalayan Slab in the Garhwal Himalaya. *In:* Treloar, P. J. Searle, M. P. (eds.), *Himalayan Tectonics.* Geological Society of London Special Publications, 74, 485-509, DOI: 10.1144/gsl.sp.1993.074.01.33.

Molina Garza, R. S., Geissman, J., Wawrzyniec, T., Weber, B., Martínez, M. L., Aranda-Gómez, J. 2009. An integrated magnetic and geological study of cataclasite-dominated pseudotachylytes in the Chiapas Massif, Mexico: a snapshot of stress orientation following slip. *Geophysical Journal International,* 177, 891-912, DOI: 10.1111/j.1365-246X.2009.04046.x.

Montési, L. G. J. 2013. Fabric development as the key for forming ductile shear zones and enabling plate tectonics. *Journal of Structural Geology,* 50, 254-266, DOI: 10.1016/j.jsg.2012.12.011.

Montomoli, C., Iaccarino, S., Carosi, R., Langone, A., Visonà, D. 2013. Tectonometamorphic discontinuities within the Greater Himalayan Sequence in Western Nepal (Central Himalaya): Insights on the exhumation of crystalline rocks. *Tectonophysics,* 608, 1349-1370, DOI: 10.1016/j.tecto.2013.06.006.

Montomoli, C., Carosi, R., Iaccarino, S. 2014. Tectonometamorphic discontinuities in the Greater Himalayan Sequence: a local or a regional feature? *In:* Mukherjee, S., Carosi, R., Van Der Beek, P. K., Mukherjee, B. K. Robinson, D. M. (eds.), *Tectonics of the Himalaya.* Geological Society of London Special Publications, 412, DOI: 10.1144/sp412.3.

Mora, A., Ketcham, R. A., Higuera-Díaz, I. C., Bookhagen, B., Jimenez, L., Rubiano, J. 2014. Formation of passive-roof duplexes in the Colombian Subandes and Perú. *Lithosphere,* 6, 456-472, DOI: 10.1130/l340.1.

Morales, L. F. G., Mainprice, D., Lloyd, G. E., Law, R. D. 2011. Crystal fabric development and slip systems in a quartz mylonite: an approach via transmission electron microscopy and viscoplastic self-consistent modelling. *In:* Prior, D. J., Rutter, E. H. Tatham, D. J. (eds.), *Deformation mechanisms, rheology and tectonics.* Geological Society of London Special Publications, 360, 151-174, DOI: 10.1144/sp360.9.

Morales, L. F. G., Lloyd, G. E., Mainprice, D. 2014. Fabric transitions in quartz via viscoplastic self-consistent modeling part I: Axial compression and simple shear under constant strain. *Tectonophysics,* 636, 52-69, DOI: 10.1016/j.tecto.2014.08.011.

Morgan, S. S., Law, R. D. 2004. Unusual transition in quartzite dislocation creep regimes and crystal slip systems in the aureole of the Eureka Valley–Joshua Flat–Beer Creek pluton, California: a case for anhydrous conditions created by decarbonation reactions. *Tectonophysics,* 384, 209-231, DOI: 10.1016/j.tecto.2004.03.016.

Mottram, C. M., Argles, T. W., Harris, N. B. W., Parrish, R. R., Horstwood, M. S. A., Warren, C. J., Gupta, S. 2014a. Tectonic interleaving along the Main Central Thrust, Sikkim Himalaya. *Journal of the Geological Society, London,* 171, 255-268, DOI: 10.1144/jgs2013-064.

Mottram, C. M., Warren, C. J., Regis, D., Roberts, N. M. W., Harris, N. B. W., Argles, T. W., Parrish, R. R. 2014b. Developing an inverted Barrovian sequence; insights from monazite petrochronology. *Earth and Planetary Science Letters,* 403, 418-431 DOI: 10.1016/j.epsl.2014.07.006.

Mukherjee, S., Koyi, H. 2010. Higher Himalayan Shear Zone, Sutlej section: structural geology and extrusion mechanism by various combinations of simple shear, pure shear and channel flow in shifting modes. *International Journal of Earth Sciences,* 99, 1267-1303, DOI: 10.1007/s00531-009-0459-8.

Mukherjee, S., Mulchrone, K. 2012. Estimating the viscosity and Prandtl number of the Tso Morari crystalline gneiss dome, Indian western Himalaya. *International Journal of Earth Sciences,* 101, 1929-1947, DOI: 10.1007/s00531-012-0758-3.

Mukherjee, S. 2013a. Higher Himalaya in the Bhagirathi section (NW Himalaya, India): its structures, backthrusts and extrusion mechanism by both channel flow and critical taper mechanisms. *International Journal of Earth Sciences,* 102, 1851-1870, DOI: 10.1007/s00531-012-0861-5.

Mukherjee, S. 2013b. Channel flow extrusion model to constrain dynamic viscosity and Prandtl number of the Higher Himalayan Shear Zone. *International Journal of Earth Sciences,* 102, 1811-1835, DOI: 10.1007/s00531-012-0806-z.

Mukherjee, S. 2014. Kinematics of "top -to-down" simple shear in a Newtonian rheology. *The Journal of Indian Geophysical Union,* 18, 273-276.

Mulchrone, K., Mukherjee, S. 2015. Shear Senses and Viscous Dissipation of Layered Ductile Simple Shear Zones. *Pure and Applied Geophysics*, 1-8, DOI: 10.1007/s00024-015-1035-8.

Murphy, D. C. 1987. Suprastructure/infrastructure transition, east-central Cariboo Mountains, British Columbia: geometry, kinematics and tectonic implications. *Journal of Structural Geology,* 9, 13-29, DOI: 10.1016/0191-8141(87)90040-X.

Murphy, M., Taylor, M., Gosse, J., Silver, C., Whipp, D., Beaumont, C. 2014. Limit of strain partitioning in the Himalaya marked by large earthquakes in western Nepal. *Nature Geoscience,* 7, 38-42, DOI: 10.1038/ngeo2017.

Murphy, M. A., Copeland, P. 2005. Transtensional deformation in the central Himalaya and its role in accommodating growth of the Himalayan orogen. *Tectonics,* 24, TC4012, DOI: 10.1029/2004tc001659.

Muxworthy, A., Heslop, D., Williams, W. 2004. Influence of magnetostatic interactions on first-order-reversal-curve (FORC) diagrams: a micromagnetic approach. *Geophysical Journal International,* 158, 888-897, DOI: 10.1111/j.1365-246X.2004.02358.x.

Nábelek, J., Hetenyi, G., Vergne, J., Sapkota, S., Kafle, B., Jiang, M., Su, H. P., Chen, J., Huang, B. S., Team, H.-C. 2009. Underplating in the Himalaya-Tibet Collision Zone revealed by the Hi-CLIMB experiment. *Science,* 325, 1371-1374, DOI: 10.1126/science.1167719.

Nadin, E. S., Martin, A. J. 2012. Apatite thermochronometry within a knickzone near the Higher Himalaya front, central Nepal: No resolvable fault motion in the past one million years. *Tectonics,* 31, TC2010, DOI: 10.1029/2011tc003000.

Najman, Y., Appel, E., Boudagher-Fadel, M., Bown, P., Carter, A., Garzanti, E., Godin, L., Han, J., Liebke, U., Oliver, G., Parrish, R., Vezzoli, G. 2010. Timing of India-Asia collision: Geological, biostratigraphic, and palaeomagnetic constraints. *Journal of Geophysical Research: Solid Earth,* 115, B12416, DOI: 10.1029/2010jb007673.

Nazarchuk, J. H. 1993. *Structure and geochronology of the Greater Himalaya, Kali Gandaki region, west-central Nepal [MS thesis]*. Ottawa, Ontario, Carleton University.

Negrini, M., Stünitz, H., Nasipuri, P., Menegon, L., Morales, L. F. G. 2014. Semibrittle deformation and partial melting of perthitic K-feldspar: An experimental study. *Journal of Geophysical Research: Solid Earth,* 119, 2013JB010573, DOI: 10.1002/2013jb010573.

Nie, G., Shan, Y. 2014. Development of quartz c-axis crossed/single girdles under simple-pure shear deformation: Results of visco-plastic self-consistent modeling. *Journal of Structural Geology,* 66, 261-270, DOI: 10.1016/j.jsg.2014.05.022.

Nelson, K. D., Zhao, W. J., Brown, L. D., Kuo, J., Che, J. K., Liu, X. W., Klemperer, S. L., Makovsky, Y., Meissner, R., Mechie, J., Kind, R., Wenzel, F., Ni, J., Nabelek, J., Chen, L. S., Tan, H. D., Wei, W. B., Jones, A. G., Booker, J., Unsworth, M., Kidd, W. S. F., Hauck, M., Alsdorf, D., Ross, A., Cogan, M., Wu, C. D., Sandvol, E., Edwards, M. 1996. Partially molten middle crust beneath southern Tibet: Synthesis of project INDEPTH results. *Science,* 274, 1684-1688, DOI: 10.1126/science.274.5293.1684.

Nicolas, A., Poirier, J.-P. 1976. *Crystalline plasticity and solid state flow in metamorphic rocks*, 444, Wiley London.

O'reilly, W. 1984. *Rock and mineral magnetism,* Blackie, Glasgow.

Oesterling, N., Heilbronner, R., Stünitz, H., Barnhoorn, A., Molli, G. 2007. Strain dependent variation of microstructure and texture in naturally deformed Carrara marble. *Journal of Structural Geology,* 29, 681-696, DOI: 10.1016/j.jsg.2006.10.007.

Okudaira, T., Takeshita, T., Hara, I., Ando, J.-I. 1995. A new estimate of the conditions for transition from basal <a> to prism [c] slip in naturally deformed quartz. *Tectonophysics,* 250, 31-46, DOI: 10.1016/0040-1951(95)00039-4.

Okudaira, T., Ogawa, D., Michibayashi, K. 2010. Grain-size-sensitive deformation of upper greenschist- to lower amphibolite-facies metacherts from a low-P/high-T metamorphic belt. *Tectonophysics,* 492, 141-149, DOI: 10.1016/j.tecto.2010.06.002.

Olsen, T. S., Kohlstedt, D. L. 1985. Natural deformation and recrystallization of some intermediate plagioclase feldspars. *Tectonophysics,* 111, 107-131, DOI: 10.1016/0040-1951(85)90067-8.

Parsons, A. J., Law, R. D., Searle, M. P., Phillips, R. J., Lloyd, G. E. 2014. Geology of the Dhaulagiri-Annapurna-Manaslu Himalaya, Western Region, Nepal. 1:200,000. *Journal of Maps,* 10.1080/17445647.2014.984784, 1-11, DOI: 10.1080/17445647.2014.984784.

Passchier, C. W., Trouw, R. a. J. 2005. *Microtectonics,* 2nd ed., Springer, New York.

Paudel, L. P., Arita, K. 2000. Tectonic and polymetamorphic history of the Lesser Himalaya in central Nepal. *Journal of Asian Earth Sciences,* 18, 561-584, DOI: 10.1016/s1367-9120(99)00069-3.

Paudel, L. P., Arita, K. 2006a. Thermal evolution of the Lesser Himalaya, central Nepal: Insights from K-white micas compositional variation. *Gondwana Research,* 9, 409-425, DOI:10.1016/J.Gr.2006.01.003.

Paudel, L. P., Arita, K. 2006b. The b-spacing values of white micas and their metamorphic implications in the Lesser Himalaya, central Nepal. *Journal of Asian Earth Sciences,* 27, 10-24, DOI: 10.1016/j.jseaes.2005.01.008.

Pearson, O. N., Decelles, P. G. 2005. Structural geology and regional tectonic significance of the Ramgarh thrust, Himalayan fold-thrust belt of Nepal. *Tectonics,* 24, TC4008, DOI: 10.1029/2003tc001617.

Pêcher, A., Le Fort, P. Origin and significance of the Lesser Himalayan augen gneisses. *Colloque International CNRS,* 268, 319–329.

Pêcher, A. 1989. The metamorphism in the Central Himalaya. *Journal of Metamorphic Geology,* 7, 31-41, DOI: 10.1111/j.1525-1314.1989.tb00573.x.

Pêcher, A. 1991. The Contact between the Higher Himalaya Crystallines and the Tibetan Sedimentary Series - Miocene Large-Scale Dextral Shearing. *Tectonics,* 10, 587-598, DOI: 10.1029/90TC02655.

Pêcher, A., Bouchez, J.-L., Le Fort, P. 1991. Miocene dextral shearing between Himalaya and Tibet. *Geology,* 19, 683-685, DOI: 10.1130/0091-7613(1991)019<0683:mdsbha>2.3.co;2.

Pennacchioni, G., Menegon, L., Leiss, B., Nestola, F., Bromiley, G. 2010. Development of crystallographic preferred orientation and microstructure during plastic deformation of natural coarse-grained quartz veins. *Journal of Geophysical Research: Solid Earth,* 115, B12405, DOI: 10.1029/2010jb007674.

Piazolo, S., Jessell, M. W., Bons, P. D., Evans, L., Becker, J. K. 2010. Numerical simulations of microstructures using the Elle platform: A modern research and teaching tool. *Journal of the Geological Society of India,* 75, 110-127, DOI: 10.1007/s12594-010-0028-6.

Pick, T., Tauxe, L. 1994. Characteristics of magnetite in submarine basaltic glass. *Geophysical Journal International,* 119, 116-128, DOI: 10.1111/j.1365-246X.1994.tb00917.x.

Pieri, M., Kunze, K., Burlini, L., Stretton, I., Olgaard, D. L., Burg, J. P., Wenk, H. R. 2001. Texture development of calcite by deformation and dynamic recrystallization at 1000 K during torsion experiments of marble to large strains. *Tectonophysics,* 330, 119-140, DOI: 10.1016/S0040-1951(00)00225-0.

Pike, C. R., Roberts, A. P., Verosub, K. L. 1999. Characterizing interactions in fine magnetic particle systems using first order reversal curves. *Journal of Applied Physics,* 85, 6660-6667, DOI: 10.1063/1.370176.

Platt, J. P. 1986. Dynamics of orogenic wedges and the uplift of high-pressure metamorphic rocks. *Geological Society of America Bulletin,* 97, 1037-1053, DOI: 10.1130/0016-7606(1986)97<1037:doowat>2.0.co;2.

Pokorný, J., Suza, P., Hrouda, F. 2004. Anisotropy of magnetic susceptibility of rocks measured in variable weak magnetic fields using the KLY-4S Kappabridge. *In:* Martin-Hernandez, F., Luneburg, C. M., Aubourg, C., Jackson, M. (eds.), *Magnetic fabric: Methods and applications*. Geological Society of London Special Publications*,* 238, 69-76, DOI: 10.1144/GSL.SP.2004.238.01.07.

Price, R. A. 1986. The southeastern Canadian Cordillera: Thrust faulting, tectonic wedging, and delamination of the lithosphere. *Journal of Structural Geology,* 8, 239-254, DOI: 10.1016/0191-8141(86)90046-5.

Prior, D. J., Boyle, A. P., Brenker, F., Cheadle, M. C., Day, A., Lopez, G., Peruzzi, L., Potts, G., Reddy, S., Spiess, R., Timms, N. E., Trimby, P., Wheeler, J., Zetterstrom, L. 1999. The application of electron backscatter diffraction and orientation contrast imaging in the SEM to textural problems in rocks. *American Mineralogist,* 84, 1741-1759.

Ramsay, J., Huber, M. 1983. *The techniques of modern structural analysis; Volume 1: Strain analysis*. London, Academic Press.

Randle, V., Ralph, B. 1986. A practical approach to the determination of the crystallography of grain boundaries. *Journal of Materials Science,* 21, 3823-3828, DOI: 10.1007/bf02431617.

Randle, V. 1993. *The measurement of grain boundary geometry,* Institute of Physics Publishing, Bristol.

Rapine, R., Tilmann, F., West, M., Ni, J., Rodgers, A. 2003. Crustal structure of northern and southern Tibet from surface wave dispersion analysis. *Journal of Geophysical Research-Solid Earth,* 108, DOI: 10.1029/2001jb000445.

Ratschbacher, L., Frisch, W., Liu, G., Chen, C. 1994. Distributed deformation in southern and western Tibet during and after the India-Asia collision. *Journal of Geophysical Research: Solid Earth,* 99, 19917-19945, DOI: 10.1029/94jb00932.

Rippe, D., Unsworth, M. 2010. Quantifying crustal flow in Tibet with magnetotelluric data. *Physics of the Earth and Planetary Interiors,* 179, 107-121, DOI: 10.1016/j.pepi.2010.01.009.

Roberts, A. P., Cui, Y., Verosub, K. L. 1995. Wasp-waisted hysteresis loops: Mineral magnetic characteristics and discrimination of components in mixed magnetic systems. *Journal of Geophysical Research: Solid Earth,* 100, 17909-17924, DOI: 10.1029/95jb00672.

Roberts, A. P., Pike, C. R., Verosub, K. L. 2000. First-order reversal curve diagrams: A new tool for characterizing the magnetic properties of natural samples. *Journal of Geophysical Research: Solid Earth,* 105, 28461-28475, DOI: 10.1029/2000jb900326.

Roberts, A. P., Liu, Q. S., Rowan, C. J., Chang, L., Carvallo, C., Torrent, J., Horng, C. S. 2006. Characterization of hematite (α-Fe_2O_3), goethite (α-FeOOH), greigite (Fe_3S_4), and pyrrhotite (Fe_7S_8) using first-order reversal curve diagrams. *Journal of Geophysical Research: Solid Earth,* 111, B12S35, DOI: 10.1029/2006jb004715.

Robinson, D. M., Pearson, O. 2013. Was Himalayan normal faulting triggered by initiation of the Ramgarh–Munsiari thrust and development of the Lesser Himalayan duplex? *International Journal of Earth Sciences,* 102, 1773-1790, DOI: 10.1007/s00531-013-0895-3.

Robinson, D. M., Decelles, P. G., Garzione, C. N., Pearson, O. N., Harrison, T. M., Catlos, E. J. 2003. Kinematic model for the Main Central thrust in Nepal. *Geology,* 31, 359-362, DOI: 10.1130/0091-7613(2003)031<0359:KMFTMC> 2.0.CO;2.

Robinson, D. M., Decelles, P. G., Copeland, P. 2006. Tectonic evolution of the Himalayan thrust belt in western Nepal: Implications for channel flow models. *Geological Society of America Bulletin,* 118, 865-885, DOI: 10.1130/B25911.1.

Robinson, D. M. 2008. Forward modeling the kinematic sequence of the central Himalayan thrust belt, western Nepal. *Geosphere,* 4, 785-801, DOI: 10.1130/Ges00163.1.

Robinson, D. M., Khanal, S., Kohn, M. J., Mandal, S. 2014. A new model for building the Himalaya using the Greater Himalayan Thrust System. *GSA Annual Meeting*, 2014 Vancouver, BC.

Robinson, D. M., Martin, A. J. 2014. Reconstructing the Greater Indian margin: A balanced cross section in central Nepal focusing on the Lesser Himalayan duplex. *Tectonics,* 33, 2014TC003564, DOI: 10.1002/2014tc003564.

Rochette, P., Aubourg, C., Perrin, M. 1999. Is this magnetic fabric normal? A review and case studies in volcanic formations. *Tectonophysics*, 307, 219-234, DOI: 10.1016/S0040-1951(99)00127-4.

Rolfo, F., Groppo, C., Mosca, P. 2014. Petrological constraints of the 'Channel Flow' model in eastern Nepal. *In:* Mukherjee, S., Carosi, R., Van Der Beek, P. K., Mukherjee, B. K. Robinson, D. M. (eds.), *Tectonics of the Himalaya.* Geolgoical Society of London Special Publications, 412, DOI: 10.1144/sp412.4.

Rosenberg, C. L., Medvedev, S., Handy, M. 2007. Effects of melting on faulting and continental deformation. *In:* Handy, M. R., Hirth, G. Hovius, N. (eds.), *Tectonic faults, agents of change on a dynamic Earth.* MIT Press, Cambridge, Massachusetts, 95, 357-401.

Rosenberg, C. L., Stünitz, H. 2003. Deformation and recrystallization of plagioclase along a temperature gradient: an example from the Bergell tonalite. *Journal of Structural Geology,* 25, 389-408, DOI: 10.1016/S0191-8141(02)00036-6.

Rosenberg, C. L., Handy, M. R. 2005. Experimental deformation of partially melted granite revisited: implications for the continental crust. *Journal of Metamorphic Geology,* 23, 19-28, DOI: 10.1111/j.1525-1314.2005.00555.x.

Royden, L. H., Burchfiel, B. C. 1987. Thin-skinned N–S extension within the convergent Himalayan region: gravitational collapse of a Miocene topographic front. *In:* Coward, M. P., Dewey, J. F. Hancock, P. L. (eds.), *Continental Extensional Tectonics.* Geological Society of London Special Publications, 28, 611-619, DOI: 10.1144/GSL.SP.1987.028.01.40.

Rutter, E. H. 1999. On the relationship between the formation of shear zones and the form of the flow law for rocks undergoing dynamic recrystallization. *Tectonophysics,* 303, 147-158, DOI: 10.1016/S0040-1951(98)00261-3.

Rutter, E. H., Brodie, K. H., Irving, D. H. 2006. Flow of synthetic, wet, partially molten "granite" under undrained conditions: An experimental study. *Journal of Geophysical Research: Solid Earth,* 111, B06407, DOI: 10.1029/2005jb004257.

Scaillet, B., France-Lanord, C., Le Fort, P. 1990. Badrinath-Gangotri plutons (Garhwal, India): petrological and geochemical evidence for fractionation processes in a high Himalayan leucogranite. *Journal of Volcanology and Geothermal Research,* 44, 163-188, DOI: 10.1016/0377-0273(90)90017-A.

Scaillet, B., Pêcher, A., Rochette, P., Champenois, M. 1995. The Gangotri granite (Garhwal Himalaya): Laccolithic emplacement in an extending collisional belt. *Journal of Geophysical Research: Solid Earth,* 100, 585-607, DOI: 10.1029/94jb01664.

Schmid, S. M., Casey, M. 1986. Complete Fabric Analysis of Some Commonly Observed Quartz C-Axis Patterns. *Mineral and Rock Deformation: Laboratory Studies: The Paterson Volume.* American Geophysical Union, 263-286, DOI: 10.1029/GM036p0263.

Schulmann, K., Mlčoch, B., Melka, R. 1996. High-temperature microstructures and rheology of deformed granite, Erzgebirge, Bohemian Massif. *Journal of Structural Geology,* 18, 719-733, DOI: 10.1016/S0191-8141(96)80007-1.

Schulmann, K., Lexa, O., Stipska, P., Racek, M., Tajcmanova, L., Konopasek, J., Edel, J. B., Peschler, A., Lehmann, J. 2008. Vertical extrusion and horizontal channel flow of orogenic lower crust: key exhumation mechanisms in large hot orogens? *Journal of Metamorphic Geology,* 26, 273-297, DOI: 10.1111/j.1525-1314.2007.00755.x.

Schulte-Pelkum, V., Monsalve, G., Sheehan, A., Pandey, M. R., Sapkota, S., Bilham, R., Wu, F. 2005. Imaging the Indian subcontinent beneath the Himalaya. *Nature,* 435, 1222-1225, DOI: 10.1038/Nature03678.

Searle, M. 2013. Crustal melting, ductile flow, and deformation in mountain belts: Cause and effect relationships. *Lithosphere,* 5, 547-554, DOI: 10.1130/rf.l006.1.

Searle, M. P., Windley, B. F., Coward, M. P., Cooper, D. J. W., Rex, A. J., Rex, D., Tingdong, L., Xuchang, X., Jan, M. Q., Thakur, V. C., Kumar, S. 1987. The closing of Tethys and the tectonics of the Himalaya. *Geological Society of America Bulletin,* 98, 678-701, DOI: 10.1130/0016-7606(1987)98<678:tcotat>2.0.co;2.

Searle, M. P., Rex, A. J. 1989. Thermal-model for the Zanskar Himalaya. *Journal of Metamorphic Geology,* 7, 127-134, DOI: 10.1111/j.1525-1314.1989.tb00579.x.

Searle, M. P., Waters, D. J., Dransfield, M. W., Stephenson, B. J., Walker, C. B., Walker, J. D., Rex, D. C. 1999. Thermal and mechanical models for the structural and metamorphic evolution of the Zanskar High Himalaya. *In:* Macniocall, C. Ryan, P. D. (eds.), *Continental Tectonics.* Geological Society of London Special Publications 164, 139–156, DOI: 10.1144/GSL.SP.1999.164.01.08.

Searle, M. P., Godin, L. 2003. The South Tibetan Detachment and the Manaslu Leucogranite: A structural reinterpretation and restoration of the Annapurna-Manaslu Himalaya, Nepal. *Journal of Geology,* 111, 505-523, DOI: 10.1086/376763.

Searle, M. P., Simpson, R. L., Law, R. D., Parrish, R. R., Waters, D. J. 2003. The structural geometry, metamorphic and magmatic evolution of the Everest massif, High Himalaya of Nepal-South Tibet. *Journal of the Geological Society, London,* 160, 345-366, DOI: 10.1144/0016-764902-126.

Searle, M. P., Szulc, A. G. 2005. Channel flow and ductile extrusion of the high Himalayan slab - the Kangchenjunga-Darjeeling profile, Sikkim Himalaya. *Journal of Asian Earth Sciences,* 25, 173-185, DOI: 10.1016/j.jseaes.2004.03.004.

Searle, M. P., Law, R. D., Jessup, M. J. 2006. Crustal structure, restoration and evolution of the Greater Himalaya in Nepal-South Tibet: implications for channel flow and ductile extrusion of the middle crust. *In:* Law, R. D., Searle, M. P. Godin, L. (eds.), *Channel Flow, Ductile Extrusion and Exhumation in Continental Collision Zones.* Geological Society of London Special Publications, 268, 355-378, DOI: 10.1144/GSL.SP.2006.268.01.17.

Searle, M. P., Law, R. D., Godin, L., Larson, K. P., Streule, M. J., Cottle, J. M., Jessup, M. J. 2008. Defining the Himalayan Main Central Thrust in Nepal. *Journal of the Geological Society, London,* 165, 523-534, DOI: 10.1144/0016-76492007-081.

Searle, M. P. 2010. Low-angle normal faults in the compressional Himalayan orogen; Evidence from the Annapurna-Dhaulagiri Himalaya, Nepal. *Geosphere,* 6, 296-315, DOI: 10.1130/Ges00549.1.

Searle, M. P., Cottle, J. M., Streule, M. J., Waters, D. J. 2010. Crustal melt granites and migmatites along the Himalaya: melt source, segregation, transport and granite emplacement mechanisms. *Sixth Hutton Symposium on the Origin of Granites and Related Rocks: Proceedings of a Symposium.* Transactions of the

Royal Society of Edinburgh, 100, 219–233, DOI: 10.1017/S175569100901617X.

Searle, M. P., Elliott, J. R., Phillips, R. J., Chung, S. L. 2011. Crustal-lithospheric structure and continental extrusion of Tibet. *Journal of the Geological Society, London,* 168, 633-672, DOI: 10.1144/0016-76492010-139.

Shapiro, N. M., Ritzwoller, M. H., Molnar, P., Levin, V. 2004. Thinning and flow of Tibetan crust constrained by seismic anisotropy. *Science,* 305, 233-236, DOI: 10.1126/science.1098276.

Sidman, D., Ferré, E. C., Teyssier, C., Jackson, M. 2005. Magnetic fabric and microstructure of a mylonite: example from the Bitterroot shear zone, western Montana. *In:* Bruhn, D., Burlini, L. (eds.), *High-Strain Zones: Structure and Physical Properties*. Geological Society of London Special Publications, 245, 143-163, DOI: 10.1144/gsl.sp.2005.245.01.07.

Skemer, P., Katayama, I., Jiang, Z., Karato, S.-I. 2005. The misorientation index: Development of a new method for calculating the strength of lattice-preferred orientation. *Tectonophysics,* 411, 157-167, DOI: 10.1016/j.tecto.2005.08.023.

Skemer, P., Warren, J. M., Kelemen, P. B., Hirth, G. 2010. Microstructural and Rheological Evolution of a Mantle Shear Zone. *Journal of Petrology,* 51, 43-53, DOI: 10.1093/petrology/egp057.

Snoke, A. W. 1980. Transition from infrastructure to suprastructure in the northern Ruby Mountains, Nevada. *In:* Crittenden, M. D., Coney, P. J., Davis, G. H. Davis, G. H. (eds.), *Cordilleran metamorphic core complexes.*Geological Society of America Memoirs, 153, 287-334, DOI: 10.1130/MEM153-p287.

Soper, N. J., Barber, A. J. 1982. A model for the deep structure of the Moine thrust zone. *Journal of the Geological Society, London,* 139, 127-138, DOI: 10.1144/gsjgs.139.2.0127.

Sorkhabi, R. B., Stump, E. 1993. Rise of the Himalaya: a geochronologic approach. *GSA Today,* 3, 87-92.

Spencer, C. J., Harris, R. A., Dorais, M. J. 2012. The metamorphism and exhumation of the Himalayan metamorphic core, eastern Garhwal region, India. *Tectonics,* 31, TC1007, DOI: 10.1029/2010tc002853.

Srivastava, P., Mitra, G. 1994. Thrust geometries and deep structure of the outer and lesser Himalaya, Kumaon and Garhwal (India): Implications for evolution of the Himalayan fold-and-thrust belt. *Tectonics,* 13, 89-109, DOI: 10.1029/93tc01130.

St-Onge, M. R., Searle, M. P., Wodicka, N. 2006. Trans-Hudson Orogen of North America and Himalaya-Karakoram-Tibetan Orogen of Asia: Structural and thermal characteristics of the lower and upper plates. *Tectonics,* 25, TC4006, DOI: 10.1029/2005tc001907.

Stallard, A., Shelley, D. 1995. Quartz c-axes parallel to stretching directions in very low-grade metamorphic rocks. *Tectonophysics,* 249, 31-40, DOI: 10.1016/0040-1951(95)00040-T.

Stephenson, A. 1994. Distribution anisotropy: two simple models for magnetic lineation and foliation. *Physics of the Earth and Planetary Interiors,* 82, 49-53, DOI: 10.1016/0031-9201(94)90101-5.

Stipp, M., Stunitz, H., Heilbronner, R., Schmid, S. M. 2002. The eastern Tonale fault zone: a 'natural laboratory' for crystal plastic deformation of quartz over a

temperature range from 250 to 700 degrees C. *Journal of Structural Geology,* 24, 1861-1884, DOI: 10.1016/S0191-8141(02)00035-4.

Stöcklin, J. 1980. Geology of Nepal and Its Regional Frame. *Journal of the Geological Society,* 137, 1-34, DOI: 10.1144/gsjgs.137.1.0001.

Streule, M. J., Searle, M. P., Waters, D. J., Horstwood, M. S. A. 2010a. Metamorphism, melting, and channel flow in the Greater Himalayan Sequence and Makalu leucogranite: Constraints from thermobarometry, metamorphic modeling, and U-Pb geochronology. *Tectonics,* 29, TC5011, DOI: 10.1029/2009tc002533.

Streule, M. J., Strachan, R. A., Searle, M. P., Law, R. D. 2010b. Comparing Tibet-Himalayan and Caledonian crustal architecture, evolution and mountain building processes. *In:* Law, R. D., Butler, R. W. H., Holdsworth, R. E., Krabbendam, M. Strachan, R. A. (eds.), *Continental tectonics and mountain building: The legacy of Peach and Horne.* Geological Society of London Special Publications, 335, 207-232, DOI: 10.1144/SP335.10.

Stünitz, H., Fitz Gerald, J. D., Tullis, J. 2003. Dislocation generation, slip systems, and dynamic recrystallization in experimentally deformed plagioclase single crystals. *Tectonophysics,* 372, 215-233, DOI: 10.1016/S0040-1951(03)00241-5.

Styron, R. H., Taylor, M. H., Murphy, M. A. 2011. Oblique convergence, arc-parallel extension, and the role of strike-slip faulting in the High Himalaya. *Geosphere,* 7, 582-596, DOI: 10.1130/GES00606.1.

Sylvester, A. G., Christie, J. M. 1968. The origin of crossed-girdle orientations of optic axes in deformed quartzites. *The Journal of Geology,* 76, 571-580, DOI: 10.2307/30066182.

Tagami, M., Takeshita, T. 1998. C-axis fabrics and microstructures in quartz schist from the Sambagawa metamorphic belt, central Shikoku, Japan. *Journal of Structural Geology,* 20, 1549-1568, DOI: 10.1016/S0191-8141(98)00044-3.

Takeshita, T., Kocks, U. F., Wenk, H. R. 1989. Strain path dependence of texture development in aluminum. *Acta Metallurgica,* 37, 2595-2611, DOI: 10.1016/0001-6160(89)90293-9.

Tarling, D. H., Hrouda, F. 1993. *The magnetic anisotropy of rocks,* 1st ed., Chapman and Hall, London.

Tauxe, L., Mullender, T. a. T., Pick, T. 1996. Potbellies, wasp-waists, and superparamagnetism in magnetic hysteresis. *Journal of Geophysical Research: Solid Earth,* 101, 571-583, DOI: 10.1029/95jb03041.

Tauxe, L. 2002. *Paleomagnetic principles and practice,* 1st ed., Springer, Dordrecth.

Tauxe, L., Bertram, H. N., Seberino, C. 2002. Physical interpretation of hysteresis loops: Micromagnetic modeling of fine particle magnetite. *Geochemistry Geophysics Geosystems,* 3, 1-22, DOI: 10.1029/2001GC000241.

Toy, V. G., Prior, D. J., Norris, R. J. 2008. Quartz fabrics in the Alpine Fault mylonites: Influence of pre-existing preferred orientations on fabric development during progressive uplift. *Journal of Structural Geology,* 30, 602-621, DOI: 10.1016/j.jsg.2008.01.001.

Tripathy, N. R. 2009. Degree of magnetic anisotropy as a strain-intensity gauge in a saturated finite-strain zone. *Journal of the Geological Society,* 166, 9-12, DOI: 10.1144/0016-76492008-078.

Trullenque, G., Kunze, K., Heilbronner, R., Stünitz, H., Schmid, S. M. 2006. Microfabrics of calcite ultramylonites as records of coaxial and non-coaxial deformation kinematics: Examples from the Rocher de l'Yret shear zone (Western Alps). *Tectonophysics,* 424, 69-97, DOI: 10.1016/j.tecto.2006.06.004.

Tullis, J. 1977. Preferred orientation of quartz produced by slip during plane strain. *Tectonophysics,* 39, 87-102, DOI: 10.1016/0040-1951(77)90090-7.

Tullis, J., Yund, R. A. 1991. Diffusion creep in feldspar aggregates: experimental evidence. *Journal of Structural Geology,* 13, 987-1000, DOI: 10.1016/0191-8141(91)90051-J.

Turcotte, D. L., Schubert, G. 2002. *Geodynamics,* Cambridge University Press, Cambridge.

Unsworth, M. J., Jones, A. G., Wei, W., Marquis, G., Gokarn, S. G., Spratt, J. E., Team, I.-M. 2005. Crustal rheology of the Himalaya and Southern Tibet inferred from magnetotelluric data. *Nature,* 438, 78-81, DOI: 10.1038/Nature04154.

Upreti, B. N. 1999. An overview of the stratigraphy and tectonics of the Nepal Himalaya. *Journal of Asian Earth Sciences,* 17, 577-606, DOI: 10.1016/S1367-9120(99)00047-4.

Valdiya, K. S. 1980. *Geology of Kumaun Lesser Himalaya,* Wadia Institute of Himalaya, Dehra Dun, India.

Vanderhaeghe, O. 2009. Migmatites, granites and orogeny: Flow modes of partially-molten rocks and magmas associated with melt/solid segregation in orogenic belts. *Tectonophysics,* 477, 119-134, DOI: 10.1016/j.tecto.2009.06.021.

Vannay, J.-C., Steck, A. 1995. Tectonic evolution of the High Himalaya in Upper Lahul (NW Himalaya, India). *Tectonics,* 14, 253-263, DOI: 10.1029/94tc02455.

Vannay, J. C., Hodges, K. V. 1996. Tectonometamorphic evolution of the Himalayan metamorphic core between the Annapurna and Dhaulagiri, central Nepal. *Journal of Metamorphic Geology,* 14, 635-656, DOI: 10.1046/j.1525-1314.1996.00426.x.

Vannay, J. C., Grasemann, B. 2001. Himalayan inverted metamorphism and syn-convergence extension as a consequence of a general shear extrusion. *Geological Magazine,* 138, 253-276, DOI: 10.1017/S0016756801005313.

Vernon, R. H. 2004. *A practical guide to rock microstructure*, Cambridge University Press, Cambridge.

Vollmer, F. W. 1990. An application of eigenvalue methods to structural domain analysis. *Geological Society of America Bulletin,* 102, 786-791, DOI: 10.1130/0016-7606(1990)102<0786:aaoemt>2.3.co;2.

Walker, J. D., Martin, M. W., Bowring, S. A., Searle, M. P., Waters, D. J., Hodges, K. V. 1999. Metamorphism, melting, and extension: Age constraints from the High Himalayan Slab of southeast Zanskar and northwest Lahaul. *Journal of Geology,* 107, 473-495, DOI: 10.1086/314360.

Wallis, D. 2014. *Micro-geodynamics of the Karakoram Fault Zone, Ladakh, NW Himalaya [PhD thesis].* School of Earth & Environmenty, University of Leeds.

Wallis, D., Parsons, A. J., Phillips, R. J., Searle, M. P. Ferré, E. C. 2014. Comment on: "Interplay of deformation and magmatism in the Pangong Transpression Zone, Eastern Ladakh, India: Implications for remobilization of the trans-

Himalayan magmatic arc and initiation of the Karakoram Fault" by K. Sen, B. K. Mukherjee & A. S. Collins, Journal of Structural Geology, 16 (2014), 13-24. *Journal of Structural Geology,* 65, 117-119, DOI: 10.1016/j.jsg.2014.03.008.

Wallis, S. R., Kobayashi, H., Nishii, A., Mizukami, T., Seto, Y. 2011. Obliteration of olivine crystallographic preferred orientation patterns in subduction-related antigorite-bearing mantle peridotite: an example from the Higashi–Akaishi body, SW Japan. *In:* Prior, D. J., Rutter, E. H. Tatham, D. J. (eds.), *Deformation mechanisms, rheology and tectonics: Microstructures, mechanics and anisotropy.* Geological Society of London Special Publications, 360, 113-127, DOI: 10.1144/sp360.7.

Wang, J. M., Zhang, J. J., Wang, X. X. 2013. Structural kinematics, metamorphic P–T profiles and zircon geochronology across the Greater Himalayan Crystalline Complex in south-central Tibet: implication for a revised channel flow. *Journal of Metamorphic Geology,* 31, 607-628, DOI: 10.1111/jmg.12036.

Wang, J. M., Dai, J., Zhao, X., Li, Y., Graham, S. A., He, D., Ran, B., Meng, J. 2014. Outward-growth of the Tibetan Plateau during the Cenozoic: A review. *Tectonophysics*, 621, 1-48, DOI: 10.1016/j.tecto.2014.01.036.

Wasilewski, P. J. 1973. Magnetic hysteresis in natural materials. *Earth and Planetary Science Letters,* 20, 67-72, DOI: 10.1016/0012-821X(73)90140-4.

Webb, A. A. G., Yin, A., Harrison, T. M., Celerier, J., Burgess, W. P. 2007. The leading edge of the Greater Himalayan Crystalline complex revealed in the NW Indian Himalaya: Implications for the evolution of the Himalayan orogen. *Geology,* 35, 955-958, DOI: 10.1130/G23931a.1.

Webb, A. A. G., Schmitt, A. K., He, D. A., Weigand, E. L. 2011a. Structural and geochronological evidence for the leading edge of the Greater Himalayan Crystalline complex in the central Nepal Himalaya. *Earth and Planetary Science Letters,* 304, 483-495, DOI:10.1016/j.epsl.2011.02.024.

Webb, A. A. G., Yin, A., Harrison, T. M., Célérier, J., Gehrels, G. E., Manning, C. E., Grove, M. 2011b. Cenozoic tectonic history of the Himachal Himalaya (northwestern India) and its constraints on the formation mechanism of the Himalayan orogen. *Geosphere,* 7, 1013-1061, DOI: 10.1130/ges00627.1.

Webb, A. A. G., Yin, A., Dubey, C. S. 2013. U-Pb zircon geochronology of major lithologic units in the eastern Himalaya: Implications for the origin and assembly of Himalayan rocks. *Geological Society of America Bulletin,* 125, 499-522, DOI: 10.1130/b30626.1.

Weber, J. C., Ferrill, D. A., Roden-Tice, M. K. 2001. Calcite and quartz microstructural geothermometry of low-grade metasedimentary rocks, Northern Range, Trinidad. *Journal of Structural Geology,* 23, 93-112, DOI: 10.1016/S0191-8141(00)00066-3.

Wegmann, C. 1935. Zur Deutung der Migmatite. *Geologische Rundschau,* 26, 305-350.

Wei, W. B., Unsworth, M., Jones, A., Booker, J., Tan, H. D., Nelson, D., Chen, L. S., Li, S. H., Solon, K., Bedrosian, P., Jin, S., Deng, M., Ledo, J., Ray, D., Roberts, B. 2001. Detection of widespread fluids in the Tibetan crust by magnetotelluric studies. *Science,* 292, 716-718, DOI: 10.1126/science.1010580.

Wenk, H. R., Shore, J. 1975. Preferred orientation in experimentally deformed dolomite. *Contributions to Mineralogy and Petrology,* 50, 115-126, DOI: 10.1007/bf00373331.

Wenk, H. R., Kern, H., Van Houtte, P., Wagner, F. 1986. Heterogeneous Strain in Axial Deformation of Limestone, Textural Evidence. *Mineral and Rock Deformation: Laboratory Studies: The Paterson Volume.* American Geophysical Union, 287-295, DOI: 10.1029/GM036p0287.

Wenk, H. R., Takeshita, T., Bechler, E., Erskine, B. G., Matthies, S. 1987. Pure shear and simple shear calcite textures. Comparison of experimental, theoretical and natural data. *Journal of Structural Geology,* 9, 731-745, DOI: 10.1016/0191-8141(87)90156-8.

Wenk, H. R., Christie, J. M. 1991. Comments on the interpretation of deformation textures in rocks. *Journal of Structural Geology,* 13, 1091-1110, DOI: 10.1016/0191-8141(91)90071-P.

Whipp, D. M., Beaumont, C., Braun, J. 2014. Feeding the “aneurysm”: Orogen-parallel mass transport into Nanga Parbat and the western Himalayan syntaxis. *Journal of Geophysical Research: Solid Earth*, 119, 5077–5096, DOI: 10.1002/2013jb010929.

Whipple, K. X., Meade, B. J. 2004. Controls on the strength of coupling among climate, erosion, and deformation in two-sided, frictional orogenic wedges at steady state. *Journal of Geophysical Research: Earth Surface,* 109, F01011, DOI: 10.1029/2003jf000019.

White, N. M., Pringle, M., Garzanti, E., Bickle, M., Najman, Y., Chapman, H., Friend, P. 2002. Constraints on the exhumation and erosion of the High Himalayan Slab, NW India, from foreland basin deposits. *Earth and Planetary Science Letters,* 195, 29-44, DOI: 10.1016/S0012-821X(01)00565-9.

White, R. W., Powell, R., Holland, T. J. B. 2001. Calculation of partial melting equilibria in the system Na2O–CaO–K2O–FeO–MgO–Al2O3–SiO2–H2O (NCKFMASH). *Journal of Metamorphic Geology,* 19, 139-153, DOI: 10.1046/j.0263-4929.2000.00303.x.

Willett, S., Beaumont, C., Fullsack, P. 1993. Mechanical model for the tectonics of doubly vergent compressional orogens. *Geology,* 21, 371-374, DOI: 10.1130/0091-7613(1993)021<0371:MMFTTO>2.3.CO;2.

Williams, P. F., Jiang, D., Lin, S. 2006. Interpretation of deformation fabrics of infrastructure zone rocks in the context of channel flow and other tectonic models. *In:* Law, R. D., Searle, M. P. Godin, L. (eds.), *Channel flow, ductile extrusion and exhumation in continental collision zones.* Geological Society of London Special Publications, 268, 221-235, DOI: 10.1144/gsl.sp.2006.268.01.10.

Wilson, C. J. L. 1984. Shear bands, crenulations and differentiated layering in ice-mica models. *Journal of Structural Geology,* 6, 303-319, DOI: 10.1016/0191-8141(84)90054-3.

Wobus, C. W., Hodges, K. V., Whipple, K. X. 2003. Has focused denudation sustained active thrusting at the Himalayan topographic front? *Geology,* 31, 861-864, DOI: 10.1130/G19730.1.

Woodcock, N. H. 1977. Specification of fabric shapes using an eigenvalue method. *Geological Society of America Bulletin,* 88, 1231-1236, DOI: 10.1130/0016-7606(1977)88<1231:sofsua>2.0.co;2.

Woodcock, N. H., Naylor, M. A. 1983. Randomness testing in three-dimensional orientation data. *Journal of Structural Geology,* 5, 539-548, DOI: 10.1016/0191-8141(83)90058-5.

Xu, Z., Wang, Q., Pêcher, A., Liang, F., Qi, X., Cai, Z., Li, H., Zeng, L., Cao, H. 2013. Orogen-parallel ductile extension and extrusion of the Greater Himalaya in the late Oligocene and Miocene. *Tectonics,* 32, 191-215, DOI: 10.1002/tect.20021.

Xypolias, P., Kokkalas, S. 2006. Heterogeneous ductile deformation along a mid-crustal extruding shear zone: an example from the External Hellenides (Greece). *In:* Law, R. D., Searle, M. P. Godin, L. (eds.), *Channel flow, ductile extrusion and exhumation in continental collision zones.* Geological Society of London Special Publications, 268, 497-516, DOI: 10.1144/gsl.sp.2006.268.01.23.

Yakymchuk, C., Godin, L. 2012. Coupled role of deformation and metamorphism in the construction of inverted metamorphic sequences: an example from far-northwest Nepal. *Journal of Metamorphic Geology,* 30, 513-535, DOI: 10.1111/j.1525-1314.2012.00979.x.

Yan, D.-P., Zhoub, M.-F., Robinsonb, P. T., Grujic, D., Malpas, J., Kennedy, A., Reynoldsc, P. H. 2011. Constraining the mid-crustal channel flow beneath the Tibetan Plateau: data from the Nielaxiongbo gneiss dome, SE Tibet. *International Geology Review,* 54, 1-18, DOI: 10.1080/00206814.2010.548153.

Yang, Y., Ritzwoller, M. H., Zheng, Y., Shen, W., Levshin, A. L., Xie, Z. 2012. A synoptic view of the distribution and connectivity of the mid-crustal low velocity zone beneath Tibet. *Journal of Geophyical Research,* 117, B04303, DOI: 10.1029/2011jb008810.

Yin, A., Harrison, T. M., Murphy, M. A., Grove, M., Nie, S., Ryerson, F. J., Feng, W. X., Le, C. Z. 1999. Tertiary deformation history of southeastern and southwestern Tibet during the Indo-Asian collision. *Geological Society of America Bulletin,* 111, 1644-1664, DOI: 10.1130/0016-7606(1999)111<1644:TDHOSA>2.3.CO;2.

Yin, A. 2006. Cenozoic tectonic evolution of the Himalayan orogen as constrained by along-strike variation of structural geometry, exhumation history, and foreland sedimentation. *Earth-Science Reviews,* 79, 163-164, DOI: 10.1016/j.earscirev.2006.08.005.

Zeitler, P. K., Chamberlain, C. P.,Smith, H. A. 1993. Synchronous Anatexis, Metamorphism, and Rapid Denudation at Nanga-Parbat (Pakistan Himalaya). *Geology,* 21, 347-350, DOI: 10.1130/0091-7613(1993)021<0347:SAMARD> 2.3.CO;2.

Zhang, H., Harris, N., Parrish, R., Kelley, S., Zhang, L., Rogers, N., Argles, T., King, J. 2004. Causes and consequences of protracted melting of the mid-crust exposed in the North Himalayan antiform. *Earth and Planetary Science Letters,* 228, 195-212, DOI: 10.1016/j.epsl.2004.09.031.

Zhang, Z. J., Klemperer, S. 2010. Crustal structure of the Tethyan Himalaya, southern Tibet: new constraints from old wide-angle seismic data. *Geophysical Journal International,* 181, 1247-1260, DOI: 10.1111/j.1365-246X.2010.04578.x.

Zwart, H. J. 1979. The geology of the Central Pyrenees. *Leidse Geologische Mededelingen,* 50, 1 – 74.